# Clean Coal Program Research Activities

## Final Report

*Institute for Clean and Secure Energy*
*380 INSCC*
*University of Utah*
*Salt Lake City, UT 84112*

Reporting Period: 07/01/2006 - 05/31/2009

Authors:
Larry L. Baxter, Brigham Young University
Eric G. Eddings, University of Utah
Thomas H. Fletcher, Brigham Young University
Kerry E. Kelly, University of Utah
JoAnn S. Lighty, University of Utah
Ronald J. Pugmire (coPI), University of Utah
Adel F. Sarofim (coPI), University of Utah
Geoffrey D. Silcox, University of Utah
Philip J. Smith, University of Utah
Jeremy N. Thornock, University of Utah
Jost O.L. Wendt, University of Utah
Kevin J. Whitty, University of Utah

*Issue Date: May 2010*

DOE Cooperative Agreement DE-FC26-06NT42808

INSTITUTE FOR *Clean and Secure Energy*
THE UNIVERSITY OF UTAH

## DISCLAIMER

## Abstract

Although remarkable progress has been made in developing technologies for the clean and efficient utilization of coal, the biggest challenge in the utilization of coal is still the protection of the environment. Specifically, electric utilities face increasingly stringent restriction on the emissions of $NO_x$ and $SO_x$, new mercury emission standards, and mounting pressure for the mitigation of $CO_2$ emissions, an environmental challenge that is greater than any they have previously faced. The Utah Clean Coal Program addressed issues related to innovations for existing power plants including retrofit technologies for carbon capture and sequestration (CCS) or green field plants with CCS.

The Program focused on the following areas: simulation, mercury control, oxycoal combustion, gasification, sequestration, chemical looping combustion, materials investigations and student research experiences. The goal of this program was to begin to integrate the experimental and simulation activities and to partner with NETL researchers to integrate the Program's results with those at NETL, using simulation as the vehicle for integration and innovation. The investigators also committed to training students in coal utilization technology tuned to the environmental constraints that we face in the future; to this end the Program supported approximately 12 graduate students toward the completion of their graduate degree in addition to numerous undergraduate students. With the increased importance of coal for energy independence, training of graduate and undergraduate students in the development of new technologies is critical.

# Table of Contents

# Executive Summary

The Utah Clean Coal Program's ($UC^3$) mission was the generation of scientific and technical information to allow for the clean and efficient utilization of coal in a carbon-constrained world. It was organized to support the Department of Energy's (DOE's) goals and focused on the following eight thrust areas:

*Simulation*. $UC^3$ investigators enhanced the capability of the ARCHES large-eddy simulation (LES) entrained-flow code by coupling it with the direct quadrature method of moments (DQMOM) to produce a tool for realistic time- and space-dependent simulations of coal-laden, reaction systems in the near-burner region. They demonstrated stand-alone one-dimensional turbulence (ODT) calculations of planar jets, with and without, particles. They are also developed validation hierarchies for the oxycoal burner and the entrained-flow gasifier and performed a benchmark demonstration of the LES tool with coal particles.

*Mercury control.* The Mercury Team developed mercury oxidation and adsorption data from experiments and fixed-bed and single-particle modeling. The fixed-bed model incorporates Langmuir adsorption kinetics and accounts for competitive adsorption between mercury, $SO_2$, and $NO_2$. The single-particle model simulates in-flight capture of elemental mercury as a function of Langmuir and Freundlich adsorption kinetics, sorbent feed rate, and intraparticle diffusion. At the conditions examined, the capture of elemental mercury by single particles is highly sensitive to particle diameter, and accurate predictions of capture required the use of a particle-size distribution. The fixed-bed experimental experiments showed that at 150°C and in the absence of HCl or HBr, the efficiency of mercury capture was about 20%. The addition of 50 ppm HCl caused complete capture of all elemental and oxidized mercury species. In the absence of halogens, $SO_2$ increased the mercury adsorption efficiency to 30%. The efficiency of adsorption decreased with increasing $SO_2$ concentration when halogens were present. Increasing the HCl concentration to 100 ppm lessened the effect of the $SO_2$.

*Oxycoal combustion*. The Oxycoal Team explored the effects of variations in $O_2$ partial pressure and $CO_2$ concentration on coal jet ignition. They constructed a 100 kW pilot-scale oxy-fired furnace with a coaxial zero swirl burner and optical ports, collected thousands of images of flames at a variety of conditions, and developed automated image-processing methods to determine stand-off distance. The results indicate that primary $PO_2$ has a dominant effect on flame stability and axial coal jet ignition and secondary preheat temperature plays a critical role in coal ignition. In addition to the oxy-fired furnace, a pilot-scale fluidized bed (CFB) was used to examine cold- and hot-flow conditions in addition to cold-flow validation techniques for minimum fluidization tests. Cold-flow studies resulted in determining minimum fluidization velocities that were within 35% of the theoretical value. Also, hot-flow tests revealed vital information concerning CFB operation, which will be beneficial for future testing.

*Gasification*. The Gasification Team developed and enhanced experimental capabilities including modifying a pressurized flat-flame burner to study carbon conversion, modifying the University of Utah's entrained-flow gasifier so that it could process coal, and developing a high-temperature entrained-flow reactor to study char properties at high conversion where char collapses into molten slag. The goal of these facilities was to provide data that will address two problems encountered in entrained-flow gasifiers, those of the shorter than desired lifetimes of the refractory linings and the lower efficiencies of carbon conversion. In addition, in conjunction with the Simulation Team a validation hierarchy and preliminary computational modeling tools were developed to simulate entrained-flow gasifiers.

*Sequestration.* The Sequestration Team studied the impact of contaminant gases, such as $SO_2$, on sequestration chemistry and vertical mixing of $CO_2$ and brine in their newly constructed high-temperature, high pressure experimental assembly and in simulation studies. Their experimental results revealed changes in rock chemistry that mirrored those in the brine chemistry, and when $SO_2$ was added

to the experiments the dissolution patterns changed with precipitation of anhydrite, gypsum and bassinite. They also developed an experimental assembly to study the effect of $SO_2$ on injectivity. The simulations studies found that the distribution of $CO_2$ depends of the absolute permeabilities of the seals and the relative permeabilities.

*Combustion chemical looping (CLC).* The CLC Team investigated Ni/NiO and Cu/$Cu_2O$/CuO systems to provide mechanistic understanding and chemical reaction rates for oxygen carriers in CLC. The oxidation reactions of the Ni and Cu metals were studied by thermogravimetric analysis (TGA) and by temperature programmed oxidation (TPO). The NiO produced in the oxidation reaction was found to be stable, but the CuO produced in the oxidation reactions was not stable at elevated temperatures. It spontaneously decomposed under $N_2$ atmosphere. The Cu/$Cu_2O$/CuO material performed very well as an oxygen carrier in the simulated CLC for up to 200 cycles.

*Materials investigations*. This task supported the Oxycoal combustion and Gasification areas via the development of materials expertise for fuel-conversion systems with an emphasis on (ultra)super critical steam generation systems. The investigators established interactions with the Albany and Pittsburgh offices of NETL to study materials issues and developed material interaction models that compliment the ash sintering and melting models developed under the Gasification Tasks.

*NETL student research experience*. These research experiences offered one University of Utah and one Brigham Young undergraduate student the opportunity to work with NETL researchers to develop measurements for CFBs.

# Objectives

The $UC^3$ mission was the generation of scientific and technical information to allow for the clean and efficient utilization of coal in a carbon-constrained world. Building on the existing core-competencies developed over a long history of basic and applied research in coal science and combustion processes, the $UC^3$ objectives were to support DOE's goals in the following eight thrust areas:

- Simulation – developing a new generation of LES-based, entrained-flow computational fluid dynamic (CFD) models and developing a validation and verification environment that integrates experimental results and submodels developed in the thrust areas.

- Mercury control – providing mechanistic understanding and kinetic rates for sorbents of interest to DOE and integrating these submodels into NETL's models of sorbent injection.

- Oxycoal combustion – exploring effects of variations in the partial pressure of $O_2$ and $CO_2$ on coal jet ignition in retrofit oxycoal combustion applications and providing fundamental rate parameters and sub-scale model validation for CFBs.

- Gasification – providing data that will address two problems encountered in entrained-flow gasifiers, those of the shorter than desired lifetimes of the refractory linings and the lower efficiencies of carbon conversion.

- Sequestration – studying the impact of contaminant gases on sequestration chemistry and vertical mixing of $CO_2$ and brine.

- Combustion chemical looping – providing a mechanistic understanding and chemical reaction rates for oxygen carriers of interest to the DOE.

- Materials investigations – supporting the Oxycoal combustion and Gasification thrust areas via the development of materials expertise for fuel-conversion systems with an emphasis on (ultra)super critical steam generation systems.

- NETL student research experience - offering select University of Utah graduate and undergraduate research opportunities at NETL.

# Approach and Results by Task

## Task 1.0 – Identification of an Appropriate LES Algorithm and Suitable Framework for the Computations

Under this task, the LES simulation capability (ARCHES) (Spinti et al. 2008) at the University of Utah was coupled with DQMOM (Fox 2003) to produce a unique tool for realistic time- and space-dependent simulations of coal-laden, reacting systems in the near-burner region.

### *Approach*

*Large-Eddy Simulation.* The LES modeling approach involves an application of a filter to the governing equations of mass, momentum, and energy balance. The filter effectively separates resolved and unresolved scales for the cardinal variables. Resolved scales are directly represented on the computational mesh while the unresolved scales are modeled. The major advantage to LES is that it captures a relatively large range of spatial and temporal scales (ideally 80% of the entire energy) of the flow. This makes LES an ideal approach for modeling systems such as the near-burner region of a coal burner where a large range of scales exist and where unsteady phenomena play an important role in the physical processes.

### *Algorithm Selection*

In this work, an existing LES code, ARCHES, was used that solves the balances of mass, momentum and energy using explicit time-stepping methods. The code has been verified and validated for many different gas combustion applications. The numerical algorithms include second-order spatial and temporal discretization schemes. The code is parallelized using the Uintah computational framework (www.uintah.utah.edu) and has been demonstrated to run efficiently on up to two thousand processors.

*Direct Quadrature Method of Moments.* DQMOM solves for statistical moments of the particle number density function (NDF) on the computational mesh. The NDF is the full statistical description of the particle phase and contains all information regarding the particle phase. DQMOM is one specific approach of moment methods. In general, tracking moments creates a closure problem. That is, source terms in the transport equation for each moment depend on other, higher-order moments, requiring the solution to high-order moments. In some cases, an infinite set of moments would be required to completely close the set of equations. This problem is overcome by the use of numerical quadrature. Numerical quadrature provides a way to numerically integrate unknown or complex functions by evaluating them at a set of independent variable values called abscissas and their respective weights. The value of the integral is then evaluated by summing the set of weighted abscissas. In DQMOM, the weights and weighted abscissas are tracked directly on the computational mesh and moments of the NDF are reconstructed from the numerical quadrature.

A major advantage to DQMOM is that it allows for tracking NDFs that are functions of multiple variables (i.e., particle size, temperature, coal mass fraction). The set of variables parameterizing the distribution in coal particle distributions includes composition, energy, and momentum. Thus, DQMOM has the ability to track a multivariate particle distribution, allowing for easy incorporation of particle physics into the overall method.

*Coal Particle Abstraction.* Following Smoot and Smith (1985) we characterize the coal particle as composed of four components:

1. Raw Coal
2. Char

3. Moisture
4. Ash (mineral matter)

Using α to represent mass fraction and r to represent a reaction rate, the coal particle is illustrated along with the important reaction processes in Figure 1. In this figure, we have used j to represent that the reaction rates and mass fractions are associated with a $j^{th}$ particle. Note that the reaction rates can actually represent a distribution of rates. For example, $r_{vj}$ can represent a series of parallel devolatilization rates for a specific coal type.

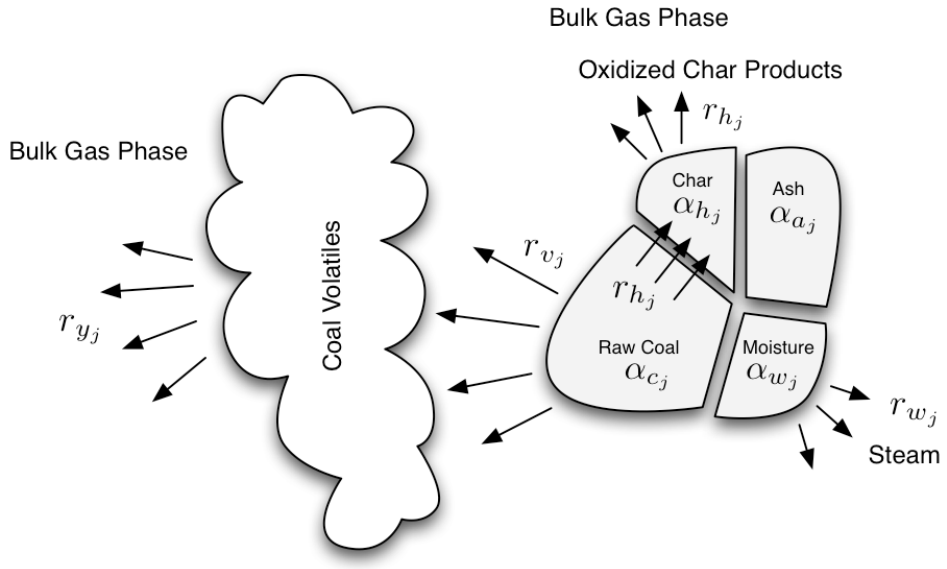


**Figure 1.** Description of a reacting coal particle with the coal components highlighted along with the important coal reactions.

Using Figure 1 as a starting point, transport of the particle phase in LES was derived using a moment description. In other words, four parameters were chosen to represent the coal particle NDF. These parameters include:

- L, a characteristic length scale of the particle
- U, a particle velocity vector
- c, a raw coal mass fraction of a particle
- h, a particle enthalpy

Using these sets of internal coordinates, a full moment description for the particle phase was derived and the DQMOM approach was used to solve the set of resulting equations.

*Length/Time Scale Analysis of the Coal Particle*. When coupling LES with the particle-phase representation, the issue of resolution must be considered. In LES, a filtering operation is applied (with a filter width of size Δ) to the cardinal variables that filter out smaller scales with wave numbers higher than the Nyquist limit. This creates the notion of "resolved" velocities that are those velocities solved for on the LES computational mesh and "unresolved" velocities that exist at the subgrid level, which are accounted for by a turbulence model. Particles, in general, may be affected by all velocities at all scales. In our proposed coal model, we must consider if the subgrid scale affects the particles, thus requiring representation in the number distribution. The following arguments are proposed for determining when subgrid effects of momentum and reaction must be considered for the particle phase.

Using the definitions of Damkohler (Da, indication of chemical reaction scales relative to the scalar mixing scales) and Schmidt number (Sc, indication of the molecular to scalar diffusion), relationships were derived to show the minimum required filter width that would be required when considering scalar mixing and reaction. In this case, two relationships were found:

*Case 1: Sc > 1*

$$Da \sim Sc^{-1}\left(\frac{\eta}{\Delta}\right)^2, \quad (1)$$

*Case 2: Sc < 1*

$$Da \sim Sc^{-\frac{3}{2}}\left(\frac{\eta}{\Delta}\right)^2, \quad (2)$$

where η is the fluid Kolmogorov scale. These arguments help in establishing a minimum grid resolution for resolution of the mixing and reaction scales directly on the mesh.

Using the definitions of the Stokes number (St, indication of the particle time scale to the fluid time scale) and particle relaxation time, relationships where derived to show a minimum required filter width needed to resolve the significant particle motions,

*Case 1:* $\tau_c < \tau_e$

$$St \sim \frac{\tau_p \bar{u}_p}{\Delta} \sim \frac{\tau_p^2 g}{\Delta}, \quad (3)$$

*Case 2*: $\tau_c > \tau_e$

$$St \sim \frac{\tau_p \nu}{\Delta^2}. \quad (4)$$

where $\tau_c$ is the eddy cross over time and $\tau_e$ is the eddy lifetime. These arguments help to establish a minimum filter width required to resolve the significant particle motions.

**Task 2.0 – Verification of the LES Code**

***Approach***

The term verification refers to the mathematical accuracy of the computer code and not the physical accuracy of the results. Typically, there are two verification activities; code verification and solution verification. Code verification activities are software quality assurance activities. In other words, code verification should ensure that computer "bugs" are not present in the code that could affect the quantity of interest in the computed output. In solution verification, one attempts to verify that the discretized equations and numerical algorithm behave mathematically as one would expect (i.e., an expected numerical convergence). Both code and solution verification activities do not cease unless, perhaps, development on the code is abandoned as the introduction of new code requires that verification be repeated to ensure reliability. Since the LES code is continuously being updated and changed to suit the current project, we present here the verification techniques that are used to ensure that verification activities are sufficient and that the LES verification milestone is complete.

Code verification activities include nightly, automated regression testing on the LES code using a set of predetermined cases. Results from the nightly regression test are compared to a set of gold-standard results. Any deviation of the results to within machine precision of the gold standard results in a failure of the regression test. Automated emails are set out after the completion of the regression test to notify developers of the regression status.

Two solution verification activities used here include the method of manufactured solutions (MMS) and grid convergence error estimators. In MMS, a solution to the cardinal variables is proposed upfront. For example, the velocities (in two-dimensions) could be determined with the following expression,

$$u(\mathbf{x},t) = sin(2\pi x/L_x)e^{-\lambda t} \qquad (5)$$
$$v(\mathbf{y},t) = cos(2\pi y/L_y)e^{-\lambda t}.$$

These expressions for the velocity components are then passed through the governing equation. Any remainder terms are added as source terms to the governing equations. For example, consider the simplified governing equation in one-dimension,

$$\frac{\partial u}{\partial t} + \frac{\partial u}{\partial x} = 0. \qquad (6)$$

Using the expression for velocity from Equation 1, one can determine that the MMS source term is

$$S_{mms} = \frac{2\pi}{L_x} cos(2\pi x/L_x) - \lambda sin(2\pi x/L_x)e^{-\lambda t} \qquad (7)$$
.

When performing the actual verification test for this simplified example, one initializes *u* according to Equation 5 and then solves the transport equation with the extra source term added (Equation 7). With MMS, one may compare the solution to the exact solution at any time or spatial location.

While comparing to the MMS solution on a single grid is useful, is it perhaps more useful to check the order of numerical convergence. That is, if a governing equation is approximated with a discretization scheme, the leading order error term in the discretization scheme is usually known *a priori*. If error is checked on a series of successively refined grids, the convergence of the error in the asymptotic regime should reduce by order *p* where *p* is the order of the discretization scheme.

MMS offers a method for verification for arbitrarily chosen functions of the cardinal variables. The functions can be as simple or as complex as one desires. Particularly useful is the ability to choose functions of the cardinal variables that exercise all terms in the governing equation, unlike using analytical solutions to the Navier Stokes equations which must remove terms to get a solution. MMS is also useful in that specific terms in the governing equation can be singled out and verified. This is useful when the order discretization scheme is not common among all terms in the equation. Thus, convergence of terms can be checked individually to ensure consistency.

MMS becomes less useful when one is interested in knowing the verification error associated with the intended application (i.e., a coal burner) because the MMS functions are typically not representative of

the flow field of interest[1]. It is possible that for the intended application, some error modes may become important as the components/models are combined into one multi-physics code to generate a result for the intended application. In order to assess the verification error for the intended application, we have used the methods suggested by Logan and Nitta (2005). These methods use Richardson extrapolation techniques to determine the order of convergence of the solution, coupled with a notion of a factor of safety (to account for regions of non-monotonic convergence) and confidence intervals. These methods provide quantification of error, in the form of an error bar with a given confidence, for a given mesh resolution. Details of the approach can be found in Logan and Nitta.

***Highlighted Results***

Verification studies were performed to test both the molecular viscous diffusion process and the stochastic eddy events process. The tests were performed by simulating a planar jet with an inlet velocity of 20 m/s and a co-velocity of 2m/s. Two different initial density profiles were used to study the effects of density on convergence of the model. One condition used a constant density profile while the other used a random initial density profile:

$$\rho=0.1*1.29+0.9*1.29*(\textit{Rand Num}) \quad (8)$$

Note that this density profile allows for one order magnitude variation in the velocity.

*Spatial Integration.* Three types of integrators were tested to determine the stability of the spatial integration scheme. These integrators were a first-order forward Euler approach, a second-order Crank-Nicolson approach, and a fourth-order Runge-Kutta approach. The Crank-Nicolson approach offered reasonable stability with lower cost than the Runge-Kutta approach. The forward Euler approach offered a relatively strict restriction on the spatial step of the integrator.

*Conservation.* Verification tests were performed to ensure that conservation of mass, momentum and kinetic energy were maintained through a triplet map. Various initial conditions in cell size and density profiles were tested. All tests showed that the conserved variables were indeed maintained since the difference of their initial and final values were (machine) zero.

*Model parameter calibration.* Calibration tests were accomplished by changing crucial modeling parameters and then observing the results of the different runs. The effects of the main parameters of C, α and Z on the flow field were as follows.

- The possibility of an eddy occurrence was proportional to C. It was observed that the decay of the axial velocity will increase with increasing C.
- When α increased, there was a stronger kinetic energy exchange among three velocity components resulting in a significant change of the Reynolds stress profile.
- A larger Z resulted in the suspension of eddies during the eddy trial events.

Using experimental data (Bradbury and Riley, 1969) in coordination with the previous observations, the final parameters were determined to be: C=2.3, α=1/6 and Z=15 for the planar jet case.

[1] Although some researchers have tried to find functions that are representative of the intended application. Of particular note is a variation on MMS called the method of generated solutions (MGS) where the computed solution of the intended application is fit with a series of splines, generating mathematical expressions for inserting into the governing equation. This process has been explored by Kris Sokorski (Department of CS, University of Utah) and the Simulation team but is not being used in the current project.

**Task 3.0 – Development of Stand-Alone, Multiphase ODT Submodel with Appropriate Manifold Parameters**

***Subtask 3.1 – Identification of the ODT Algorithm***

ODT, an outgrowth of the linear eddy mixing (LEM) modeling strategy (Kerstein et al. 2001), models the effect of mixing by turbulent stirring separately from molecular diffusion and reaction on a highly resolved one-dimensional line of sight through the computational domain. In ODT, turbulent eddies are represented using a stochastic process, called the triplet map, which captures the range of length scales in the turbulent flow along the line of sight. Diffusion scales are directly represented using a Newtonian diffusion processes. Although the low-dimensional nature of the ODT model limits its application to full scale systems, it proves to be a valuable tool to understand subgrid turbulent mixing and coal combustion chemistry because of its low computational cost coupled with high resolution in one-dimension.

In this work, a Lagrangian particle tracking method was coupled with a spatially developing ODT model to allow for modeling of reacting coal systems.

***Subtask 3.2 – Verification and Validation of the ODT Code***

The Simulation Team performed verification of the ODT code and demonstrations of planar jets, with and without particles. Using the results from a reacting coal jet from a series of ODT simulations, data were extracted showing possible manifolds for reducing the dimensionality of the chemistry for the LES calculation.

*Planar Jets and Plumes*. The ODT model requires a series of constants to be calibrated for the triplet map kernels. In order to determine appropriate values of the constants and to verify correct physical behavior of the code, a number of planar jets and plumes were simulated. Examples of the results are shown in Figure 2. Along with the contour plot of velocity, the u-velocity component for each case is plotted against values of u-velocity obtained from similarity theory (Bradbury et a. 1967). One observes that the ODT simulation is capturing the correct trend for jets and plumes.

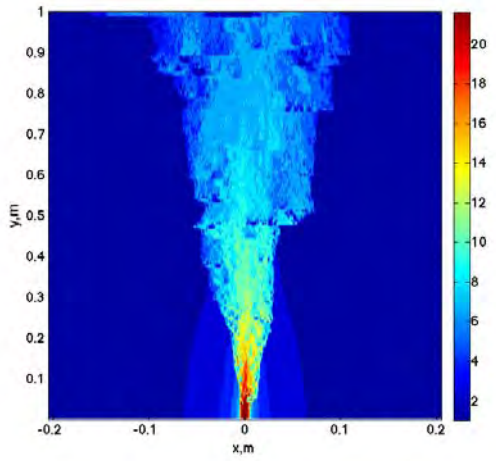


(a)

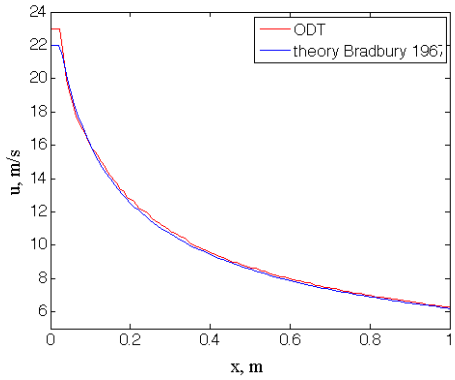


(b)

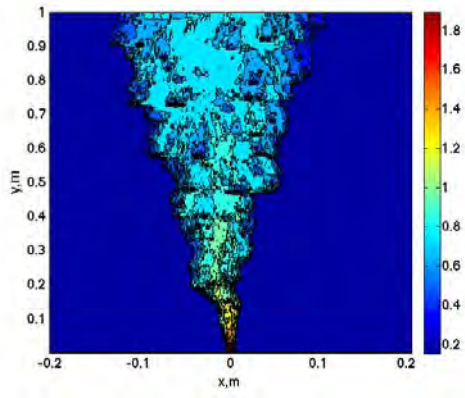


(c)

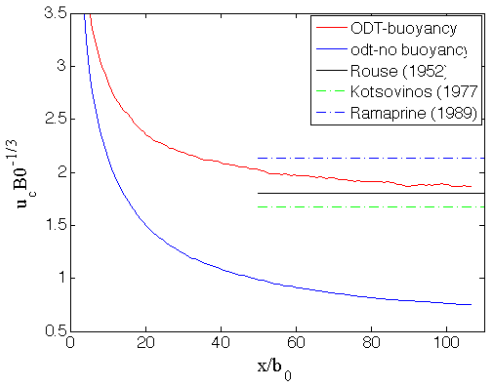


(d)

**Figure 2.** Verification and calibration plots of ODT jet simulations (a-b) and ODT buoyant plume simulations (c-d).

*Particle Dispersion in Jets Using ODT.* A Lagrangian particle tracking method was combined with the ODT code to simulate particle dispersion in a turbulent jet. Important issues were addressed, including determining a time integration strategy that handled the ODT modeling approximation that creates two separate timescales of the particle motion and eddy events. Particle motion for three differently sized particles is show by their path lines in Figure 3. The simulation is an inert, particle-laden jet. Particles are introduced into the center of the jet with three particle sizes; 10 μm, 70 μm, and 130 μm. Triplet mapping

(representing turbulent eddies) of the fluid causes instantaneous lateral displacement of the particles. Note that small particles are greatly affected by the turbulent eddies while large particles are less affected.

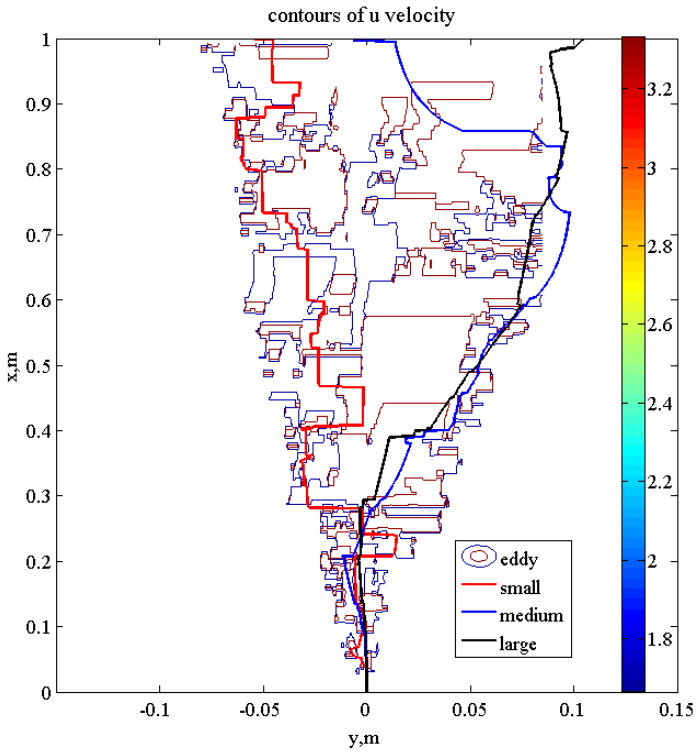


**Figure 3.** Path lines of three particle sizes in a turbulent jet.

Size effects are noticeable when viewing the contours of particle mass flux for each particle size as shown in Figure 4. Small particles are quickly dispersed by the turbulent eddies while larger particles are showing a tendency to cluster near the edges of the jet.

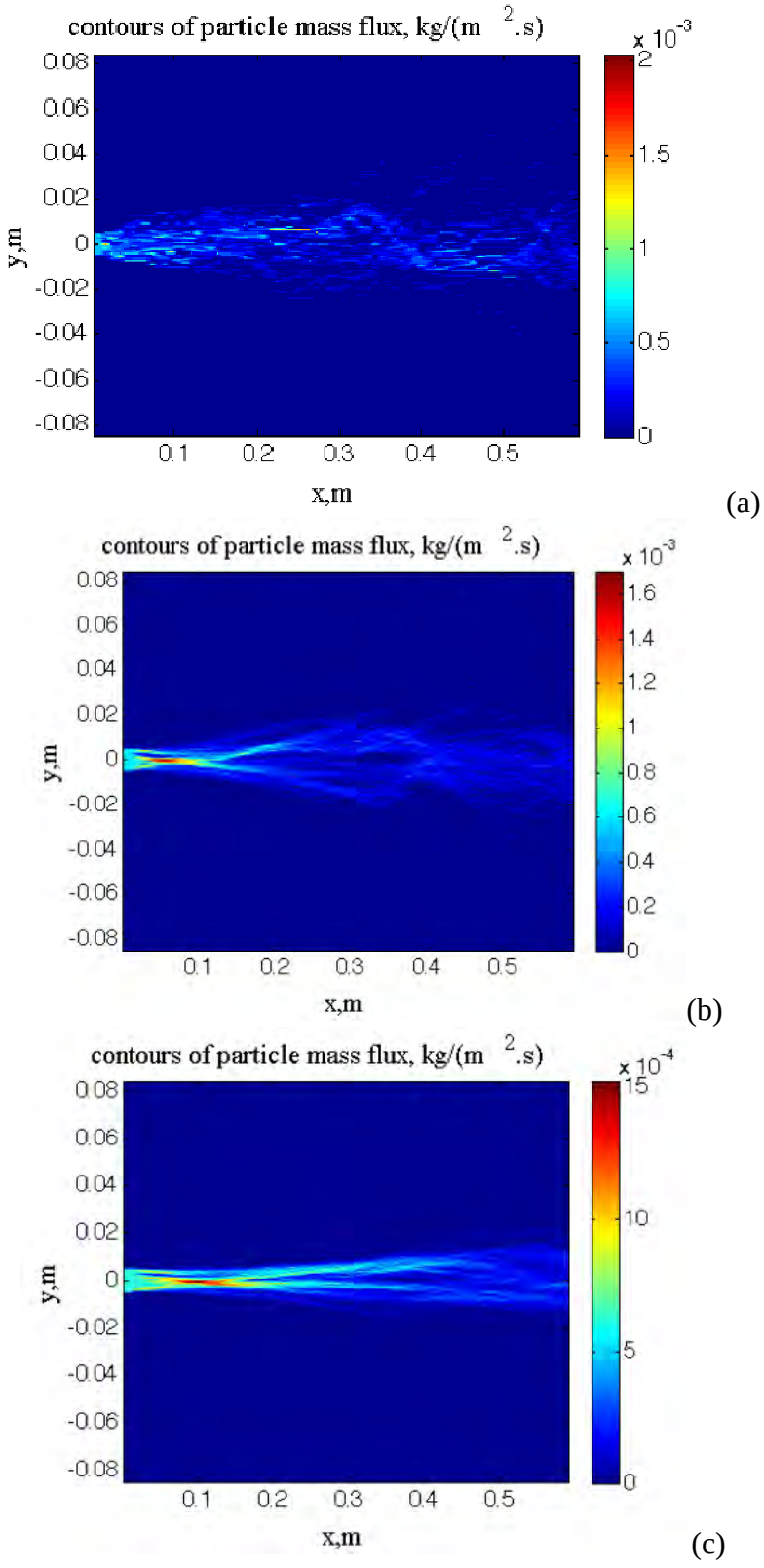


**Figure 4.** Mass flux of particles for (a) small (b) medium and (c) large particle sizes.

*Oxycoal Simulations with ODT*. The ODT model was used to simulate an oxycoal combustor. The operating conditions and the geometry of the test bed developed by Utah are found in (Zhang et al. 2007). This simulation focused on the near-burner region. Because ODT is, by definition, resolving the flow only in one dimension, the near-burner region was represented with a double-planar channel nozzle. The oxidizer in the primary channel was composed of 20.6% $O_2$ and 79.4% $CO_2$, and the oxidizer in the secondary channel was composed of 44.5% $O_2$ and 55.5% $CO_2$. The initial temperature and species composition of gas mixture in the co-flow region were estimated from a Fluent® simulation.

The coal particle phase was represented using 1800 Lagrangian particles. The particle phase was divided into three groups according to the size of the particles. Small particles had a diameter of 10μm, medium particles had a diameter of 65μm, and large particles had a diameter of 130μm. A top-hat distribution of the number density was assumed. Multiple realizations of the flow field were obtained, and the average flow field was computed by averaging 200 realizations.

Figure 5 shows the real flame from the experiment, temperature contours obtained from an ODT simulation, and a profile of the instantaneous eddy profile. The eddy profile showed the highest concentration of eddies at the edge of the flame. Also, the larger eddies predicted by the ODT model coincided with the large axial velocity and temperature gradients.

The gas-particle coupling is illustrated in Figure 6. In this figure, dashed lines show the instant velocity profiles, and solid lines show the instant particle velocities. Small particles tended to follow the flow field very closely while larger particles deviated. The largest particle size showed a remarkably smooth velocity compared to the chaotic fluid velocities. Figure 7 illustrates the same trend, but in the particle temperature field.

Figure 8 shows the averaged flow fields from the ODT realizations. The averaged flow fields clearly show the fast devolatilization of the raw coal near the burner and then the slower char combustion processes further down stream. These results are qualitatively correct. However, more validation work is needed, including obtaining the necessary data to quantitatively validate these and future results.

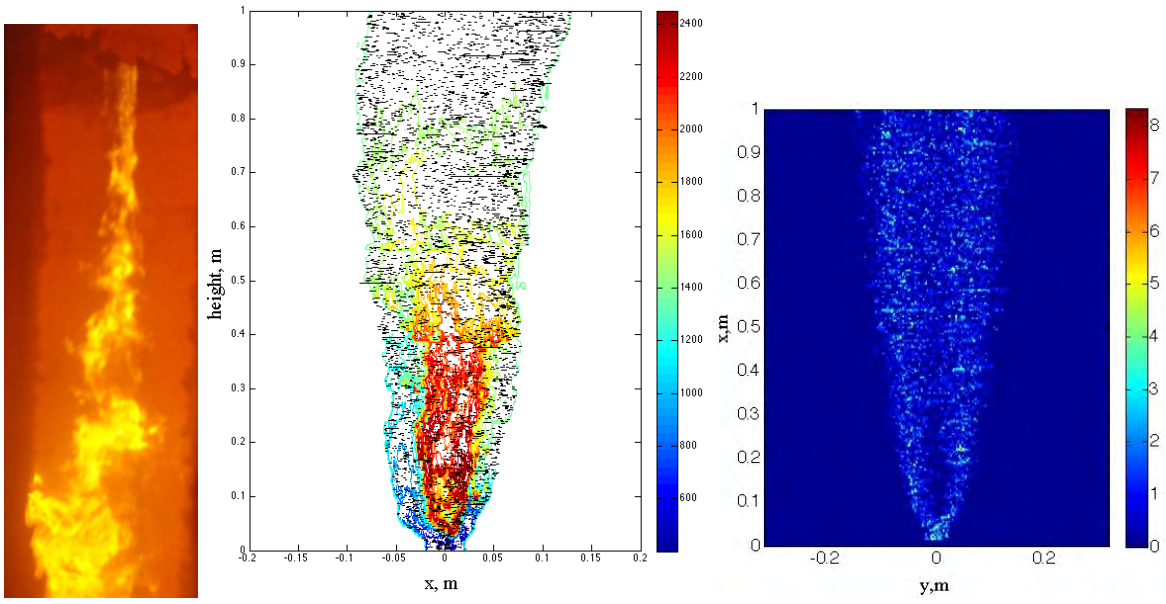


(a) (b) (c)

**Figure 5.** (a) The experimental flame (b) The ODT instantaneous temperature profile (c) The ODT instantaneous eddy distribution.

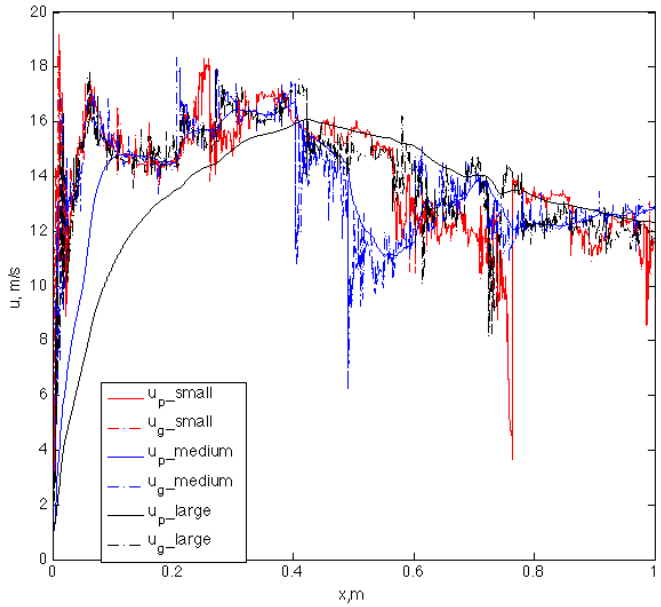


**Figure 6.** Instantaneous particle and gas velocities as a function of radius.

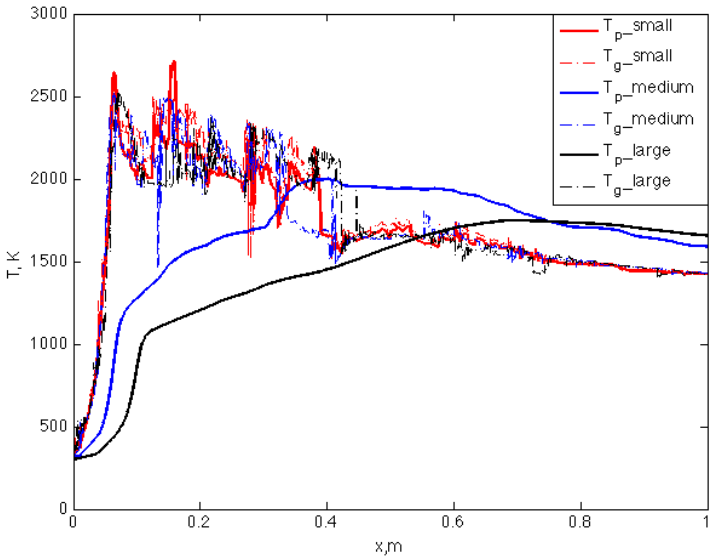


**Figure 7.** Instantaneous particle- and gas-phase temperatures as a function of radius.

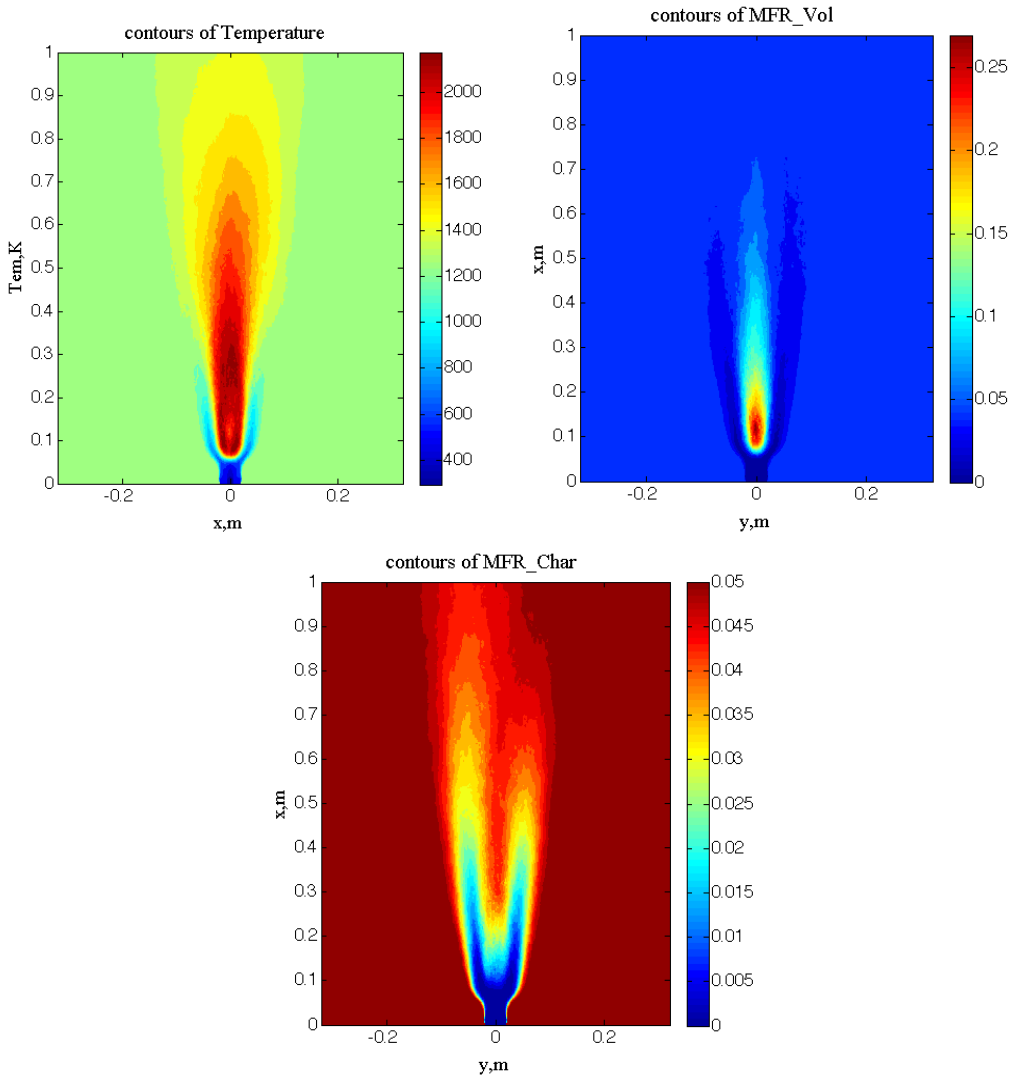


**Figure 8**. Profiles of the temperature, raw coal volatilization reaction, and char oxidation reactions.

***Subtask 3.3 – Identification of Manifold Parameters***

Multiscale simulations require hierarchical models to address the nonlinear coupling across the multitude of length and time scales, many of which remain unresolved in practical simulations. In the context of turbulent combustion, it is widely recognized that low-dimensional attractive manifolds exist (see, *e.g.* Mass and Pope, 1992; 1995; Schmidt et al. 1988; Valorani et al. 2003). The effect of such manifolds is to produce correlations in state variables (*e.g.* temperature and composition). Direct numerical simulation (DNS) remains the most detailed method to analyze turbulence chemistry interactions, and hence the manifestation of manifolds in the thermochemical state (Sutherland et al. 2007; Hawkes et al. 2007). Principal Component Analysis (PCA) provides a systematic methodology to identify correlations among variables in reacting flow systems. The investigators have shown that PCA can be used to represent the vast majority of state-space information in reacting flows using a small number of parameters (Parente et al. 2009; Sutherland and Parente, 2009). Furthermore, we have proposed a full modeling approach based on PCA that relies on the linearity of the PCA reduction to derive transport equations for the principal components themselves (Sutherland and Parente, 2009).

PCA not only identifies parameters which capture the data optimally, it also provides an ordering of the parameters so that incorporation of additional parameters results in the best possible reduction of reconstruction error. This is shown in Table 1 for PCA reduction of a 12-dimensional system representing $CO/H_2$-air combustion with extinction. Also shown in Table 1 are the results for a parameterization using the scalar dissipation rate ($c$), a common parameter for nonpremixed flamelet combustion modeling. These results are presented at stoichiometric conditions. Interestingly, the PCA model shows a marked improvement over the flamelet models (which use $c$ as a parameter). Results for simulations under two different conditions (corresponding to different Reynolds numbers) are presented as Case A and Case B, respectively. Additional details can be found in (Sutherland and Parente, 2009). PCA reduction of experimental data has shown analogous results (Parente et al. 2009). The primary limitation of the PCA model for application as a predictive model for combustion is the fact that the transport equations for the principal components include source terms which must be accurately parameterized by the principal components. To date, there has been relatively little success in obtaining an accurate representation of the principal component source terms, despite the fact that many of the state variables are well parameterized.

**Table 1.** $R^2$ values as a function of the number of retained principal components. Also shown is the $\chi$ parameterization. All results are at $f = f_{st} = 0.4375$.

| | $n_\eta$ | T | $H_2$ | $O_2$ | O | OH | $H_2O$ | H | $HO_2$ | $H_2O_2$ | CO | $CO_2$ | HCO |
|---|---|---|---|---|---|---|---|---|---|---|---|---|---|
| Case A | $\chi$ | 0.789 | 0.344 | 0.811 | 0.718 | 0.165 | 0.085 | 0.695 | 0.839 | 0.816 | 0.803 | 0.827 | 0.828 |
| | 1 | 0.983 | 0.259 | 0.976 | 0.930 | 0.240 | 0.178 | 0.823 | 0.986 | 0.916 | 0.978 | 0.956 | 0.980 |
| | 2 | 0.983 | 0.936 | 0.968 | 0.958 | 0.963 | 0.924 | 0.964 | 0.980 | 0.985 | 0.969 | 0.976 | 0.980 |
| Case B | $\chi$ | 0.801 | 0.509 | 0.807 | 0.697 | 0.426 | 0.186 | 0.648 | 0.665 | 0.729 | 0.810 | 0.058 | 0.817 |
| | 1 | 0.967 | 0.370 | 0.910 | 0.614 | 0.736 | 0.531 | 0.524 | 0.940 | 0.849 | 0.907 | 0.094 | 0.901 |
| | 2 | 0.996 | 0.845 | 0.982 | 0.882 | 0.931 | 0.990 | 0.858 | 0.974 | 0.941 | 0.981 | 0.378 | 0.984 |
| | 3 | 0.990 | 0.904 | 0.982 | 0.984 | 0.979 | 0.991 | 0.985 | 0.977 | 0.933 | 0.981 | 0.854 | 0.980 |

Because of the extraordinarily high cost of direct numerical simulation, where all length and time scales are resolved, alternative modeling techniques are needed that introduce various levels of approximation to reduce computational cost. The ODT model has been shown to quantitatively reproduce statistics observed in DNS in nonreacting flow, and the ODT model has been extended to include basic coal combustion and gasification models with equilibrium gas-phase chemistry in Subtask 3.2.

**Task 4.0 – Construction of a Validation Hierarchy based on Intended Uses and Identification of Experimental Data Requirements**

***Subtask 4.1 – Construction of Validation Hierarchies***

*Description of Approach.* A verification and validation/uncertainty quantification approach was developed for modeling the near-burner region of the oxycoal burner and the entrained-flow gasifier at the University of Utah. The strategy used here is unique and puts an emphasis on combining data from experiments and simulations to quantify error in models from validation and predictive scenarios. Quantification of error from models is necessary but not common practice in traditional modeling. This approach provides a rigorous methodology for enabling better understanding of the physical phenomena from the experiments and the predictive capabilities of the model.

This validation and uncertainty quantification (V/UQ) methodology seeks to establish the validity of a model and to quantify the uncertainty in a model's prediction. While the model itself is deterministic, it reflects our concept of reality and attempts to represent the stochastic physical process. As the observation of the physical process is inherently uncertain, the deterministic model must also include quantified uncertainty. Uncertainty in the model prediction originates from three sources: uncertainty in model inputs (boundary and initial conditions and model parameters), uncertainty due to numerical approximations, and uncertainty in data used for model validation. These uncertainties must be quantified

and reduced in order to calculate and minimize the uncertainty in the model prediction.

Figure 9 shows a simplified block flow diagram of the V/UQ approach developed here. We wish to quantify the uncertainty in a model output (y) given uncertainty in the inputs (x) to produce a probability density function (f) for both inputs and outputs. Starting with a specific objective, inputs (boundary/initial conditions, model parameters, numerical error) to the model(s) are identified along with their respective uncertainties. Modeling activities result in a probability density function (PDF) conditioned on the uncertainty of the input. The model output is examined for consistency with the PDF obtained from (ideally) multiple experimental observations. Consistency is a formal approach driven by concepts of Bayesian inference. The result is a modified PDF of the model inputs, model output, and potentially experimental observations. In other words, consistency between experimental observations and our conceptual model of the world is determined along with a statistical distribution describing the uncertainty in the analysis.

*Highlighted Results.* The uncertainty is determined through the efficient use of a validation hierarchy, which decouples the overarching problem of interest into smaller problems that are more amenable to V/UQ procedures. Each brick in the hierarchy is treated as an individual V/UQ objective. Inputs into the model originate from bricks in the lower hierarchy. Model output uncertainty from the current brick then becomes input uncertainty into the next hierarchical brick. In this manner, uncertainty from all levels of the hierarchy is propagated upward to the overall V/UQ objective. Figure 10 and Figure 11 demonstrate the validation hierarchies that were developed for the oxycoal and gasifier tasks.

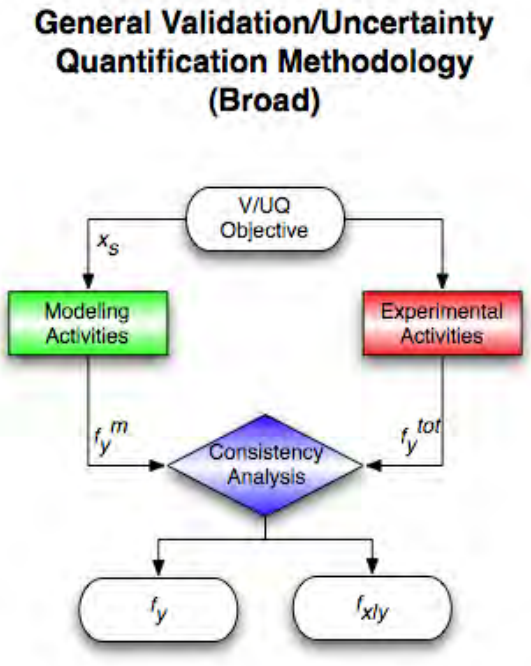


**Figure 9.** The flow diagram for the approach to uncertainty quantification that combines computational data with experimental data to produce quantified uncertainty in the model outputs.

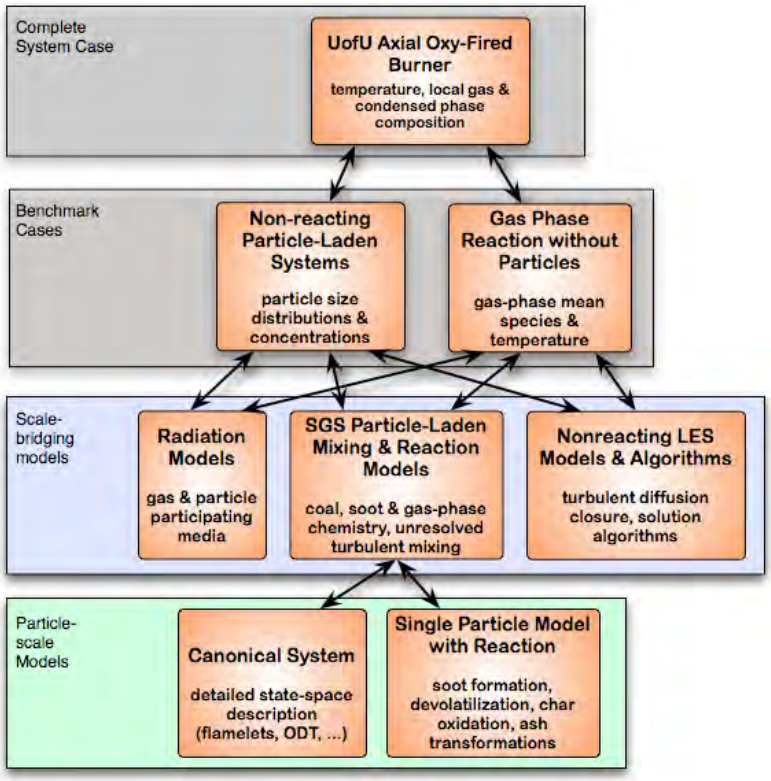


**Figure 10.** The validation hierarchy for the oxy-fired burner.

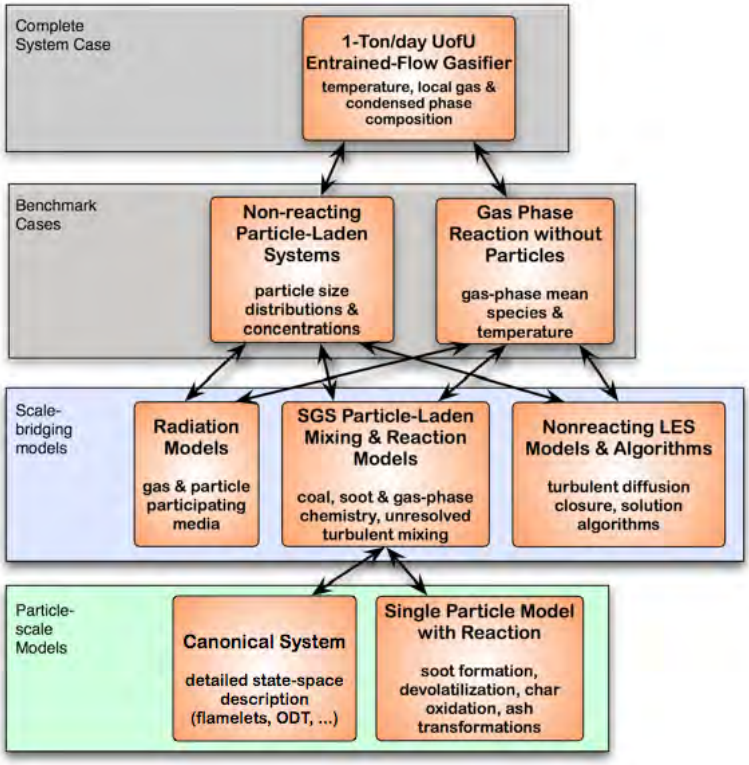


**Figure 11.** The validation hierarchy for the entrained-flow gasifier.

***Subtask 4.2 – Validation Hierarchy Demonstration using a Coupled Problem***

*Benchmark demonstration of an LES simulation with coal particles.* The discussion of Task 1 described the development of the DQMOM and its integration into the LES capabilities. Here, we present the first results of a benchmark pyrolysis validation test. For this test, three significant phenomena were observed: 1) particle inertia effects 2) particle size segregation 3) devolatilization of the raw coal. After a brief description of the problem set, each phenomenon in the simulation is discussed.

*Problem Setup*. The nozzle geometry of this problem matched the nozzle geometry of the oxycoal furnace built by the University of Utah (Task 8). Coal was fed in the center, primary inlet, and the secondary stream was coal-free. The simulation used an inert carrier gas (nitrogen) in both the primary and secondary inlets. The primary and secondary inlet temperature is 298°K and the reactor has an initial temperature of 1800°K. The simulation domain focuses on the near-burner region of the flow with dimensions being (76m, 0.31m, 0.31m) and the case resolution is roughly $7.4\times10^6$ computational cells.

DQMOM provides a way to represent the full particle distribution, which is a function of the internal coordinates (particle properties) of the distribution. One of the crucial steps of using DQMOM for any problem is deciding on which internal coordinates most represent the distribution. For this problem, we are interested in examining particle size effects and raw coal devolatilization. Thus, the distribution was represented using two internal coordinates; particle diameter and raw coal mass per particle. All other coal properties were assumed constant across all particles. Two quadrature nodes were used to represent the distribution requiring boundary conditions for two weights, two length abscissas, and two raw coal mass abscissas. The quantities were scaled using the properties of a 100 μm particle at the inlet. Unscaled values for the inlet distribution are shown in Table 2.

**Table 2.** Boundary conditions for the inlet particle distribution.

| Weight | Length | Raw Coal Mass |
|---|---|---|
| *#/vol* | *microns* | *Kg* |
| 2.00E+10 | 35 | 1.91E-11 |
| 2.00E+10 | 75 | 2.10E-10 |
| *Abscissa 1* | | |
| *Abscissa 2* | | |

*Highlighted Results*. Figure 12 - Figure 14 show volume-rendered fields of the various solution variables. Figure 12 plots the gas mixture fraction (mass of hot gas / mass of gas mixture) and demonstrates the structure of the gas field. Figure 13 and Figure 14 represent the number of particles per unit volume for small and large particles respectively. These three figures demonstrate that particles were moving differently than the gaseous field and that small particles were moving differently than the large particles. Note that the larger particles were demonstrating larger coherent structures axially than the smaller particles. This behavior is expected as small particles are dispersed faster than the larger, higher inertial particles.

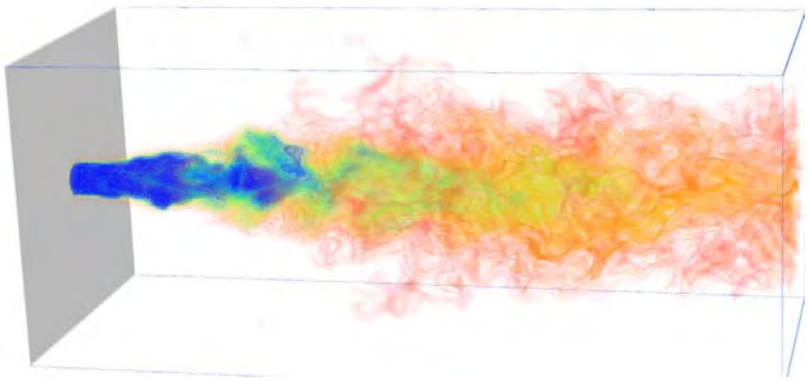

**Figure 12.** Volume rendering of the mixture fraction field.

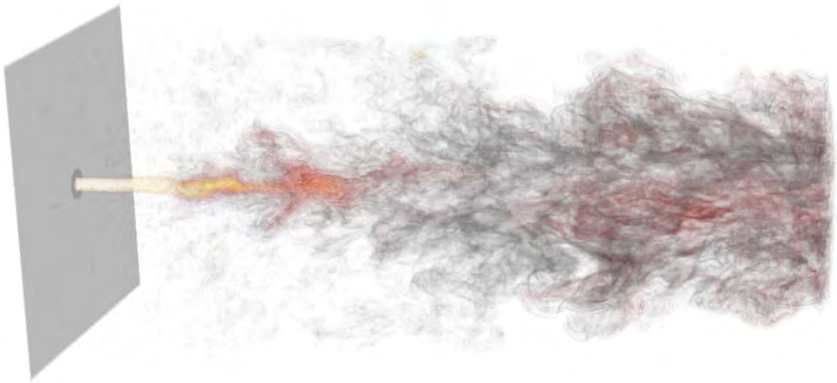

**Figure 13.** Volume rendering of the number density of the small particles.

**Figure 14.** Volume rendering of the number density of the small particles.

Figure 15 shows radial plots 20 primary diameters downstream of the inlet of the scaled number density of small and large particles. Instantaneous data and averaged data are presented. Along the radius, clustering of particles was observed. Also smaller particles were observed dispersing from the center of the jet earlier (in terms of axial location) than the larger particles.

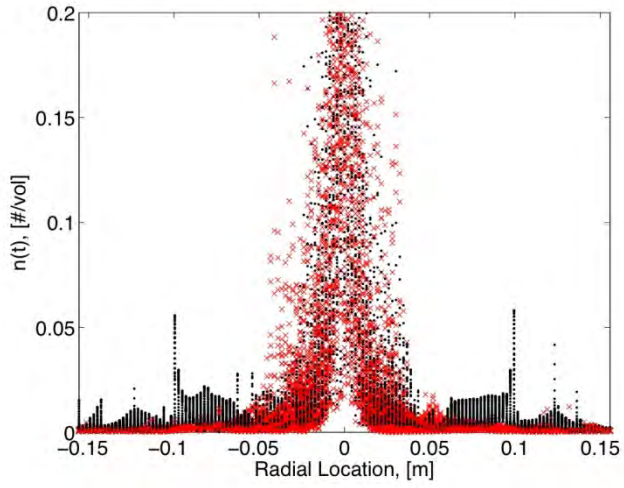


(a)

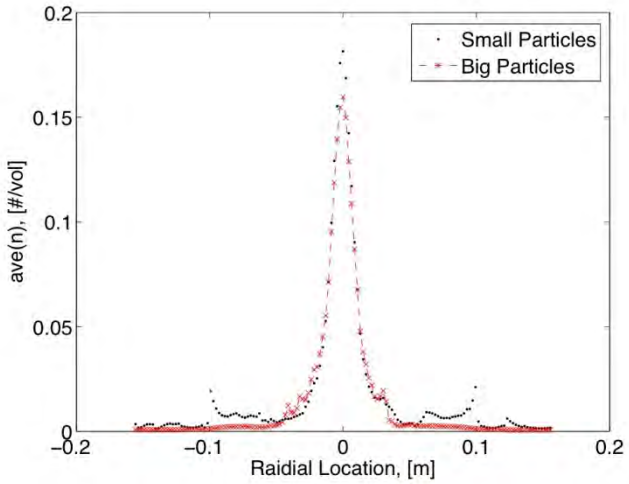


(b)

**Figure 15.** Volume rendering of the number density of the small particles.

Figure 16 shows radial plots 20 primary diameters downstream of the inlet of the mass of the raw coal in the particles for small and large particle sizes. Instantaneous and averaged data area presented. The raw coal mass for each particle size showed smooth transitions from the cold central core to the hot portion of the flow.

Figure 17 shows the distribution mean raw coal mass. The figure shows that for this reactor, complete particle pyrolysis occurs after roughly 0.35m downstream, or 25 primary inlet diameters, from the inlet.

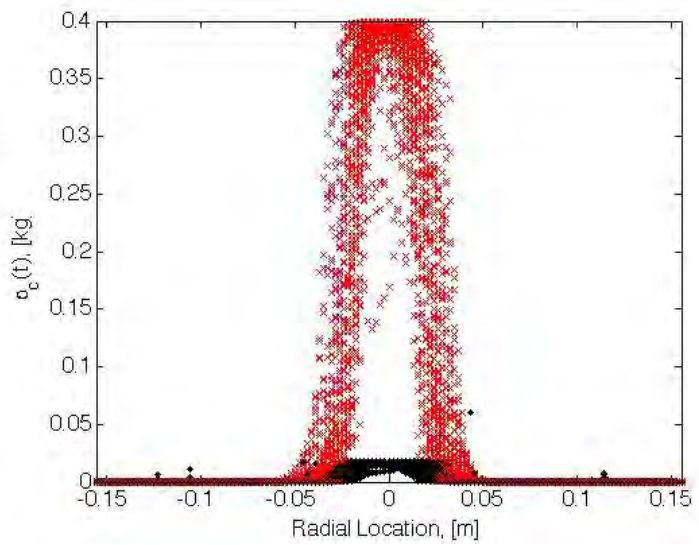


(a)

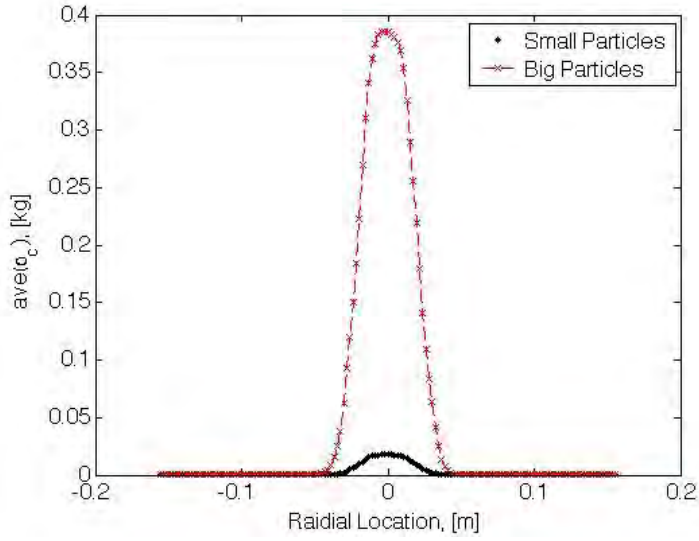


(b)

**Figure 16.** Instantaneous (a) and averaged (b) raw coal mass values for small and large particles.

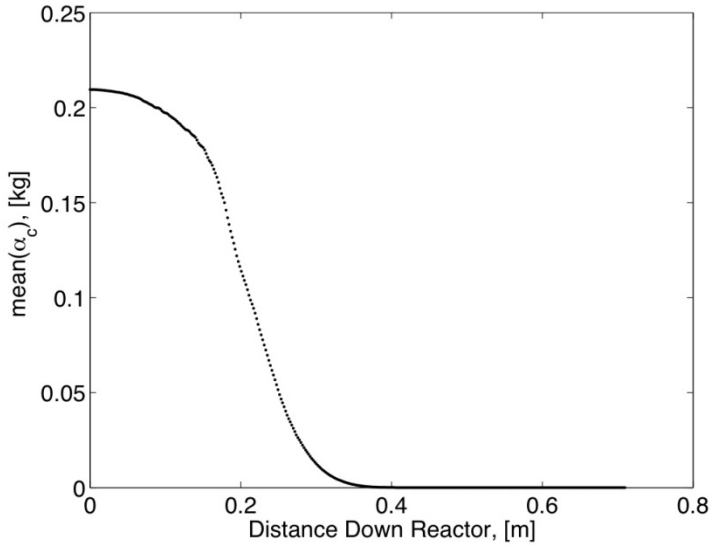


**Figure 17.** Mean raw coal mass as a function of the distance down the reactor. Note that complete pyrolysis occur after 3.5m downstream from the inlet.

## MERCURY CONTROL

In the Mercury Control thrust area, the investigators worked toward providing mechanistic understanding and kinetic rates for sorbents of interest to DOE. Complete results of the Mercury Control Task can be found in the Mercury Topical Report (Appendix A).

### Task 5.0 – Determination of the Capacities and Rates of Adsorption of Sorbents in Packed-Bed Studies

#### *Subtask 5.1 – Review/Summary of Existing Oxidation and Adsorption Data and Models*

Extensive literature exists on the oxidation and retention of mercury on fly ash and activated carbon. The literature consistently highlights the importance of using actual or simulated flue gas containing $SO_2$, $NO_x$, water, and HCl. The mechanism sketched in Figure 18 is from Olson and Mibeck (2005) and is able to explain the complex oxidation and adsorption data that researchers have observed on carbon. A parallel mechanism is believed to hold for HBr.

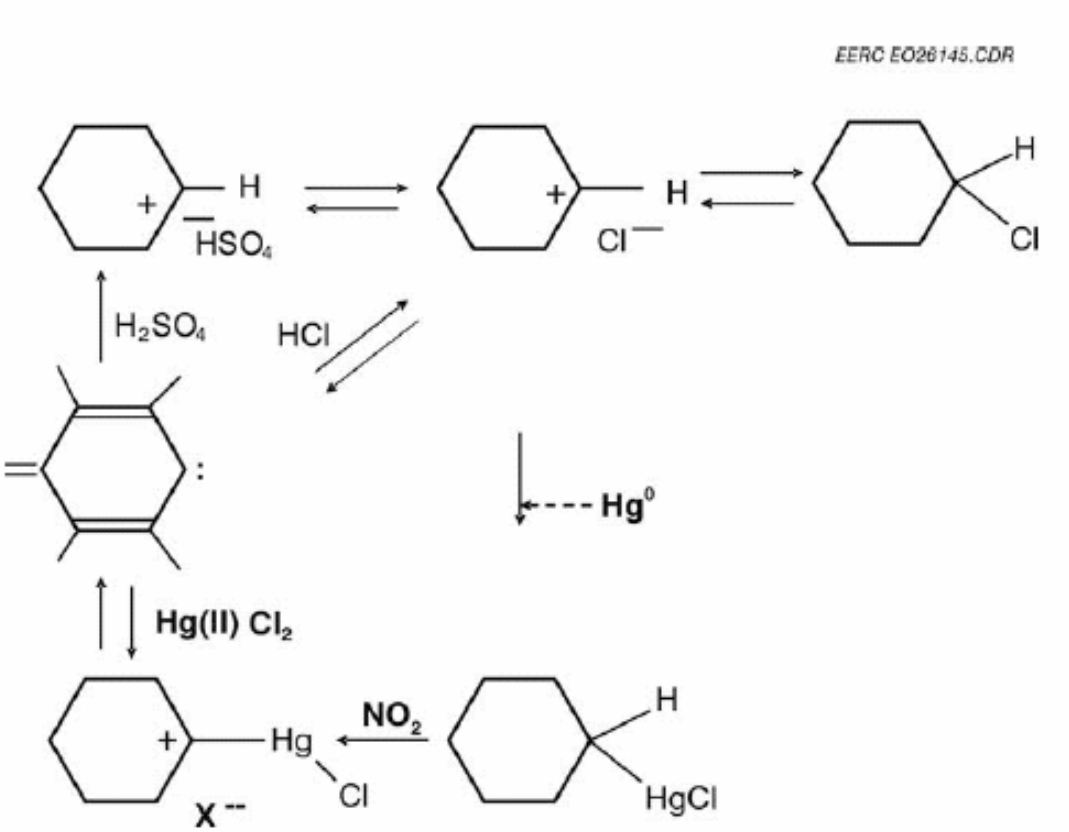


**Figure 18**. Proposed heterogeneous oxidation and adsorption mechanism for mercury capture on carbon (Olson and Mibeck, 2005).

Presto et al. (2007) studied the effect of $SO_2$ on mercury adsorption using Norit Darco flue gas desulfurization (FGD) and Norit Darco Hg-LH activated carbons at a bed temperature of 149°C. They suggested that the $SO_2$ mainly has an inhibitory effect on mercury adsorption that could be explained by the competitive adsorption of mercury and $SO_2$ on the available adsorption sites. Other studies suggest that the $SO_2$ could improve the elemental mercury adsorption on the surface of the carbon. Ghorishi and Gullett (1998) studied the effect of acid gases on mercury species sorption. At a temperature of 100-140°C, using a FGD activated carbon and a flue gas composed of nitrogen, $HgCl_2$ and 1000 ppm $SO_2$, they concluded that $SO_2$ reacted with the activated carbon and created sulfur active sites that captured elemental mercury through the formation of solid-phase, S-Hg bonds.

Miller et al. (2000) observed an initial mercury capture of 50%, which decreased to only 10% capture after 1 hour, with no oxidation of elemental mercury in the presence of 1600 ppm $SO_2$. The flue gas composition was 6 % $O_2$, 12 % $CO_2$, 8% $H_2O$, balance $N_2$. The activated carbon was LAC, and the temperature was 107°C. They concluded that $SO_2$ alone has a small benefit on elemental mercury capture.

The effect of hydrochloric acid on mercury oxidation and adsorption is to increase mercury adsorption on activated carbon; however, its effect is not well understood with respect to mercury oxidation. Using a flue gas composition that was 6 % $O_2$, 12 % $CO_2$, 8% $H_2O$, balance $N_2$ and a lignite activated carbon at 107°C, Miller et al. (2000) observed nearly 100% mercury capture in the presence of 50 ppm HCl. A similar effect of HCl with FGD sorbent was also observed by Carey et al. (1997), who concluded that despite the lower gas-phase concentration, HCl had a more pronounced enhancement effect on elemental mercury capture than other species present in the flue gas such as $SO_2$, suggesting that the Cl sites are

more active than the S sites. Using a FGD carbon exposed to a flue gas composed of nitrogen, elemental mercury and 50 ppm HCl, Ghorishi and Gullett (1998) found that HCl can react with the FGD sorbent and create chlorine (Cl) sites; these sites are instrumental in capturing elemental mercury through formation of Cl-Hg bonds in the solid phase.

The effect of nitrogen oxide (NO) on the ability of carbon to capture and oxidize mercury was studied by Liu et al. (2000) using a fixed-bed reactor charged with 100 mg of 60-80 U.S. Mesh size virgin or sulfur-impregnated activated carbon (SIAC) at 140$^{o}$C using a carrier gas flow rate of 1 L/min. The authors concluded that both virgin and SIAC samples showed no mercury uptake after 5 h exposure to 100 ml/min of 400 ppm NO in $N_2$ at 140$^{o}$C. They believe that NO was not adsorbed by the carbon at the conditions they examined.

The investigation of the oxidation rate of elemental mercury by $Br_2$ under flue gas conditions downstream from the air preheater and upstream from the particulate collectors was performed by Liu et al. (2007). They monitored the concentration of elemental mercury as a function of time in Pyrex flasks by a mercury cold vapor atomic absorption spectrophotometer. The elemental mercury concentrations ranged from 0.01 ppm-0.20 ppm, with $Br_2$ ranging between 4 and 60 ppm, and fly ash was used as sorbent. The $SO_2$ slightly inhibited the elemental mercury removal by fly ash at the typical flue gas temperatures. In contrast, a small increase in the elemental mercury removal by $Br_2$ was observed when NO was present in the flue gas. At 298$^{o}$K, fly ash significantly promoted the oxidation of elemental mercury by $Br_2$, and the unburned carbon acted primarily by the rapid adsorption of $Br_2$ with subsequent removal of elemental mercury from the gas phase.

***Subtask 5.2 – Evaluation of Mercury Analyzer***

A Tekran 2537A mercury analyzer coupled with a wet sample conditioning system designed by Southern Research Institute provided measurement of total and elemental mercury in the exhaust gas. In this system sample gas was pulled in two streams from the last section of the quartz reaction tube into a set of conditioning impingers. One stream was bubbled through a solution of stannous chloride to reduce the oxidized mercury to elemental form and then through a solution of sodium hydroxide to remove acid gases. This stream represented the total mercury concentration in the reactor. The second stream was first treated with a solution of potassium chloride to remove oxidized mercury species and then was treated with a caustic solution for acid gas removal. This stream was representative of the elemental mercury concentration in the reactor. Oxidized species were calculated by the difference between total and elemental mercury concentrations. A chiller removed water from the sample gas and then each stream was intermittently sent to the analyzer.

The wet sample conditioning system included an impinger that is filled with a 10%-by-weight solution of KCl in water. The investigators found that molecular chlorine ($Cl_2$) was reacting with the water in the KCl impinger of the experimental system to form hydrogen hypochlorite:

$$Cl_2 + 2H_2O = HOCl + H_3O+ + Cl-$$

The hypochlorite readily oxidizes elemental mercury to give high apparent levels of mercury oxidation, and the addition of sodium thiosulfate to the impinger solution prevents the formation of hypochlorite. In the absence of thiosulphate, ppm-levels of chlorine oxidize most of the elemental mercury that enters the impinge from the experimental reactor. The Mercury Team's measurements and predictions clearly show that the addition of thiosulphate is essential in order to measure the extent of mercury oxidation.

***Subtask 5.3 – Fixed-Bed Experiments***

*Approach.* The homogeneous mercury reactor used in this study is a 50-mm O.D. x 47-mm I.D. quartz tube (132 cm in length) located along the center of a high-temperature Thermcraft heater. The reaction tube extended 79 cm below the heater, was temperature controlled, and had a quartz sample section attached at the bottom with a capped end.

A methane-fired, premixed burner made of quartz glass supplied realistic combustion gasses to the reactor. All reactants were introduced through the burner and passed through the flame to create a radical pool representative of real combustion systems. The design burner heat input was about 300-W, producing 3.7 SLMP of combustion gases.

The heterogeneous tests were performed in the fixed-bed reactor using activated carbon from coconut shells. The 1.2-cm-I.D., quartz, fixed-bed reactor was connected to the existing, methane-fired tube furnace. The tests were conducted by loading the heterogeneous reactor with one gram of carbon particles of about 3 mm, wrapping it with heating tape and insulation, and regulating the temperature to 150$^{o}$C. The thickness of the bed was about 2 cm.

For all the tests, the tubular reactor was operated with the high quench profile (440$^{o}$K/s) and an inlet mercury concentration of 25 $\mu g/m^3$. Initially, a mercury mass balance was closed with the homogeneous reactor in order to check the mercury concentrations entering the packed bed. The flue gases were then allowed to enter the heterogeneous reactor to study the effect of the sorbent. The baseline composition for all tests was: 25 $\mu g/m^3$ Hg, 0.88% $O_2$, 33 ppmv NO, 10.5 % $CO_2$, 9 ppmv CO. To study the effects of other flue gas components such as $SO_2$, NO, $NO_2$, HCl, and HBr, different concentrations of these species were added to the baseline flue gas. All were introduced through the burner.

Figure 19 shows the effects of starting the fixed-bed adsorption process with 50 ppm chlorine (as HCl equivalent) and then adding increasing amounts of $SO_2$. Of most interest in this figure is the almost complete lack of mercury adsorption when chlorine is absent at 150°C. The addition of $SO_2$ causes significant reductions in the amount of mercury adsorbed. The extent of the reduction is roughly proportional to the $SO_2$ concentration.

However, when the chlorine concentration is increased from 50 ppm to 100 ppm the effect of $SO_2$ becomes negligible at concentrations ranging from 100 to 500 ppm. The order of injection for $SO_2$ and HCl also seems to play some role in the extent of mercury adsorption by the carbon. The addition of 50 ppm HCl at different $SO_2$ concentrations always results in an increase of the mercury uptake by the carbon; this increase is again nearly proportional to the $SO_2$ concentration. The $SO_2$ interferes with the ability of the carbon to adsorb mercury.

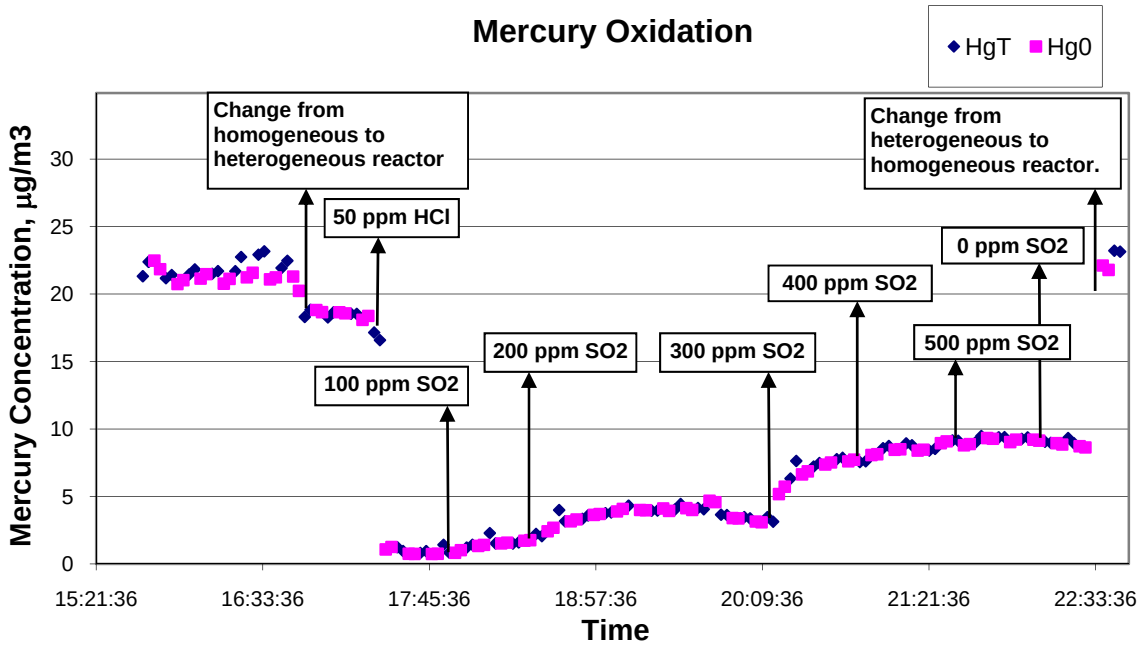


**Figure 19.** Elemental (Hg0) and total (HgT) mercury concentrations at the exit of the carbon bed as a function of time (hours) at a temperature of 150°C at chlorine concentrations of 50 ppm (as HCl equivalent) and $SO_2$ concentrations ranging from 100 to 500 ppm.

The effect of bromine on mercury adsorption was also studied. Figure 20 shows the bromine caused an increase in mercury adsorption by the carbon, and this increase was not affected significantly by either chlorine when added at 50 ppm (as HCl equivalent) or by $SO_2$ when added at 500 ppm. Bromine as a promoter of adsorption or oxidation on activated carbon was less sensitive to $SO_2$ than chlorine.

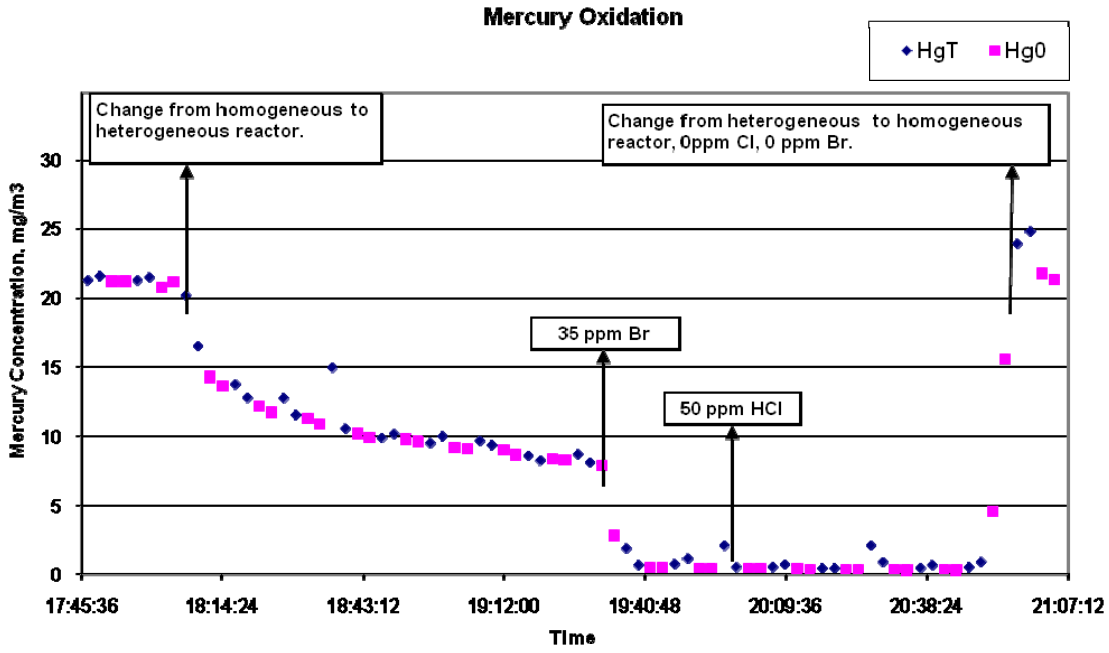


**Figure 20.** Elemental (Hg0) and total (HgT) mercury concentrations at the exit of the carbon bed as a function of time (hours) at a temperature of 150°C at a bromine concentration of 35 ppm (as HBr equivalent) and a chlorine concentration of 50 ppm (as HCl equivalent).

***Subtask 5.4 – Modeling of Full-Scale Performance***

*Fixed-bed model.* Following the Langmuir theory, the net rate of mercury adsorption on the activated carbon particle for species i can be written as the difference between the local adsorption rate and desorption rate:

$$\frac{dW_i}{dt} = k_{1i}\left(W_{\max,i} - \sum_{i=1}^{n} W_i\right)C_i - k_{2i}W_i$$

where

$W_{max,i}$: Asymptotic adsorbate concentration (g Hg / g carbon).
$K_1$: Kinetic constant of the adsorption reaction ($m^3$ / g min).
$K_2$: Kinetic constant of the desorption ($min^{-1}$).
$C_i$: Gas-phase concentration of component A (g / $m^3$).
$W_i$: Solid-phase concentration of component A (g Hg / g carbon).
n: Number of species in the flue gas.

For the packed-bed, the mass balance on species i in the gas phase in the axial direction is:

$$V\frac{dC_i}{dz} - \rho\frac{dW_i}{dt} = \varepsilon\frac{dC_i}{dt}$$

where

ρ: Bulk density of the carbon (g carbon/$m^3$).
ε: Porosity of the bed (void fraction).

Equations for the adsorbed phase and for the gas phase species were discretized using forward discretization for the time derivatives and upwind discretization for the spatial derivatives. The discretized equations were solved using MATLAB®.

As a first approach, breakthrough data and Langmuir constants from Karatza et al. (1998) for $HgCl_2$ were used to determine the accuracy of the model and method of solution. The model provided a rough fit of Karatza's data. Other sources of experimental data (Miller et al. 2000) were used with the objective of finding the model constants for mercury and some of the other flue-gas species (HCl, $SO_2$, and $NO_2$).

Miller et al. (2000) used a quartz filter loaded with 150.5 mg of a carbon-based sorbent and exposed it to a simulated flue gas. The temperature was kept at 225°F (107°C), and a Semtech 2000 mercury analyzer was used to continuously measure the elemental mercury at the outlet. The baseline flue gas composition was $O_2$ 6%, $CO_2$ 12%, $H_2O$ 8%, and $N_2$ balance. Experimental results obtained by Miller et al. are shown in Figure 21 as well as the model results. A rough fitting of experimental and calculated data is observed using the parameter values fromTable 3. As seen in this table, parameters can vary by orders of magnitude (e.g., maximum carbon uptake), particularly as the flue gas composition changes.

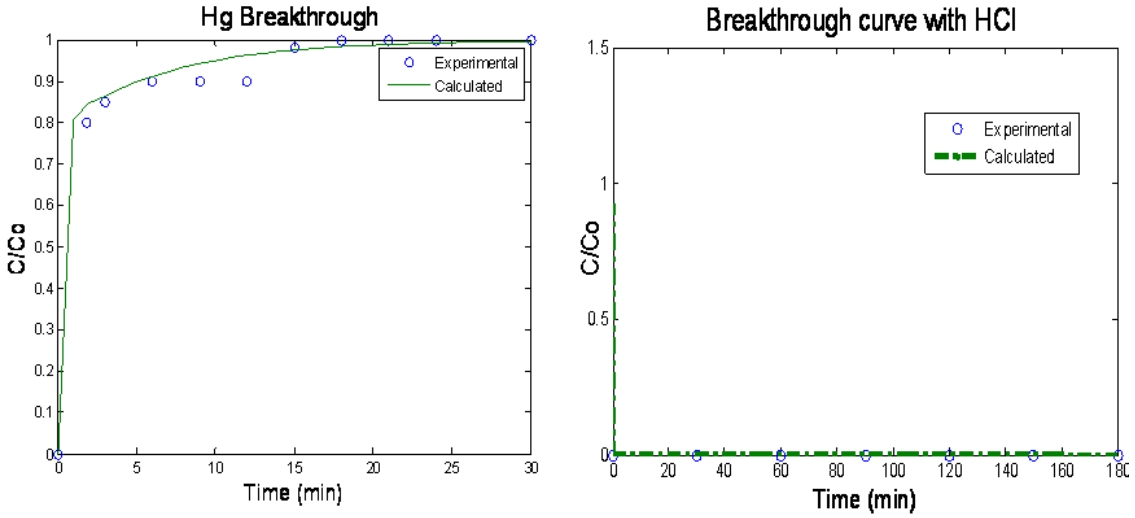


**Figure 21.** Breakthrough curves for lignite activated carbon with a bed temperature of 107°C. (A) Mercury and baseline gases, (B) Mercury, 50 ppm HCl and baseline gases. Experimental data were from Miller et al. (2000), and calculated data obtained with the heterogeneous model.

**Table 3.** Calculated heterogeneous model parameters for Miller et al. (2000) experimental data.

| Flue gas Composition | $K_{1i}$ ($m^3$/g min ) | $K_{2i}$ ($min^{-1}$) | $W_{maxi}$ (g Hg/g Carbon) |
|---|---|---|---|
| Mercury and Baseline gases (i=1) | 5.9212 | 0.1476 | 0.009105 |
| Mercury, 1600 ppm $SO_2$ and baseline gases (i=2) | 0.02870 | 0.5874 | 0.00751 |
| Mercury, 20 ppm $NO_2$ and baseline gases (i=3) | 2.8720 | 587.4 | 0.0751 |

**Task 6.0 – Identify the Effects of Gas Composition on Mercury Kinetics and Capture in Entrained-Flow Systems**

***Subtask 6.1 – Evaluation of Entrained-Flow Mercury Reactor***

The modifications to the mercury analyzer are discussed under Subtask 5.2. The Mercury Team evaluated the University of Utah's entrained-flow mercury reactor, calibrated the feeding system for sorbent injection, and identified unsolvable problems with static. In addition, to the issues regarding the reactor, there were several questions regarding the kinetics so the team focused on packed-bed studies (Subtask 5.3) and single-particle modeling efforts (Subtask 6.2).

***Subtask 6.2 – Entrained-Flow Mercury Reactor Experiments***

Because of challenges with the mercury analyzer and problems with static in the entrained-flow reactor, the Mercury Team focused on a single-particle entrained flow model.

*Single-particle model for in-flight sorbent capture of mercury*. A mercury mass balance on the gas phase can be constructed using a conventional balance on an entire spherical sorbent particle or on adjacent, concentric shells within the particle. The sign convention of the model treats flux into the particle as "positive" and flux out of the particle as "negative." This balance may be expressed in differential form and the spatial orientation of the concentration terms may be standardized with respect to index i to give:

$$\frac{dC_{cv,i}}{dt} = \frac{D_{eff}}{V_{cv,i}\epsilon_P \Delta r}\left(C_{i-1}A_{i-1} - C_i(A_{i-1} + A_i) + C_{i+1}A_i\right) - \frac{R_{ads}}{\epsilon_P}$$

where

$C_{cv,i}$: Gas phase mercury concentration in the void space of the particle at the node i (g Hg/$m^3$)
$V_{cv,i}$: Volume of the shell at the node i ($m^3$).
$\varepsilon_p$: Porosity of the particle ($m^3$ void/ $m^3$ particle).
$A_i$: Surface area of the particle side shell of the control volume ($m^2$).
$R_{ads}$: Rate term for solid phase uptake of mercury (g Hg/s $m^3$).
$D_{eff}$: Effective diffusivity of gaseous, elemental mercury inside the particle($m^2$/s).
$\Delta r$: Radial distance between adjacent shells (m).

The form of $R_{ads}$ is dependent upon the apparent density of the sorbent particle, $\rho_p$, and a solid phase rate model. In this work, two different rate models are employed. The first and simplest uses a difference between adsorption and desorption, assuming equilibrium at the particle surface:

$$k_2\omega_i = k_1(\omega_{max} - \omega_i)C_{cv,i}$$

where

$\omega_i$: Solid phase, elemental mercury concentration at node i (g Hg/g carbon).
$\omega_{max}$: Maximum elemental mercury uptake capacity of the sorbent (g Hg/ g carbon).
$k_1$: Adsorption constant ($m^2$/ g Hg s).
$k_2$: Desorption constant (1/s).

The second rate model uses the Freundlich isotherm,

$$\omega_i = \frac{C_{cv,i}^{1/n}}{K_{fr}}$$

where
$K_{fr}$: Sorption constant for Freundlich isotherm.

The single-particle model calculated mercury uptake with respect to time, porosity, feed rate, average particle pore size, and particle radius. It can also calculate solid and gas-phase concentrations inside the sorbent particle. The model used the MATLAB® function "ode23s," a stiff ordinary differential equation solver, to obtain solutions. The set of constants required - $\omega_{max}$, $k_1$, and $k_2$ for the standard adsorption/desorption model, $\omega_{max}$ and K for the Langmuir isotherm model, and n and $K_{fr}$ for the Freundlich isotherm model are extracted from a packed bed isotherm (Meserole et al. 1999).

The results from the rate law and Langmuir isotherm models can be compared directly as identical parameters may be applied to their governing equations. $K_{lang}$ from the Langmuir isotherm is simply the quotient of $k_1$ and $k_2$ from the rate model. The parameters for these two adsorption models are shown in Table 4.

**Table 4.** Constants used in Rate law and Langmuir isotherm adsorption models.

| Parameter | Magnitude | Units |
|---|---|---|
| $K$ | 580.8 | $\frac{m^3}{g}$ |
| $k_1$ | 0.41 | $\frac{m^3}{g \cdot s}$ |
| $k_2$ | 7.06e-4 | $\frac{1}{s}$ |
| $w_{max}$ | 1000 | $\frac{\mu g_{Hg}}{g_{carbon}}$ |
| $D_{ab}$ | 2.55e-5 | $\frac{m^2}{s}$ |
| $D_{kn}$ | 7.0e-6 | $\frac{m^2}{s}$ |
| $F.R.$ | 10.0 | $lb/MMacf\left(0.08\frac{g_{carbn}}{m^3}\right)$ |
| $R_P$ | 14.5 | $\mu m$ |
| $D_{pore}$ | 3.0 | $nm$ |
| $t_{residence}$ | 2.0 | $s$ |

The results from the Langmuir isotherm adsorption model for low residence times (Figure 22) showed higher uptake levels than do the rate-based model results. The rate-based model showed negligible uptake under standard operating conditions. Similar results were obtained by Flora et al. (2003).

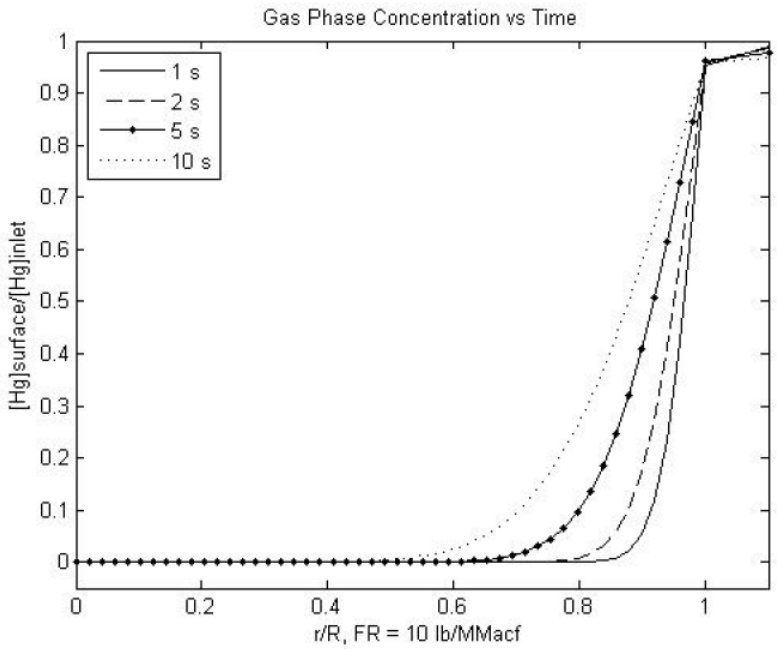


**Figure 22.** Mercury concentration normalized with inlet concentration inside the sorbent particle using Langmuir isotherm model.

The Freundlich isotherm parameters, determined from a sorbent used in full-scale tests at Pleasant Prairie, are shown in Table 5 (Cremer et al. 2005). They are used in the Freundlich model calculations in Figure 23 along with reactor parameters similar to the ones used in the rate-based and Langmuir isotherm models.

**Table 5.** Constants used in Freundlich isotherm adsorption model.

| Parameter | Magnitude | Units |
|---|---|---|
| $K_{fr}$ | 0.01490 | $\frac{g_{carbon}}{m^3}$ |
| $n$ | 1 | |
| $D_{ab}$ | 2.55e-5 | $\frac{m^2}{s}$ |
| $D_{kn}$ | 7.0e-6 | $\frac{m^2}{s}$ |
| $F.R.$ | 10.0 | $lb/MMacf\left(0.08\frac{g_{carbn}}{m^3}\right)$ |
| $R_P$ | 14.5 | $\mu m$ |
| $D_{pore}$ | 3.0 | $nm$ |
| $t_{residence}$ | 2.0 | $s$ |

Using the above magnitude for the necessary parameters, Figure 23 shows mercury uptake under the Freundlich isotherm adsorption model. At normal residence times, a steep gas-phase intraparticle concentration gradient was observed in the Freundlich model. This gradient was much steeper than that seen in the Langmuir adsorption model.

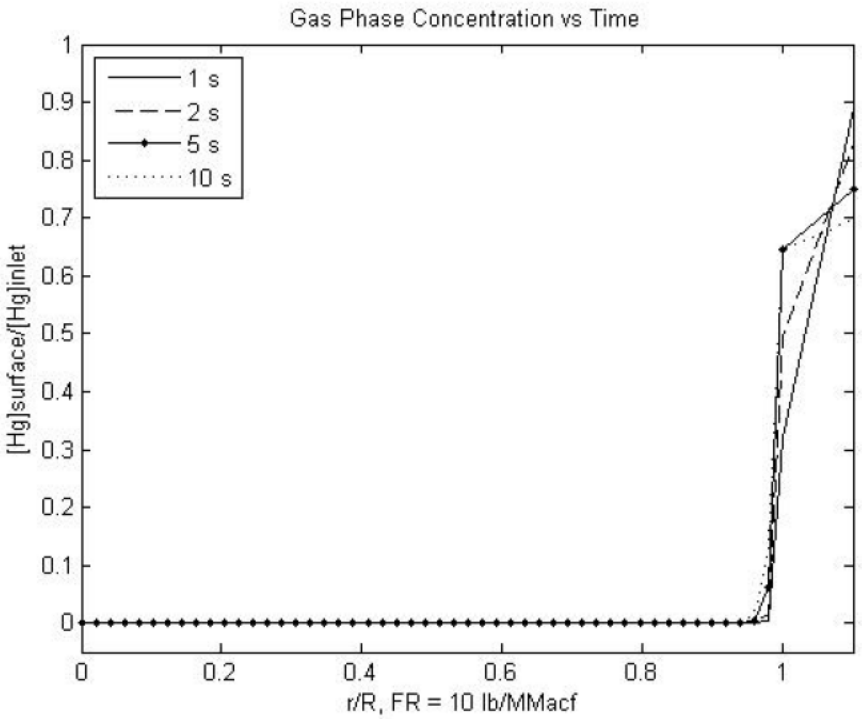


**Figure 23.** Mercury uptake normalized with inlet concentration over time using Freundlich isotherm model.

Multiple full-scale reports have shown (Cremer et al. 2005, Scala 2004, Bustard et al. 2004) that particle diameter does not affect mercury uptake as implied by the models. An explanation for this lack of convergence between the model and full-scale data is that particle distributions are not properly addressed in models. With the exception the work by Meserole et al. (2004), all published models assume monodisperse size distributions. However, the sorbents used in full-scale settings have polydisperse size distributions. In order to capture this effect, sorbent PSDs in a model may be discretized to the desired resolution.

### *Subtask 6.3 – Integration into Heterogeneous and Homogeneous Reaction Models*

The full-scale results suggest much greater adsorption rates compared to the results shown by entrainment alone. One of the reasons is that the sorbents have a PSD versus a single size. This distribution, shown in Figure 24, changes the results of the model as suggested by Figure 25, where a typical distribution has been “binned”.

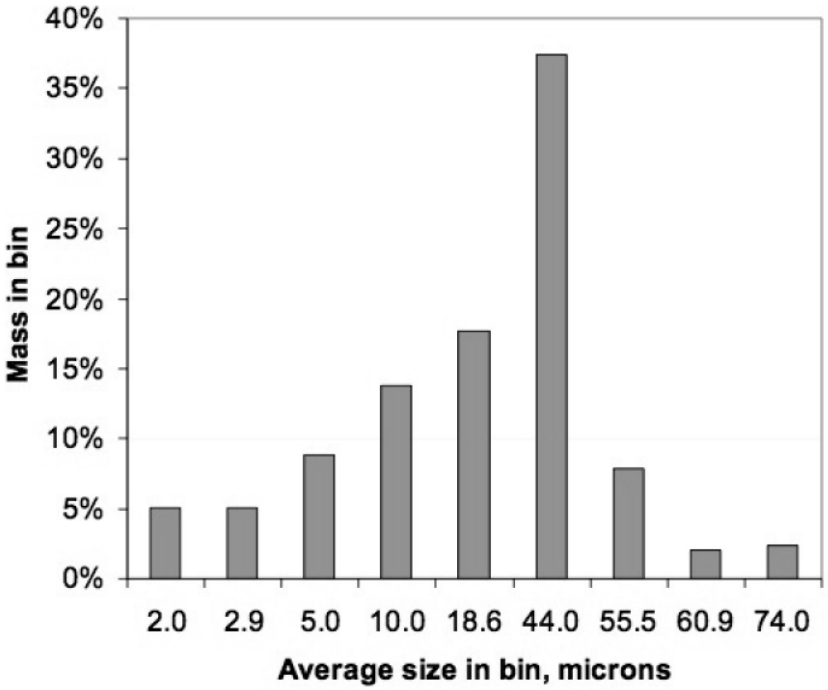


**Figure 24**. One example of activated carbon PSD.

Figure 25 shows a direct comparison of the 1 and 10 lb/MMacf lines from a single particle size compared to a distribution of particle sizes, which has an average diameter equivalent to the single size, 29 μm. The PSD results showed significantly more uptake than does the single particle size model due to the presence of smaller than average particles that, per capita, have more surface area exposed directly to the bulk.

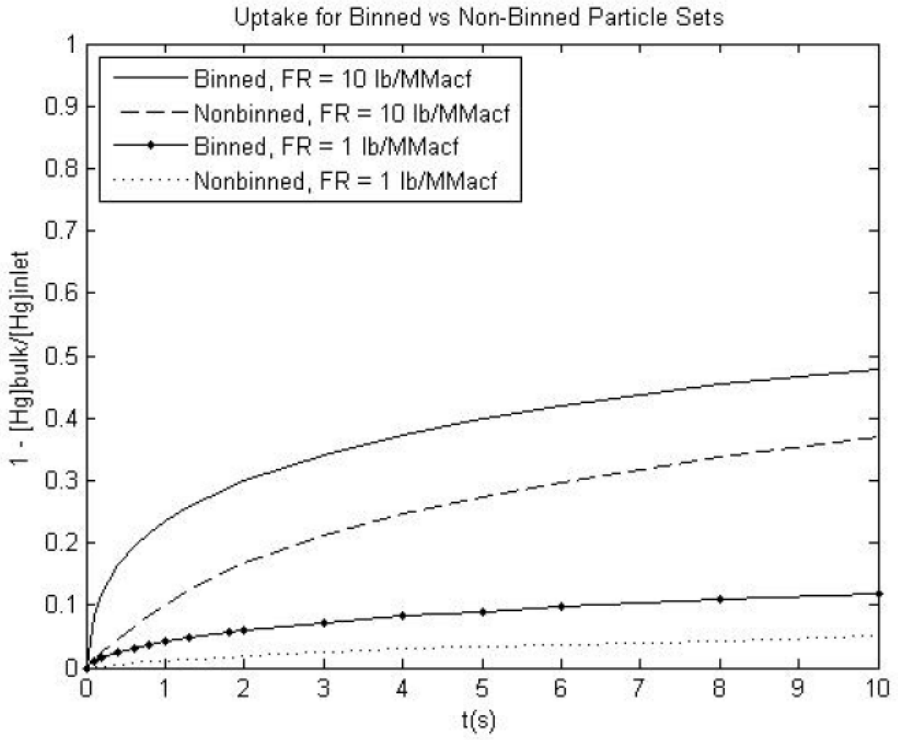


**Figure 25.** A comparison of uptake for "binned" and "nonbinned" particle sets for two different feed rates. "Binned" represents a PSD size range from 2 μm to 75 μm and an average of 30 μm which is the size used in the "nonbinned" model.

Furthermore, the uptake results in Figure 25 are lower than those seen in the full-scale results (Figure 26). If a 25% correction is added, noted as "in-flight + deposit", the full-scale data may be more closely simulated as shown in Figure 26. Admittedly, this correction factor is highly qualitative, but it does allow for a predictive capacity that comes within 10% of full-scale values reported by Cremer et al. (2005).

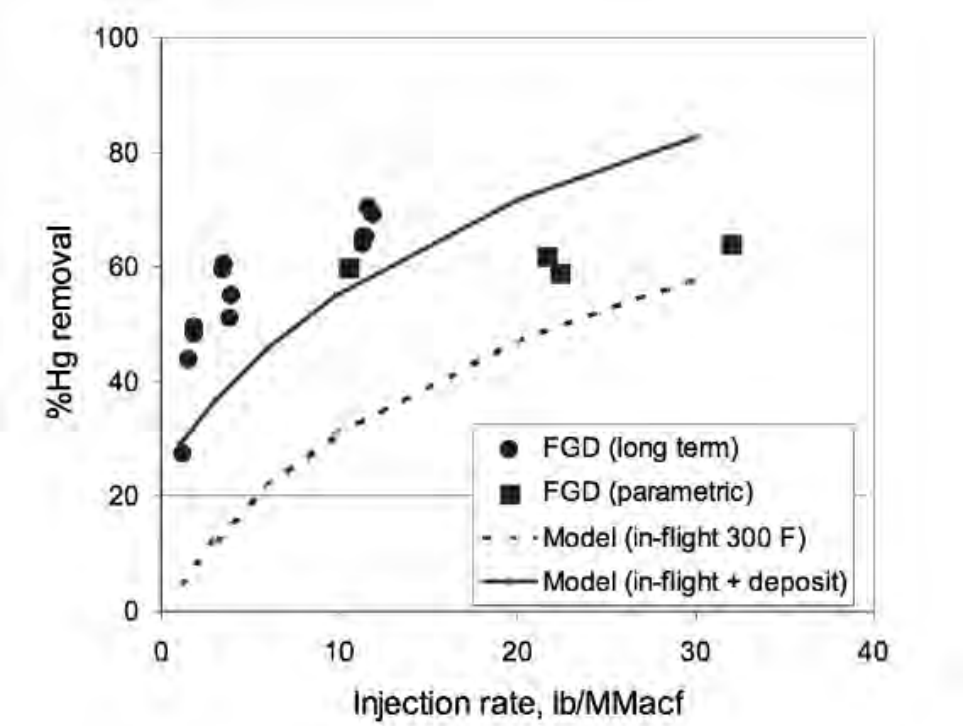


**Figure 26.** Full-scale mercury uptake at Pleasant Prairie as reported by Cremer et al. (2005).

Figure 27 shows results that may be directly compared to Figure 26. The range of factors was 1.25 (representing 25%) to 1.5. The basic 25% correction seemed to match the full-scale data more closely, which points to the conclusion that the "packed bed" that forms on the wall of the duct likely does so quickly and does not change throughout the duration of the test. In addition, the results suggested that in-flight predictions are not sufficient to conclude the total mercury adsorption capacity of the system. Some wall effects must be included.

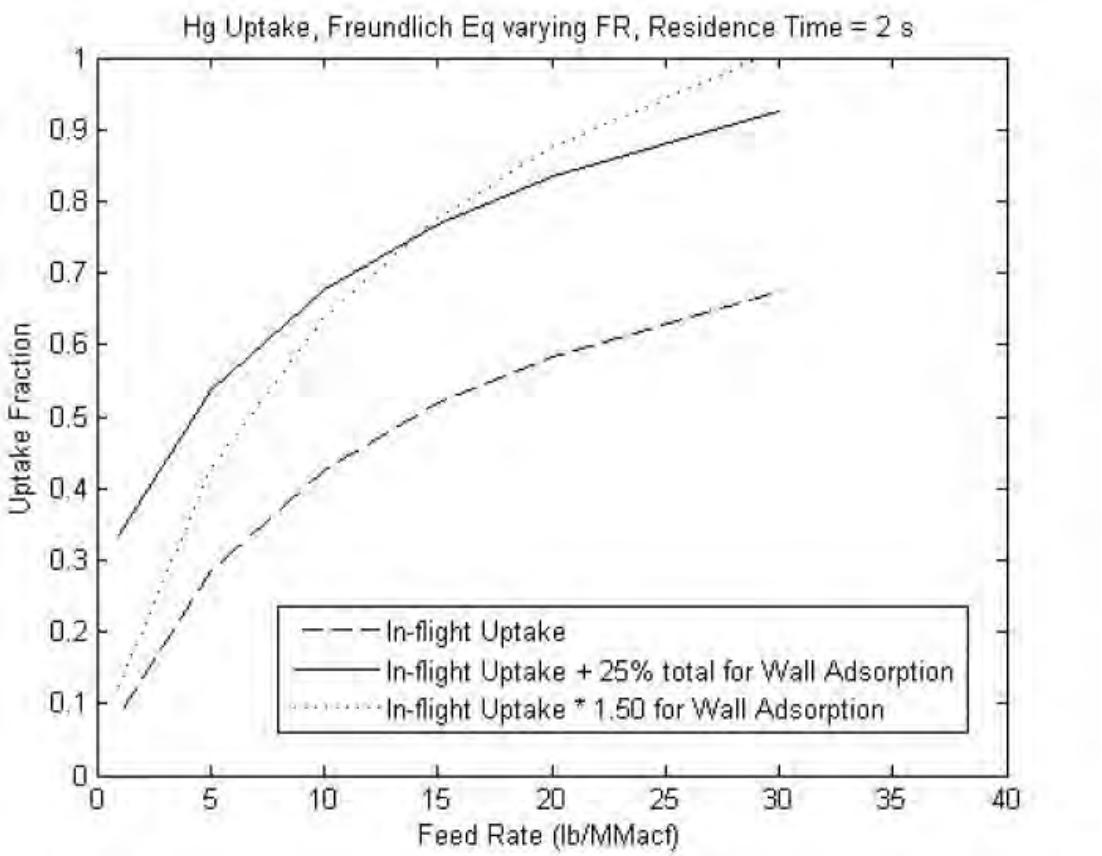


**Figure 27.** Mercury uptake normalized with inlet concentration inside the particle using the Freundlich isotherm adsorption model. The particles are "binned", and a total uptake 25% or 50% proportional uptake increase is added as a correction factor to simulate "wall effects".

**Task 7.0 – Development of Mechanistic Insight into the Chemical Bonding between Mercury and Ligands used as Model Compounds**

This Task planned to study the chemical bonding interactions of sorbents utilized in packed-bed and entrained-flow studies using NMR data coupled with theoretical calculations. However, due to the loss of two students this task was discontinued.

## OXYCOAL COMBUSTION

The primary focus of the Oxyfuel Combustion Thrust Area was to investigate the effects of variations in the partial pressure of $O_2$ and $CO_2$ on coal jet ignition in *retrofit* oxycoal combustion applications and to provide fundamental rate parameters and sub-scale model validation for CFBs. The experimental oxycoal studies focus on the same suite of four common fuels, as described and characterized in Subtask 11.1.

**Task 8.0 – Investigation of the Effects of $O_2$ and $CO_2$ Partial Pressure on Coal Jet Ignition**

Additional details for this task can be found in the topical report in Appendix B.

***Subtask 8.1 – Design and Construction of an Oxycoal Combustion Furnace***

The Oxycoal Team completed the design, construction, and troubleshooting of a new down-fired, 100 kW, oxycoal combustion furnace with quartz windows for optical access, which will permit flame detachment studies and future optical diagnostics. The new furnace simulates the environment experienced by pulverized coal jet flames in tangentially fired furnaces or cement kilns, and provides for the systematic control of burner momentum and velocity variables, as well as wall temperatures. It consists of an oxy-fuel combustion chamber, followed by downstream controlled temperature cooling to simulate practical furnace conditions. The furnace allows for stabilization of axial Type 0 (no swirl) pulverized coal, diffusion flames, through the use of heated walls, and variations of oxygen content of transport and secondary air streams. It employs a K-tron loss-in-weight twin-screw coal feeder with modified eductor design is installed to provide steady and consistent coal feeing, which is the key to study the coal jet flame stability.

The experiments discussed in the following subtasks were performed using a Utah bituminous pulverized coal with the particle size ranging from 35 μm to 75 μm (average particle size is 50 μm).

***Subtask 8.2 – Coal Jet Ignition Experiments***

The effect of $O_2$ partial pressure in the transport stream and in oxidant stream on the near-burner aerodynamics, flame stability and detachment, was investigated and quantified. The experiments focused on effects of $P_{O2}$ in the transport stream on flame stability, CO and $NO_x$ emissions, and temperature for natural-gas jet ignition, coal-jet ignition in air, and coal-jet ignition in enriched air/oxygen the.

The natural-gas experiments provided key operational parameters, such as the maximum firing rate of 130,000 btu/hr and the time the combustor required to reach steady state. They also showed that CO levels were near zero regardless of $P_{O2.}$

Figure 28 shows the effect of $P_{O2}$ in the transport (primary) stream on the flame stability, as indicated by the stand-off distance. With overall $P_{O2}$, primary stream velocity, and secondary stream velocity, total stoichiometric ratio, wall temperature, preheat temperature, coal feeding rate, and camera setting fixed, increasing $P_{O2}$ in the transport stream from 0 to 20.9%, can change flame stability. Stand-off distance decreased when $P_{O2}$ in transport stream increased. The bottom pictures show flame structure in the near-burner zone. The effect of $P_{O2}$ in the transport stream is more significant than the effect of $P_{O2}$ in secondary stream because oxygen in transport stream is premixed with pulverized coal and reacts with coal directly and rapidly under high temperatures, while secondary oxygen needs a mixing mechanism to reach the center coal jet.

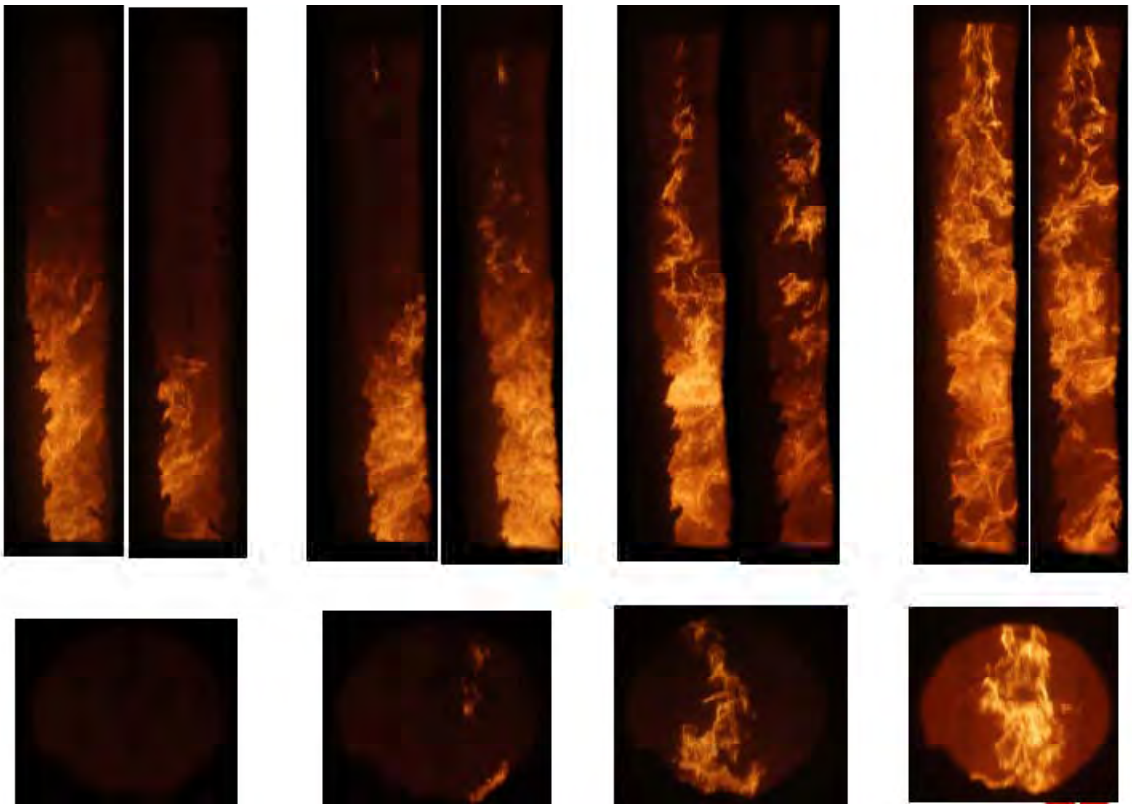

**Figure 28.** The effect of $P_{O2}$ in transport stream on flame stability and near-burner flame structure**.** $P_{O2}$ in transport stream =

0 0.099 0.144 0.207

Figure 29 shows the $NO_x$ formation and $P_{O2}$ in the secondary stream. Increasing $P_{O2}$ tended to lead to higher $NO_x$ formation due to the greater temperature. Once the flame became attached, when $P_{O2}$ in the secondary stream was higher than 25.4%, $NO_x$ formation decreased slightly, due to the different mixing pattern and fluid mechanics caused by the flame attachment. The lower $NO_x$ formation curve in Figure 29 indicates that almost no thermal $NO_x$ was generated without the presence of $N_2$, and almost all the $NO_x$ came from the nitrogen in the fuel under oxycoal combustions.

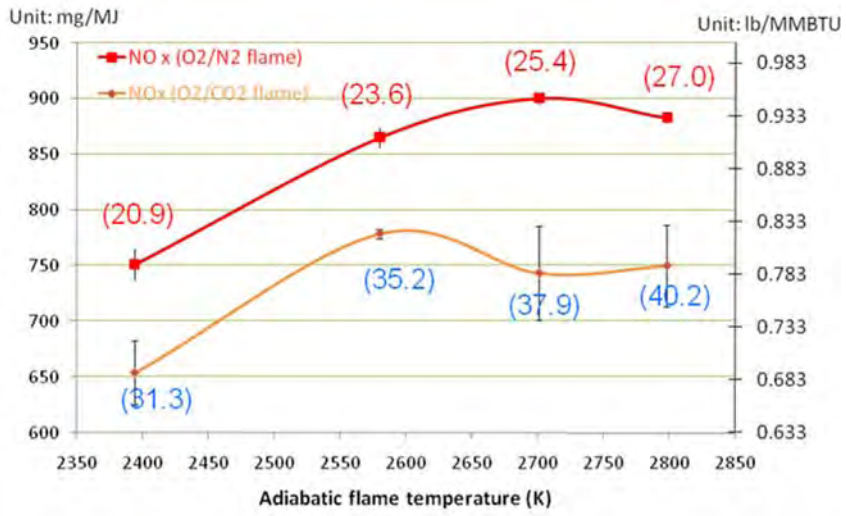


**Figure 29.** Comparison of $NO_x$ formation under $O_2/N_2$ environment and $O_2/CO_2$ environment (red and blue numbers show $PO_2$ in percentage in secondary stream of each case, $PO_2$ in transport stream is always 20.9%).

***Subtask 8.3 – Preliminary Validation of Coal Jet Ignition Models***

Examination of the data from Subtask 8.2 and 8.5 suggests the following interpretations:

- The composition of the *primary* jet fluid is very important in determining coal-jet stability in co-axial turbulent diffusion jet flames. This was evident in the data showing the effect of partial pressure of oxygen in the primary jet on flame attachment.
- The temperature (and probably also the composition) of the *secondary* jet fluid is also extremely important. Flame stabilization was very sensitive to secondary flow temperatures.

These results, showing that chemical and thermal properties of *both* the primary jet ($P_{O2}$) *and* the secondary jet (T) controlled the turbulent diffusion flame stand-off distance, are consistent with the following physical view of the interactions between turbulent mixing and coal particle ignition mechanisms: Large eddies transport packets of coal particles, *and their surrounding primary fluid*, into the secondary fluid. The primary oxygen concentration determines the initial concentration of $O_2$ at the particle surface. In order for the coal to ignite, this must be increased to a required ignition level of $O_2$ at the surface through molecular diffusion of oxygen to the particle surface. This molecular diffusion flux through a film of primary fluid can be enhanced by a) increases in the concentration of $O_2$ in the secondary fluid, and b) increases in the diffusion coefficient of $O_2$ in the primary fluid ($N_2$ versus $CO_2$). Additional data are required to test these specific hypotheses, and these are being generated in subsequent work.

The presence of bi-and multi-modal probability density functions (PDFs) is interesting and has implications for a simulation model. Multiple modes occur under conditions of flame near-instability. Very slight changes in either initial or boundary conditions can determine large changes in the flame location, which, however, appear only to occur at specific locations. There appear to be distances from the burner where the flame can never be stabilized – it can only appear either before or after this distance. These locations are represented by the locations of the various modes of the PDFs and appear to be the result of physical, not random, phenomena.

The experimental work has therefore suggested that the simulation must be able

- To predict multiple modes in the flame stand-off distance PDFs
- To explain the physics (possibly due to the largest eddy size) behind this observation
- To predict the large *discrete* effects on flame stand-off distance, of small changes in input or boundary conditions.

In summary, these results support a LES approach to properly predict ignition in large co-axial turbulent diffusion oxycoal jet flames.

***Subtask 8.4 – Preparation of Oxycoal Combustion Furnace for Pure Oxygen Combustion and Associated Safety Training***

The oxycoal furnace designed and constructed under Subtask 8.1 was modified to allow for combustion with pure $O_2$ instead of air. The modifications included the installation of a vaporizer to vaporize the liquid oxygen, cleaning and running the lines from the oxygen tank to the combustor, and installation of a $CO_2$ supply system. This subtask also included installation of all appropriate safety systems and training of research personnel. The oxycoal furnace now allows pulverized coal combustion in mixtures of pure oxygen and carbon dioxide without the presence of air.

***Subtask 8.5 – Coal-Jet Ignition Studies with Pure $O_2$ and $CO_2$ in both Primary and Secondary Jets***

*Approach*. In order to quantify the flame stand-off distance and other flame measurements from a large number of images and to begin to obtain statistics on these measurements, the Oxycoal Team developed an automated image-processing method. A special CMOS sensor based camera, which is more sensitive to the near infrared wavelength (responsivity: 1.4 V/lux-sec (550nm)), captured type 0 axial turbulent diffusion flame shape for statistical studies of stand-off distance at different operational parameters, such as systematic variations of partial oxygen pressure in both transport and secondary oxidant stream. During the coal-jet ignition process, the sequences of flame images were collected at 24 frames per second and were analyzed by a MATLAB®-based image processing. The image-processing code detected the flame edges using the Sobel (maximum gradient) and used the average intensity at the edges to set a threshold for the conversion to black and white image (Figure 30c). This code automatically determined the following parameters:

- average intensity of the entire image
- average intensity within the flame envelope
- visible flame length(luminous zone)
- mean stand-off distance
- stand-off distance in the centerline
- total area of the flame
- number of blobs
- flame width at different locations

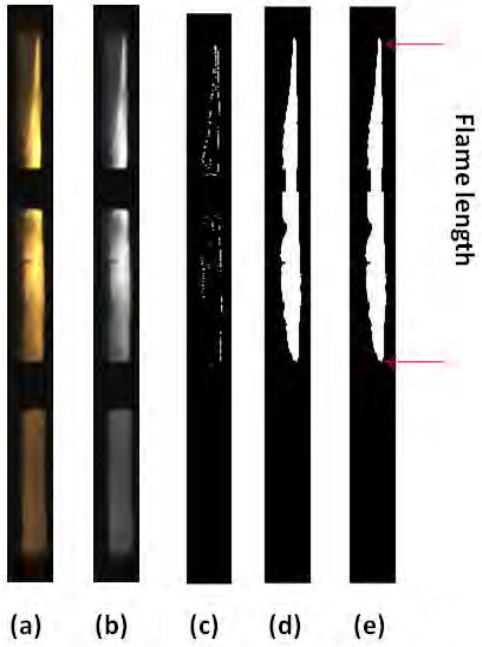


**Figure 30.** Image processing method: (a) original image, (b) image converted to grayscale, (c) edge detection using the Sobel method, (d) image converted to black and white using the threshold calculated from the Sobel method, (e) measurement of stand-off distance (if any), flame length, and intensity within flame envelope.

Summaries of the flame stand-off distance are presented as PDFs, which is computed by,

$$\rho = \frac{1}{N}\frac{dn_i}{dx_i}$$

where

$\rho$ = probability density function for the standoff distance (units 1/m or 1/cm)

N = total number of images

$n_i$ = frequency of flames starting with the $i^{th}$ bin

$x_i$ = standoff distance of the $i^{th}$ bin (m or cm)

The integration of probability density function of stand-off distance should be unity, which is $\int \rho \, dx = 1$.

Figure 31– Figure 34 depict the PDF of stand-off distance when increasing primary $P_{O2}$ from 0 to 0.207. Error bars were calculated using five replicates from different days. Other burner operating parameters were: overall $P_{O2}$ = 40%, preheat temperature = 489°K, wall temperature = 1283°K, coal type: Utah Bituminous. Two blind spots exist in the range of 0 to 11 cm and 35.1 to 41.6 cm (x-axis) due to the location of the quart windows.

The flame was detached when primary $P_{O2}$ was lower than 14.4%. Unsteady attachments were observed in the primary $P_{O2}$ = 14.4% case, which indicates that 14.4% of primary oxygen partial pressure was transition point under the above burner operating conditions. Under the condition of $P_{O2}$ = 20.7%, the

coal flame became attached. Therefore stand-off distance appears to not be a continuous variable, and attachment/detachment passes through a sudden transition when varying $P_{O2}$ in transport stream.

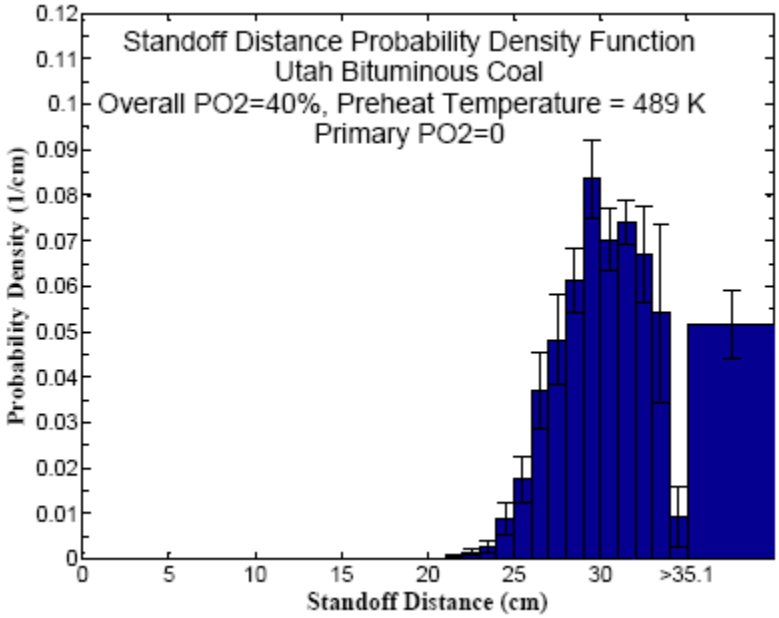


**Figure 31.** PDF of stand-off distance, an oxycoal combustion case (Primary $P_{O2}$ = 0, overall $P_{O2}$ = 40%, Preheat temperature = 489 K, S.R. = 1.15, Utah Bituminous Coal).

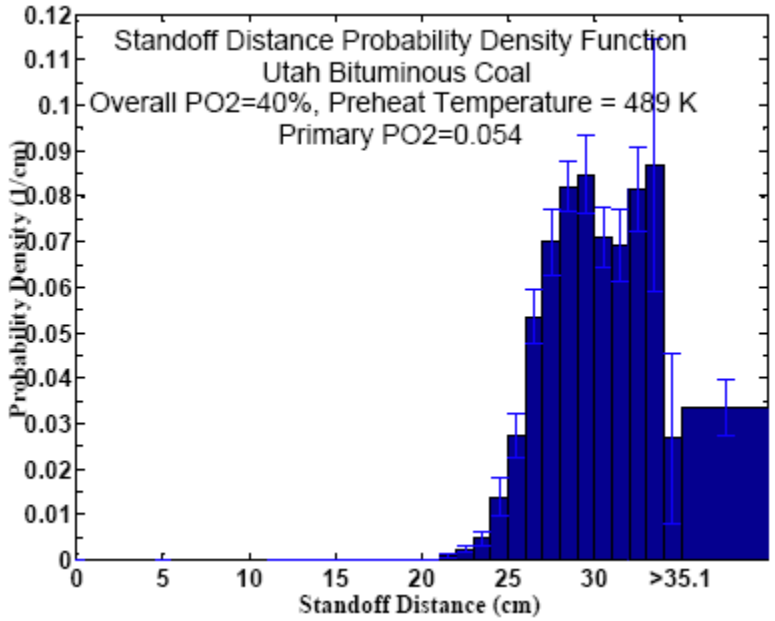


**Figure 32.** PDF of stand-off distance, an oxycoal combustion case (Primary $P_{O2}$ = 0.054, overall $P_{O2}$ = 40%, Preheat temperature = 489 K, S.R. = 1.15, Utah Bituminous Coal).

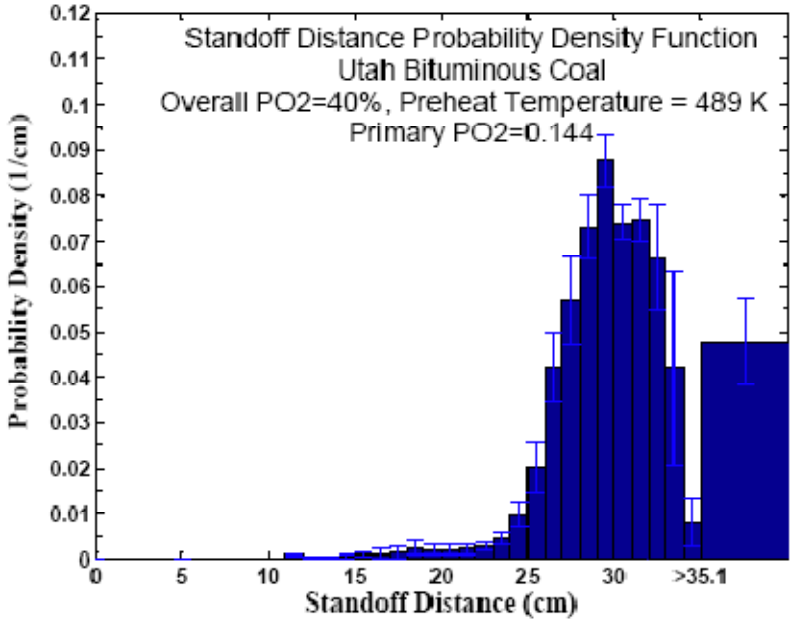


**Figure 33.** PDF of stand-off distance, an oxycoal combustion case (Primary $P_{O2}$ = 0.144, overall $P_{O2}$ = 40%, Preheat temperature = 489 K, S.R. = 1.15, Utah Bituminous Coal).

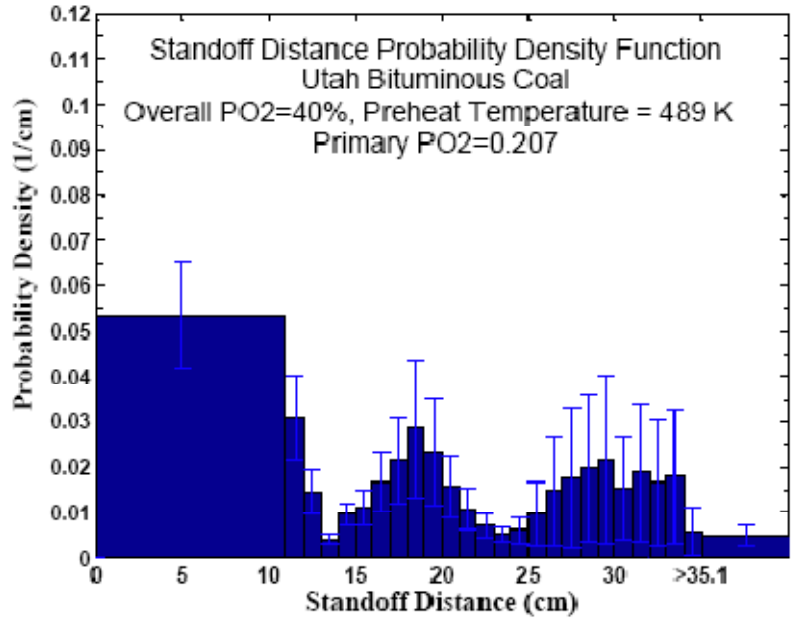


**Figure 34.** Probability density function of stand-off distance, an oxycoal combustion case (Primary $P_{O2}$ = 0.207, overall $P_{O2}$ = 40%, Preheat temperature = 489 K, S.R. = 1.15, Utah Bituminous Coal).

Figure 35 – Figure 38 shows the PDFs of stand-off distance when varying primary $P_{O2}$ from 0 to 20.7% at a higher secondary stream preheat temperature (544°K). The results are based on five replicates. The purpose of these tests was to understand the effect of preheat temperature of secondary stream on coal ignition and flame stability. Increasing primary $P_{O2}$ from 0 to 5.4% decreased stand-off distance, indicating that the flame front was moving upstream to the burner. As shown in Figure 37, primary $P_{O2}$ = 9.9% was a transition point for flame detachment and flame attachment at the elevated preheat

temperature of secondary stream. Compared with Figure 32, the secondary preheat temperature contributed significantly to the coal ignition process and flame stability.

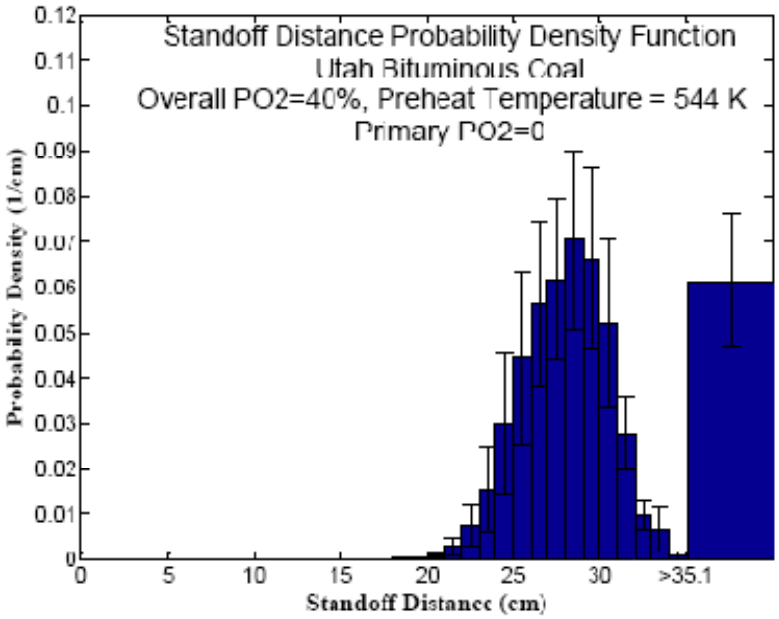


**Figure 35.** PDF of stand-off distance, an oxycoal combustion case (Primary $P_{O2}$ = 0, overall $P_{O2}$ = 40%, Preheat temperature = 544 K, S.R. = 1.15, Utah Bituminous Coal)

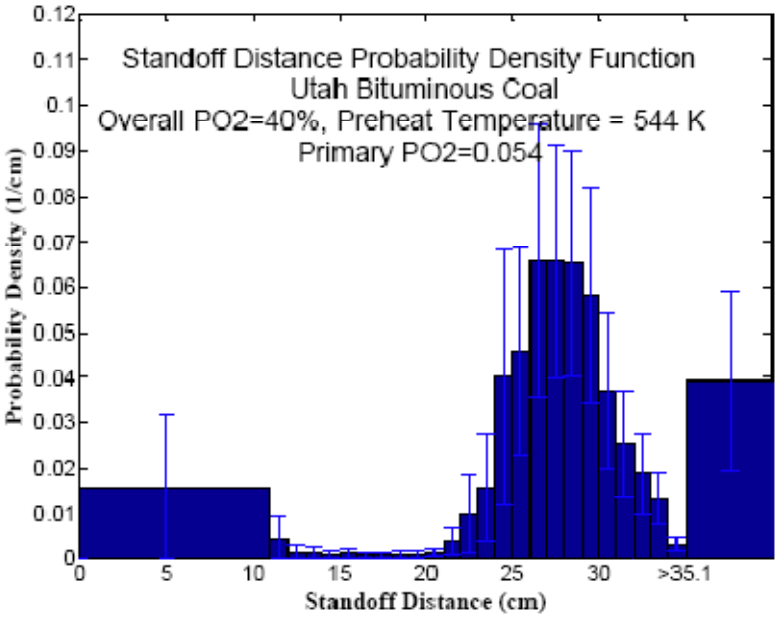


**Figure 36.** PDF of stand-off distance, an oxycoal combustion case (Primary $P_{O2}$ = 0.054, overall $P_{O2}$ = 40%, Preheat temperature = 544 K, S.R. = 1.15, Utah Bituminous Coal).

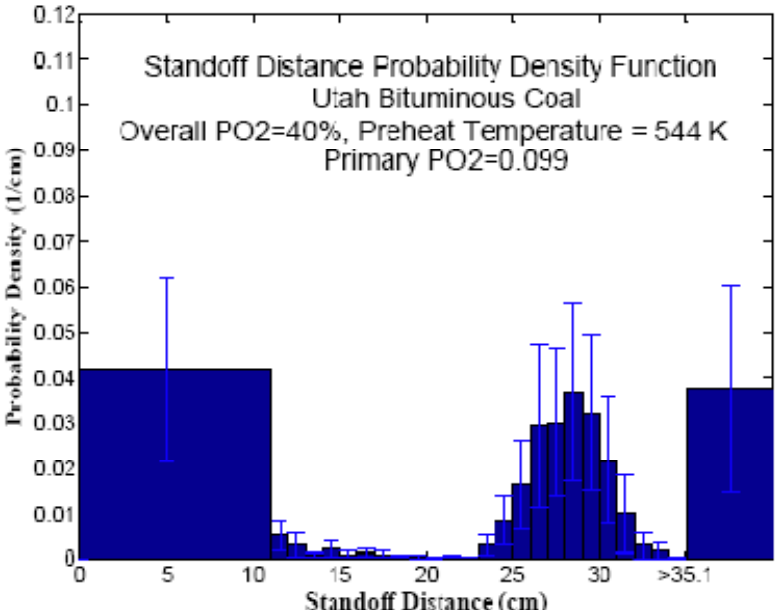


**Figure 37.** PDF of stand-off distance, an oxycoal combustion case (Primary $P_{O2}$ = 0.099, overall $P_{O2}$ = 40%, Preheat temperature = 544 K, S.R. = 1.15, Utah Bituminous Coal).

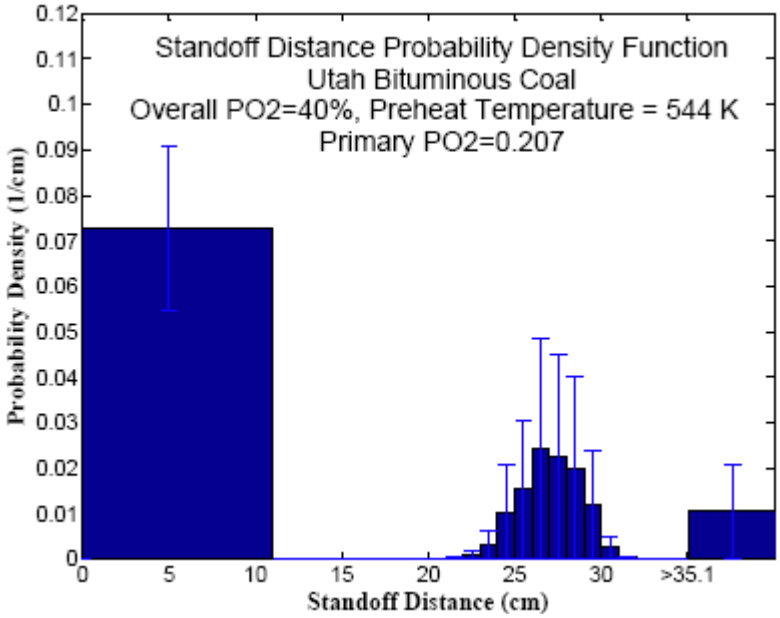


**Figure 38.** PDF of stand-off distance, an oxycoal combustion case (Primary $P_{O2}$ = 0.207, overall $P_{O2}$ = 40%, Preheat temperature = 544 K, S.R. = 1.15, Utah Bituminous Coal).

$NO_x$ emissions did not change as primary $P_{O2}$ varied as long as the overall $P_{O2}$ and stoichiometric ratio were fixed. In addition, temperature appears to have an insignificant effect on fuel $NO_x$ formation.

***Subtask 8.6 – Preliminary Comparison of Fly Ash Partitioning under Oxycoal and Air-Coal Combustion Conditions***

This subtask focused on the fate of ash and mineral matter under oxycoal combustion conditions. This has been identified as an important problem for retrofit applications.

*Approach.* Preliminary tests were conducted to examine the effect of oxycoal combustion on fly ash PSD and composition. PSDs and ash samples were collected from the OFC described in Subtask 8.1 under air-fired, air enriched, and oxy-fired conditions (Table 6).

**Table 6.** Experimental conditions.

| Setting | Air | Oxy Case 3 | Oxy Case 4 | Units |
|---|---|---|---|---|
| Coal feed | 4.54 | 4.54 | 4.54 | kg/hr |
| Primary air | 4.58 | - | - | kg/hr |
| Secondary air feed | 43.45 | - | - | kg/hr |
| Primary $CO_2$ feed | - | 5.53 | 5.53 | kg/hr |
| Primary $O_2$ feed | - | 1.04 | 1.04 | kg/hr |
| Secondary $CO_2$ feed | - | 28.12 | 17.24 | kg/hr |
| Secondary $O_2$ feed | - | 10.07 | 10.07 | kg/hr |
| Adiabatic flame temperature | 2396 | 2394 | 2797 | Kelvin |

Two particle probes were used to draw samples for analysis (Figure 39). The first collected total ash samples for loss-on-ignition measurements, and it did not utilize dilution. It featured a 7/8" I.D. pipe located inside a 1.5" water-cooled sleeve. Ash samples flowed into the filter enclosed in the probe. A vacuum pump drew the sample, and a rotameter controlled the flow at 50 SCFH. The second probe was an isokinetic dilution probe from a previous DOE-sponsored project. It utilized a stainless steel water jacket and contained a nitrogen jet at the tip of the probe allowing for dilution of the sample. It quenched reactions and reduced the amount of coagulation of small particles (Hinds, 1999).

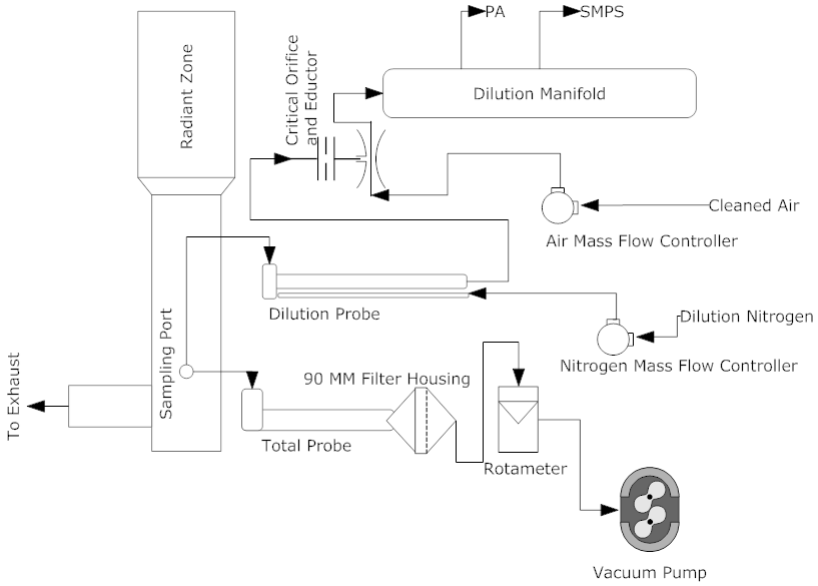


**Figure 39.** Sample collection schematic**.**

This second dilution probe was used for all scanning mobility particle sizer (SMPS), photoacoustic analyzer (PA), and Berner Low Pressure Impactor (BLPI) measurements. Dilution rates were controlled

with a mass flow controller. The BLPI samples were collected directly downstream of the dilution probe. The SMPS and PA samples were withdrawn from the probe using an eductor, which utilized filtered clean dry motive air for secondary dilution. Flow through the probe was controlled by a critical orifice at flow rate of 8.45 lpm. After flowing through the critical orifice and eductor, the diluted sample stream was sent into the dilution manifold where the SMPS and the PA simultaneously drew samples. Unfortunately, the same dilution rates are not idea for the SMPS and PA measurements.

The ash samples were prepared using EPA method SW846 3050A and analyzed using EPA method 6010B. Samples were also collected using the BLPI for SEM/EDS analysis for major species. Postdoctoral researcher Dr. Dunxi Yu performed these analyses, including Si, which required a special acid digestion.

*Highlighted results.* The loss-on-ignition (LOI) results showed that burner-influenced fluid dynamics played an important role in determining the char burnout. This affects the mixing of the $O_2$ and fuel, and in the case of the oxyfired conditions a higher $O_2$ concentration resulted in a greater average LOI. However, when comparing the oxyfired and air-fired combustion cases at matched adiabatic flame temperatures, the oxyfired cases revealed a lower LOI as a function of S.R. (Figure 40). When evaluating the LOI as a function of percent $O_2$ in the furnace or the flue gas, the air-fired conditions were actually more efficient with lower LOI results. This is consistent with drop-tube experiments (Borrego and Alvarez, 2007). This is a significant concern because not only does a full-scale oxy-fired plant lose efficiency by requiring energy to operate an air separation unit, recycle system, and $CO_2$ compressor, but it also appears that it loses combustion efficiency as well.

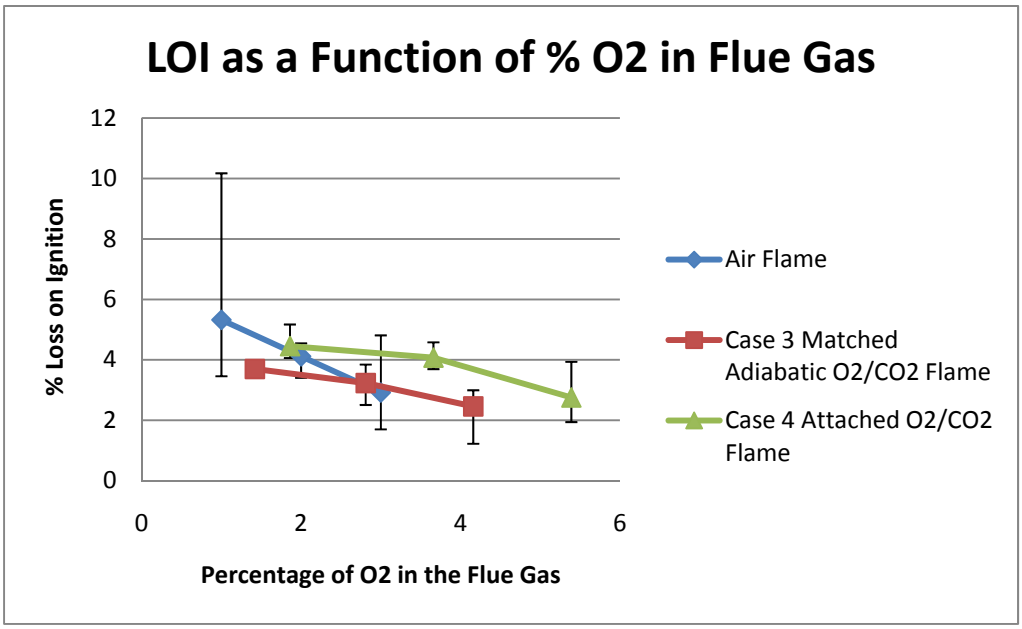


**Figure 40.** Ignition loss as a function of $O_2$ percentage in the flue gas for three flame scenarios.

Based on these preliminary experiments, it would appear that PSDs are more sensitive at the smaller end of the submicron range (Figure 41- Figure 43). The matched adiabatic flame temperature cases for air- and oxyfired conditions had very similar PSDs with a few subtle differences in modal peaks that could be driven by changes in the combustion environment. However, there was a significant difference in the ultrafine region of the high temperature case 4 suggesting greater metal vaporization. The higher concentration of ultrafine particles in a smaller volume of flue gas in the furnace under high oxygen oxy-cases facilitates greater coagulation due to less effective dilution (Hinds 1999). The greater residence

time in the furnace due to lower gas velocities caused greater metal vaporization. This may be beneficial as it will enhance the efficiency of particle capture devices.

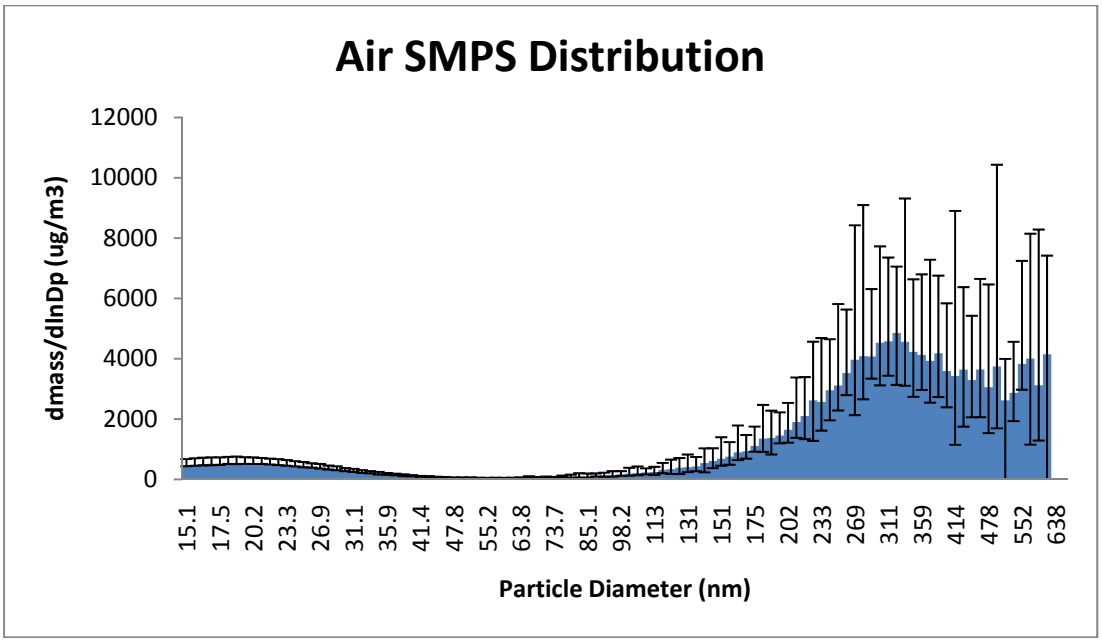


**Figure 41.** Average air-fired particle mass distribution for 15-660 nm diameter particles.

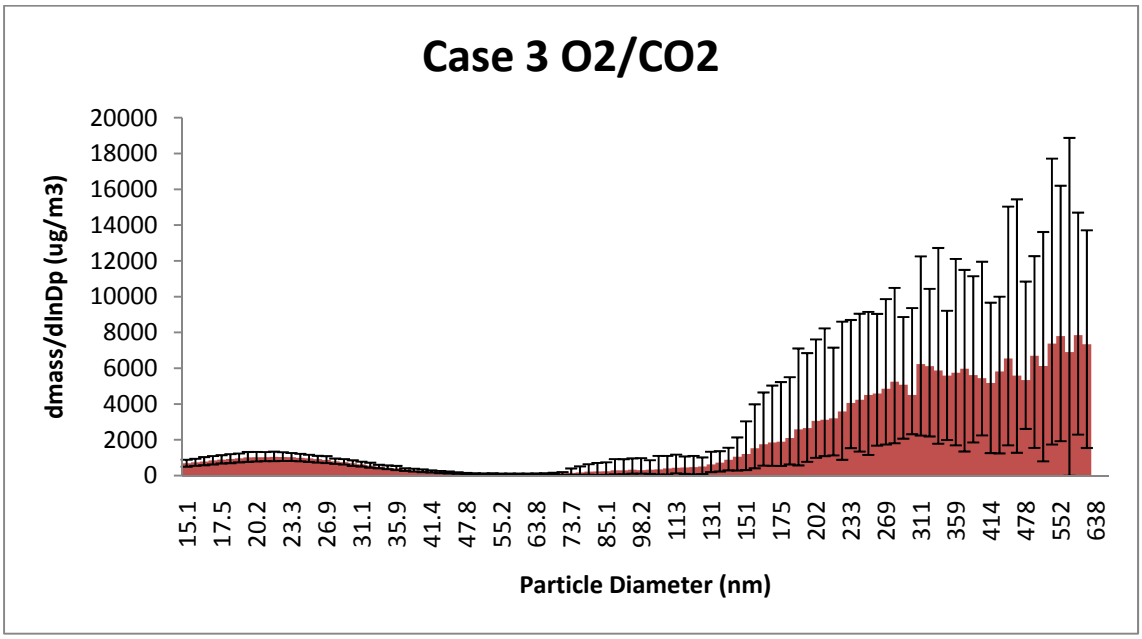


**Figure 42.** Averaged SMPS mass distribution of case 3 oxy fired conditions.

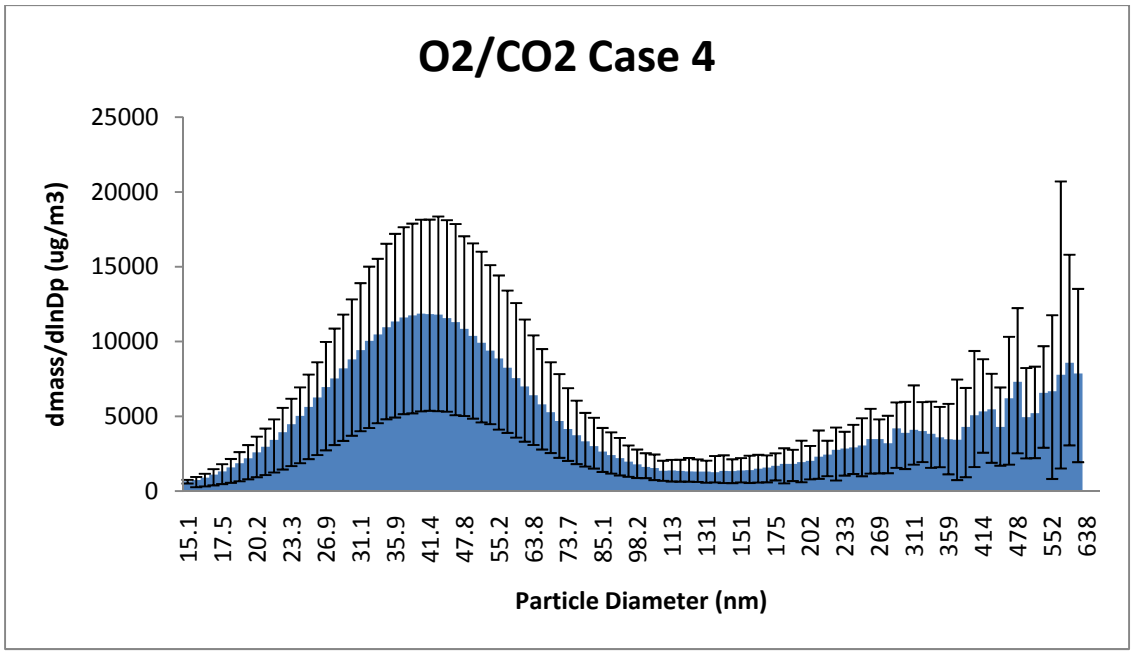


**Figure 43.** Averaged SMPS mass distribution for higher temperature case 4 oxy fired conditions.

In addition, the ash samples from the high-temperature (case 4) revealed many elements in higher relative concentrations in the submicron mode. The elements Ca, Mg, and Fe were all found in higher relative concentrations in the oxyfired cases compared to the air-fired cases, while K and Na were present in relatively higher abundance in air-fired cases. The Al concentrations were similar throughout all experiments. It can be assumed that the composition of the coal was constant, and any changes in volatility were not the result of coal composition.

The trends suggest that elements with the same type of chemical structure behave similarly. However, it is not clear what mechanism was driving the relatively higher concentrations of metals forming 2+ ions and the relatively lower concentrations of metals forming 1+ ions under the oxyfired conditions. It seems as though the $CO_2$-rich combustion environment does effect the equilibrium formation of certain compounds that form aerosols.

## Task 9.0 – Development of Fundamental Rate Parameters for Circulating Fluidized Beds

### *Subtask 9.1 – Development of a New Single-Particle, Fluidized-Bed Reactor*

*Approach.* A single-particle reactor designed for oxycoal combustion was developed with two specific objectives:

- to analyze gases produced during oxycoal combustion experiments by means of Fourier transform infrared spectroscopy (FTIR) and CO-NO infrared analyzer, and
- to extract the coal particle after specific times of reaction to evaluate changes in surface complexes and structural properties.

In addition to designing the reactor, carbonaceous materials for use in oxycoal combustion experiments were prepared. These included a bituminous Utah coal and a char obtained from pyrolysis of polyacrylonitrile ($C_3H_3N$), prepared at 600°C (PAN-6) and 800°C (PAN-8). This material was prepared with the aim of obtaining a char with a high nitrogen content. Both materials were characterized by proximate, elemental analysis, and by surface area analysis. The particle sizes ranged from 3.5 – 4.6 mm,

and particles were extracted after a pre-determined reaction time. In this way it was possible to characterize the evolution of oxygen and nitrogen complexes and identify physical changes in the char during the oxy-combustion.

The combustion temperature in the single-particle fluid-bed reactor was approximately 770°C. This temperature was not constant for all experiments due to its variation with gas composition. The fluidization velocity was 0.04 m/s (0.14 ft/s); this corresponds to a volumetric flowrate of 4 L/min. This velocity was selected after evaluating a range of velocities for its high and uniform fluidization.

Initial efforts were focused on combustion in a mixture of gases composed of $O_2$ and $CO_2$ at several concentrations; however, to determine the role of $CO_2$ concentration on oxycoal combustion it was also necessary to evaluate several concentrations for $O_2$ in $N_2$.

*Highlighted Results.* In order to obtain a char with low reactivity it was necessary to prepare it with a pyrolysis heating ramp = 20°C/min. This material was characterized by proximate and elemental analysis as shown in Table 7.

**Table 7.** Proximate and elemental analysis for coal, PAN-6 and PAN-8.

| | C % | H % | N % | O(diff) % | S % | Vol. Matter % | Fixed C % |
|---|---|---|---|---|---|---|---|
| PAN-6 | 73.03 | 2.2 | 19.61 | 4.8 | <0.05 | 34 | 65 |
| PAN-8 | 77.32 | 1.12 | 16.37 | 4.9 | <0.05 | 27 | 73 |
| Coal | -- | -- | -- | -- | -- | 43.3 | 46.9 |

Surface area analysis results are shown in Table 8 for both $N_2$ and $CO_2$ sorption. It is important to note that the heating ramp had a small effect on surface area, increasing slightly the meso- and micro-porous areas. However, the maximum temperature employed had an important effect, especially changing the distribution of porosity in the char.

**Table 8.** Surface area measurements for chars.

| | PAN-6 (4°C/min) | PAN-6 (20° C /min) | PAN-8 (20° C /min) |
|---|---|---|---|
| $N_2$ | 14.3 $m^2/g$ | 16.7 $m^2/g$ | 123.7 $m^2/g$ |
| $CO_2$ | 288.8 $m^2/g$ | 311.6 $m^2/g$ | 158.6 $m^2/g$ |

A quantitative analysis of $N_2O$ and $NO_x$ emissions was performed. Figure 44 shows an overall trend that the $NO_2$ concentration was greater under $O_2$-$CO_2$ combustion than in $O_2$-$N_2$. In addition, it shows an overall trend that $N_2O$ emissions were slightly higher under $O_2$-$N_2$ combustion than under $O_2$-$CO_2$ combustion although the effect was not as pronounced at very high oxygen concentrations.

Overall trends showed $N_2O$ increases with higher $O_2$ % for both $O_2$-$CO_2$ and $O_2$-$N_2$ combustion. For the $O_2$-$CO_2$ system an interesting effect occurred: $NO_2$ decreased with a higher $O_2$ concentration, while $N_2O$ increased, which indicated a change in the mechanism for $NO_x$ emissions when shifting from $N_2$ to $CO_2$ as the diluent.

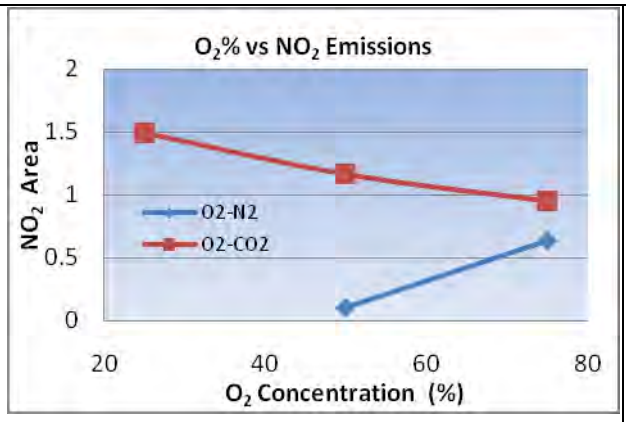


**Figure 44.** $O_2$ concentration vs. $NO_2$ emissions.

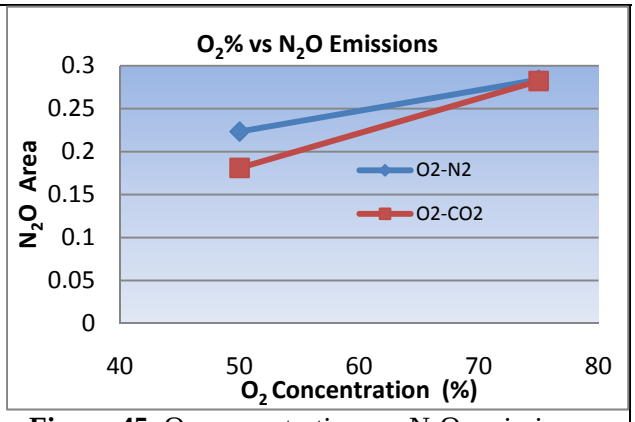


**Figure 45.** $O_2$ concentration vs. $N_2O$ emissions.

Figure 46 indicates that NO emissions increased with higher oxygen concentrations, independent of which balance gas was used ($N_2$ or $CO_2$). However, when $O_2$-$CO_2$ was the reacting gas, NO emissions were higher than the NO produced with $O_2$-$N_2$ as the reacting gas. Although these tests were repeated, the trends were not always evident due to variations in the coal mass. Therefore, the reported data were normalization by coal mass to account for variations in fuel-N loading in the reactor (Figure 46). When the data are reported in this fashion, the trend was always consistent with that indicated in Figure 46.

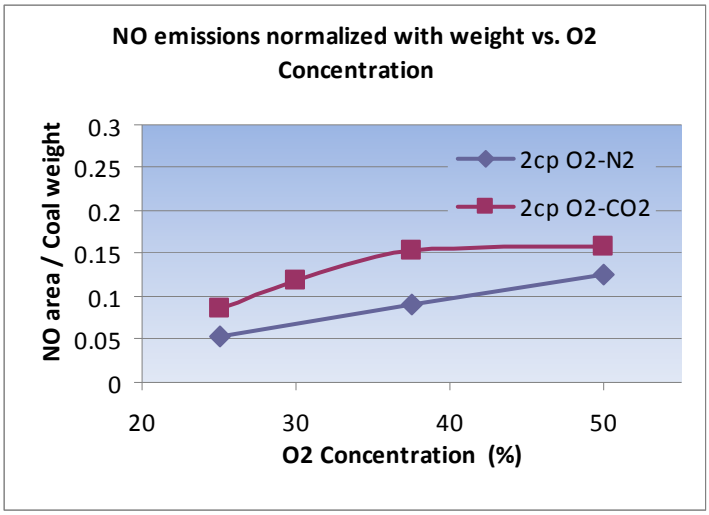


**Figure 46.** $O_2$ concentration vs. NO emissions normalized by coal weight for 2 coal particles in the reactor.

Only a qualitative analysis of CO observations could be reported due to its high production. However, it was observed that CO emissions rise with higher $CO_2$ concentrations.

It is important to note that the primary signal for $N_2O$ is close to the CO frequency absorption, which made it difficult to quantify this important component by means of FTIR. Consequently, the secondary signal was used although this represents a higher level of uncertainty due to its lower intensity. Another difficulty encountered in this study was the presence of water, since this signal interferes with $NO_2$ and NO frequency absorption.

***Subtask 9.2 – Collection of Experimental CFB Data for Model Validation***

*Approach.* The CFB facility stands approximately 21 feet in height with an outside shell diameter of 24 inches. The internal cross-section is 10 inches in diameter. The furnace consists of five main sections: plenum/distributor; lower bed; freeboard. A significant effort was put into modifying the CFB in order to conduct flow experiments. All necessary measurement devices were installed including mass flow controllers, thermocouples, pressure transmitters, etc., and they have been integrated with the OPTO 22 data acquisition hardware/software platform. The plumbing necessary to allow recirculation of flue gas was added, as well as a method for ash removal. More detailed information regarding the CFB facility, along with several labeled schematics, is provided in Appendix C.

Cold-flow testing was conducted to determine minimum fluidization velocities and to attempt to validate pressure measurements through the aid of literature references. Each minimum fluidization test was run in triplicate so that statistical analyses could be made, and 6 to 10 pressure measurements were made for each pressure test, which were run with both gauges and computer data acquisition programs. In addition, pressure measurements were made through the various portions of the CFB facility.

The bed was loaded with both 100 lb and 50 lb of 4095 quartz. The gas mass flow was measured as it varied and was subsequently converted to gas velocity values. The pressure drop measured was between the bottom of the bed and a point along the freeboard of the fluidized bed, and the gas velocity represents the superficial gas velocity. The method from Kunii and Levenspiel (1991) provided a general form for the calculation of this velocity.

To validate pressure data, six additional pressure ports were added to the CFB facility, and pressure measurements collected made through the ten ports of the CFB facility.

After the new distributor was fabricated and installed, the furnace was then heated up and coal was fed into the furnace. Initial testing was performed with 25 lbs/hr of coal in order to show the temperature profile and emissions data of the furnace.

Although the original statement of project objectives included testing with natural gas instead of coal due to the limited budget, the investigators received complementary funding (from Praxair Inc.) to develop oxycoal firing capabilities and were able to perform oxycoal tests. Consequently, the Oxycoal Team performed three campaigns for oxygen firing and flue gas recycle (FGR). The first focused on developing the procedure for switching from air-firing to oxy-firing with FGR, preliminary temperature and outlet $CO_2$ data. The second was to demonstrate firing with a low $N_2$ content in exhaust. The last was to obtain CO, NOx and $SO_2$ concentrations for varying bed oxygen concentrations, as well as for baseline air conditions.

Since the first tests of coal testing proved successful, additional tests were performed with increasing the firing rate. In the final test it was possible to run up to 40 lbs/hr of coal. Temperature, emissions and pressure were measured for all sectors of the CFB. Solids sampling ports were added at various locations by installing a small pipe with a ball valve that could be opened periodically to allow solids to flow out of the reactor.

*Highlighted Results.* The minimum fluidization velocity for a bed of 100 pounds of 4095 size sand was determined from the data shown in Figure 47, and was calculated to be 1.89 feet per second. The value obtained from a theoretical correlation was 1.22 feet per second, and the deviation between these two values is 35.45%.

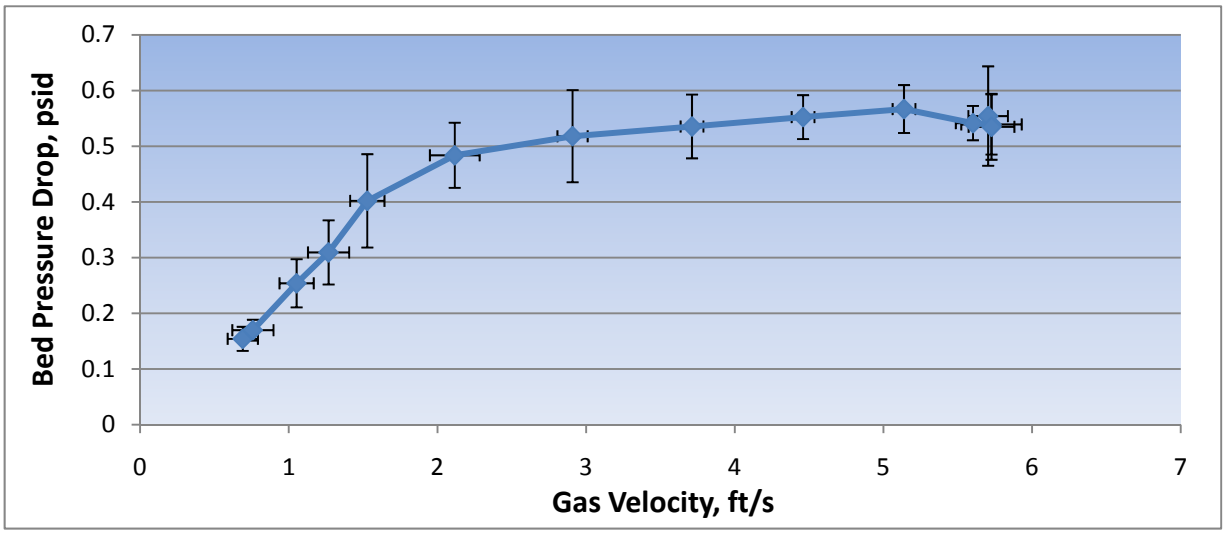


**Figure 47.** Average aeration curve for a 100 pound loading of 4095 quartz with associated error calculated to within a 95% confidence level.

Pressure transmitters used for both minimum fluidization and pressure validation tests were corrected to a constant gauge pressure. These measurements were correlated with Bernoulli's equation for pressure drops across the distributor plate and found to agree with a least-squares fit of 0.999.

For validation of pressure measurements it was concluded that a more sensitive and higher resolution sensor is required.

During hot flow, temperatures of sections 1 through 5 and the transition section were well controlled. Initial testing was performed with 25 lbs/hr of coal. Figure 48 and Figure 49 illustrate the temperature profile and emissions data. All of the temperatures throughout the furnace converged to approximately 1650°F. At lower temperatures, the CO concentration was fairly high, but as the furnace heated up this concentration decreased.

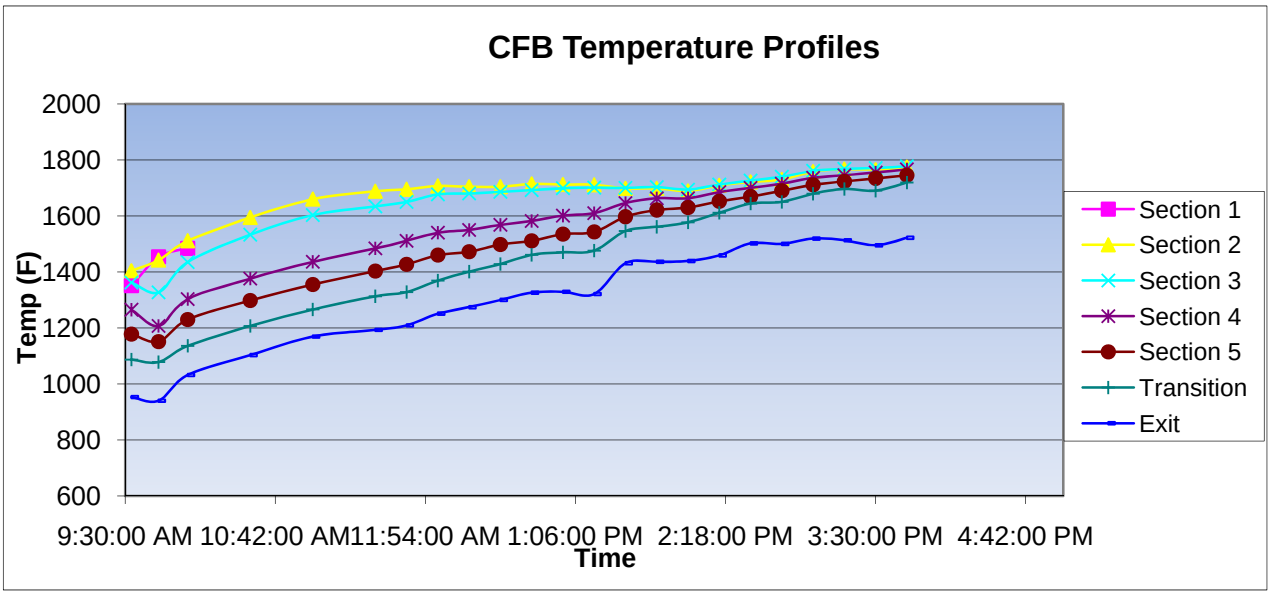


**Figure 48.** CFB temperature profile (25 lbs/hr coal).

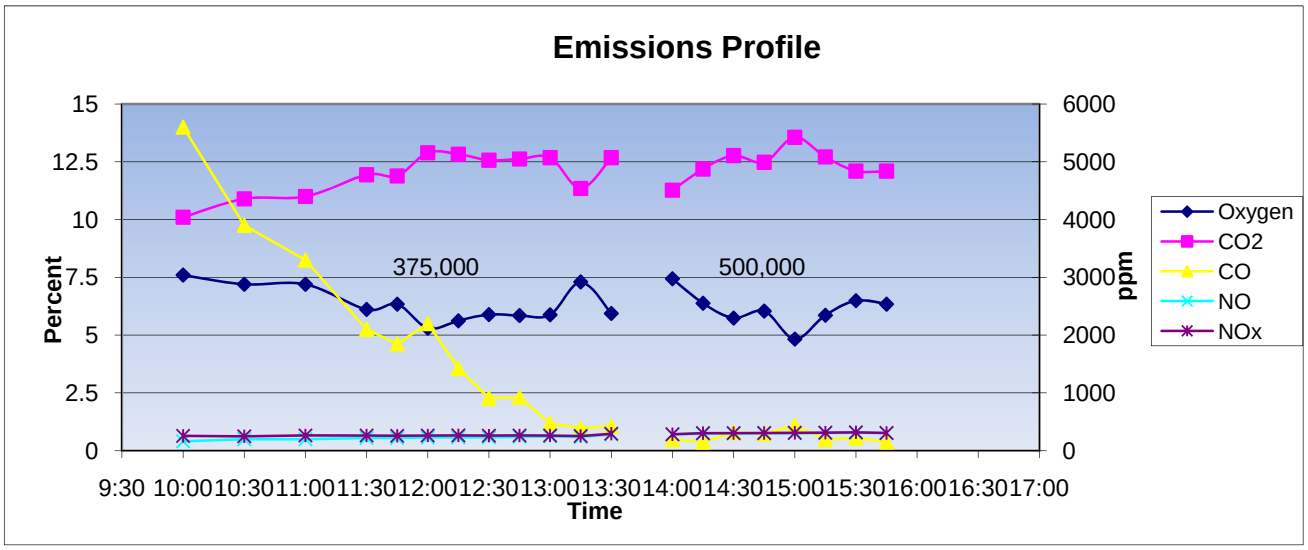


**Figure 49.** CFB emissions profile (25 lbs/hr coal).

Pressure measurements in Figure 50 were relatively constant or asymptotic with the exception of a perturbation after the system was reinitialized at about 14:40 due to pluggage in the cyclone. A plug in the system was even more evident when analyzing the pressure data because as the plenum, bed, and loop seal pressures decrease, the cyclone pressure increases. The decrease in pressures showed that the bed was no longer fluidizing and would soon cease circulating altogether, while the increase in cyclone pressure showed a back-pressure through the transition section, forcing more material out the top of the cyclone.

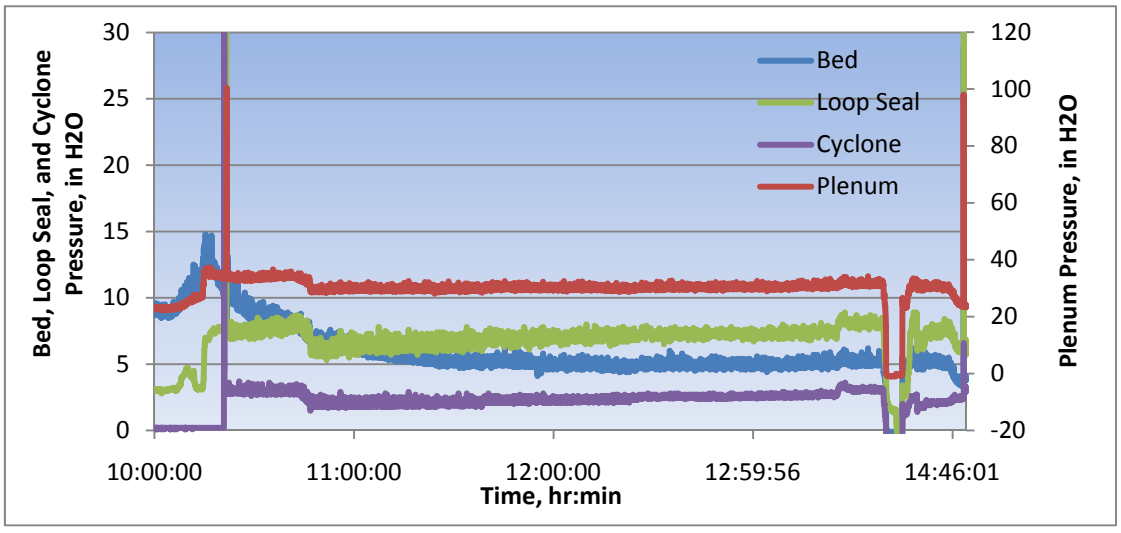


**Figure 50.** Pressure profiles of the plenum, bed, cyclone, and loop seal versus testing time.

While the above temperature profiles are indicative of the heat transfer effects, the carbon-conversion data are important when considering the reactions within the bed. Table 9 shows the data for loss on LOI tests performed on the carbon samples extracted from the CFB during the testing. The locations of port numbers given in Table 9 are provided in the detailed information in Appendix C (Figure 3).

**Table 9.** LOI data for hot flow testing of Utah bituminous coal.

| | Port 7 | Port 7 | Port 7 | Port 7 | Port 5 (1) | Port 5 (2) |
|---|---|---|---|---|---|---|
| Sample Time | 11:30 | 13:00 | 14:00 | Shut Down | 12:00 | 12:00 |
| Percent LOI | 5.74% | 5.62% | 3.67% | 3.84% | 4.47% | 3.62% |

Most of the samples were collected at Port 7, which is in the freeboard region in Section 4. A few samples were collected at Port 5, which is slightly lower than Port 7 but still above the coal feed location.

## GASIFICATION

The overall aim of the Gasification area was to improve the understanding of coal conversion in high-pressure, high-temperature, entrained-flow gasifiers, and to develop simulation submodels for such systems. A more comprehensive summary of the Gasification area can be found in the Gasification Topical Report (Appendix D).

### Task 10.0 – Coal Conversion Studies

The objective of this task was to improve the understanding of coal conversion under high-temperature, high-pressure gasification conditions.

#### *Subtask 10.1 – Investigation of Pressurized Pyrolysis and Char Conversion*

The purpose of this subtask was to characterize chars generated at pressures of up to 15 atm, temperatures of up to 1700°K, and residence times of up to 0.5 seconds. These measurements and tests on chars generated at high heating rates (~$10^5$°K/s) in a pressurized flat-flame burner (PFFB) allow existing devolatilization and gasification models to be enhanced.

*Approach.* Significant challenges were encountered and overcome in the pursuit of the research objectives. In the beginning of the project the original PFFB required a new pressure vessel to comply with state legal requirements. The opportunity was taken to implement other improvements to the system. The burner was changed from a down-flow configuration to up-flow to reduce thermal degradation. New heating/insulating units were installed to maintain a high temperature in the reaction zone. The collection probe was replaced with a moveable version. Figure 51 illustrates the redesigned system. These and other changes necessitated the development of new operating procedures and support systems such as ignition, reliable particle entrainment, temperature control and flow control.

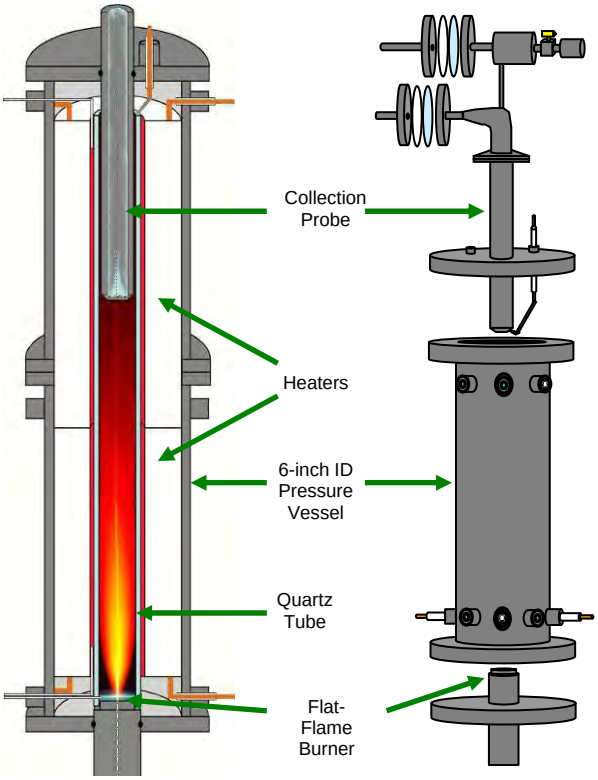


**Figure 51.** BYU HPFFB interior (left) and exterior (right).

The PFFB system upgrades were completed, and its range of operating conditions was extended through changes in fuel mixture and burner geometry. The PFFB system is capable of heating rates on the order of $10^5$ °K/s, gas temperatures of 1200-1800°K, and pressures of 2.5-15 atm. These operating conditions are particularly well-suited to the study of the development of char structure and surface area during pyrolysis and gasification. The surface area and particle size available for gasification strongly influence the overall gasification rate. Heating rate has been observed to have a strong impact on the size and physical structure of chars at atmospheric pressure. The size and structure of chars strongly influences the gasification rate. The PFFB facility permits the investigation of particle size, structure, and intrinsic reactivity at high heating rates and pressures relevant to the gasification industry. Previous gasification studies have been performed in facilities with lower heating rates that produce chars that are highly swollen and not representative of chars produced in industrial facilities at ~$10^6$ °K/s.

*Highlighted results.* Pyrolysis and char gasification experiments were conducted with a Wyodak subbituminous coal at 2.5 atm, a peak flame temperature of 1640°K, and residence times of 30 ms, 60 ms, and 220 ms. Little if any swelling of the coal occurred, and the chars were highly porous (Figure 52). The mass release due to gasification was large. Under subsequent studies, further analysis is being conducted on these chars and the soot produced.

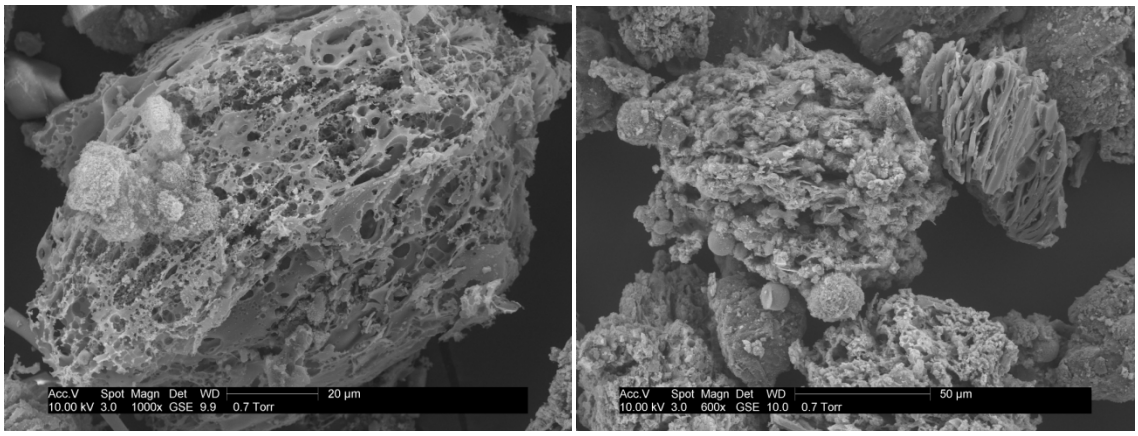


**Figure 52.** Wyodak Char produced at 2.5 atm, residence time of 60 ms (left) and 220 ms (right).

### *Subtask 10.2 – Investigation of Soot Formation during Gasification*

The purpose of this subtask was to improve the understanding of soot formation from coal tar under gasification conditions by choosing model compounds to represent coal tar and subjecting them to high heating rates in flat-flame burner systems. The resulting soot was captured and analyzed to determine how the chemical structure of the model compound changes when it is subjected to different pyrolysis conditions.

The model compound 2,6-dimethylnaphtalene was studied as a precursor for soot in an atmospheric flat-flame burner. Information regarding changes in cluster size and aliphatic groups was obtained through $^{13}$C-NMR (nuclear magnetic resonance) analysis, and FTIR was used to obtain qualitative information about gaseous species that were formed. However, the yield of products at the optimum experimental temperature was too low to perform more extensive analysis.

A review of coal tar characteristics was conducted to facilitate the selection of future model compounds. On average aromatic clusters in tar molecules contained at least one oxygen atom. Nitrogen atoms occurred once in every 2-3 clusters on average. Other characteristics such as cluster size and the number of attachments per cluster were quantified. New model compounds were selected based on these characteristics. 6-(5H)-Phenanthridinone was chosen for the first experiments because it has both oxygen and nitrogen. However, the Gasification Team found that phenanthridinone was much easier to handle than the dimethylnaphthalene and had a much higher product yield of products.

Experiments with the model compound 6-(5H)-phenanthridinone were conducted on the atmospheric flat-flame burner. An eastern bituminous coal and a Wyodak subbituminous coal were subjected to the same experimental conditions. The tar and soot from the model compound and the two coals were collected for analysis. The yield of gas-phase species was determined using FTIR. The NMR data obtained on the PDN did not exhibit as much structural change as that observed in the coal data (Figure 53). This was an unusual result, and further consideration of the time/temperature profile will be necessary in order to understand the validity of these data.

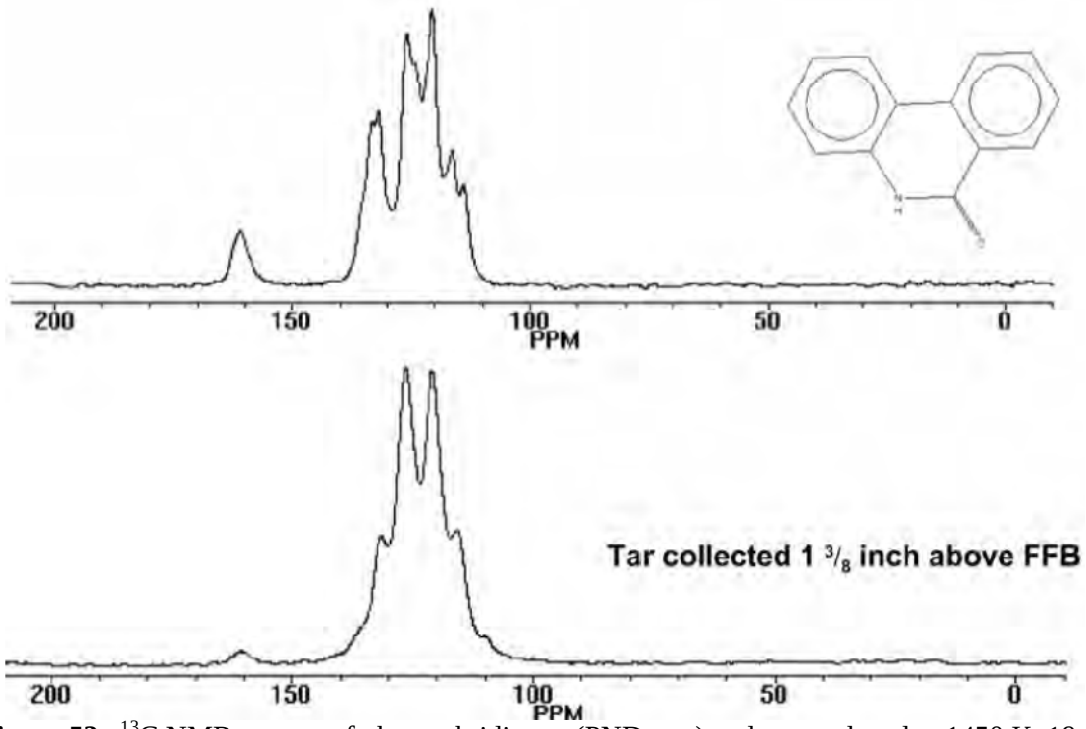


**Figure 53.** $^{13}C$ NMR spectra of phenanthridinone (PND, top) and tar produced at 1450 K, 19 ms.

***Subtask 10.3 – Investigation of Char Burnout***

*Approach.* Under this subtask, a new high-temperature atmospheric pressure laminar entrained-flow reactor (LEFR) was constructed at the University of Utah. This system was used to prepare coal char in either inert or reacting conditions to allow study of char properties at high conversion near the point where the char collapses into molten slag.

The LEFR used in this study for char and ash preparation is shown in Figure 54. It consists of a high temperature furnace, a coal feeder, a sample collector, gas supply and cooling water circulator. Two co-axial alumina tubes (89 mm O.D. × 75 mm I.D. × 1500 mm long and 57mm O.D. × 50 mm I.D. × 1000 mm long, respectively) were mounted vertically inside the furnace (Carbolite, single zone, 1600 °C maximum operation temperature and 610 mm heated length) and sealed with flanges. The inside tube was used as the reactor. The reaction gas (a premixed air–nitrogen mixture) was injected through three injection ports on the bottom flange and was preheated as it flowed upwards through the annulus between the two co-axial tubes. When the reaction gas reached the top of the annulus, it turned and flowed down into the inner tube through an alumina honeycomb flow straightener. The flow straightener had a sufficient pressure drop to generate a uniform and laminar flow. Coal particles were fed into the reactor through an injection probe using a vibrating syringe-pump-type coal feeder with nitrogen as carrier gas. The injection probe was water-cooled to prevent the coal particles from being heated before reaching the reaction zone. Upon injection into the reactor, the coal particles underwent pyrolysis and reacted with the reaction gas to produce char particles. The reacting products exited the reactor through a water-cooled collection probe. Nitrogen was injected into the collection probe through a sintered stainless steel tube to quench the product stream and reduce the thermophoresis deposit of the char particles on the cold surface of the probe. Char particles were collected using a cyclone separator followed by a filter.

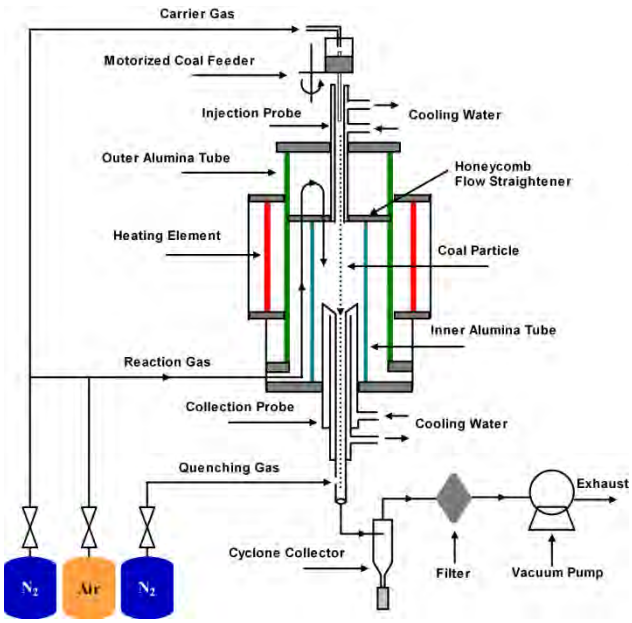


**Figure 54**. Schematic diagram of the LEFR used for preparing char and ash samples.

A pulverized Illinois # 6 bituminous coal was sieved to 104 μm or less for this study. The coal was dried in a muffle furnace at 104 °C for 24 hours to remove the moisture before sieving. Properties of the coal sample are presented in Table 10.

**Table 10.** Properties of the Illinois #6 coal used in this study.

| Analysis | |
|---|---|
| Proximate analysis (wt%, dry) | |
| Moisture[a] | 3.63 |
| Ash | 10.89 |
| Volatiles | 36.42 |
| Fixed carbon | 52.69 |
| Ultimate analysis (wt%, dry ash free) | |
| C | 74.52 |
| H | 4.96 |
| N | 1.48 |
| S | 4.66 |
| O | 14.56 |
| Ash fusion analysis (oxidizing, °C) | |
| IT | 1244 |
| ST | 1254 |
| HT | 1286 |
| FT | 1343 |

[a]As received

For the experiments performed in this study, the pressure inside the reactor was maintained at local atmospheric pressure, 0.84 atm (in Salt Lake City). Experiments were carried out at four temperatures (1200, 1300, 1400 and 1500 °C), which cover the range below and above the ash fusion temperatures. Two kinds of experiments were performed: devolatilization experiments and oxidation experiments. In the devolatilization experiments, the residence time was fixed at 2 s. The devolatilization gas was pure nitrogen, which provided an inert gas environment. The residence time was controlled by adjusting the flow rate of devolatilization gas at different temperatures. The flow rate of coal carrier gas flowing through the injection probe was set to maintain the same velocity as the devolatilization gas in the reactor. In the oxidation experiments, the residence time varied from 1.5 s to 6 s to achieve various carbon conversions. The use of long residence time was due to the low oxygen content (1.8%–5.7%) in the reaction gas for the low coal feeding rates (20 mg/min). The residence time was controlled by adjusting the flow rate of nitrogen while fixing the flow rate of air in the reaction gas. This also varied the oxygen concentration in the reaction gas. The flow rate of the air in the reaction gas was set to be 0.24 SLPM (standard liter per minute), which was 50% more than necessary for complete combustion of coal. The flow rate of the coal carrier gas was set to maintain the same velocity as the reaction gas in the reactor. The flow rate of nitrogen in the reaction gas was equal to the total gas flow rate minus the air and the carrier gas rates in the reactor.

The carbon content of the char particles was determined using a hot foil LOI instrument (FERCO, HF400). Using ash as a tracer, which assumes conservation of the ash in the char before and after the reaction, the corresponding conversion $X$ was calculated as

$$X = \left(1 - \frac{(Carbon\ Content)_{char} \cdot (Ash\ Content)_{coal}}{(1-(Carbon\ Content)_{char}) \cdot (Fixed\ Carbon\ Content)_{coal})}\right) \cdot 100\%$$

The surface area and pore size distribution of the char particles were measured by gas adsorption analysis using a surface area and porosimetry analyzer (Micromeritics, ASAP 2010) with $N_2$ as adsorptive gas at 77 K (liquid nitrogen bath). Each sample was degassed under 10 μm Hg pressure and 350 °C for 2 hours in order to remove moisture before the analysis. The surface area was calculated using the BET (Brunauer–Emmett–Teller) method.

Microimages of the char and ash particles were captured using a scanning electron microscope (FEI Nova nano). The accelerating voltage was 10–15 kV and the working distance was 5 mm. Particles were adhered to the sample holder using silver paste as conductive base.

*Highlighted results.* The conversions of coal chars prepared under various reaction temperatures are plotted as a function of residence time in Figure 55. The data points are the averaged result of three experimental runs. As expected, it took less time to reach the same carbon conversion at higher temperature than that at lower temperature.

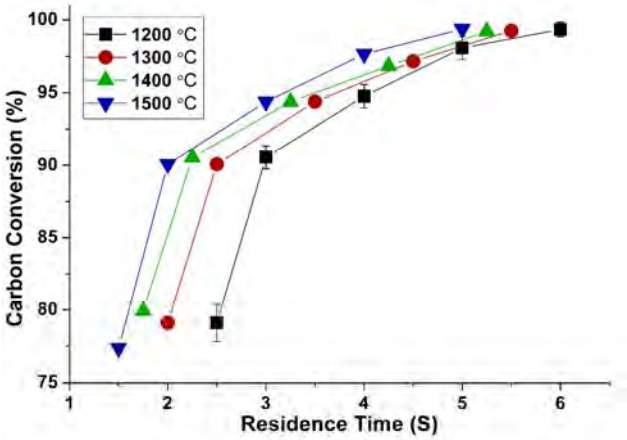


**Figure 55.** Coal conversion of char particles prepared at different temperatures.

Surface areas of fresh chars prepared at 1200, 1300, 1400 and 1500°C are 41, 45, 49, 62 $m^2/g$, respectively. In order to allow comparison of samples prepared under different conditions and to follow the evolution of surface area during conversion, the normalized surface was used instead of the specific surface area. To normalize the data, the surface area per unit mass of oxidized char was divided by the surface area per unit mass of the fresh char prepared at the same temperature, which is defined as the initial surface area. The surface area profile of the oxidized char particles at various temperatures is plotted versus carbon conversion in Figure 56. For all four temperatures, the normalized surface areas decreased with conversion and fall below the initial surface area at around 90% conversion. This trend is consistent with observations from other researchers (Simons, 1983; Hurt et al., 1991).

Remarkable differences existed in the surface area profile at high conversion (above 90%). The normalized surface areas decreased more rapidly at higher temperatures than those at lower temperatures. In particular, the normalized surface areas of chars prepared at 1400 and 1500 °C eventually fell below those at 1200 and 1300 °C. This indicates that temperature had an effect on the surface area of the char at high conversion. Liu et al. (2006) attributed the decrease of char surface area at high temperatures to ash melting, which closed the pores of the char resulting in an inaccessibility of the pores to adsorptive gas. Lin et al. (1994) also pointed out that the ash melting contributes to the decrease in the surface area of micropores and mesopores, especially at high conversion because the ash content increased with increasing conversion. The Illinois # 6 coal used in this study had an ash fluid temperature of 1343 °C, which is above 1200 and 1300°C and below 1400 and 1500°C. Therefore, the more rapid decrease in the surface areas of char particles at 1400 and 1500 °C indicates melting of ash minerals in the char.

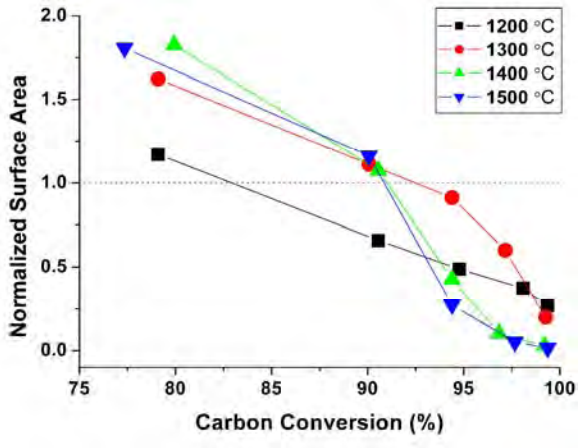


**Figure 56**. Evolution of surface area per unit mass of char at various temperatures.

Scanning electron microscopy (SEM) images of chars prepared at 1200°C (below ash fusion temperature) and 1400°C (above ash fusion temperature) are presented in Figure 57 and highlight important structural and morphological features during the transition. The images of char reacted at 1200°C did not show significant change throughout conversion. It can be observed that the fresh char had a porous structure. The char oxidized to 80% conversion still looked porous. Although some mineral grains can be seen on the char surface, the non-spherical shape suggested that they were not melted. The unmelted minerals are unlikely to close the micropores and mesopores in the carbon, which create the surface area of the char. Therefore, the char still had relatively high surface area. As conversion increased to about 94% and 99%, most of the carbon in the char was consumed and the char transformed to ash particles. These ash particles did not melt throughout the oxidation process at 1200°C, as indicated by their rough surface and irregular shape. This agrees with the results in Figure 57 that surface areas of the char oxidized at 1200 and 1300°C do not decrease.

In contrast, the images of char oxidized at 1400 °C showed significant change throughout the oxidation process. The fresh char had a porous structure, similar to that of the char prepared 1200 °C. However, at around 80% conversion, some melted (as indicated by the droplet shape) mineral grains started to appear on the char surface. As conversion increased to about 94%, many melted mineral droplets (molten slag) were observed while some porous char still exists. The melted minerals presumably had a tendency to close the micropores and mesopores in the carbon. The closing of micropores and mesopores in the carbon resulted in the decrease of surface area as shown in Figure 57. As conversion increased to about 99%, the material appeared to have completely melted, as indicated by its smooth surface and spherical shape. The melted material can be classified as molten slag due to its smooth surface and solid structure. Consequently, the transition from porous char to molten slag at 1400 and 1500 °C was responsible for the sharp decrease in the surface area at around 90% conversion.

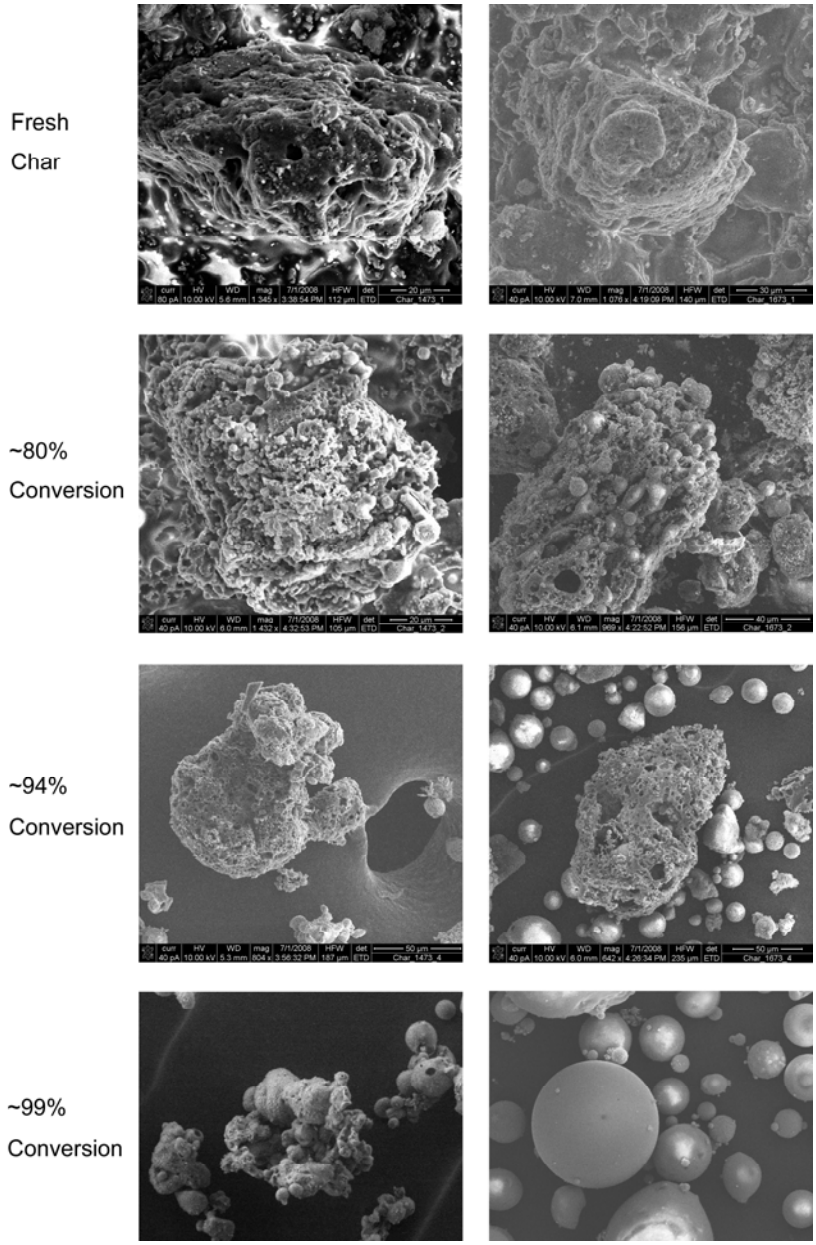


**Figure 57.** SEM images of char particles: left, 1200 °C; right, 1400 °C.

### Task 11.0 – Study the Effect of Ash Characteristics and Deposition on Refractory Wear

#### Subtask 11.1 – *Coal Selection and Characterization*

The four coals chosen for the experimental work were Pittsburgh #8, Illinois #6, Black Thunder PRB and Beulah Zap lignite. Typical proximate and ultimate analyses of these fuels, as well as the heating value, are presented in Table 11. Due to the cost of transporting and pulverizing these fuels, it was impractical to purchase large quantities of all fuels at once. Rather, the experimental teams worked with existing inventories of these fuels and subjected these coals to proximate, ultimate and heating value analyses as necessary. During subsequent studies, it may be necessary to procure large inventories of particular fuels

for testing in the University of Utah's large-scale facilities. When new coal is procured it will be analyzed in a similar manner and records will be kept for the various coals.

**Table 11.** Target fuels with typical proximate, ultimate and heating value analyses.

| **Coal** | **Pittsburgh #8** | **Illinois #6** | **Black Thunder** | **Beulah Zap** |
|---|---|---|---|---|
| **Coal Type** | Bituminous | Bituminous | Sub-Bituminous PRB | Lignite |
| **Proximate Analysis** | | | | |
| Moisture (wt% of as-received fuel) | 1.08 | 2.54 | 21.30 | 26.89 |
| Ash (wt% dry) | 9.00 | 12.33 | 6.46 | 13.86 |
| Volatile matter (wt% dry) | 38.22 | 39.40 | 54.26 | 42.78 |
| Fixed carbon (wt% dry) | 52.64 | 48.28 | 39.28 | 43.36 |
| **Ultimate Analysis** (wt% dry ash-free) | | | | |
| Carbon | 84.07 | 78.91 | 74.73 | 70.49 |
| Hydrogen | 5.58 | 5.50 | 5.40 | 4.75 |
| Nitrogen | 1.53 | 1.38 | 1.00 | 1.22 |
| Sulfur | 3.86 | 4.00 | 0.51 | 2.14 |
| Oxygen | 4.96 | 10.09 | 18.27 | 21.36 |
| Chlorine | n/a | 0.11 | 0.08 | 0.05 |
| **Heating Value** | | | | |
| HHV, dry (Btu/lb) | 13,859 | 12,233 | 12,815 | 10,040 |

### *Subtask 11.2 – Modeling of Coal Ash Sintering and Melting*

*Model Development*. Figure 58 illustrates the geometries used to define the terms in this sintering discussion. In this derivation, two spheres of radius R initially touch at a point. The distance along their common symmetry axis, designated z, originates at the initial point of contact. As sintering proceeds, the sphere radius does not change, but the point of contact grows to a neck, with the extent of sintering, $Z_s$, given by the difference between the original point of contact and the horizontal symmetry line between the spheres, which also corresponds to the narrowest section of the neck. The portion of the spheres that is overlapped on either side of $Z_s$ is transferred to the neck, forming a neck that connects with the original spherical body at a point $Z_c$. This model presumes a conservation of both mass and volume during this process.

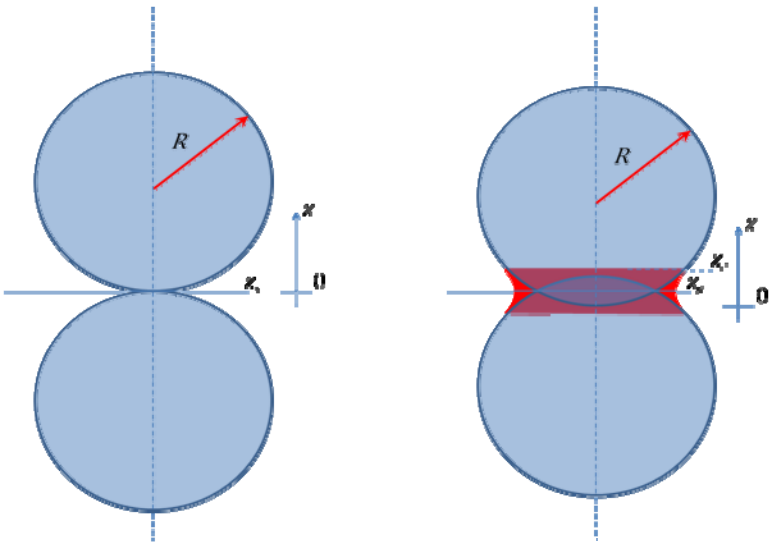


**Figure 58.** Illustration of the geometries used in the sintering discussion.

An axisymmetric body, or volume of revolution, contains a volume determined from the formula

$$V = \int_0^L \pi f^2(z)\, dz$$

Where *f*(z) is the thickness (distance from the symmetry axis) of the body of revolution as a function of and *L* is the length of the body in the *z* direction. In the case of sphere with *z* = 0 at the bottom of the sphere as illustrated,

$$f^2(z) = R^2 - (R - z)^2 = (2R - z)z$$

so

$$V_{sphere} = V_s = \int \pi(2R - z)z\, dz = \frac{1}{3}\pi(3R - z)z^2$$

Later it will be important to calculate the volume between two locations, which volume is given by

$$V_{z_1 - z_2} = \frac{1}{3}\pi[z_1^3 - z_2^3 + 3R(z_2^2 - z_1^2)]$$

The neck thickness (distance from the symmetry axis) must always be larger than the original sphere thickness at any value of *z* within the neck region, must be a minimum at the point $z = Z_s$, must have the same value as the sphere radius at the point $z = Z_c$ and must asymptotically approach the sphere surface at the point $z = Z_c$. A quadratic function in *z* satisfies all these criteria with appropriately defined coefficients and represents the simplest polynomial that can do so, namely

$$r_n(z) = a + b\, z + c\, z^2$$

The following equations express these conditions mathematically

$$r_n(Z_s \le z \le Z_c) \ge r_s(Z_s \le z \le Z_c)$$

$$\left.\frac{dr_n}{dz}\right|_{z=Z_s} = 0 = b + 2cZ_s$$

$$\left.\frac{d^2 r_n}{dz^2}\right|_{z=Z_c} > 0$$

$$r_n(z = Z_c) = a + bZ_c + cZ_c^2 = r_s(z = Z_c) = \sqrt{(2R - Z_c)Z_c}$$

$$\left.\frac{d^2 r_n}{dz^2}\right|_{z=Z_c} > 0$$

$$r_n(z = Z_c) = a + bZ_c + cZ_c^2 = r_s(z = Z_c) = \sqrt{(2R - Z_c)Z_c}$$
$$\left.\frac{dr_n}{dz}\right|_{z=Z_c} = b + 2cZ_c = \left.\frac{dr_s}{dz}\right|_{z=Z_c} = \frac{R - Z_c}{\sqrt{(2R - Z_c)Z_c}}$$

where $r_n$ and $r_s$ are functions of $z$ and represent the neck and sphere thicknesses, respectively, and the other symbols have already been defined. The solution to these equations provides the coefficients for the polynomial, namely,

$$r_n(Z_s - Z_c \le z \le Z_c) = \frac{z^2(R - Z_c)}{2\sqrt{Z_c(2R - Z_c)}(Z_c - Z_s)} - \frac{z(R - Z_c)Z_s}{\sqrt{Z_c(2R - Z_c)}(Z_c - Z_s)} - \frac{Z_c(Z_c^2 - 3RZ_c + 2RZ_s)}{2\sqrt{Z_c(2R - Z_c)}(Z_c - Z_s)}$$
$$= \frac{R[z^2 + 3Z_c^2 - 2(z + Z_c)Z_s] - Z_c(z^2 + Z_c^2 - 2zZ_s)}{2\sqrt{Z_c(2R - Z_c)}(Z_c - Z_s)}$$

and, as previously indicated,

$$r_s(Z_c \le z \le 2R) = \sqrt{z(2R - z)}$$

Expressed in dimensionless variables designated by primes, where all dimensions are normalized by $R$ $\left(z' = \frac{z}{R}, Z_s' = \frac{Z_c}{R}, Z_s' = \frac{Z_s}{R}, r_n' = \frac{r_n}{R}\right)$, these expressions, now independent of $R$ except as a normalization variable, become

$$r_n'(Z_s' - Z_c' \le z' \le Z_c') = \frac{\left[z'^2 + 3{Z_c'}^2 - 2(z' + Z_c')Z_s'\right] - Z_c'(z'^2 + {Z_c'}^2 - 2z'Z_s')}{2\sqrt{Z_c'(2 - Z_c')}(Z_c' - Z_s')}$$

and

$$r_s'(Z_c' \le z' \le 2) = \sqrt{z'(2 - z')}$$

Figure 59 illustrates the details of the structure near the neck at a relatively high (50%) and a relatively low (1%) extent of sintering. The neck has a well defined minimum, in these cases about 78% and 12% of the original sphere diameter, respectively, and asymptotically approaches the original sphere surface. The local minimum neck diameters are indicated and also represent the symmetry plane, or point where the second sphere initial diameter would meet the first sphere initial diameter, located at about 18% and 0.05% of the initial sphere diameter along the symmetry axis (z axis), respectively.

Placing $r_n$ in the equation for a volume of a solid of rotation yields the total volume (including that of the included portion of the sphere) of the sintered body in the region of the neck ($Z_s' \le z' \le Z_c'$), which is

$$V_t = \frac{\pi(Z_s - Z_c)\{Z_c^2(42R^2 - 34RZ_c + 7Z_c^2) + 2Z_s(\mathrm{R} - Z_c)[Z_c(8R - 3Z_c) + Z_s(\mathrm{R} - Z_c)]\}}{15(2R - Z_c)Z_c}$$

The incrementally added volume, $V_n$, that is, the volume of material added to the spheres in the region of the neck, is

$$V_n = \frac{\pi(Z_s - Z_c)\{Z_c^2(42R^2 - 34RZ_c + 7Z_c^2) + 2Z_s(\mathrm{R} - Z_c)[Z_c(8R - 3Z_c) + Z_s(\mathrm{R} - Z_c)]\}}{15(2R - Z_c)Z_c}$$
$$- \frac{1}{3}\pi[(3R - Z_c)Z_c^2 - (3R - Z_s)Z_s^2]$$
$$= \frac{\pi(Z_c - Z_s)^2[2Z_c^3 + 6RZ_c(2R - Z_s) - 2R^2Z_s + 3Z_c^2(-3R + Z_s)]}{15(2R - Z_c)Z_c}$$

The volume of a sphere between two arbitrary positions along the z-axis is

$$V_s(z_2) - V_s(z_1) = \frac{1}{3}\pi(3R - z)z^2\Big|_{z_1}^{z_2}$$

where $z_1$ and $z_2$ represent the two locations. The total sphere volume that lies between 0 and $Z_s$ is displaced by sintering and must fill the neck region outside the sphere between $Z_c$ and $Z_s$. Mathematically,

$$\underbrace{\frac{\pi}{3}(3R - Z_s)Z_s^2}_{\substack{volume\ displaced \\ by\ sintering}}$$
$$= \underbrace{\frac{\pi(Z_s - Z_c)[Z_c^2(42R^2 - 34RZ_c + 7Z_c^2) + 2(8R - 3Z_c)(R - \mathrm{zc})Z_cZ_s + 2(R - Z_c)^2Z_s^2]}{15(2R - Z_c)Z_c}}_{\substack{total \\ neck\ volume}}$$
$$- \underbrace{\frac{1}{3}\pi[(3R - Z_c)Z_c^2 - (3R - Z_s)Z_s^2]}_{\substack{initial\ sphere\ volume \\ inside\ neck}}$$

or

$$\frac{1}{3}\pi(3R - Z_s)Z_s^2 = \frac{\pi(Z_c - Z_s)^2[2Z_c^3 + 6RZ_c(2R - Z_s) - 2R^2Z_s + 3Z_c^2(-3R + Z_s)]}{15(2R - Z_c)Z_c}$$

or,

$$(3R - Z_s)Z_s^2 = \frac{(Z_c - Z_s)^2[2Z_c^3 + 6RZ_c(2R - Z_s) - 2R^2Z_s + 3Z_c^2(-3R + Z_s)]}{5(2R - Z_c)Z_c}$$

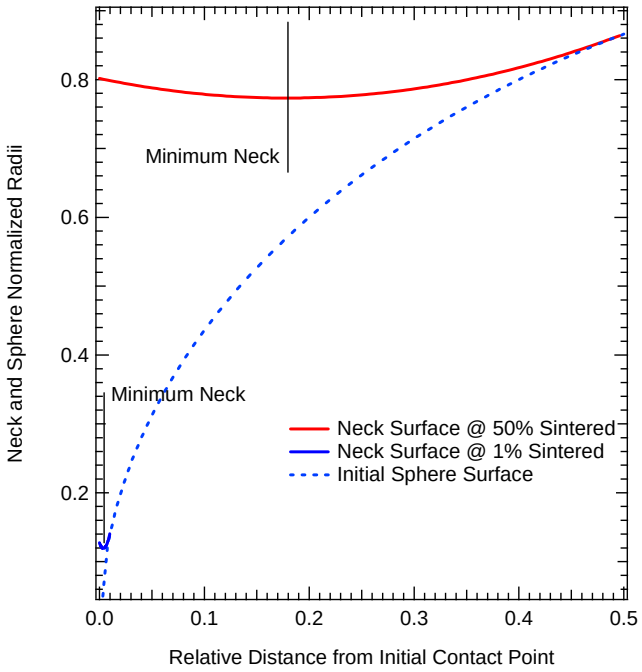


**Figure 59.** Example predicted surface shape as a function of *z* showing the initial sphere shape and the current neck shape at the point where the relative sintering extent is 0.5 (that is, 50% of the maximum possible sintering).

This function provides the relationship between $Z_c$ and $Z_s$ for a given value of $R$ that conserves volume and mass. This implicit expression is fifth order in $Z_c$ and third order in $Z_s$. It does not lend itself to explicit solution for $Z_c$ as a function of $Z_s$ and $R$. There are three explicit solutions for $Z_s$,and all are complex in some regions. However, the only one that has a real-valued domain over the physically meaningful range of range of $Z_c$, that is, $0 < Z_c < R$, is as follows

$$Z_s = \frac{Z_c[A_1^2 + 10(2R - Z_c)^2 - A_1(14R - 4Z_c)]}{6A_1(R - Z_c)}$$

where

$$A_1 = \left\{10(2R - Z_c)\left[59R^2 - 8Z_c(4R - Z_c) - 3\sqrt{369R^4 + 6Z_c[8RZ_c(4\mathrm{R} - Z_c) - 64R^3 + Z_c^3]}\right]\right\}^{1/3}$$

The maximum values of $Z_c$ and $r_n$ are both $R$, that is, sintering will continue until the neck is as thick as the original particle. However, as discussed later, the rate of sintering is a strong function of the extent of sintering, decreasing dramatically with increasing sintering extent. The limiting value of $Z_s$ is 1/3 as $Z_c$ approaches $R$, that is

$$\lim_{Z_c \to R} Z_s = \frac{1}{3}$$

Despite the complexity of the previous function, the parameters $Z_c$ and $Z_s$ are nearly proportional to each other. A quadratic fit to the solution of this equation forced to pass through the origin yields

$$\frac{Z_s}{R} = 0.37936\frac{Z_c}{R} - 0.047103\left(\frac{Z_c}{R}\right)^2$$

which is a completely adequate fit for nearly any purpose. An optimized proportional fit is

$$\frac{Z_s}{R} = 0.34457\frac{Z_c}{R}$$

The rigorous endpoint of the proportional line should be 1/3 when $\frac{Z_c}{R}$ is at unity, so 0.3333 is an alternative proportionality constant in the above equation. The nearly proportional fit of these two parameters represents a significant reason for casting the problem in this form.

The surface radius of curvature, $R_c$, plays an important role in sintering. The definitions of the radius of curvature and its inverse, the curvature ($C$), for an arbitrary, one-dimensional curve are

$$R_c = \frac{\{1 + [f'(x)]^2\}^{3/2}}{f''(x)}$$

and

$$C = \frac{f''(x)}{\{1 + [f'(x)]^2\}^{\frac{3}{2}}} = \frac{1}{R_c}$$

where $f(x)$ describes the surface profile. Since the functions involve only derivatives of $f(x)$, the point of reference for the measurement to the surface is unimportant, that is, the surface curvature depends only on the shape of the surface and not the size of body on which the surface exists. In three dimensions, the curvature has two components, expressible as one each in the $z$ and $\theta$ directions of a cylindrical coordinate system for this application. Negative radii of curvatures designate convex surfaces in this discussion.

In this model, using the results from above, the radius of curvature in the $z$ direction is

$$R_{c,z} = \begin{cases} -R & Z_c < z < R \\ \dfrac{(Z_c - Z_s)\sqrt{(2R - Z_c)Z_c}}{R - Z_c}\left[1 + \dfrac{(R - Z_c)^2(z - Z_s)^2}{Z_c(2R - Z_c)(Z_c - Z_s)^2}\right]^{3/2} & Z_s \le \mathrm{z} \le Z_c \end{cases}$$

The minimum radius of curvature (maximum curvature) occurs at the neck ($Z_s$),

$$R_{c,\,Z_s,min} = \frac{\sqrt{(2R - Z_c)Z_c}(Z_c - Z_s)}{R - Z_c}$$

Which, prior to sintering contacts at a point ($Z_c = 0$), making the neck radius of curvature zero as expected. Figure 60 illustrates how the minimum radius of curvature at the neck increases with increasing sintering.

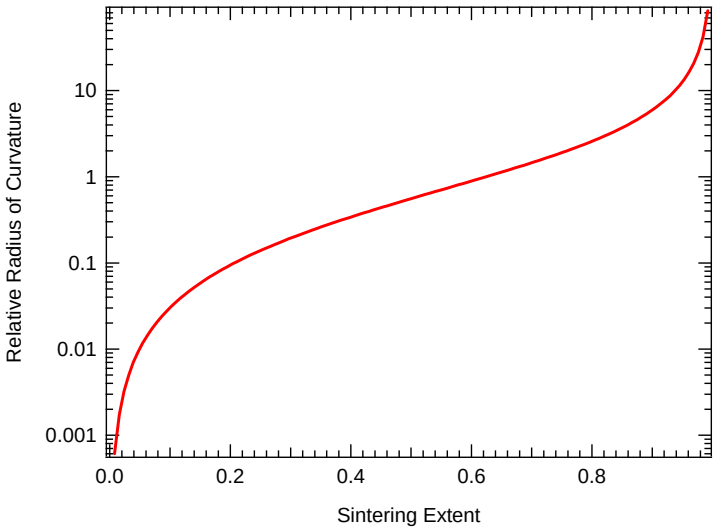


**Figure 60.** Radius of curvature normalized by the initial sphere diameter as a function of extent of sintering. Note that extent of sintering is not linear with time, with sintering slowing dramatically as extent increases.

In the $\theta$ direction, the radius of curvature is the same as the neck thickness at that location and is always convex (negative),

$$R_{c,\theta} = \begin{cases} -\sqrt{(2R - z)z} & Z_c < z < R \\ -\dfrac{R[z^2 + 3Z_c^2 - 2(z + Z_c)Z_s] - Z_c(z^2 + Z_c^2 - 2zZ_s)}{2\sqrt{Z_c(2R - Z_c)}(Z_c - Z_s)} = r_n & Z_s \leq \mathrm{z} \leq Z_c \end{cases}$$

It is significant, as will be mentioned later, that this expression does not depend on $\theta$, or more to the point, its derivative with respect to $\theta$ is zero.

The surface curvature in the $z$ direction varies from convex to concave and is constant (and convex/negative) for values of $z$ greater than $Z_c$, where it is identical to that of the original sphere. Between $Z_s$ and $Z_c$, the surface curvature is concave and varies with $z$. The radius of curvature is smallest (curvature is largest) at $z = Z_s$, as would be expected at the neck.

Surface curvature varies as expected with the degree of sintering, with maximum curvature occurring when sintering is a minimum and vice versa. Since $Z_s$ is a function of $Z_c$ and vice versa, albeit somewhat complex functions, this function provides the radius of curvature for this idealized system as a smooth function of the extent of sintering. This formalism describes sintering continuously from point contact to formation of a neck the same diameter as the sphere. The substantial current sintering literature rather arbitrarily divides this process into several zones as characterized by curvature. This work contributes to the existing literature by eliminating the need for such divisions, allowing a single model to describe the entire process.

Sintering rates depend on radii of curvature because vapor pressures and surface energies depend on them. For example, the vapor pressure on a concave surface is lower than that on a convex surface if composition and temperature are equal, representing one of the several mechanisms by which molecules move from the bulk particles with low curvature and generally convex surfaces to the point contacts that have very high curvature and concave surfaces. Other mechanisms include viscous and plastic flow and volume, grain, and surface diffusion. All are driven by the curvature or, more precisely, the gradient in the

curvature. Since the gradient in the radii of curvature is zero in the $\theta$ direction for both the sphere and the neck, there should be no net tangential material transport. Therefore, the focus is on transport in the $z$ direction.

Sintering rates for most materials can be expressed as

$$\frac{dV_n}{dt} = \frac{B}{kTR_{c,z}} = \frac{B(R - Z_c)}{kT(Z_c - Z_s)\sqrt{(2R - Z_c)Z_c}\left[1 + \frac{(R - Z_c)^2(z - Z_s)^2}{(2R - Z_c)Z_c(Z_c - Z_s)^2}\right]^{3/2}}$$
$$= \frac{d}{dt}\frac{\pi(Z_c - Z_s)^2[2Z_c^3 + 6RZ_c(2R - Z_s) - 2R^2Z_s + 3Z_c^2(-3R + Z_s)]}{15(2R - Z_c)Z_c}$$
$$= \frac{\pi(Z_c - Z_s)}{15Z_c^2(2R - Z_c)^2}\{2(3R^2Z_c - 3RZ_c^2 + Z_c^3 - R^2Z_s)[(8R - 3Z_c)Z_c + 2(R - Z_c)Z_s]Z_c{}'$$
$$+ Z_c(-2R + Z_c)[Z_c^3 + 2RZ_c(13R - 9Z_s) - 6R^2Z_s + Z_c^2(-12R + 9Z_s)]Z_s{}'\}$$

where $k$ and $T$ are the Boltzman constant and absolute temperature, respectively, and $B$ is a material property that depends on the sintering mechanism and generally exponentially on temperature. Both $Z_c$ and $Z_s$ depend on time, but not independently on time since they are functions only of one another and $R$. $Z_c{}'$ and $Z_s{}'$ here denote the time derivatives of the functions. The last equality can be approximated by assuming that the functions and their derivatives are proportional has been shown to be nearly the case. With this approximation,

$$\frac{dV_n}{dt} = \frac{B}{kTR_{c,z}} = \frac{B(R - aZ_s)}{(-1 + a)kTZ_s\sqrt{aZ_s(2R - aZ_s)}\left[1 + \frac{(z - Z_s)^2(R - aZ_s)^2}{(-1 + a)^2aZ_s^3(2R - aZ_s)}\right]^{3/2}}$$
$$= -\frac{(1 - a)^2\pi Z_s}{15a(2R - aZ_s)^2}\{8(1 - 6a)R^3$$
$$+ aZ_s[2(17 + 33a)R^2 + aZ_s(-2(18 + 17a)R + 3a(3 + 2a)Z_s)]\}Z_s{}'$$

where $a$ is the proportionality constant (about 1/0.34457 or 2.90217 according to the fit discussed earlier or the value 3 if the initial and endpoints are to be correct), which yields

$$Z_s{}' = -\frac{15aB(R - aZ_s)(2R - aZ_s)^2}{C(a - 1)^3k\pi TZ_s^{5/2}\sqrt{a(2R - aZ_s)}}$$

where

$$C = 8(1 - 6a)R^3 + aZ_s\{2(17 + 33a)R^2 + aZ_s[3a(3 + 2a)Z_s - 2(18 + 17a)R]\}$$

assuming the function is evaluated at $z = Z_s$.

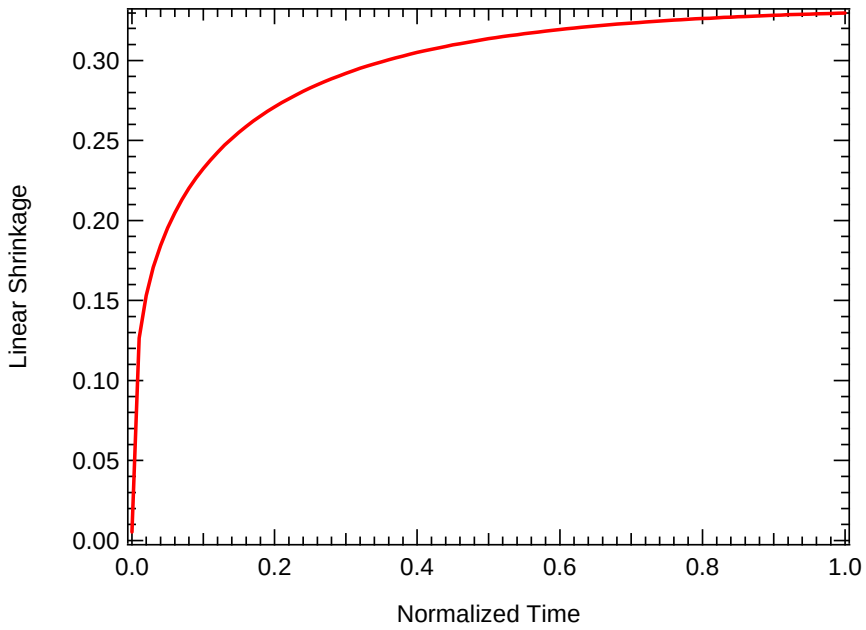


**Figure 61.** Dimensionless linear shrinkage as a function of normalized time according to this sintering model.

This equation closely approximates the more rigorous sintering rate expression given previously, both of which describe the time dependence of $Z_s$ in terms of the materials property $B$, which depends on temperature, $T$, and on a variety of physical and empirical constants. There is no analytical solution to this function, but it is an implicit ordinary differential equation, the numerical solution to which is relatively easily obtained. The plot can be made quite generic if $\frac{Z_s}{R}$ is plotted with respect to $\frac{tB}{kT}$, which is a measure of linear shrinkage as a function of normalized time. Such a diagram appears as Figure 61.
Given a generally empirically determined value of $B$, these equations provide estimates of sintering rates. Figure 62 illustrates how the neck initially grows very rapidly, with growth rate falling much more rapidly than exponentially during initial growth stages. Over a broad range of subsequent growth, from approximately 15% to about 85% of the ultimate sintering extent, growth rate decreases approximately exponentially. During the last stages of growth, when surface curvature is minimal, growth rate again drops off at super-exponential rates.

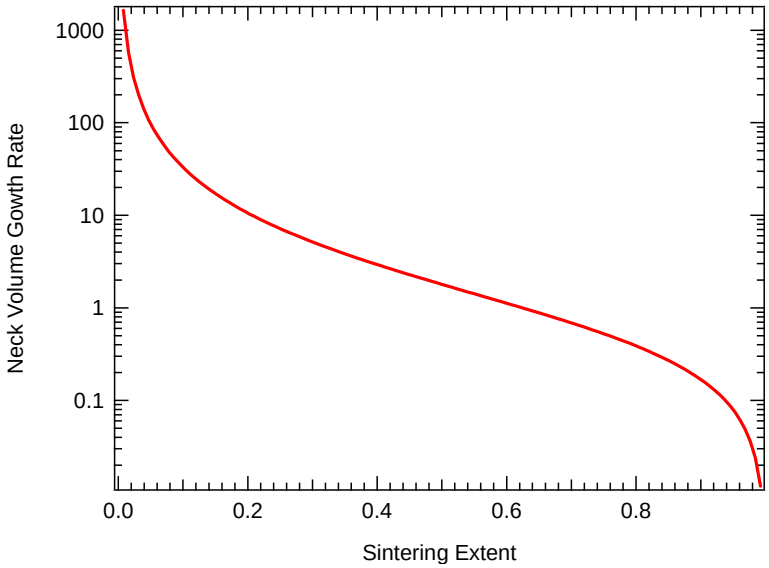


**Figure 62.** Volumetric neck growth rate as a function of sintering extent.

The minimum neck radius critically affects the strength and amount of heat transfer through sintered particles. The minimum neck radius as a function of the extent of sintering follows from the above development, namely,

$$r_n(z = Z_S) = \frac{R(3Z_c^2 - Z_s^2 - 2Z_cZ_s) - Z_c(Z_c^2 - Z_s^2)}{2\sqrt{Z_c(2R - Z_c)}(Z_c - Z_s)}$$

where, as before, $Z_s$ could be written as a function of $Z_c$ and there is only one independent variable on the right side. Figure 63 illustrates how the minimum neck radius changes with changing extent of sintering. The minimum neck area is,

$$A_{min} = \pi r_{n.min}^2 = \pi \left[\frac{R(3Z_c^2 - Z_s^2 - 2Z_cZ_s) - Z_c(Z_c^2 - Z_s^2)}{2\sqrt{Z_c(2R - Z_c)}(Z_c - Z_s)}\right]^2$$

Deposit properties such as strength and thermal conductivity depend critically on the minimum neck area relative to the overall sphere cross sectional area and should develop with increased sintering approximately in proportion to this equation, or the square of the function shown in Figure 63.

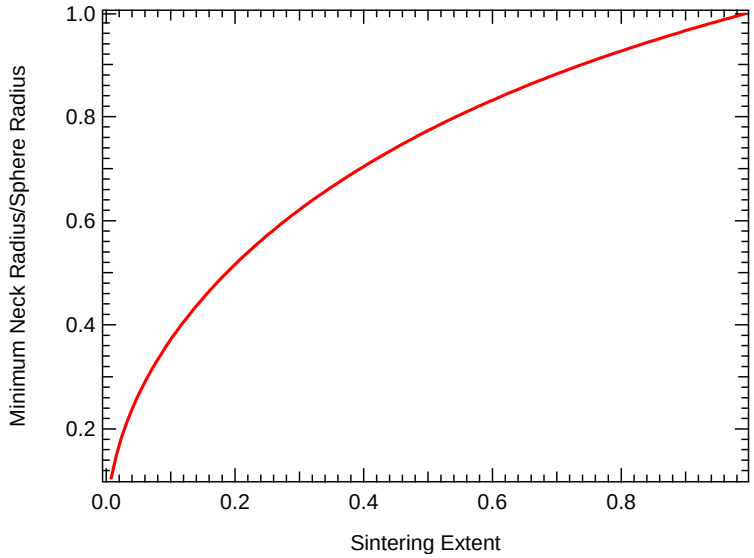


**Figure 63.** Minimum neck radius normalized by the initial sphere radius as a function of sintering extent.

Local deposit properties such as thermal conductivity and strength depend directly on $A_{min}$. Since all particles in a deposit are, through some path, connected to the deposit target surface, there are no particles hanging in space or unattached by any path to the target surface. Under such conditions, the thermal conductivity through any series of equally sized, connected particles closely corresponds to

$$k_{eff} = \frac{\phi k_s}{\tau}\left(\frac{r_{n,min}}{R}\right)^2 + (1-\phi)k_g$$

where $\phi$ is the local solid volume fraction, $\tau$ is the tortuosity defined as the ratio of the path length through connected particles to the straight-line path length, and $k_{eff}$, $k_s$ and $k_g$ represent the effective, solid-, and gas-phase thermal conductivities, respectively. This result draws in part on previous fundamental work [1]. This function shows how thermal conductivity depends on $\frac{r_{n,min}}{R}$, the function illustrated in Figure 63. Similarly, the local deposit strength is given by

$$S_{eff} = \phi S_s \left(\frac{r_{n,min}}{R}\right)^2$$

where $S$ represents strength and subscripts are as before and there is no dependence on tortuosity that compares to that in the thermal conductivity.

*Literature Experimental Results.* Figure 64 illustrates the efficacy of this approach and typical data. In this experiment, the measured thermal conductivity normalized by its maximum value as predicted from the equations above appears as a function of time in an experiment during which coal flow halted at about 80 minutes and temperature increased to more fully sinter the deposit. The success of the sintering is seen by a decrease in deposit thickness without changing deposit mass, that is, an increase in bulk density. As seen, the initial deposit exhibits a thermal conductivity near its lower bound, consistent with a structure of particles minimally connected at their contact points, or with minimal neck formation and little sintering. As the temperature increases, the deposit thermal conductivity rises to near its maximum value, consistent with substantial neck growth approaching its maximum. The thermal conductivity reliably tracks and provides a quantitative measure of the deposit structure.

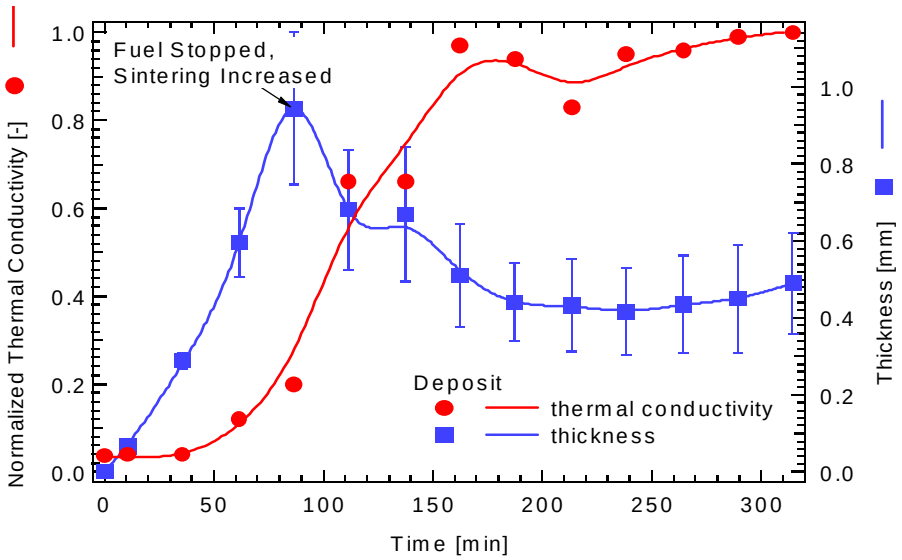


**Figure 64.** Normalized thermal conductivity (normalized by maximum value) as a function of time in an experiment during which coal flow halted, temperature increased, and probe deposit sintered appreciably.

Data collected without increasing the temperature and sintering the deposit during the experiment appear in Figure 65. The deposit still densifies, but it does so as a consequence of deposit growth and the associated increased temperature and not as a consequence of increasing the overall temperature. As indicated, the deposit conductivity initially rises to near its upper limit when the deposit is young but reaches a plateau and does not change appreciably as the deposit matures and densifies. The deposit behaves very much like the illustration of neck diameter growth earlier.

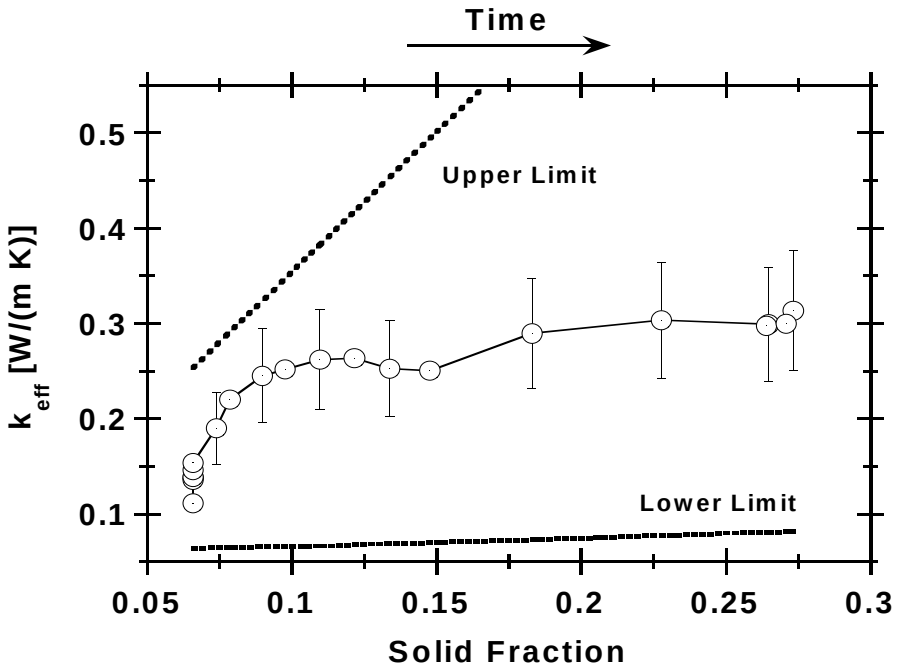


**Figure 65.** Thermal conductivity change with solid fraction as measured for real ash deposits.

***Subtask 11.3 – Acquisition of Data for Melting Model Verification***

The Gasification Team completed investigations and drafted papers on in situ and ex situ measurements of ash emittance, thermal conductivity, sintering rates, and related properties under both reducing and oxidizing conditions. These are detailed in the Gasification Topical Report (Appendix D). Among the most important findings, nearly all of which are supported by both experimental and modeling work, are the following:

- ash deposit structure, independent of porosity, has a major impact on deposit thermal conductivity and sintering.
- deposits tend to initially exhibit tenuous connectedness among deposited ash.
- fine particles, in the absence of disruptive large particle impacts, form filaments on the surface and exhibit primarily intra-filamentary, as opposed to inter-filamentary, sintering. That is, particle necks along individual filaments thicken but filaments do not sinter to one another.
- deposit porosity decreases only modestly during initial deposition, but thermal conductivity changes from very low values to near the upper bound for a given porosity, largely because of neck thickening driven by sintering.
- subbituminous ash forms deposits with lower thermal conductivity than bituminous ash.
- thermal conductivities of both ashes are essentially independent of local stoichiometry if all else (deposit composition and morphology, deposit thickness, and deposit porosity) remain constant.

- reducing conditions favor sintering, especially for bituminous coals, so functionally reducing conditions often increase conductivity.
- deposit emittance is also significantly lower for subbituminous ash than bituminous ash, in part because of differing composition (lower iron content and higher calcium and sodium content) and in part because subbituminous ash has smaller particle sizes.
- the effective total emittance (Planck-weighted values) decreases with increasing deposit temperature for both types of deposits and for both reducing and operating conditions.
- subbituminous ash emittance is relatively independent of local stoichiometry while reducing conditions often increase bituminous coal ash emittance, which is in any case higher than that of subbituminous coal ash.
- the primary reason for the change with stoichiometry is a shift in oxidation state of iron (from +3 under oxidizing conditions to +2 under reducing conditions).
- slag exhibits uniformly higher emittance than non-molten or non-sintered ash for all fuels, but the emittance retains some spectral character and also decreases with increasing deposit temperature.
- temperature dependence in emittance primarily arises from a largely temperature-independent spectral emittance signature that is characteristically higher at high wavelengths than at low wavelengths.
- physical changes in deposit structure, including sintering/slag formation, change both the spectral and total emittance values.
- models can fundamentally capture some of the chemical effects but continue to rely on empirical indications of spalling frequency, though spalling depth can be predicted.
- refractory wear rate depends critically on slag flow rate and temperature, and can be highly localized in systems where ash impacts the walls or with large gas temperature gradients.
- experimental simulations of refractory wear using either a spinning cup sample or a static immersion do not accurately reflect actual slag-refractory interactions.
- refractory wear produces only subtle changes to reactor performance that can be observed externally, with the single largest influence being on wall temperature (though this is small) and essentially no observable influence on gas or slag properties.

These experimental and modeling results benefitted from and were in many cases at least partially funded by other research programs on related topics in the laboratory.

## Task 12.0 – Develop and Validate Computational Modeling Tools to Accurately Simulate Entrained-Flow Gasifiers

### *Subtask 12.1 – Heat Flux Modeling*

Heat transfer plays a key role in performance of a gasification system and is largely responsible for limited refractory and injector lifetimes. The entrained-flow gasifier simulation tool currently being developed under other funding at the University of Utah will improve the understanding of heat transfer to the walls and will allow identification of areas prone to excessive heat transfer.

The Gasification Team identified factors which play a key role in heat transfer within a gasification system. This analysis was based partly on an understanding of the environment within an entrained-flow gasifier, partly on experience with simulation of industrial combustion systems and partly on results from the experimental tasks in this program (e.g., Subtask 10.2). The resulting parameters include:

- *Soot***.** As indicated previously, coal gasification can result in production of carbon-rich soot, which has a very high emissivity and a key player in radiative heat transfer.

- *Char*. Char also has a high emissivity and like soot contributes strongly to radiative heat transfer. Char may exist either entrained in the gas phase or be captured in the slag flowing down the wall of the gasifier.
- *Slag.* The walls of a slagging gasifier are not bare refractory, but instead refractory coated with a layer of viscous slag. Heat transfer from the reacting environment to the refractory walls is thus very dependent on properties of the slag (e.g., emissivity, thickness, coverage).
- *Gas.* Radiation from the gas is more important in entrained-flow gasification systems than combustion systems, primarily because the gas is much denser due to the pressure, which can exceed 60 atmospheres.

These parameters are expected to be the major contributors to heat flux, which is expected to be driven almost exclusively by radiation at gasification temperatures. The relative importance of each of these will depend on several factors including operating conditions, coal conversion behavior and refractory properties. Models for the first three of these (soot, char, and slag) were being developed within the gasification research area (Subtasks 10.2, 10.3 and 11.2) and are continuing to be developed under other funding sources. Gas-phase radiation is well enough understood that it can be incorporated into the simulation using existing experience.

The University of Utah simulation team is continuing to pursue a multi-phase modeling approach for coal gasification systems using LES as the turbulence closure under follow-on funding. In this approach, gas transport is represented by the standard, filtered, Navier-Stokes equations wherein LES subgrid closure models are applied to represent the fluctuating scales. The particle phase is represented by transport of the NDF. Practical representation of the NDF requires some approximation, which in this case leads to directly tracking moments, with numerical quadrature, of the number density function. This approach is termed the DQMOM.

The number density function that DQMOM attempts to represent is a function of properties of the particle phase it is representing. One identifies a set of orthogonal properties, termed internal coordinates, that then approximate the NDF. In other words, if $\xi$ is the set of internal coordinates, then the NDF (n) is described by $n(\xi, X, i)$ where $X$ is spatial location and $t$ is time. The distribution then changes through local changes in the internal coordinates, $\xi$ that are dependent on $X$ and $t$. The transport of $\xi$ in internal coordinate space is usually termed phase-space velocity and occurs because of physical processes that affect the NDF. For example, if $\xi$= length, then one may have a distribution of particles that change size depending on a local concentration of some other quantity, $\phi$. This model then affects the NDF through its affect on an internal coordinate.

### *Subtask 12.2 – Entrained-Flow Gasifier Modification*

The aim of this task was to modify the University of Utah's existing pressurized entrained-flow gasifier (Figure 66) so that it could process coal. The system was originally designed to process spent pulping liquor (black liquor) under U.S. Department of Energy cooperative agreement DE-FC26-04NT42261. That program was terminated after the first year due to lack of funding and a redirection of priorities within the Office of Biomass Programs. Consequently, construction of the entrained-flow gasifier was never fully completed and the system was never operated.

Pressurized entrained-flow gasification of coal and black liquor are overall very similar processes. However, there are several important differences between the two processes:

- Black liquor gasification takes place at approximately 975°C while coal gasifiers typically operate much hotter, near 1400°C.

- Black liquor is a homogeneous aqueous solution that does not need to be constantly mixed. Concentrated black liquor does, however, need to be heated in order to flow or to be pumped. Coal slurry is more challenging because the coal will rapidly settle and "harden" if the slurry is not constantly kept well mixed.
- The "ash" or molten smelt from black liquor gasification is soluble in water so no specific solids handling system is necessary. Coal slag, on the other hand, will solidify and settle to the bottom of the water bath below the quench part of the reactor.
- Black liquor smelt is caustic so the quench bath has a high pH (~12). Coal slag is somewhat acidic. Materials of construction must be carefully selected.
- Molten black liquor smelt has a relatively low viscosity and flows readily down the wall of a gasifier. Coal slag is very viscous even at the much higher operation temperature of a coal gasifier, presenting a risk for buildup of slag within the reactor.

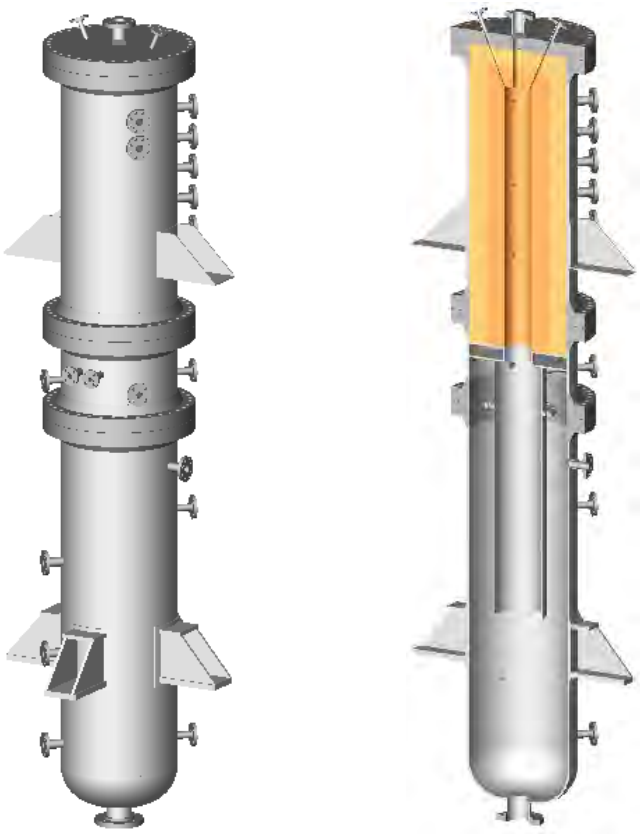

**Figure 66**. Rendering of the entrained-flow gasifier and split view of same.

In order to estimate conditions and performance of the existing entrained-flow gasifier when operating on coal, two Excel-based models were developed. One was simple and assumed complete conversion of coal slurry to slag and a synthesis gas comprising only CO, $H_2$, $CO_2$ and $H_2O$. Such assumptions result in a maximum volumetric production of syngas and a minimum residence time in the reactor. This model was used to estimate limits of operation and approximate "worst case" flow rates for slurry, oxygen, quench water and syngas. These flow rates were used to specify ranges of the various flow meters, etc. Based on this analysis and a residence time in the reactor of 6 seconds, it is expected that the gasifier

should be able to process coal slurry at a rate corresponding to more than 1 ton/day (dry) of coal when operating at pressures greater than 20 bar (300 psi).

The other model developed under this subtask was more involved and used a Gibbs Free Energy minimization approach to predict the composition of the syngas, syngas flow rate and adiabatic flame temperature based on coal composition, slurry concentration, oxygen/fuel ratio and coal feed rate. This model considered approximately one dozen components in the synthesis gas. Although there are commercial packages such as Aspen® and Hysys® which can perform equilibrium calculations such as this, it is desirable to have a portable simulator that can be used without needing expensive, specialized software.

Modification of the gasifier initially focused on the quench system, since it was imperative that the system was able to adequately cool the product from the gasifier before contacting metal components downstream. Water for the primary quench sprays was changed from city water to softened water since deposits quickly formed within the nozzles when using city water. No deposits were observed after this change. A new safety loop was added to the control system which shuts off oxygen and fuel flow if quench recirculation stops, quench spray flow stops or the temperature downstream of the primary quench exceeds a preset temperature (default 500°F). The quench system was tested during operation on natural gas standby and during gasification of isopropyl alcohol and found to efficiently cool the gas exiting the reactor.

Temperature measurement in entrained-flow coal gasifiers is notoriously difficult since the harsh environment quickly corrodes thermocouples. Temperature measurement is critical for this system, however, since it is a research reactor and will ultimately provide validation data to the simulations that are being performed. Two B-type thermocouples were ordered from SynTemp, Inc., a company that specializes in gasifier thermocouples. The thermocouples are able to measure temperatures to 1800°C (3270°F). The thermocouples were installed near the burner and near the exit of the gasifier, positioned such that they protrude approximately 1 cm from the wall of the reactor. Initial testing indicates that the thermocouples perform as intended. The control system was programmed to trip the system if either of the thermocouples exceeds a preset temperature.

The other major activity associated with rebuild of the system was development of a coal slurry preparation and feed system. The University of Utah has no experience making or handling coal slurry. Due to costs associated with a complete feed system able to match the full capacity of the gasifier, it was decided to develop a prototype system using existing components available at the University's Industrial Combustion and Gasification Research Facility. The prototype system (Figure 67) comprises a 20-gallon slurry preparation and mixing tank, 2-hp recirculation pump, mixing paddle and a small progressive cavity pump for feeding the coal slurry.

**Figure 67.** Prototype coal slurry feed system. The progressive cavity pump body is seen below the tank, the motor for the mixer is vertically mounted in the upper-left corner of the photo. The recirculation pump is near the center of the photo.

The coal slurry feed system has proven to be able to easily mix and circulate slurry exceeding 60% coal by weight. It was found that the recirculation motor was so powerful that it would actually heat the mixture over time, causing water to evaporate from the slurry, thereby increasing its concentration. The final design will have a variable frequency drive on the motor which will allow it to be operated at lower rotational speeds. The progressive cavity pump was not able to deliver a stable flow of slurry, nor was it able to pressurize the material beyond roughly 15 psi. This was surprising, since several sources indicated that this design of pump is the most appropriate for handling coal slurry in this flow range. Ultimately, after consultation with the pump manufacturer and disassembly of the pump it was observed that the stator was cracked, likely due to its age and lack of contact with fluids for many years. A new rotor and stator set was ordered which should allow pressurizing to approximately 10 bar (150 psi), but these components had a very long lead time and had not arrived by the end of the program.

Most of the effort under this subtask focused on establishing safe operability of the system when processing coal slurry. The quench and downstream systems have been proven to work well. Because the coal slurry feed system was not yet functioning, a test campaign involving gasification of isopropyl alcohol was conducted over several days. The fuel was fed using a 10-gallon vessel pressurized with compressed air to force the fuel out. This test was successful because it provided an opportunity to test heating the reactor on natural gas for several days, establishing a safe procedure for initiating gasification of the fuel, and experiencing operation at various pressures and oxygen/fuel ratios. The system was operated at pressures to 5 bar (75 psi), and the pressure control valve worked well. Although the objective of this task, getting the system completely ready for operation on coal, was not fully achieved the gasifier has been tested and is expected to be available for future research.

## SEQUESTRATION

The primary objective of the Sequestration Thrust Area was to study the impact of contaminant gases on sequestration chemistry and vertical mixing of $CO_2$ and brine. Appendix E contains more detailed results of the Sequestration Task.

### Task 13.0 – Impact of Contaminant Gases on Sequestration Chemistry

In this task, the impact of contaminant gases on sequestration chemistry was studied by measuring reaction rates for $CO_2$, brine, and rocks in a newly designed high-temperature, high pressure experimental assembly.

#### *Subtask 13.1 – Development of an Experimental Assembly*

A high-pressure, high-temperature experimental assembly was developed to analyze $CO_2$, brine and rock reactions. The experimental apparatus is illustrated in Figure 68. It consists of series of four stainless-steel reactors made of 316-grade stainless steel, which were rated for 4000 psi at 600°C. The reactors were pressure sealed with high-pressure SWAGELOK® fittings. The reactor has the provision for retrieving the rock sample without disturbing it through a detachable cap at the bottom. The $CO_2$ was pressurized in the reactor using a single cylinder high-pressure positive displacement pump. The flow of $CO_2$ into the reactor was controlled using high-pressure needle valves. Dry $CO_2$ (drawn from a $CO_2$ cylinder equipped with a siphon) was used in all the experiments. High-purity nitrogen provided pressure test the entire setup at 3000 psi. The temperature was controlled using a bench-top temperature controller with SPECVIEW® as the interface via K-type thermocouples.

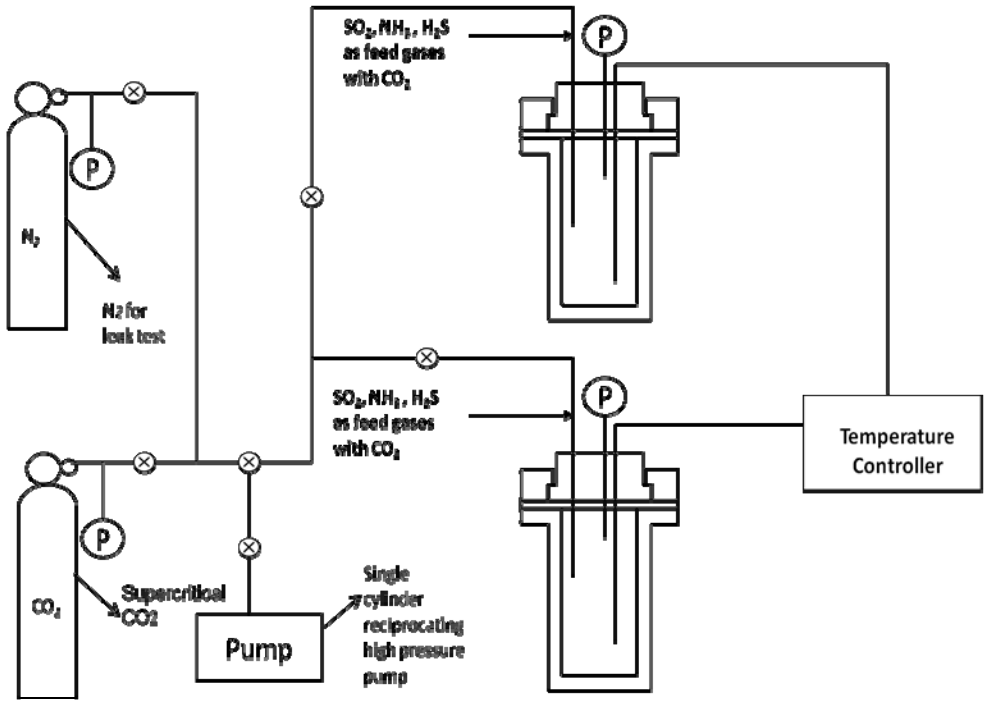


**Figure 68.** Schematic diagram of the experimental setup.

#### *Subtask 13.2 – Study of Reaction Kinetics for $CO_2$, Brines and Rocks*

*Approach.* The Sequestration Team performed experiments to study the kinetics of the reactions between $CO_2$, brines and rocks. Dirty sandstone was selected as the reacting material because of its diverse geochemical reaction basis and common occurrence in sedimentary basins (Kaszuba et al. 2005). The

dirty sandstone used in our experiments is comprised of equal proportions of calcite, dolomite, quartz, microcline, andesine and chlorite. The physical properties of these materials are provided in Table 12. The minerals were crushed to 100μm and mixed to create the initial mineral assemblage.

**Table 12.** Physical properties of the rocks used to construct the dirty sandstone.

| Rock | Quartz | Andesine | Dolomite | Chlorite | Microcline | Calcite |
|---|---|---|---|---|---|---|
| Formula | $SiO_2$ | $Na_xCa_yAlSi_2O_8$ | $CaMg(CO_3)_2$ | $(Fe, Mg, Al)_6(Si, Al)_4O_{10}(OH)_8$ | $KAlSi_3O_8$ | $CaCO_3$ |
| Class | Silicates | Silicates | Carbonates | Silicates | Silicates | Carbonates |

Brine was prepared from laboratory-grade NaCl with the initial composition shown in Table 13.

**Table 13.** Initial composition of the brine for all the experiments (<=detection limits).

| **Na** | **Mg** | **K** | **Ca** | **Al** | **Mn** | **Fe** | **Ba** | **Si** | **S** | **Cl** |
|---|---|---|---|---|---|---|---|---|---|---|
| mg/L | mg/L | mg/L | mg/L | μg/L | μg/L | μg/L | μg/L | mg/L | mg/L | mg/L |
| 23032 | 1 | <6 | <4 | <8 | <1 | 54 | <2 | 0.4 | <6 | 26542 |

Table 14 provides the experimental conditions.

**Table 14.** The conditions adopted for each of the experiments.

| Experiment | Temperature ($^oC$) | Pressure (psi) | Gas Composition |
|---|---|---|---|
| Set A | 200 | 2000 | $CO_2$ |
| Set B | 100 | 2000 | $CO_2$ |
| Set C | 100 | 600 | $90\%CO_2+10\%SO_2$ |

*Highlighted results*

**Experimental set A (200$^o$C and 2000 psi).** Calcium carbonate was observed to grow on the sample as layers (Figure 69). Calcium carbonate deposition is a clear indication of the consumption of $CO_2$ in this reaction. Ankerite, (iron carbonate) was also seen growing as aggregates on the reacted surface usually intergrown with the initial minerals (usually quartz).

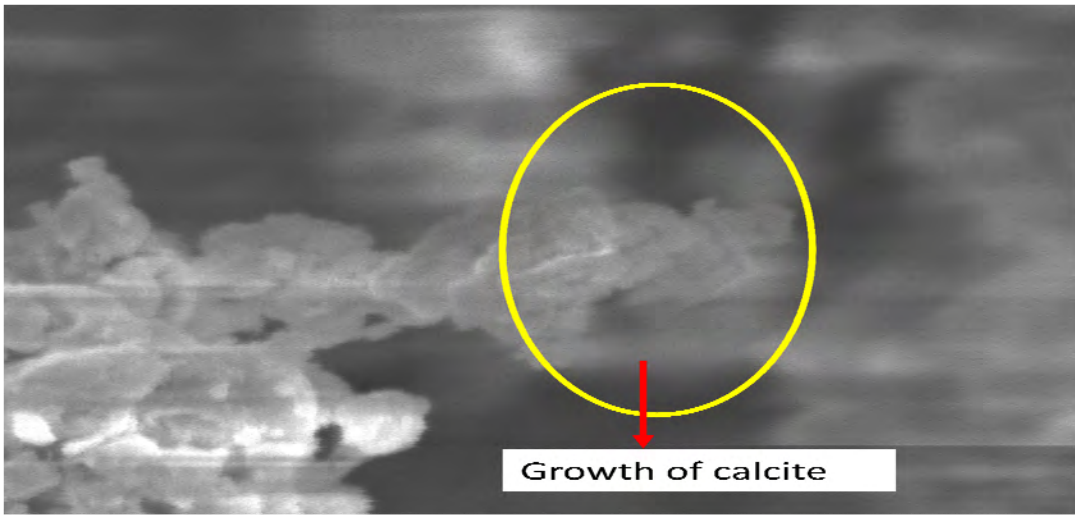


**Figure 69.** SEM image of Calcite growth in the final sample.

**Experimental set B (100°C and 2000 psi).** Figure 70 shows the changes in the principal ions in the brine during the course of the experiment. These results are corroborated with brine chemistry in Figure 71, which provides a complete picture of the geochemical alterations taking place in brine and rock chemistries with Ca ion as the reference. The precipitate from this experiment was analyzed by x-ray diffraction and by SEM. After 62 days the samples showed pronounced dissolution patterns. Dissolution occurs mainly by the formation of few deep etch pits and some shallow ones, almost at the same position in the initial dissolution of the surface. The samples also revealed precipitated calcite crystals, which were highly irregular in shape.

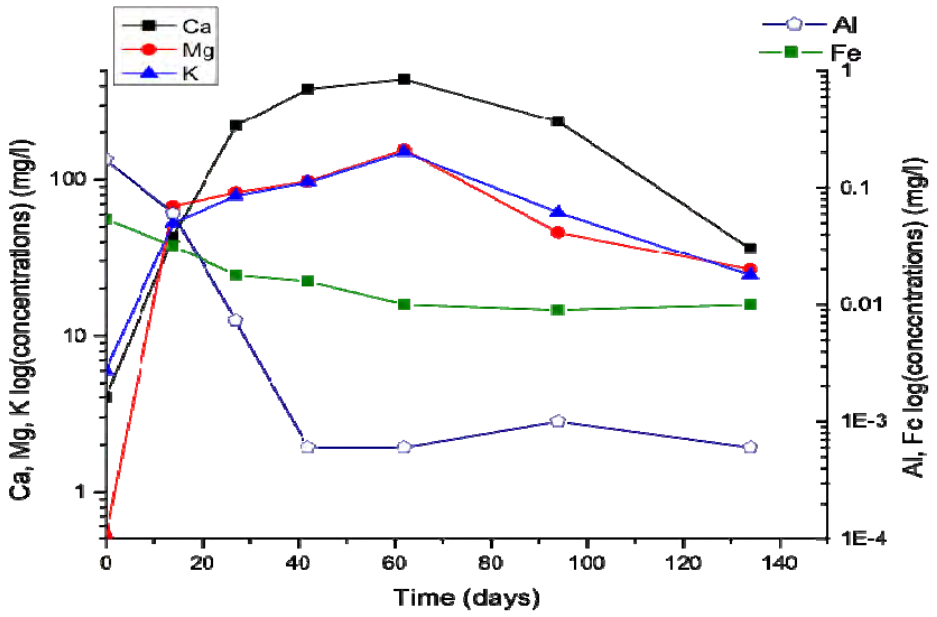


**Figure 70.** Changes in concentrations of the principal ions during the experiment

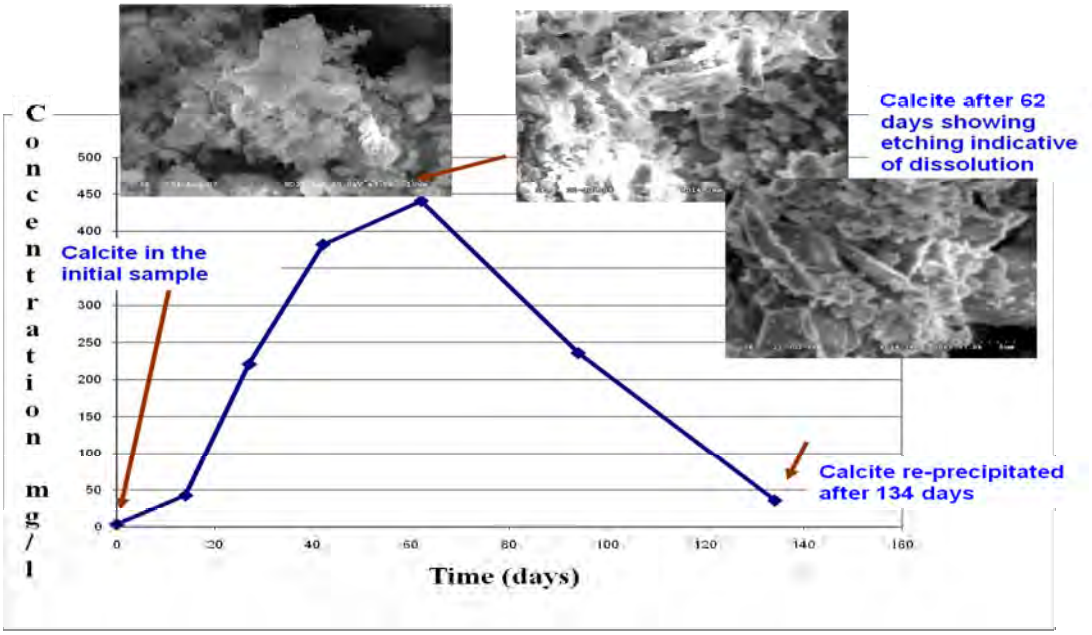


**Figure 71.** Rock chemistry results corroborated with brine chemistry.

### *Subtask 13.3 – Investigation of the Effect of $SO_2$*

Experimental Set C in Table 14 was designed to determine the dissolution/precipitation tendencies of the realistic gas mixtures, such as those containing $SO_2$, in comparison to the pure $CO_2$ stream. The only change in this set of experiments compared to Set B was the feed-gas composition, which contained 10% $SO_2$ with 90% $CO_2$. The gas was a calibrated mixture provided by AIRGAS in cylinders with a maximum deliverable pressure of 600 psi.

Figure 72 shows the brine chemistry analysis during the experiment, and a comprehensive picture with the corroboration of brine and rock chemistries is presented in Figure 73. The product also exhibited widespread deposition of anhydrite crystals. SEM analysis revealed anhydrite as large discrete bladed crystals on the surface of the host

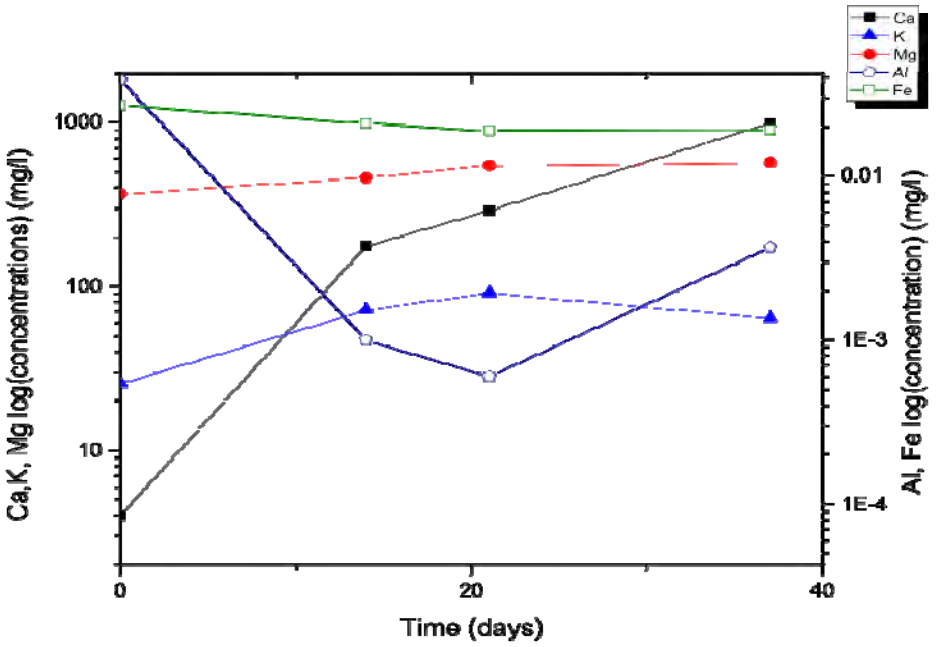


**Figure 72.** Changes in the brine chemistry of principal ions during the experiment.

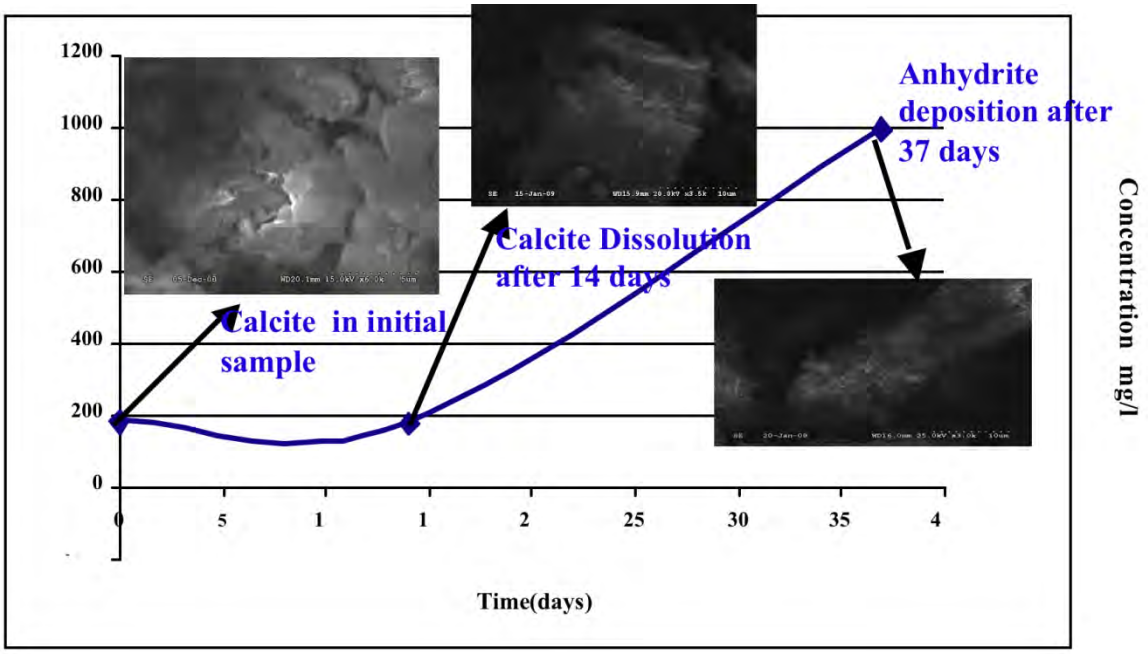


**Figure 73.** Rock chemistry results corroborated with brine chemistry.

### *Subtask 13.4 - Optimizing Injectivity in the Presence of $SO_2$*

Although research in geologic carbon sequestration is maturing, numerous practical aspects of implementing field trials of carbon sequestration must be addressed, such as the potential loss of injectivity related to the presence of contaminant gases (e.g., $SO_2$, $H_2S$, $NH_3$, NO), which poses environmental and economic risks. This subtask aimed to provide critical experimental data for engineering and modeling strategies for optimizing $CO_2$ injectivity in the presence of contaminant gases, and minimizing associated risks at the injection well.

*Approach.* The experimental setup consisted of three dual cylinder Quizix pumps for $CO_2$, brine and the fluid for the overhead burden (Figure 74). The flow was regulated using high pressure gate valves rated to 15000 psi. All the pumps wee automated; the flow was controlled via pump-works software. The flow of the $CO_2$ and brine were directed to a core holder where the absolute and the differential pressures across the core were measured using sensitive pressure transducers. The brine after the breakthrough was collected on a digital scale and preserved for analysis. The whole assembly was mounted in a well insulated oven maintained at 100°F. The experimental assembly was completed and the system was evaluated for experiments. Special provisions were necessary for injecting $SO_2$ into the system.

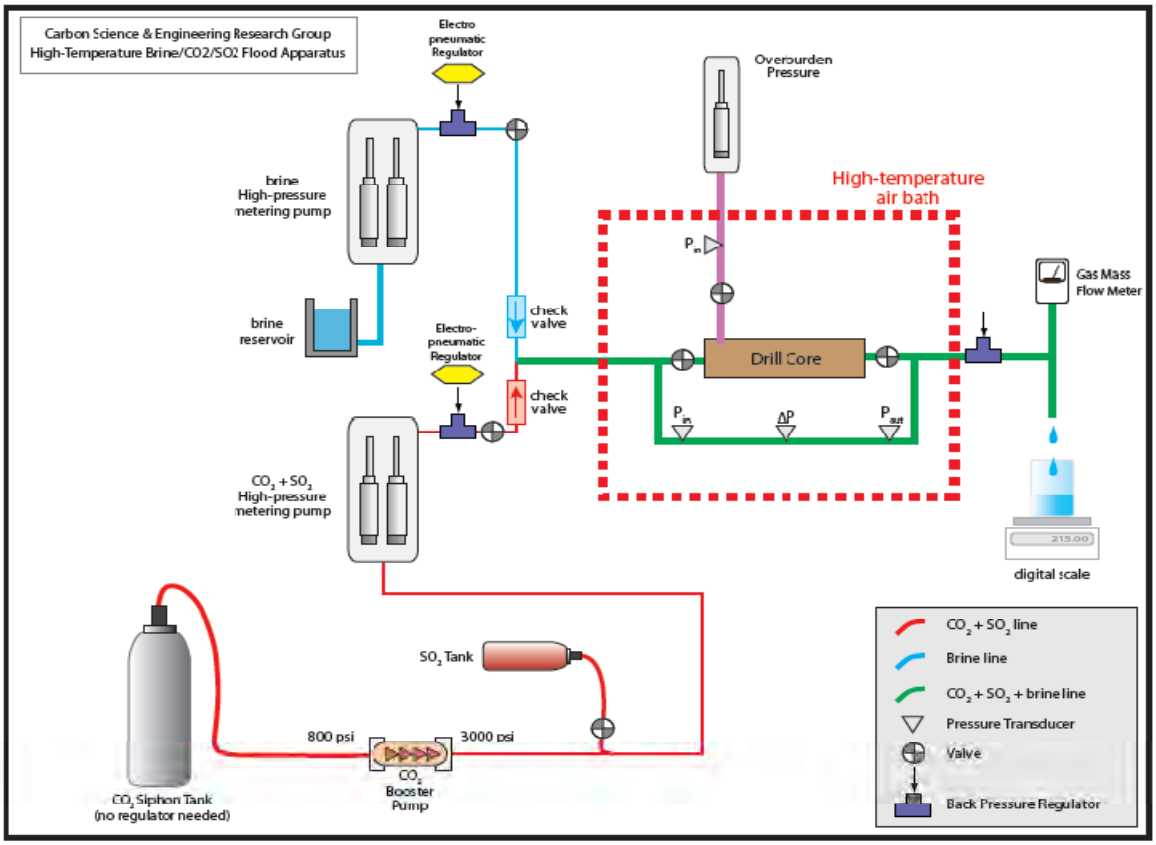


**Figure 74.** Schematic diagram of the experimental setup.

*Highlighted results.* Design of the experimental system and assembly of the equipment was more complicated than originally envisioned, and flow experiments were not conducted during the project. Injectivity studies with $CO_2$ and $CO_2$+$SO_2$ mixtures, using the experimental setup described above, were planned to measure the following changes in the rock/core: matrix lithology (diagenetic), porosity, and

permeability during long-term injection tests (several hours to days), when saturations in the core stabilized.

San Juan Basin rock core samples were acquired for laboratory testing. The San Juan Basin of northern New Mexico was selected for this research because it is the site of a pilot-demonstration of $CO_2$ injection under the auspices of the Southwest Regional Partnership on Carbon Sequestration, a consortium sponsored by NETL. The Partnership is in its sixth year and currently deploying multiple injection tests throughout the region. The subject formations for deep saline sequestration testing are the Jurassic-aged Entrada sandstone and the Mississippian-aged Leadville limestone. The core samples were analyzed for fractures and other heterogeneities. Results of these analyses indicated that these formations possess many minor chemical constituents. To maximize applicability (transferability/portability) of our results to other studies, we elected to focus on pure end-member archetypes of these formations represented by the Indiana Limestone and the Berea Sandstone. In the last few months of this project, the Sequestration Team acquired Indiana and Berea core from Fisher Scientific Inc. and repeated mineralogic and hydrologic (porosity and permeability) analyses of the core.

**Task 14.0 – Study the Vertical Mixing of $CO_2$ and Brine**

The Sequestration Team studied vertical mixing and equilibration times using TOUGHREACT. Simulations have shown that due to the density difference between carbonated brine (denser and at the top) and brine (lighter and at the bottom) gravity-driven plumes of $CO_2$-laden water result, enhancing the mixing process in the formation. There is some uncertainty in the development and progression of these plumes, which significantly impacts the overall time of equilibration in an aquifer.

*Approach.* For all simulation experiments, the TOUGHREACT simulator was utilized (Xu et al. 2006), which includes full thermal-hydrologic-chemical coupling – multiphase $CO_2$ flow, heat flow, and reactive transport. TOUGHREACT utilizes the finite-volume method to solve the multiphase groundwater flow equations and uses a generalized form of Darcy's Law to evaluate flow velocities. Because all flow experiments and simulations involve brine, a robust chemical model of brine-$CO_2$-$SO_2$ interactions was needed. The original TOUGHREACT code (Xu et al. 2006) computed activity coefficients of charged aqueous species using an extended Debye-Huckel (DH) equation. The DH model can handle ionic strengths from dilute to moderately saline water. During the course of the Yucca Mountain project, a Pitzer ion-interaction model was implemented into TOUGHREACT (Zhang et al., 2008) using the model formulated by Harvie et al. (1984). The vertical migration studies were performed by using a multiphase flow simulator (TOUGHREACT) with different seal properties.

*Highlighted results.* Vertical migration of $CO_2$ in the formation into which it is injected is an important phenomenon. On a macro-scale, it is important to capture such a buoyancy-driven transport, since it affects all aspects of $CO_2$ trapping. The gravity fingers created can range in scale from millimeters to several meters. This particular component of the process embodies all of the elements of the parent sequestration process in the sense that equilibration does not occur over engineering time scales, and several spatial scales govern how the dissolution and equilibration proceeds.

In this task the Sequestration Team studied the vertical migration of $CO_2$ in the aquifer and the parameters that control the migration and subsequent distribution of $CO_2$ in the various phases. Table 15 summarizes the simulation conditions. In addition to studying the sensitivity of parameters to the absolute permeability of the seal and the formation, additional simulations were performed with relative permeabilities where both the phases were essentially immobile (a situation that is termed "permeability jail" in some other gas flow applications).

**Table 15.** Simulation conditions for the study of vertical migration.

| Parameter | Values |
|---|---|
| Grid | 1*60*60 |
| Grid block size | 100ft*10ft*10ft |
| Model size | 100ft*600ft*600ft |
| Porosity | 0.30 (0.15 for seal) |
| Permeability (matrix) | 100md |
| Permeability (seal) | 1~100md |
| Temperature | 75 °C |
| Pressure | 200bar |
| Salinity | 3-6.0wt% |
| Injection rate | 2.3177*10$^3$kg/hr |
| Injection period | 258.4 days |

Distributions of free and dissolved $CO_2$ concentrations are shown in Figure 75. In the uniform permeability case, the free-$CO_2$ concentration was highest at the top of the formation. If the top of the formation was breached, the $CO_2$ leaked outside of the target zone. If permeability-jail type relative permeabilities were used in the seal, the seal became an effective trapping layer, and $CO_2$ was better distributed in the aqueous phase as well.

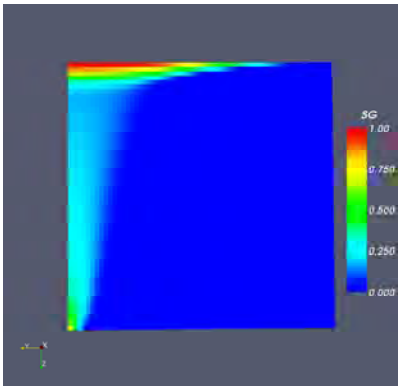


Free $CO_2$: k=100md, uniform

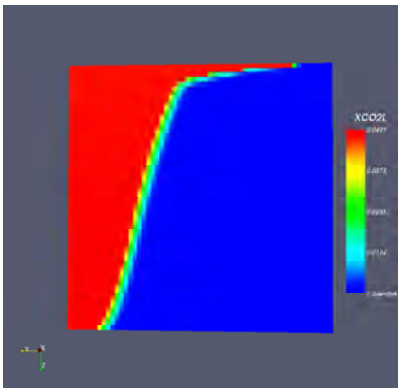


dissolved $CO_2$: k=100md, uniform

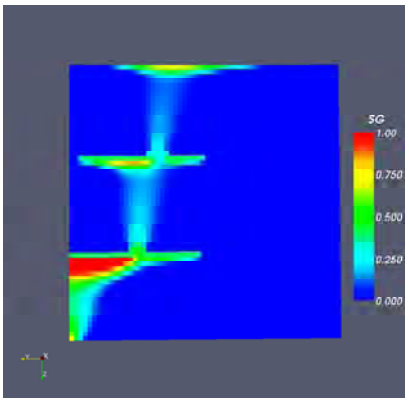


Free $CO_2$: k=100md, permeability jail

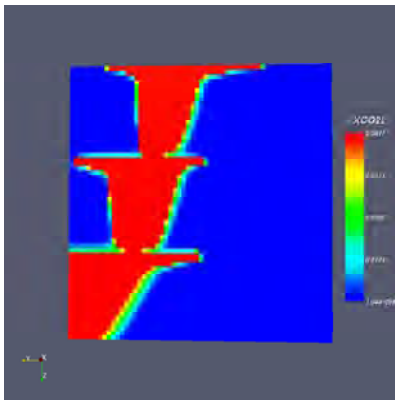


dissolved CO2: k=100md, permeability jail

**Figure 75.** Vertical distribution of CO2 (as free gas phase, and in the dissolved state) for the domain with uniform permeabilities and in the system with "permeability-jail" relative permeabilities in the seal.

When the permeability of the seal was reduced to 1 md, the vertical migration of $CO_2$ predominantly occurred through the holes in the low permeability seal, and the permeability jail-type relative permeabilities did not change the distributions of the free and dissolved $CO_2$ concentrations significantly (Figure 76).

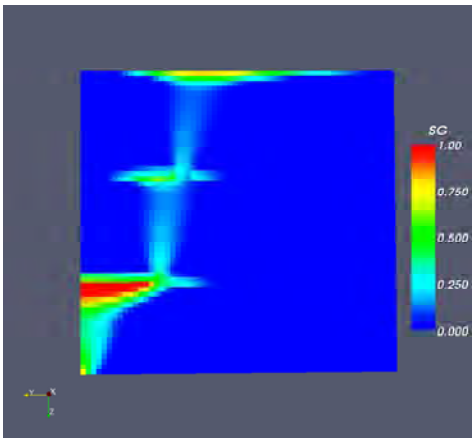


Free $CO_2$: k=1md, low permeability

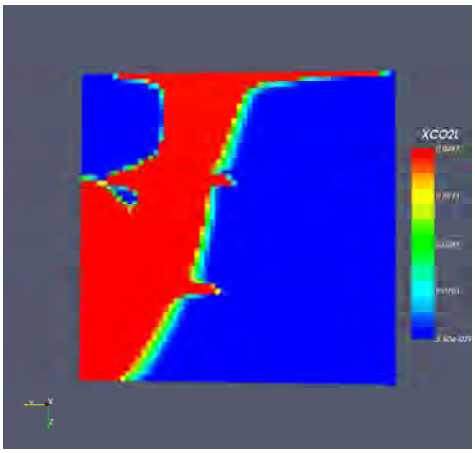


dissolved $CO_2$: k=1md, low permeability

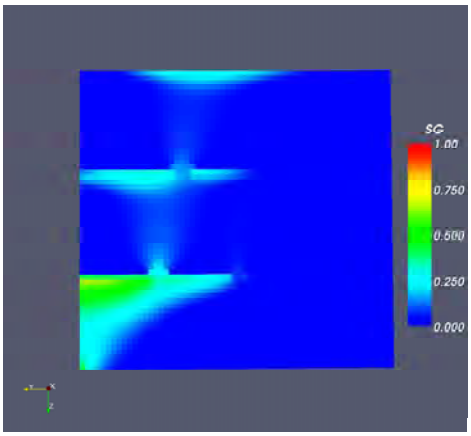


Free $CO_2$: k=1md, permeability jail

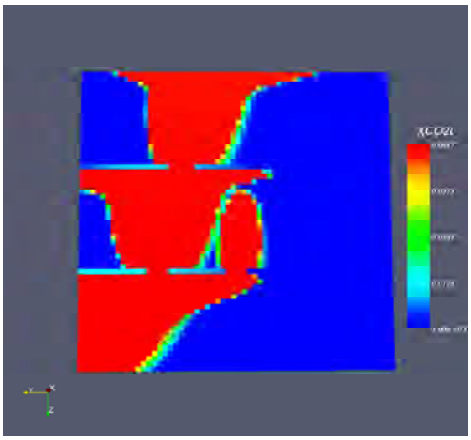


dissolved $CO_2$: k=1md, permeability jail

**Figure 76.** Vertical distribution of CO2 (as free gas phase, and in the dissolved state) for the domain with uniform permeabilities and in the system with "permeability-jail" relative permeabilities in the seal. The seal permeability is 1 md in all the simulations.

## Task 15.0 – Overarching UC$^3$ Activities

### *Subtask 15.1 – Form a Technical and Industrial Advisory Board*

The Utah Clean Coal Program began forming a Technical and Industrial Advisory Board; however, this Board was modified as part of the University of Utah's Clean and Secure Energy Program (FC26-08NT0005015), and it now encompasses the Coal and the Unconventional Fuels programs. The Board includes representatives from energy industries, national and regional government, and environmental organizations.

***Subtask 15.2 – Host a Conference to Disseminate Results and Publish a Conference Summary***

In May of 2007, the University of Utah's Institute for Clean and Secure Energy hosted a Future of Coal Conference. The presentations and publications are now housed in the ICSE repository (http://repository.icse.utah.edu/dspace/index.jsp).

***Subtask 15.3 – Prepare progress and final reports of activities***

As required by DOE, the Utah Clean Coal Program has submitted regular reports including: progress reports, quarterly milestone updates, and annual accomplishments.

**Task 16.0 – Chemical Looping Combustion**

CLC is an efficient method of capturing high-purity $CO_2$ from the combustion of fuel gases. In essence, a fuel such as syngas or methane is brought into contact with an oxygen carrier (OC) such as NiO(s) in the complete absence of air in the first of two interconnected reactors. In the first, the fuel reactor (FR), the oxygen of the OC reacts with the fuel to produce $CO_2$ + $H_2O$ and the reduced form of the OC (still in particulate form). The exit gases, after condensation of the water, yield pure $CO_2$ suitable for sequestration. The reduced OC is moved into the second, the Air Reactor (AR), where the OC is reoxidized by the combustion air to its original oxidized state and is ready to initiate a second cycle as the refreshed OC returns to the FR thus closing the "Loop." Depending on the choice of oxygen carrier the chemical reaction in the FR can be either exothermic or endothermic.

Under this task, the CLC Team worked toward determining the reactivity of a number of OCs. The work included a literature survey, procurement of a high-pressure TGA, and an experimental program to develop new insights to the CLC process. A more comprehensive summary of these efforts can be found in the CLC Topical Report (Appendix F).

***Subtask 16.1 – Review Published Studies of CLC Experiments***

The review began with Lewis and Gilliland (1954) and Richter and Knoche (1983), the forerunners to Ishida and Jin (1994), who are the widely credited "inventors" of CLC. The search revealed only one publication for CLOU (chemical looping with oxygen uncoupling). This concept was introduced by Chalmers University of Technology in Sweden for which refereed papers are beginning to appear in print (Mattisson et al. 2009). CLOU permits combustion of solid fuels in gas-phase oxygen without resorting to an energy-intensive air separation unit. Furthermore, few of the titles found in this literature survey mention rate studies of metal oxide reductions and metal particle oxidations carried out at high temperatures. More recently the CLC research community has been considering long-term experiments of 30 hours or more carried out with lab-scale fluidized bed CLC reactors rather than with simple TGAs (Shen et al. 2009, Chandel et al. 2009). Another growing dimension of CLC research is the computer modeling of the fuel and air reactors (Deng et al. 2008). None of these papers appears to report CLC experiments carried out at high pressures.

***Subtask 16.2 – Acquire and Test a High Temperature, Elevated Pressure TGA***

The CLC Team purchased and installed a high-pressure TGA (TherMax 500). However, the TherMax 500 has never operated satisfactorily, and fundamental problems remain unidentified. This delayed experiments performed at pressures exceeding one atmosphere as well as all experiments involving "fuels" (syngas, hydrogen, etc.). I n spite of these handicaps, the CLC Team has made significant progress in completing our experimental matrix using generously "loaned" time on an atmospheric pressure TGA in the Department of Chemistry.

***Subtask 16.3 – CLC Experiments***

*Approach.* The CLC Team performed thermogravimetric analysis using the TherMax 500 and a TA Q500, and temperature-programmed oxidations and reductions using the Micromeritics ChemiSorb 2720. Thermogravimetric analysis is based on the observation of the weight of a solid sample suspended on a microbalance, enclosed in a temperature controlled environment. To obtain the data necessary to describe the reaction kinetics, the experiments can be executed under isothermal (constant temperature) and non-isothermal (programmed temperature changes) conditions.

For isothermal experiments the sample was prepared under ambient conditions (temperature, pressure), and was heated to the target temperature in an inert ($N_2$, He) atmosphere. When the target temperature was stabilized, the flow of the inert gas was replaced with flow of a reacting gas (air, $H_2$), and the change of the sample weight was recorded. The rate constant at the target temperature ($k_T$) could be determined, according to an assumed reaction mechanism. The experiment was repeated at several temperatures to construct an Arrhenius plot ($\ln(k_T)$ vs $1/T$).

For non-isothermal experiments the sample was prepared under ambient conditions (temperature, pressure). The inert gas flow was terminated, and the system was switched to the reacting gas. The sample was heated to the target temperature according to a (linear) heating program (°C/min). The experiment was repeated several times, using different heating rates. The kinetic information was extracted by using the IsoKin program. This approach has no initial assumptions of the reaction mechanism.

The temperature programmed oxidations (TPO) and reductions (TPR) were conducted by monitoring the composition of the gas before and after the reaction zone using a thermal conductivity detector (TCD). In the Micromeritics ChemiSorb 2720 the full gas flow is monitored, in a time-delayed manner, by comparing the gas composition before and after the sample, respectively. To optimize the TCD signal the gas mixtures were chosen as ultra high purity helium as the (neutral) carrier gas; 10% $H_2$ in ultra high purity argon for the reduction experiments; and 5% $O_2$ in UHP helium for the oxidation experiments. During the experiment, the sample temperature was raised according to a linear heating program, and the consumption of the component of interest was measured by the TCD detector.

These techniques complement each other. The TGA data provide information about the changes in the solid, and the TPR/TPO experiments reveal the participation of the gases.

During the course of the experiments, improvements were made in the instruments. An external gas mixing system, consisting of four mass-flow controllers to deliver gases under high pressure was developed to provide the reaction gas for the TherMax 500 apparatus. In the same instrument, the original sample holders suspended by a metal wire were replaced by all-quartz buckets. The piece of wire was not durable and required tedious the cleaning. An all-quartz sample holder was designed and fabricated at the University of Utah, for a fraction of the commercial replacement cost. Similarly, quartz replicas of the platinum sample holding pans were used in the TA Q500 instrument. The platinum pans were not suitable for the experiments, due to sintering of the metal samples.

*Highlighted results.* Figure 77 illustrates the non-isothermal oxidation of Ni with air. The observed 27.7% weight gain at the end of the reaction indicated the complete oxidation of the Ni to NiO (27.3% calculated weight gain). The oxidation occurred in a single process.

$$2Ni(s) + O_2(g) \rightleftharpoons 2NiO(s)$$

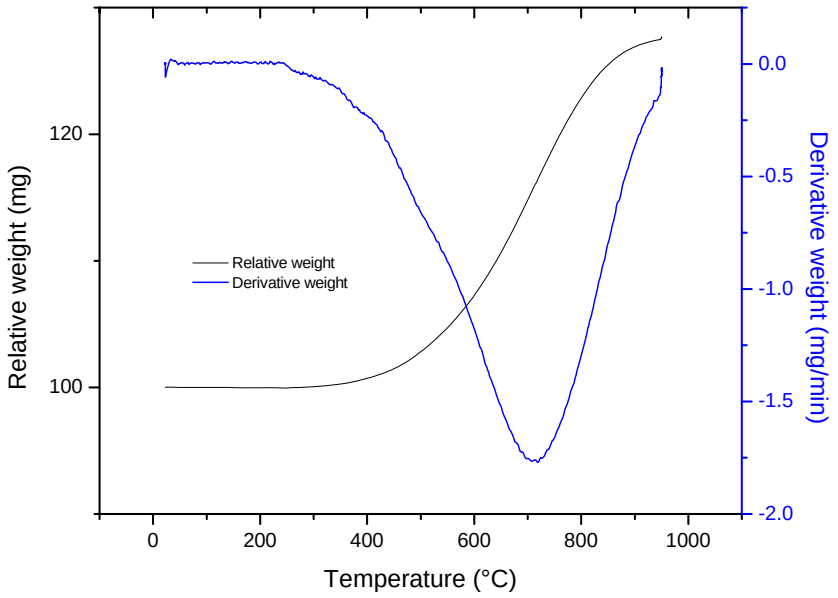


**Figure 77.** Non-isothermal oxidation of Ni with air.

Figure 78 presents the isothermal oxidation of Ni with air at 950 °C. The reaction was complete. Similar isothermal data sets were collected for evaluation at several temperatures in the 600 – 950 °C range. After the completion of the experiment the sample was cooled under $N_2$, without any substantial loss of weight. The minor change shown in the figure was due to the effect of the buoyancy on the mass, arising from the changing density of the air. While the Ni/NiO system is a good candidate for the CLC, it is not a good choice for CLC with oxygen uncoupling.

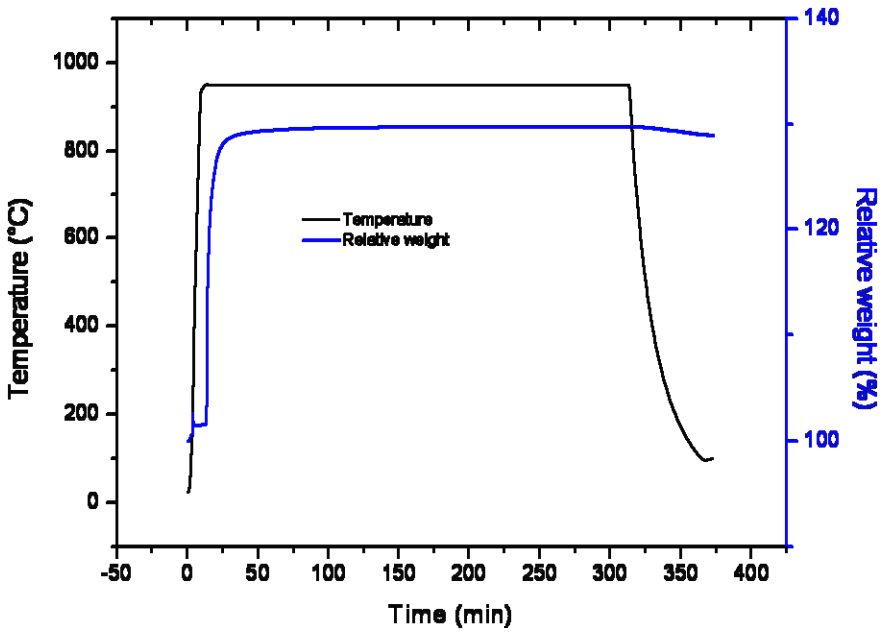


**Figure 78.** Isothermal oxidation of Ni with air at 950 °C.

Figure 79 shows the reduction of NiO with 50% $H_2$ in $N_2$ as simulated fuel. The 19.3% weight loss was close to the 21.4% change expected for the complete reduction

$$NiO(s) + H_2(g) \rightleftharpoons Ni(s) + H_2O(g)$$

Interestingly, this reaction takes place at a comparatively low temperature.

Figure 80 shows that the non-isothermal oxidation of Cu is not simple. The observed 24.3% weight gain was close to the expected 25.2%, but it did not occur in a single step. The difference is clearly indicated by the derivative curves. The three oxidation reactions of the copper

$$2Cu(s) + O_2(g) \rightleftharpoons 2CuO(s)$$

$$4Cu(s) + O_2(g) \rightleftharpoons 2Cu_2O(s)$$

$$2Cu_2O(s) + O_2(g) \rightleftharpoons 4CuO(s)$$

did not satisfactorily explain the observed trace, characterized by more than three steps. These steps were clearly revealed by considering the derivative of the weight change.

The isothermal oxidation of Cu with air at 950 °C as shown in Figure 81 was not yet complete after a 45-minute isothermal holding period. The weight gain was 22.5%. After the 45 minutes, the air was replaced with $N_2$, and the sample was allowed to cool. The change of gas immediately initiated a weight loss. In the absence of oxygen, the CuO decomposed. The decomposition was not complete because the temperature dropped quickly, and the reaction stopped.

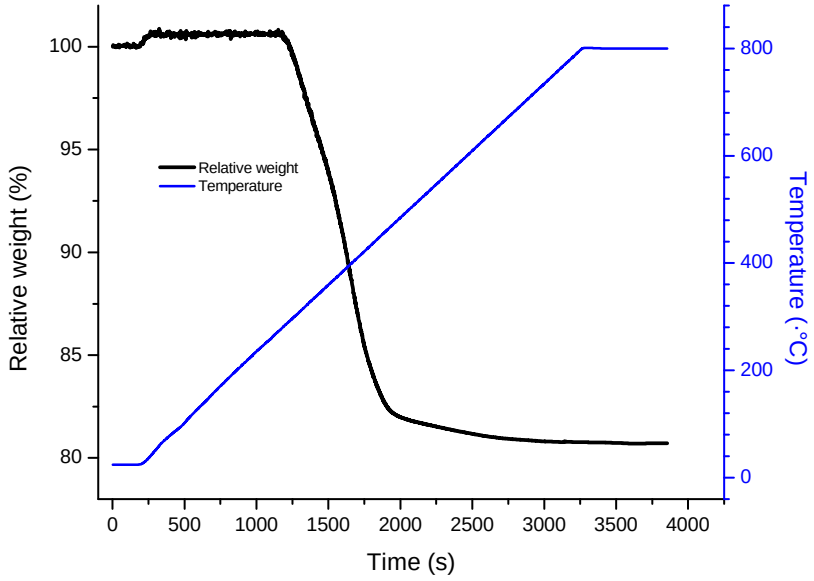


**Figure 79.** Reduction of NiO with 50% $H_2$.

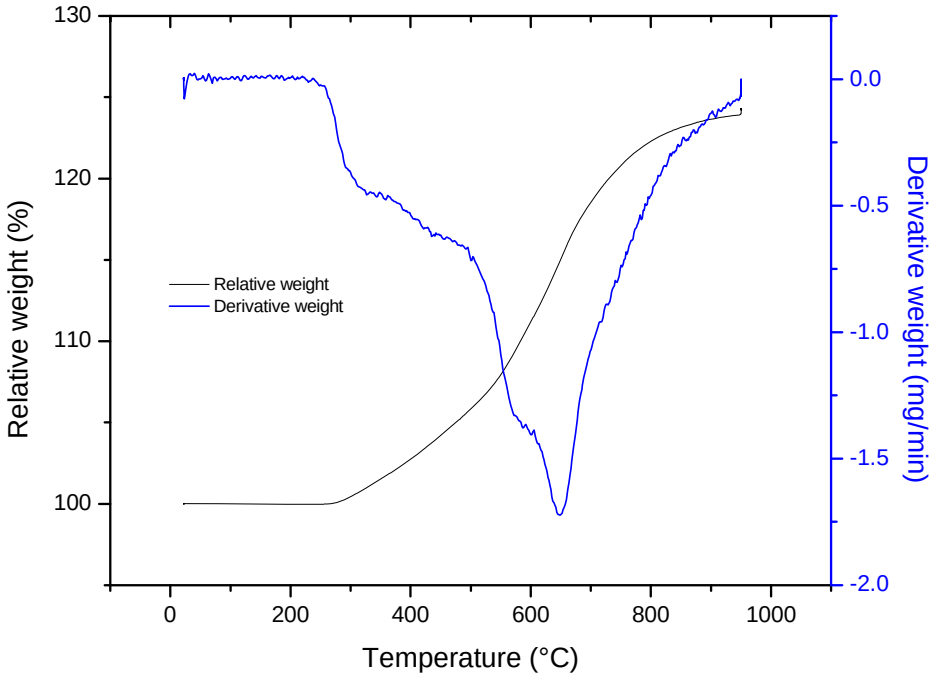


**Figure 80.** Non-isothermal oxidation of Cu with air.

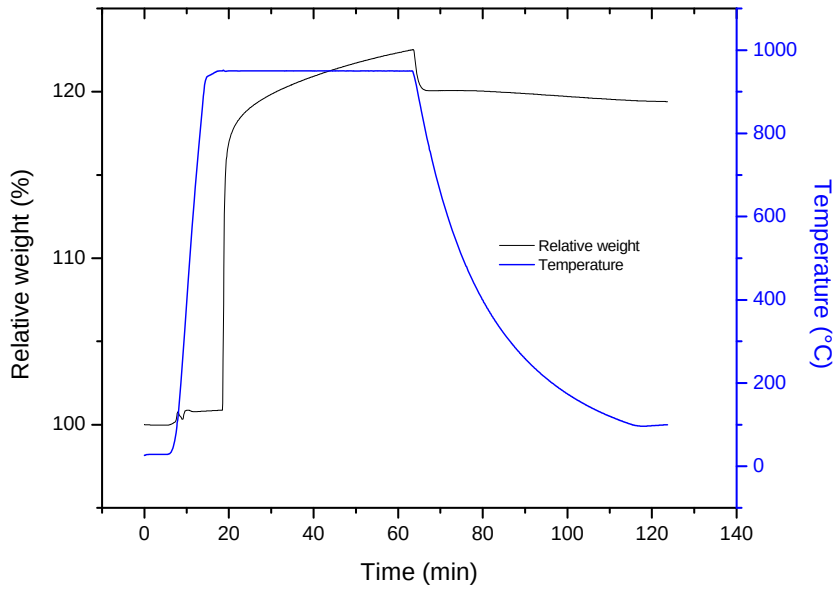


**Figure 81.** Oxidation of Cu with air at 950 °C.

Figure 82 shows the spontaneous decomposition of CuO under nitrogen. When the sample temperature exceeded 770°C, decomposition occurred. The weight loss was approximately 10%. For the conversion of CuO to Cu metal the expected weight loss is 20.1%. The observed value agrees well with the 10.1% weight loss expected for the conversion of CuO into $Cu_2O$. Under the same experimental conditions NiO did not decompose.

The oxygen carrying capability of the $CuO/Cu_2O$ system was further investigated in simulated looping experiments with both Cu and CuO as starting materials. After 6 or 7 cycles the systems exhibited a consistently repeatable behavior. The weight changes indicated a swing between CuO and $Cu_2O$ (129.2% and 115.8%, relative to 100% Cu, respectively). The oxidation segments with air were faster and more complete, as indicated by the constant weights, than the decomposition segments under $N_2$.

This behavior can be tuned, by selecting the temperature of the reaction and the times of exposure to the different gases. Figure 83 shows an experiment with 20 minutes under air exposure and 20 minutes under $N_2$. The oxidation cycles went to completion (for practical purposes), while the decomposition cycles did not. The looping was successfully extended up to 200 cycles.

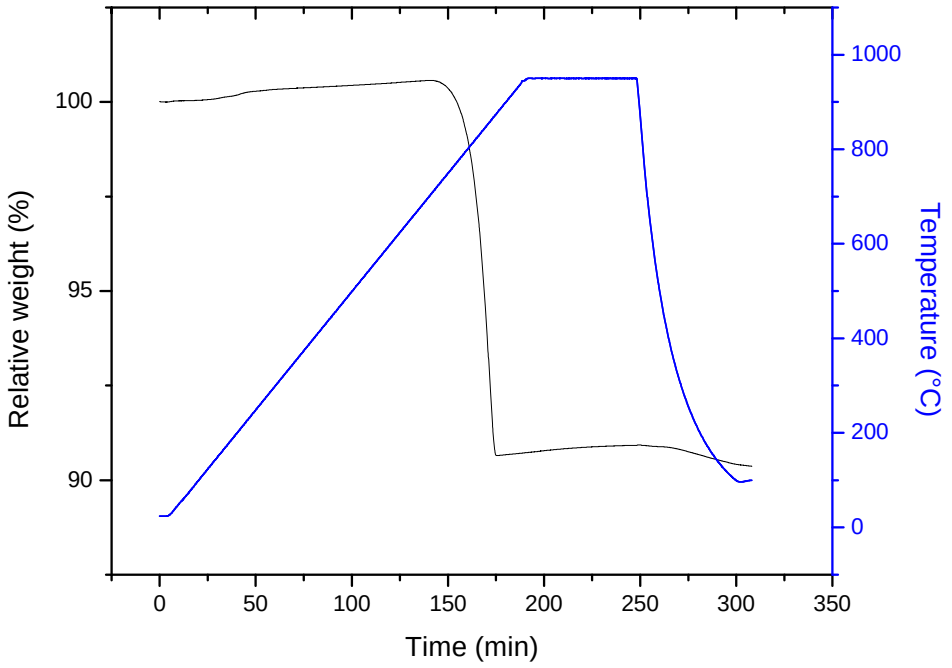


**Figure 82.** Decomposition of CuO in nitrogen.

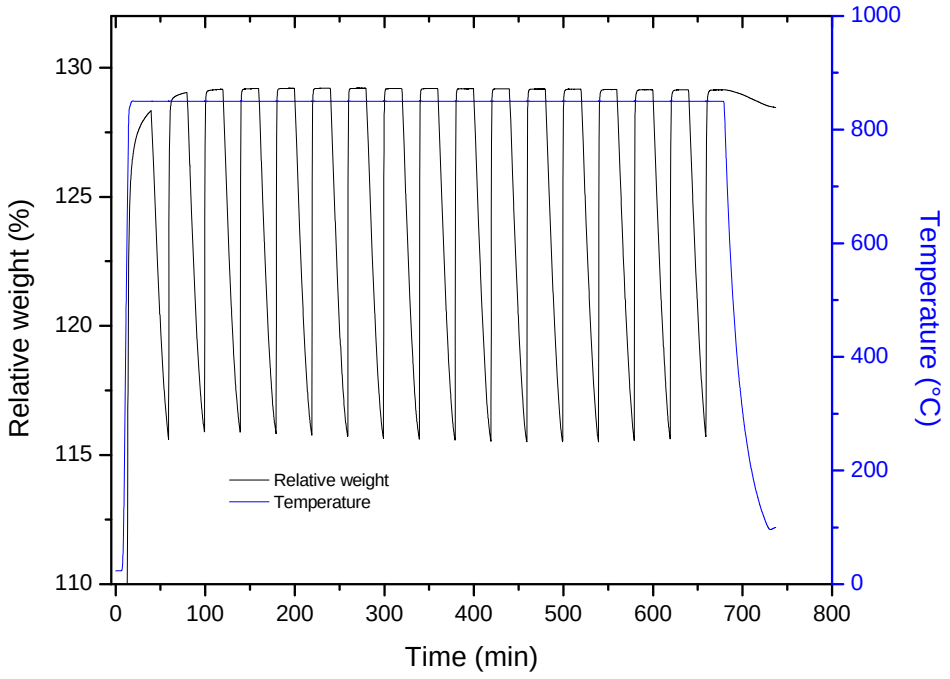


**Figure 83.** Looping of $Cu/Cu_2O/CuO$, with air and $N_2$.

***Subtask 16.4 – Process Model***

Because of the challenges associated with the high-pressure TGA, the CLC Team did not begin the task of developing a simple process model of two interconnected well-stirred reactors.

**Task 17.0 – Material Investigations for Fuel-Conversion Systems**

***Subtask 17.1 – Institutional Cooperation***

Utah Clean Coal Program began establishing long-term interactions with the Albany and Pittsburgh offices of NETL to study materials issues, including defining operating windows and conditions for fuel-conversion processes, especially ultra-supercritical steam generators.

***Subtask 17.2 – Submodel Development***

One major challenge in modeling ash/slag phase equilibrium is that the ash/slag system involves many solid compounds that are stable over different ranges of temperatures and compositions. In addition, if the structures of solids are similar, solid solutions may be formed, resulting in more complex computation. In this study, the liquidus temperature is defined as the point where lowering temperature will result in new solid phase formation (i.e., solid precipitation). Likewise, the solubility is defined as the weight fraction of the added solute in the saturated liquid slag. Note that the solubility definition indicates that the liquid slag is saturated with respect to any possible solid species or solid solutions whose addition may decrease the total Gibbs energy of the system. These solid species may or may not be the solute or any species that have the same formula forms as the liquid species. It is assumed in this study that compounds with the same formulae but in different phases are taken as different species. In practice, the definition of solubility implies that the dissolution process will be restricted when the solute is covered with a solid layer that is saturated with the liquid slag. Figure 84 shows a typical dissolution process for an $Al_2O_3$-based refractory material dissolving in a coal slag. Once a precipitated solid layer (e.g., $Ca_2Al_2SiO_7$) completely covers the solute surface, it blocks the direct contact of the solute and the slag and thus limits further $Al_2O_3$ dissolution. One specific application example of the solubility defined in this study is the design of the water cooled gasifiers where less anti-corrosive materials (e.g., $Al_2O_3$-based materials) are used as refractories. Though these materials might still be thermodynamically dissolvable in the liquid slag, they are protected by the precipitated/frozen solid layer that is saturated with the liquid slag along the gasifiers.

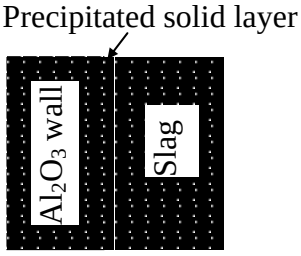


**Figure 84**. Solid precipitation protects solute from further dissolution.

The liquid slag phase is assumed to be the base phase in this study, and the $\omega_i$s of all solid phases are computed based on the liquid composition. One major advantage of this assumption is that the chemical potentials of the liquid phase only need to be computed once in each computational cycle. In other words, the liquid phase can be taken as a new pure species phase with fixed ratios of elements, and thus, the computation of the sub-optimization problem defined in the following equation is avoided for the liquid solution.

$$Q_2^T \vec{\mu} = 0$$

Oxide compositions, as opposed to elemental compositions, are usually used in typical ash chemistry analyses because the majority of ash/slag is comprised of oxides. The quasi-chemical model[3, 4] is used for the liquid slag solution because this model can use a set of generalized parameters when correlating slags with many different oxides. Another advantage of using oxide compositions for the slag is that, as shown in the following solubility section, it can simplify the computation for species with complex elemental compositions. Based on the above modeling description, the algorithms used to find the liquidus temperature and solubility are summarized in Table 16.

**Table 16**. Simplified algorithm used to find the liquidus temperature and species solubility.

| Liquidus temperature | Species solubility |
|---|---|
| (1) Assume slag is liquid | (1) Assume slag is liquid |
| (2) Determine temperature range | (2) Determine solubility range |
| (3) Guess a liquidus temperature $T_q$ | (3) Guess a composition $x_i$ |
| (4) Calculate chemical potentials for all possible species comprised of slag elements | (4) Calculate chemical potentials for all possible species comprised of slag elements |
| (5) Calculate $\omega_i$ of non-present solids | (5) Calculate $\omega_i$ of non-present solids |
| (6) If min($\omega_i$) != 0, goto (3) | (6) If min($\omega_i$) != 0, goto (3) |
| | (7) Obtain $w_{sat}$ |

The solubility ($w_{sat}$) in Table 16 is defined as the weight fraction of the added solute in the saturated solution comprised of the original unsaturated slag and the added solute. Solid precipitation will occur as long as at least one of the $\omega_i$ is less than zero. Therefore, the minimal $\omega_i$ value is used in Table 16 for a system with more than two possible phases. If only one phase is currently not present, Steps (6) in Table 16 can be further simplified using the following equation.

*Approach.* A general phase equilibrium algorithm using the Gibbs energy minimization approach can be expressed by the following equations

Minimize:

$$G = \sum_{i=1}^{I} n_i \mu_i \tag{9}$$

Subject to:

$$\sum_{i=1}^{I} a_{ij} n_i = b_j,\ j = 1, \ldots, J \tag{10}$$

$$n_i \geq 0, i = 1, \ldots, I \tag{11}$$

where $G$ is the total Gibbs energy of the system, $\mu_i$ is the chemical potential of species $i$, $n_i$ is the number of moles of species $i$, $a_{ij}$ is the stoichiometric coefficients (as moles of element $j$ in 1 mole of species $i$), $b_j$ is the number of moles of element $j$, and $I$ and $J$ are the total number of species and elements, respectively. The minimization problem formulated in Equations (9)-(11) can be restated using the Lagrangian method as

$$\text{Minimize } L = \sum_{i=1}^{I} n_i \mu_i - \sum_{j=1}^{J} \pi_j \left( \sum_{i=1}^{I} a_{ij} n_i - b_j \right) - \sum_{i=1}^{I} \omega_i n_i \tag{1}$$

where $\pi_j$ and $\omega_i$ are the mass balance and non-negative constraint Lagrange multipliers, respectively, and $L$ is the unconstrained Lagrangian function. At equilibrium, the system satisfies the following conditions:

$$\frac{\partial L}{\partial n_i} = \mu_i + \sum_{k=1}^{I} n_k \frac{\partial \mu_k}{\partial n_i} - \sum_{j=1}^{J} \pi_j a_{ij} - \omega_i = 0 \tag{12}$$

$$\frac{\partial L}{\partial \pi_j} = \sum_{i=1}^{I} a_{ij} n_i - b_j = 0,\ j = 1, \ldots, J \tag{13}$$

$$\frac{\partial L}{\partial \omega_i} = n_i = 0 \tag{14}$$

Equation (12) can be further simplified into,

$$\frac{\partial L}{\partial n_i} = \mu_i - \sum_{j=1}^{J} \pi_j a_{ij} - \omega_i = 0 \tag{15}$$

using the Gibbs-Duhem equation. A vector form of Equation (15) is expressed as follows,

$$\vec{\mu} = A\vec{\pi} + C\vec{\omega} \tag{16}$$

where $A$ is the matrix of $a_{ij}$, and each column of $C$ ($\vec{c}_j$) is a unit vector defined as:

$$c_{ij} = \begin{cases} 1, \text{species } i \text{ is not present} \\ 0, \text{species } i \text{ is present} \end{cases} \tag{17}$$

From Equation (14), at equilibrium, $\frac{\partial L}{\partial \omega_i} = 0$ is valid only if $n_i = 0$, or species $i$ is not present in the system. In other words, if species $i$ is present in the system, $\omega_i$ will not be in the non-negative constraint set, which implies $\omega_i = 0$, and Equation (15) can be further simplified into

$$\frac{\partial L}{\partial n_i} = \mu_i - \sum_{j=1}^{J} \pi_j a_{ij} = 0 \quad \text{for } n_i > 0 \tag{18}$$

Since Lagrange multipliers must be positive at a global optimal, a negative $\omega_i$ value indicates that the addition of species $i$ into the current system can possibly lower the system Gibbs energy. Therefore, we can use the $\omega_i$ values of non-present species to determine if the present phases are stable at a given temperature.

Greenberg (1986) developed a phase equilibrium algorithm based on the Newton's method where a QR decomposition procedure was used to account for the linear and nonnegative constraints,

$$Q^T (A \mid C) = R \tag{19}$$

where $Q$ is an ($I \times I$) orthonormal matrix, $A|C$ is the combined matrix consisting of active constraints, and $R$ is an upper triangular matrix. The $Q^T$ matrix can be partitioned as

$$\begin{pmatrix} Q_1^T \\ Q_2^T \\ Q_3^T \end{pmatrix} (A \mid C) = \begin{pmatrix} R_{11} & R_{12} \\ 0 & R_{22} \\ 0 & 0 \end{pmatrix} \tag{20}$$

where $Q_1^T$ is a ($J$×$I$) matrix, $Q_2^T$ is a (($M$-$J$)×$I$) matrix, $Q_3^T$ is a (($I$-$M$)×$I$) matrix, and ($A$|$C$) is the total constraint matrix constructed by appending the non-present species constraint vector after the mass balance matrix. The value of $M$ is the summation of the mass balance and active non-negative constraints (for non-present species). The $\vec{\omega}$ vector can be solved by multiplying $Q_2^T$ on both sides of Equation (16) as shown in Equation (21).

$$Q_2^T \vec{\mu} = Q_2^T A \vec{\pi} + Q_2^T C \vec{\omega} \tag{21}$$

From Equation (20), we have,

$$Q_2^T A = 0 \tag{22}$$

and Equation (21) can be simplified into

$$Q_2^T \vec{\mu} = Q_2^T C \vec{\omega} \tag{23}$$

The values of $\omega_i$s can be easily solved using Equation (23) since $Q_2^T C$ is an upper triangular matrix.

Equation (23) is only valid for pure non-present species phases. If a solution phase is to be added into the system, we then want to find the solution $\omega_i$ values at the composition where the addition of the phase can mostly decrease the total Gibbs energy. A more negative $\omega_i$ value implies that the addition of the corresponding phase is more likely to decrease the system Gibbs energy. Therefore, the minimum $\omega_i$ values are used for non-present solution phases, which can be obtained by solving Equation (24),

$$\min \sum_{i=1}^{p} x_i \omega_i, \qquad \text{subject to} \quad \sum_{i=1}^{p} x_i = 1 \tag{24}$$

where $p$ is the number of species in the non-present solution phase, and $x_i$ is the mole fraction of each species in the phase.

$$\mu_i - \omega_i = \sum_{j=1}^{J} \pi_j a_{ij} \tag{25}$$

which implies that the value of $\mu_i - \omega_i$ is only a function of present species. Therefore, the value of $\omega_i$ at any given composition, $x$, can be found by

$$\omega_i(x) = \mu_i(x) - (\mu_i^0 - \omega_i^0) \tag{27}$$

where $\mu_i^0 - \omega_i^0$ is the $\mu_i - \omega_i$ value calculated using Equation (25) at the limiting concentration. It is assumed that below this concentration, the corresponding species are assumed to be non-present. To avoid computational overflow for certain functions, such as ln($x$) in typical solid phases, this limiting

concentration is defined as a small positive number, having insignificant effect on the system Gibbs energy and its dominant species.

Equation (24) can be solved using the following unconstrained Lagrangian function,

$$\text{Minimize} \quad Lp = \sum_{i=1}^{p} x_i \omega_i - \lambda \left( \sum_{i=1}^{p} x_i - 1 \right) \tag{28}$$

where *Lp* is the Lagrangian multiplier function for the non-present solution phase.

Equation (28) shows the derivatives of *Lp* with respect to $x_i$.

$$\frac{\partial Lp}{\partial x_i} = \omega_i - \lambda = \mu_i - (\mu_i^0 - \omega_i^0) - \lambda \tag{29}$$

A modified conjugate gradient method[2] is used in this work to solve Equation (29) to avoid evaluating the second-order derivatives of Gibbs energy with respect to $x_i$,. Once all $\omega_i$ are calculated, they are compared with zero to determine if the present solution is stable ($\omega_i > 0$ for all non-present species) or unstable (at least one $\omega_i < 0$), which can be used to find the liquidus temperature or the solubility of solute for a given system.

*Liquidus temperature computation.* In the liquidus temperature computation, the temperature range in Step (2) of Table 1 can be estimated using (i) a high limiting temperature that guarantees the existing single phase (i.e., liquid phase) is stable (e.g., 3000 K) and (ii) a low limiting temperature that guarantees the occurrence of solid precipitation (e.g., 298.15 K).

Figure 85 depicts a liquidus temperature computation example of liquid slag in equilibrium with pure solid species computed using the proposed algorithm and the thermodynamic data reported by Wu et al.[5] It can be found that each intermediate compound (e.g., $Na_2SiO_3$, $Na_2Si_2O_5$, etc.) is stable and only impacts the liquidus temperature curve over a limited range of compositions.

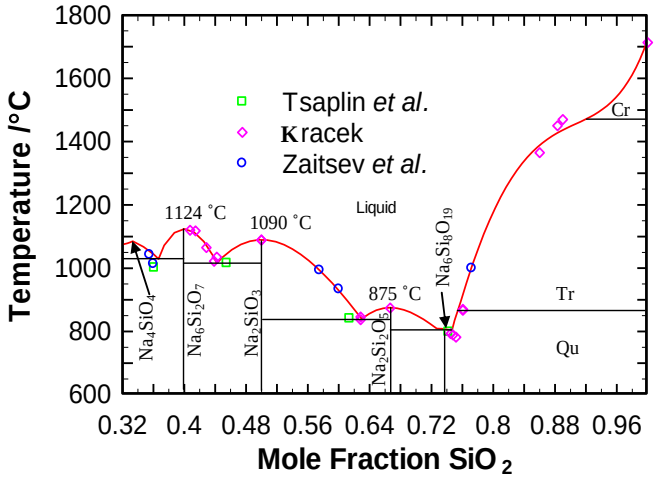


**Figure 85**. *T-x* of $Na_2O$-$SiO_2$. Experimental data: □ Tsaplin et al. (2000), ◊ Kracek (1930), ○ Zaitsev et al. (1999) (—) : Results calculated using the present algorithm.

Figure 86 illustrates the liquidus temperature vs. composition for a FeO-$SiO_2$ system computed based on the thermodynamic data reported by Romero-Serrano and Pelton (1999). An immiscible liquid region is formed over the $SiO_2$ composition range of 0.57~0.99, which is computed by introducing a second liquid solution phase (with quite different initial compositions from the original liquid solution) into the computational system.

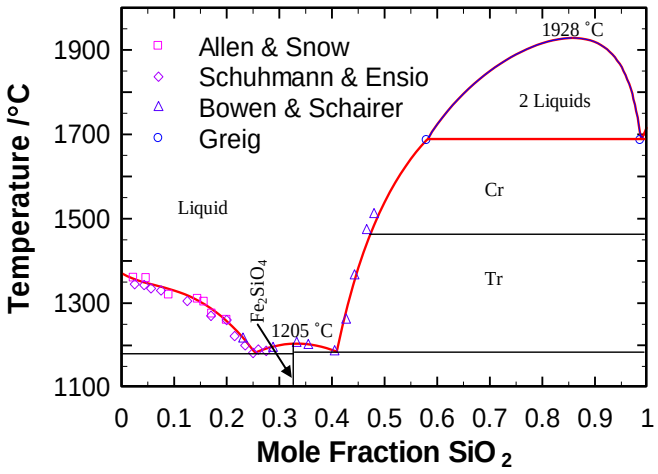


**Figure 86**. T-x of FeO-$SiO_2$. Experimental data: □ Allen and Snow (1955), ◊ Schuhmann and Ensio (1951), Δ Bowen and Schairer (1932), ○ Greig (1927) (—): Results calculated using the present algorithm.

Figure 87 depicts the melting point graph of the CaO-$Al_2O_3$-$SiO_2$ system computed using the thermodynamic data reported by Eriksson and Pelton (1993). Because no solid solution has been observed within the CaO-$Al_2O_3$-$SiO_2$ system, the liquidus temperature is equal to the melting temperature. Figure 87 is plotted based on 1524 melting points calculated every 0.025 mole fraction of each species. On a computer with an Intel Xeon 3.2 GHz CPU and 2.0 GB memory, it takes ~ 0.01 seconds in average to compute each point with temperature convergence accuracy up to $10^{-3}$ $^{o}$C. The melting point computation using the proposed methodology is only a function of composition, which is different from common commercial algorithms whose computation is usually based on both temperature and element/component compositions. Notice that there is no direct computational comparison between the proposed algorithm and those used in commercial software because the software package used in the present work does not have a similar graphic user interface and supporting functions present in commercial software. Regardless of these differences, the proposed algorithm is believed to run more efficiently than general Gibbs energy minimization-based commercial software because it only requires solving a one-variable nonlinear equation given chemical potentials of non-present species.

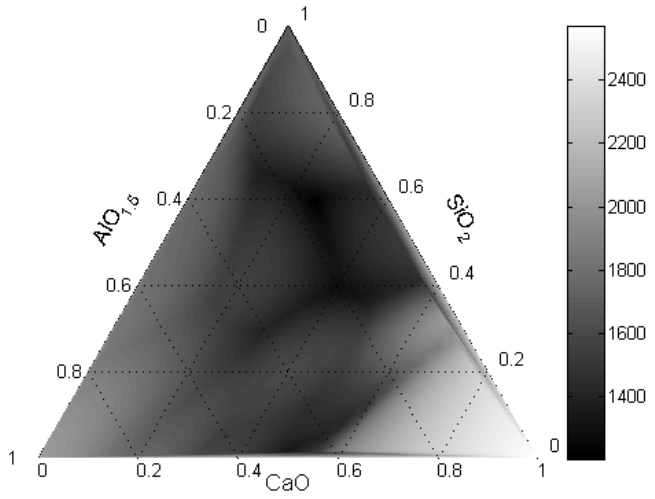


**Figure 87**. Temperature($^{o}$C)-composition of CaO-$Al_2O_3$-$SiO_2$ as a function of mole fraction.

*Solubility examples.* Figure 88 depicts the solubility of $Al_2O_3$ in several binary $Al_2O_3$-$SiO_2$ slags (an example as shown in Case (a) of Figure 89). The transition temperature corresponds to the melting temperature of $Al_6Si_2O_{13}$, which impacts the solubility curve greatly.

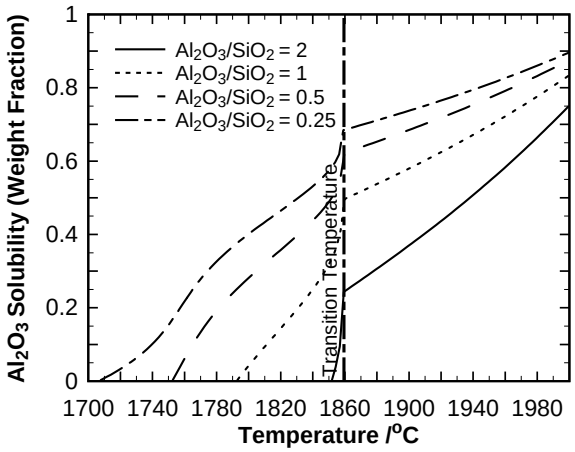


**Figure 88**. Solubility of $Al_2O_3$ as a function of temperature.

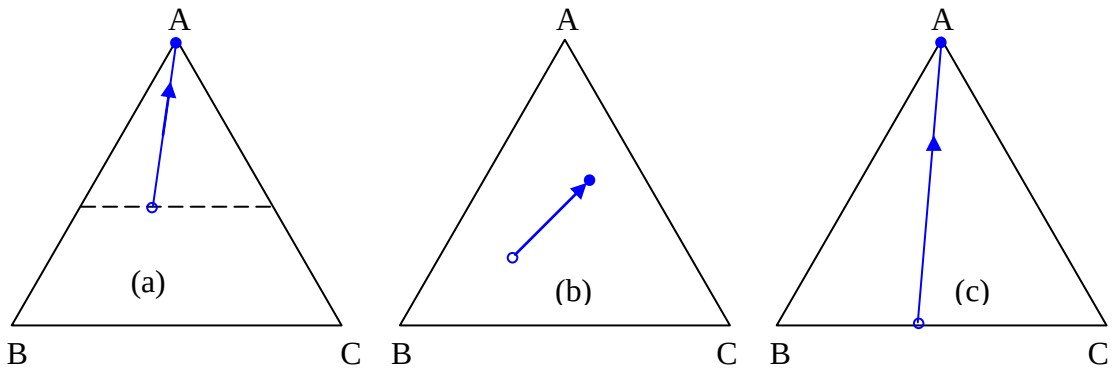


**Figure 89**. Diagram of solubility computation path. (◦) represents the liquid composition point, arrow represents solute addition direction, and (•) represents the solute composition point.

Figure 90 shows a solubility example as discussed in Case (b) of Figure 89. The solubility of $Ca_2Al_2SiO_7$ in the $CaO$-$Al_2O_3$-$SiO_2$ slag is computed by adding $CaO$, $Al_2O_3$, and $SiO_2$ in the liquid with a fixed molar ratio of $CaO$:$Al_2O_3$:$SiO_2$ = 2:1:1.

Both Figure 89 and Figure 90 are computed using the thermodynamic data reported by Eriksson and Pelton (1993).

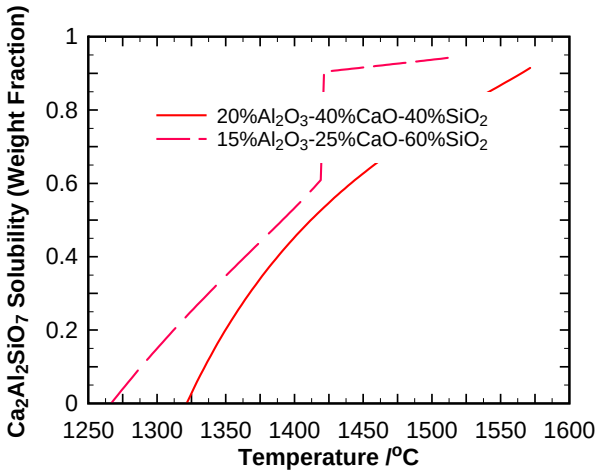


**Figure 90**. Solubility of $Ca_2Al_2SiO_7$ as a function of temperature.

Figure 91 and Figure 92 illustrate two examples as described in Case (c) of Figure 89, computed using the thermodynamic data reported by Eriksson and Pelton (1993) and Degterov and Pelton (1997), respectively. To compute the solubility of $Al_2O_3$ and $Cr_2O_3$ in $CaO$-$SiO_2$, two ternary slags, $CaO$-$Al_2O_3$-$SiO_2$ and $CaO$-$Cr_2O_3$-$SiO_2$, are created. The solubility is calculated with the initial weight fraction of $Al_2O_3$ and $Cr_2O_3$ at $10^{-3}$ %.

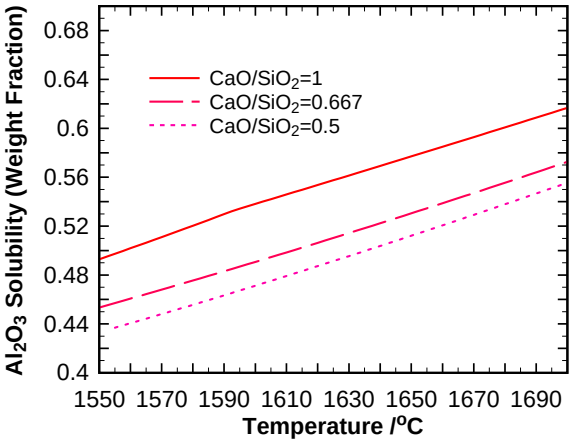


**Figure 91**. Solubility of $Al_2O_3$ in $CaO\text{-}SiO_2$ solutions.

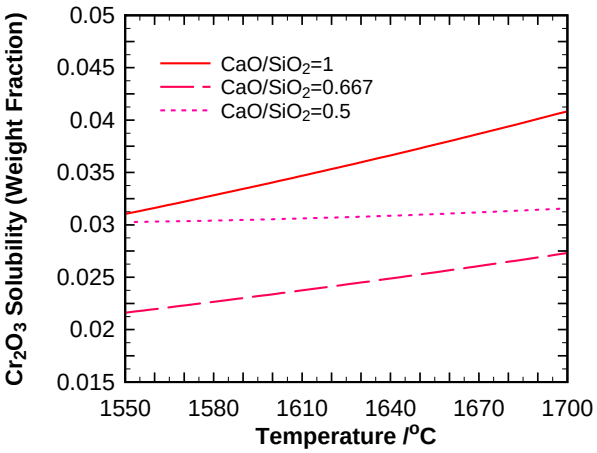


**Figure 92**. Solubility of $Cr_2O_3$ in $CaO\text{-}SiO_2$ solutions.

A that the solubility of $Cr_2O_3$ is much less than that of $Al_2O_3$, which indicates that $Cr_2O_3$-based refractories are more anti-corrosive and therefore more durable than $Al_2O_3$-based refractories under harsh operating conditions such as those found in coal gasification processes.

Figure 93 depicts the optimized fraction of the $Al_2O_3\text{-}Cr_2O_3$ sesquioxide solution in a saturated ternary slag, attentively computed using the thermodynamic data reported by Degterov and Pelton (1996a, 1996b, 1997). (The modeling parameters of the quaternary slag, $Al_2O_3\text{-}Cr_2O_3\text{-}CaO\text{-}SiO_2$, have not been critically evaluated and validated in literature; however, the predicted results are expected to be reasonable and representative based on the available thermodynamic data and quasi-chemical modeling approach). Because $Al_2O_3$ and $Cr_2O_3$ have different transport properties (e.g., diffusivities), the solubility of solid solutions is indefinite. On the other hand, the insolubility of the solid solution can be evaluated, which corresponds to the fraction where the solid solution is most likely precipitated at the given liquid slag composition.

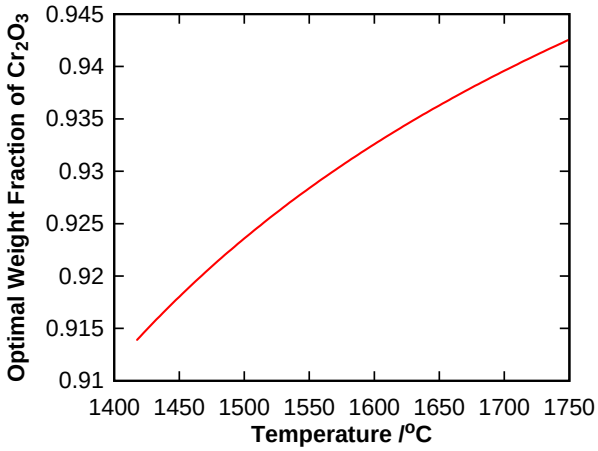


**Figure 93**. Most insoluble weight fraction of $Cr_2O_3$ in the $Al_2O_3$-$Cr_2O_3$ refractory with respect to a 20%$Al_2O_3$-40%CaO-40%$SiO_2$ liquid slag.

*Summary*. Under this subtask, a simplified phase diagram algorithm was developed to calculate the slag liquidus temperature at given compositions and solute solubility at given temperatures and compositions. Several binary and ternary systems have been used as examples to verify the algorithm and illustrate its applications. This algorithm runs quickly since only a one-variable root-finding method and the first-order derivatives (chemical potentials) of the Gibbs energy are needed for its computation. However, the algorithm cannot be used to calculate the species and phase distribution if phase transition does occur. If knowledge of the species/phase distribution is needed, a normal Gibbs energy minimization routine is called to calculate the moles and corresponding phases of species at equilibrium.

The algorithm presented in this study has been integrated into the INL gasification and refractory wear package (Liu et al. 2008) as a subroutine to compute phase equilibrium-related estimations where the species/phase distribution is not a concern (e.g., slagging gasifier temperature design, chemical corrosion, and spalling of refractories).

### Task 18.0 – Student Research Experience at DOE NETL

The University of Utah, in cooperation with DOE NETL, offered two students, David Ray Wagner and David Johnson, an opportunity to perform research at NETL. David Ray Wagner worked on the dynamics of a cold-flow circulating fluidized (CFCFB) beds using two sets of existing experimental data and performing tracer studies. The tracer technique excited phosphorescent polyethylene beads, which contain a dye at 10% by weight, by flashing a bright xenon flash tube. This intense light then excited the surfaces of the particles and was read downstream by fiber optic probes. The resulting curves were then integrated or differentiated, yielding concentration and therefore void fractions as well as particle velocities.

David Johnson also worked on the CCCFB. He designed, built, and installed a new air-sparger system. In the system air was injected into the reactor through six soaker hoses lying along the bottom of the L-valve. The air was separated into these six hoses through a PVC manifold. This system performed well, helping the particles in the reactor run more smoothly and quickly. He also worked on a fiber-optic probe, including methods to calibrate the fiber-optic probe to make concentration measurements.

# Conclusions

The Utah Clean Coal Program's mission was to generate scientific and technical information to allow for the clean and efficient utilization of coal in a carbon-constrained world. It generated key findings in the following areas:

*Simulation.* The Simulation Team successfully verified the molecular viscous diffusion and the stochastic eddy event processes in the enhanced ARCHES LES coded. In addition, they verified the ODT code and demonstrated it for planar jets, with and without particles. They found that small particles were greatly affected by the turbulent eddies while large particles are less affected. Small particles were quickly dispersed by the turbulent eddies while larger particles tended to cluster near the edges of the jet. The larger particles demonstrated larger coherent structures axially than the smaller particles. They also demonstrated that for the OFC reactor, complete particle pyrolysis occurred after roughly 0.35 m downstream, or 25 primary inlet diameters, from the inlet.

*Mercury.* The Mercury Team focused on fixed-bed experiments and models. They identified the highest efficiency of the sorbent for mercury capture, near 100 percent, for exposure of the coconut-shell carbon either to 50 ppm chlorine (as HCl equivalent) or 50 ppm bromine (as HBr equivalent) at 150$^{o}$C. In addition, the Langmuir-based, fixed-bed model showed a reasonable ability to fit fixed-bed breakthrough data from a variety of sources for powdered activated carbons. It is important to include the PSD in fixed-bed models because mercury uptake is strongly related to particle size. Furthermore, intraparticle diffusion was found to offer significant resistance to adsorption for larger particles.

*Oxycoal combustion.* The Oxycoal Team investigated the effects of variations in the $P_{O2}$ and $CO_2$ concentration on coal jet ignition in *retrofit* oxycoal combustion applications and provided fundamental rate parameters and sub-scale model validation for CFBs. The $P_{O2}$ in the transport (primary) stream effected flame stability, as measured by flame stand-off distance; flame stability increased as $P_{O2}$ in transport stream increased. The effect of $P_{O2}$ in the transport stream was more significant than the effect of $P_{O2}$ in secondary stream. In addition, increasing the preheat temperature increased flame stability. The single-particle reactor studies revealed that as $O_2$ concentration increased, $NO_2$ emissions decreased in $O_2$-$CO_2$ combustion, a trend that was opposite to that observed in $O_2$-$N_2$ combustion. Also, overall $N_2O$ emissions are somewhat higher when $N_2$ was used instead of $CO_2$ as balance gas, although this observation needs further verification. Successful oxycoal combustion in the pilot-scale CFB demonstrated its potential for subsequent oxycoal research. Cold-flow studies in the CFB determined minimum fluidization velocities, and hot-flow tests provided initial temperature, pressure, LOI and emissions.

*Gasification.* The Gasification Team focused on an improved understanding of carbon conversion, char to slag transformation, and the development of experimental and simulation tools to predict the performance of an entrained-flow gasifier. The investigators explored soot formation using model compounds in an atmospheric flat-flame burner, and their preliminary results showed that soot from the model compound, PDN, did not exhibit as much structural change as that observed in the coal soot. In addition, using the new high-temperature, entrained-flow reactor system the Gasification Team produced a series of coal chars with varying carbon contents corresponding to various degrees of conversion. At temperatures in excess of the coal's ash fusion temperature, a significant decrease in internal surface area was observed at a conversion of roughly 92%. This was a result of the char transitioning ("collapsing") from a highly porous, solid material into a melted, much less porous slag-type material, and it appeared to be associated with migration of mineral inclusions to the surface of the char. The Team also investigated ash emittance, thermal conductivity, and sintering rates under reducing and oxidizing conditions. They found that ash deposit structure, independent of porosity, had a major impact on deposit thermal conductivity and sintering; subbituminous ash formed deposits with lower thermal conductivity and

emittance than bituminous ash; thermal conductivities of both ashes were essentially independent of local stoichiometry if all else remain constant; and reducing conditions favored sintering, especially for bituminous coals.

*Sequestration.* The Sequestration Team's most significant conclusions related to the simulation of vertical migration of $CO_2$ and the reaction kinetics for $CO_2$, brines and rocks. In all of the kinetic experiments, changes in mineralogy were evident, and in general changes in rock chemistry mirrored those seen in brine. In experiments with $CO_2$, one of the most important conclusions was the observation of calcite re-precipitation indicating that permanent mineralogical sequestration is possible. Chlorite dissolution and analcime and ankerite precipitation were common features in all $CO_2$ experiments. In experiments containing $SO_2$, the mineralogical reactions differed in that the dissolution patterns continued and no calcite re-precipitation was observed. The most significant findings in these experiments were the precipitation of anhydrite, gypsum and bassanite. The Sequestration Team studied vertical mixing and equilibration times of $CO_2$ in the free gas and dissolved forms in a layered reservoir and found that distribution depends on the absolute permeability of the seals and on the relative permeabilities.

*CLC*. The CLC Team investigated oxidation/reduction kinetics of metal oxides. The oxidation experiments in air showed the complete oxidation of Ni to NiO in a single step. The limited data for the reduction of NiO with 50% $H_2$ in $N_2$ indicated the complete reduction of NiO to Ni at a comparatively low temperature (below 500°C). Cu oxidation experiments in air revealed a more complex oxidation process reflecting the multiple oxidation states of Cu. In addition, CuO underwent decomposition to yield oxygen gas and $Cu_2O$ under $N_2$ at elevated temperatures, in contrast to NiO which did not decompose at temperatures of interest. The investigators successfully demonstrated limited cycling of the oxidation/decomposition of copper oxide over times as long as thirty hours with a single charge of unsupported Cu/CuO.

*Material investigations*. Under this subtask, a simplified phase diagram algorithm was developed to calculate the slag liquidus temperature and solute solubility at given temperatures and compositions. The algorithm was verified using several binary and ternary systems, and it has been integrated into the INL gasification and refractory wear package (Liu et al. 2008).

## Acknowledgement

This material is based upon work supported by the Department of Energy under Award Number DE-FC26-06NT42808.

## References

Allen, W. C.; Snow, R. B. The orthosilicate-iron oxide portion of the system CaO-"FeO"-$SiO_2$. *Journal of the American Ceramic Society 38* (1955) 264-280.

Borrego, A.G.; Alvarez, D. Comparison of chars obtained under oxy-fuel and conventional pulverized coal combustion atmospheres, *Energy & Fuels* 21 (2007) 3171-3179.

Bowen, N. L.; Schairer, J. F., The system: FeO-$SiO_2$. *American Journal of Science 24* (1932) 177-213.

Bradbury, L.J.S.; Riley, J. The spread of a turbulent plane jet issuing into a parallel moving airstream. *J. Fluid Mech*., 27 (1967) 381–394.

Bustard, J.; Durham, M.; Starns, T.; Lindsey, C.; Martin, C.; Schlager, R.; Baldrey, K. *Fuel Processing Technology* 85 (2004) 549-562.

Carey, T.R.; Hargrove, O.W.; Richardson, C.F.; Change, R.; Meserole, F. Performance of activated carbon for mercury control in utility flue gas using sorbent injection. In: *Proceedings of the First*

*EPRI-DOE-EPA Combined Utility Air Pollutant Control Symposium*, Washington, DC, USA, August 25-29, 1997.

Chandel, M. K.; Hoteit, A.; Delebarre, A., Experimental investigation of some metal oxides for chemical looping combustion in a fluidized bed reactor. *Fuel* 2009, 88, (5), 898-908.

Cremer, M.; Senior, C.; Chiodo, A.; Wang, D.; Valentine, J. CFD modeling of activated carbon injection for mercury control in coal-fired power plants. *REI Technical Report*, 2005.

Degterov, S.; Pelton, A. D. Critical evaluation and optimization of the thermodynamic properties and phase diagrams of the $CrO$-$Cr_2O_3$-$SiO_2$ and $CrO$-$Cr_2O_3$-$SiO_2$-$Al_2O_3$ systems. *Journal of Phase Equilibria 17* (6) (1996a) 488-494.

Degterov, S.; Pelton, A. D., Critical evaluation and optimization of the thermodynamic properties and phase diagrams of the $CrO$-$Cr_2O_3$, $CrO$-$Cr_2O_3$-$Al_2O_3$, and $CrO$-$Cr_2O_3$-$CaO$ Systems. *Journal of Phase Equilibria 17* (6) (1996b) 476-487.

Degterov, S.; Pelton, A. D., Critical evaluation and optimization of the thermodynamic properties and phase diagrams of the $CrO$-$Cr_2O_3$-$SiO_2$-$CaO$ system. *Metallurgical and Materials Transactions B-Process Metallurgy and Materials Processing Science 28* (2) (1997) 235-242.

Deng, Z.; Xiao, R.; Jin, B.; Song, Q.; Huang, H., Multiphase CFD modeling for a chemical looping combustion process (fuel reactor). *Chem. Eng. Technol*., 31, 12 (2008) 1754-1766.

Eriksson, G.; Pelton, A. D. Critical evaluation and optimization of the thermodynamic properties and phase diagrams of the $CaO$-$Al_2O_3$, $Al_2O_3$-$SiO_2$, and $CaO$-$Al_2O_3$-$SiO_2$ Systems. *Metallurgical Transactions B 24* (5) (1993) 807-816.

Flora, J.R.V.; Hargis, R.A.; O'Dowd, W.J.; Pennline, H.W.; Vidic, R.D. *J. Air & waste Manage. Assoc.* 53 (2003) 478-488.

Fox, R.O. *Computational Models for Turbulent Reacting Flows*. Cambridge University Press, 2003.

Ghorishi, B.; Gullett, B. K. Sorption of mercury species by activated carbons and calcium-based sorbents: effect of temperature, mercury concentration and acid gases, *Waste Manage. Res. 16,* 6 (1998) 582-593.

Greenberg, J. P. The Design of Chemical Equilibrium Computation Algorithms and Investigations into the Modeling of Silicate Phase Equilibria. Dissertation, University of California, San Diego, San Diego, 1986.

Greig, J. W. Liquid immiscibility in the system: $FeO$-$Fe_2O_3$-$Al2O_3$-$SiO_2$. *American Journal of Science 14* (5) (1927) 473-84.

Harvie, C.E.; Moller. N.; Weare, J.H. The prediction of mineral solubilities in natural waters: The Na-K-Mg-Ca-H-Cl-SO4-OH-$HCO_3$-$CO_3$-$H_2O$-system to high ionic strengths at 25°C, *Geochim. Cosmochim. Acta*, 48, 4 (1984) 723-751.

Hawkes, E.R.; Sankaran, R.; Sutherland, J.C.; Chen. J.H. Scalar mixing in direct numerical simulations of temporally-evolving plane jet flames with detailed $CO/H_2$ kinetics. In *Proc. Combust. Inst*., 31, (2007) 1633–1640.

Hinds, W. *Aerosol Technology*, 2nd Edition, John Wiley and Sons, Inc., 1999.

Hurt, R. H.; Sarofim, A.F.; Longwell, J.P. *Fuel* 70 (1991). 1079–1082.

Ishida, M.; Jin, H. A new advanced power-generation system using chemical-looping combustion. *Energy*, 19, 4, (1994) 415-422.

Kerstein, A.R; Ashurst, W.T.; Wunsch S.; et al. One-dimensional turbulence: vector formulation and application to free shear flows. *J. Fluid Mech*. 447 (2001) 85-109.

Karatza, D.; Lancia, A.; Musmarra, D. *Environ. Sci. Technol.* 32 (1998) 3999-4004.

Kaszuba, J.P.; Janecky, D.R.; Snow, M.G. Experimental evaluation of mixed fluid reactions between supercritical carbon dioxide and brine: Relevance to the integrity of a geologic carbon repository. *Chem. Geol.* 217 (2005) 277-293.

Kracek, F. C., The System Sodium Oxide-Silica. *Journal of Physical Chemistry 34* (1930) 1583-98.

Kunii, D.; Levenspiel, O. *Fluidization Engineering*, 2nd Ed., Butterworth-Heinemann, 1991.

Jackson. J.E. *A User's Guide to Principal Component Analysis*. Wiley Series in Probability and Statistics, 1991.

Lewis, W.K.; Gilliland, E.R. Production of Pure Carbon Dioxide. Patent 2665972, 1954.

Lin, S. Y.; Hirato, M.; Horio, M. *Energy & Fuels*, 8 (1994) 598–606.

Liu, B.; Baxter, L. L.; Garcia, H. E., Refractory Wear in Entrained Flow Coal Gasifiers, Unpublished Work. Idaho National Laboratory: Idaho Falls, Idaho, 2008.

Liu, H.; Luo, C.; Kato, S.; Uemiya, S.; Kaneko, M.; Kojima, T. *Fuel Processing Technology*, 87 (2006) 775–781.

Lui, W.; Vidic, R.D.; Brown, T. D. Impact of flue gas conditions on mercury uptake by sulfur-impregnated activated carbon. *Environ. Sci. Technol.* 34 (2000) 154-159.

Liu, S.; Yan, N.; Liu, Z.; Qu, Z.; Wang, H.P.; Chang, S.; Miller, C. Using bromine gas to enhance mercury removal from flue gas of coal-fired power plants. *Environ. Sci. Technol.* 41 (2007) 1405-1412.

Logan R.W.; Nitta, C.K. *Comparing 10 methods for solution verification, and linking to model validation*, March 2005, LLNL Report, UCRL-TR-210837.

Maas, U.; Pope, S.B. Implementation of simplified chemical kinetics based on intrinsic low-dimensional manifolds. In: *Proc. Combust. Inst*., 24 (1992) 103–112.

Maas, U.; Pope, S.B. Laminar flame calculations using simplified chemical kinetics based on intrinsic low-dimensional manifolds. In: *Proc. Combust. Inst*., 25 (1994) 1349–1356.

Mattisson, T.; Lyngfelt, A.; Leion, H., Chemical-looping with oxygen uncoupling for combustion of solid fuels. *Int. J. Greenhouse Gas Control* 3, 1 (2009) 11-19.

Meserole, F.B.; Change, R.; Carey, T.R.; Machac, J.; Richardson, C.F. *J. Air & Waste manage. Assoc.* 19 (1999) 694-704.

Miller, S.J.; Dunham, G.E.; Olson, E.S.; Brown, T.D. Flue gas effects on a carbon-based mercury sorbent, *Fuel Processing Technology*, 65-66 (2000) 343-363.

Olson, E. S.; Mibeck, B. A. Oxidation kinetics and the model for mercury capture on carbon in flue gas, *International Conference on Air Quality V*, Arlington, VA, September 19-21, 2005.

Presto, A.; Granite, E.J. Impact of sulfur oxides on mercury capture by activated carbon, *Environ. Sci. Technol.*, 41 (2007) 6579-6584.

Richter, H. J.; Knoche, K. F. Reversibility of combustion processes. *ACS Symp. Ser*. 1983, 235, 71-85.

Romero-Serrano, A.; Pelton, A. D. Thermodynamic analysis of binary and ternary silicate systems by a structural model. *Isij International 39* (5) (1999) 399-408.

Scala, F. *Industrial & Engineering Chemistry Research* 43 (2004) 2575-2589.

Schmidt, D.; Blasenbrey, T.; Maas, U. Intrinsic low-dimensional manifolds of strained and unstrained flames. *Combust. Theory Modelling*, 2 (1998) 135–152.

Shen, L.; Wu, J.; Xiao, J.; Song, Q.; Xiao, R., Chemical-looping combustion of biomass in a 10 kWth reactor with iron oxide as an oxygen carrier. *Energy & Fuels* 23, 5 (2009) 2498-2505.

Schuhmann, R., Jr.; Ensio, P. J. Thermodynamics of iron silicate slags: slags saturated with γ iron. *Journal of Metals 3* (1951) 401-11.

Simons, G.A. *Progress in Energy and Combustion Science*, 9 (1983) 269–290.

Smoot L.D.; Smith, P.J. *Coal Combustion and Gasification*. Plenum Press, 1985.

Spinti, J.; Thornock, J.N.; Eddings, E.G.; Smith, P.J.; Sarofim, A.F. Heat transfer to objects in pool fires, in: *Transport Phenomena in Fires*, M. Faghri and B. Sundeen. WIT Press, Southampton, B, UK, 2008.

Sutherland J.C.; Parente, A. Combustion modeling using principal component analysis. In *Proc. Combust. Inst.*, 32 (2009) 1563–1570.

Sutherland, J.C.; Smith, P.J.; Chen, J.H. A quantitative method for a priori evaluation of combustion reaction models. *Combust. TheoryModelling* 11(2) (2007) 287–303.

Tsaplin, A. A.; Zaitsev, A. I.; Shelkova, N. E.; Mogutnov, B. M., Thermodynamic properties and phase equilibria in $Na_2O$-$SiO_2$ and $K_2O$-$SiO_2$ systems. *Schriften des Forschungszentrums Juelich, Reihe Energietechnik/Energy Technology 15* (Pt. 1, High Temperature Materials Chemistry, Part 1) (2000) 59-62.

Xu, T.; Sonnenthal, E.L.; Spycher, N.; Pruess, K. TOURGHREACT: A simulation program for non-isothermal multiphase reactive geochemical transport in variably saturated geologic media. *Computer & Geosciences* 32 (2006)145-165.

Valorani, M. Habib N. Najm, and D. A. Goussis. CSP analysis of a transient flame-vortex interaction: time scales and manifolds. Combust. Flame, 134(1-2):35–53, 2003.

Zhang, J.; Okerlund, R.; Eddings, E.G.; Wendt. J.O.L. Ignition of axial pulverized coal jets in a specially designed 100 kw oxyfuel combustor. In Chuguang Zheng, editor, 6th International Symposium of Coal Combustion, pp. 1387–1393, Wuhan, China, 2007.

Zhang, G.,N.; Spycher, E.; Sonnenthal, C.; Steefel, Xu, T. Implementation of a Pitzer Activity Model into TOUGHREACT for modeling concentrated solutions, *Nuclear Technology*, 164 (2008) 180-195.

Zaitsev, A. I.; Shelkova, N. E.; Lyakishev, N. P.; Mogutnov, B. M., Thermodynamic properties and phase equilibria in the $Na_2O$-$SiO_2$ system. *Physical Chemistry Chemical Physics 1* (8) (1999) 1899-1907.

# List of Abbreviations

| | |
|---|---|
| Al | Aluminum |
| AR | Air reactor |
| $A_i$ | Surface area of the particle side shell of the control volume ($m^2$) |
| Btu | British thermal unit |
| BLPI | Berner low-pressure impactor |
| $C_{cv,i}$ | Gas phase mercury concentration in the void space of the particle at the node i (g $Hg/m^3$) |
| Ca | Calcium |
| $Cu_2O$ | Cuprous oxide |

| | |
|---|---|
| CFD | Computational fluid dynamics |
| CFB | Circulating fluidized bed |
| CFCFB | Cold flow circulating fluidized |
| $C_i$ | Gas phase concentration of component A (g / $m^3$) |
| Cl | Chlorine |
| CLC | Chemical looping combustion |
| $CO_2$ | Carbon dioxide |
| CLOU | Chemical looping with oxygen uncoupling |
| Cu | Copper |
| CuO | Cupric oxide |
| Da | Damkohler number |
| $D_{eff}$ | Effective diffusivity of gaseous, elemental mercury inside the particle ($m^2$/s) |
| DQMOM | Direct quadrature method of moments |
| DNS | Direct numerical simulation |
| DOE | Department of Energy |
| FGD | Flue gas desulfurization |
| FGR | Flue gas recycle |
| FR | Fuel reactor |
| HCl | Hydrogen chloride |
| Hg | Mercury |
| HBr | Hydrogen bromide |
| I.D. | Inner diameter |
| K | Potassium |
| $k_1$ | Adsorption constant ($m^2$/ g Hg s). |
| $k_2$ | Desorption constant (1/s). |
| $K_1$ | Kinetic constant of the adsorption reaction ($m^3$ / g min) |
| $K_2$ | Kinetic constant of the desorption ($min^{-1}$) |
| $K_{fr}$ | Sorption constant for Freundlich isotherm |
| KW | Kilowatt |
| LEFR | laminar entrained-flow reactor (LEFR) |
| LES | Large-eddy simulation |
| Lpm | Liters per minute |
| Md | millidarcy |
| Mg | Magnesium |
| MGS | Method of generated solutions |
| MMS | Method of manufactured solutions (MMS) |
| NDF | Number density function |
| NETL | National Energy Technology Laboratory |
| n | Number of species in the flue gas |
| N | Number of images |
| $N_2$ | Nitrogen |
| Na | Sodium |
| Ni | Nickle |
| NiO | Nickle oxide |
| Nm | Nanometer |
| NMR | Nuclear magnetic resonance |
| NO | Nitric oxide |
| $NO_2$ | Nitrogen dioxide |
| $NO_x$ | Mono-nitrogen oxides |
| $O_2$ | Oxygen |
| ODT | One dimensional turbulence |

| | |
|---|---|
| O.D. | Outer diameter |
| OC | Oxygen carrier |
| PA | Photoacoustic analyzer |
| PCA | Principal component analysis |
| PFFB | Pressurized flat-flame burner |
| $P_{O2}$ | Partial pressure of oxygen |
| ppm | parts per million |
| ppmv | parts per million by volume |
| $R_{ads}$: | Rate term for solid phase uptake of mercury (g Hg/s $m^3$) |
| Sc | Schmidt number |
| SCFH | Standard cubic feet per hour |
| SEM | Scanning electron microscopy |
| SIAC | Sulfur-impregnated activated carbon |
| SLPM | Standard liters per minute |
| SMPS | Scanning mobility particle sizer |
| $SO_2$ | Sulfur dioxide |
| TGA | Thermogravimetric analysis |
| TPO | Temperature programmed oxidation |
| TPR | Temperature programmed reduction |
| TCD | Thermal conductivity detector |
| $UC^3$ | Utah Clean Coal Program |
| $V_{cv,i}$: | Volume of the shell at the node i ($m^3$). |
| V/UQ | Validation and uncertainty quantification |
| W | Watt |
| $W_i$ | Solid phase concentration of component A (g Hg / g carbon) |
| $W_{max,i}$ | Asymptotic adsorbate concentration (g Hg / g carbon) |
| $\Delta r$ | Radial distance between adjacent shells (m) |
| $\varepsilon$ | Porosity of the bed (void fraction) |
| $\varepsilon_p$ | Porosity of the particle ($m^3$ void/ $m^3$ particle) |
| $\rho$ | Bulk density of the carbon (g carbon/$m^3$) |
| $\rho_p$ | Apparent density of the sorbent particle |
| $\omega_i$: | Solid phase, elemental mercury concentration at node i (g Hg/g carbon). |
| $\omega_{max}$: | Maximum elemental mercury uptake capacity of the sorbent (g Hg/ g carbon). |

# List of Figures

# List of Tables

# Modeling and Experimental Studies of Mercury Oxidation and Adsorption in a Fixed-Bed Reactor

Topical Report

Reporting period: July 1, 2006 to March 31, 2009

Authors: Paula A. Buitrago, Mike Morrill, JoAnn S. Lighty, Geoffrey D. Silcox.

June 2009

DOE Award Number: DE-FC26-06NT42808
Tasks 5 and 6

University of Utah
Institute for Clean & Secure Energy
380 INSCC, 155 South, 1452 East
Salt Lake City, UT 84112

# Disclaimer

# ABSTRACT

This report presents experimental and modeling mercury oxidation and adsorption data. Fixed-bed and single-particle models of mercury adsorption were developed. The experimental data were obtained with two reactors: a 300-W, methane-fired, tubular, quartz-lined reactor for studying homogeneous oxidation reactions and a fixed-bed reactor, also of quartz, for studying heterogeneous reactions. The latter was attached to the exit of the former to provide realistic combustion gases. The fixed-bed reactor contained one gram of coconut-shell carbon and remained at a temperature of 150$^{o}$C. All methane, air, $SO_2$, and halogen species were introduced through the burner to produce a radical pool representative of real combustion systems. A Tekran 2537A Analyzer coupled with a wet conditioning system provided speciated mercury concentrations. At 150°C and in the absence of HCl or HBr, the mercury uptake was about 20%. The addition of 50 ppm HCl caused complete capture of all elemental and oxidized mercury species. In the absence of halogens, $SO_2$ increased the mercury adsorption efficiency to up to 30 percent. The extent of adsorption decreased with increasing $SO_2$ concentration when halogens were present. Increasing the HCl concentration to 100 ppm lessened the effect of $SO_2$.

The fixed-bed model incorporates Langmuir adsorption kinetics and was developed to predict adsorption of elemental mercury and the effect of multiple flue gas components. This model neglects intraparticle diffusional resistances and is only applicable to pulverized carbon sorbents. It roughly describes experimental data from the literature. The current version includes the ability to account for competitive adsorption between mercury, $SO_2$, and $NO_2$.

The single particle model simulates in-flight sorbent capture of elemental mercury. This model was developed to include Langmuir and Freundlich isotherms, rate equations, sorbent feed rate, and intraparticle diffusion. The Freundlich isotherm more accurately described in-flight mercury capture. Using these parameters, very little intraparticle diffusion was evident. Consistent with other data, smaller particles resulted in higher mercury uptake due to available surface area. Therefore, it is important to capture the particle size distribution in the model. At typical full-scale sorbent feed rates, the calculations underpredicted adsorption, suggesting that wall effects can account for as much as 50 percent of the removal, making it an important factor in entrained-mercury adsorption models.

# TABLE OF CONTENTS

# EXECUTIVE SUMMARY

The heterogeneous mercury adsorption tests were completed in the fixed-bed reactor using activated carbon from coconut shells. The 1.2-cm-ID, quartz, fixed-bed reactor was connected to the existing, methane-fired tube furnace. The mean size of the carbon particles was 3 mm and the quartz frit that supports them was perforated with several 1-mm-diameter holes to reduce the pressure drop across the bed. For all tests the tubular reactor was operated with the high quench profile (440 K/s), an inlet mercury concentration of 25 $\mu g/m^3$, and a NO concentration of 20-30 ppm from the methane-fired burner.

The fixed-bed tests were performed at 150°C, 25 $\mu g$ $Hg/m^3$, and included conditions with and without chlorine, bromine and $SO_2$. One gram of coconut-shell-based carbon was placed on the quartz frit. The thickness of the bed was about 2 cm and its temperature was controlled at 150°C. The presence of chlorine (50 ppm as HCl equivalent) dramatically increased mercury adsorption by the carbon, although the efficiency of the bed was reduced from 95 percent to 50 percent in the presence of 500 ppm $SO_2$. This reduction is no longer observed when the HCl concentration is increased to 100 ppm.

The addition of $SO_2$ also caused an increase in mercury adsorption by the carbon, although the extent of this increase was small compared to that obtained with HCl alone. The efficiency of mercury adsorption by the carbon in the presence of $SO_2$ was enhanced considerably when chlorine was added to the system.

Tests completed with bromine (35 ppm as HBr equivalent) showed an increase in mercury uptake by the carbon, similar to that obtained with HCl alone. No significant effect on the extent of adsorption was observed when either HCl, $SO_2$ or both were added to the system.

Preliminary adsorption tests made with 20 ppm of $NO_2$, in the absence of halogens, showed no effect on mercury adsorption. In the presence of $NO_2$ alone the carbon bed captured no elemental mercury at 150°C.

Modeling efforts focused on predicting mercury uptake for both a packed-bed and entrained-flow reactors. The packed-bed model is based on the Langmuir isotherm, neglects intraparticle diffusion resistances and is only applicable to pulverized-carbon sorbents. It roughly describes experimental data from the literature including the competitive effect between different flue gas components such $SO_2$ and $NO_2$.

The entrained-flow model for in-flight mercury capture was used to examine the suitability of the Langmuir and the Freundlich isotherms. Using parameters from a full-scale test, the Freundlich was better able to predict in-flight capture; little

intraparticle diffusional resistance was found with steep gradients near the particle surface. The model was used to help define the relative importance of in-flight capture and capture by sorbent on duct walls. Smaller particles, which result in more accessible surface area, showed more mercury uptake because of lower intraparticle diffusional resistance. Therefore, it is important to include particle size distribution in the model. In this study, this was accomplished by “binning” the particle sizes.

# EXPERIMENTAL METHODS

The homogeneous mercury reactor used in this study is a 50-mm OD x 47-mm ID quartz tube (132 cm in length) located along the center of a high-temperature Thermcraft heater. The reaction tube extends 79 cm below the heater, is temperature controlled, and has a quartz sample section attached at the bottom with a capped end [(1)]. Peak gas temperature in the electrically heated zone was about 1080°C.

A methane-fired, premixed burner made of quartz glass supplied realistic combustion gasses to the reactor. All reactants were introduced through the burner and passed through the flame to create a radical pool representative of real combustion systems. The design burner heat input was about 300-W, producing 3.7 SLMP of combustion gases.

The heterogeneous tests were performed in the fixed bed reactor using activated carbon from coconut shells. The 1.2-cm-ID, quartz, fixed-bed reactor was connected to the existing, methane-fired tube furnace. The mean size of the carbon particles was 3 mm and the quartz frit that supported them was perforated with several 1-mm-diameter holes to reduce the pressure drop across the bed. The tests were conducted by loading the heterogeneous reactor with carbon, wrapping it with heating tape and insulation, and regulating the temperature to 150$^{o}$C.

For all the tests, the tubular reactor was operated with the high quench profile (440 K/s) and an inlet mercury concentration of 25 $\mu g/m^3$. One gram of coconut-shell-based carbon was placed on the quartz frit. The thickness of the bed was about 2 cm. Initially, a mercury mass balance was closed with the homogeneous reactor in order to check the mercury concentrations entering the packed bed. The flue gases were then allowed to enter the heterogeneous reactor to study the effect of the sorbent. The baseline composition for all tests was: 25 ug/m$^3$ Hg, 0.88% $O_2$, 33 ppmv NO, 10.5 % $CO_2$, 9 ppmv CO.

To study the effects of other flue gas components such as $SO_2$, NO, $NO_2$, HCl, and HBr, different concentrations of these species were added to the baseline flue gas. All were introduced through the burner.

A Tekran 2537A mercury analyzer coupled with a wet sample conditioning system designed by Southern Research Institute (SRI) provided measurement of total and elemental mercury in the exhaust gas. In this system sample gas was pulled in two streams from the last section of the quartz reaction tube into a set of conditioning impingers. One stream was bubbled through a solution of stannous chloride to reduce the oxidized mercury to elemental form and then through a solution of sodium hydroxide to remove acid gases. This stream represented the total mercury concentration in the reactor. The second stream was first treated

with a solution of potassium chloride to remove oxidized mercury species and then was treated with a caustic solution for acid gas removal. This stream was representative of the elemental mercury concentration in the reactor. Oxidized species were calculated by the difference between total and elemental mercury concentrations. A chiller removed water from the sample gas and then each stream was intermittently sent to the analyzer [(1)] .

# RESULTS AND DISCUSSION

## *Experimental Results*

Due to the high pressure drop developed through the reactor it was not possible to use powdered activated carbon. Particles of larger size were used. Besides the particle size difference, the adsorption capacity of the coconut-shell carbon is typically higher than that for a coal-based carbon. The key factor affecting the adsorptive capacity of the bed is the sample size. One gram of carbon was used here and the large sample size is the reason that breakthrough curves were not observed in the periods of time considered.

Figure 1 shows the effects of starting the fixed bed adsorption process with 50 ppm chlorine (as HCl equivalent) and then adding increasing amounts of $SO_2$. Of most interest in Figure 1 is the almost complete lack of mercury adsorption when chlorine is absent at 150°C. The addition of $SO_2$ causes significant reductions in the amount of mercury adsorbed. The extent of the reduction is roughly proportional to the $SO_2$ concentration.

However, when the chlorine concentration is increased from 50 ppm to 100 ppm, as shown in Figure 2, the effect of $SO_2$ becomes negligible at concentrations ranging from 100 to 500 ppm. The order of injection for $SO_2$ and HCl also seems to play some role in the extent of mercury adsorption by the carbon. As shown in Figure 3, the addition of 50 ppm HCl at different $SO_2$ concentrations always results in an increase of the mercury uptake by the carbon; this increase is again nearly proportional to the $SO_2$ concentration. The $SO_2$ interferes with the ability of the carbon to adsorb mercury.

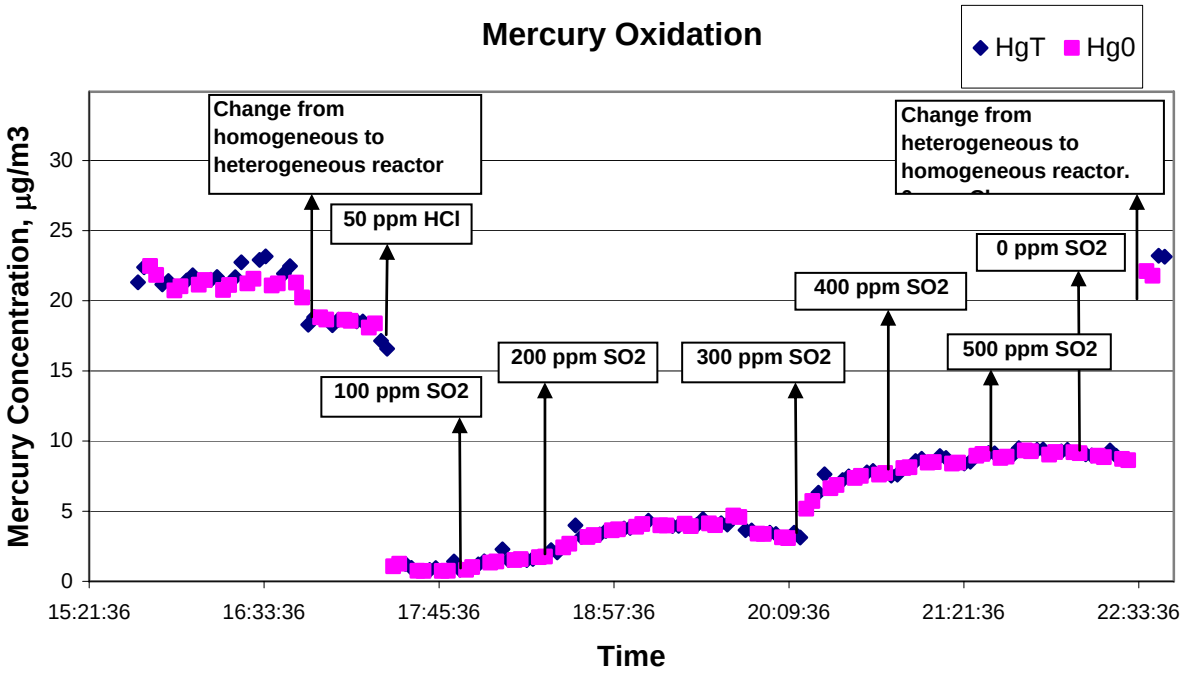


Figure 1 Elemental ($Hg^0$) and total ($Hg^T$) mercury concentrations at the exit of the carbon bed as a function of time (hours) at a temperature of 150°C at chlorine concentrations of 50 ppm (as HCl equivalent) and $SO_2$ concentrations ranging from 100 to 500 ppm.

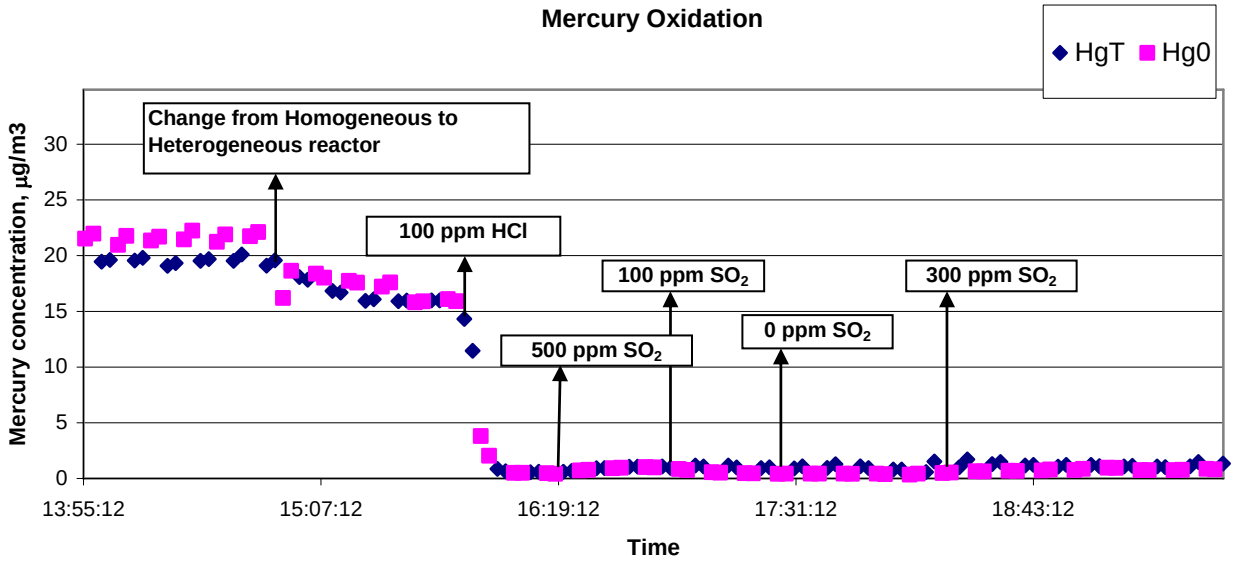


Figure 2 Elemental ($Hg^0$) and total ($Hg^T$) mercury concentrations at the exit of the carbon bed as a function of time (hours) at a temperature of 150°C at chlorine concentration of 100 ppm (as HCl equivalent) and $SO_2$ concentrations of 500, 100, and 300 ppm.

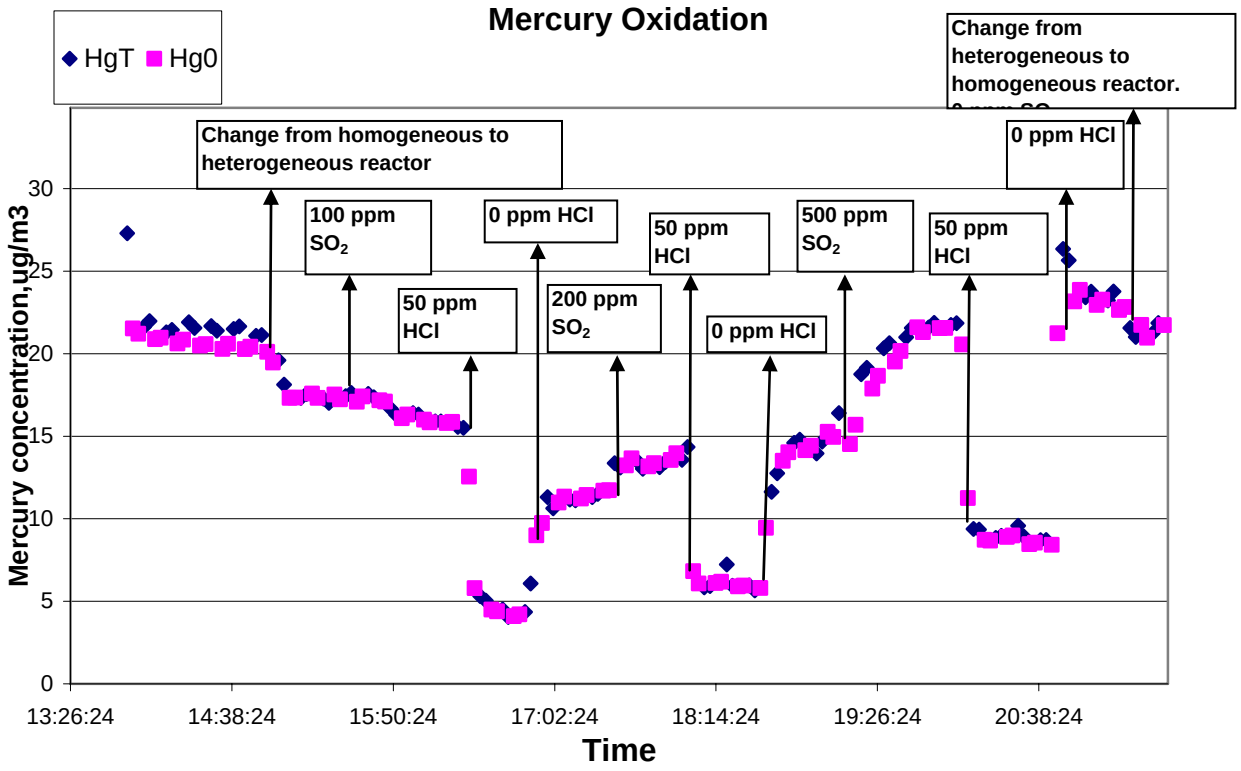


Figure 3 Elemental ($Hg^0$) and total ($Hg^T$) mercury concentrations at the exit of the carbon bed as a function of time (hours) at a temperature of 150°C at $SO_2$ concentrations of 100, 200, 500 ppm and a chlorine concentration of 50 ppm (as HCl equivalent).

The effect of bromine on mercury adsorption was also studied. As shown in Figure 4, the bromine causes an increase on mercury adsorption by the carbon and this increase is not affected significantly by either chlorine when added at 50 ppm (as HCl equivalent) or by $SO_2$ when added at 500 ppm, according to the results in Figure 5. Bromine as a promoter of adsorption or oxidation on activated carbon is less sensitive to $SO_2$ than chlorine.

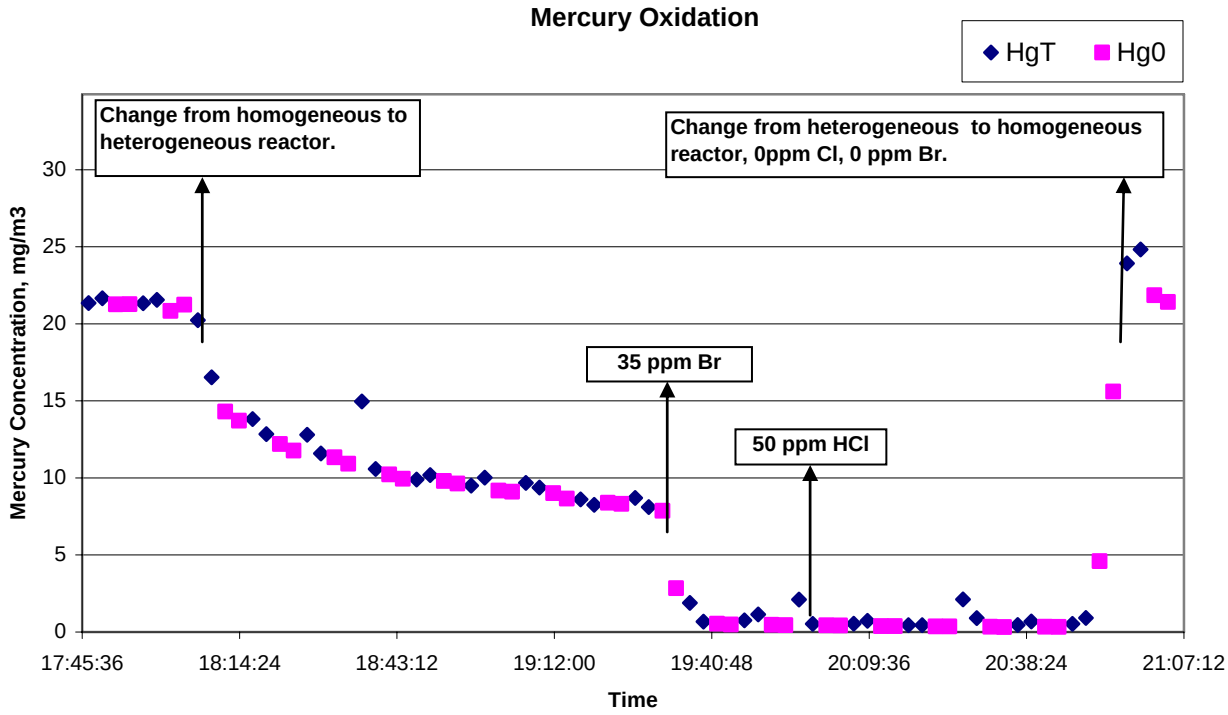


Figure 4 Elemental ($Hg^0$) and total ($Hg^T$) mercury concentrations at the exit of the carbon bed as a function of time (hours) at a temperature of 150$^o$C at a bromine concentration of 35 ppm (as HBr equivalent) and a chlorine concentration of 50 ppm (as HCl equivalent).

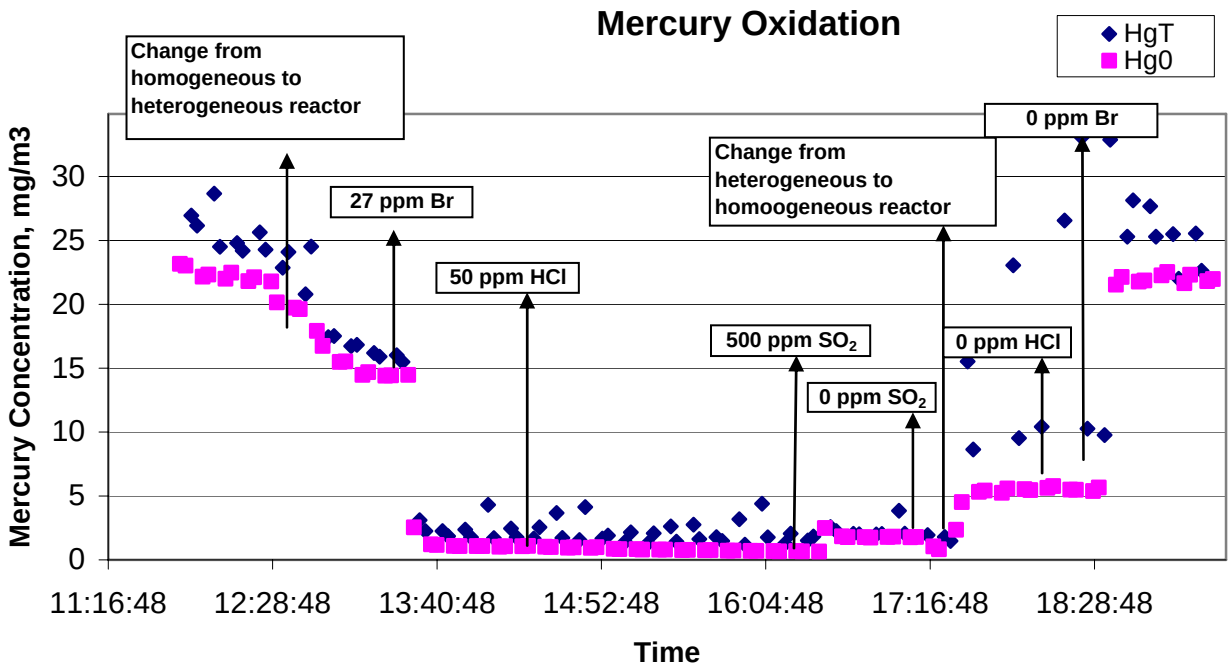


Figure 5 Elemental ($Hg^0$) and total ($Hg^T$) mercury concentrations at the exit of the carbon bed as a function of time (hours) at a temperature of 150°C at a bromine concentration of 27 ppm (as HBr equivalent) , chlorine concentration of 50 ppm (as HCl equivalent) and $SO_2$ concentration of 500 ppm.

A preliminary test was performed to study the effect of $NO_2$ on mercury adsorption and oxidation by the coconut-shell carbon. Because $NO_2$ is such a strong oxidant, this initial test was made by injecting the $NO_2$ through one of the bottom ports of the homogeneous reactor, instead of through the burner as is usual. Two $NO_2$ concentrations, 5 and 20 ppm, were used. For the homogeneous part of the test, no change was observed in elemental and total mercury concentrations at the exit of the homogeneous reactor at either concentration. Similar results were obtained with the heterogeneous reactor. Both sets of data are shown in Figure 6. Additional tests are planned to confirm these preliminary findings.

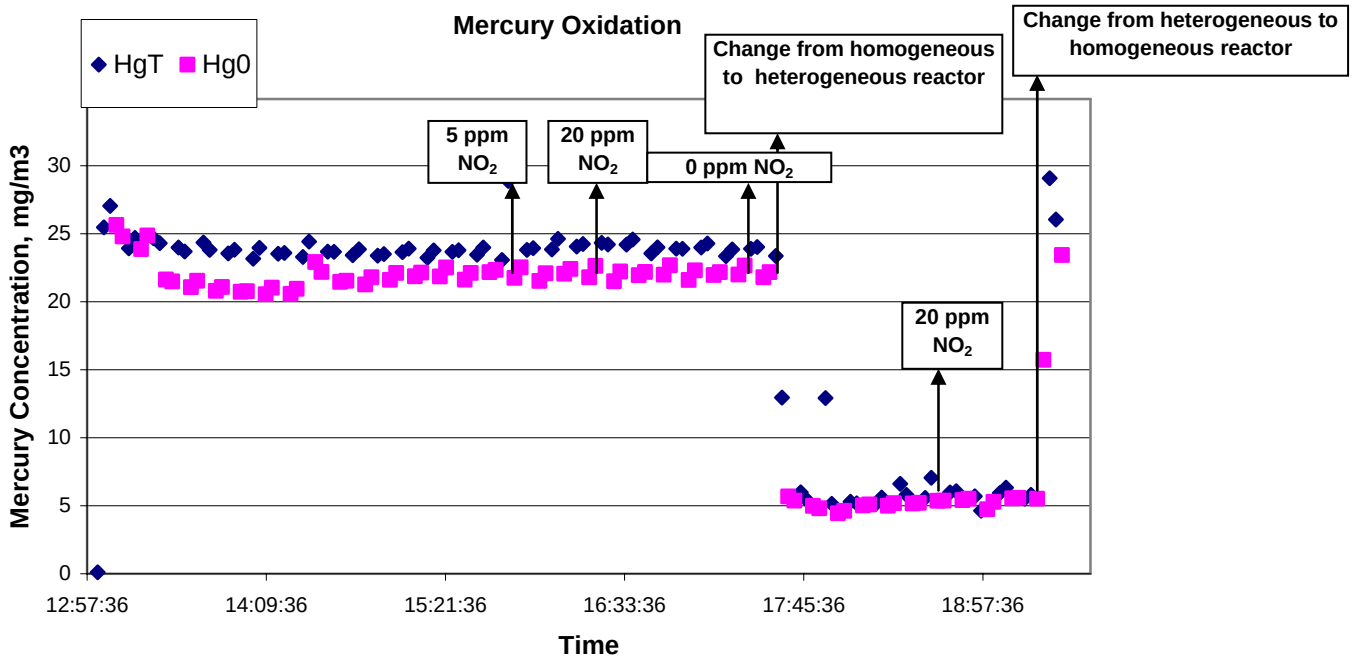


Figure 6 Elemental ($Hg^0$) and total ($Hg^T$) mercury concentrations at the exit of the carbon bed as a function of time (hours) at a temperature of 150°C at $NO_2$ concentrations of 5 and 20 ppm.

## *Heterogeneous Model*

### Packed bed

Following the Langmuir theory, the net rate of mercury adsorption on the activated carbon particle for species i can be written as the difference between the local adsorption rate and desorption rate:

$$\frac{dW_i}{dt} = k_{1i}\left(W_{\max,i} - \sum_{i=1}^{n} W_i\right)C_i - k_{2i}W_i \qquad (1)$$

where

$W_{max,i}$: Asymptotic adsorbate concentration (g Hg / g carbon).
$K_{1i}$: Kinetic constant of the adsorption reaction ($m^3$ / g min).
$K_{2i}$: Kinetic constant of the desorption ($min^{-1}$).
$C_i$: Gas phase concentration of component A (g / $m^3$).
$W_i$: Solid phase concentration of component A (g Hg / g carbon).
n: Number of species in the flue gas.
t: Time (min).

The mass balance in the gas phase in axial coordinates for species i is:

$$V\frac{dC_i}{dz}-\rho\frac{dW_i}{dt}=\varepsilon\frac{dC_i}{dt} \qquad (2)$$

where

$\rho$: Bulk density of the carbon (g carbon/$m^3$).
$\varepsilon$: Porosity of the bed (void fraction).

and

$$\varepsilon=\frac{Void\ volume}{Bed\ volume}=\frac{Bed\ volume-Carbon\ volume}{Bed\ volume} \qquad (3)$$

$$Bed\ volume=\frac{\pi}{4}D^2L-\frac{m_q}{\rho_q} \qquad (4)$$

$$Carbon\ volume=\frac{g_c}{\rho} \qquad (5)$$

where

D: Diameter of the packed bed (m).
$m_q$: Mass of quartz beads in the packed bed (g).
$\rho_q$: Quartz density (g/$m^3$).
L: Length of the packed bed (m).
A: Cross- Sectional area of the bed ($m^2$).
$\Delta Z$ : Distance between nodes (m).
V: Superficial velocity (m/min).

Equations (1) and (2), one for the gas phase and the other one for the solid phase, for all species, were discretized using forward discretization for the time derivatives and upwind discretization for the spatial derivatives .The discretized equations were solved using MATLAB.

As a first approach, breakthrough data and Langmuir constants from Karatza et al. [3] for $HgCl_2$ were used to determine the accuracy of the model and method of solution. Karatza's bed consisted of 50 mg of fly ash mixed with 3 grams of inert glass beads. The thickness of the bed was 2.5 mm, and an additional 57.5 mm of glass beads were provided upstream of the bed in order to distribute the gas flow over the entire cross section.

Using values of $W_{max}$ = 0.00103 (g/g), $k_1$ =22.2 $m^3$/g min, $k_2$ = 0.033 $min^{-1}$ from Karatza et al. [3] a fair fitting of the experimental data is observed, as shown in

Figure 7, where two sets of experimental data taken at 150°C were used. In A an initial $HgCl_2$ concentration of 2.8 mg/m$^3$ was used while in B this concentration was 10 mg/m$^3$.

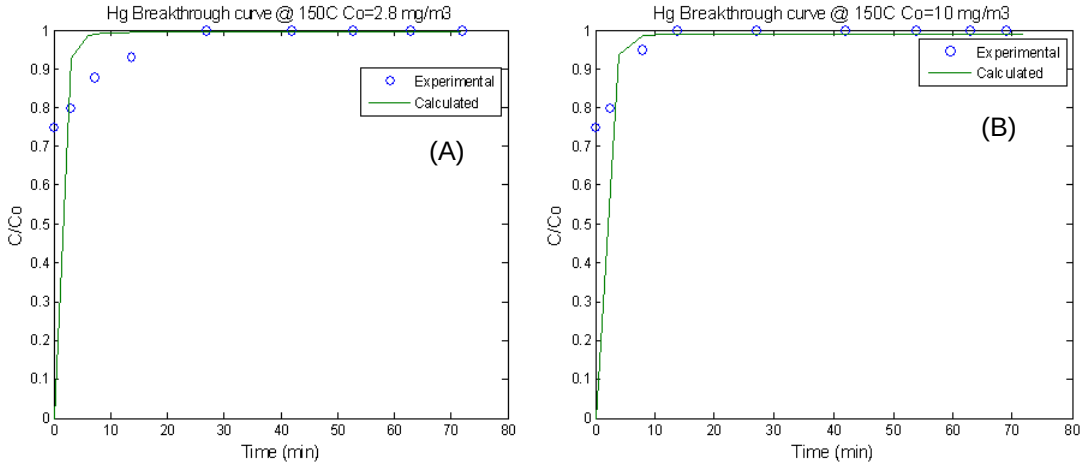


Figure 7 Breakthrough curves for fly ash with a bed temperature of 150°C. (A) Initial mercury concentration, $C_o$=2.8 mg/m3, (B) $C_o$=10mg/m$^3$. Experimental data from Karatza et al. [3]. Calculated values obtained with the heterogeneous model.

Figure 7 illustrates the accuracy of the heterogeneous model and method of solution for the two model equations. Other sources of experimental data [4] were used with the objective of finding the model constants for mercury and some of the other species in the flue gas (HCl, $SO_2$, and $NO_2$).

Miller et al. [4] used a quartz filter loaded with 150.5 mg of a carbon based sorbent and exposed it to a simulated flue gas. The temperature was kept at 225°F (107°C) and a Semtech 2000 mercury analyzer was used to continuously measure the elemental mercury at the outlet. A $SnCl_2$ reduction cell was used prior to the analyzer to convert all forms of mercury for analysis. With the reduction cell in place, the analyzer measured total mercury, but without the reduction cell only $Hg^0$ was measured. The baseline flue gas composition was $O_2$ 6%, $CO_2$ 12%, $H_2O$ 8%, $N_2$ balance. Experimental results obtained by Miller et al. are shown in Figure 8 as well as the model results. A rough fitting of experimental and calculated data is observed using the parameter values from Table 1. As seen in this table, parameters can vary by orders of magnitude (e.g., maximum carbon uptake), particularly as the flue gas composition changes.

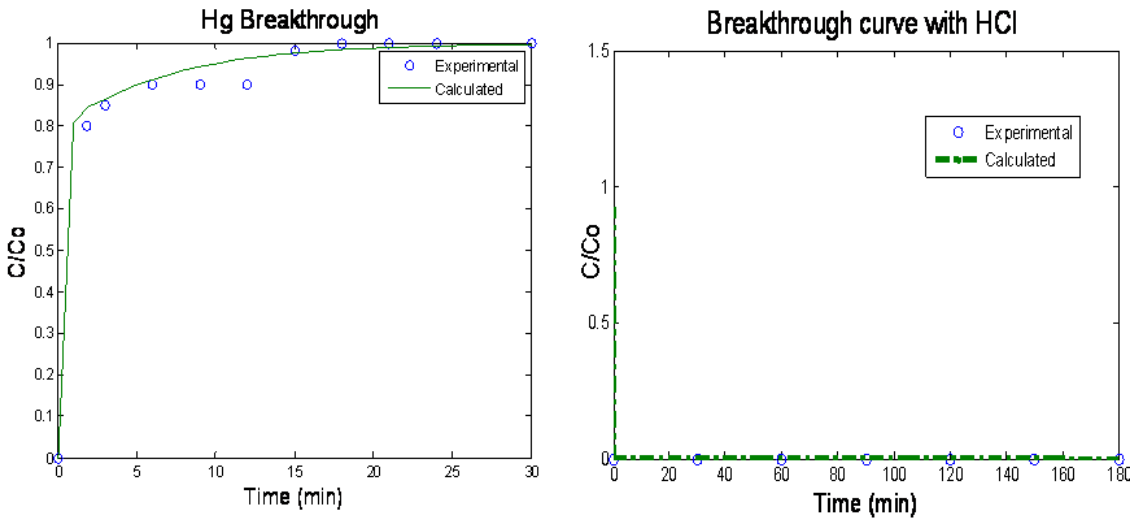


Figure 8 Breakthrough curves lignite activated carbon with a bed temperature of 107°C. (A) Mercury and baseline gases, (B) Mercury, 50 ppm HCl and baseline gases. Experimental data o from Miller et al. [4] Calculated data obtained with the heterogeneous model.

Table 1 Calculated heterogeneous model parameters for Miller et al. [4] experimental data.

| Flue gas Composition | $K_{1i}$ ($m^3$/g min ) | $K_{2i}$ ($min^{-1}$) | $W_{maxi}$ (g Hg/g Carbon) |
|---|---|---|---|
| Mercury and Baseline gases (i=1) | 5.9212 | 0.1476 | 0.009105 |
| Mercury, 50 ppm HCl and baseline gases (i=2) | 3.05 | 268.992 | 0.091 |

Miller et al. [4] also used 0.15 g of lignite activated carbon to make a bed of 6.35 cm ID and 0.00947 cm depth at 225°F (107°C) and exposed it to a different flue gas compositions. The baseline composition was $O_2$ 6%, $CO_2$ 12%, $H_2O$ 8%. In this case the fitting of the data is shown in Figure 9, using the model parameters shown in Table 2.

Table 2 Calculated heterogeneous model parameters for Miller et al. [4] experimental data.

| Flue gas Composition | $K_{1i}$ ($m^3$/g min ) | $K_{2i}$ ($min^{-1}$) | $W_{maxi}$ (g Hg/g Carbon) |
|---|---|---|---|
| Mercury and Baseline gases (i=1) | 5.9212 | 0.1476 | 0.009105 |
| Mercury, 1600 ppm $SO_2$ and baseline gases (i=2) | 0.02870 | 0.5874 | 0.00751 |
| Mercury, 20 ppm $NO_2$ and baseline gases (i=3) | 2.8720 | 587.4 | 0.0751 |

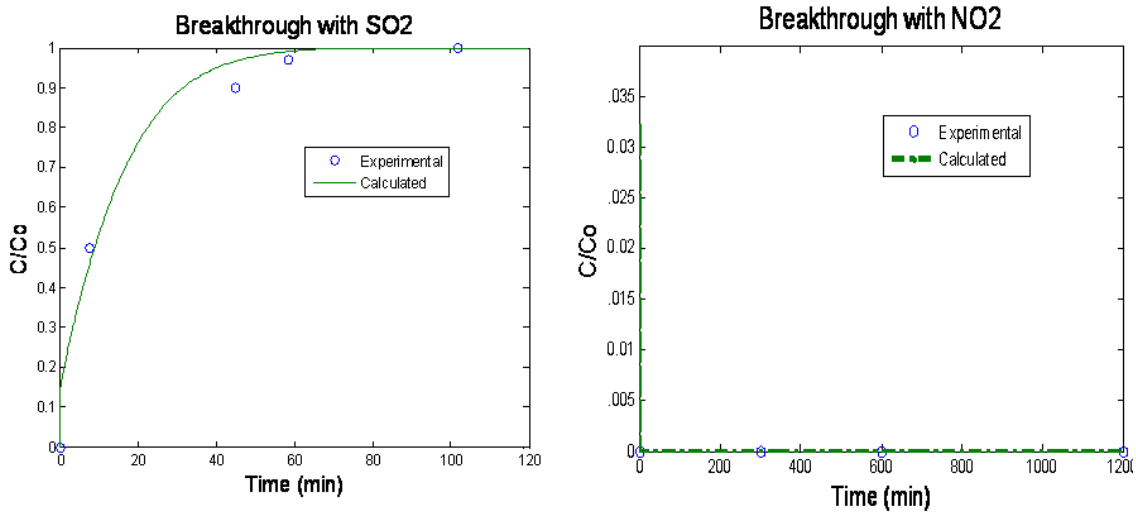


Figure 9 Breakthrough curves lignite activated carbon with a bed temperature of 107°C. (A) Mercury, 1600 ppm $SO_2$ and baseline gases, (B) Mercury, 20 ppm $NO_2$ and baseline gases. Experimental data o from Miller et al [4], Calculated data obtained with the heterogeneous model.

## Single particle model for in flight sorbent capture of mercury

A mercury mass balance on the gas phase can be constructed using a conventional balance on an entire spherical sorbent particle or on adjacent, concentric shells within the particle where,

$$\text{Accumulation} = \text{Flux In} - \text{Flux Out} - \text{Adsorbed} \qquad (6)$$

The sign convention of the model treats flux into the particle as "positive" and flux out of the particle as "negative." Equation 6 may be expressed in differential form as,

$$\frac{\partial C_{cv}}{\partial t} V_{cv,i} \epsilon_P = J_{in} A_{in} - J_{out} A_{out} - R_{ads} V_{cv} \quad (7)$$

where

$C_{cv,i}$: Gas phase mercury concentration in the void space of the particle at the node i (g Hg/$m^3$)
$V_{cv,i}$: Volume of the shell at the node i ($m^3$).
$\varepsilon_p$: Porosity of the particle ($m^3$ void/ $m^3$ particle).
$J_{in}$: Gas phase mercury flux through the “in” side shell of the control volume (g Hg/ $m^2$ s).
$A_{in}$: Surface area of the particle side shell of the control volume ($m^2$).
$J_{out}$: Gas phase mercury flux through the “out” side shell of the control volume (g Hg/$m^2$ s).
$A_{out}$: Surface area of the bulk side shell of the control volume ($m^2$).
$R_{ads}$: Rate term for solid phase uptake of mercury (g Hg/s $m^3$).

The flux terms in Equation 7 follow Fick's law,

$$J = -D_{eff} \frac{\partial C}{\partial r} \quad (8)$$

where

Deff: Effective diffusivity of gaseous, elemental mercury inside the particle ($m^2$/s).
r: Radial distance from the center of the particle (m).

Once designated spatially, they may be discretized as,

$$J_{in} = -D_{eff} \frac{C_{center} - C_{in}}{\Delta r} \quad (9)$$

$$J_{out} = D_{eff} \frac{C_{center} - C_{out}}{\Delta r} \quad (10)$$

where:

$C_{center}$: Gas phase mercury concentration at the node inside of the control (g Hg/$m^3$).
$C_{in}$: Gas phase mercury concentration at the “in” side shell of the control Volume (g Hg/$m^3$).
$C_{out}$: Gas phase mercury concentration at the “out” side shell of the control

volume (g Hg/$m^3$).

$\Delta r$: Radial distance between adjacent shells (m).

and substituted back into Equation 7 to form Equation 11,

$$\frac{\partial C_{cv}}{\partial t} V_{cv,i} \epsilon_P = -D_{eff} \left( \frac{C_{center} - C_{in}}{\Delta r} \right) A_{in} - D_{eff} \left( \frac{C_{center} - C_{out}}{\Delta r} \right) A_{out} - R_{ads} V_{cv} \quad (11)$$

The spatial orientation of the concentration terms may be standardized with respect to index i.

$$C_{center} = C_i \quad (12)$$

$$C_{in} = C_{i-1} \quad (13)$$

$$C_{out} = C_{i+1} \quad (14)$$

Additionally, the volume and area terms may also be spatially specified with index value i. Once the terms are given a spatial index, they may be regrouped and equation 11 simplifies to,

$$\frac{dC_{cv,i}}{dt} = \frac{D_{eff}}{V_{cv,i} \epsilon_P \Delta r} \left( C_{i-1} A_{i-1} - C_i (A_{i-1} + A_i) + C_{i+1} A_i \right) - \frac{R_{ads}}{\epsilon_P} \quad (15)$$

Graphically, the concentration, area, and volume terms from Equation 15 may be represented as shown in Figure 10. The adjacent shells in the mass balance are organized by index value, i, into nz nodes. At i=nz, the nodes terminate at the particle's surface where the subscript R maybe used interchangeably with nz. The organization of the general mass balance terms is shown in Figure 11.

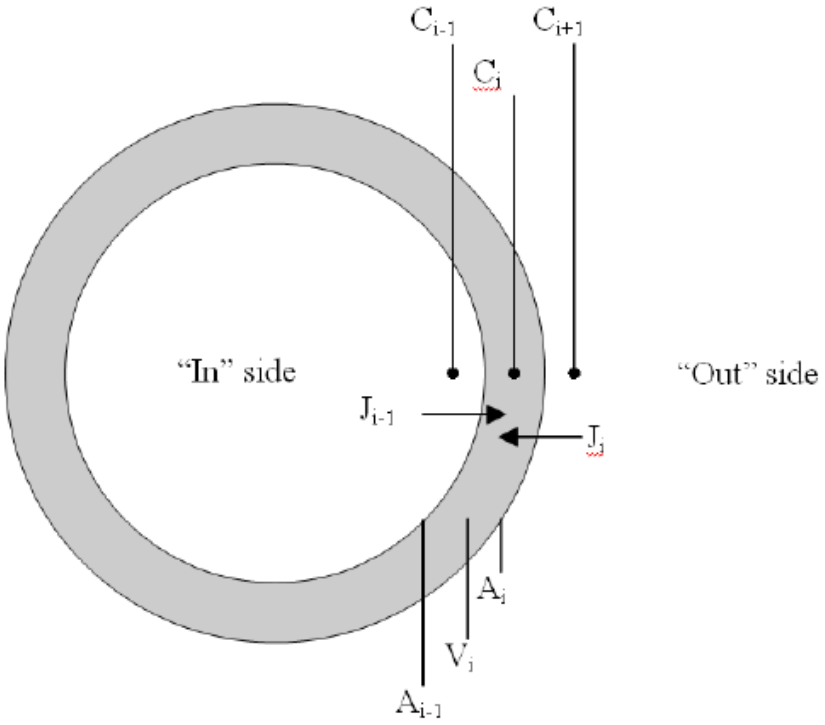


Figure 10 The basic mass balance scheme used in a shell inside a uniform, spherical sorbent particle.

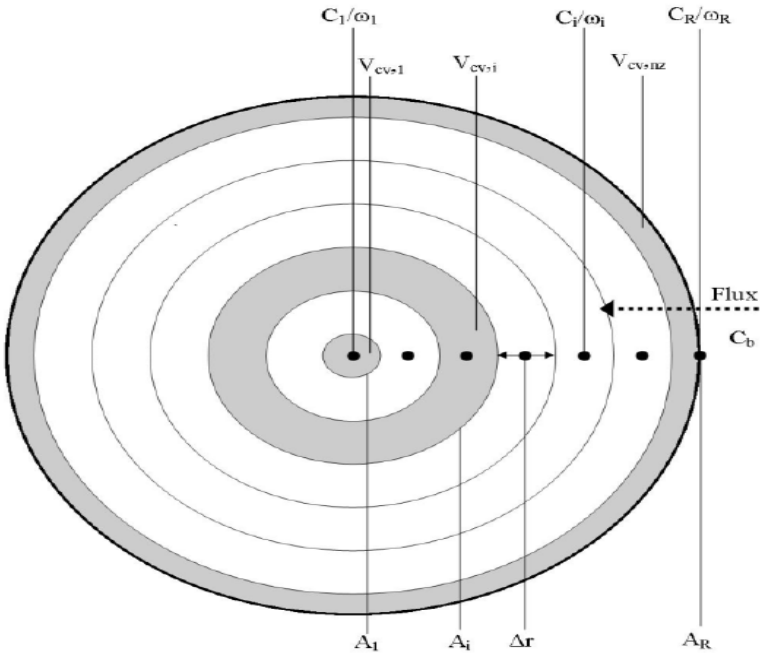


Figure 11 The organization of the discretization scheme used in the model.

## Rate Models

The effective diffusion coefficient from Equations 9 and 10 may be calculated by combining the Knudsen and binary diffusion coefficients:

$$D_{eff} = \frac{\tau_P^{-1}}{1/D_{ab} + 1/D_{kn}} \quad (16)$$

where

$\tau$: Sorbent particle tortuosity
$D_{ab}$: Binary diffusion constant between gaseous mercury and air ($m^2/s$).
$D_{kn}$: Knudsen diffusion coefficient ($m^2/s$).

The binary diffusion coefficient may be computed using the classic Chapman-Enskog equation and the appropriate constants [5,6]. The Knudsen diffusion coefficient and tortuosity may be computed using Equations 17 and 18.

$$D_{kn} = \frac{97}{2} d_{pore} \left(\frac{T}{MW_{Hg}}\right)^{0.5} \quad (17)$$

$$\tau_P = \epsilon_P^{-1.5} \quad (18)$$

where

$d_{pore}$: Average pore diameter of the sorbent particle (m).
T; Reactor temperature (K).
$MW_{Hg}$: Molecular weight of mercury (g Hg/mole).

The form of $R_{ads}$ in the Equation 15 is dependent upon the apparent density of the sorbent particle, $\rho_p$, and a solid phase rate model. In this work, three different rate models are employed. The first and simplest uses a difference between adsorption and desorption,

$$\frac{\partial \omega_i}{\partial t} = k_1(\omega_{max} - \omega_i)C_{cv,i} - k_2\omega_i \quad (19)$$

where

$\omega_i$: Solid phase, elemental mercury concentration at node i (g Hg/g carbon).
$\omega_{max}$: Maximum elemental mercury uptake capacity of the sorbent (g Hg/ g carbon).
$k_1$: Adsorption constant ($m^2$/ g Hg s).
$k_2$: Desorption constant (1/s).

If equilibrium is assumed at the surface of the particle,

$$k_2\omega_i = k_1(\omega_{max} - \omega_i)C_{cv,i} \tag{20}$$

$$k_2\omega_i = k_1\omega_{max}C - k_1\omega_i C_{cv,i} \tag{21}$$

$$(k_2 + k_1 C_{cv,i})\omega_i = k_1\omega_{max}C_{cv,i} \tag{22}$$

$$\omega_i = \left(\frac{k_1\omega_{max}C_{cv,i}}{k_2 + k_1 C_{cv,i}}\right) \tag{23}$$

$$\omega_i = \left(\frac{K_{lang}\omega_{max}C_{cv,i}}{1 + K_{lang}C_{cv,i}}\right), \quad K_{lang} = \frac{k_1}{k_2} \tag{24}$$

where

$K_{lang}$: Sorption constant for Langmuir Isotherm ($m^3$/g Hg).

Equation 24 is the adsorption component of the second rate model and is known as the Langmuir isotherm. Finally a Freundlich isotherm may also be used in the rate model,

$$\omega_i = \frac{C_{cv,i}^{1/n}}{K_{fr}} \tag{25}$$

where

$K_{fr}$: Sorption constant for Freundlich isotherm.

Both the Langmuir and Freundlich models must be differentiated with respect to time before they can be used in the general mass balance in equation.

The boundaries of the shell balance require the initial conditions,

$$@t = 0, \quad C_{cv,i} = 0 \tag{26}$$

$$\omega_i = 0 \tag{27}$$

$$C_b = C_{bo} \tag{28}$$

where

$C_b$; Bulk, gas phase mercury concentration (g Hg/m$^3$).
$C_{bo}$: Inlet mercury concentration (g Hg/m$^3$).

The flux boundary condition,

$$@r = 0, \frac{\partial C_{cv,i}}{\partial r} = 0 \tag{29}$$

is also necessary in the solution of the shell balance. Mercury flux through the particle surface is equal to the amount lost from the bulk phase,

$$-D_{eff}\frac{\partial C_R}{\partial r} = k_{mt}(C_R - C_b) \tag{30}$$

where

$C_R$: Gas phase mercury concentration at particle surface (g Hg/m$^3$).
$k_{mt}$: External mass transfer coefficient (m/s).

When multiplied by the available external particle surface area, $\Omega$, this quantity is equal to the change in bulk mercury concentration with respect to time as shown in Equation 31.

$$\frac{\partial C_b}{\partial t} = \Omega k_{mt}(C_R - C_b) \tag{31}$$

The mass transfer coefficient may be computed given the assumption that the boundary layer is stationary. As a sorbent particle falls through a duct, its terminal velocity may be computed by balancing the gravitational forces with the buoyant and kinetic forces as discussed by Bird, Stewart, and Lightfoot [7]. The force balance may be solved for the terminal velocity term to yield Equation 32.

$$v_{terminal} = \frac{2R_P^2(\rho_{Pactual} - \rho_{gas})g}{9\mu} \tag{32}$$

where

$R_p$: Sorbent particle radius (m).
$\rho_{Pactual}$: Actual density of the sorbent particle (g carbon/m$^3$).
g: Acceleration due to gravity (m/s$^2$).
vterminal: Speed at which a sorbent particle of radius Rp travels due to gravity alone (m/s).

Given a range of particle diameters from 1 to 75 microns, a flue gas composition comparable to air, and a temperature of 150°C, the terminal velocities of particles in a full scale duct will range from $7.4 \times 10^{-4}$ to 4.1 meters per second whereas the linear velocity of flu gas in a full-scale duct is usually on the order of 20+ meters per second[8]. By the standard correlation [9]

$$N_{sh} = (4.0 + \frac{1.21(v_{terminal} * 2R_P}{D_{ab}})^{2/3})^{1/2} \quad (33)$$

where

$N_{sh}$: Sherwood number.
$D_{ab}$: Binary diffusion constant between gaseous mercury and air ($m^2/s$).

The Sherwood number then varies from 2.0 to 3.2. Small sorbent particles will travel roughly the same speed as the flue gas while the larger particles will travel slightly faster. The question may be asked as to whether a momentum balance is necessary to model in-flight uptake. Scala et al. [10] found that assuming a stationary boundary layer resulted in no more than 10 % error into the results and for that reason a similar assumption is made in this model.

The mass transfer coefficient is defined as,

$$k_{mt} = \frac{ShD_{ab}}{2R_P} \quad (34)$$

On account of the boundary condition in Equation 29, the "inner flux" term on the mass balance at the centermost node of the particle is zero. Therefore, Equation 15 when applied at that node is,

$$\frac{dC_{cv,1}}{dt} V_{cv,1} \epsilon_P = \frac{D_{eff} A_r}{\Delta r} \left( C_2 - C_1 \right) - R_{ads} V_{cv,1} \quad (35)$$

At the particle surface, the "outer" flux term must be expressed via Equation 15 as the index nz+1 does not exist on the sorbent particle.

In the mass balance, adsorption may also be assumed to take place only at the particle surface. In such a case, the governing equations are just as they were before only all of the "inner" flux terms are zero, and the balance on the particle surface is slightly simpler:

$$\frac{dC_R}{dt} = \frac{k_{mt}}{V_{cv,nz}\epsilon_P}(C_{Bulk} - C_R)A_R - \frac{R_{ads}}{\epsilon_P} \quad (36)$$

The balance for the bulk mercury concentration change is the same as Equation 31.

## Model Solution

Equation 15 can be discretized into a series of adjacent shells and combined with Equations 31 and 36 to form a complete mass balance on the system. Before the equations can be solved, however, the user must specify a number of parameters. In each of the three $R_{ads}$ models, a set of constants is required - $\omega_{max}$, $k_1$, and $k_2$ for the standard adsorption/desorption model, $\omega_{max}$ and K for the Langmuir isotherm model, and n and $K_{fr}$ for the Freundlich isotherm model. These parameters are commonly extracted from a packed bed isotherm [11]. Finally, $\rho_P$ and the number of nodes to be used inside the particle must be specified.

The model calculates mercury uptake with respect to time, porosity, feed rate, average particle pore size, and particle radius. It can also calculate solid and gas phase concentrations inside the sorbent particle itself. Before running the code, parameter(s) to be varied and isotherm model(s) to be used must be specified. The model uses the MATLAB function "ode23s," a stiff ordinary differential equation solver, to obtain solutions.

The results from the rate law and Langmuir isotherm models can be compared directly as identical parameters may be applied to their governing equations. $K_{lang}$ from the Langmuir isotherm is simply the quotient of $k_1$ and $k_2$ from the rate model. The parameters shown in the results for these two adsorption models are shown in Table 3.

Table 3 Constants used in Rate law and Langmuir isotherm adsorption models.

| Parameter | Magnitude | Units |
|---|---|---|
| $K$ | 580.8 | $\frac{m^3}{g}$ |
| $k_1$ | 0.41 | $\frac{m^3}{g \cdot s}$ |
| $k_2$ | 7.06e-4 | $\frac{1}{s}$ |
| $w_{max}$ | 1000 | $\frac{\mu g_{Hg}}{g_{carbon}}$ |
| $D_{ab}$ | 2.55e-5 | $\frac{m^2}{s}$ |
| $D_{kn}$ | 7.0e-6 | $\frac{m^2}{s}$ |
| $F.R.$ | 10.0 | $lb/MMacf\left(0.08\frac{g_{carbn}}{m^3}\right)$ |
| $R_P$ | 14.5 | $\mu m$ |
| $D_{pore}$ | 3.0 | $nm$ |
| $t_{residence}$ | 2.0 | $s$ |

Of the three $R_{ads}$ models, the rate of adsorption/desorption model shows the lowest uptake. Under typical, full-scale conditions, mercury uptake under this model is virtually zero as can be seen in Figure 12. This negligible uptake is not

entirely unexpected as equilibrium, which is highly favorable for adsorption, is not fixed at the particle surface. Equilibrium at the particle surface allows for a solid phase concentration to exist as soon as gas phase mercury reaches the solid surface.

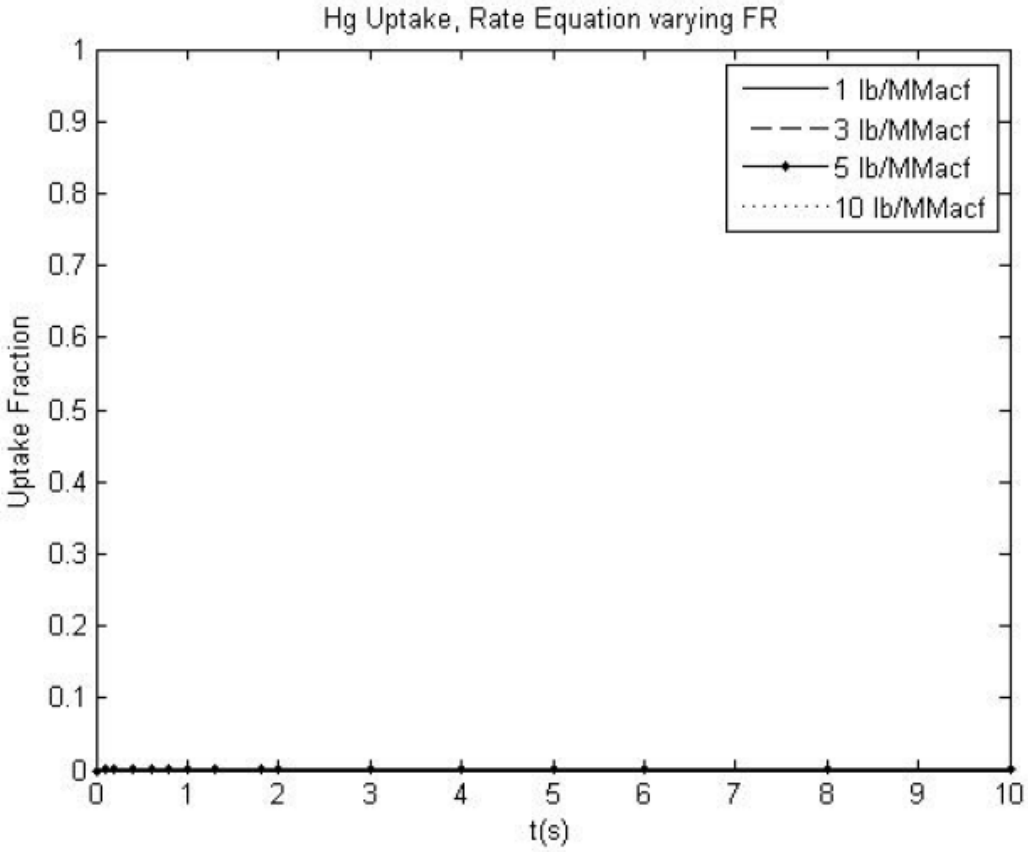


Figure 12 Mercury uptake normalized with inlet concentration over time using the rate model.

Figure 13 shows that even at a residence time as low as 2 seconds, gaseous mercury can enter the particle. Because the adsorption process takes more time to complete, the solid phase concentration is zero. In this figure and all subsequent figures containing solid phase concentrations, the intraparticle solid phase concentrations,_ωi, must be multiplied by feed rate, FR, and normalized with the inlet concentration, $C_{bo}$, in order to be compared directly to gas phase concentration.

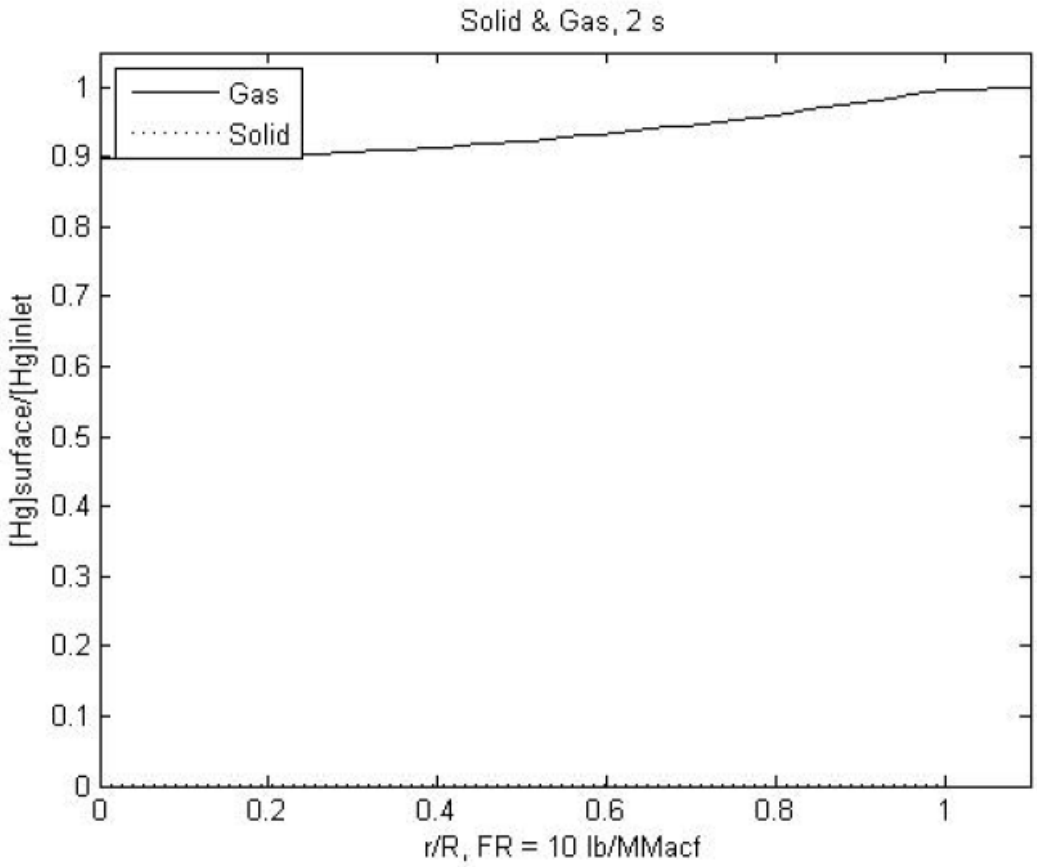


Figure 13 Mercury uptake normalized with inlet concentration in both the solid and gas phases using the rate model.

The results from the Langmuir isotherm adsorption model in Figure 14 show higher uptake levels than do the rate model results, but as stated for the rate model, this uptake is almost negligible under standard operating conditions. Similar results were obtained by Flora et al. [12] .

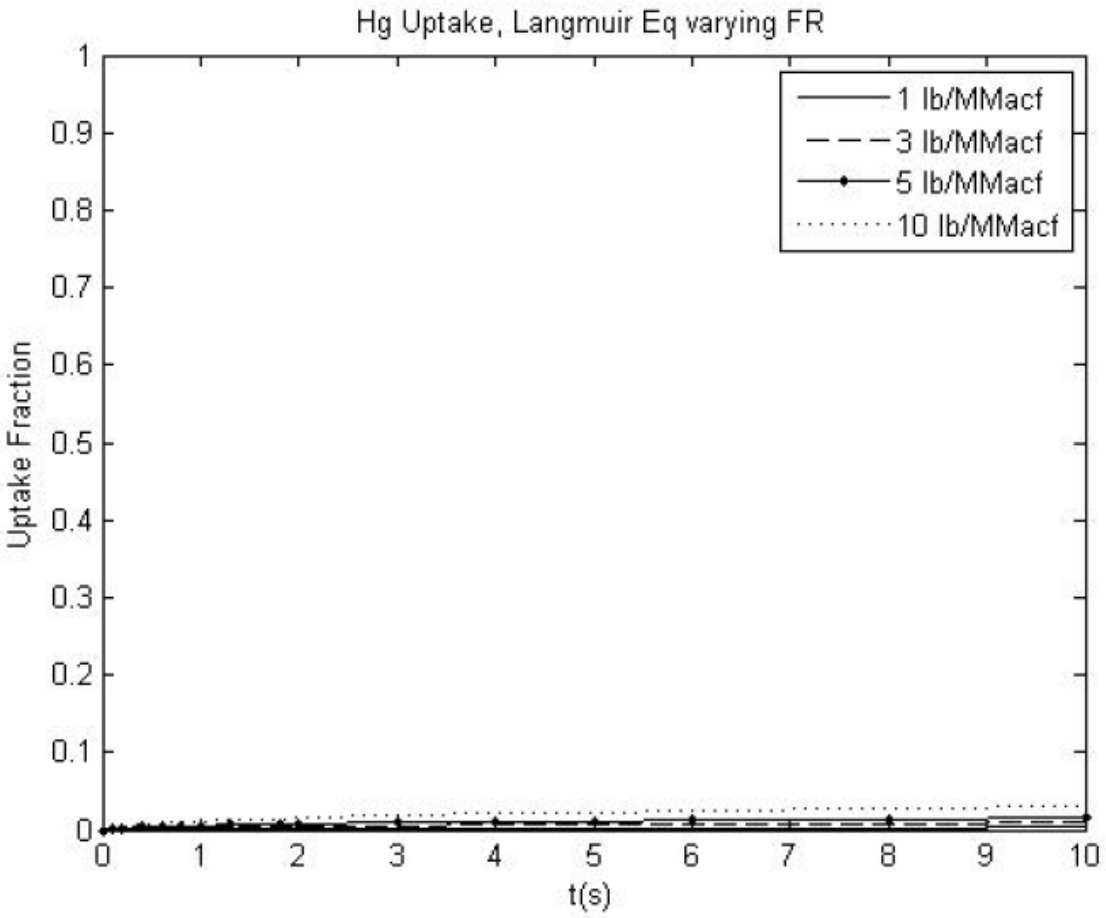


Figure 14 Mercury uptake normalized with inlet concentration over time using the Langmuir isotherm model.

At low residence times, some gas phase intraparticle concentration can be observed in the Langmuir model as shown in Figure 15.

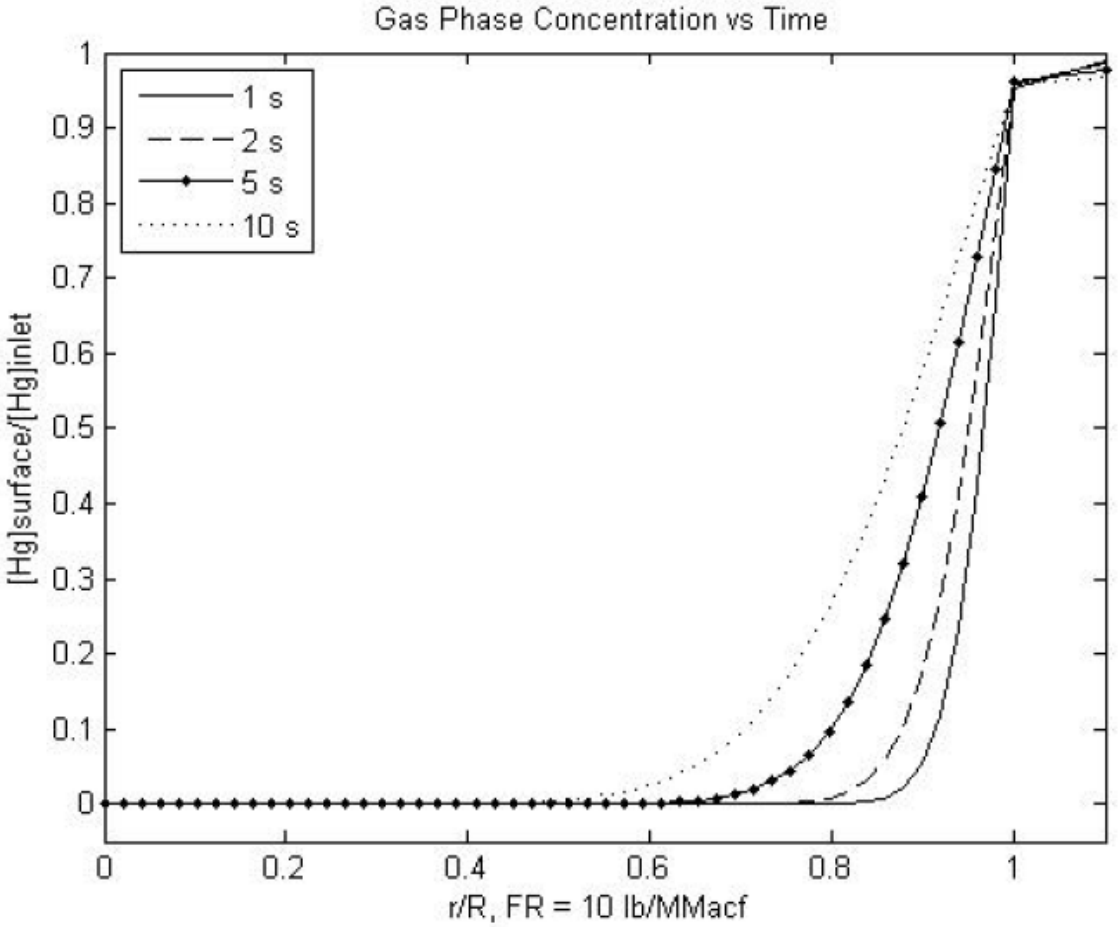


Figure 15 Mercury concentration normalized with inlet concentration inside the sorbent particle using Langmuir isotherm model.

The Freundlich isotherm parameters experimentally determined from a sorbent used in full-scale tests at Pleasant Prairie [8] are shown in Table 4. They are used in the Freundlich model results below along with reactor parameters similar to the ones used in the rate and Langmuir isotherm models.

Table 4 Constants used in Freundlich isotherm adsorption model.

| Parameter | Magnitude | Units |
|---|---|---|
| $K_{fr}$ | 0.01490 | $\frac{g_{carbon}}{m^3}$ |
| $n$ | 1 | |
| $D_{ab}$ | 2.55e-5 | $\frac{m^2}{s}$ |
| $D_{kn}$ | 7.0e-6 | $\frac{m^2}{s}$ |
| $F.R.$ | 10.0 | $lb/MMacf\left(0.08\frac{g_{carbn}}{m^3}\right)$ |
| $R_P$ | 14.5 | $\mu m$ |
| $D_{pore}$ | 3.0 | $nm$ |
| $t_{residence}$ | 2.0 | $s$ |

Using the above magnitude for the necessary parameters, Figure 16 shows mercury uptake under the Freundlich isotherm adsorption model.

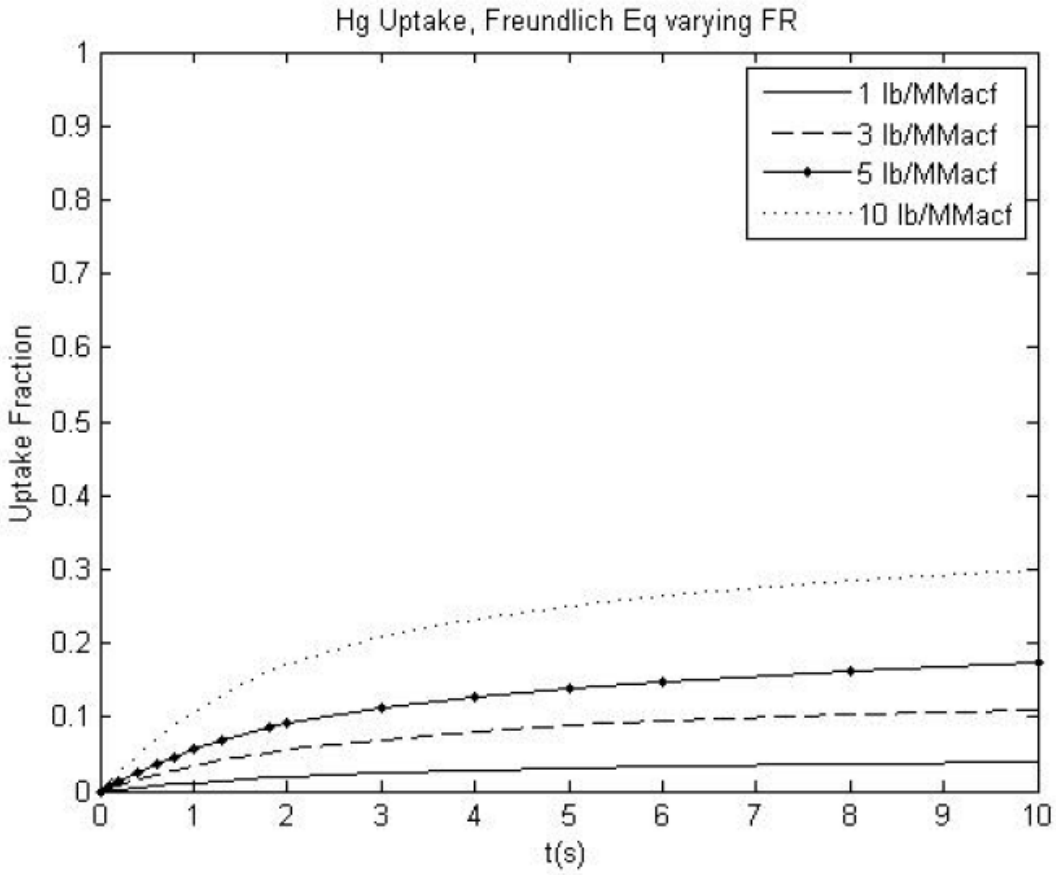


Figure 16 Mercury uptake normalized with inlet concentration over time using Freundlich isotherm model.

At normal residence times, a steep gas phase intraparticle concentration gradient can be observed in the Freundlich model as shown in Figure 17. This gradient is much steeper than that seen in the Langmuir adsorption model

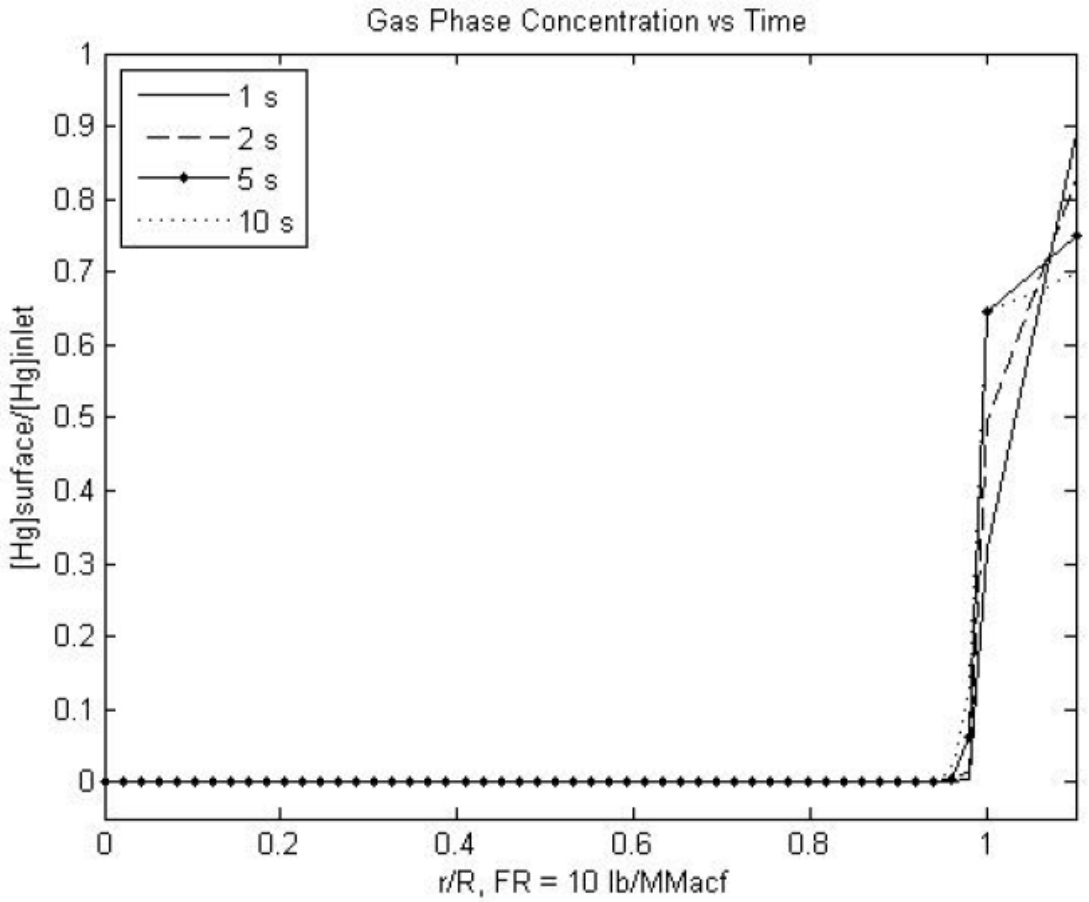


Figure 17 Mercury uptake normalized with inlet concentration over time using Freundlich isotherm model.

## Effect of Individual Sorbent Properties

Theoretically, particle diameter greatly affects mercury uptake as shown in Figure 18. These results are similar to that seen in the other published work [11] . Mercury uptake is inversely proportional to particle diameter. As sorbent diameter decreases, more surface area is available for uptake. However, that diameter crosses a certain minimum values, external mass transfer becomes the primary resistive force to uptake.

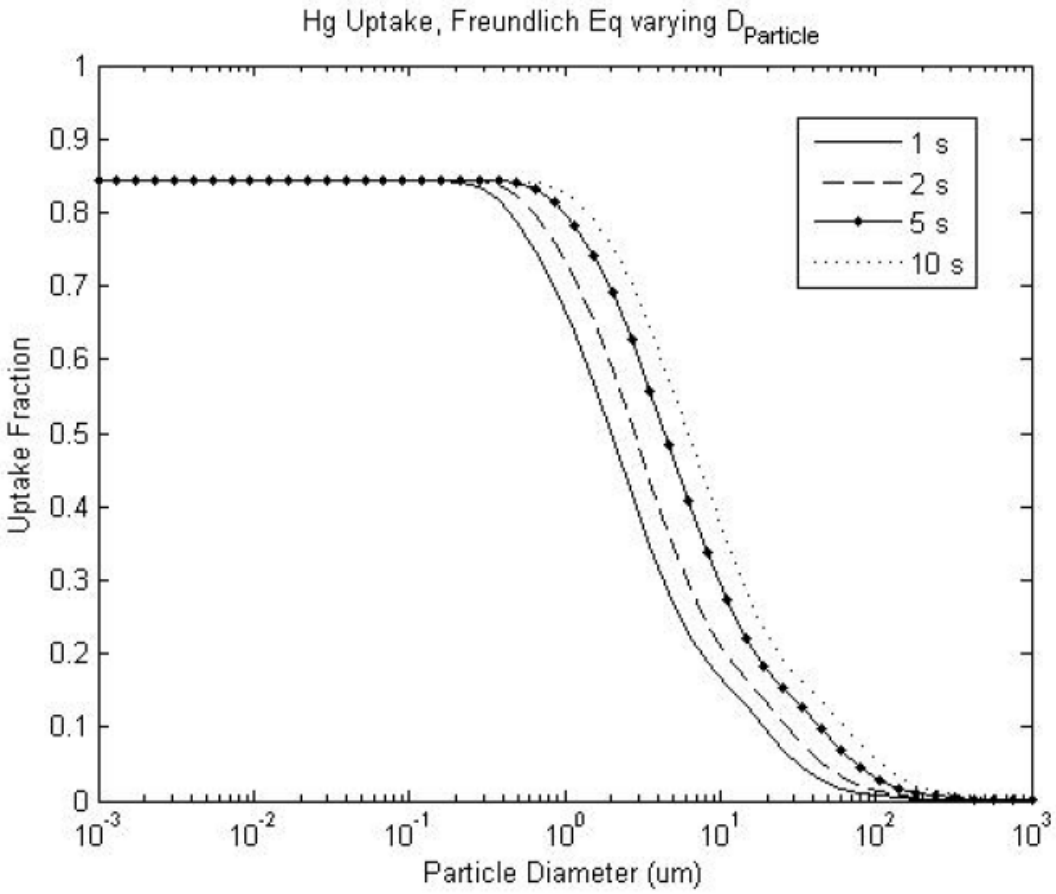


Figure 18 Mercury uptake normalized with inlet concentration over time using Freundlich isotherm model and varying particle diameter.

Multiple full scale reports have shown [8,13,14], however, that particle diameter does not affect mercury uptake as implied by models. This contradiction may likely be accounted for by poor dispersion of the particles as they are injected into the ducts. The Pollack report [14] commented on some attempts to verify this hypothesis by varying injection geometry to get different adsorption results. Adsorption under these altered conditions proved no different than the original test.

An alternate explanation lack of convergence between the model and full-scale data is that particle distributions are not properly addressed in models. With the exception the work by Meserole et al. [15], all published models assume a monodisperse size distributions. However, the sorbents used in full-scale settings have polydisperse size distributions. In order to capture this effect, sorbent particles in a model may be "binned" at any resolution desired. The "binned" conditions modeled in Figure 20 simulate the distribution reported by Cremer et al [8] in Figure 19.

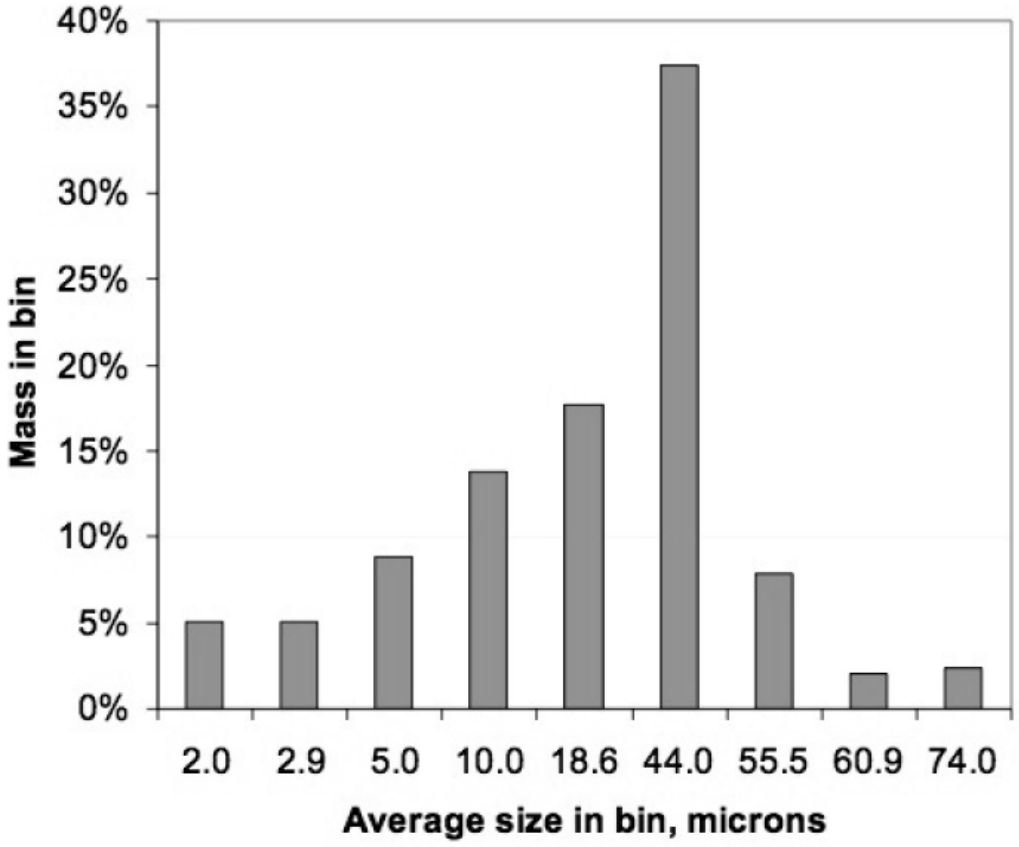


Figure 19 One example of how activated carbon particles may be distributed in "bin" form.

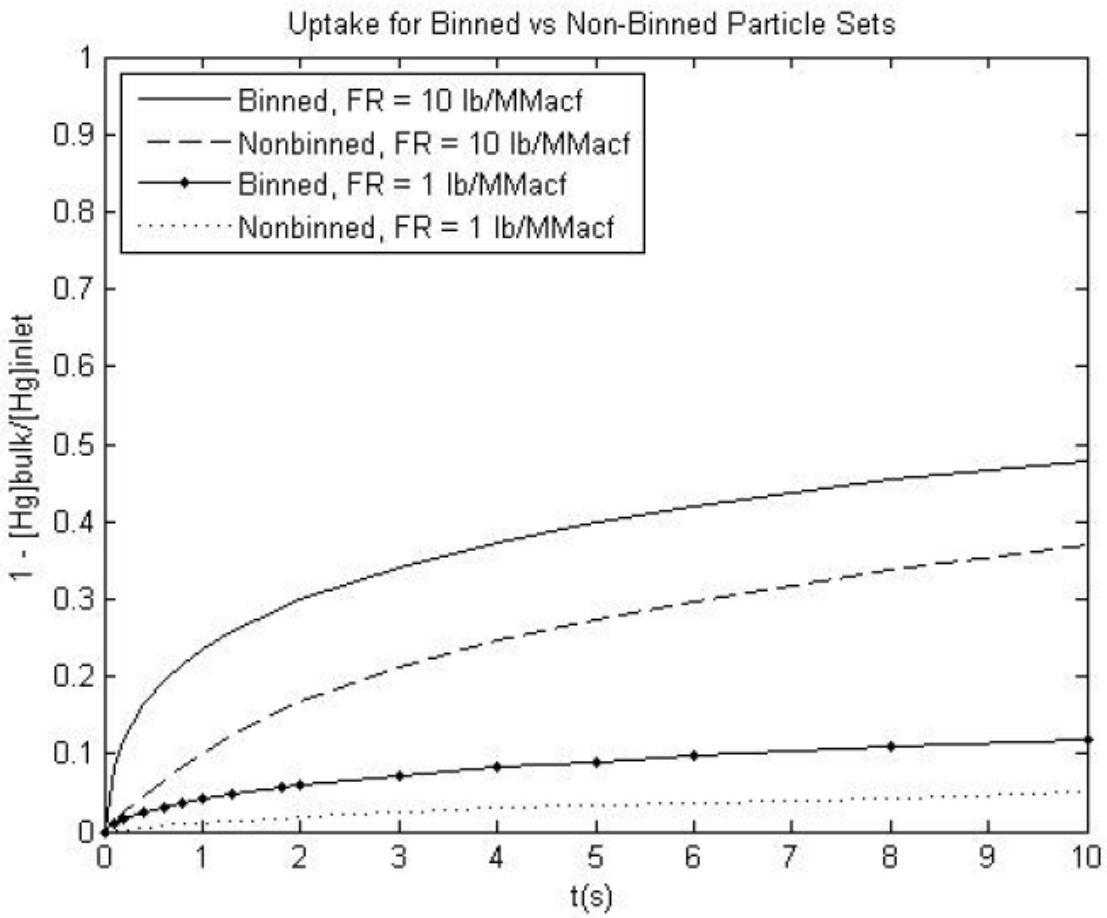


Figure 20 A comparison of uptake for “binned” and “nonbinned” particle sets for two different feed rates. “Binned” at size range from 2 μm to 75 μm and averaging 30 μm which is the size angle used in the “nonbinned” model.

Figure 21 shows a direct comparison of the 1 and 10 lb/MMacf lines from the "nonbinned" particles in Figure 20 and the "binned" particles previously described. The "binned" model show significantly more uptake than does the "nonbinned" model due to the presence of smaller than average particles that, per capita, have more surface area exposed directly to the bulk. The "nonbinned" particle set has an average diameter of 29 μm which is identical to the average diameter of the "binned" set.

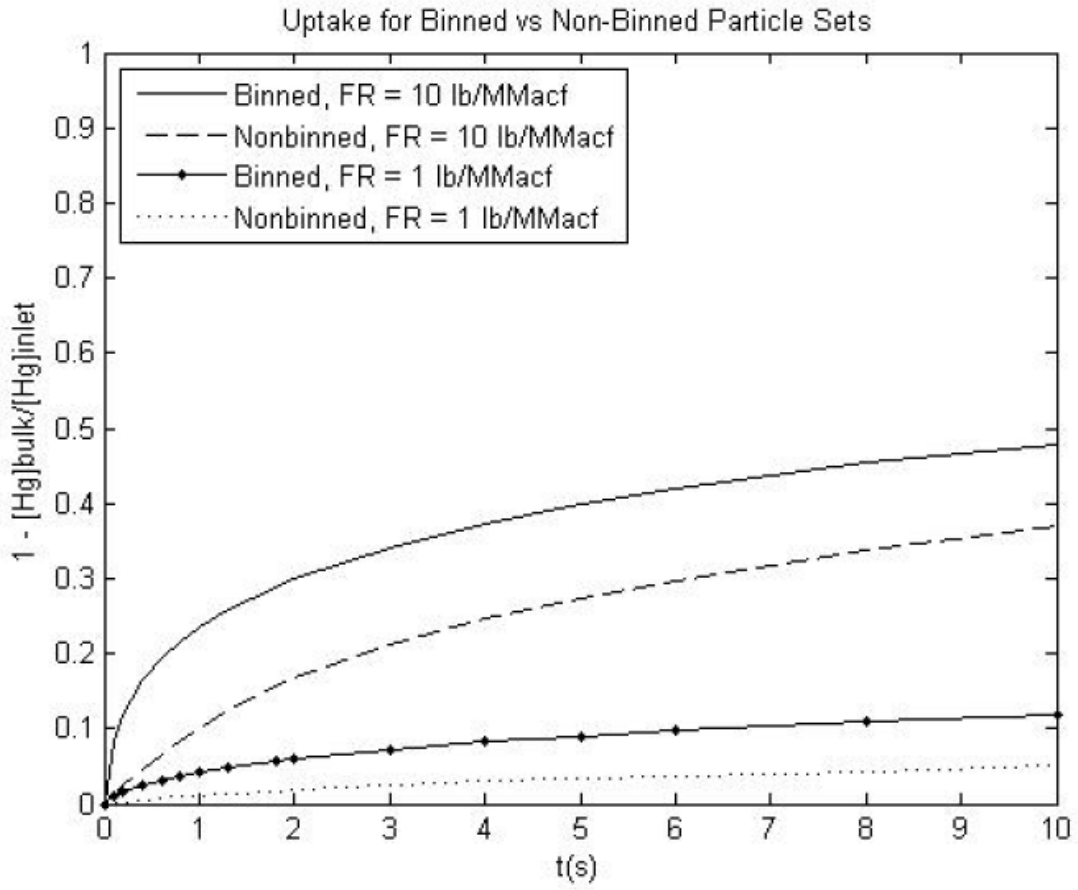


Figure 21 A comparison of uptake for "binned" and "nonbinned" particle sets for two different feed rates. "Binned" at size range from 2 μm to 75 μm and averaging 30 μm which is the size angle used in the "nonbinned" model.

These results show that the two systems with the same average particle diameter may have different adsorptive capacities depending on the actual distribution and the need for including particle size distribution in a model.

## Nonlinearity of Feed Rate influence on uptake

Full scale data has shown that mercury uptake does not increase linearly with feed rate [8]. While this effect is observed in Figure 22, the cause is likely different. Most full scale data show that mercury uptake maximizes between 10 and 15 lb/MMacf. As shown in the figure, the model requires a great deal more sorbent before the maximum limit is reached. One possible case as discussed by the Pollack report [14] could be an actual change in adsorptive capacity due to lowering chlorine concentrations in the full-scale results. This was found in the packed bed study as well (see Table 1). Another possibility mentioned by the Pollack report is the hypothesis that the injection lances are not properly distributing the sorbent.

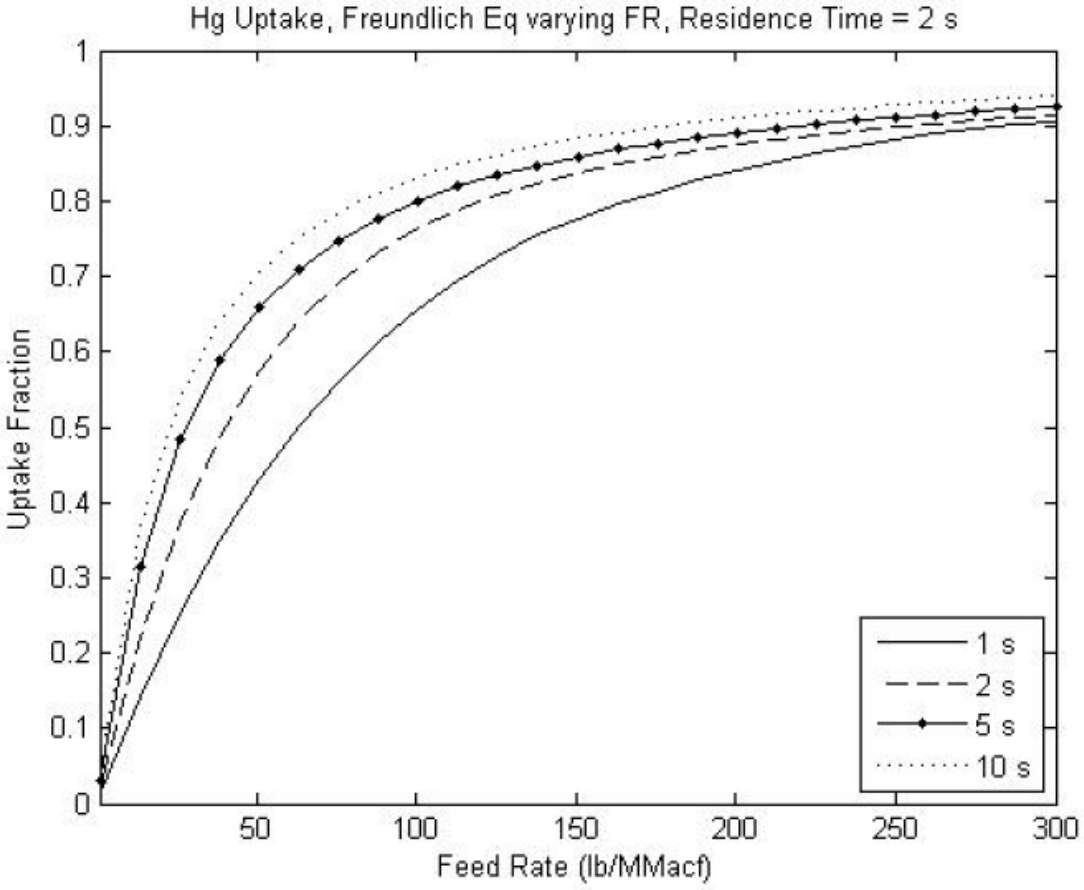


Figure 22 Mercury uptake normalized with inlet concentration over time using the Freundlich isotherm model and varying the feed rate (Rp=15 μm).

## Consolidation of Adsorption Models

Calculations with actual sorbents, realistic reactor settings, and the Langmuir isotherm results in Figure 14 are significantly lower than what is shown in full-scale data [8,13]. In order to understand this inconsistency, several parameters must be investigated.

External mass transfer easily becomes a resistive force when particle size is large enough. By increasing $D_{ab}$ by 4 orders of magnitude, external mass transfer can effectively be removed from the Langmuir model. The results are shown in Figure 23. Mercury uptake is still low overall, so external mass transfer is clearly not the limiting factor in adsorption.

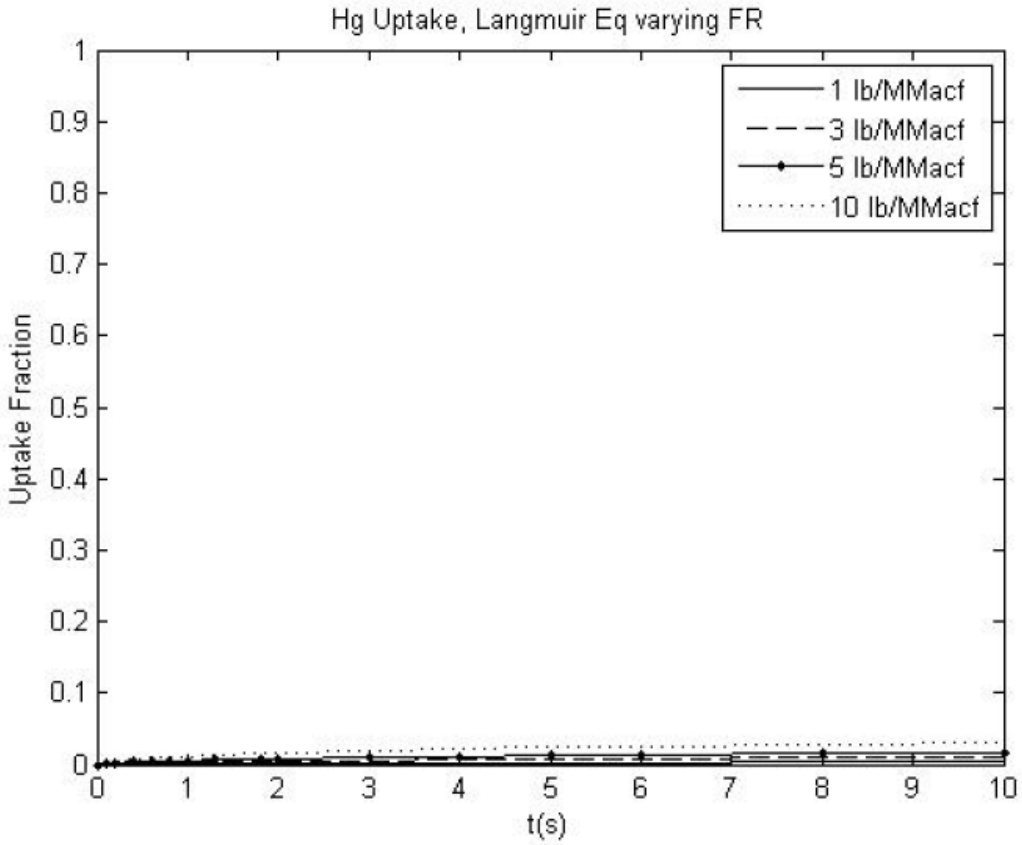


Figure 23 Mercury uptake normalized with inlet concentration over time using the Freundlich isotherm model and maximizing Dab to minimize resistance from external mass transfer ($R_p$=15μm).

Additionally, the Langmuir isotherm also takes around 100 seconds to reach its maximum value - much longer than any residence time in a full scale system. This observation is consistent with the results from the Langmuir model constructed by Flora et al. [12] who reported no more than 2% uptake in the entire entrained portion of a reactor using Darco-FGD carbon.

The uptake results from the Freundlich isotherm adsorption model shown in Figure 16 are higher than those in the other two models, but it is not immediately clear that the Freundlich isotherm model itself more closely simulates the adsorption of mercury onto activated carbon. Though the Freundlich and Langmuir isotherms have different forms, at standard flue gas concentrations and $\omega_{max}$ values seen in realistic settings, they are mathematically similar.

As $K_{lang}C$ gets smaller, the Langmuir isotherm, Equation 24, simplifies to

$$\omega_i = K_{lang}\omega_{max}C_{cv,i} \qquad \text{(Eq. 37)} \quad (37)$$

If n from the Freundlich isotherm is assumed to be 1 and the Freundlich sorption constant, $K_{fr}$, is defined as,

$$K_{fr} = \frac{1}{K\omega_{max}} \tag{38}$$

The Freundlich isotherm takes the form,

$$\begin{aligned} \omega_i &= \frac{C_{cv,i}}{K_{fr}} \\ &= \frac{C_{cv,i}}{\frac{1}{K_{lang}\omega_{max}}} \\ &= K_{lang}\omega_{max}C_{cv,i} \end{aligned} \tag{39}$$

Typically, these assumptions are valid in full-scale conditions, so both isotherms should yield similar results. The Figure 24 verifies this analysis. The parameters used in this model were taken from the full-scale values reported in the Pleasant Prairie study [8] .

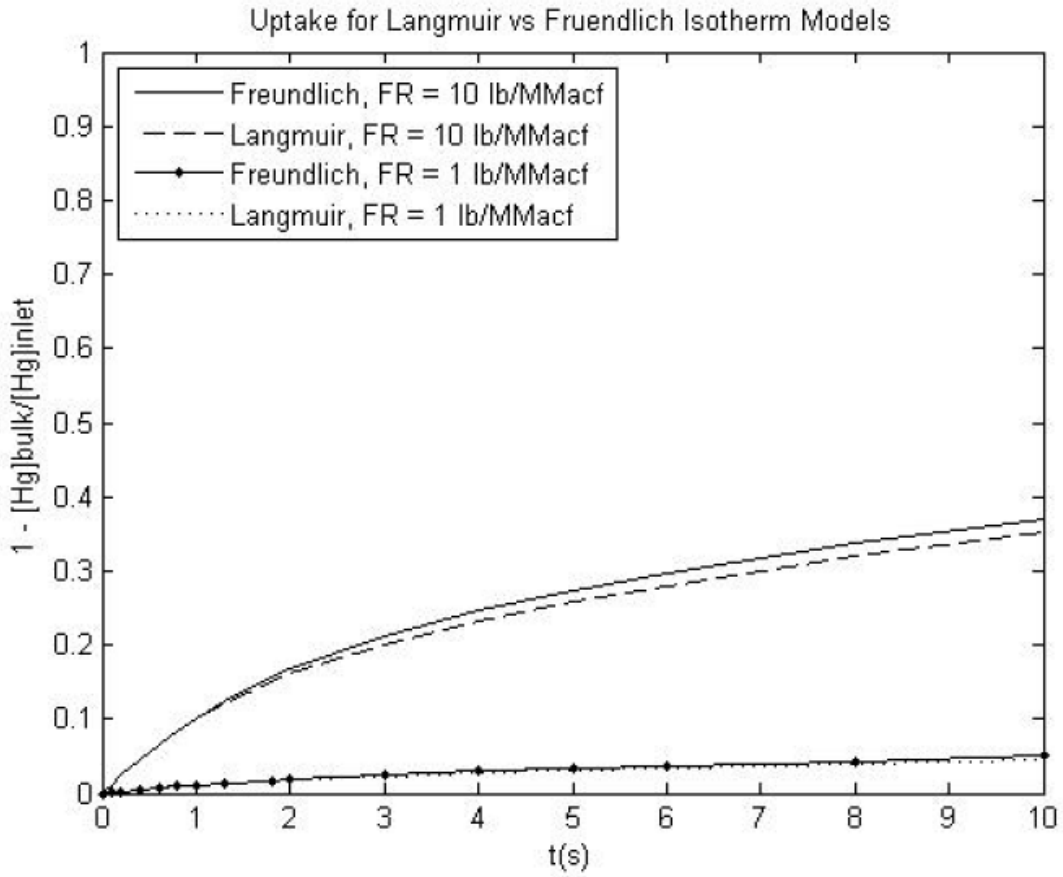


Figure 24 Mercury uptake normalized with inlet concentration over time using the Freundlich and Langmuir isotherm models. These results used “bined” activated carbon as described by Cremer et al. [8] (Kfr=1/Klang max=0.0149).

## Intraparticle Diffusion

As shown in Figures 15 and 17, intraparticle diffusion can be observed at short residence times in varying degrees. The concentration gradient inside the particle largely depends on the size of the particle itself. At a diameter of 30 μm as shown in the previous figures, mercury cannot diffuse to the center of the particle in short residence times if the solid and gas phases remain in equilibrium. However, when particle diameter is decreased to 5 μm, mercury has a shorter distance to travel and the concentration gradients are more apparent as shown in Figure 25.

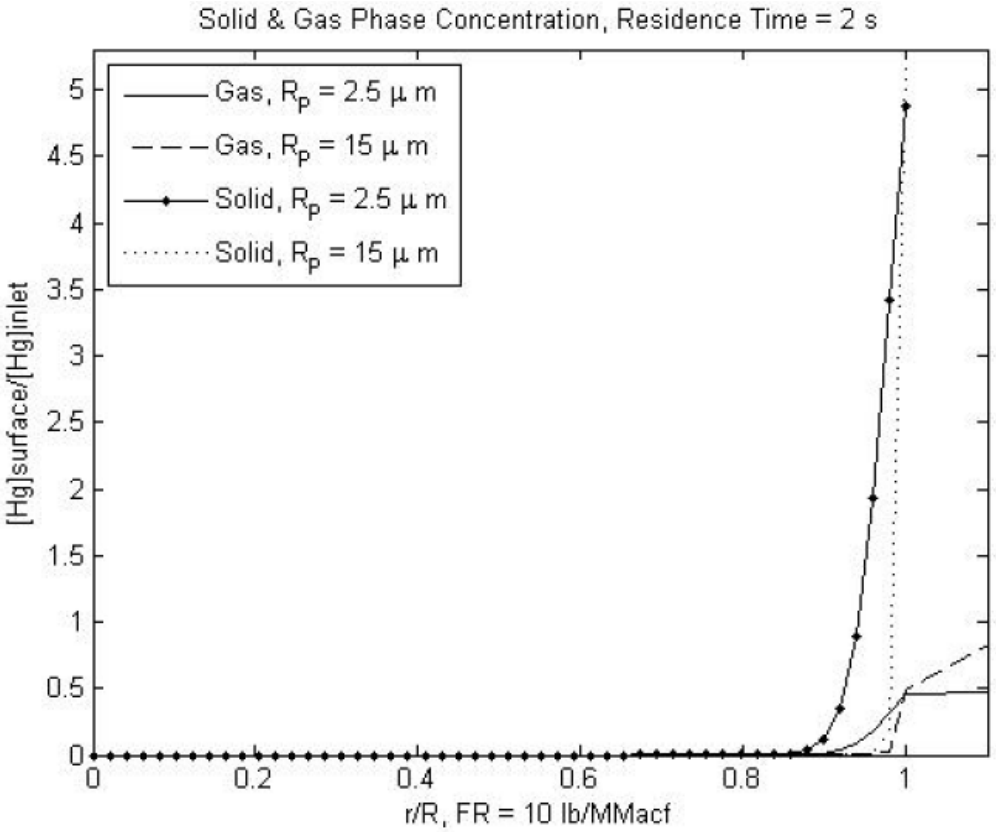


Figure 25 Comparison of gas and solid phase mercury concentration normalized with the inlet concentration inside the particle using the Freundlich adsorption model using different particles diameters.

The Langmuir isotherm adsorption model shows an even more dramatic gradient change when particle size is decreased as shown in Figure 26.

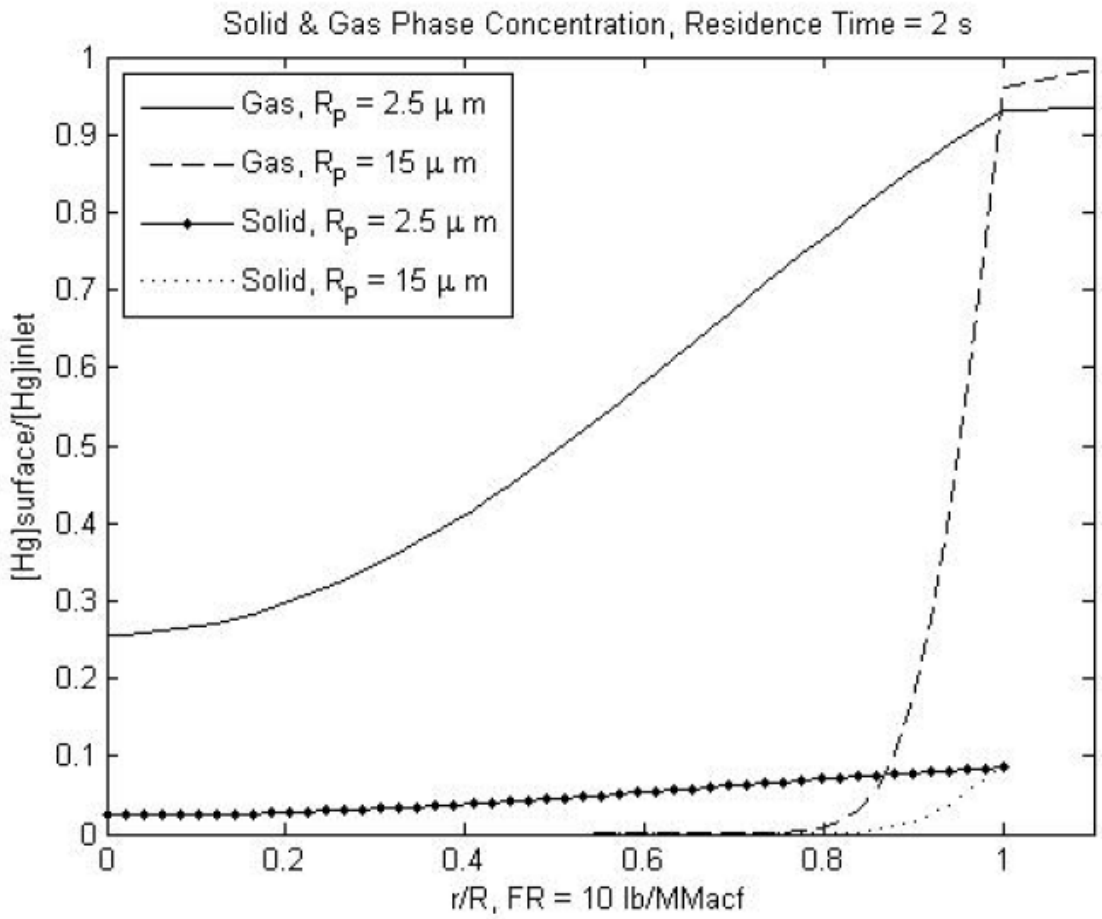


Figure 26 Comparison of gas and solid phase mercury concentration normalized with the inlet concentration inside the particle using the Langmuir adsorption model using different particles diameters.

## Explanation of Wall Effects

The uptake results for the binned particles in Figure 20 are lower than that seen in the full-scale results shown in Figure 27. If a 25% correction is added to the uptake shown in Figure 21, the full-scale data may be more closely simulated as shown in Figure 28. Admittedly, this correction factor is highly qualitative, but it does allow for a predictive capacity that comes within 10% of full-scale values reported by Cremer et al. [8] .

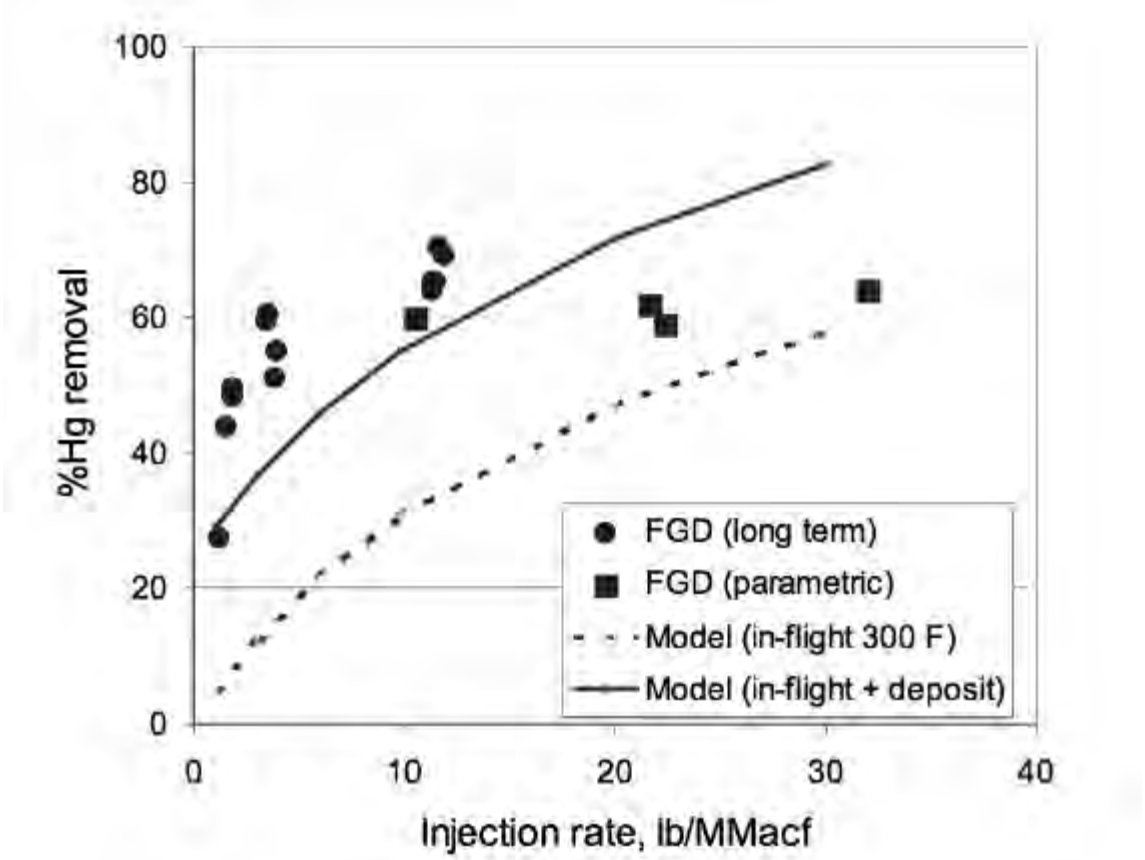


Figure 27 Full-scale mercury uptake at Pleasant Paire as reported by Cremer et al. (8)

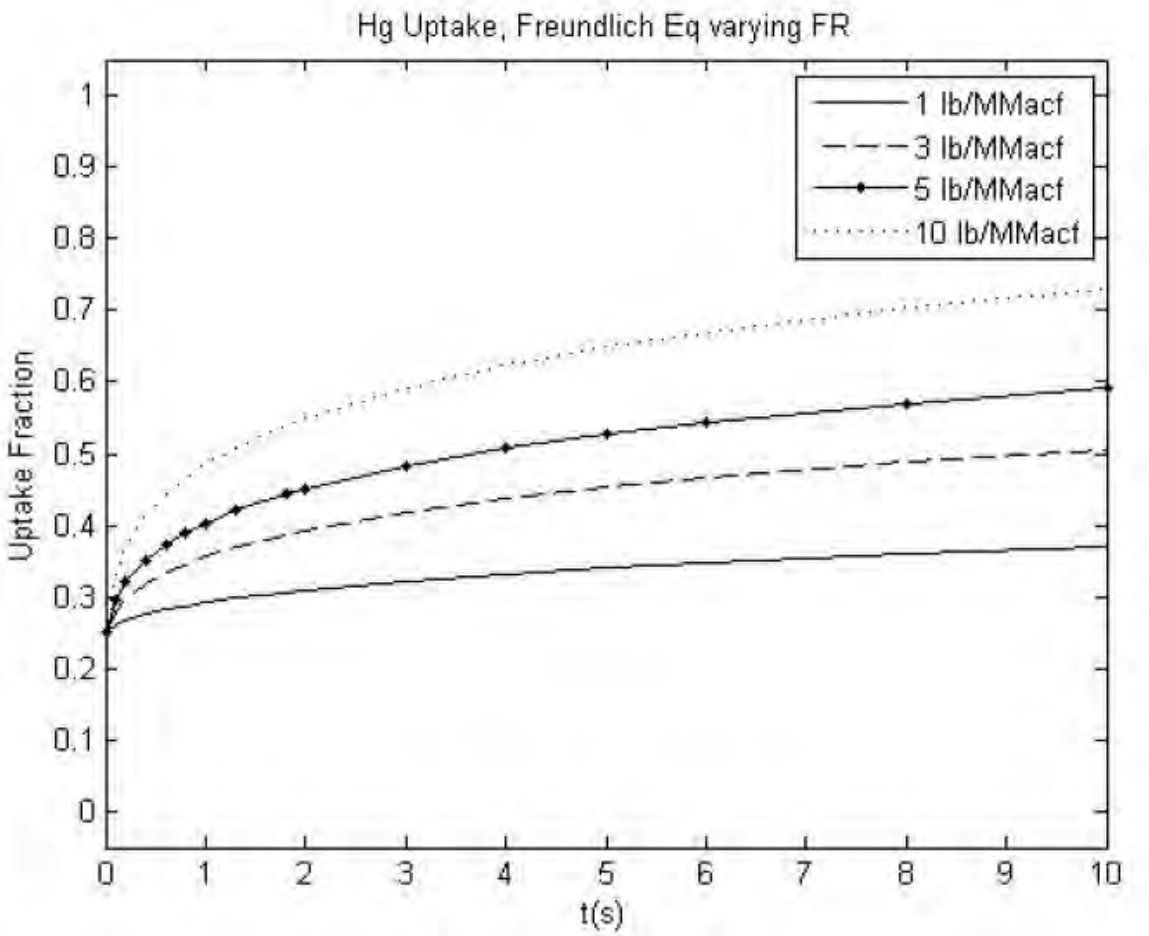


Figure 28 Mercury uptake using Freundlich isotherm adsorption model. The particles are “binned” and a 25 % correction factor is added to simulate “wall effects”.

Figure 29 shows results that may be directly compared to Figure 27. The solid line represents a 25% total uptake correction as shown in Figure 28 while the dotted line shows uptake that is 66% in-flight and 33% wall effect. The basic 25% correction seems to match the full scale data more closely, which points to the conclusion that the "packed bed" that forms on the wall of the duct likely does so quickly and does not change throughout the duration of the test.

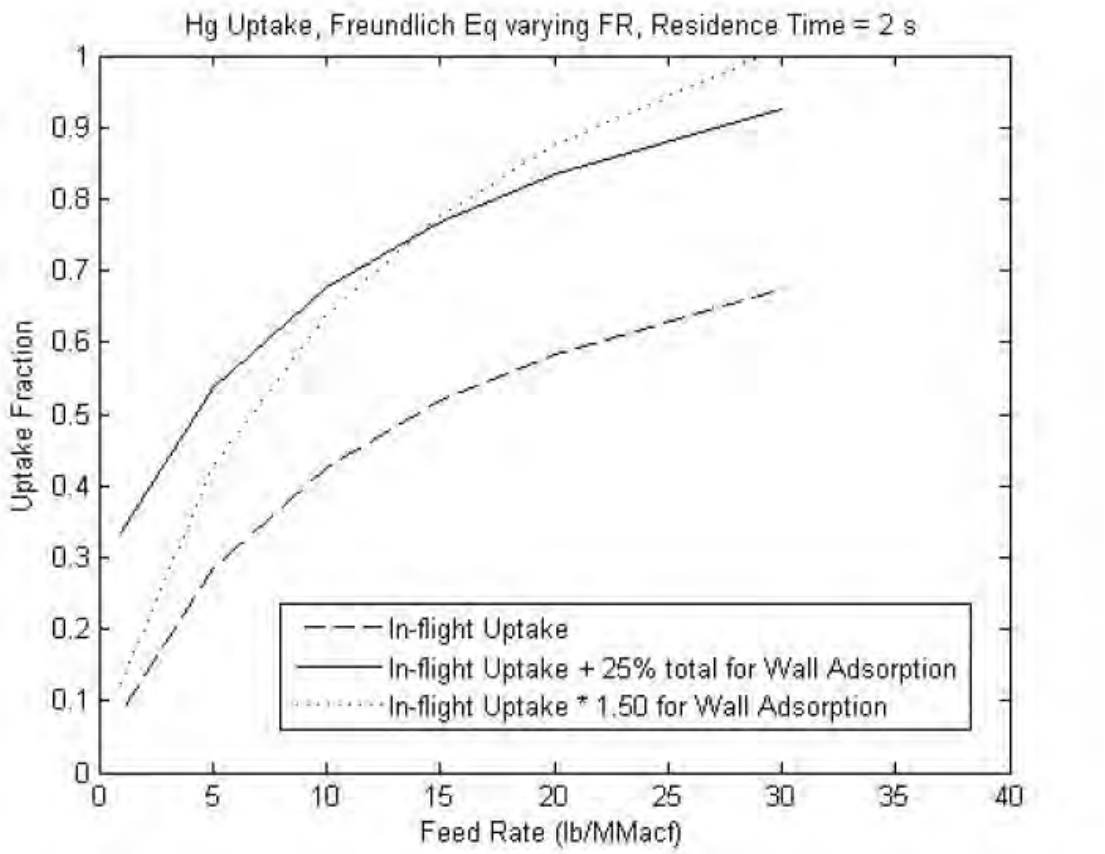


Figure 29 Mercury uptake normalized with inlet concentration inside the particle using the Freundlich isotherm adsorption model . The particles are “binned”, and a total uptake 25% or 50% proportional uptake increase is added as a correction factor to simulate “wall effects”.

# CONCLUSIONS

- The experimental setup does not allow the use of powdered activated carbons as sorbents due to the high pressure drop across the fixed-bed reactor.

- Classical breakthrough curves were not observed with the coconut-shell activated carbon under the periods of time and flue gas compositions considered in this report because of the large sample size.

- Without halogen species, the coconut-shell activated carbon provided negligible mercury capture at 150$^{o}$C. Under these conditions the sorbent is not effective for mercury capture.

- The highest efficiency of the sorbent for mercury capture, near 100 percent, was obtained upon exposure of the coconut-shell carbon either to 50 ppm chlorine (as HCl equivalent) or 50 ppm bromine (as HBr equivalent) at 150$^{o}$C.

- When the carbon was exposed to 100 ppm $SO_2$ in the absence of halogens, the sorbent adsorption efficiency increased from 20 percent to 30 percent. When 50 ppm chlorine (as HCl equivalent) was added to the flue gas after the addition of $SO_2$ at concentrations ranging from 100 ppm to 500 ppm, the adsorption efficiency increased. In contrast, when the $SO_2$ was added at concentrations ranging from 100 ppm to 500 ppm after the addition of 50 ppm HCl, the sorbent adsorption capacity decreased. The extent of this decrease was proportional to the $SO_2$ concentration. This reduction was not observed when the HCl concentration increased to 100 ppm.

- In presence of 50 ppm bromine (as HBr equivalent) almost 100% adsorption was observed, the extent of this adsorption was not significantly affected by the addition of HCl or $SO_2$.

- The Langmuir-based, fixed-bed model shows a reasonable ability to fit fixed-bed breakthrough data from a variety of sources for powdered activated carbons.

- Wall effects are extremely important in entrained particle models. They can account for as much as 50 percent of removal perceived to be “in-flight”. As of yet, the wall effects cannot be quantitatively modeled, but enough is known about them to generate a qualitative correction factor that can place mercury uptake predictions within 10 percent or 20 percent of full-scale tests. As more full-scale data is complied and reported, this correction factor may be improved.

- Several options exist for solid-phase adsorption models. An adsorption/desorption rate model was insufficient in predicting full-scale entrained mercury capture. Freundlich and Langmuir isotherm models are both mathematically adequate.

- It is important to include the particle size distribution, in this study as bins of particles. Uptake is strongly related to particle size. Furthermore, intraparticle diffusion was found to offer significant resistance to adsorption for larger particles.

## Acknowledgement

This material is based upon work supported by the Department of Energy under Award Number DE-FC26-06NT42808.

# LIST OF FIGURES

**Figure 1** Elemental ($Hg^0$) and total ($Hg^T$) mercury concentrations at the exit of the carbon bed as a function of time (hours) at a temperature of 150$^oC$ at HCl concentration of 50 ppm and $SO_2$ concentrations ranging from 100 to 500 ppm.

**Figure 2** Elemental ($Hg^0$) and total ($Hg^T$) mercury concentrations at the exit of the carbon bed as a function of time (hours) at a temperature of 150$^oC$ at HCl concentration of 100 ppm HCl and$SO_2$ concentrations of 500 ppm, 100 ppm and 300 ppm.

**Figure 3** Elemental ($Hg^0$) and total ($Hg^T$) mercury concentrations at the exit of the carbon bed as a function of time (hours) at a temperature of 150$^oC$ at $SO_2$ concentrations of 100, 200, 500 ppm and HCl concentration of 50 ppm.

**Figure 4** Elemental ($Hg^0$) and total ($Hg^T$) mercury concentrations at the exit of the carbon bed as a function of time (hours) at a temperature of 150$^oC$ at a bromine concentration of 35.28 ppm (as HBr equivalent) and 50 ppm HCl.

**Figure 5** Elemental ($Hg^0$) and total ($Hg^T$) mercury concentrations at the exit of the carbon bed as a function of time (hours) at a temperature of 150$^oC$ at a bromine concentration of 35.28 ppm (as HBr equivalent) , HCl concentration of 50 ppm and $SO_2$ concentration of 500 ppm.

**Figure 6** Elemental ($Hg^0$) and total ($Hg^T$) mercury concentrations at the exit of the carbon bed as a function of time (hours) at a temperature of 150$^oC$ at $NO_2$ concentrations of 5 and 20 ppm $NO_2$.

**Figure** 7 Breakthrough curves for fly ash with a bed temperature of 150$^oC$. (A) Initial mercury concentration, $C_o$=2.8 mg/$m^3$, (B) $C_o$=10mg/$m^3$. Experimental data

o from Karatza et al [3]. , Calculated values obtained with the heterogeneous model.

**Figure 8** Breakthrough curves lignite activated carbon with a bed temperature of 107$^{o}$C. (A) Mercury and baseline gases, (B) Mercury, 50 ppm HCl and baseline gases. Experimental data o from Miller et al [4]. , Calculated data obtained with the heterogeneous model.

**Figure 9** Breakthrough curves lignite activated carbon with a bed temperature of 107$^{o}$C. (A) Mercury, 1600 ppm $SO_2$ and baseline gases, (B) Mercury, 20 ppm $NO_2$ and baseline gases. Experimental data from Miller et al [4], Calculated data obtained with the heterogeneous model.

**Figure 10** The basic mass balance scheme used in a shell inside a uniform, spherical sorbent particle.
**Figure 11** The organization of the discretization scheme used in the author's model.

**Figure 12** Mercury uptake normalized with inlet concentration over time using the rate model.

**Figure 13** Mercury uptake normalized with inlet concentration in both the solid and gas phases using the rate model.

**Figure 14** Mercury uptake normalized with inlet concentration over time using the Langmuir isotherm model.

**Figure 15** Mercury concentration normalized with inlet concentration inside the sorbent particle using Langmuir isotherm model.

**Figure 16** Mercury uptake normalized with inlet concentration over time using Freundlich isotherm model.

**Figure 17** Mercury uptake normalized with inlet concentration over time using Freundlich isotherm model.

**Figure 18** Mercury uptake normalized with inlet concentration over time using Freundlich isotherm model and varying particle diameter.

**Figure 19** One example of how activated carbon particles may be distributed in "bin" form.

**Figure 20** A comparison of uptake for "binned" and "nonbinned" particle sets for two different feed rates. "Binned" at size range from 2 μm to 75 μm and averaging 30 μm which is the size angle used in the "nonbinned" model.

**Figure 21** A comparison of uptake for “binned” and “nonbinned” particle sets for two different feed rates. “Binned” at size range from 2 μm to 75 μm and averaging 30 μm which is the size angle used in the “nonbinned” model.

**Figure 22** Mercury uptake normalized with inlet concentration over time using the Freundlich isotherm model and varying the feed rate ($R_p$=15 μm).

**Figure 23** Mercury uptake normalized with inlet concentration over time using the Freundlich isotherm model and maximizing Dab to minimize resistance from external mass transfer ($R_p$=15μm).

**Figure 24** Mercury uptake normalized with inlet concentration over time using the Freundlich and Langmuir isotherm models. These results used “bined” activated carbon as described by Cremer et al. [8] ($K_{fr}=1/K_{lang}\omega_{max}$=0.0149).

**Figure 25** Comparison of gas and solid phase mercury concentration normalized with the inlet concentration inside the particle using the Freundlich adsorption model using different particles diameters.

**Figure 26** Comparison of gas and solid phase mercury concentration normalized with the inlet concentration inside the particle using the Langmuir adsorption model using different particles diameters.

**Figure 27** Full-scale mercury uptake at Pleasant Paire as reported by Cremer et al. [8]

**Figure 28** Mercury uptake using Freundlich isotherm adsorption model. The particles are “binned” and a 25 % correction factor is added to simulate “wall effects”.

**Figure 29** Mercury uptake normalized with inlet concentration inside the particle using the Freundlich isotherm adsorption model . The particles are “binned”, and a total uptake 25% or 50% proportional uptake increase is added as a correction factor to simulate “wall effects”.

# REFERENCES

(1) Fry, A., Cauch, B., Silcox, G., Lighty, J., Senior, C. *Proceedings of the Combustion Institute* **2007**, 31, 2855-2861.
(2) Schaeffer K., Potwora, R. Coconut Shell versus Bituminous Coal Activated carbon. June 2008. Carbon Resources.
(3) Karatza, D., Lancia, A., Musmarra, D. *Environ. Sci. Technol.* **1998**, 32, 3999-4004.
(4) Miller, S., Dunham, G., Olson, E., Brown, T. *Fuel Processing Technology* **2000,** 65-66, 343-363.

(5) Gardner, P.J., Pang, P., Preston, S.R. *J. Chem. Eng. Data* **1991**, 36, 265-268.
(6) Massman, W.J. *Atmospheric Environment* **1991,** 33, 453-457.
(7) Bird, S., Lightfoot, *Transport phenomena,* 2nd ed.; WILEY-VCH, 2000.
(8) Cremer, M., Senior, C., Chiodo, A., Wang, D., Valentine, J. *CFD Modeling of Activated Carbon Injection for Mercury Control in Coal-Fired Power Plants.* Technical report, 2005.
(9) McCabe, W., Smith, J., Harriot, P.P. *Unit Operations of Chemical Engineering.* McGraw Hill Inc., 1993.
(10) Scala, F. *Envirionmental Science & Technology.***2001**, 35, 4367-4372.
(11) Scala, F. *Industrial & Engineering Chemistry Research* **2004,** 43, 2575-2589.
(12) Flora, J.R.V., Hargis, R. A., O'Dowd, W.J., Pennline, H.W., Vidic, R.D. *J. Air & waste Manage. Assoc.* **2003,** 53, 478-488.
(13) Bustard, J., Durham, M., Starns, T., Lindsey, C.,Martin, C., Schlager, R., Baldrey, K. *Fuel Processing Technology* **2004**, 85, 549-562.
(14) Pollack, N.R. *Sorbent Injection: taking the technology from R&D to Comercial Launch.* Technical Report, 2008.
(15) Meserole, F.B., Change, R.,Carey, T.R., Machac, J., Richardson, C.F. *J. Air & Waste manage. Assoc.* **1999**, 19, 694-704.

# ABBREVIATIONS

| | |
|---|---|
| g/g: | Grams of Mercury per Grams of Carbon |
| g $Hg/m^3$: | Grams of Mercury per Cubic Meter |
| $\mu g/m^3$: | Micrograms per Cubic Meter |
| $\mu m$: | Micrometers |
| nm: | Nanometers |
| $m^3$/g min: | Cubic meter per gram per minute |
| $min^{-1}$: | 1/minute |
| $mg/m^3$: | Milligram per Cubic Meter |
| C: | Celsius |
| Co: | initial Mercury Concentration |
| cm: | Centimeters |
| CO: | Carbon Monoxide |
| $CO_2$: | Carbon Dioxide |
| F: | Fahrenheit |
| g; | Grams |
| HCl: | Hydrochloric Acid |
| HBr: | Hydrogen Bromide |
| Hg: | Mercury |
| $HgCl_2$: | Mercuric Chloride |
| $Hg^o$: | Elemental Mercury |
| $Hg^T$: | Total Mercury |
| $H_2O$: | Water |

| | |
|---|---|
| ID: | Internal Diameter |
| K: | Kelvin |
| lb: | Pounds |
| m: | meters |
| $m^2$: | Square Meters |
| $m^3$: | Cubic Meter |
| mg: | Milligrams |
| min: | Minutes |
| mm: | Millimeters |
| $N_2$: | Nitrogen |
| NO: | Nitrogen Monoxide |
| $NO_2$: | Nitrogen Dioxide |
| $O_2$: | Oxygen |
| OD: | Outer Diameter |
| ppm: | Parts Per Million |
| ppmv: | Parts Per Million by Volume |
| s: | Seconds |
| SLPM: | Standard Liters per Minute |
| $SnCl_2$: | Stannous Chloride |
| $SO_2$: | Sulfur Dioxide |
| W: | Watts |

# EFFECTS OF PARTIAL PRESSURE OF OXYGEN ON THE STABILITY OF AXIAL, OXY-COAL, TURBULENT DIFFUSION FLAMES

Topical Report Task 8

July 31st, 2009

Co-operative Agreement: DE-FC26-06NT42808

Reporting Period: July 1, 2006 to March 31, 2009

Prepared for:

U.S. Department of Energy,

National Energy Technology Laboratory (NETL)

Prepared by

Jingwei Zhang and Jost O.L. Wendt

Department of Chemical Engineering and

Institute for Clean and Secure Energy,

University of Utah, Salt Lake City, UT 84108

**Email: Jost.Wendt@utah.edu**

DISCLAIMER

ABSTRACT

Oxy-fuel combustion of pulverized coal with flue gas recirculation is potentially one of the few technologies that may allow $CO_2$ sequestration technologies to be applied to existing coal-fired boilers. One issue of interest is to understand and predict the effects of the near-burner zone environment consisting of $O_2$ and $CO_2$ (instead of $N_2$). The purpose of this research is to better understand the effect of partial pressure of $O_2$ ($P_{O2}$) on flame stability, which becomes another degree of freedom not present during air combustion. The data obtained were designed to form an experimental basis for validation of coal-jet ignition models. These models can play a useful role in predicting flame attachment and flame stability for retrofit of oxy-coal combustion into existing boilers. Type 0 axial flames, which can be accurately characterized, are chosen to represent the near-burner zones of tangentially fired furnaces or cement kilns, where burner swirl is absent.

This topical report describes:

- the design attributes of a 100 kW test oxy-fuel combustor, together with an ancillary $O_2$ and $CO_2$ supply system. One challenge that was satisfactorily resolved was the steady feeding of 2 – 5 kg/hr coal into an axial burner to produce Type 0 axial turbulent diffusion flames in a steady enough fashion to allow quantification of the data.
- the methodology developed to quantify flame stand-off distance, flame length, and flame luminosity using image processing techniques.
- the results showing the effect of $P_{O2}$ in secondary $O_2/CO_2$ stream on flame stability, flame length and flame luminosity at the same adiabatic flame. temperature comparing with $O_2/N_2$ environment.
- the results showing the effect of $P_{O2}$ in the primary (transporting) stream on the axial flame stand-off distance. Statistical studies, including probability distribution function (PDF) data, on the flame stand-off distance, are provided to quantify this effect.

The results indicated that flame stand-off distance is not a continuous variable, and attachment/detachment passes through a sudden transition. In addition, the secondary stream preheat plays an important role on the coal ignition. Primary $P_{O2}$ has a first-order effect on flame stability and axial coal jet ignition.

## Contents

## EXCUTIVE SUMMARY

The purpose of this research is to better understand and to scale the effect of partial pressures of $O_2$ and $CO_2$, two additional degrees of freedom for oxy-coal combustion, on coal jet ignition and flame stability in the near-burner zone. A novel methodology is developed to quantify the flame stability and flame length by introducing an image processing technique. In addition, the experiment is designed to provide data for simulation validation studies that can be used to predict how air fired combustors may be retrofitted to oxy-coal.

Specifically the objective is to explore effects of the partial pressure of $O_2$ and $CO_2$ on coal jet flame stability, which is quantified by stand-off distance, the distance between burner tip and the base of the detached flame. The experiments are carried out in a 100 kW pilot-scale laboratory furnace outfitted with a coaxial, zero swirl burner and arrays of electrically heated panels in the burner zone in order to control variations in near-burner heat loss. The design of the combustor is described in detail. Currently, fresh, once-through $CO_2$ (rather than flue gas recycle), and $O_2$ streams are introduced into the burner. The furnace has visual access to the burner zone through quartz windows, and this allows for optical measurements. Data consist, in part, of sequences of photo-images of the flame. A special complementary metal–oxide–semiconductor (CMOS) sensor based camera, which is more sensitive to the near infrared wavelength, is employed to capture quantitative information on Type 0 axial turbulent diffusion flame shapes. This information is subsequently analyzed to yield statistical data with error quantification, of flame stand-off distance as functions of variations of various operational parameters, including systematic variations of partial oxygen pressure in both transport and secondary oxidant streams. These analyses are used to determine the effect of oxygen partial pressure in both transport and secondary stream on coal jet ignition and flame stability.

This work has led to the following conclusions:

- Systematic measurements of axial flame stand-off distance versus primary $O_2$ concentration ($P_{O2}$) have been obtained, together with uncertainty quantification.
- Flame lift-off distance is not a continuous variable and attachment/detachment appears to pass through a sudden transition.
- Secondary stream preheat plays a critical role in coal ignition. However primary $P_{O2}$ has a dominant effect on flame stability and axial coal jet ignition.

## OBJECTIVES

Oxy-coal combustion, in which air is replaced by an $O_2$/ $CO_2$ mixture, is one of the technologies that may allow $CO_2$ sequestration technologies to be applied to existing coal-fired boilers. One issue of interest is to understand and predict the effects of inlet oxidant mixture composition, now consisting of $O_2$ and $CO_2$ instead of $O_2$ and $N_2$, on flame stability. The objectives of the research presented here are:

1. to better understand, the effects of partial pressure of $O_2$ in the coal transport jet, on axial coal jet ignition and flame stability;
2. to contribute to *validated*, turbulent diffusion coal flame simulations that predict the effects on flame stability of conversion from air fired to oxy-fired conditions in existing units.

Furthermore, although the well defined axial flame type under consideration here was chosen because of its simplicity and suitability for simulation, it does have direct practical relevance to certain industrial oxy-coal combustion configurations, such as tangentially fired boilers and cement kilns. Therefore, this work comprises the first steps towards understanding the stability of turbulent oxy-coal flames in general.

## SCOPE

One measure of coal jet flame stability is the stand-off distance, the distance between burner tip and the base of a detached flame. To explore how oxygen partial pressure ($P_{O2}$) of the oxidant streams may affect this parameter, experiments have been completed in a newly designed and constructed 100 kW pilot-scale laboratory furnace. These experiments employed a well-defined pulverized coal (PC) axial turbulent diffusion flame similar to those depicted on Figure 1. These relatively simple, zero swirl, axial flames (designated here as Type 0 flames) are better defined for companion simulation studies, and may also have similarities to practical flames in cement kilns and in tangentially fired boilers.

The scope of this Topical Report encompasses the following:

1. A brief exposition of background material relevant to this project.
2. The design and construction of the new 100kW oxy-fuel combustor (OFC), the co-axial jet burner, and supporting piping and instrumentation created for this project.
3. Results of screening experiments, using air, performed to validate this new facility under essentially conventional combustion conditions.
4. Engineering details on the incorporation of the $O_2$ and $CO_2$ supply system provided by Praxair, Inc.
5. A description of necessary modifications to the coal feeder to allow sufficiently steady coal feeding conditions for flame stability studies, at coal feed rates of 2-5 kg/h.

6. The development of a photo-imaging technique to allow quantification of flame structure, including stand-off distance, flame length, and (relative) flame luminosity.
7. Results of additional screening tests used to validate the photo-imaging quantification techniques. These included determination of effect of secondary $PO_2$ on flame length and flame luminosity.
8. Initial results showing the effects of $PO_2$ in the primary jet on flame stand-off distance, for oxy-coal combustion with once-through $CO_2$.

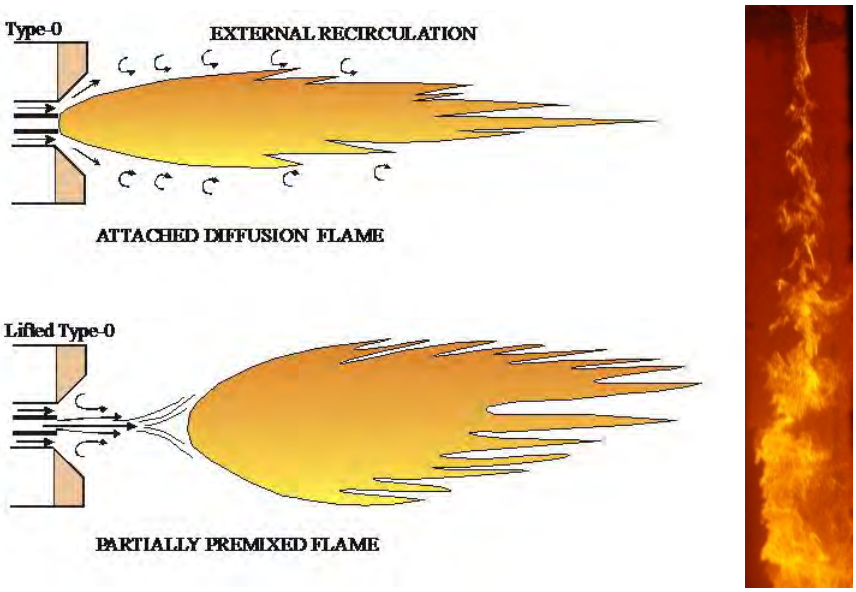


**Figure 1.** Type 0 flame: picture on the left shows attached and detached Type 0 flame; picture on the right shows a typical Type 0 attached oxy-coal flame (shutter speed 0.25 ms)

## BACKGROUND

Global warming, one of the largest environmental challenges of our time, is due to increased carbon dioxide levels in the atmosphere [1]. The world currently depends on the use of fossil fuels, especially coal, for its energy supply, and will continue to do so for a long time. According to the Kyoto Protocol, by 2008-2012, Annex I countries must reduce their greenhouse gas emissions by a collective average of 5% below their 1990 levels. One approach to diminish $CO_2$ emissions into the atmosphere is to capture the carbon emissions from fossil fuel combustion units and sequester them deep in the earth. This is carbon capture and sequestration (CCS). In post combustion process, $CO_2$ capture requires absorption into and subsequent regeneration of an absorbent, usually a solution. Another CCS process currently under consideration involves burning coal with relatively pure oxygen, together with recycled flue gases, to produce a highly concentrated (up to 95% $CO_2$) flue gas stream, suitable for immediate compression to a supercritical state and subsequent transportation and sequestration. This is oxy-fuel combustion, one of the promising technologies to reduce $CO_2$ emissions, and one that has attracted world-wide attention[1, 2, 3, 4].

Sarofim et al (2004) have summarized the major scientific questions on oxy-coal combustion in PC furnace with $CO_2$ recycle in terms of the following issues:

1. Can we predict heat transfer profile, fouling, slagging, ash partitioning and char burnout under oxy-coal combustion conditions?
2. Can we predict ignition/kinetic/aerodynamic interactions here at the burner?
3. How much residual $N_2$, NO, Hg, $SO_2$, trace metals etc. can be removed with the $CO_2$ to be sequestered?
4. From where shall the recycled flue gases be taken? Should they be extracted from the flue gas after ash removal, after $H_2O$ removal, or after $SO_2$ removal, or after any combination of these three?

This work focuses on the second question, related to ignition. To study the coal jet ignition and flame stability, it is very important to understand both the chemistry (such as, single coal particle ignition mechanisms, kinetics rates of char oxidation, and so on) and the aerodynamics (such as mixing, particle trajectories and flow patterns) occurring in the near-burner zone. It is also of interest to study the $NO_x$ formation under oxy-coal combustion conditions, because measurements of $NO_x$ are achieved with little extra effort as by-products of this work, and because $NO_x$ from coal flames is sensitive to flame attachment and flame jet aerodynamics. Therefore this literature review summarizes the previous studies on: 1) coal particle ignition mechanism; 2) near-burner phenomena studies and flame stability; 3) pollutant formation under oxy-coal combustion conditions.

## Single coal particle ignition mechanism

To understand coal jet ignition, it is useful first to study ignition of a single coal particle. Over the last decade, there have been numerous studies of coal particle ignition mechanisms [5-20]. Essenhigh et al. [8] completed a classical review on coal particle ignition mechanisms in 1980. Both homogenous, gas phase ignition(GI), and heterogeneous (HI) mechanisms have been proposed to describe the ignition process [8-15]. The greatest controversy lies on which mechanism is controlling: devolatilization followed by gas phase ignition (first proposed by Faraday) or gas/solid reaction (whole coal ignition). The heterogeneous reaction involves the direct attack of oxygen on the whole coal particle, not just char, and also removes material, which would otherwise be expelled as volatiles [8]. In the GI mechanism the initial step is pyrolysis and subsequent ignition of the volatiles (Faraday mechanisms), followed by (heterogeneous) ignition of the char. The heterogeneous mechanism neglects the influence of volatile matter and depends on heat generation by combustion on the coal surface (either externally or internally), whereas the homogeneous mechanism involves the combustion of evolved volatile matter in the vicinity of the particle with its heating by conduction from the volatile flame. [11]

Wall and Gururajan [10, 11 ] applied analyses of both heterogeneous and homogenous mechanisms to data obtained in their study and showed that:

1. Although a flame sheet model for the ignition of a single particle by a homogeneous mechanism predicts the observed particle size dependence of the ignition temperature, it fails to predict the observed oxygen concentration dependence [11].
2. Analysis of the ignition temperature data (at temperatures ranging from 650K-1200K and particle sizes less than 500 $\mu m$ ) to determine the reactivity of coal or char, requires a) the assumption of heterogeneous ignition, b) an assumption on the nature of the product of combustion (generally $CO_2$ rather than CO), and c) the reaction order with respect to oxygen (if experiments were not preformed over a range of oxygen partial pressures) [10].
3. When both surface oxidation (heterogeneous mechanism) and volatile combustion (homogeneous mechanism) are considered to occur simultaneously, surface oxidation dominates the ignition behavior (as far as ignition temperature is concerned) of only small particles, or at high oxygen concentrations [11].

Sun [15] suggested that when weight loss occurs before ignition, it can be assumed that pyrolysis occurs first, so that ignition is homogeneous. On the other hand, when ignition occurs before or at almost same time as weight loss, ignition can be assumed to be heterogeneous. It is possible that both heterogeneous reaction and pyrolysis occur simultaneously. However, at the early stage of pyrolysis it is likely that the volatile matter evolved cannot attain the flammability limit. In this case it is more likely that the ignition of coal particles occurs earlier than the ignition of volatile matter and also that the heterogeneous reaction removes material, which would otherwise be expelled as volatiles [8]. This situation suggests the HI mechanism. In 1979, Juntgen [8] drew a map of ignition regimes as a function of heating rate and particle size, and

suggested that if coal particle size is larger than 100 $\mu m$ and heating rate lower than 100 K/s, GI mechanism should be applied; otherwise HI is more favored [8].

Many criteria, such as temperature, pyrolysis rate, local gas phase combustible concentration, local gas phase reaction rate, local gas phase heat release rate, local gas phase heating rate [10,11,15], and spatial concentration distribution of combustibles, have been developed to define the ignition of coal particles.

The increased coal particle temperature was found to be controlled by the following factors:

1. Heat transfer from the ambient gas.
2. Radiative heat transfer from the chamber's walls. Before ignition the temperature of these walls was low and radiation effects on ignition temperature can be assumed to be negligible [10-12].
3. Heat generated by chemical reaction.
4. Heat loss when the temperature of the particles was higher than that of the ambient gas and chambers' walls.

From these results and others in the literature, numerous factors, such as coal properties, particularly particle size and volatile content [7-9, 15], heating rate [8, 15], oxygen concentration [5, 6, 12, 15], pressure [15-17] and nature of the gas flow surrounding the particle[5, 6, 13] may all impact coal ignition.

Zhang, et al, [18-20] developed a moving flame front (MFF) model and an improved moving flame front (IMFF) model, taking into account the effect of CO oxidizing in the boundary layer around the particle and the influence of the finite rate heterogeneous reduction of $CO_2$ during combustion of a carbon particle. This model has better agreement with the experimental data compared with the traditional single-film model. It is applicable to the burnout of coal char particles in a practical PC flame.

With the exception of the recent work of Molina and Shaddix [5, 6], most studies have not considered the effect of elevated levels of $CO_2$, as present in oxy-coal combustion systems, on the ignition of coal particles. The different properties of $CO_2$ in comparison to $N_2$ have been shown to cause differences in flame and furnace operation parameters such as ignition time and gas temperature profiles [21]. Molina and Shaddix used a combination of particle statistics and one color pyrometry to measure the particle temperature and CH radical chemiluminescence as a tool for the detection of flame sheet and ignition regions [5, 6]. Single particle imaging, shows that the substitution of $N_2$ by $CO_2$ increases the time required for ignition. It also shows that the temperature and size of the diffusion flame of soot cloud that surrounds the particle are lower and larger respectively when $CO_2$ is used instead of $N_2$, due to the fact that $N_2$ has a higher thermal diffusivity than $CO_2$. They also quantified the characteristic devolatilization time and ignition time and found that ignition occurs at higher oxygen concentrations, and that the presence of $CO_2$ retards coal and char ignition, but has a negligible effect on the duration of devolatilization.

An understanding of coal particle ignition mechanisms can help elucidate the detailed kinetics near a coal particle when that is ignited. However, another point should be always kept in mind, namely that the particles injected always contain a size distribution. Therefore, the experimental data results from a range of oxidation rates. Thus, the assumption of a single particle size cannot explain some aspects of the experimental results (e.g., the "curvature" of the burn-off curve) and may lead to significant deviations in calculated kinetics parameters. Only Ballester and Jimenez took the particle size distribution into account [7].

## Near-burner phenomena studies and flame stability

The near-burner region can be defined by the following Figure 2 [29],

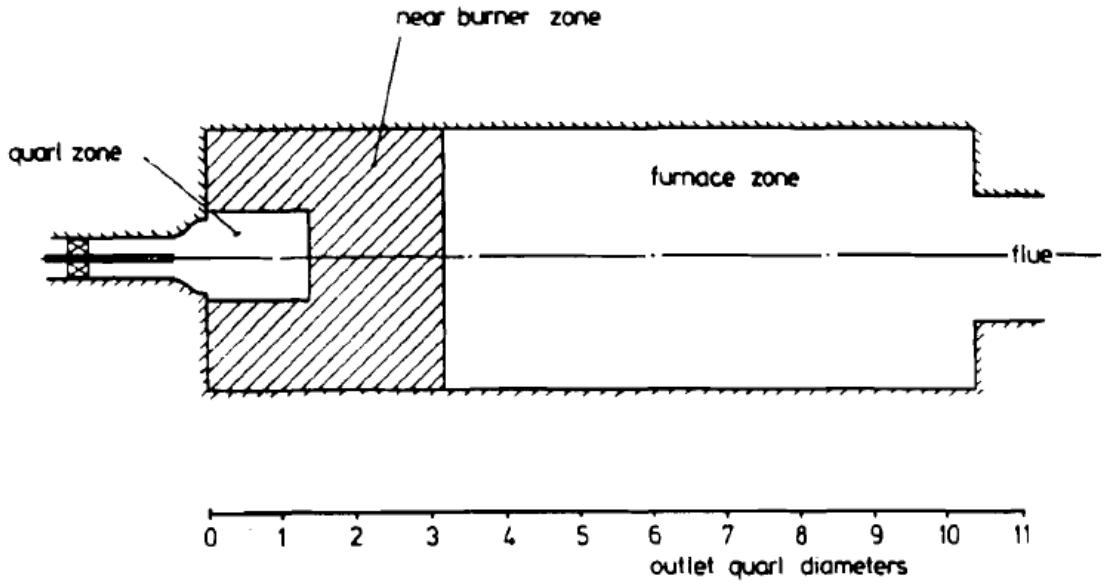


**Figure 2.** International Flame Research Foundation (IFRF) furnace No. 1; definition of quarl zone, near-burner zone and furnace zone

Measurements in industrial swirling flames of high and medium volatile bituminous coals [29] show that $NO_x$ production and destruction can take place in a region close to the burner, as defined above. Char burnout as high as 80% and $NO_x$ concentrations representative of the flue gas concentrations levels are typically measured within two quarl diameter downstream of the burner outlet. The flow pattern in the quarl zone and consequent mixing determine the pollutant formation characteristics of swirl-stabilized flames. Unfortunately, there has seldom been good agreement between the simulation and the experimental data in the near-burner zone. This may be due to various reasons [29-32]. One reason is that the detailed fluid dynamics and flame structure in the near-burner zone are really complex. Another reason for discrepancies between simulation and data may be due to the intrusive in-flame measurement techniques employed. Once a probe is inserted into the flame, it is difficult to quantify the disturbance introduced to the flame and the continuous reaction inside the probe. Non-intrusive optical diagnostics may be a good technique to quantify the flame without influencing it. Examples in the literature are by

Olivani, et al. [34], who used PIV (particle image velocimetry) and LDV (laser Doppler velocimetry) to obtain a comprehensive analysis of the velocity field, and optical still photography for the detection of flame front and main visible flames [34]. From the point of view in the simulation side, the accuracy of the model could not be definitively established due to a lack of detailed measurements in the near-burner region of the combustor and an incomplete understanding of the devolatilization and char combustion of the chosen coal [27]. Another example of the complexity in turbulent jets in the near-burner region is given by Budilarto [35] and Budilarto and Sinclair [36], who suggested that coal ignition sub-model should capture observations that smaller particles preferentially migrate to the jet edge due to turbulent eddies, while larger particles keep travelling in the center of coal jet due to the inertia.

Flame stability, is often quantified as a function of many parameters, such as swirl number, stoichiometry, coal loading, temperature, and coal type [29, 30, 32, 33]. Flame stability can also be described by the attachment or detachment in the experiments. Stand-off distance (also called Lift-off distance), is a parameter to describe the flame stability. When stand-off distance is zero, it means the flame is attached and stable. For unstable detached flames, stand-off distance is usually defined in the experiments as the distance from the burner tip to the base of the flame. Truelove et al, [30] suggested the flame stand-off is taken as the distance at which three percent of the coal mass is devolatilized for prediction purposes. The stability limits of a non-premixed burner arrangement are quantified as a function of swirl number, quarl length, burner confinement and mixtures of pulverized solid fuel and natural gas. Most scientists focused on the above parameters which influence the flame stability. But few studies considered the effect of oxygen partial pressure, which becomes another degree of freedom in oxy-coal combustion. Axelbaum's group at Washington University [40] reported that an increase in $O_2$ concentration improves flame stability while replacing $N_2$ with $CO_2$ results in reduced flame stability. They characterize flame stability by the primary oxidizer Reynolds number at flame blow off (Type I PC flames). They found the air-fired flame and the 30% $O_2$/70% $CO_2$ flame have similar blow-off velocity limits. The flame with 6% $O_2$ in the primary oxidizer and 35% $O_2$ in the secondary oxidizer also has comparable blow-off velocity limits suggesting the potential for reduced $NO_x$ due to the removal of $O_2$ from the high temperature region of the flame without sacrificing flame stability [40].

## Pollutant reduction during oxy-coal combustion

The reduction of $SO_x$ and $NO_x$ in oxy-coal combustion has been reported by many scientists [21-28]. Most of the studies were done either in lab scale or pilot scale furnaces.

Under oxy-coal combustion conditions, because $N_2$ is absent, theoretically there is no thermal $NO_x$ formation. Fuel $NO_x$ is dominant. Liu and Okazaki [23] reported that the conversion ratio from fuel-N to exhaust NO was automatically reduced to less than about one fourth of conventional PC, mainly due to the reduction (or reburning) of recycled NO into the combustion zone. The detailed mechanisms were also discussed by Okazaki and Ando [25]. Ogden and Wendt studied the flame attachment and $NO_x$ emissions using oxygen enrichment for Type 0 PC

flame [38, 39]. Liu et al. [21] found air/oxidant staging is a very effective method in reducing $NO_x$ emissions for both coal combustion in air and coal combustion in 30% $O_2$/70% $CO_2$. Croiset and Thambimuthu [25] from CANMET compared the coal combustion in once-through $O_2/CO_2$ mixtures and experiments with recycled flue gas. They found that combustion with recycled flue gas leads to lower $NO_x$ emission rate than for once-through combustion in $O_2/CO_2$ mixtures, with also agreed with the results of [25,26]. Hu and Kobayashi et al [22] discussed the effect of temperature on $NO_x$ emissions in the presence of recycled flue gas. Increasing the temperature in the presence of excess oxidants will accelerate the oxidation of fuel nitrogen components to NO; on the other hand, at higher temperature, volatiles are predicted to be more rapidly evolved and hence will have a higher average concentration in the early stage of combustion, resulting in fuel rich zones for enhanced NO reduction to $N_2$. NO reduction by char is also enhanced at higher temperature due to the increased rates of reaction, although it provides only a marginal contribution to the total NO reduction. Therefore the net results depend on the combustion conditions and the coal type [22].

# EXPERIMENTAL METHODS

## Design and construction of the new experimental furnace

A new 100 kW down-fired, oxy-coal combustion furnace (OFC) was designed and constructed to allow for the systematic investigation of near-burner aerodynamics of axial diffusion flames using a mixture of oxygen/carbon dioxide to replace the combustion air. It has heated walls and quartz windows for optical access that permit flame detachment studies and future optical diagnostics (Figure 3). The new furnace will simulate the environments experienced by PC jet flames in certain boilers (such as tangentially fired units) and will provide for the systematic control of burner momentum and velocity variables, as well as wall temperatures. The furnace consists of an oxy-fuel combustion chamber, followed by downstream section with controlled temperature cooling to simulate practical furnace conditions. It allows stabilization of axial Type 0 (no swirl) PC diffusion flames, through the use of heated walls, and variations of oxygen content of transport and secondary air streams. It also represents those typical of existing tangentially fired boilers or cement kilns. The time-temperature history, for combustion with air, represents that of existing boilers.

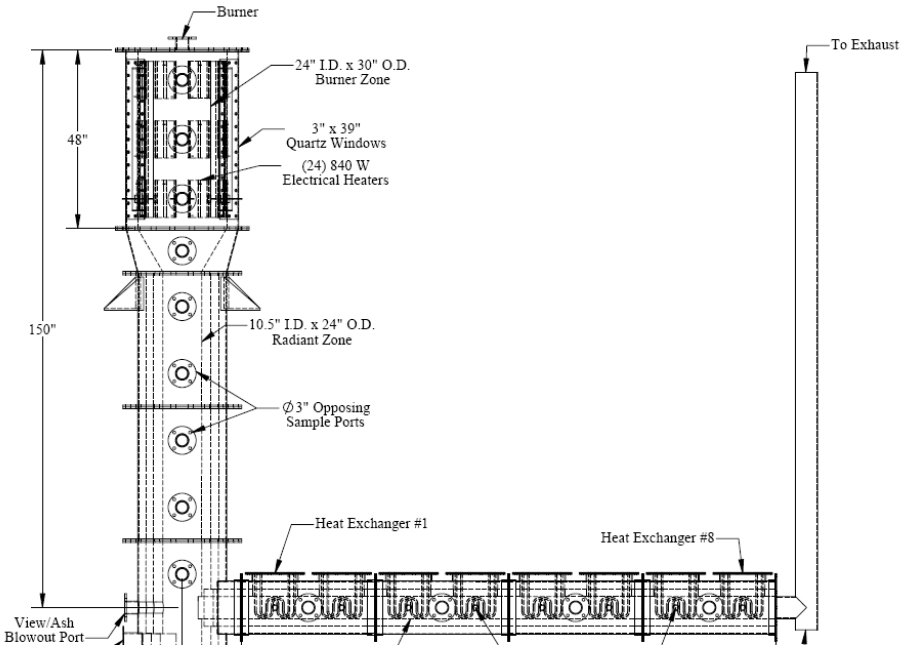


**Figure 3.** Design sketch of the new 100 kW oxy-coal combustion furnace

The top section (Figure 4, Figure 5) is the burner zone, with dimensions of 0.610 m I.D., 0.914 m O.D. and 1.219 m in height. It is insulated by 2600 fiberboard with a thickness of 76 mm. The burner zone is heated electrically by 24 × 840 W flanged ceramic plate heaters (3 rows and 8 heaters per row, as shown in Figure 2). Each row of heaters is embedded with K-type thermocouples to control or monitor the temperature. The independent control of wall temperature provides another degree of freedom, which may impact PC ignition or flame attachment/detachment during the combustion process.

Three layers of insulation are installed in the downstream radiant zone: 1900 fiberboard (thickness of 51 mm), 2600 fiberboard (thickness of 76 mm), and 700 ultra green castable refractory(thickness of 127 mm). Two layers of insulation are installed in the convective zone: 2600 fiberboard (thickness of 76 mm), and 700 ultra green castable refractory (thickness of 51 mm). Eight heat exchangers in the convection section, which allow the simulation of super heaters in an industrial boiler, cool the flue gas before entering the exhaust system. A preheater is also installed to heat the inlet oxidant to temperatures as high as 700 K.

**Figure 4.** View of inside of top section chamber, showing electric heaters and view of optical windows

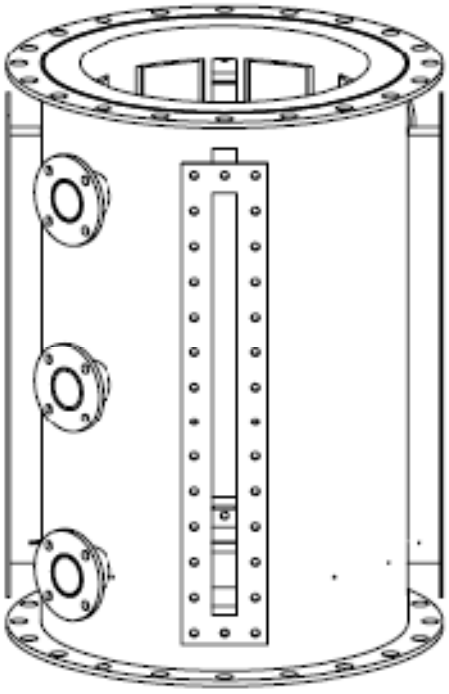

**Figure 5.** Design sketch of the top section

Figure 6 and 7 show OFC, and Figure 7 shows the burner applied in our tests.

**Figure 6.** OFC constructed in University of Utah. Left: top section when burning NG; Right: a whole view

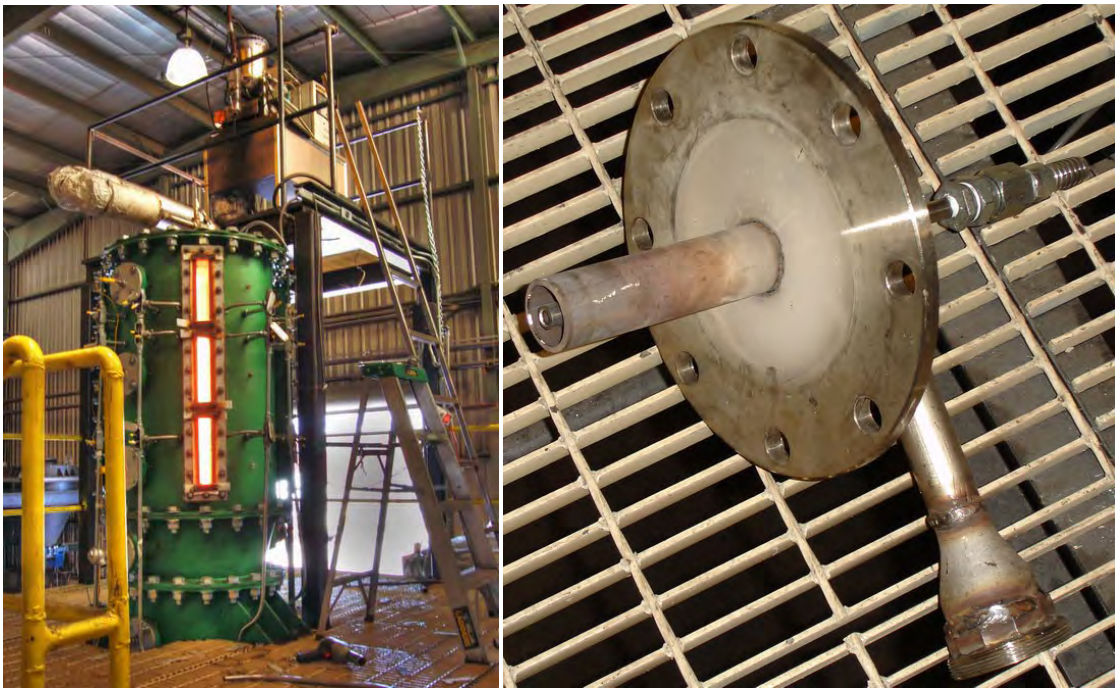

**Figure 7.** OFC constructed in University of Utah. Left: a picture of the furnace during the test; right: a burner applied

Figure 8 shows the designed temperature history of the OFC reactor.

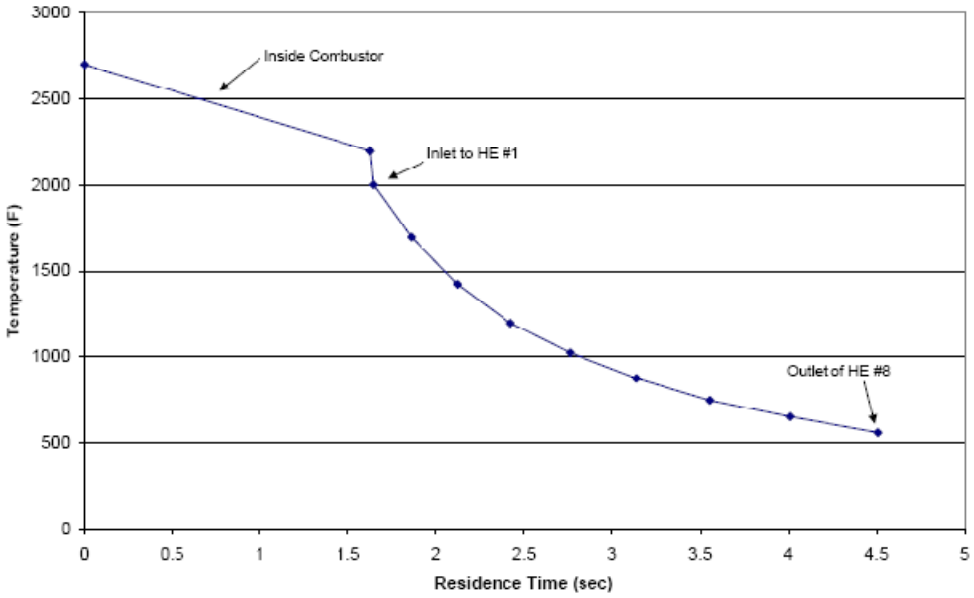


**Figure 8.** Designed OFC Time/Temperature History

A new K-Tron twin-screw loss-in-weight coal feeder with a modified eductor is installed to provide steady PC feeding.

The entire system is controlled by Opto22 commercial software. The data, including measurements of temperature, pressure, and gas components, etc. can be also acquired by the Opto22 instantaneously and automatically. Safety features prevent accidents or unnecessary damage. Figure 9 shows the control box where Opto22 modules and other automatic control modules installed. Figure 10 shows the interface of the Opto22 Software.

Gas species in the exhaust are monitored by two sets of gas analysers:

- $O_2$: Yokogawa - Zirconia oxygen analyser ZA8 (Qty: 1), Horiba - Paramagnetic oxygen analyser (Qty: 1)
- $CO_2$: California Analytical Instrument - Infrared gas analyzer: ZRH(Qty: 2), and ZRE (Qty: 1)
- $NO_x$: Thermal Environmental Instrument – Chemiluminescense $NO_x$ analyzer (Qty: 1), Horiba - Chemiluminescense $NO_x$ analyzer CLA-510SS (Qty: 1)

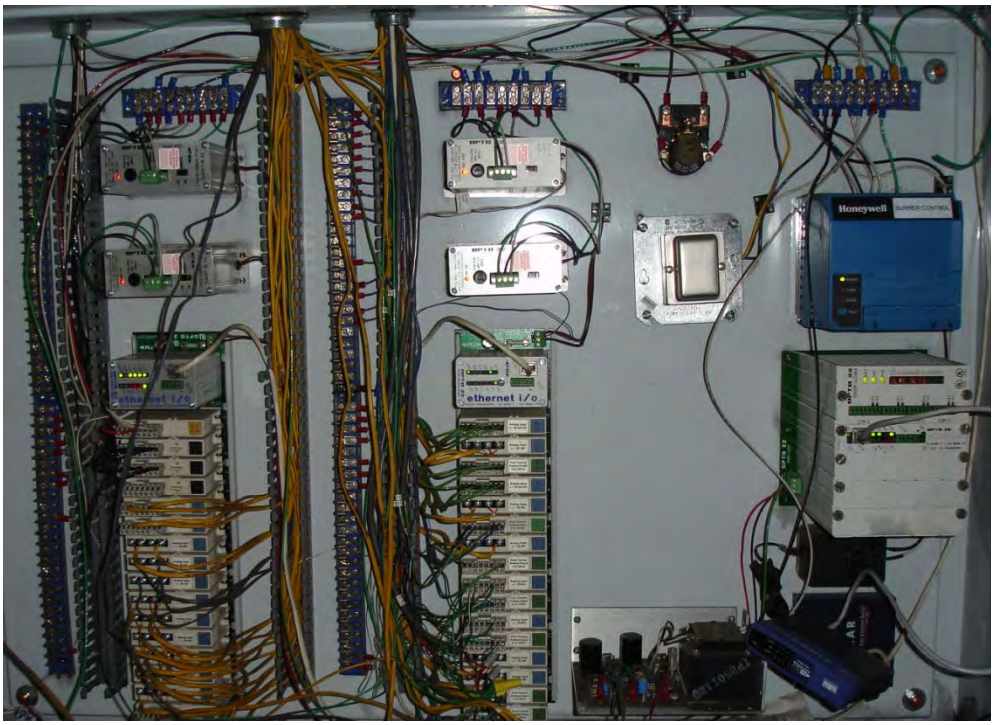

**Figure 9.** Opto22 Control box

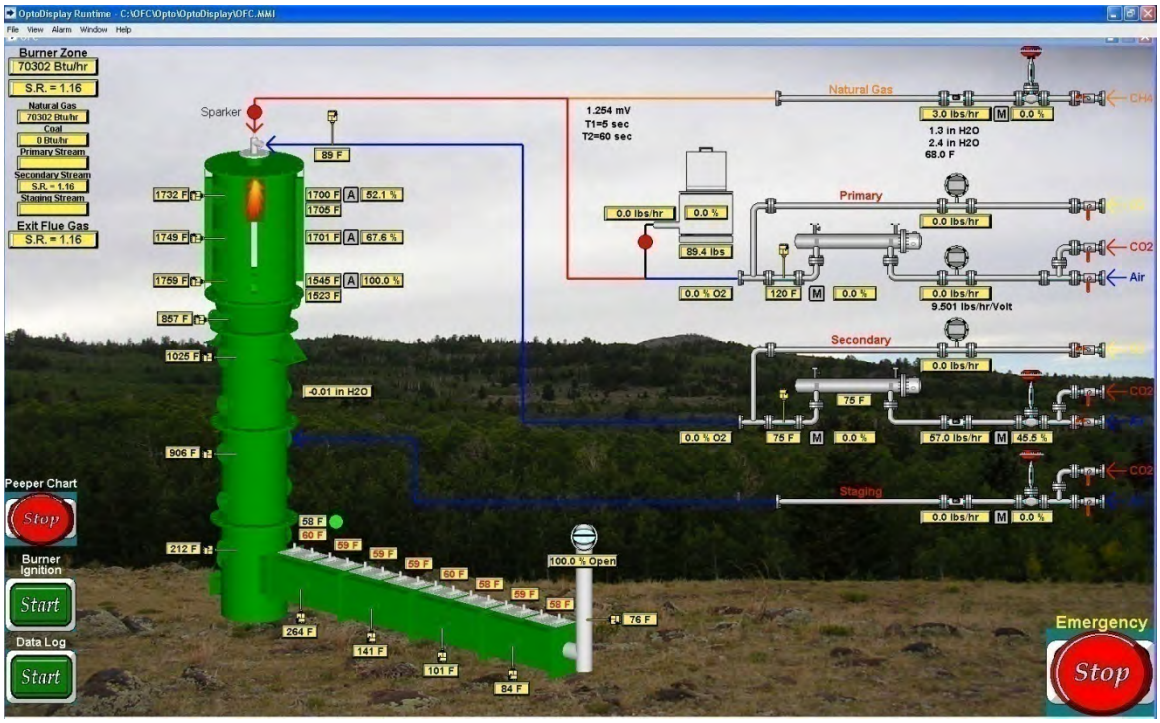


**Figure 10.** An Opto22 commercial software interface to control our oxy-coal combustor and to acquire the data

## Preliminary screening tests to validate the equipment and operating envelope under air firing conditions

The new oxy-coal combustor was characterized by gas combustion initially. Figure 11 shows a natural gas flame. Characteristic times for the reactor to reach steady state (Table 1), temperature profiles (Tables 2 and 3), and measured exhaust components, including $NO_x$ (Tables 4 and 5) have been obtained for various natural gas combustion conditions. These results can help to understand the characteristics of the reactor. The effect of variations in the wall temperature was also investigated (Table 3). Wall temperatures can be adjusted as an independent variable, using the electric heaters in the burner chamber wall, and comprises another degree of freedom for controlling the jet ignition process in the combustor.

**Figure 11.** A natural flame applied to characterize the combustor

**Table 1.** Time required to reach steady state under different natural gas firing rates

| Change of condition | | Time needed |
|---|---|---|
| **Depart from** | **Destination** | (hours) |
| Room temperature | 16.1 kW, SR=1.50 | 12 |
| 16.1 kW, SR=1.50 | 16.1 kW, SR=1.15 | 1 |
| Flame off, T = 783 K | 29.9 kW, SR=1.50 | 5 |
| 29.9 kW, SR=1.50 | 29.9 kW, SR=1.15 | 2 |
| 29.9 kW, SR=1.15 | 38.4 kW, SR=1.47 | 2 |
| 38.4 kW, SR=1.47 | 38.4 kW, SR=1.15 | 2 |
| 38.4 kW, SR=1.15 | 31.4 kW, SR=1.50 | 5 |
| 31.4 kW, SR=1.50 | 16.1 kW, SR=1.50 | 6 |

The results shown in Table 1 suggest that the design was successful, and the furnace materials performed well, such that unsteady thermal behavior did not last for unreasonably long times. Table 2 shows how wall and gas temperatures, with heaters off, depend on firing rate. Top, mid and bottom refer to 16.5 cm, 57.2 cm, and 97.8 cm, respectively, away from the burner face in the axial direction. They all represent the gas temperatures close to the wall. Table 3 shows effects of external heating at the furnace walls on the measured wall temperatures and measured gas temperatures, at a firing rate of 40.2 kW and a stoichiometric ratio (SR) of 1.15.

**Table 2.** Typical wall and gas temperatures at different firing rates.

| Firing rate ( kW ) | S.R. | Gas Temperature (K) | | | Wall Temperature (K) | | |
|---|---|---|---|---|---|---|---|
| | | top | middle | bottom | top | middle | bottom |
| 17.0 | 1.15 | 1001 | 1004 | 1005 | | | |
| 31.7 | 1.15 | 1170 | 1179 | 1209 | 1099/1100 | 1103 | 1013/983 |
| 41.3 | 1.13 | 1231 | 1240 | 1266 | 1169/1169 | 1172 | 1089/1066 |
| 17.6 | 1.50 | 963 | 964 | 985 | 907/909 | 905 | 790/753 |
| 31.7 | 1.50 | 1118 | 1125 | 1155 | 1051/1052 | 1051 | 950/928 |
| 33.1 | 1.50 | 1129 | 1136 | 1166 | 1061/1063 | 1061 | 955/928 |
| 41.6 | 1.72 | 1139 | 1145 | 1174 | 1071/1073 | 1067 | 959/963 |
| 31.7 | 0.89 | 1186 | 1195 | 1223 | 1125/1125 | 1129 | 1062/1027 |

**Table 3.** Effect of wall heating on measured gas and wall temperatures at a firing rate of 40.2 kW, and SR =1.15.

| Conditions | Gas Temperatures (K) | | | Wall Temperatures (K) | | |
|---|---|---|---|---|---|---|
| | top | middle | bottom | top | middle | bottom |
| Without wall heated | 1263 | 1274 | 1305 | 1185 | 1191 | 1114 |
| Wall heated to 1200 K | 1293 | 1306 | 1338 | 1214 | 1221 | 1198 |
| Wall heated to 1228 K | 1304 | 1318 | 1351 | 1228 | 1233 | 1226 |
| Wall heated to 1255 K | 1324 | 1337 | 1370 | 1257 | 1256 | 1255 |
| Wall heated to 1283 K | 1345 | 1357 | 1388 | 1285 | 1284 | 1284 |
| Wall heated to 1311 K | 1365 | 1376 | 1405 | 1311 | 1312 | 1312 |

**Table 4.** Exhaust components measured in the end of convection zone when burning natural gas.

| Components | 16.1 kW SR = 1.11 | 39.3 kW SR = 1.13 | 29.5 kW SR = 1.17 | 31.4 kW SR = 1.50 |
|---|---|---|---|---|
| O2 (v%) | 2.8 | 2.8 | 3.6 | 8.7 |
| CO2 (v%) | 9.8 | 9.9 | 9.4 | 6.5 |
| CO (ppm) | 7 | 1 | 1 | 1 |
| NO (ppm) | 65 | 71.7 | 70.4 | 43.8 |

**Table 5.** Calculated (from mass balance) values of $O_2$ and $CO_2$ when burning natural gas.

| Components | SR = 1.11 | SR = 1.13 | SR = 1.15 | SR = 1.17 | SR = 1.50 |
|---|---|---|---|---|---|
| O2 (v%) | 2.28 | 2.64 | 2.99 | 3.32 | 7.47 |
| CO2 (v%) | 10.59 | 10.39 | 10.19 | 10.00 | 7.64 |

Table 4 shows exhaust gas measurements at the end of convection zone when burning natural gas. NO emissions are similar to what might be expected for unpreheated gas flames and consist of only thermal NO (from $N_2$ fixation). Table 4 shows calculated $O_2$ and $CO_2$ values for the same conditions measured and reported in Table 5. The comparison suggests that there may be a very slight leak of air either into the system, or into the sampling line, due to the slightly negative operating pressure of the reactor.

These natural gas tests showed that data gleaned from this furnace had good reproducibility. The system reached a steady thermal state fairly rapidly, and the allowable load that kept wall temperatures below the electric heater danger point was determined. The reactor is well-designed and well-built. It is also well-insulated to prevent heat loss and well-sealed to prevent leaking.

The next step of preliminary tests involved firing PC with air or oxygen enhanced air. Temperature profiles, exhaust components, and flame stand-off distances were measured during the tests. According to the temperature history, in order to protect wall heaters, coal firing rate started at 4.3 lb/hr (1.95 kg/hr). Wall temperature plays an important role in PC ignition. Moreover, increasing wall temperatures also helps with the flame attachment. For the conditions of 1.95 kg/hr coal feeding rate, S.R. of 1.15, and wall temperatures fixed at 1366 K, the corresponding gas temperatures are (from top to bottom at the same locations as noted in Table 3): 1393 K, 1400 K, and 1405 K. The typical exhaust components (at air-fired condition) measured are: $O_2$ 2.88 v%, $CO_2$ 15.97 v%, CO 17 ppm, NO 363 ppm, and $NO_2$ 21 ppm. Comparing with the calculated results for exhaust components based on measured feed rates ($O_2$ 2.78 v%, $CO_2$ 16.27 v%), the mass balance is enclosed.

Systematic experimental tests were performed to understand the effect of partial pressure of oxygen ($P_{O2}$) in secondary stream on coal jet ignition under an oxy-enhanced environment. During the tests the following parameters were fixed:

- S.R. = 1.15 = 0.15 $_{\text{primary air}}$ + 1.00 $_{\text{secondary air}}$
- Coal feeding rate = 1.95 kg/hr
- Wall temperature = 1361 K
- Secondary stream preheat temperature = 589 K

The following parameters are varied: velocities of both primary air and secondary air, especially the ratios of primary stream velocity ($v_p$) vs. secondary air velocity ($v_s$) to test the burner design.

During the tests, gas species in the exhaust are monitored to ensure the mass balance of the reaction. $NO_x$, as an indicator of flame attachment or mixing process, is measured to help monitor the stability of the flame. For instance, Figure 12 shows how $NO_x$ concentration drops and rises, when flame turns from detached to attached, then detached again.

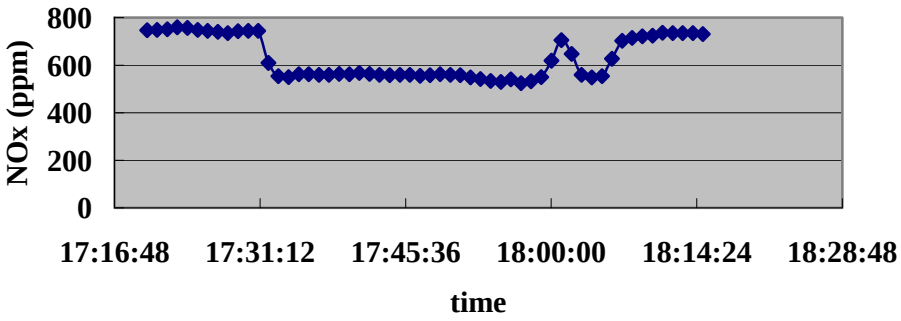


**Figure 12.** $NO_x$ level, an indicator of flame detachment/attachment
($v_p = v_s$ = 9.14 m/s, oxy-enriched case, primary stream is pure air, secondary stream is a mixture of $O_2/N_2$, in which $P_{O2}$ is 30%, 3% excessive $O_2$ in exhaust)

1) Under conditions of $v_p / v_s = 1$.

Figure 13 and 14 show how flame attachment/detachment changes when varying PO2 in secondary stream under oxy-enriched cases. The difference between Figure 13 and Figure 14 is the velocity. In Figure 13, both primary jet and secondary jet have higher velocities and higher momentums compared with Figure 14 cases. Higher momentum leads to better turbulent mixing and shorter flame length. Yet lower momentum generates longer but less luminous flames, which are difficult to measure with the CMOS camera, which relies on the luminosity of the flame.

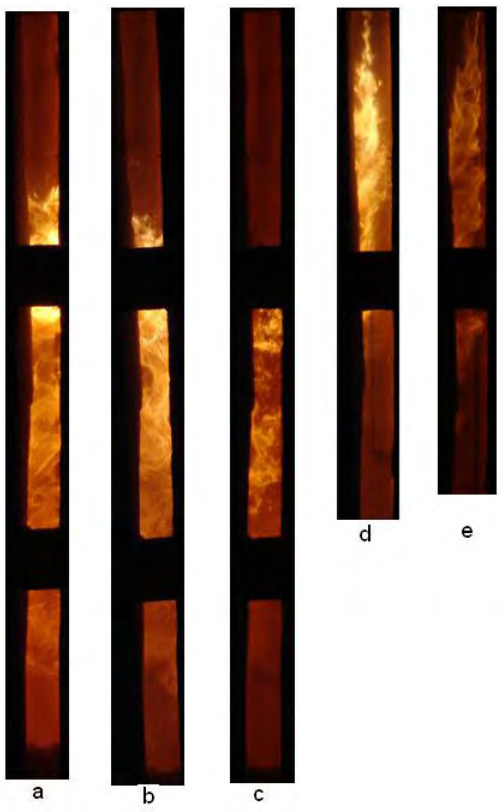


**Figure 13.** Different flame shape under different $P_{O2}$ in secondary stream when $v_p = v_s = 9.14$ m/s. (a – 30% $O_2$ in secondary stream; b – 24% $O_2$ in secondary stream; c – 21% $O_2$ in secondary stream; d - 30% $O_2$ in secondary stream; e – 21% $O_2$ in secondary stream) Primary streams are all air and secondary streams are mixtures of $O_2$ and $N_2$.

2) Under conditions of $v_p / v_s = 0.5$ ($v_p = 4.57$ m/s; $v_s = 9.14$ m/s).

Detached flames are always observed when primary jet momentum is higher than secondary jet momentum, it is difficult for secondary oxidant to diffuse to the primary coal jet to help ignition in the near-burner zone. Therefore, the coal jet must travel a longer time to be well mixed with the secondary oxidant.

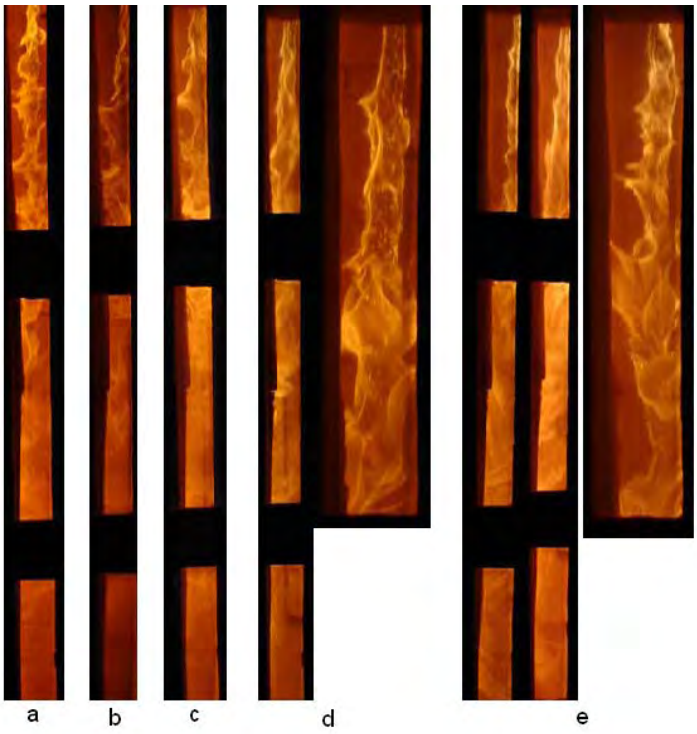


**Figure 14**. Different flame shape under different PO2 in secondary stream when $v_p = v_s = 4.57$ m/s. (a – 21% $O_2$ in secondary stream; b – 24% $O_2$ in secondary stream; c – 26% $O_2$ in secondary stream; d - 28% $O_2$ in secondary stream; e – 30% O2 in secondary stream) Primary streams are all air and secondary streams are mixtures of $O_2$ and $N_2$.

3) Under conditions of $v_p / v_s = 2$ ($v_p = 9.14$ m/s; $v_s = 4.57$ m/s).

More attached flames are observed during the tests when $P_{O2}$ in the secondary jet is increased. Due to the momentum difference of the primary stream and the secondary stream, better mixing, when secondary stream has a higher momentum, is achieved by the shear stress and turbulence. Therefore flame stability is enhanced and the flame is shortened.

Compared with case 1 and case 2, case 3 produces flames, which are most easily measured with the optical technique.

At the end of this research phase, the coal feeding rate was adjusted to 4.8 kg/hr to increase the thermal load to reach steady state more quickly. Thus shortening flame in the range of optical windows becomes a challenge, which requires a new burner design.

The new burner design must help keep the flame in the range of optical measurement and help stabilize the flame with a optimized velocity ratio under 4.8 kg/hr's coal feeding rate.

The new operating parameters at air-firing condition are:

$v_p = 6.2$ m/s; $v_s = 32.9$ m/s, secondary stream preheat temperature = 489 K, $v_p / v_s = 1 / 5.4$, coal feeding rate = 4.8 kg/hr, S.R. =1.15, inside secondary air sleeve, Re = 13,300.

Figure 15 and 16 show oxy-enriched flames using the above burner design. $PO_2$ in primary stream is kept as 21% (pure air), while $PO_2$ in secondary stream is elevated by injecting pure oxygen to air, namely in these two figures, 28% and 30%.

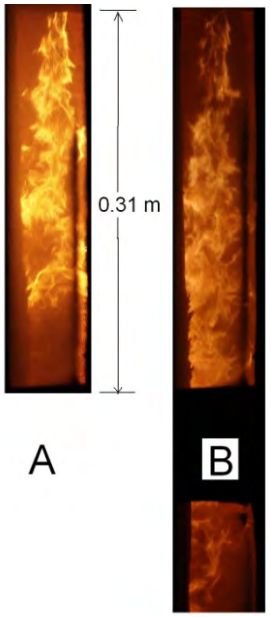


**Figure 15.** Flame structure and flame length: A – 28% $O_2$ in secondary stream; B – 32% $O_2$ in secondary stream

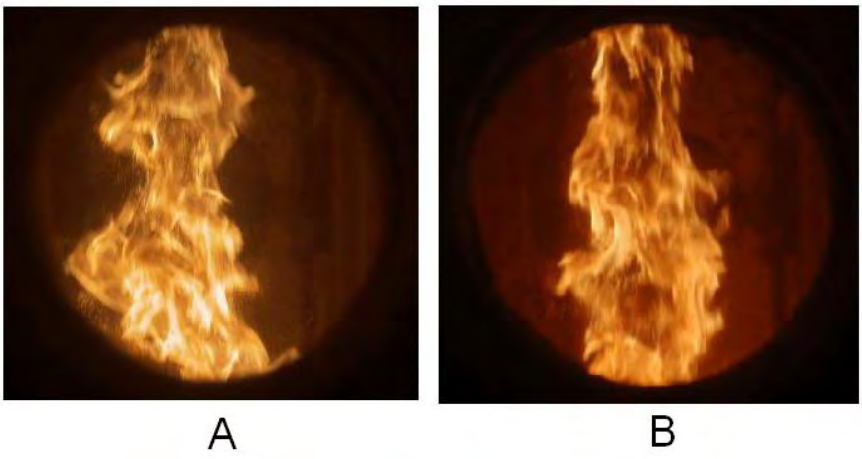


**Figure 16.** Flame structure (near-burner view): A – 28% O2 in secondary stream; B – 32% O2 in secondary stream.

## Incorporation of $O_2$ supply and once through $CO_2$ to allow for oxy-firing conditions

The purpose of building two tanks ($O_2$ and $CO_2$) is to provide a once-though $O_2/CO_2$ mixture for the OFC system. Figure 17 and 18 show the $O_2$ tank and $CO_2$ tank constructed, respectively, with

the help of Praxair Inc. As shown in figure 22, a large vaporizer was constructed to vaporize the liquid oxygen. To accomplish this research phase, two years of effort and much professional staff time were required.

**Figure 17.** Praxair $O_2$ tank (capacity: 6,000 gallon)


**Figure 18.** Praxair $CO_2$ tank 3 (capacity: 400 gallon)

## Establishment of steady coal feeding conditions through coal feeder modifications

Coal feeding is a critical factor in this research. Unsteady feeding can cause the following problems:

1) Coal feeding is not uniform.
2) The flame fluctuates heavily because of the poor feeding, instead of the nature of turbulent coal flame itself.
3) The gas components in exhaust vary due to the coal feed pulsing. PC is difficult to fully combust. Oxygen concentration measured in the exhaust does not agree with the calculated one.
4) Flame stability studies cannot be carried on due to the large error introduced by the unsteady coal feeding.

To ensure a steady PC feeding, numerous technical details are summarized here:

1) Any large pressure drop in the primary coal jet line downstream of coal feeder should be avoided.
2) Vibration of eductor can help improve the coal feeding. However it is not viable when the eductor is attached to a loss-in-weight coal feeder because vibration is harmful for the loss-in-weight function, which monitors the mass loss on the scale and adjust the feeding instantaneously and automatically.
3) The selection of the coal feeder should match its optimum working range. A PC feeder works best at 40% to 60% motor's range. In general, 1000 rpm is the best choice for uniform feeding. However higher rpms can cause PC stick in the feeder outlet. Therefore 1000 rpm is the optimal for motor speed.
4) A twin-screw loss-in-weight feeder (Figure 19) works better than a single-screw non-loss-in-weight feeder.
5) An agitator installed in the hopper can prevent bridging when feeding coal.
6) An optimized design of an eductor.


**Figure 19.** K-Tron loss-in-w eight twin-screw coal feeder applied in oxy-coal combustion lab, University of Utah

The unique design of the eductor includes the following features:

1) A purging loop was installed, as shown in Figure 20. This design can introduce a local high velocity swirl inside the eductor, removing PC from the augers at the exit.
2) A mesh was set up in the exit of the twin screws as shown in Figure 21. The mesh can break up the PC clumps in the feeder exit, which significantly improves the feeding and reduces the pulsing.

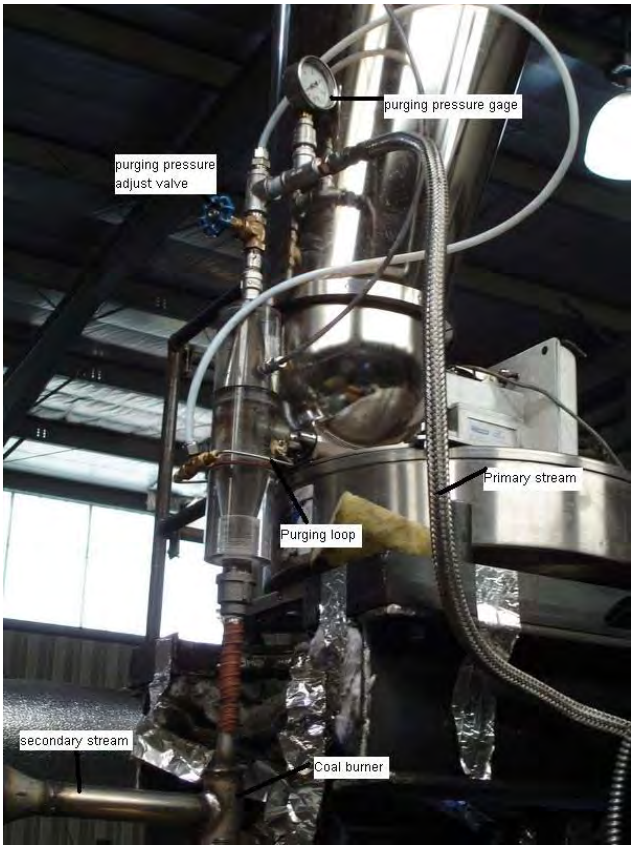


**Figure 20**. An eductor design schematic in oxy-coal combustion lab, University of Utah

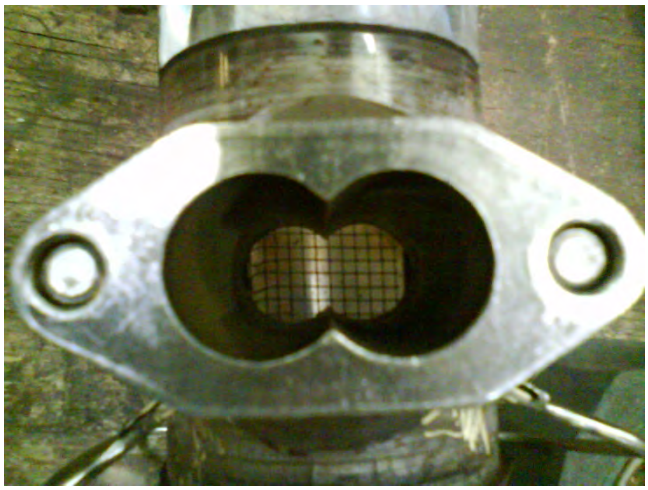

**Figure 21.** A mesh installed inside the eductor at the exit of feeder screws

Four methods have been used to verify the steady feeding behavior:

1) The coal jet and the flame were visually inspected to ensure the steady feeding during the test.
2) Total 500 continuous pictures were collected by the Epix CMOS camera (SV5C10) in approximately 20 seconds using the frequency of 24 fps (frame per second). Although the

fluctuating nature of the flame is observed in the pictures, the relatively steady flame shape was also captured in each picture, which indicates steady feeding behavior.

3) $O_2$, $CO_2$, and $NO_x$ level in the exhaust were all monitored during the test. Mass balance was obtained. The $O_2$ level matched the results of theoretical calculation and was always steady under different running conditions.
4) Loss-on-ignition (LOI) ash samples were collected during the combustion, and a high conversion rate of the carbon is always observed, which shows full combustion of coal particles, and which will not be expected during the unsteady feeding process.

## Development of photo-imaging technique to allow quantification of flame stability

A special CMOS sensor based camera, which is more sensitive to the near infrared wavelength (response: 1.4 V/lux-sec (550nm)), captures Type 0 axial turbulent diffusion flame shape for statistical studies of stand-off distance at different operational parameters, such as systematic variations of partial oxygen pressure in both transport and secondary oxidant stream. Statistical analysis is used to understand the effect of oxygen partial pressure in both the transport and the secondary stream on coal jet ignition and flame stability. Ultimately the statistics help to generate PDFs, which can be used to evaluate the experiment precision and to validate simulation models.

Because inserting a probe in the near-burner zone influences Type 0 PC flame and coal jet ignition, detailed 2D temperature profiles and gas component concentrations are difficult to measure. Therefore, to quantify the flame stability, novel optical measurements and an image processing technique have been developed.

The image processing work began with comparing XCAP-standard commercial software package of EPIX Inc. and MatLab code developed in house. Figure 22 shows the comparison of the results from the different codes. All the pictures have been rotated 90 degrees from the real down-fired orientation (left represents the top, while right represents the bottom). The top picture is over exposed on purpose to test the codes under extreme conditions. The middle picture shows the result of the first version MatLab code developed by oxy-coal combustion group in University of Utah. The bottom one shows the result by using Epix XCAP-standard software from the camera manufacture. The results show that even under extreme conditions, both the MatLab code and XCAP-standard commercial software can quantify the flame envelope reasonably well. Due to the unfriendly interface and limited ability to process large image sets of XCAP-standard, the University of Utah team developed their own MatLab code.

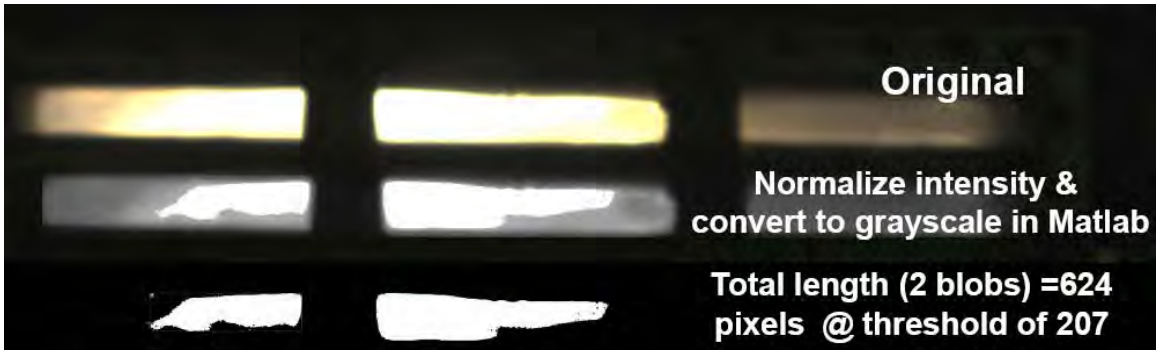


**Figure 22.** Results of image processing using MatLab and XCAP.

Table 6 shows an example of flame length measurement of an attached oxy-enriched flame, with $P_{O2}$ in secondary stream = 0.28. Table 7 shows an example of stand-off distance and flame length measurements of a detached air-fired flame. In both tables, length means the luminous zone length, while STD represents standard deviation of the measurements. Threshold values range between 0 and 1, and these were manually selected.

**Table 6.** An example of flame length measurement of an attached oxy-enriched flame

| Date | Length(in) | Length STD(in) | Threshold | Aperture |
|---|---|---|---|---|
| 29-Oct | 23.39 | 2.36 | 0.45 | 8 |
| 29-Oct | 26.49 | 2.77 | 0.80 | 6 |
| 31-Oct | 24.55 | 4.07 | 0.28 | 8 |
| 31-Oct | 24.80 | 4.18 | 0.80 | 6 |
| 3-Nov | 20.28 | 2.61 | 0.42 | 8 |
| 4-Nov | 26.33 | 5.64 | 0.50 | 8 |
| Average | 24.30 | 2.29 | | |

**Table 7.** An example of flame length measurements of a detached air-fired flame

| Length (in) | Length STD(in) | Stand-off Distance (in) | Stand-off distance STD(in) | Threshold | Aperture |
|---|---|---|---|---|---|
| 14.66 | 5.21 | 20.28 | 3.08 | 0.26 | 6 |
| 11.52 | 5.07 | 24.00 | 5.02 | 0.56 | 4 |
| 7.16 | 4.73 | 26.68 | 5.77 | 0.40 | 6 |
| 13.98 | 10.04 | 19.19 | 5.04 | 0.40 | 4 |
| 7.50 | 10.05 | 24.59 | 5.04 | 0.75 | 4 |
| 8.83 | 3.11 | 24.04 | 4.54 | 0.73 | 4 |

A tentative conclusion can be drawn from the results of Table 6 and 7: image processing results of flame length and stand-off distance depend on selection of threshold value to quantify the flame envelope. In order to reduce the effect of manual threshold selection, the University of Utah team updated the image processing code to employ the Sobel (maximum gradient) method to detect the flame edge, which is less subjective. Instead of manually selecting the threshold to convert the grayscale image to the black and white image, the edges of the flame are detected using the Sobel method in Matlab (Figure 23 c). This method returns edges at those points where the gradient of the grayscale intensity is at a maximum. The above methodology is shown in Figure 23.

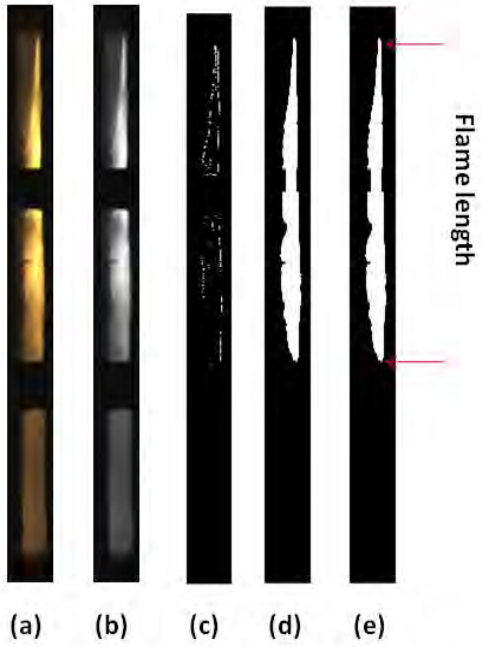


**Figure 23**. Procedures of flame image processing: (a) original image, (b) image converted to grayscale, (c) edge detection using the Sobel method, (d) image converted to black and white using the threshold calculated from the Sobel method, (e) measurement of image statistics: stand-off distance (if any), flame length, and intensity within flame envelope.

During the PC ignition process, the sequences of images of flames are taken by a CMOS sensor based camera with at least 24 fps. Then all the images are analyzed by the MatLab code. This code can automatically analyze the following parameters:

a) average intensity of the whole image
b) average intensity within the flame envelope
c) visible flame length(luminous zone)
d) mean stand-off distance
e) stand-off distance in the centerline
f) total area of the flame
g) number of blobs
h) flame width at different locations

## Screening tests of photo-imagining techniques with a view to determining effect of secondary $PO_2$ on flame length and flame luminosity

Air-fired cases, oxy-enriched cases and oxy-fired cases were tested and analyzed. The purpose is to compare the luminosity, $NO_x$ formation, and flame stability under $O_2/N_2$ environment and $O_2/CO_2$ environment by varying the partial pressure of $O_2$ in secondary stream to match the same adiabatic flame temperature. Matching adiabatic flame temperature is one of the two criteria to compare air-fired combustion and oxy-fired combustion. The other one is to match the heat transfer flux, which is difficult at this point.

The burner design parameters are:

- primary sleeve: O.D. = 21.34 mm, $\delta$ = 2.769 mm;
- secondary sleeve: I.D. = 42.16 mm, $\delta$ = 3.556 mm;
- $v_p$ is always fixed as 6.16 m/s, $v_s$ to $v_p$ ratio varies from 2.5 to 5.4.

The fixed parameters are: Overall S.R. = 1.15 = 0.11 (primary) + 1.04 (secondary); $T_{primary\ stream}$ = room temperature, $T_{secondary\ stream}$ = 561 K, $T_{wall}$ = 1255 K, Primary $P_{O2}$ = 0.21. Coal feeding rate = 10.7 lb/hr = 4.8 kg/hr, Coal type: Utah bituminous (Ultimate(wt%, daf): C 77.75%, H 5.03%, N 1.44%, S 0.45%, O 15.33%; Proximate: Moisture 3.03%, Volatile Matter 38.81%, Fixed Carbon 46.44%, Ash 11.72%; high heating value (HHV) = 11731 BTU/hr = 12377 kJ/hr). The testing matrix is shown in Table 8.

**Table 8.** cases selected for the comparison between $O_2/N_2$ flame and $O_2/CO_2$ flame

| $O_2/N_2$ mixture | | | Case No. | $O_2/CO_2$ mixture | | |
|---|---|---|---|---|---|---|
| $T_{adb}$ (K) | secondary $P_{O2}$ | overall $P_{O2}$ | | $T_{adb}$ (K) | secondary $P_{O2}$ | overall $P_{O2}$ |
| 2334 | 0.209 | 0.209 | I | 2289 | 0.330 | 0.313 |
| 2434 | 0.240 | 0.236 | II | 2389 | 0.380 | 0.352 |
| 2488 | 0.260 | 0.254 | III | 2447 | 0.415 | 0.379 |
| 2528 | 0.280 | 0.270 | IV | 2490 | 0.445 | 0.402 |

Photo images captured from experiments comparing $O_2/N_2$ environments and $O_2/CO_2$ environments can be found in Figure 24. In group I, both air-fired flames and oxy-fired flames are very unstable and hard to capture a scene of ignition, due to the fluctuation of flame itself instead of the feeding.

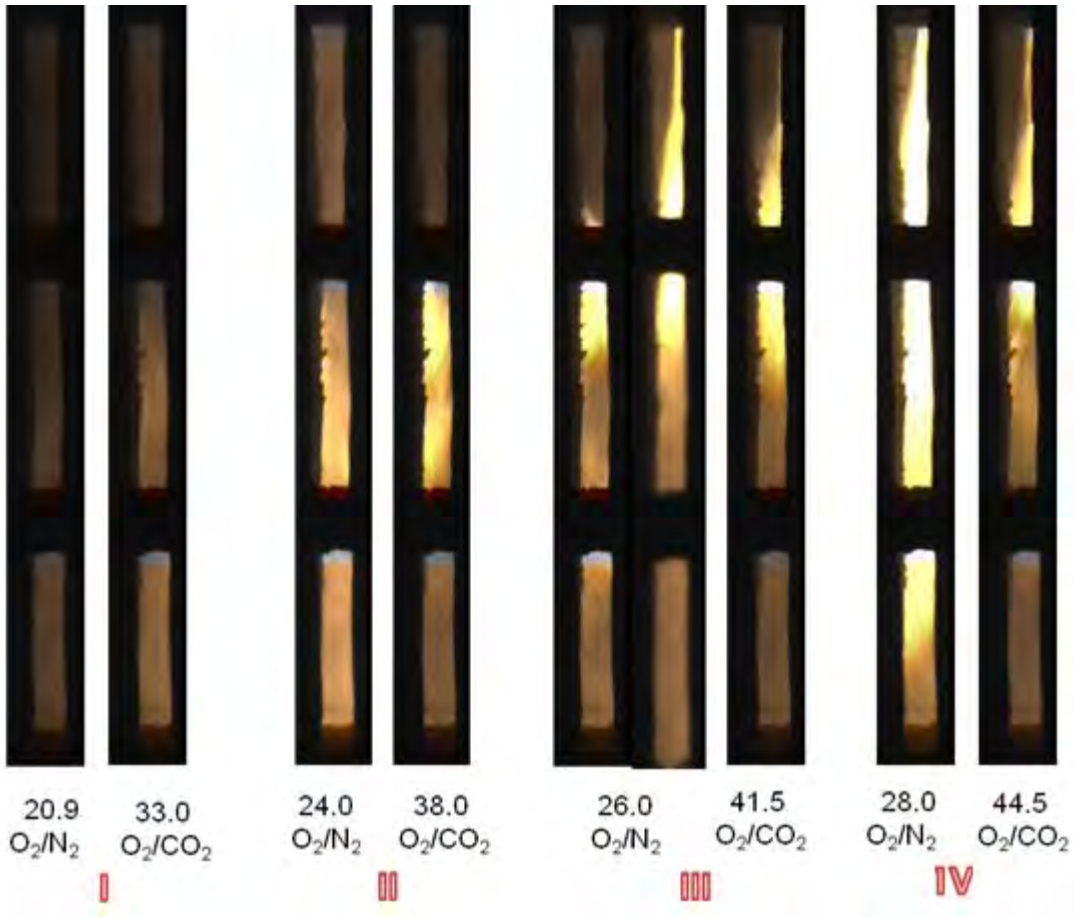


**Figure 24.** Photo images captured from experiments showing the flame attachments/detachments

Figure 25 shows the $NO_x$ formation, when varying $P_{O2}$ in the secondary stream. $NO_x$ was measured at the exit of the exhaust close to the entrance of the stack. The top curve represents $O_2/N_2$ flame (both air flame and oxygen enriched flame), which shows the tendency that increasing $P_{O2}$ leads to a higher $NO_x$ formation due to higher temperature. Once the flame becomes attached to the burner, when $P_{O2}$ in the secondary stream is higher than 25.4% in these tests, $NO_x$ formation is slightly lower, due to the different mixing pattern and fluid mechanics caused by the flame attachment. However, the bottom $NO_x$ formation curve shows that under oxy-coal combustion conditions, $NO_x$ is not influenced by $P_{O2}$ or flame temperature that much because theoretically there is no thermal $NO_x$ generated without the presence of $N_2$. Almost all the $NO_x$ comes from the nitrogen compounds in the fuel under oxy-coal combustions.

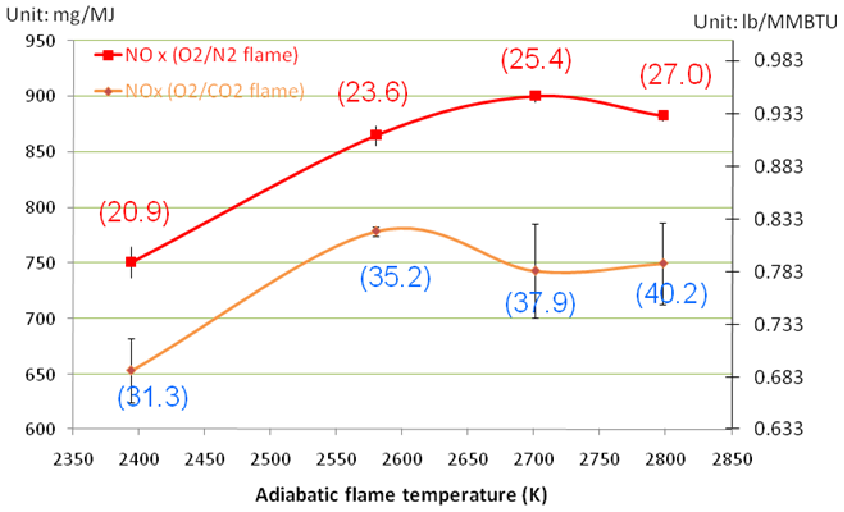


**Figure 25.** Comparison of $NO_x$ formation under $O_2/N_2$ environment and $O_2/CO_2$ environment (red and blue numbers show $P_{O2}$ in percentage in secondary stream of each case, $P_{O2}$ in transport stream is always 20.9%)

Figure 26 shows the comparison of the average flame luminosity over the entire image between an $O_2/CO_2$ flame and an $O_2/N_2$ flame. Flame luminosity, often related to soot formation in the flame, is of interest if one assumes flame luminosity is proportional to the flame intensity. Consequently when matching adiabatic flame temperature, an $O_2/CO_2$ flame tends to be more luminous than an $O_2/N_2$ flame, which is contrary to the experimental observations. To improve the methodology, a new concept of "average intensity within a flame envelope" has been developed. Figure 27 and 28 show the histograms of average intensity within the flame envelope for an $O_2/N_2$ flame and an $O_2/CO_2$ flame. The results show that for case IV in Table 8, when an $O_2/N_2$ flame and an $O_2/CO_2$ flame with an approximately matched adiabatic flame temperature are both attached, an oxy-coal flame is less luminous than an oxygen-enriched flame. This result may indicate that under oxy-coal combustion conditions, less soot is expected.

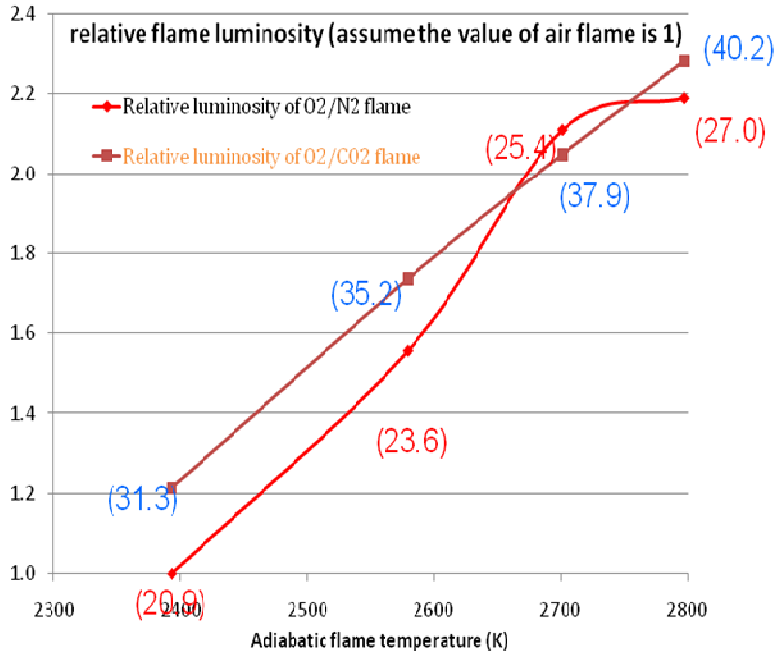


**Figure 26.** Comparison of relative flame luminosity between $O_2/N_2$ environment and $O_2/CO_2$ environment

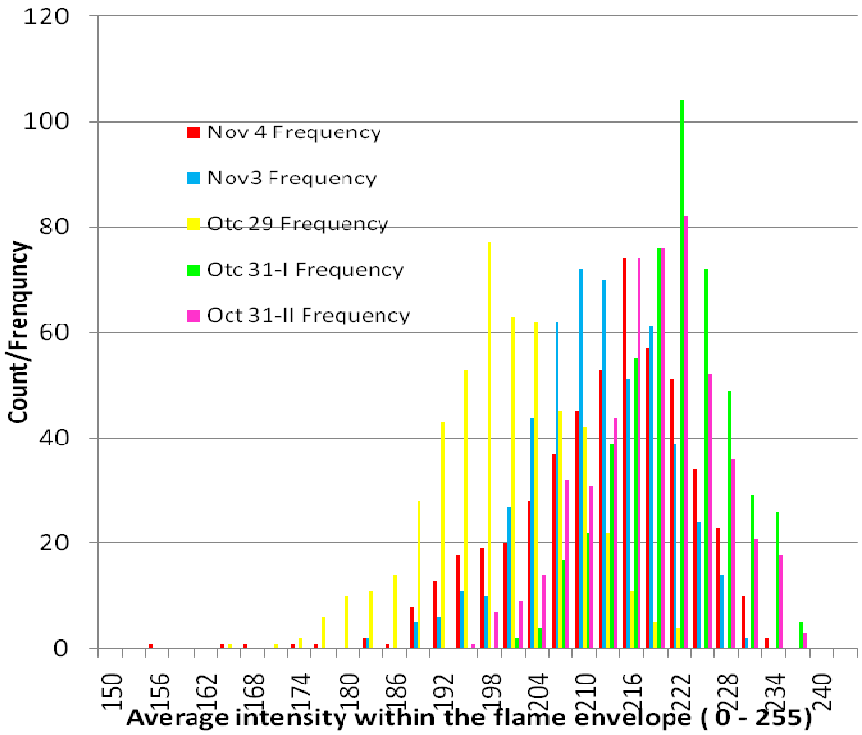


**Figure 27.** Histograms of average intensity within flame envelope for an oxygen enriched ($O_2/N_2$) case IV(see Table 1) attached flame

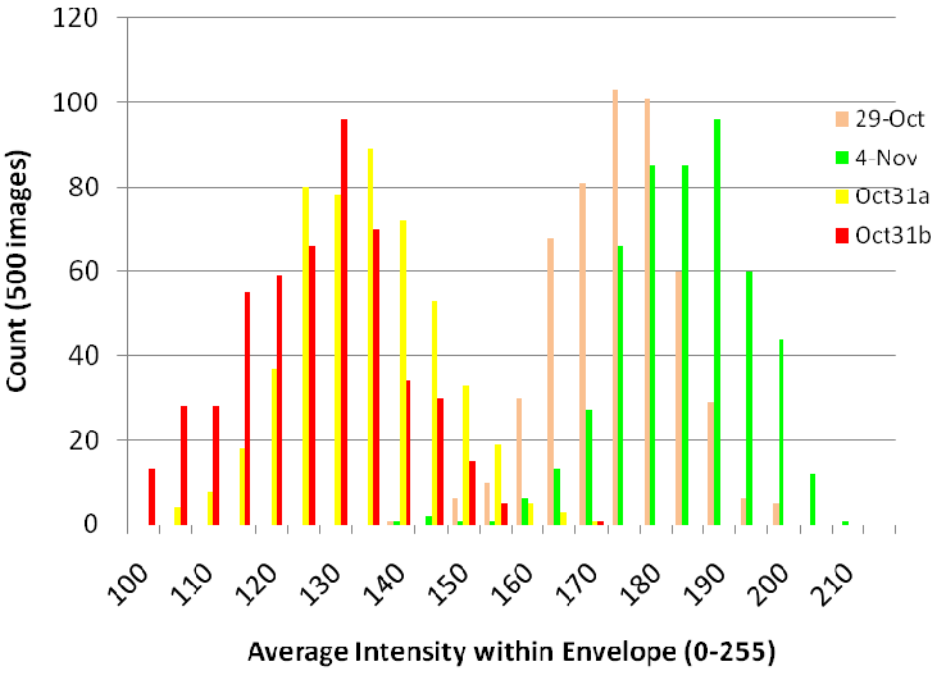


**Figure 28.** Histograms of average intensity within flame envelope for an oxy-coal ($O_2/CO_2$) case IV (see Table 1) attached flame

Figure 29 shows how $P_{O2}$ in the secondary stream influences flame stability (attachment/detachment) and visible flame length (luminous zone) under oxy-coal combustion conditions. The primary stream partial pressure of $O_2$ is always kept as 20.9%. Increasing $P_{O2}$ in secondary stream helped the flame become attached. It also reduced the stand-off distance, which also means the coal particles are ignited more quickly. The total flame length is defined here as the sum of luminous zone length and stand-off distance. The results may also suggest that when a flame is attached, $P_{O2}$ may have minor effects on the flame length; however changing burner operation parameters, such as velocity and momentum, can also influence the flame length.

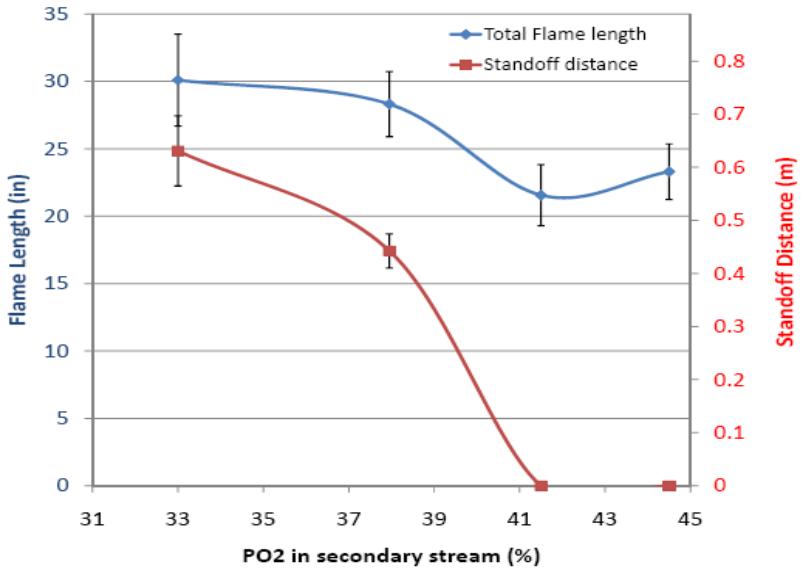


**Figure 29.** Flame length vs $P_{O2}$ in secondary stream under oxy-coal combustion conditions

## Final studies on effects of $P_{O2}$ in the primary coal jet on flame stand-off distance, and other data for simulation studies

### a) Statistical studies

Under more realistic operating condition, experimental data are often noisy due to operator inconsistency, limitations in instrumentation accuracy, coal feeding rates, etc. Because of the turbulent nature of flame in addition, it is always fluctuating. Therefore two questions need to be addressed:

1) How to quantify the accuracy/error of the experiments?
2) How to quantify the reproducibility of the experiments?

Figure 29 expresses average values with error bars. With a goal of providing validation data for large eddy simulation (LES) model development, the precision and accuracy of the OFC experiments are critical. Statistical analyses were performed to begin to quantify the accuracy, the error and the reproducibility of the experiments. For instance, Figure 30 shows the histograms of visible flame length of oxy-coal case IV (see Table 8, an attached flame). Ultimately the histograms will be used to generate PDFs, which will be used for LES model validation to quantify the model precision. Figure 30 also shows a good repeatability of the experiments.

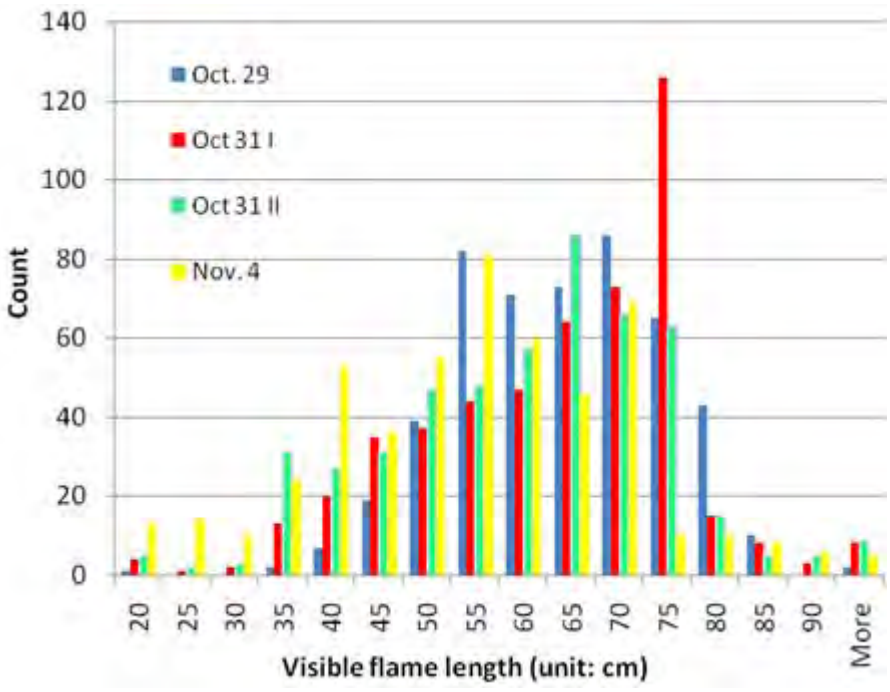


**Figure 30.** Histograms of flame length of oxy-coal case IV (see Table 1). Flames are attached.

Table 9 compares the mean stand-off distances of two replicates for the same conditions on different days. The t-statistic is 1.077, less than 1.96, indicating that the two means are not significantly different at a 95% confidence level.

**Table 9**. T-statistic comparison of two days for primary $P_{O2}$ = 14.4%, oxy-coal case IV (see Table 8), secondary preheat temperature 489 K.

| Date | May 14th | May 15th |
|---|---|---|
| Mean | 24.4826 | 23.81816 |
| Median | 26 | 23.22373 |
| Mode | 31 | 26 |
| Standard Deviation | 4.476499 | 5.214789 |
| Sample Variance | 20.03904 | 27.19403 |
| Kurtosis | -1.26547 | 0.0208 |
| Skewness | -0.12994 | -0.48414 |
| Range | 18.59492 | 30.77966 |
| Minimum | 12.40508 | 0.220339 |
| Maximum | 31 | 31 |
| Count | 3000 | 3000 |
| Confidence (95.0%) | 0.160251 | 0.186681 |
| | 0.664435 | |
| | 0.616733 | |
| t-statistic | 1.077347 | |

## b) Determining sample size

To determine how representative the samples were, two long data sets were collected for both an attached and a detached oxy-fired flame. The visible flame length and flame intensity were statistically analyzed, for the first 500 images, 1000 images, 2000 images, 3000 images, 5000 images, 8000 images and 11,000 images.

For attached flames, the results are shown in Figure 31 and 32. All data sets are normalized to 500-image sample size. Even for 500 images, the frequency polygons yield the same trend and values compared with an 11,000-images sample size. The conclusion was 3000 images are adequate. The reason that the averaged intensity within the flame envelope keeps decreasing with the long data set is due to the ash accumulating on the quartz windows. The two narrow peaks located beside the main peak in the flame length measurement, represent the intervals between quartz windows. According to the code, if a flame edge is located between the intervals of quartz windows, it is assumed to exist in the middle of the intervals.

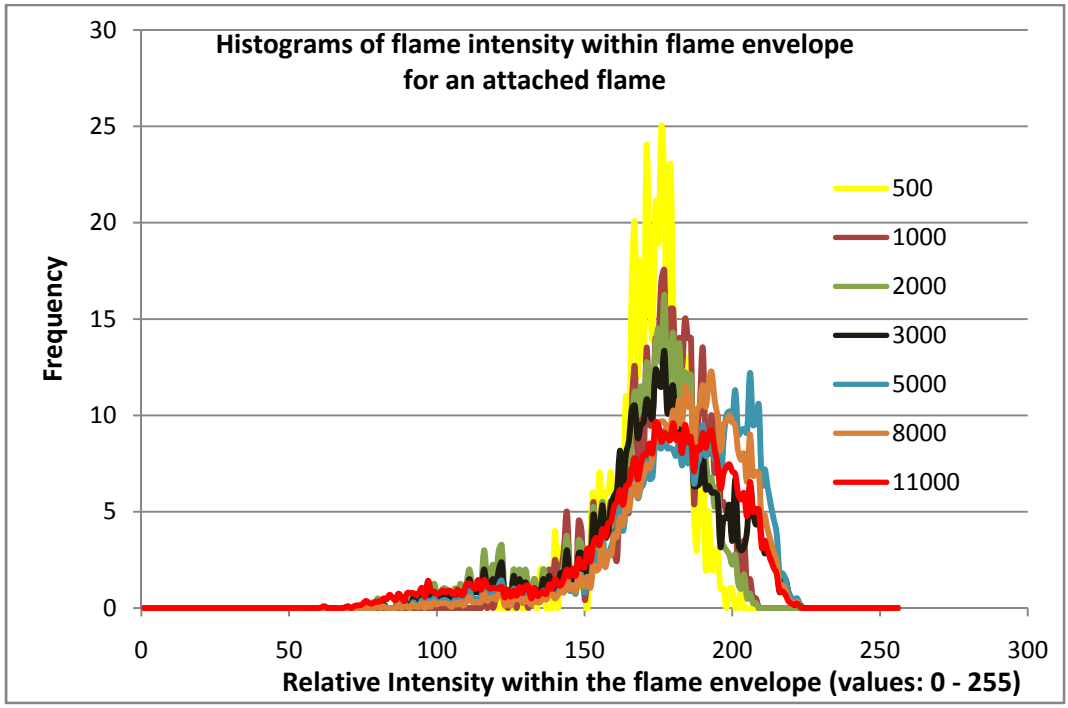


**Figure 31.** Histograms of flame intensity within flame envelope for an attached flame (long data set)

For detached flames, the stand-off distance is of interest. Figure 32 shows the histograms of a long data set of detached flames (similar to oxy-fired case IV in Table 8, the same overall $P_{O2}$, but $P_{O2}$ in primary stream is 0). It shows that from the first 500 images to the first 1000, 3000, 5000, 10000, or 11000 images, the histograms yield the same trend. Statistically, the reproducibility of the experiments is good. A total of 3000 is chosen as the sample size. The long

bars in the right of Figure 33 show the counts of flames starting in the interval between the top and the middle quartz windows, accounting for approximately 40% of the images.

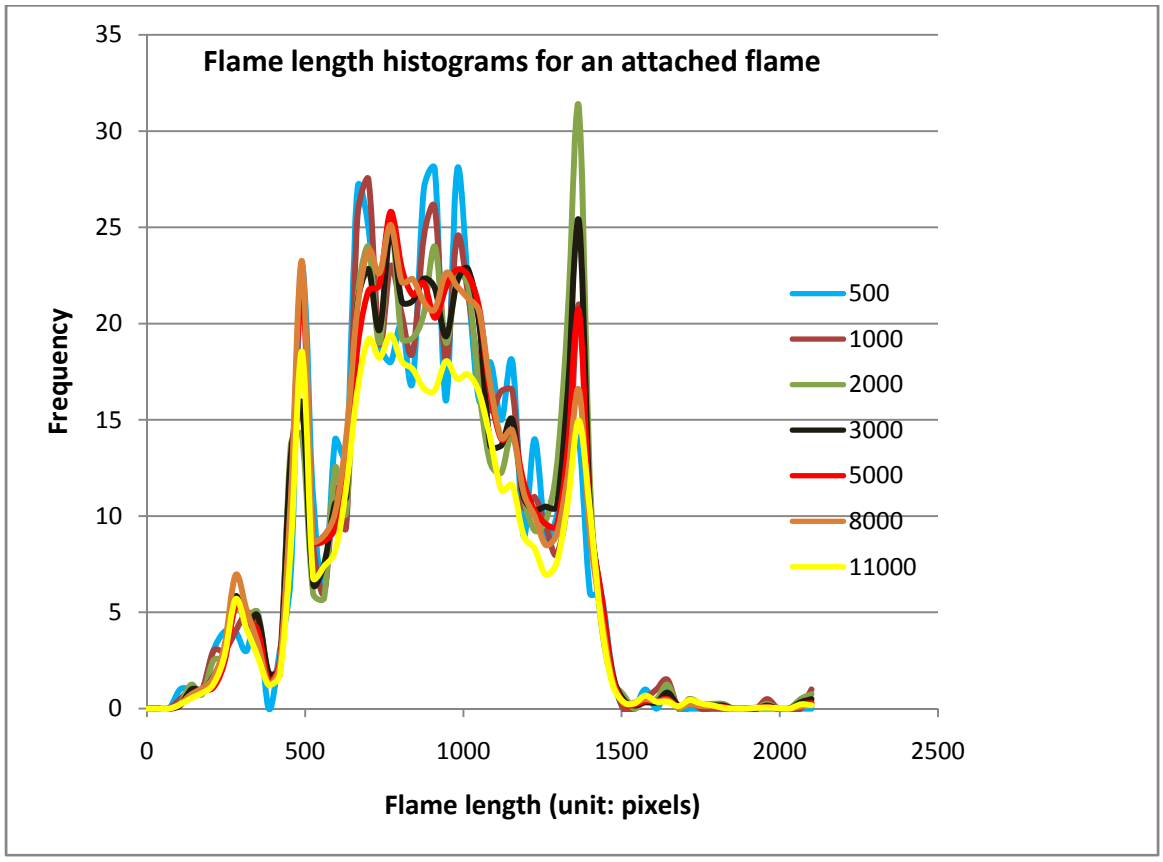


**Figure 32.** Histograms of flame length for an attached flame (long data set)

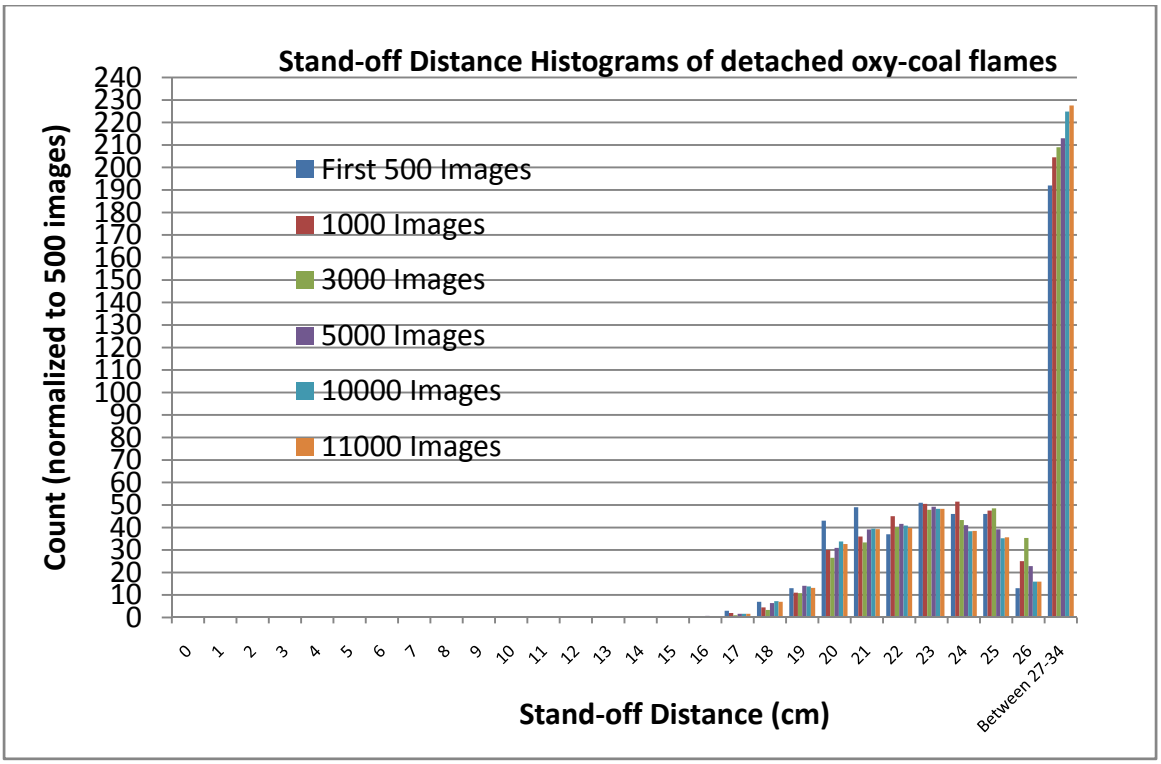


**Figure 33.** Histograms of Lift-off (stand-off) distance of a detached oxy-coal flame (long data set)

### c) The effect of $P_{O2}$ in transport stream on flame stability

Figure 34 shows the effect of $P_{O2}$ in the transport (primary) stream on the flame stability, quantified by the stand-off distance. With overall $P_{O2}$, primary stream velocity, and secondary stream velocity, total stoichiometric ratio, wall temperature, preheat temperature, coal feeding rate, and camera setting fixed, increasing $P_{O2}$ in the transport stream from 0 to 20.9%, can change flame stability. Stand-off distance decreased when $P_{O2}$ in transport stream increased. The bottom pictures show flame structure in the near-burner zone. The effect of $P_{O2}$ in the transport stream is more significant than the effect of $P_{O2}$ in secondary stream because oxygen in transport stream is premixed with PC and reacts with coal directly and rapidly under high temperatures, while secondary oxygen needs a mixing mechanism to reach the center coal jet.

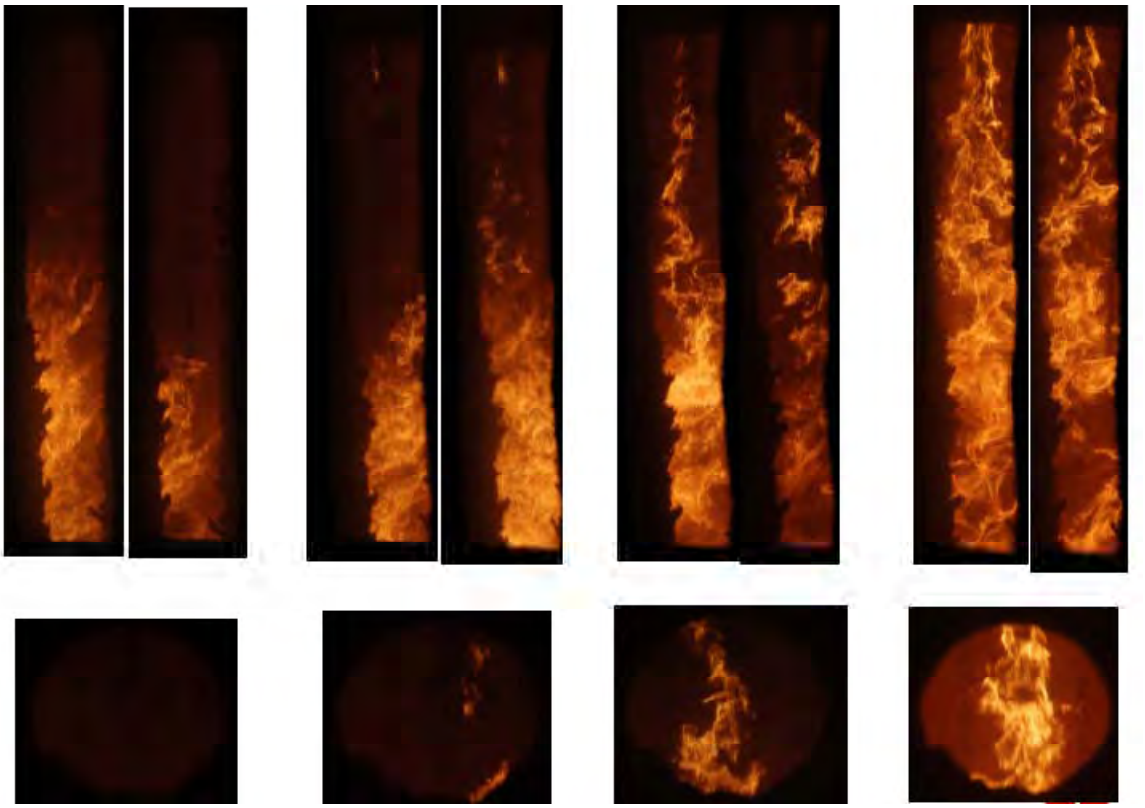

**Figure 34.** The effect of PO2 in transport stream on flame stability and near-burner flame structure
$P_{O2}$ in transport stream =
0 0.099 0.144 0.207

**d) The PDF of stand-off distance to quantify the effect of PO2 in transport stream on coal jet flame stability**

A PDF of stand-off distance is computed by,

$$\rho = \frac{1}{N}\frac{dn_i}{dx_i}$$

where $\rho = probability\ density\ function\ of\ standoff\ distance\ (unit: \frac{1}{m}\ or\ \frac{1}{cm})$

$$N = the\ number\ of\ total\ images$$

$$n_i = frequency\ of\ flames\ starting\ in\ the\ i^{th}\ bin$$

$$x_i = Standoff\ distance\ of\ i^{th}\ bin\ (unit: m\ or\ cm)$$

The integration of probability density function of stand-off distance should be unity, which is, $\int \rho\, dx = 1$,

where $\rho = probability\ density\ function\ of\ standoff\ distance (unit: \frac{1}{m}\ or\ \frac{1}{cm})$

$$x = standoff\ distance\ (unit: m\ or\ cm)$$

Figures 35 – 39 depict the probability density function curves of stand-off distance when increasing primary $P_{O2}$ from 0 to 0.207. Error bars are quantified by fiver replicates running on different days. Other burner operating parameters are: overall $P_{O2}$ = 40%, preheat temperature = 489 K, wall temperature = 1283 K, coal type: Utah Bituminous. Burner design is the same as described in the section on preliminary tests. Two blind spots exit in the range of 0 to 11 cm and 35.1 to 41.6 cm in the x-axis due to the construction of the quart windows.

The flame is detached when primary $P_{O2}$ is lower than 14.4%. Unsteady attachments are observed in primary $P_{O2}$ = 14.4% case, which indicate that 14.4% of primary oxygen partial pressure is a transit point under the above burner operating conditions. Under the condition of $P_{O2}$ = 20.7%, coal flame gets attached steadily. Therefore stand-off distance is not a continuous variable and attachment/detachment pass through a sudden transition when varying PO2 in transport stream.

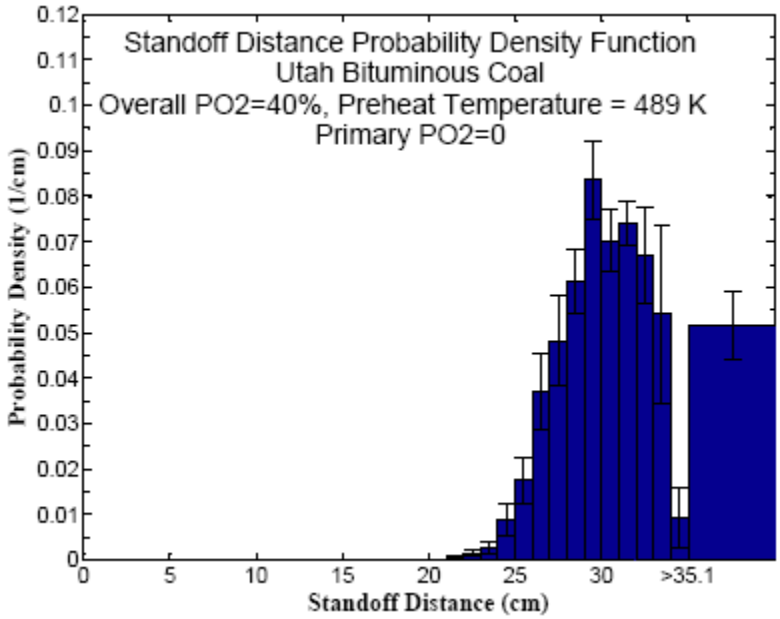


**Figure 35.** Probability density function of stand-off distance, an oxy-coal combustion case (Primary $P_{O2}$ = 0, overall $P_{O2}$ = 40%, Preheat temperature = 489 K, S.R. = 1.15, Utah Bituminous Coal)

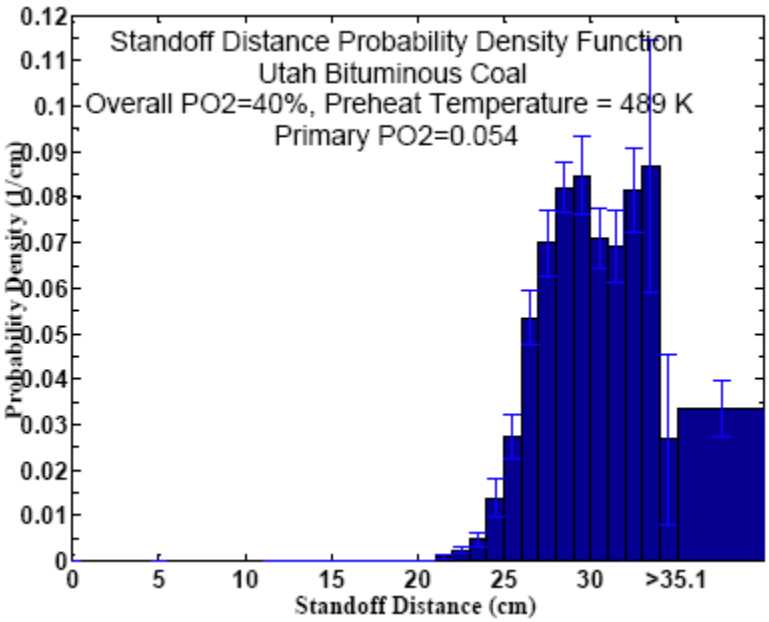


**Figure 36**. Probability density function of stand-off distance, an oxy-coal combustion case (Primary $P_{O2}$ = 0.054, overall $P_{O2}$ = 40%, Preheat temperature = 489 K, S.R. = 1.15, Utah Bituminous Coal)

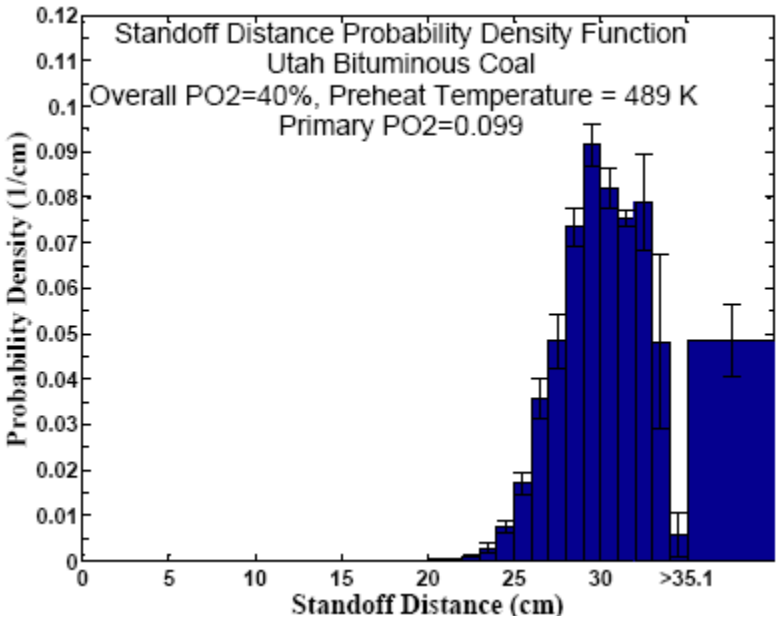


**Figure 37.** Probability density function of stand-off distance, an oxy-coal combustion case (Primary $P_{O2}$ = 0.099, overall $P_{O2}$ = 40%, Preheat temperature = 489 K, S.R. = 1.15, Utah Bituminous Coal)

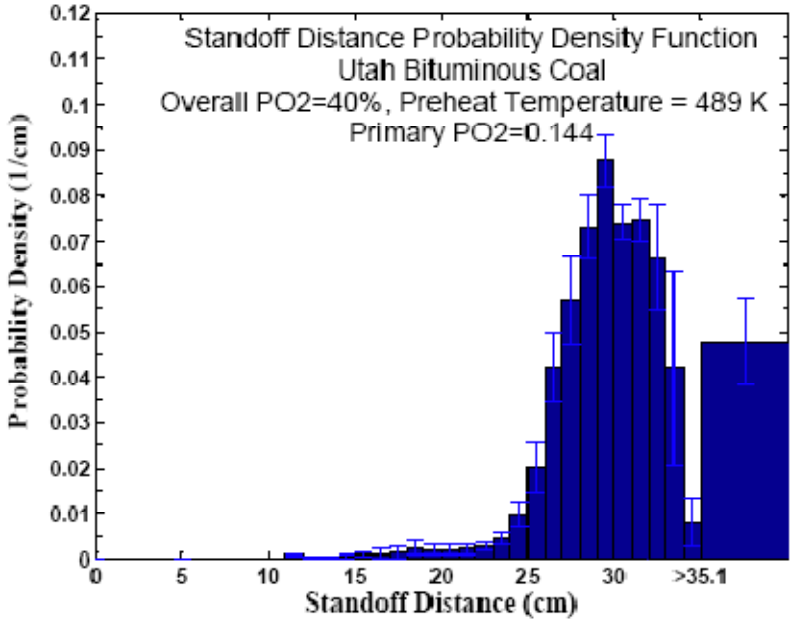


**Figure 38.** Probability density function of stand-off distance, an oxy-coal combustion case (Primary $P_{O2}$ = 0.144, overall $P_{O2}$ = 40%, Preheat temperature = 489 K, S.R. = 1.15, Utah Bituminous Coal)

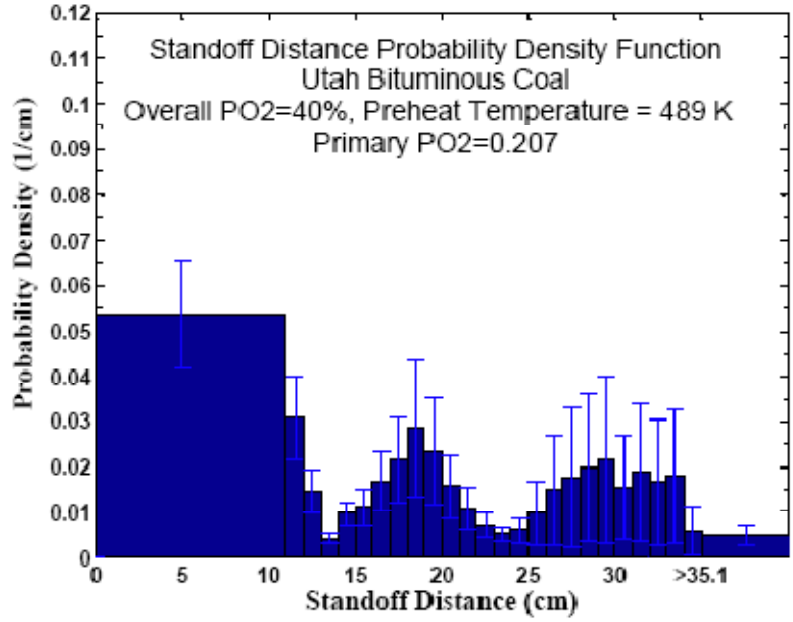


**Figure 39.** Probability density function of stand-off distance, an oxy-coal combustion case (Primary $P_{O2}$ = 0.207, overall $P_{O2}$ = 40%, Preheat temperature = 489 K, S.R. = 1.15, Utah Bituminous Coal)

Figure 40 – 44 show probability density function curves of stand-off distance when varying primary $P_{O2}$ from 0 to 20.7% at a higher secondary stream preheat temperature (544K). The

results are based on two of the five replicates. Therefore error bars will be quantified when the analysis of the five replicates is accomplished. The purpose of these tests is to understand the effect of preheat temperature of secondary stream on coal ignition and flame stability. Increasing primary $P_{O2}$ from 0 to 5.4% decreased stand-off distance, which means the flame front is moving upstream to the burner. As shown in Figure 41, primary $P_{O2}$ = 9.9% is a transition point for flame detachment and flame attachment at the elevated preheat temperature of secondary stream. Compared with Figure 36, the secondary preheat temperature contributed significantly to the coal ignition process and flame stability.

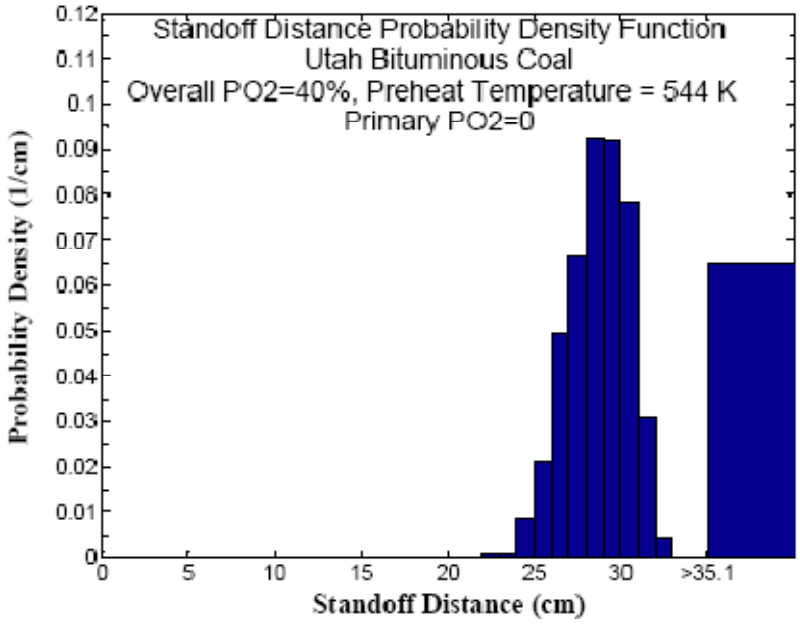


**Figure 40.** Probability density function of stand-off distance, an oxy-coal combustion case (**Primary $P_{O2}$ = 0**, overall $P_{O2}$ = 40%, Preheat temperature = 544 K, S.R. = 1.15, Utah Bituminous Coal)

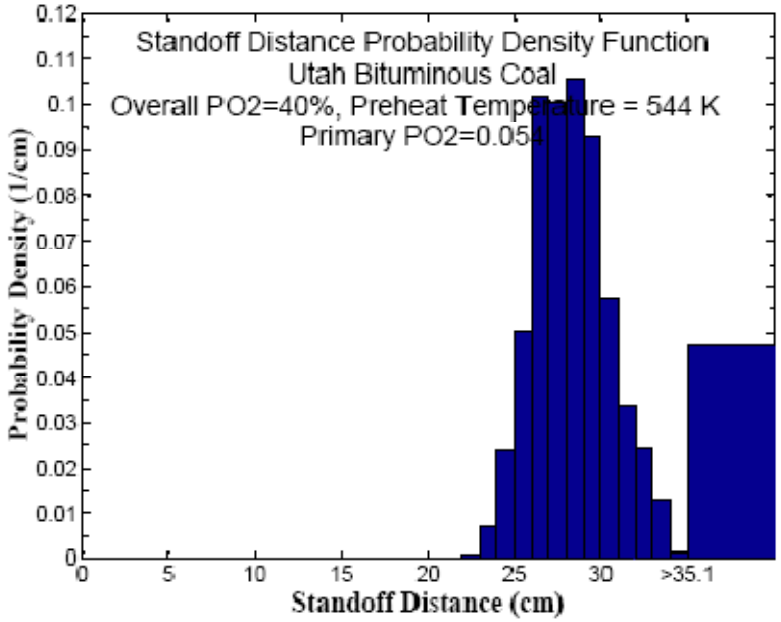


**Figure 41.** Probability density function of stand-off distance, an oxy-coal combustion case (Primary $P_{O2}$ = 0.054, overall $P_{O2}$ = 40%, Preheat temperature = 544 K, S.R. = 1.15, Utah Bituminous Coal)

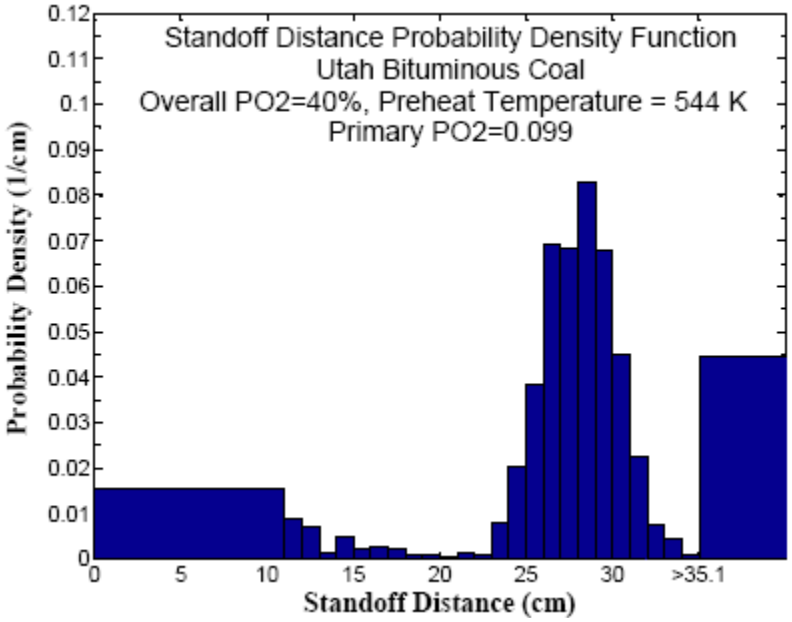


**Figure 42.** Probability density function of stand-off distance, an oxy-coal combustion case (Primary $P_{O2}$ = 0.099, overall $P_{O2}$ = 40%, Preheat temperature = 544 K, S.R. = 1.15, Utah Bituminous Coal)

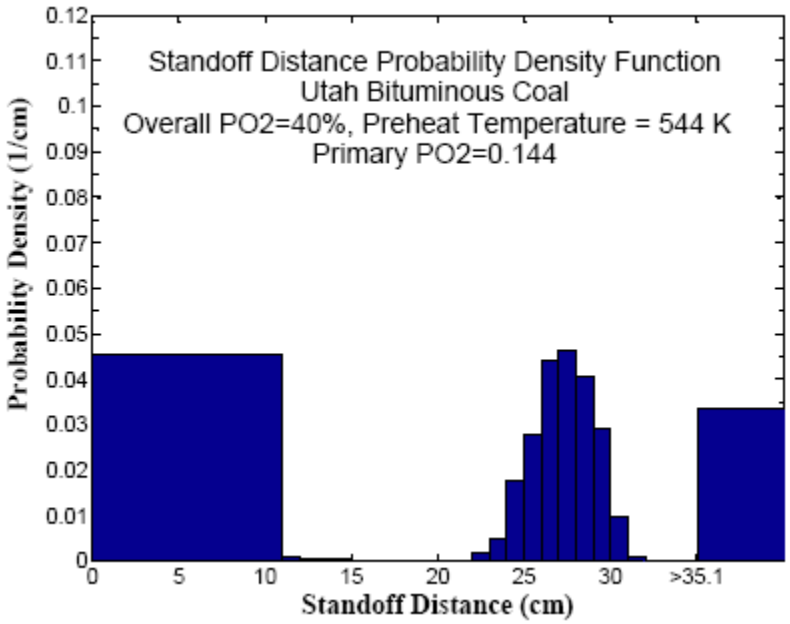


**Figure 43.** Probability density function of stand-off distance, an oxy-coal combustion case (Primary $P_{O2}$ = 0.144, overall $P_{O2}$ = 40%, Preheat temperature = 544 K, S.R. = 1.15, Utah Bituminous Coal)

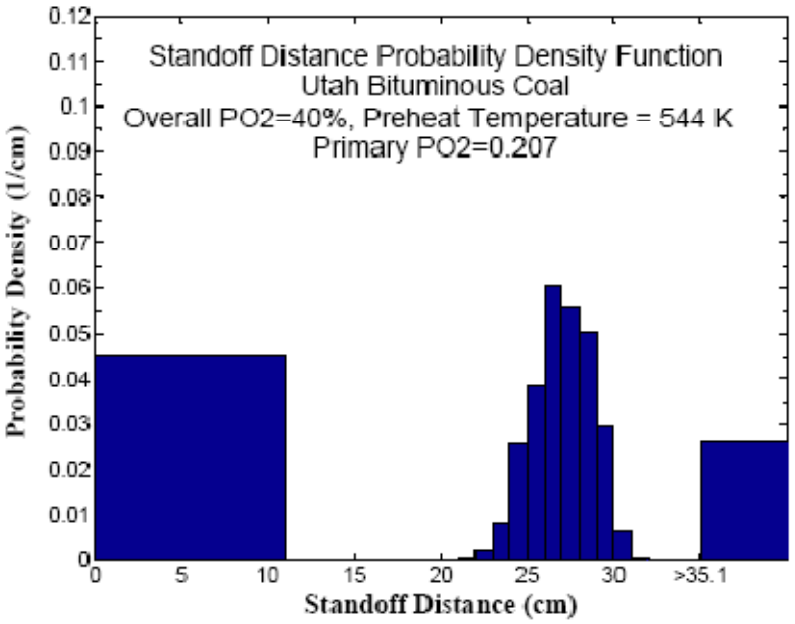


**Figure 44.** Probability density function of stand-off distance, an oxy-coal combustion case (Primary $P_{O2}$ = 0.207, overall $P_{O2}$ = 40%, Preheat temperature = 544 K, S.R. = 1.15, Utah Bituminous Coal)

## CONCLUSIONS

A new 100 kW oxy-coal combustor with controlled heated walls and optical access has been built to perform the tests on effects of $P_{O2}$ on coal jet flame stability. A new methodology for image processing has been applied to quantify the flame stability by measuring stand-off distance using high-speed camera measurements.

The major conclusions are:

- Systematic measurements of stand-off distance versus primary $O_2$ concentration ($P_{O2}$) have been obtained, together with uncertainty quantification.
- Flame stand-off distance is not a continuous variable and attachment/detachment pass through a sudden transition.
- The secondary stream preheat plays an important role on the coal ignition. Primary $P_{O2}$ has the first order effect on flame stability and axial coal jet ignition.

## ACKNOWLEDGEMENT

This material is based upon work supported by the Department of Energy under Award Number DE-FC26-06NT42808.

## LIST OF FIGURES

## LIST OF TABLES

## REFERENCES

[1] B. Metz, et al. IPCC Special Report on Carbon dioxide Capture and Storage. Cambridge University Press, UK, 2007.

[2] D J Dillon, et al. Oxy-Combustion Processes for $CO_2$ capture from advanced supercritical PF and NGCC Power Plant, IEA Greenhouse Gas R&D Program, UK

[3] K. Jordal, et al. Oxyfuel Cobustion for Coal-Fired Power Generation with $CO_2$ Capture – Opportunities and Challenges, Vattenfall, Sweden

[4] Development of Oxy-Coal Combustion for Power Generation Industry Issue Paper, IEA Greenhouse Gas R&D Programme

[5] A. Molina; C. Shaddix. Coal particle ignition and devolatilization during oxygen-enhanced and oxygen/carbon dioxide pulverized coal combustion. *2005 Fall Meeting Western States Section of the Combustion Institute*, Stanford, CA, U.S.A., Oct. 17-18, 2005; Paper 05F-20.

[6] A. Molina; C. Shaddix. Effect of $O_2/CO_2$-firing on coal particle ignition. *22nd Internationl Pittsburgh Coal Conference*, Pittsburgh, PA, U.S.A. Sept. 12-15, 2005; Paper 268.

[7] J. Ballester; S. Jimenez. Kinetic parameters for the oxidation of pulverized coal as measured from drop tube tests. *Combustion and Flame* **2005**, 142, 210-222.

[8] R.H. Essenhigh; M.K. Misra; etc. Ignition of coal particles: a review. *Combustion and Flame* **1989**, 77, 3-30.

[9] H. Karcz; etc. Evaluation of kinetic parameters of coal ignition. *Fuel* **1980**, 59, 799-802.

[10] T.F. Wall; V.S. Gururajan. Combustion kinetics and the heterogeneous ignition of pulverized coal. *Combustion and Flame* **1986**, 66, 151-157.

[11] V.S. Gururajan; T. F. Wall; etc. Mechanisms for the ignition of pulverized coal particles. *Combustion and Flame* **1990**, 81, 119-132.

[12] X.Y Du.; K. Annamalai. Transient ignition of isolated coal particle. *Combustion and Flame* **1994**, 97(3-4), 339-354.

[13] H. Katalambula; J. Hayashi; etc. Dependence of single coal particle ignition mechanism on the surrounding volatile matter cloud. *Energy and Fuels* **1997**, 11(5), 1033-1039.

[14] DK Zhang, Laser-Induced Ignition of Pulverized Fuel Particles, Combustion and Flame 1992, 90: 134 -142

[15] C. L. Sun, et al, Ignition of Coal Particles at High Pressure in a Thermogravimetric Analyzer, Combustion and Flame 1998, 115: 267-274

[16] C. Monson, Char Oxidation at Elevated Pressure, PhD dissertation, BYU, 1992

[17] D. Zeng, Effects of Pressue on Coal Pyrolysis at High Heating Rates and Char Combustion, PhD dissertation, BYU 2005

[18] M.C. Zhang, et al., A New Flame Sheet Model to Reflect the Influence of the Oxidation of CO on the Cobustion of a Carbon Particle, Combustion and Flame 2005, 143: 150-158

[19] M.C. Zhang, et al, An Improved Moving Flame Front Model for Combustion of A Carbon Particle with Finite-rate Heterogeneous Oxidation and Reduction, 6th Asia-Pacific Conference on Combustion, Nagoya, Japan, May 2007

[20] M.C. Zhang, et al, Further Discussion on the Reality and Usability of the Moving Flame Front Model for Combustion of A Carbon Particle, 6th Asia-Pacific Conference on Combustion, Nagoya, Japan, May 2007

[21] H. Liu; R. Zailani; B.Gibbs. Comparisons of pulverized coal combustion in air and in mixtures of $O_2/CO_2$. *Fuel* **2005**, 84(7-8), 833-840.

[22] Y.Q. Hu; N. Kobayashi; M. Hasatani. The reduction of recycled-$NO_x$ in coal combustion with $O_2$/recycled flue gas under low recycling ratio. *Fuel* **2001**, 80(13), 1851-1855.

[23] H. Liu; K. Okazaki. Simultaneous easy $CO_2$ recovery and drastic reduction of $SO_x$ and $NO_x$ in $O_2/CO_2$ coal combustion with heat recirculation. *Fuel* **2003**, 82(11), 1427-1436.

[24] E. Croiset; K.V. Thambimuthu. $NO_x$ and $SO_2$ emissions from $O_2/CO_2$ recycle coal combustion. *Fuel* **2001**, 80(14), 2117-2121.

[25] K. Okazaki, T. Ando, $NO_x$ reduction mechanism in coal combustion with recycled $CO_2$. Energy 1997, 22(2/3):207-215

[26] T. Nozaki, et al, Analysis of the flame formed during oxidation of pulverized coal by an $O_2$-$CO_2$ mixture. Energy 1997, 22(2/3): 199-205

[27] E. Chui, et al, Modeling of oxy-fuel combustion for a western Canadian sub-bituminous coal, Fuel 2003, 82: 1201-1210

[28] E. Chui, et al, Numerical investigation of oxy-coal combustion to evaluate burner and combustor design concepts, Energy 2004, 29: 1285-1296

[29] B.M. Visser; J.P. Smart; etc. Measurements and predictions of quarl zone properties of swirling pulverized coal flames. *23rd Symposium (International) on Combustion/The Combustion Institute*, 1990, 949-955.

[30] J.S. Truelove; D. Holcombe. Measurement and modeling of coal flame stability in a pilot-scale combustor. *23rd Symposium (International) on Combustion/The Combustion Institute*, 1990, 963-971.

[31] M. Costa; P. Costen; etc. Detailed measurements in and modeling of an industry-type pulverized-coal flame. *23rd Symposium (International) on Combustion/The Combustion Institute*, 1990, 973-980.

[32] V.D. Miosavljevic; etc. Stability of pulverized coal burners. *23rd Symposium (International) on Combustion/The Combustion Institute*, 1990, 957-962.

[33] F. El-Mahallawy, et al, Mixing and nozzle geometry effects on flame structure and stability, *MCS 4*, Lisbon, Portugal, October 2005

[34] A. Olivani, et al, Near field flow structure of isothermal swirling flows and reacting non-premixed swirling flames, *MCS 4*, Lisbon, Portugal, October 2005

[35] S.G. Budilarto, 2003. "An experimental study on effects of fluid aerodynamics and particle size distribution in particle-laden jet flows." *Ph.D. Thesis*, Purdue University, West Lafayette, IN.

[36] S.G. Budilarto, and J.L. Sinclair, "An experimental study on effect of particle size distribution in particle-laden jet flows". *2003 Annual AIChE Meeting*, San Francisco, CA, November 2003.

[37] P. Heil, et al, Drvelopment of an oxycoal swirl burner operating at low $O_2$ concentrations, *Fuel* 2009, 88: 1269 -1274

[38] G. Ogden. Pulverized coal combustion: flame attachment and $NO_x$ emissions. *Ph.D. Thesis*, The University of Arizona, 2002.

[39] G. Ogden and J Wendt, Using oxygen enrichment and coal fines to diminish $NO_x$ emissions from pulverized coal axial diffusion flames, *2003 AFRC Fall Meeting*, Livermore, California, October 2003

[40]M. Holtmeyer, R. Axelbaum, et al, Flame stability in oxygen-enhanced combustion of coal, *AIChE Annual Conference*, Salt Lake City, UT, November 2007

[41] J. Beer and N. Chigier, *Combustion Aerodynamics*, Halsted Press Division, John Wiley and Sons, Inc., New York, 1972

[42] M. Field, et al, *Combustion of Pulverized Coal*, The British Coal Utilisation Research Association, Leatherhead 1967,

[43] L. Smoot and P. Smith, *Coal combustion and gasification*, Springer, 1 edition, 1985

[44] C. Baukal, *Oxygen-Enhance Combustion*, Air Products and Chemicals, Inc., Allentown, Pennsylvania, 1998 by CRC Press LLC

[45] D. Purshing, Nitrogen oxide formation in pulverized coal flames, *PhD dissertation* of University of Arizona, 1978

[46] J. Howard, Mechanisms of ignition and combustion in flames of pulverized bituminous coal, *PhD dissertation* of The Pennsylvania State University, 1965

[44] J. Smart, The effect of burner scale and coal quality on low $NO_x$ burner performance, *PhD dissertation* of the Imperial College, London, 1992

## NOMENCLATURE

CCS – carbon capture and sequestration

CMOS - complementary metal–oxide–semiconductor

CO – carbon monoxide

$CO_2$ – carbon dioxide

I.D. – inside diameter

IFRF – International Flame Research Foundation

GI – homogenous gas phase ignition

HI – heterogeneous ignition

Hg – mercury

IMFF – improved moving flame front

LDV – laser Doppler velocimetry

LOI – loss-on-ignition

MFF – moving flame front

$N_2$ – nitrogen

NO – nitric monoxide

$NO_x$ – nitrogen oxide

N – total numbers of photo images

$n_i$ – frequency of flames starting in the $i^{th}$ bin

$O_2$ - oxygen

O.D. – outside diameter

OFC – oxy-fuel combustion

PC – pulverized coal

PDF – probability density function

PIV – particle image velocimetry

$P_{O2}$ – partial pressure of oxygen

$\rho$ – probability density function

Re – Reynolds number

$SO_2$ – sulfur dioxide

S.R. – Stoichiometric Ratio

STD – standard deviation

$\delta$ – wall thickness

$v_p$– primary stream velocity

$v_s$ – secondary stream velocity

$x_i$ – stand-off distance corresponded to the $i^{th}$ bin

## Appendix C – Additional CFB Details

| Tag | Description | Manufacturer/Part |
|---|---|---|
| Bag-300 | Baghouse | |
| BV-101 | Main FGR Shut-Off Valve | |
| BV-102 | Main Air Shut-Off Valve | |
| BV-200 | Main Oxygen Shutoff Valve | |
| BV-201 | Primary Oxygen Shut-Off Valve | |
| BV-202 | Secondary Oxygen Shut-Off Valve | |
| BV-300 | Exhaust Damper | |
| BV-401 | Loop Seal CO2 Shut-Off Valve | |
| BV-402 | Loop Seal Air Shut-Off Valve | |
| DP-101 | Primary Air/FGR dP Transmitter | Honeywell STD101 (0-30 in H2O) |
| DP-102 | Secondary Air/FGR dP Transmitter | ABB 264DS (0-64 in H2O) |
| DP-201 | Primary Oxygen dP Transmitter | ABB 264DS (0-64 in H2O) |
| DP-202 | Secondary Oxygen dP Transmitter | ABB 264DS (0-64 in H2O) |
| FC-101 | Primary Air/FGR Control Valve | 3" Fisher Control Valve |
| FC-102 | Secondary Air/FGR Control Valve | 1 1/2" Fisher Control Valve |
| FC-103 | Main Blower Recirc Valve | |
| FC-201 | Primary Oxygen Control Valve | |
| FC-202 | Secondary Oxygen Control Valve | |
| FM-101 | Primary Air/FGR V-Cone | 3" Wafer (β=0. ) |
| FM-102 | Secondary Air/FGR V-Cone | 1 1/2" (β=0.55) |
| FM-201 | Primary Oxygen V-Cone | 3/4" V-Cone (β=0.65) |
| FM-202 | Secondary Oxygen V-Cone | 1/2" (β=0.60) |
| MF-401 | Loop Seal #1 Mass Flow Controller | Brooks Model #5853i |
| MF-402 | Loop Seal #2 Mass Flow Controller | Brooks Model #5851i |
| PT-101 | Primary Air/FGR P Transmitter | Dwyer 603A-6 (0-100 in H2O) |
| PT-102 | Secondary Air/FGR P Transmitter | Dwyer 603A-6 (0-100 in H2O) |
| PT-103 | Main Blower P Transmitter | |
| PT-201 | Primary Oxygen P Transmitter | ABB 264PS |
| PT-202 | Secondary Oxygen P Transmitter | ABB 264PS |
| PT-300 | Exhaust P Transmitter | |
| Reg-200 | Main Oxygen Regulator | |
| Sol-200 | Main Oxygen Solenoid Valve | |
| Sol-201 | Primary Oxygen Solenoid Valve | |
| Sol-202 | Secondary Oxygen Solenoid Valve | |
| Sol-401 | Loop Seal #1 Solenoid Vale | Asco |
| Sol-402 | Loop Seal #2 Solenoid Valve | Asco |
| TC-101 | Primary Air/FGR Thermocouple | 1/8" K-type |
| TC-102 | Secondary Air/FGR Thermocouple | 1/8" K-type |
| TC-201 | Primary Oxygen Thermocouple | 1/8" K type |
| TC-202 | Secondary Oxygen Thermocouple | 1/8" K-type |
| TC-300 | Exhaust Thermocouple | 1/8" K-type |

**Table C-1.** A list of part descriptions and manufacturers are found below with a corresponding schematic on the following page.

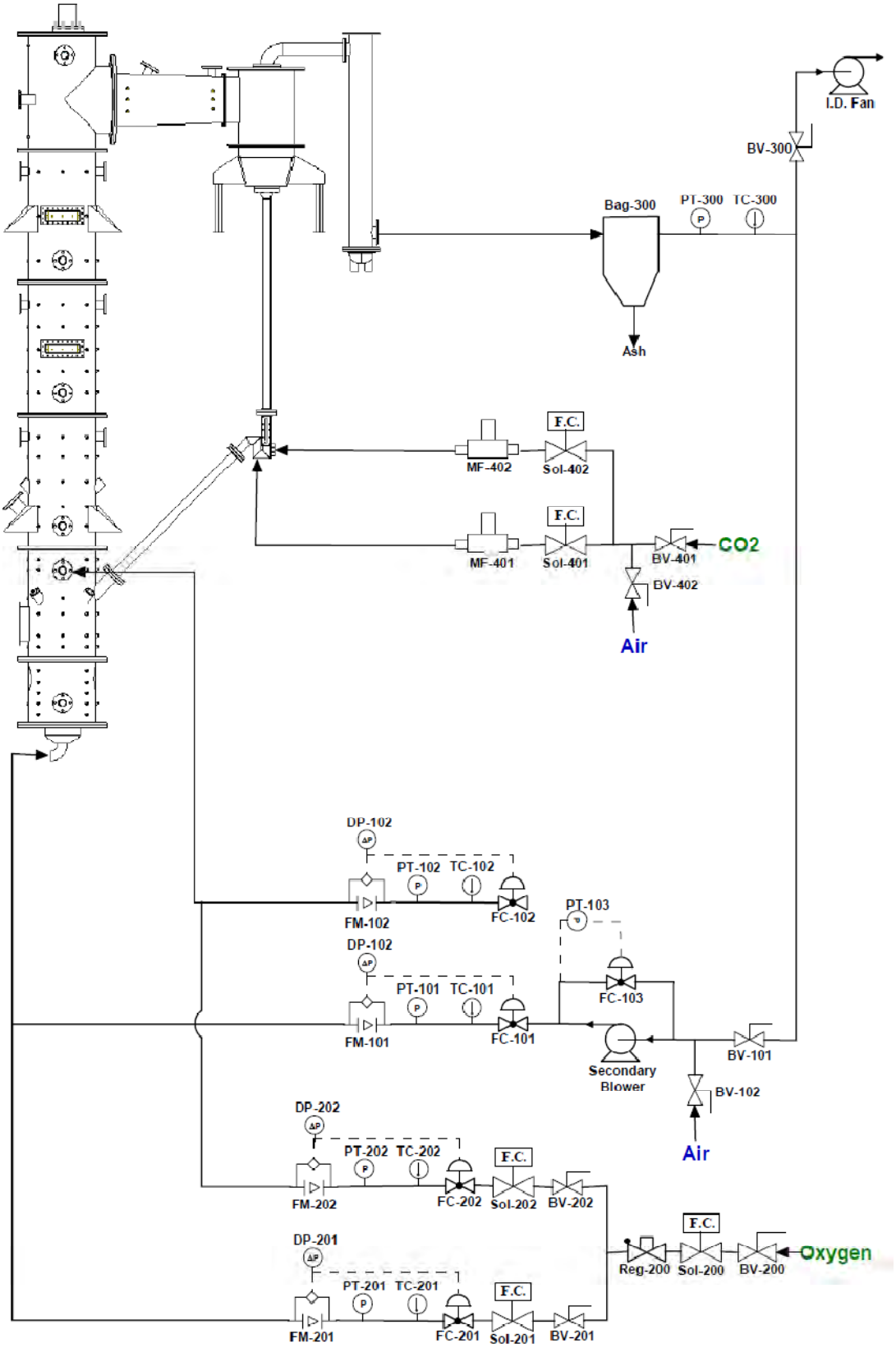


**Figure C-1.** Instrumentation diagram of the CFB.

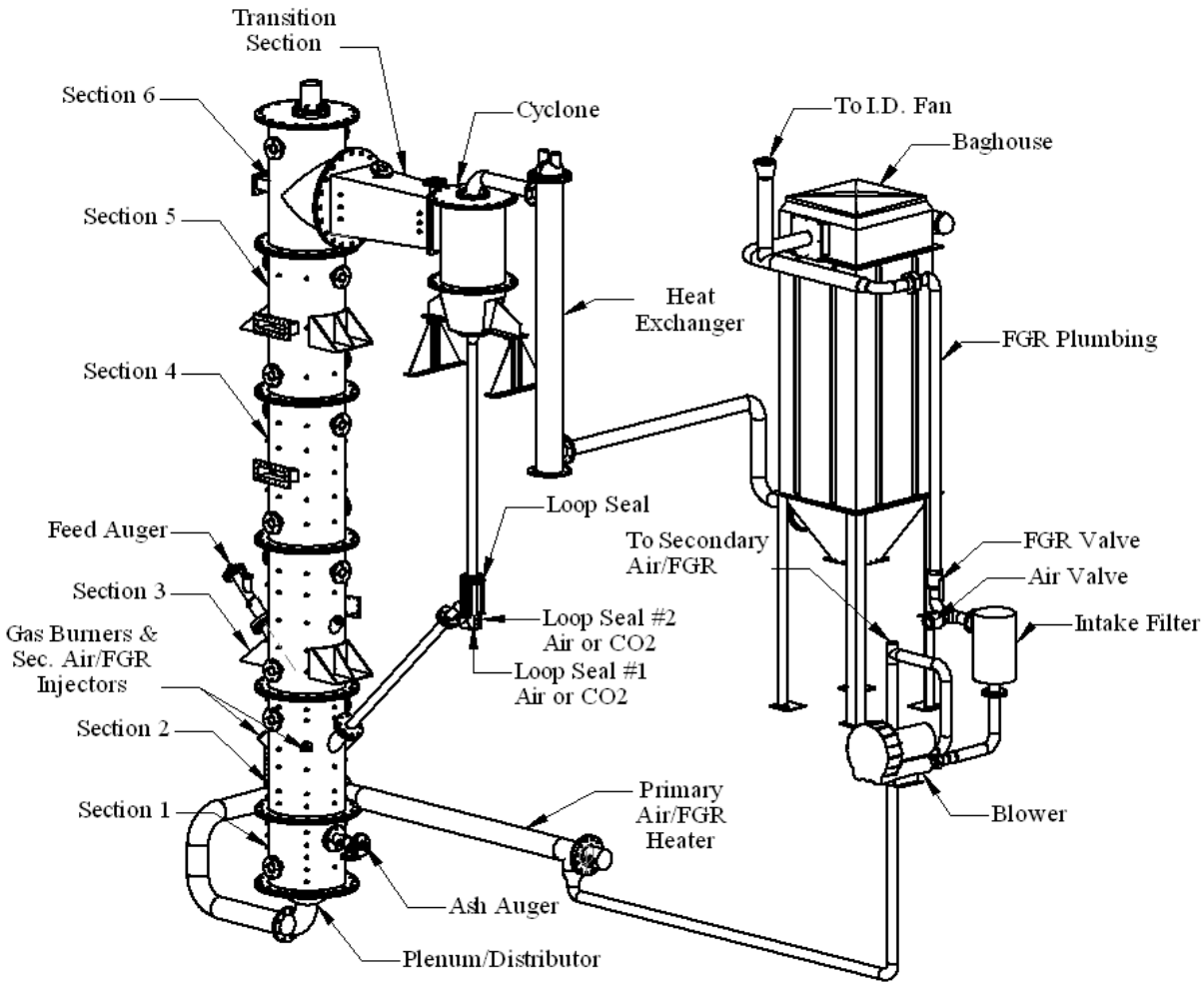


**Figure C-2.** Schematic of the current CFB facility.

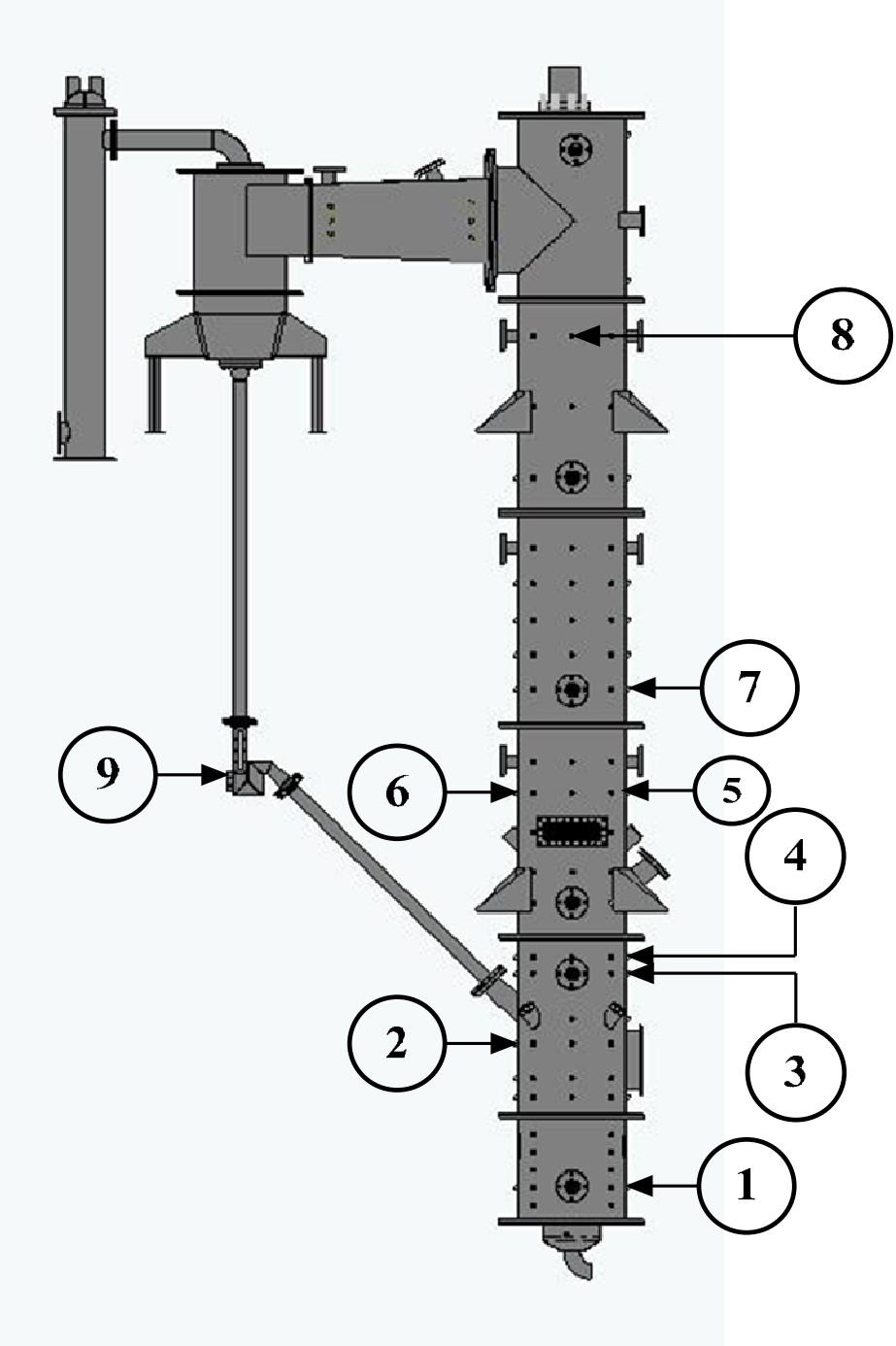


**Figure C-3.** Schematic of the CFB test facility, showing solids sampling port locations.

# UTAH CLEAN COAL CENTER: GASIFICATION RESEARCH ACTIVITIES

Topical Report

Reporting Period Start Date: 07/01/2006
Reporting Period End Date: 03/31/2009

Authors:

Larry L. Baxter, Brigham Young University
Thomas H. Fletcher, Brigham Young University
Ronald J. Pugmire, University of Utah
Jeremy N. Thornock, University of Utah
Kevin J. Whitty, University of Utah

Issue Date: September 2009

DOE Cooperative Agreement DE-FC26-06NT42808

## DISCLAIMER

# ABSTRACT

The Utah Clean Coal Center ($UC^3$) was established at the University of Utah through a cooperative agreement from the U.S. DOE / NETL. The center had five "thrust areas" critical for successful development of advanced technologies for power production from coal with minimal environmental impact. One of these areas was gasification, and it was decided to focus specifically on pressurized, oxygen-blown gasification. The overall, long-term research approach combines (1) development of an advanced computational simulation tool with (2) lab-scale experiments on fundamental processes taking place in a gasifier and (3) operation of an industrially representative, small pilot scale gasifier. Under the $UC^3$ program, experimental work was performed at the University of Utah and Brigham Young University adn focused on pressurized pyrolysis of coal, production and reaction of soot, transition from char to slag and deposition of coal ash onto surfaces. This report describes results from these studies and initial development of a computational model which will be used for simulation of entrained-flow coal gasifiers.

# TABLE OF CONTENTS

# EXECUTIVE SUMMARY

The University of Utah's Utah Clean Coal Center (UC3) was a U.S. Department of Energy program (cooperative agreement DE-FC26-06NT42808) administered through the National Energy Technology Laboratory (NETL). The program ran from July 1, 2006 to March 31, 2009 and had five major thrust areas focused on low $CO_2$ production of electric power from coal. One of the thrust areas centered on high temperature, pressurized entrained-flow gasification of coal. Although there are currently two entrained-flow gasifiers in the U.S. which produce power through an integrated gasification combined-cycle (IGCC) configuration, the technology is still relatively young and there is much to be improved before gasification is considered a fully commercial, efficient, high-availability technology. Gasification is an expensive technology to develop. Computational simulation is a useful tool for development, optimization and troubleshooting of gasification systems. However, successful simulation requires well-quantified input data taken under appropriate conditions and validation of the model with data from an operating gasifier. There are gaps in the understanding of coal conversion in entrained-flow gasifiers and very little information regarding performance of such systems is publicly available. The objectives of the gasification thrust area of the Utah Clean Coal Center were to provide such information and to begin development of a simulation tool for entrained-flow coal gasification. The experimental tasks in this area focused on development of experimental techniques and acquisition of data on pressurized coal pyrolysis, char conversion, tar formation, and slag production and interaction with gasifier refractory linings. The simulation task focused on developing the scope of a computational model for entrained-flow gasification and preparation of a system for acquisition of validation data.

Brigham Young University has developed a pressurized flat flame burner (PFFB) system which allows study of coal pyrolysis at very high heating rates ($10^5$ °C/s) representative of rates in industrial-scale coal gasifiers. Under the $UC^3$ program, modifications were made to the pressure vessel, ignition system, particle feed system and fuel system to improve safety, reliability and versatility. The system was tested using a subbituminous coal. The char that was collected allowed determination of char yield, bulk density, internal (BET) surface area and structure as determined by scanning electron microscopy.

BYU also studied production of tar during coal gasification by pyrolyzing two surrogate tar compounds (2,6-dimethylnaphthalene and 6-(5H)-phenanthridinone) as well as a subbituminous coal in a flat flame burner system. The condensed-phase materials from these tests were subjected to NMR analysis and it was discovered that the 2,6-methylnaphthalene easily loses its methyl groups to form benzene. 6-(5H)-phenanthridinone is more stable, however, and tars from the coal that was tested appeared to fall between these materials in terms of stability during high temperature pyrolysis.

The transition from coal char to molten slag was studied under atmospheric conditions in a high temperature entrained-flow reactor built specifically for this program. Coal was injected into either an inert environment or an oxygen-containing environment to form char at different degrees of conversion, from purely pyrolyzed material to molten ash with very little carbon remaining. The internal surface area of these chars was measured and the material was examined by scanning electron microscopy. It was found that, at temperatures exceeding the coal's ash fusion temperature, the char undergoes a marked decrease in internal surface area and the structure visibly changes from a very porous, sponge-like structure to a smoother, less porous morphology. For the coal studied, this occurred at a conversion between 90 and 95%. This transition point represents a shift from reactive char to unreactive slag. Due to the low porosity an internal surface area, carbon remaining in the slag will be relatively inaccessible and difficult to convert. At temperatures below the ash fusion temperature, a precipitous decrease in surface area was not observed.

A model describing the geometry of particles as they undergo sintering was developed. The model describes all geometric aspects of the sintered material and is useful for understanding deposition of coal ash onto surfaces. Experiments on sintering of coal ash and surrogate materials indicates that the sintered deposits are not simply a random packing of particles, but develop more as "pillars" of particles extending perpendicular to the surface. As a consequence, ash deposits maintain porosity longer, develop strength more slowly and to a lesser extent, and maintain anisotropic structure longer compared to random sphere structures. Low rank fuels generally sinter less than high rank fuels. This fuel-rank dependence is much larger than any detectable dependence on local stoichiometry (gasification vs. combustion) in the limit of no melting or slag formation. The dependence agrees well with known and general properties of deposit composition and particle size between these two fuels. Thermal conductivity provides a quantifiable estimate of the degree of sintering.

Long term, the objective of the research at the University of Utah is to develop a robust simulation tool for entrained-flow gasifiers. This is a multi-year undertaking. Under the Clean Coal Program, a strategy for incorporating heat transfer into the simulation was outlined. Several factors influence heat transfer, including soot and char, which strongly impact radiative heat transfer. Heat transfer to the slag layer and radiation from the gas to the walls are also important.

Results from the simulation tool that will ultimately be created will need to be validated against actual data from an operating gasifier. Under this program the University of Utah's 1 ton/day pressurized entrained-flow gasifier underwent modifications to allow operation with coal as a feedstock. Most of the effort focused on the quench system below the reactor and feed systems to the reactor. A prototype coal slurry preparation and feed system was constructed. Meanwhile, performance of the system during pressurized, oxygen-blown gasification was assessed using isopropyl alcohol as a fuel. The system performed as expected and is ready for testing with coal slurry feed.

# OBJECTIVES

The research reported herein was conducted with an overarching objective of developing robust, validated simulation tools for coal gasifiers. Specifically, the technology being targeted is pressurized, oxygen-blown slagging gasification as represented by technologies from GE, ConocoPhillips, Shell and Siemens. The specific tasks address what are considered deficiencies in the understanding of coal gasification behavior at a fundamental level, key components of computational models for simulation and actual gasifier data necessity for validation. Detailed objectives for each task are identified below.

**Task 10: Coal Conversion Studies.** Conversion of coal in high temperature systems, including gasifiers, has been studied for many years by many different groups. While much of this information is useful, the fidelity of published data is generally too low, and conditions often too unrepresentative of commercial systems, to allow incorporation into advanced computational models with any degree of confidence. The objective of this task was to fill gaps in the data available for simulation by performing experiments specifically with development of a computational tool in mind. For this program, the focus was on issues considered to have the most impact on coal conversion and gasifier performance, namely coal devolatilization (pyrolysis) under pressure, formation of soot and final burnout of the char as it transitions to molten slag.

**Task 11: Effect of Ash Characteristics and Deposition on Refractory Wear.** Limited refractory life is a critical issue affecting commercial success of high temperature coal gasification systems. The objectives of this task were to identify how ash properties affect deposition onto surfaces, and to understand and characterize the mechanisms by which those deposits form. Another objective was to develop algorithms that describe deposit and surface sintering and melting behavior, again with the ambition of ultimately incorporating these into the gasifier models.

**Task 12: Development and Validation of Computational Modeling Tools.** Development of a computational model for simulation of entrained-flow gasifiers is an ambitious undertaking that relies on information from Tasks 10 and 11 and will take several years to complete. Addressing severe refractory degradation is a priority, so the $UC^3$ program had as an objective to identify conditions and mechanisms responsible for this. Clearly, heat transfer (heat flux) to the walls of the reactor plays a significant role, so an objective was to identify key factors affecting such heat transfer. The final objective related to validation of the simulation model. The University of Utah operates a pressurized entrained-flow gasifier, originally build for processing black liquor, which can be used to provide data for validation of simulations. An objective of this program was to assess what is necessary for this gasifier to use coal as a feedstock, to make necessary modifications and to develop a coal feed system for the gasifier.

# INTRODUCTION

The Utah Clean Coal Center ($UC^3$) research program was established at the University of Utah on July 1, 2006 through a cooperative agreement (DE-FC26-06NT42808) from the United States Department of Energy, administered by the National Energy Technology Laboratory (NETL). The research program comprised 14 technical and one administrative task and was conducted over a period of approximately two years. The technical tasks focused on five "thrust areas" critical for successful development of low-impact technologies for power production from coal: (1) gasification, (2) oxy-fuel combustion, (3) computational simulation of industrial coal processing technologies, (4) mercury control, and (5) $CO_2$ sequestration. This topical report reviews activities within the gasification thrust area.

The gasification tasks were conducted by experienced researchers from the University of Utah and Brigham Young University and focus on areas important for successful, widespread implementation of gasification technology. Experience with industrial coal gasifiers shows that the refractory linings and coal injectors suffer unacceptably short lifetimes (U.S. DOE, 2002). Carbon conversion is also frequently lower than desired. Computational simulation provides a tool for evaluation of gasifier performance and can be used to model the environment (temperature, heat flux, gas composition, condensed-phase composition, local velocities) within the reactor. With appropriate inputs, simulation can help shed light on factors leading to short material lifetimes and low carbon conversion. Much of the information necessary already exists. But, for many aspects of coal gasification there is a lack of quality data and/or models describing coal conversion and the interaction between coal or coal slag and the gasifier reactor itself. Moreover, it is necessary to validate output from a simulation model by comparing to measured data from an actual system. Development of a comprehensive simulation tool for entrained-flow coal gasifiers is a multi-year effort, but under this program the Utah Clean Coal Center strove to begin filling gaps in fundamental understanding of coal gasification vital for successful simulation. The technical tasks for the gasification research program are summarized in Table 1.

**Table 1.** Tasks and subtasks for entrained-flow coal gasification research program.

| |
|---|
| **Task 10 - Coal Conversion Studies** |
| Subtask 10.1 - Investigation of pressurized pyrolysis and char conversion (T. Fletcher, BYU) |
| Subtask 10.2 - Investigation of soot formation during gasification (T. Fletcher, BYU and R. Pugmire, U.Utah) |
| Subtask 10.3 - Investigation of char burnout (K. Whitty, U.Utah) |
| **Task 11 - Effect of Ash Characteristics and Deposition on Refractory Wear** |
| Subtask 11.1 - Coal selection and characterization (L. Baxter, BYU, T. Fletcher, BYU, K. Whitty, U.Utah) |
| Subtask 11.2 - Modeling of coal ash sintering and melting (L. Baxter, BYU) |
| Subtask 11.3 - Acquisition of data for melting model verification (L. Baxter, BYU) |
| **Task 12 - Develop and Validate Computational Modeling Tools to Accurately Simulate Entrained-Flow Gasifiers** |
| Subtask 12.1 - Heat flux modeling (P. Smith, U.Utah) |
| Subtask 12.2 - Entrained-flow gasifier modification (K. Whitty, U.Utah) |

Much of the activity involved establishing experimental systems and procedures and developing the fundamental components of the simulation tool that will ultimately be used to model entrained-flow gasifiers. Additional simulation development work focused on oxy-fuel combustion. Many elements of those models are applicable to entrained-flow gasification systems. Details regarding those simulation development efforts are contained in the topical report on simulation (Tasks 2 – 4).

This report largely follows the structure of the tasks indicated in Table 1. Experimental systems are described in the following chapter. The Results and Discussion chapter details experimental results and development of models describing coal conversion and deposit formation.

# EXPERIMENTAL

Subtasks 10.1, 10.2, 10.3 and 11.3 involved experimental acquisition of data on coal conversion and ash sintering and melting behavior. Descriptions of the experimental equipment and procedures are provided in the sections below.

## Pressurized Flat Flame Burner Experiments (Subtasks 10.1 and 10.2)

Subtasks 10.1 (investigation of pressurized pyrolysis and char conversion) and 10.2 (investigation of soot formation during gasification) both used an existing pressurized flat flame burner (PFFB) system at Brigham Young University. For this research it was necessary to make several modifications to the system. These are detailed below, and a description of the experimental procedure is given.

### *PFFB Modifications – Pressure Vessel*

Significant challenges were encountered and overcome in the pursuit of the research objectives. It was found near the beginning of the project that the original PFFB was in need of a new pressure vessel to comply with state legal requirements. The opportunity was taken to implement other improvements to the system since much of it had to be redesigned anyway (Figure 1). The burner was changed from a down-flow configuration to up-flow to reduce thermal degradation. New heating/insulating units were installed to maintain a high temperature in the reaction zone. The collection probe was replaced with a moveable version. These and other changes necessitated the development of new operating procedures and support systems such as ignition, reliable particle entrainment, temperature control and flow control.

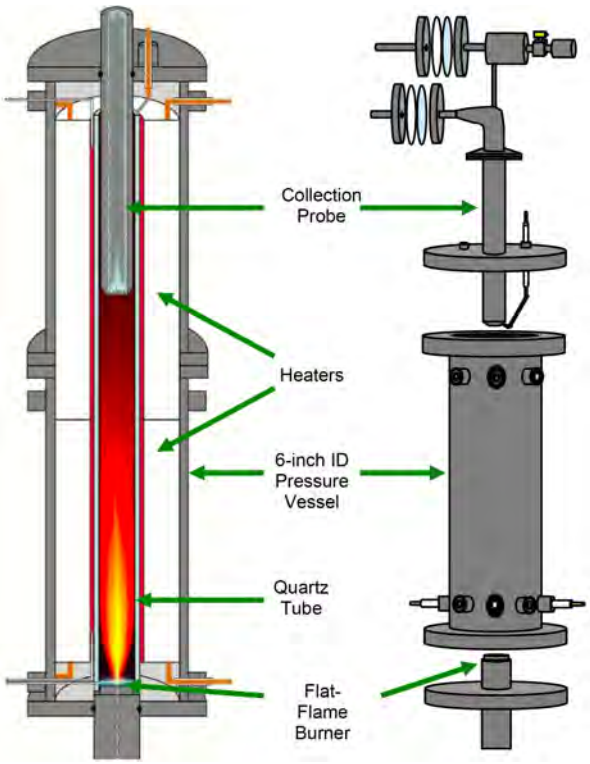


**Figure 1.** BYU High Pressure Flat-Flame Burner interior (left) and exterior (right).

## *PFFB Modifications – Ignition*

Several ignition systems for the new pressurized flat-flame burner facility were tested. A custom glow-plug system powered by a variable transformer was found to be superior to spark-ignition systems, especially at high pressure (Figure 2). Ignition has now been achieved consistently with the glow plug at pressures of up to 15 atm.

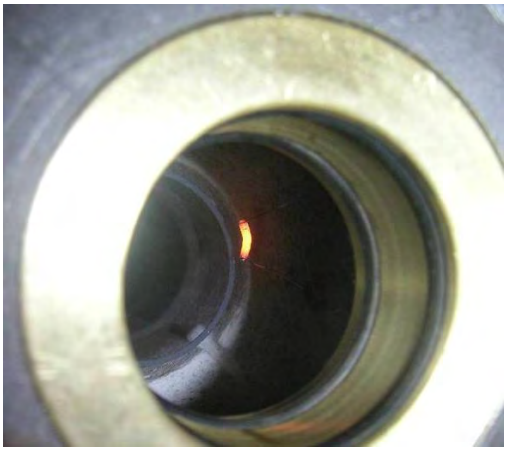

**Figure 2.** Glow plug ignition system and brass insert in vessel cap.

## *PFFB Modifications – Particle Feeding*

The PFFB was originally built with a large (5/32" ID) central entrainment tube. One of the intentions was to make it big enough to feed biomass. Using the burner in an up-flow configuration has proved to be difficult, particularly at high pressure. A large amount of nitrogen is required to keep the coal entrained in a large tube. This is undesirable because it reduces the heating rate and maximum temperature of the coal particles. As a first step, a piece of 1/8" OD tubing with an ID of 1/16" was inserted into the entrainment tube. This brought about significant improvement that was thought to be sufficient at the time. However, measurements of the centerline temperature with a thermocouple indicated that this configuration still required unacceptably high levels of entrainment gas. A tube with an ID of 0.04" was tested with success at 1, 2.5, and 5 atm. The flow rate of carrier nitrogen can be decreased by more than a factor of 2 compared to the 1/16" ID tubing.

Additional tests at higher pressures and calculations of settling velocity revealed that the 0.35-0.38 m/s velocity required to entrain the coal can be sustained in the entrainment tube, but it cannot be matched by the burner. The disparity in the velocities creates a turbulent zone that renders the temperature history of the particles unknown. It has been found that the turbulence can be minimized to an acceptable level if the ratio of carrier tube velocity to the cold burner velocity is less than ~ 4. The turbulent or laminar nature of the entrained coal stream near the burner is observable through a view port (Figure 3). By increasing the flow to the burner, a non-turbulent condition was found at 5 atm. This condition also had the advantage of generating enough extra heat to fully counter the heat loss experienced at the higher pressure. Experiments are proceeding at 2.5 and 5 atm and a system is being devised to block a portion of the burner face or switch to a different burner so that a narrower flow path may be used to increase the burner gas velocity at higher pressures with the existing flow control system.

**Figure 3.** Reacting coal stream exhibiting transition to turbulence as seen through view port.

### *PFFB Modifications – Fuel Mixture*

Soot production from the methane fuel was found to occur at very low equivalence ratios at any pressure greater than 2 atm. Several flow settings were investigated at different pressures to find conditions appropriate for experiments; any soot to be collected and analyzed should originate from coal tar rather than the methane fuel. Partial premixing was found to be somewhat helpful at lower pressures, but this option was ruled out for safety reasons at high pressure. The final solution was to change the major fuel from methane to hydrogen. This also helped with ignition; mixtures of fuel containing little or no hydrogen did not always stay lit at high pressure. Stable burner settings have been identified that use 84% hydrogen in the fuel stream. These settings eliminate soot formation at equivalence ratios of at least 1.2 and pressures of up to 15 atm.

Modifications are nearing completion to use of CO as a fuel, which should allow the use of much lower levels of hydrogen due to its low sooting potential. This will allow gasification experiments to be conducted in $CO_2$-rich atmospheres as well as $H_2O$-rich atmospheres. Using CO will have several additional benefits. Coals have been found to pyrolyze prematurely in the feeder tube, which causes bituminous coals to clog the tube at the level of the burner surface. The premature pyrolysis is thought to be due to the high flame speed of hydrogen; the burner surface is hot enough to glow (Figure 4). The lower flame speed of CO should help keep the burner surface cool enough to prevent premature pyrolysis. In the meantime, experiments have proceeded on subbituminous coal.

**Figure 4.** Atmospheric demonstration of coal feeding through burner with glowing surface.

## High Temperature Entrained Flow Reactor Experiments (Subtask 10.3)

Under subtask 10.3 (investigation of char burnout), a new high temperature atmospheric pressure laminar entrained-flow reactor (LEFR) was constructed at the University of Utah. This system was used to prepare coal char in either inert or reacting conditions to allow study of char properties at high conversion near the point where the char collapses into molten slag.

### *Experimental Apparatus*

The LEFR used in this study for char and ash preparation is shown in Figure 5. It consists of a high temperature furnace, a coal feeder, a sample collector, gas supply and cooling water circulator. Two co-axial alumina tubes (89 mm O.D. × 75 mm I.D. × 1500 mm long and 57mm O.D. × 50 mm I.D. × 1000 mm long, respectively) are mounted vertically inside the furnace (Carbolite, single zone, 1600 °C maximum operation temperature and 610 mm heated length) and sealed with flanges. The inside tube is used as the reactor. The reaction gas (a premixed air–nitrogen mixture) is injected through three injection ports on the bottom flange and is preheated when it flows upwards through the annulus between the two co-axial tubes. When the reaction gas reaches the top of the annulus, it turns and flows down into the inner tube through an alumina honeycomb flow straightener. The flow straightener has a sufficient pressure drop to generate a uniform and laminar flow, which is essential so that the entrained particles can travel along the centerline of the reactor tube experiencing identical reaction conditions. Coal particles are fed into the reactor through an injection probe using a vibrating syringe pump type coal feeder with nitrogen as carrier gas. The injection probe is water-cooled to prevent the coal particles from being heated before reaching the reaction zone. Upon injection into the reactor, the coal particles undergo pyrolysis and react with the reaction gas to produce char particles. The reacting products exit the reactor through a water-cooled collection probe. Nitrogen is injected into the collection probe through a sintered stainless steel tube to quench the product stream and reduce the thermophoresis deposit of the char particles on the cold surface of the probe. Char particles are collected using a cyclone separator followed by a filter.

### *Sample Preparation*

A pulverized Illinois # 6 bituminous coal was sieved to 104 μm or less for this study. The coal was dried in a muffle furnace at 104 °C for 24 hours to remove the moisture before sieving. Properties of the coal sample are presented in Table 2.

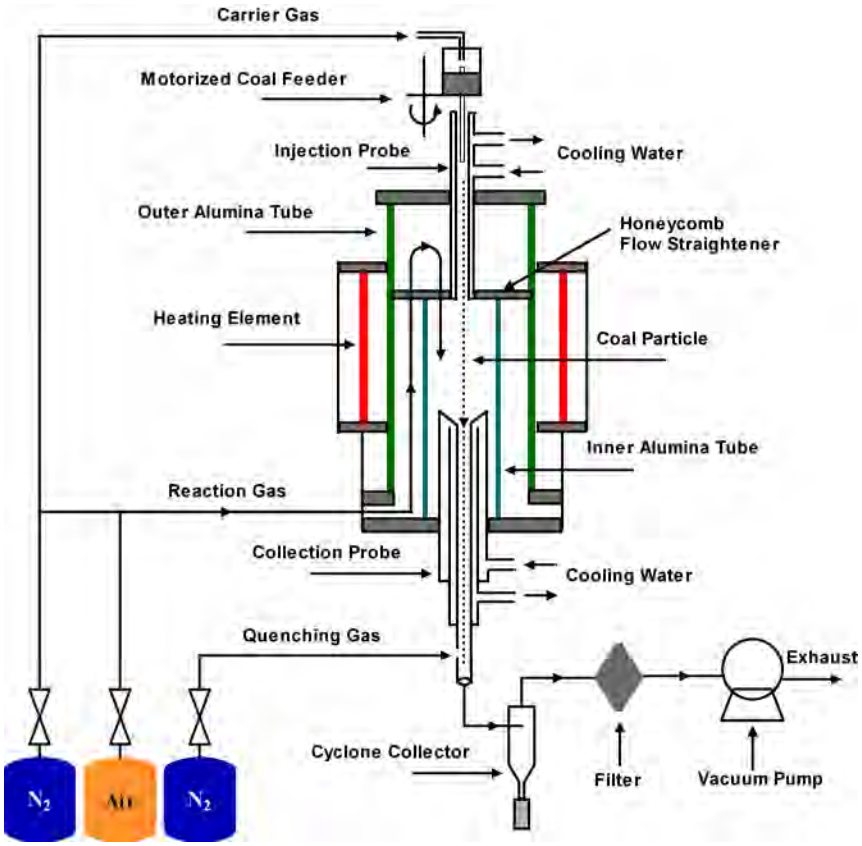


**Figure 5.** Schematic diagram of the LEFR used for preparing char and ash samples.

**Table 2.** Properties of the Illinois #6 coal used in this study.

| Analysis | |
|---|---|
| Proximate analysis (wt%, dry) | |
| Moisture[a] | 3.63 |
| Ash | 10.89 |
| Volatiles | 36.42 |
| Fixed carbon | 52.69 |
| Ultimate analysis (wt%, dry ash free) | |
| C | 74.52 |
| H | 4.96 |
| N | 1.48 |
| S | 4.66 |
| O | 14.56 |
| Ash fusion analysis (oxidizing, °C) | |
| IT | 1244 |
| ST | 1254 |
| HT | 1286 |
| FT | 1343 |

[a]As received

## *Experimental Conditions*

For the experiments performed in this study, the pressure inside the reactor was maintained at local atmospheric pressure, 0.84 atm (the altitude of Salt Lake City is about 1500 m). Experiments were carried out at four temperatures (1200, 1300, 1400 and 1500 °C) which cover the range below and above the ash fusion temperatures. Two kinds of experiments were performed: devolatilization experiments and oxidation experiments.

In the devolatilization experiments, the residence time was fixed at 2 s. The devolatilization gas was pure nitrogen, which provided an inert gas environment. The residence time was controlled by adjusting the flow rate of devolatilization gas at different temperatures. The flow rate of coal carrier gas flowing through the injection probe was set to maintain the same velocity as the devolatilization gas in the reactor.

In the oxidation experiments, the residence time was varied from 1.5 s to 6 s to achieve various carbon conversions. The use of long residence time was due to the low oxygen content (1.8%–5.7%) in the reaction gas for the very low feeding rate (20 mg/min) of coal sample. The reaction gas was an air–nitrogen mixture. The residence time was controlled by adjusting the flow rate of nitrogen while fixing the flow rate of air in the reaction gas. This also varied the oxygen concentration in the reaction gas. The flow rate of the air in the reaction gas was set to be 0.24 SLPM (standard liter per minute), which was 50% more than necessary for complete combustion of coal. The flow rate of the coal carrier gas was set to maintain the same velocity as the reaction gas in the reactor. The flow rate of nitrogen in the reaction gas was equal to the total gas flow rate minus the air and the carrier gas rates in the reactor.

Under these conditions, the Reynolds number of the gas flow inside the reactor was below 50, which ensured a laminar flow. Calculation of the terminal velocity (<0.1 m/s) and Stokes number (<1) of coal particles indicates that coal particles were entrained in the gas stream and have the same residence time as the stream.

## *Char Analysis*

The carbon content of the char particles was determined using a hot foil loss–on–ignition instrument (FERCO, HF400). Using ash as a tracer, which assumes conservation of the ash in the char before and after the reaction, the corresponding conversion $X$ was calculated as

$$X = \left(1 - \frac{(Carbon\ Content)_{char} \cdot (Ash\ Content)_{coal}}{(1-(Carbon\ Content)_{char}) \cdot (Fixed\ Carbon\ Content)_{coal}}\right) \cdot 100\% \quad (1)$$

The surface area and pore size distribution of the char particles were measured by gas adsorption analysis using a surface area and porosimetry analyzer (Micromeritics, ASAP 2010) with $N_2$ as

adsorptive gas at 77 K (liquid nitrogen bath). Each sample was degassed under 10 μm Hg pressure and 350 °C for 2 hours in order to remove moisture before the analysis. The surface area was calculated using the BET (Brunauer–Emmett–Teller) method. The pore size distribution was calculated using the HK (Horvath–Kawazoe) model in the range of 8–20 Å and the BJH (Barrett–Joyner–Halenda) model in the range of 20–2000 Å.

Microimages of the char and ash particles were captured using a scanning electron microscope ((FEI Nova nano) equipped with an Everhart–Thornley detector under high vacuum mode. The accelerating voltage was 10–15 kV and the working distance was 5 mm. Particles were adhered to the sample holder using silver paste as conductive base.

## Coal Ash Deposition Experiments (Subtask 11.3)

The coal ash deposition experiments included both subbituminous and bituminous coals under both oxidizing and reducing conditions, as indicated in Table 3. The deposit data derive from an experimental design developed previously at Sandia National Laboratories and largely replicated at BYU. The essential features of the experiment appear in Figure 6. Deposits accumulate on a probe at the exit of the multifuel reactor/combustor where (at BYU) stoichiometries can vary from gasification to combustion conditions. A tube in cross flow collects deposit material as it slowly rotates, with probe surface temperature monitored by thermocouple, deposit surface temperature measured optically, and deposit thickness monitored by a triangulation laser device. Air cools the probe at known flow rates and with measured change in temperature through the test section. Deposit mass can also be determined either by a cantilever probe mount from a dynamic scale (not illustrated) or by post mortem examination of the probe deposit. These data provide dynamic information on probe mass, porosity, thickness, and thermal conductivity. Thermal conductivity indicates a great deal about deposit structure that is difficult to quantify from SEM images or any other technique, especially with such highly structured but three dimensional systems.

**Table 3.** Equivalence ratios and fuel types used.

| coal | oxidizing | reducing |
|---|---|---|
| IL #6 1 | 0.92 | n/a |
| IL #6 2 | 0.73 | 2.33 |
| PRB | 0.71 | 3.10 |

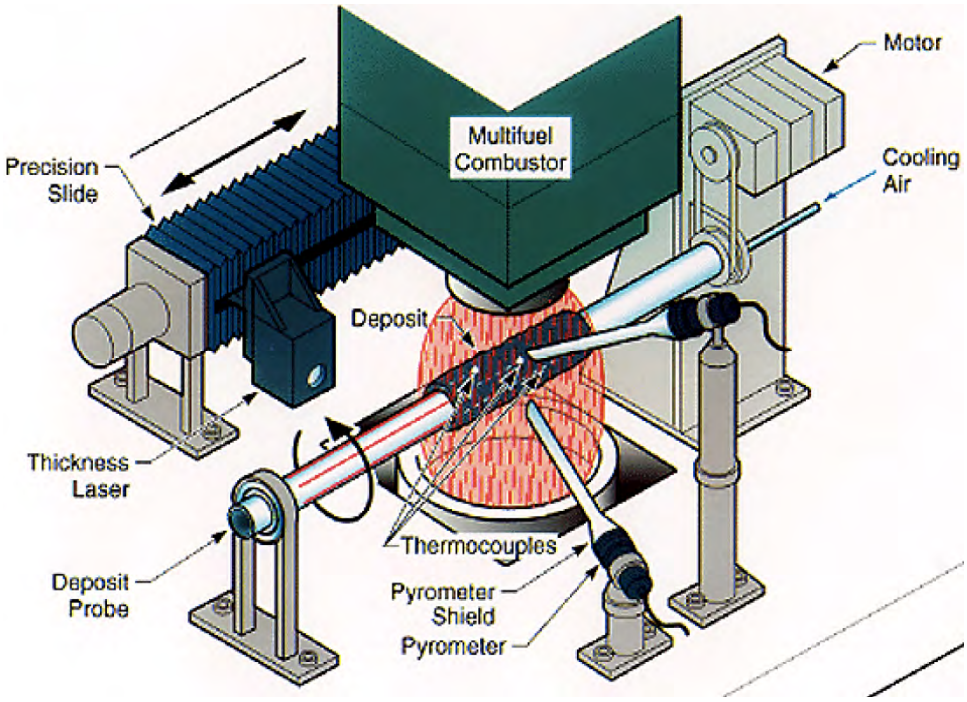


**Figure 6.** Essential experimental features of the coal experiments.

# RESULTS AND DISCUSSION

Experimental and modeling results of the gasification research program are presented by subtask in the sections below.

## Subtask 10.1 – Investigation of Pressurized Pyrolysis and Char Conversion

### *PFFB Experiments*

Experiments have been conducted on a Wyodak subbituminous coal. The mass-mean Wyodak particle size was determined to be 77 microns using a Coulter Counter. The centerline temperature that was measured previously was corrected for radiation effects. The peak centerline temperature was 1368°C. The temperature inside the probe was also measured to verify that the nitrogen jets were quenching the sample (Figure 7). The burner was fueled with a $H_2/CH_4$/Air mixture with an equivalence ratio was 1.0747. The gas composition was estimated from an adiabatic equilibrium calculation to be 27.36% $H_2O$, 3.02% $CO_2$, 1.8% $H_2$ 0.06% $O_2$, and the remainder $N_2$. The tip of the collection probe was

4.75 inches above the burner face and the quench jets are ½ inch above the probe tip, which gives the particles a residence time of ~60 ms in the hot zone.

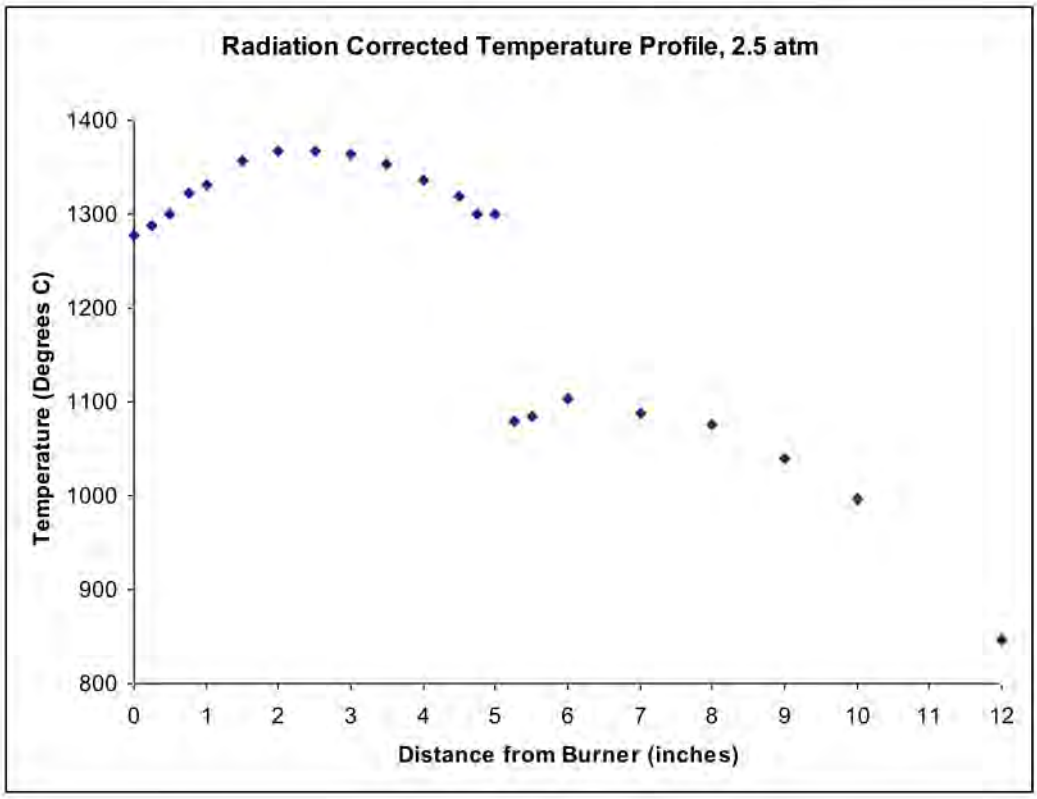


**Figure 7.** PFFB Temperature profile with quench occurring at ~5 inches.

Proximate analysis was performed for the Wyodak coal and ultimate analyses were performed for the coal and char (Table 4). The yield of char was very low due to periodic clogging of the feeder tube; future experiments may require changes to the feeding procedure or higher flow rates of entrainment gas. Ash tracer and elemental tracers (Al, Si, Ti) were used to calculate a mass release of 89.1% with a standard deviation of 1.5% on a dry, ash-free basis. Proximate analysis and CPD calculations suggest that only ~62% mass release is possible through devolatilization alone. Assumption of film-diffusion limited steam gasification (theoretical maximum rate) after 99% of the CPD-predicted devolatilization yields good agreement with the mass release vs. residence time, suggesting that this condition may be film-diffusion limited (Zone III) or nearly so for steam gasification. Further investigations will be conducted to verify whether this is the case. Catalytic properties of calcium in the ash may also play a part.

The bulk density of the coal and char was measured by the tap technique, and the apparent density was computed assuming a packing factor of 0.5. The density ratio of the char to the coal was

0.42, indicating large changes in density during this pyrolysis/gasification experiment. The $N_2$ surface area (representing macropores) was measured by the BET technique (Table 5). The value of ~360 $m^2/g$ is very high compared to previous work on bituminous coal chars. SEM images were obtained of the coal and the char (Figure 8 through Figure 10). The SEM figures are consistent with the high $N_2$ surface areas, in that a large number of pores are visible. No large voids are seen, as often observed in chars from bituminous coal pyrolysis experiments.

Char from the Wyodak coal was collected in a second experimental condition with extended residence time (18.25" above the burner, or ~220 ms) and the same gas flow rates. Enough char was collected to perform SEM analysis (Figure 11 through Figure 13). The chars from the higher residence time experiment appear very similar to those from the lower residence time experiment. A few of the particles in the 220 ms case showed signs that a small amount of softening and/or swelling occurred during pyrolysis (Figure 13). Char from the Wyodak coal was collected in a third experimental condition with lower residence time (2.25" above the burner, or ~30 ms) and the same gas flow rates. Analysis of the products is in process. Measurements of $CO_2$ reactivity with a pressurized thermogravimetric analyzer (PTGA) are being conducted on the char samples.

**Table 4.** Proximate and ultimate analyses of Wyodak coal and char

| Sample | Moisture (as rec'd) | Volatiles (daf) | Ash (dry) | C % (daf) | H % (daf) | N % (daf) | S % (daf) | O % (diff, daf) |
|---|---|---|---|---|---|---|---|---|
| Wyodak Coal | 16.30 | 50.8 | 5.8 | 72.2 | 5.4 | 1.0 | 0.6 | 20.8 |
| Wyodak Char, 2.5 atm, 60 ms | 2.00 | N/A | 33.1 | 92.5 | 1.2 | 0.9 | 0.4 | 5.1 |

**Table 5.** Density and surface area analyses of Wyodak coal and char

| Sample | Bulk Density (g/cc) | Apparent Density (g/cc) | $N_2$ (BET) Surface Area ($m^2/g$) |
|---|---|---|---|
| Wyodak Coal | 0.743 | 1.48 | N/A |
| Wyodak Char, 2.5 atm, 60 ms | 0.314 | 0.62 | 361, 355 (replicates) |

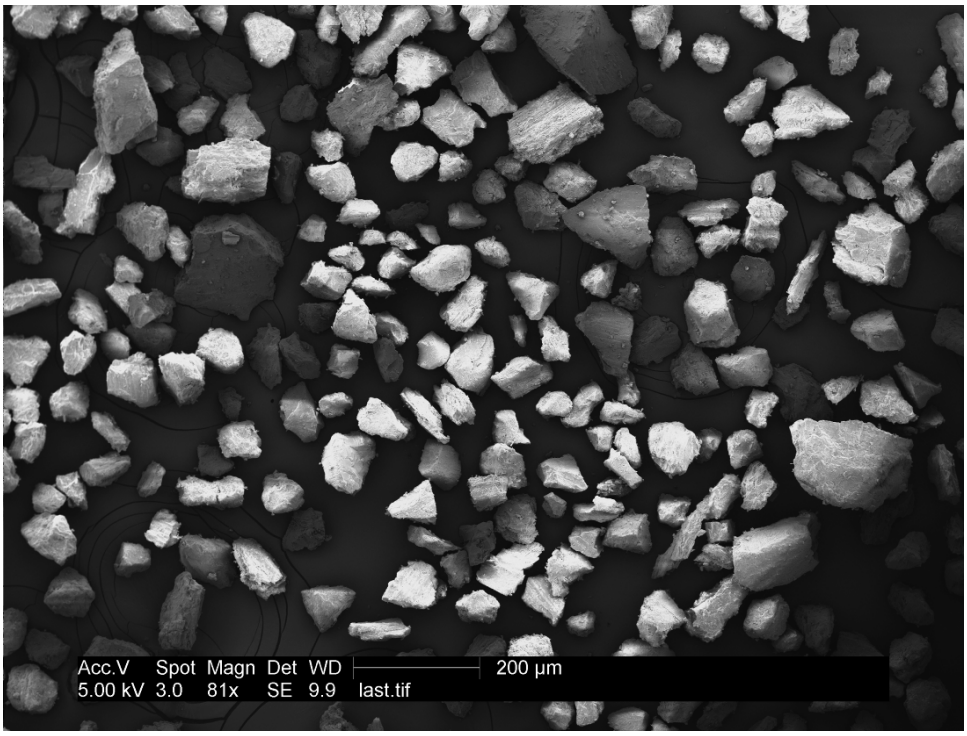


**Figure 8.** Wyodak Coal SEM.

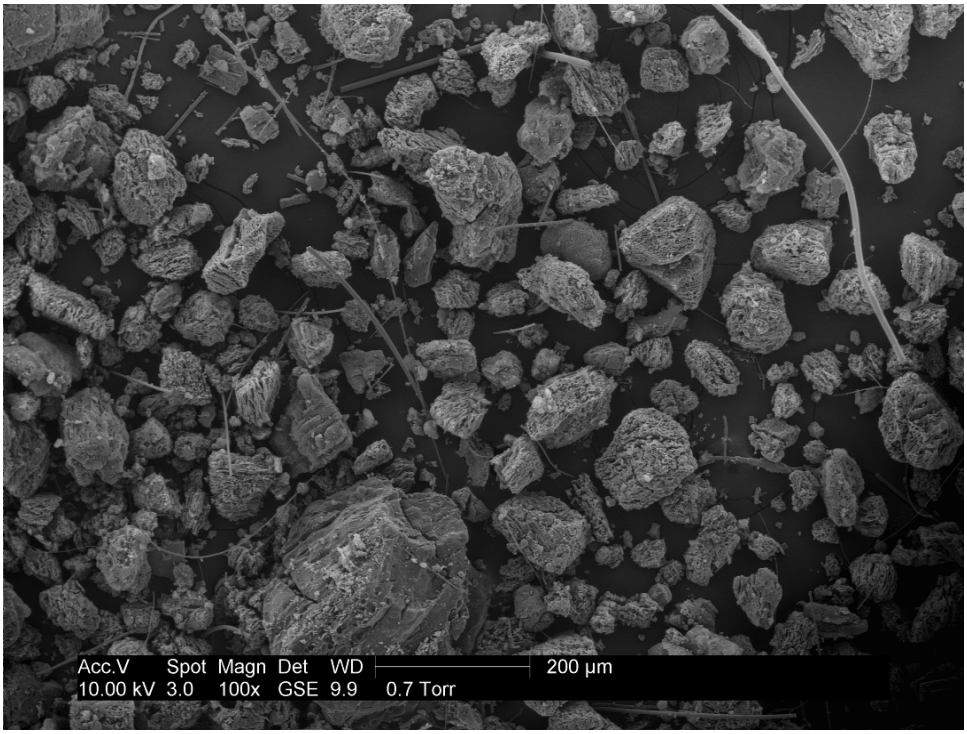


**Figure 9.** Wyodak Char produced at 2.5 atm, 60 ms.

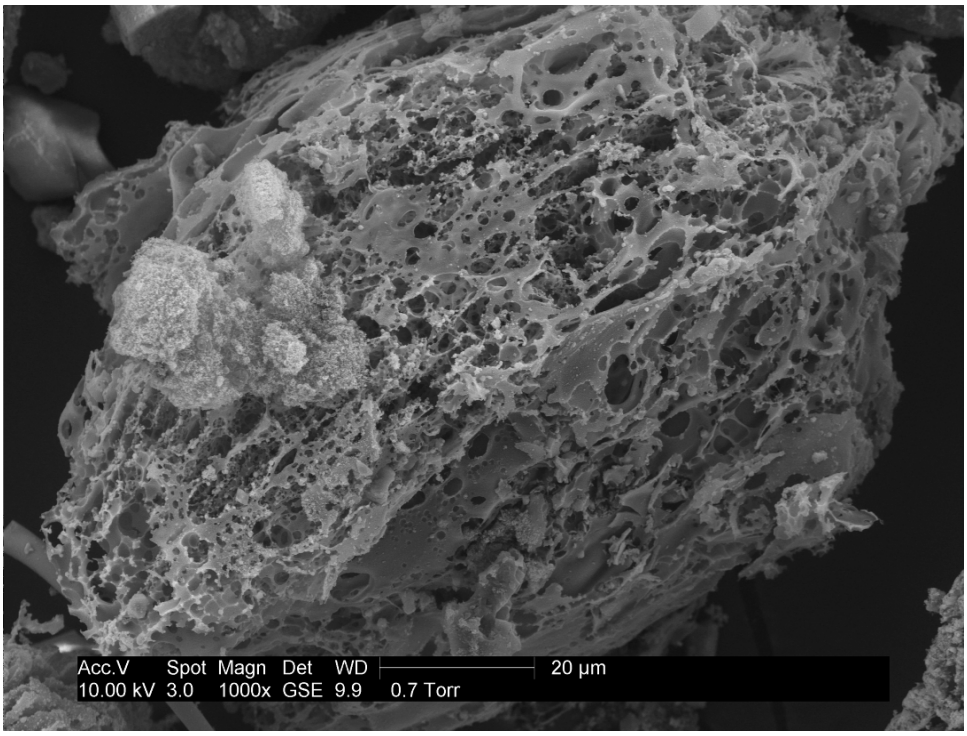


**Figure 10.** Wyodak Char particle produced at 2.5 atm, 60 ms.

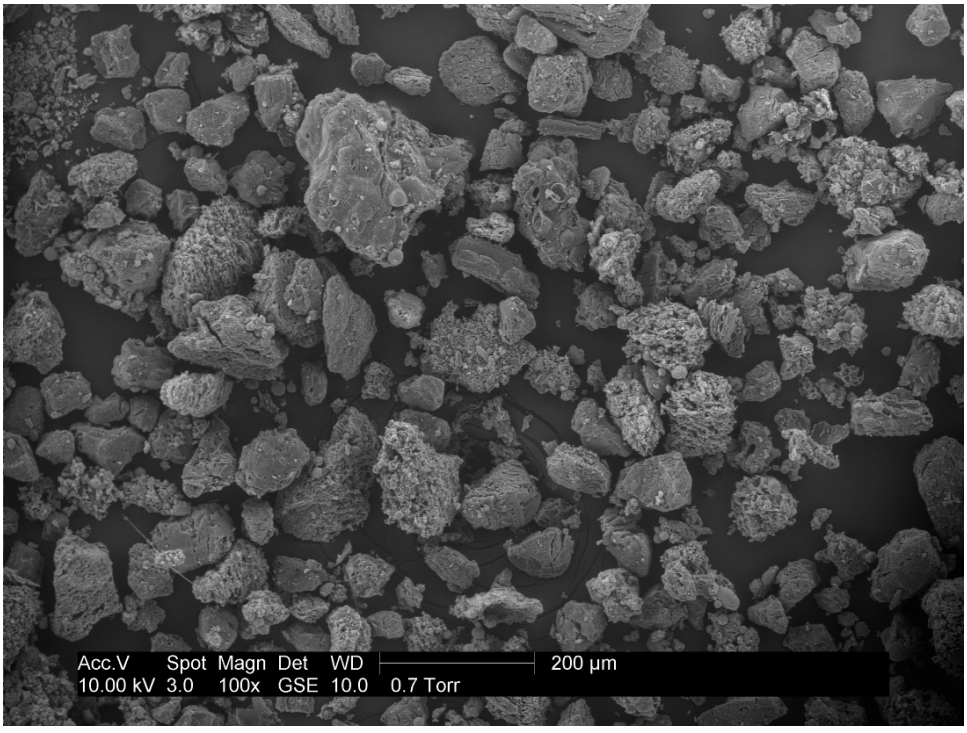


**Figure 11.** Wyodak Char produced at 2.5 atm, 220 ms.

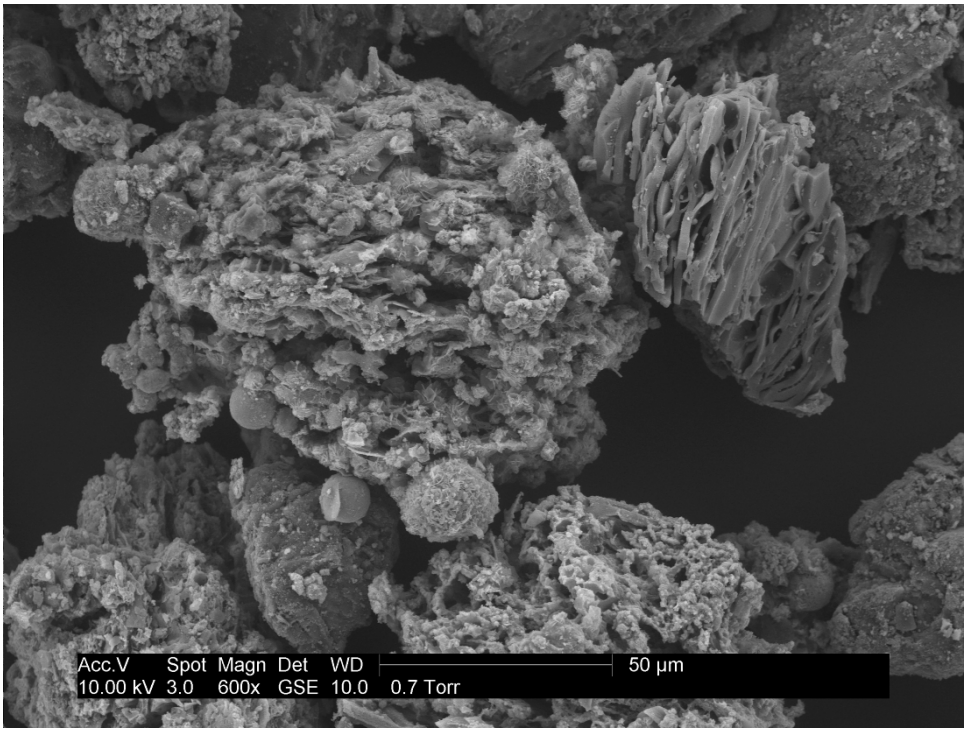


**Figure 12.** Wyodak Char produced at 2.5 atm, 220 ms.

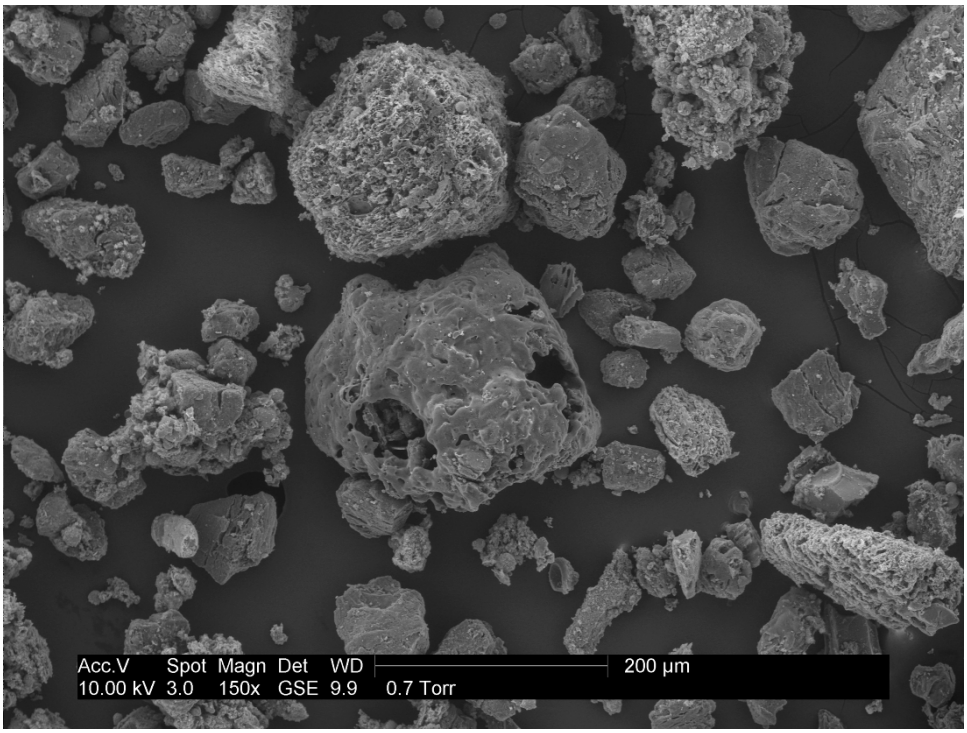


**Figure 13.** Wyodak Char produced at 2.5 atm, 220 ms.

## *Summary of PFFB Status and Capabilities*

In summary, the PFFB system is now operational, and its range of operating conditions is being extended through changes in fuel mixture and burner geometry. The PFFB system is capable of heating rates on the order of $10^5$ K/s, gas temperatures of 1200-1800 K, and pressures of 2.5-15 atm. These operating conditions are particularly well-suited to the study of the development of char structure and surface area during pyrolysis and gasification. The surface area and particle size available for gasification strongly influence the overall gasification rate. Heating rate has been observed to have a strong impact on the size and physical structure of chars at atmospheric pressure (Gale et al., 1995). The PFFB facility permits the investigation of particle size, structure, and intrinsic reactivity at high heating rates and pressures relevant to the gasification industry. Previous gasification studies have been performed in facilities with lower heating rates that produce chars that are highly swollen and not representative of chars produced in industrial facilities at ~$10^6$ K/s (Figure 14).

## *Summary of PFFB Wyodak Experiments*

Pyrolysis and char gasification experiments have been conducted with a Wyodak subbituminous coal at 2.5 atm, a peak flame temperature of 1640 K, and three residence times. Very little swelling of the coal occurred, and the chars are highly porous. The mass release due to gasification was large. Further analysis is being conducted on these chars and the soot produced. Measurements of char-$CO_2$ reactivity using PTGA have begun. Further experiments on this coal at higher pressures are ongoing and work with bituminous coals will immediately follow. This research will be continued as part of the tasks for the Center for Clean and Secure Energy (CASE).

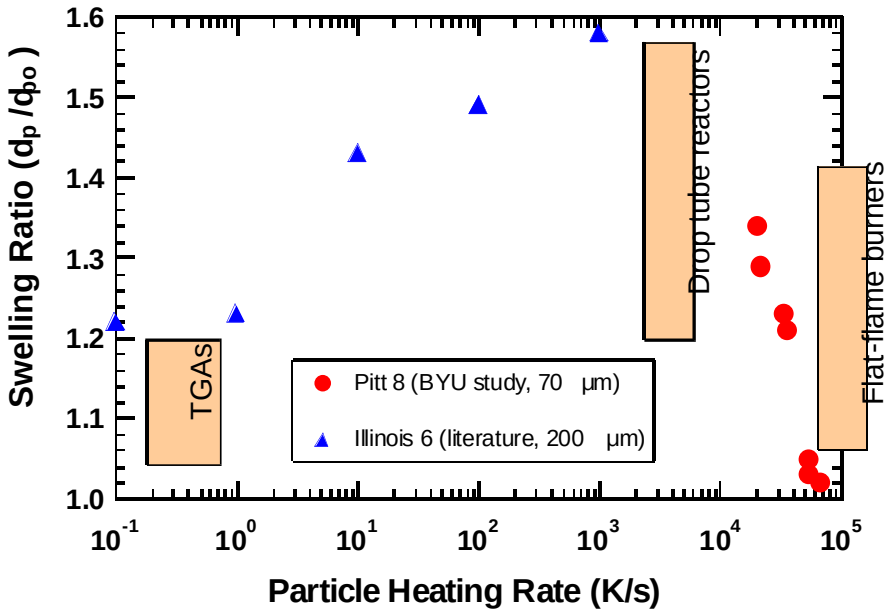


**Figure 14.** Effect of heating rate on particle swelling ratio, adapted from Gale et al. (1995).

## Subtask 10.2 – Investigation of Soot Formation during Gasification

### *Experiments with 2,6-dimethylnaphthalene*

The first model compound chosen was 2,6-dimethylnaphthalene because it was thought to be fairly representative of coal tar; it has two aromatic rings in a cluster with two aliphatic attachments. Much was learned about the chemical interaction of aromatic clusters in a previous study with pyrene and biphenyl as model compounds (Winans et al., 2007). 2,6-dimethylnaphthalene was chosen as the next model compound in order to study the effect of aliphatic attachments on soot formation chemistry. Unfortunately, 2,6-dimethylnaphthalene has a low melting point (108$^{o}$C) that made it very sticky and hence difficult to prepare and entrain. Experiments on the atmospheric flat-flame burner were conducted at several temperatures with this compound. It was difficult to find a condition with a yield of soot high enough for practical analysis and a temperature low enough to keep the aromaticity from growing too quickly. Since the aim of this research is to study the chemistry of soot development in the early stages, it is important to obtain polycyclic aromatic hydrocarbons (PAH) in the early stages of soot formation. Also, the $^{13}$C-NMR technique that has been used in these types of studies previously does not work well for very large aromatic structures due to conductivity issues.

Some FTIR and NMR data were obtained from the dimethylnaphthalene experiments (Figure 15 and Figure 16). However, not enough tar/soot was collected at the lower temperatures to make other

analyses possible and the decision was made to examine other model compounds. The FTIR spectra obtained were not of sufficient quality to be quantitative, but acetylene, methane, and naphthalene were identified in the spectrum. The NMR data shows that at a peak flame temperature of 1447 K the methyl groups had largely disappeared and $CH_2$ and/or CH groups had formed (Figure 15). By 1500 K these new aliphatic groups had largely disappeared. At about 1550 K the NMR spectra was too noisy to extract meaningful information due to conductivity of the large aromatic clusters. Another set of dimethylnaphthalene experiments was conducted at a peak flame temperature of 1425 K. Although the yield was very low (most of the products probably passed through the filters as a gas), enough tar/soot was collected for NMR analysis.

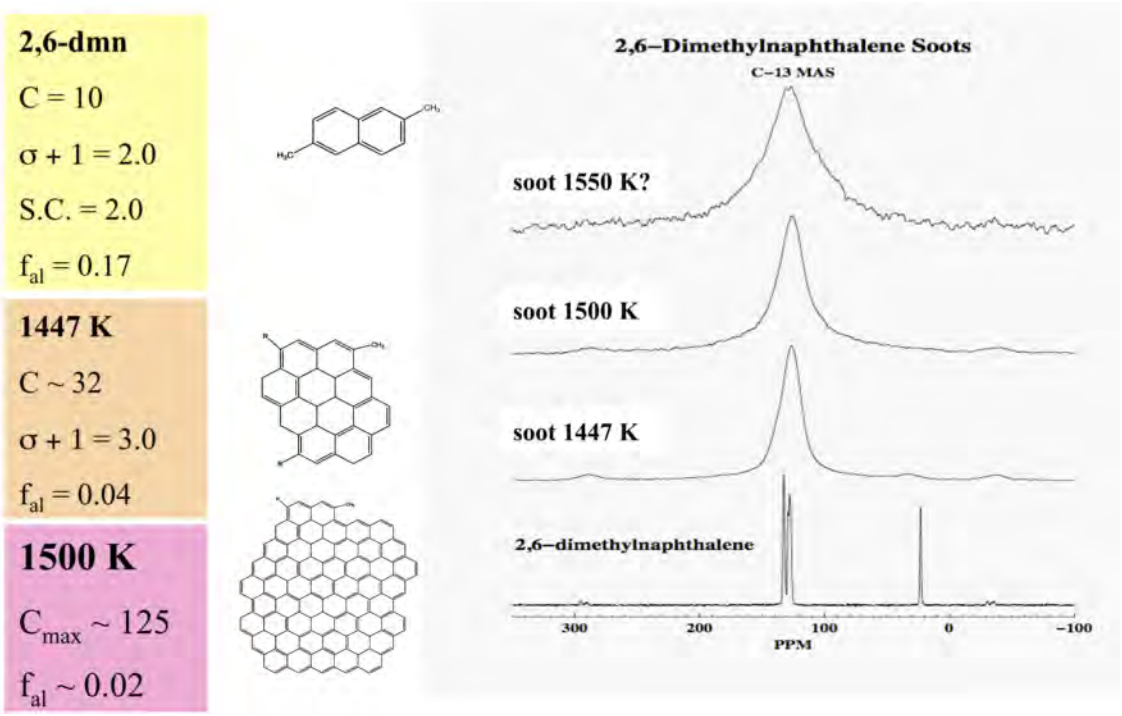


**Figure 15.** NMR spectra of soots produced on a flat-flame burner from 2,6-dimethylnaphthalene.

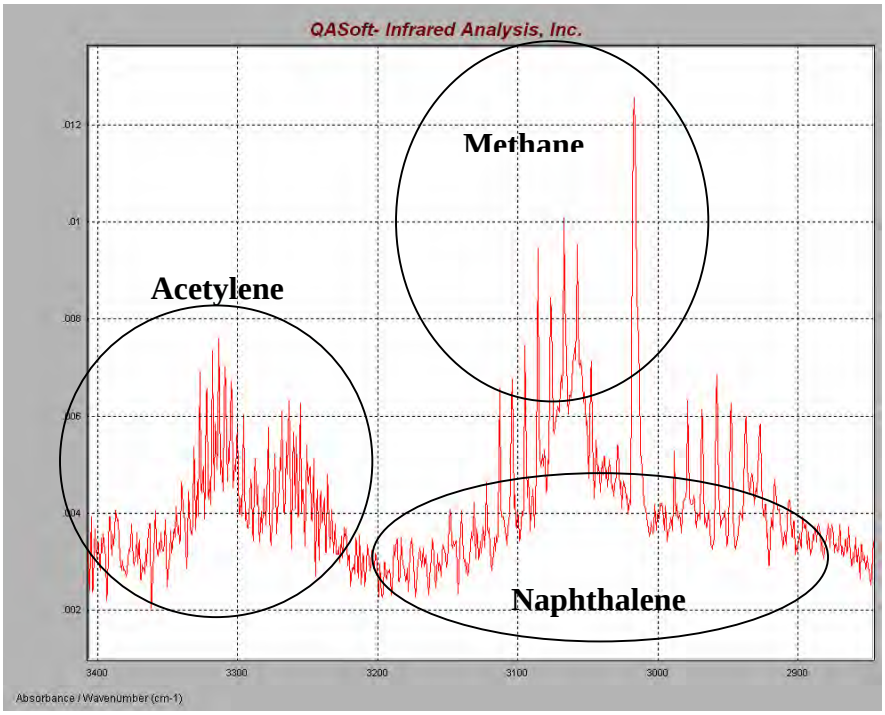


**Figure 16.** FTIR scan of 2-6-dimethylnaphthalene pyrolysis at ~1400 K.

## *Review of Tar Structure*

A review was conducted on previous experimental measurements of coal tar to allow for better selection of future model compounds. The chemical structure of coal tar differs significantly from the parent coal as evaluated by $^{13}$C-NMR (Watt et al., 1996; Perry et al., 2000). The average molecular weight of tar produced at atmospheric pressure is ~350 amu (Freihaut et al., 1989). The number of carbons per cluster and the cluster molecular weight are lower in the tar than in the parent coal due to the preferential evaporation of lighter constituents of the metaplast. The breakdown of bridges and side chains to form light gases causes the coordination number to decrease and the aromaticity to increase as the coal generates tar. At higher pressures the total tar yield and the average molecular weight of the tar decrease due to the vapor pressure effect; more of the large aromatic clusters remain in the metaplast. The cross-linking reactions that convert metaplast to char eliminate much of the aliphatic material. These reactions act on a larger reservoir of metaplast at higher pressures, leading to an increased yield of light gases.

A summary of measured tar properties (Perry et al., 2000) is quantitatively compared in Table 6. Based on these and other attempts to come up with a representative structure for tar, several characteristics become apparent. Aliphatic attachments are relatively short, 1-3 oxygen atoms will occur in most clusters, and nitrogen atoms will occur once in every 2-3 clusters. On average a tar molecule will

have 1-2 clusters of 3-4 rings each. Attempts to illustrate representative chemical structures are shown in Figure 17 based on the characteristics shown in Table 6.

**Table 6.** Average measured tar properties (Freihaut et al., 1989) with properties of suggested average tar molecules (Figure 17)

| Structural Parameter | Measured Average Range | Illustration A Values | Illustration B Values | Illustration C Values |
|---|---|---|---|---|
| Molecular Weight (amu) | 350 | 235 | 236 | 316 |
| Aromatic Rings | 3-4 | 3 | 3 | 4 |
| Carbon Aromaticity | 0.63-0.76 | 0.76 | 0.75 | 0.75 |
| Side Chains | ~2 | 2 | 2 | 2 |
| Bridges | ~2 | 2 | 2 | 2 |
| Carbon Mass Percent | 78%-82% | 87% | 81% | 76% |
| Hydrogen Mass Percent | ~4% | 7% | 6% | 4% |
| Oxygen Mass Percent | 5%-16% | 6% | 7% | 15% |
| Nitrogen Mass Percent | ~1.7% | 0% | 6% | 4% |
| Cluster MW (amu) | 240 - 290 | 235 | 236 | 316 |
| Attachments MW (amu) | 20-31 | 74 | 74 | 116 |

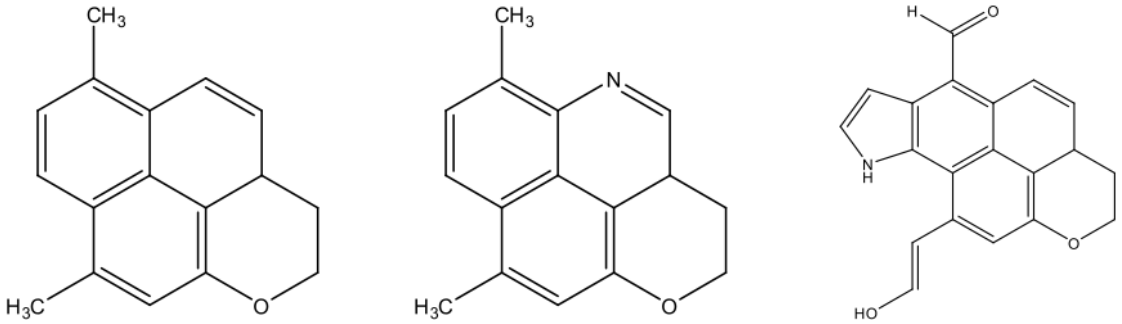


**A** **B** **C**

**Figure 17.** Illustrations A, B, and C (from left to right) of suggested average tar molecules.

### *Experiments with 6-(5H)-Phenanthridinone and Coal*

Several new compounds (see Figure 18) were selected for secondary pyrolysis studies based on this review after an extensive search through catalogs of chemical suppliers. The first of these is 6-(5H)-phenanthridinone. It has a higher molecular weight (195.22 amu) than the dimethylnaphthalene (156.22 amu) and the melting point is 291°C. 6-(5H)-phenanthridinone also contains oxygen and nitrogen, so its properties are closer to those of coal tar. Phenanthridinone has also proved easier to prepare and entrain in the atmospheric flat-flame burner than was the case with dimethylnaphthalene.

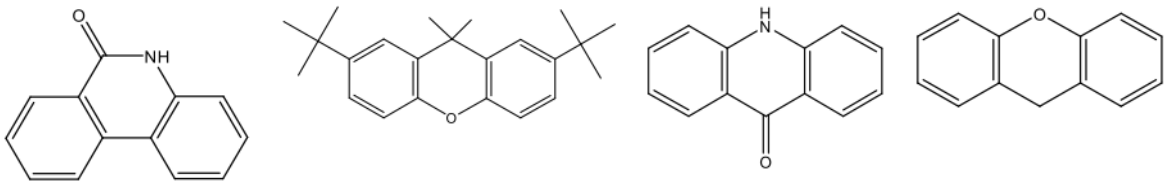


6-(5H)-phenanthridinone | 2,7-di-tert-butyl-9,9-dimethylxanthene | 9(10H)-acridone | xanthene

**Figure 18.** Proposed surrogates for coal tar in future soot formation studies.

The phenanthridinone was successfully pyrolyzed on the flat-flame burner at a peak flame temperature of 1450 K and a probe height of 1 3/8 inches. This experimental condition has a particle residence time of ~19 ms. A Wyodak subbituminous coal and an eastern bituminous coal were also pyrolyzed at the same conditions. This enables us to compare soot from real coal tar to soot produced from model compounds. The tar/soot products from the 1450 K experiments have been analyzed for both coals by $^{13}$C-NMR and further analyses on samples prepared at other temperatures are awaiting NMR instrument time for data collection.

FTIR scans of the gases produced during pyrolysis of these compounds were also obtained (Figure 19 through Figure 21). For the Phenanthridinone, the mass yields of gaseous species were 1.5% $CH_4$, 1.8% $C_2H_2$, and 1.2% HCN. For the Wyodak coal the mass yields of gaseous species were 2.8% $CH_4$, 5.8%$C_2H_2$, and 1.5% $C_2H_4$. For the eastern bituminous coal the mass yields of gaseous species were 2.9% $CH_4$, 3.4% $C_2H_2$, and 0.3% $C_2H_4$. For the Wyodak coal 30% of the nitrogen was released as HCN. For the eastern bituminous coal 32% of the nitrogen was released as HCN. No $NH_3$ was detected among the pyrolysis products for either coal. The elemental compositions of the phenanthridinone, the coals, and the soot produced from the phenanthridinone are shown in Table 7. Studies with phenanthridinone are being continued at different temperatures and residence times as part of the tasks for the Center for Clean and Secure Energy (CASE). Studies with this compound at elevated pressures will also be attempted now that the PFFB is operational (see Subtask 10.1).

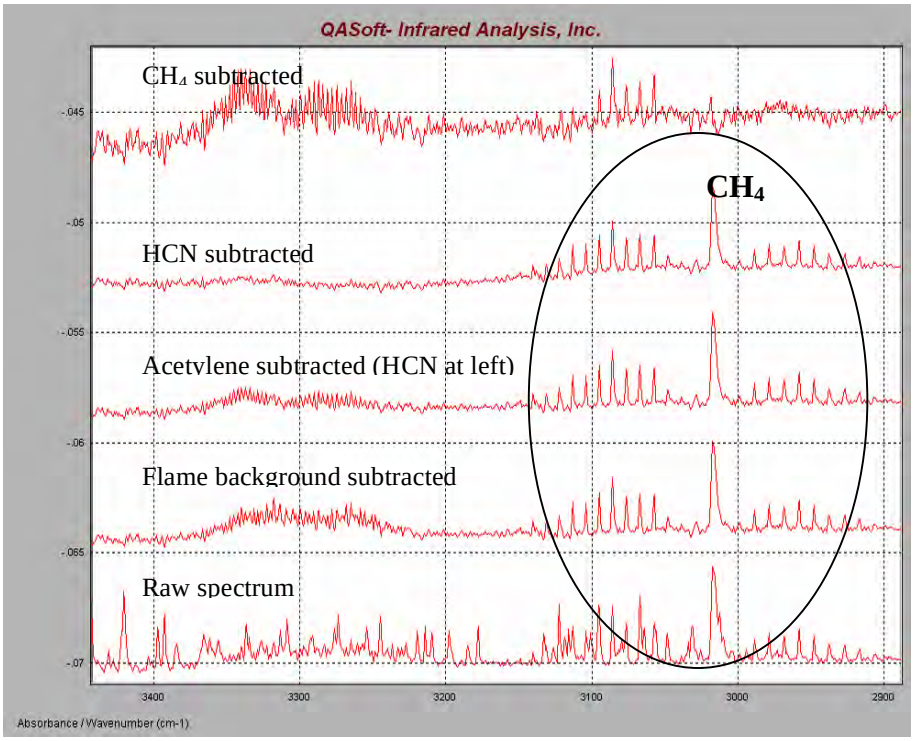


**Figure 19.** FTIR spectra of 6-(5H)-Phenanthridinone pyrolysis.

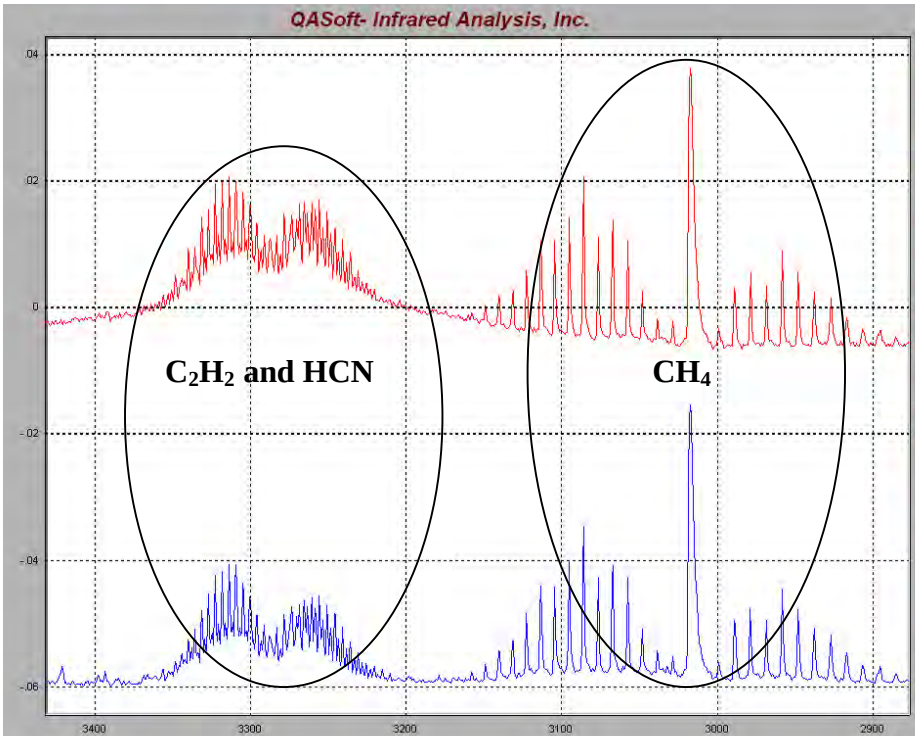


**Figure 20.** FTIR spectra of pyrolysis of eastern bituminous (top) and Wyodak (bottom).

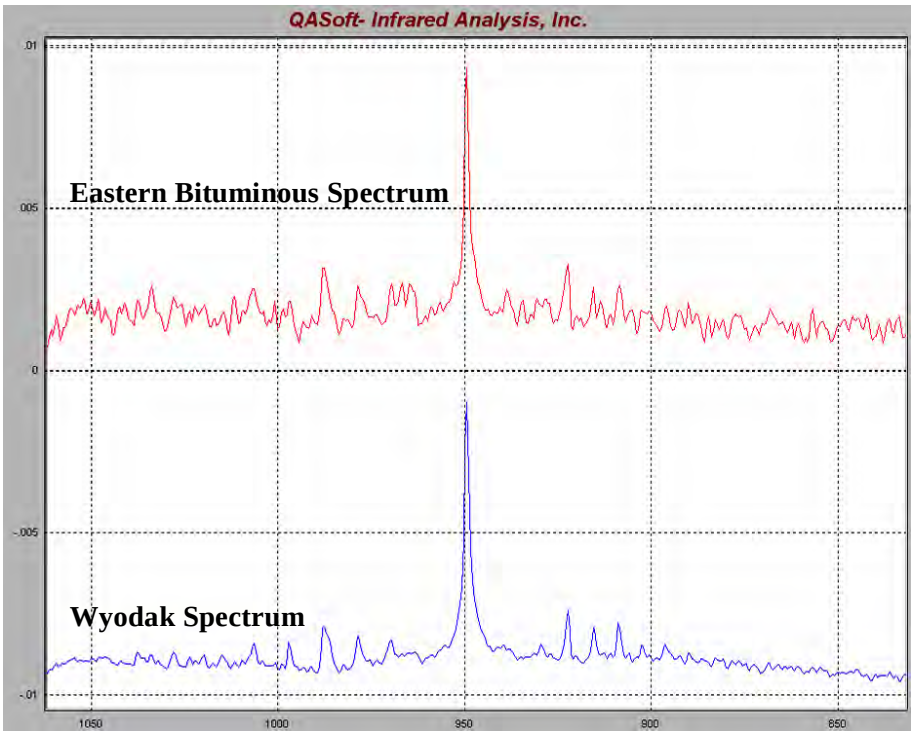


**Figure 21.** FTIR spectra of coal pyrolysis showing $C_2H_4$ peaks.

**Table 7.** Elemental Analysis (daf mass %) of model compound, soot, and coals.

| Sample | C | H | N | S | O (diff) |
|---|---|---|---|---|---|
| 6-(5H)-Phenanthridinone (exact formula values) | 80.0 | 4.6 | 7.2 | 0.0 | 8.2 |
| Phenanthridinone soot/tar (elemental analysis) | 78.9 | 3.8 | 5.9 | 0.0 | 11.4 |
| Wyodak subbituminous | 72.2 | 5.4 | 1.0 | 0.6 | 20.8 |
| Eastern Bituminous | 83.78 | 4.06 | 1.57 | 6.24 | 4.34 |

## *Summary of Model Compound Research*

The model compound 2,6-dimethylnaphtalene was studied as a precursor for soot in an atmospheric flat-flame burner. Information regarding changes in cluster size and aliphatic groups was obtained through $^{13}$C-NMR analysis and FTIR was used to obtain qualitative information about gaseous species that were formed. However, the yield of products at the optimum experimental temperature was too low to do more extensive analysis.

A review of coal tar characteristics was conducted to facilitate the selection of future model compounds. It was found that on average aromatic clusters in tar molecules contain at least one oxygen

atom. Nitrogen atoms occur once in every 2-3 clusters on average. Other characteristics such as cluster size and the number of attachments per cluster were quantified. New model compounds were selected based on these characteristics. 6-(5H)-Phenanthridinone was chosen for the first experiments because it has both oxygen and nitrogen. It was found that the phenanthridinone is much easier to work with than the dimethylnaphthalene and a much higher yield of products was observed.

Experiments with the model compound 6-(5H)-Phenanthridinone (PDN) were conducted on the atmospheric flat-flame burner. An eastern bituminous coal and a Wyodak subbituminous coal were subjected to the same experimental conditions. The tar and soot from the model compound and the two coals was collected for analysis. The yield of gas-phase species was determined using FTIR. The NMR data obtained on the PDN did not exhibit as much structural change as that observed in the coal data (see Figure 22). This is an unusual result and further consideration of the time/temperature profile will be made in order to understand the validity of these data. Further experiments on 6-(5H)-phenanthridinone at higher pressures and at different temperatures and residence times will continue as part of the tasks for the Center for Clean and Secure Energy (CASE).

An eastern bituminous coal and a Wyodak subbituminous coal were subjected to the same experimental conditions. The tar and soot from the model compound and the two coals was collected for analysis and are now awaiting the availability of NMR instrument time to complete the analyses.

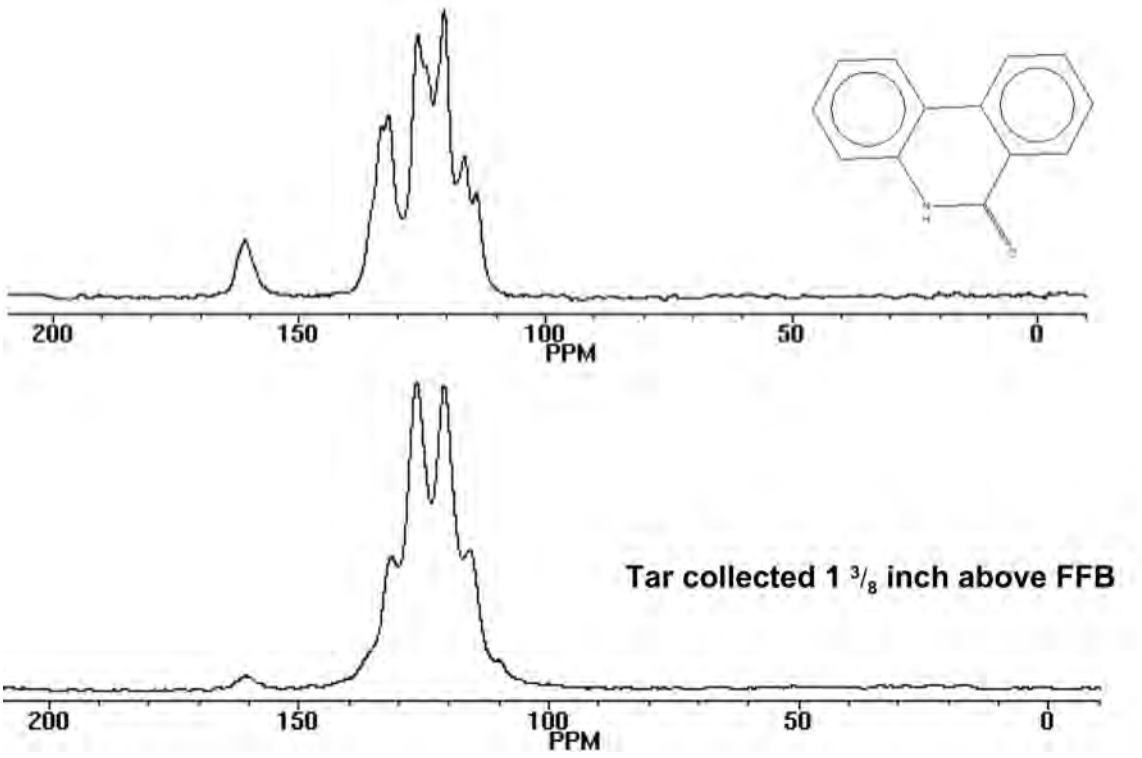


**Figure 22.** $^{13}C$ NMR spectra of phenanthridinone (PND, top) and tar produced at 1450 K, 19 ms.

## Subtask 10.3 – Investigation of Char Burnout

### *Carbon Content and Conversion*

The carbon contents and the carbon conversions of coal chars prepared under various reaction temperatures are plotted as a function of residence time in Figure 23 and Figure 24, respectively. The data points are the averaged result of three experimental runs. As expected, it took less time to reach the same carbon conversion at higher temperature than that at lower temperature. To test the reproducibility of the results, data points at 1200 °C were analyzed, and the absolute errors are plotted in the form of error bars in the figures. The relative error of the carbon content increased from around 4.3% to approximately 88% as residence time increased from 2.5 s to 6.0 s. The variations are mainly due to the variations in controlling the residence time using rotameters and are partially introduced by the use of ash tracer and the determination of carbon content using LOI. However, after converting carbon content into carbon conversion, this large relative error (88%) decreased markedly to 3%. This indicates that the reproducibility of the data is acceptable.

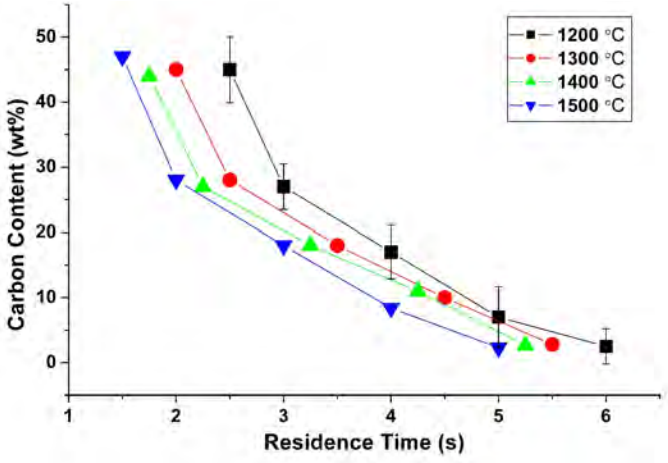


**Figure 23.** Carbon contents of chars prepared at different temperatures.

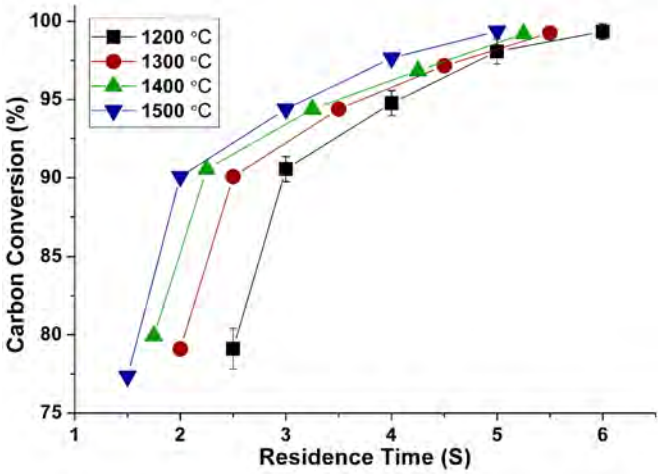


**Figure 24.** Carbon conversion of char particles prepared at different temperatures.

## *Surface Area*

Surface areas of fresh chars prepared at 1200, 1300, 1400 and 1500 °C are 41, 45, 49, 62 $m^2/g$, respectively. In order to allow comparison of samples prepared under different conditions and to follow the evolution of surface area during conversion, the normalized surface is used instead of the specific surface area. To normalize the data, the surface area per unit mass of oxidized char was divided by the surface area per unit mass of the fresh char prepared at the same temperature, which is defined as the initial surface area. In this manner, a normalized surface area larger than 1 denotes an increase in the surface area, whereas smaller than 1 indicates a decrease.

The surface area profile of the oxidized char particles at various temperatures is plotted versus carbon conversion in Figure 25. For all four temperatures, the normalized surface areas decrease with conversion and fall below the initial surface area at around 90% conversion. This trend is consistent with observations from other researchers (Simons, 1983; Hurt et al., 1991).

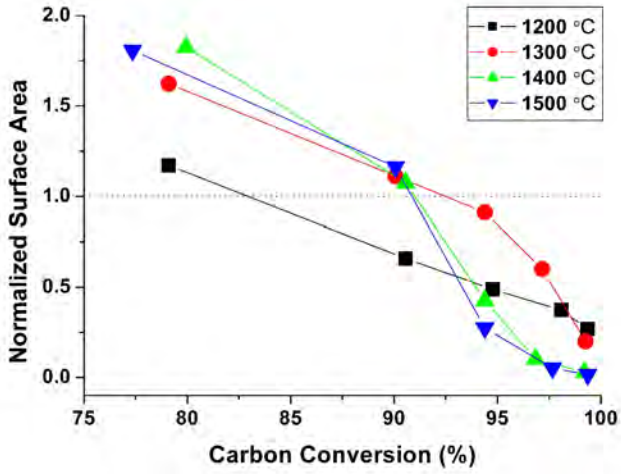


**Figure 25.** Evolution of surface area per unit mass of char at various temperatures.

However, remarkable differences exist in the surface area profile at high conversion (above 90%). The normalized surface areas decrease more rapidly at higher temperatures than those at lower temperatures. In particular, the normalized surface areas of chars undergoing conversion at 1400 and 1500 °C eventually fall below those at 1200 and 1300 °C. This indicates that temperature has an effect on the surface area of the char at high conversion.

To further illustrate this phenomenon, the normalized surface areas are evaluated on ash free basis (surface areas of pure ash prepared at 1200 and 1400 °C are 1.8 and 1.4 $m^2/g$, respectively), i.e., per unit mass of residual carbon in the char. The surface evolution is presented in Figure 26 for comparison. The difference in the surface area evolution at high conversion is much clearer in Figure 26. The surface areas of char particles oxidized at 1200 and 1300 °C keep increasing, while those of char particles oxidized at 1400 and 1500 °C start to decrease and fall below the initial surface areas. In addition, the surface area of char oxidized at 1500 °C decreases faster than that at 1400 °C. Liu et al. (2006) attributed the decrease of char surface area at high temperatures to ash melting, which closed the pores of the char resulting in an inaccessibility of the pores to adsorptive gas. Lin et al. (1994) also pointed out that the ash melting contributes to the decrease in the surface area of micropores and mesopores, especially at high conversion because the ash content increased with increasing conversion. The Illinois # 6 coal used in this study has an ash fluid temperature of 1343 °C, which is above 1200 and 1300 °C and below 1400 and 1500 °C. Therefore, the decrease in the surface areas of char particles at 1400 and 1500 °C in Figure 5 indicates melting of ash minerals in the char.

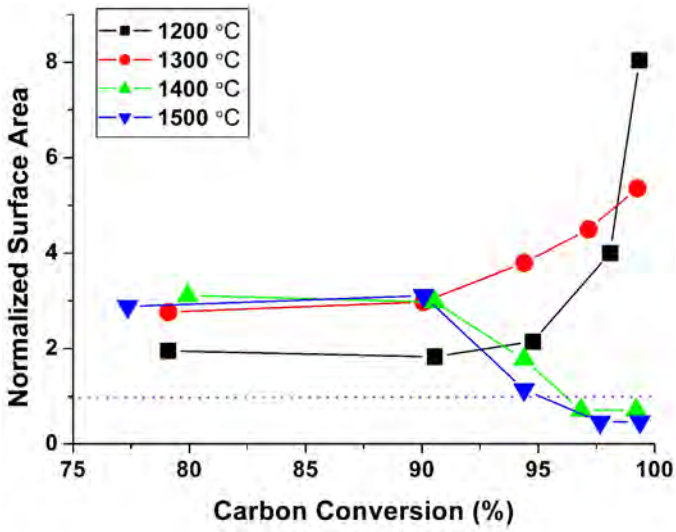


**Figure 26.** Evolution of surface area (ash free) of chars at various temperatures.

The melting of ash minerals and consumption of carbon in the char resulted in a substantial structural change: the transition from porous char to molten, low-porosity slag. In order to better understand how the char structure changes during the transition from char to slag, the samples were analyzed using SEM.

### *SEM Images*

SEM images of chars prepared at 1200 °C (below ash fusion temperature) and 1400 °C (above ash fusion temperature) are presented in Figure 27 and highlight important structural and morphological features during the transition.

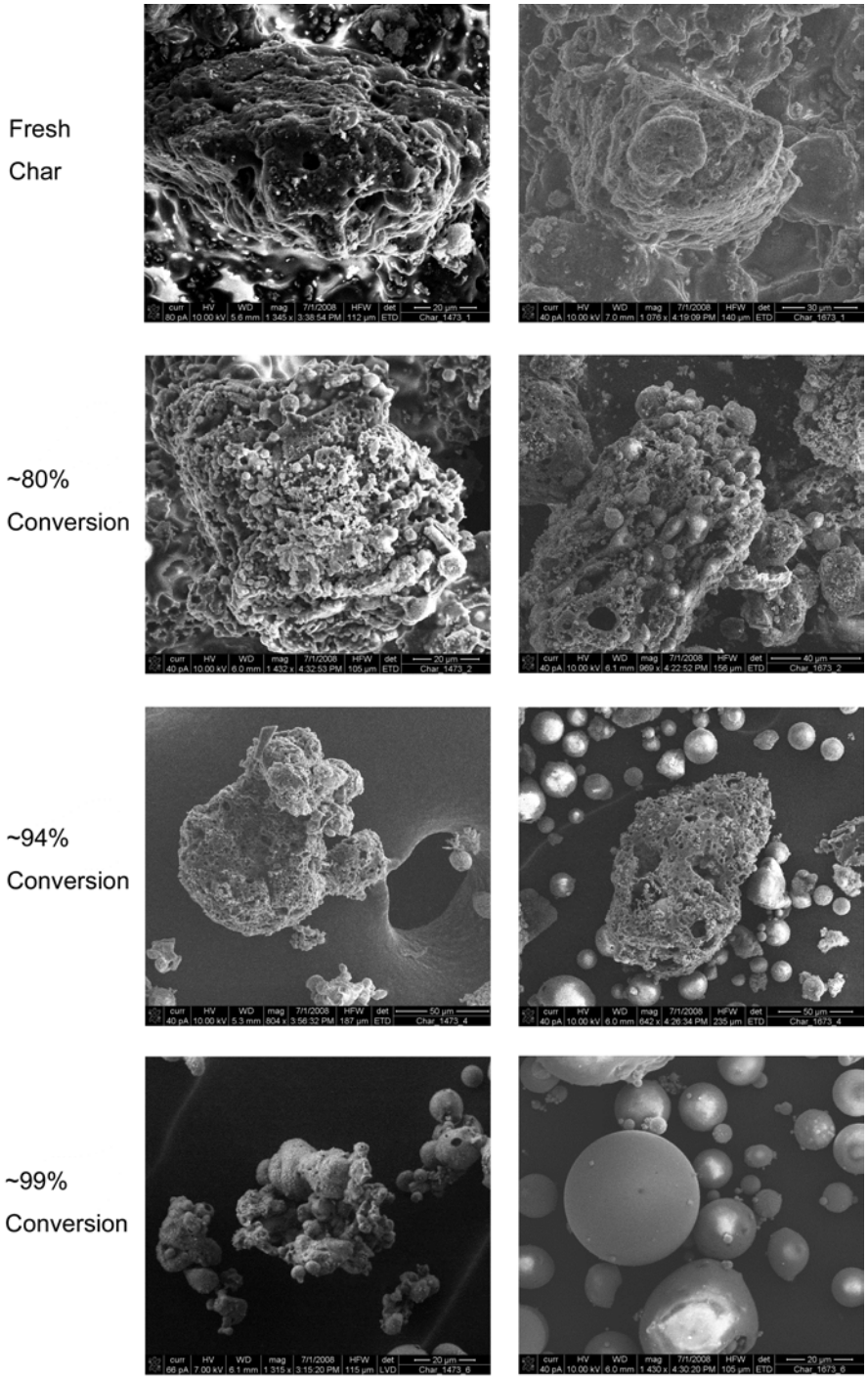


**Figure 27.** SEM images of char particles: left, 1200 °C; right, 1400 °C.

The images of char reacted at 1200 °C do not show significant change throughout conversion. It can be observed that the fresh char has a porous structure. The char oxidized to 80% conversion still looks porous. Although some mineral grains can be seen on the char surface, the non-spherical shape

suggests that they were not melted. The unmelted minerals are unlikely to close the micropores and mesopores in the carbon, which create the surface area of the char. Therefore, the char still has relatively high surface area. As conversion increased to about 94% and 99%, most of the carbon in the char was consumed and the char transformed to ash particles. These ash particles did not melt throughout the oxidation process at 1200 °C, as indicated by their rough surface and irregular shape. This agrees with the results in Figure 26 that surface areas of the char oxidized at 1200 and 1300 °C do not decrease.

In contrast, the images of char oxidized at 1400 °C show significant change throughout the oxidation process. The fresh char has a porous structure, similar to that of the char prepared 1200 °C. However, at around 80% conversion, some melted (as indicated by the droplet shape) mineral grains started to appear on the char surface. As conversion increased to about 94%, lots of melted mineral droplets (molten slag) can be observed while some porous char still exists. The melted minerals presumably have a tendency to close the micropores and mesopores in the carbon. The closing of micropores and mesopores in the carbon resulted in the decrease of surface area as shown in Figure 26. As conversion increased to about 99%, the material appears to have completely melted, as indicated by its smooth surface and spherical shape. The melted material can be classified as molten slag due to its smooth surface and solid structure. Consequently, the transition from porous char to molten slag at 1400 and 1500 °C is responsible for the sharp decrease in the surface area at around 90% conversion observed in Figure 26.

### *Char–slag Transition*

Wu et al. (1999, 2000) concluded that fragmentation plays a key role in the formation of large amounts of fine ash particles in the early and middle stage of pulverized coal combustion, while coalescence of included minerals results in the formation of coarse ash in the later stage of combustion, depending on the structure of the char. Baxter (1992) found that the fragmentation of bituminous coal char is strongly dependent on the size of the particle. Large char particles (above 80 μm) have a much higher tendency to fragment than small particles (below 20 μm). Based on these studies, the char-slag transition process can be described in three stages as follows.

The mineral grains that appeared on the surface of char with 80% conversion at 1400 °C are included minerals because all the minerals in the char after devolatilization can be classified as included minerals. These included minerals did not appear on the surface of the devolatilized char and low-conversion char because there was still sufficient residual carbon in the char to encapsulate the minerals. This is the initial stage of the transition. However, at intermediate to intermediate-high conversion (~80%), more residual carbon in the char was consumed and there was not sufficient residual carbon to encapsulate the minerals. Thus the minerals started to expose on the external surface of the char in the form of melted ash minerals due to the high temperature. The less residual carbon in the char, the more

included minerals become exposed on the char surface. This is the middle stage of the transition. At high conversion (~94%), the residual carbon in the char was consumed further and was insufficient to support the entire char structure. Consequently, fragmentation occurred and released a large amount of small char particles and molten slag particles. At very high conversion (>99%), there was almost no residual carbon in the char and the included minerals in the small particle coalesced to form large ash particles. This is the final stage of the transition.

### *Effect of Temperature and Residual Carbon on Char–slag Transition*

On the basis of the analyses of surface area evolution and SEM images, the effect of temperature and residual carbon on the char–slag transition is summarized as follows. At temperatures below ash flow temperature, porous char transforms to unmelted ash particles in the later stage of coal oxidation. At temperatures above ash flow temperature, porous char transforms to molten slag in the later stage of coal oxidation. The transition is expedited by increasing the heating temperature. The difference in the form (unmelted ash versus molten slag) of the minerals is due to ash fusion effect. The transitional point is determined by the residual carbon content in the particle. In particular, the transition starts when the residual carbon in the particle cannot encapsulate the included minerals and the minerals become exposed on the receding surface of the particle.

### *Indication of Char–slag Transition Char Conversion*

The middle stage of the char–slag transition plays a key role in affecting char conversion because of the melted minerals exposed on the char surface. The effect of char-slag transition on char conversion seems to be twofold: (1) Char particles in the middle stage of transition have a higher tendency to stick when impacting the deposition surface. Once these char particles stick on the impacting surface, their residence time is greatly increased and conversion is increased accordingly. (2) The included minerals exposed on the char surface can prevent oxidizing gas from diffusing into the porous char, decreasing the conversion. For example, the residual carbon in the slag particle (99% conversion and 1400 °C in Figure 27) is completely encapsulated by melted minerals. The low particle porosity makes the heterogeneous reaction of encapsulated carbon with oxidizing gas almost impossible.

### *Comparison with Pore Model*

Kantorovich et al. (1994) reviewed various pore models. They pointed out that the models most suitable for describing the surface features are the continuum models based on a random pore structure. These models can be divided into two categories: randomly overlapping pore model (Bhatia and Perlmutter, 1980; Gavalas, 1980; Bhatia and Perlmutter, 1981) and randomly intersecting non-overlapping pore model (Kantorovich and Bar-Ziv, 1994a; Kantorovich and Bar-Ziv, 1994b). The

randomly overlapping pore model is selected to compare with experimental data at 1200 and 1400 °C in this study.

The surface area evolution is expressed by the randomly overlapping pore model (Bhatia and Perlmutter, 1981) as

$$S_v / S_{v0} = (1-X)\sqrt{1-\psi \ln(1-X)} \tag{2}$$

in which $S_v$ and $S_{v0}$ are surface area at conversion $X$ and initial surface area per unit volume of particle, respectively. According to Feng and Bhatia (2003), the equation above can be rewritten as

$$S_X / S_0 = \sqrt{1-\psi \ln(1-X)} \tag{3}$$

where $S_X$ and $S_0$ are surface area at conversion $X$ and initial surface area per unit mass of residual carbon, respectively. That is, $S_X / S_0$ is equal to the normalized surface area evaluated per unit mass of remaining carbon in Figure 26. $\psi$ is the dimensionless structural parameter determined by

$$\psi = \frac{4\pi L_0}{\rho_0 S_0^2} \tag{4}$$

where $L_0$ is the pore length per unit mass of remaining carbon of the devolatilized char and $\rho_0$ represents the true density of remaining carbon, usually taken as 2.2 g/cm$^3$. In this study, $L_0$ was calculated from pore volume distribution (Figure 28) obtained by $N_2$ adsorption.

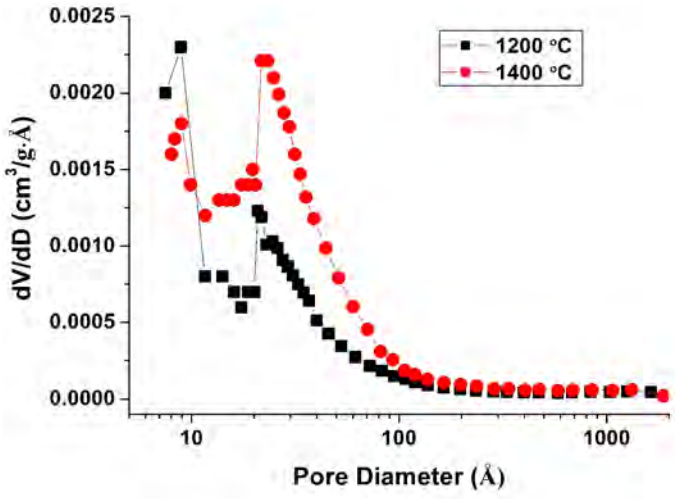


**Figure 28.** Pore volume distribution of chars devolatilized at 1200 and 1400 °C.

While the randomly overlapping pore model and the BJH method utilize cylindrical pore geometry, the HK method assumes slit pore geometry in calculating the pore size distribution. Recognizing this fact, we used the same method taken by Feng and Bhatia (2003) to convert the slit width into an equivalent cylindrical diameter. This conversion yields the slit width being equal to the pore radius, which provides the same surface area per unit pore volume. The pore characteristics for calculating $\psi$ of devolatilized chars using equation (4) are listed in Table 8.

**Table 8.** Structural parameters of devolatilized chars.

| Parameter | 1200 °C | 1400 °C |
|---|---|---|
| $L$ (m/g) | $1.6 \times 10^{10}$ | $1.7 \times 10^{10}$ |
| $\rho$ (g/cm$^3$) | 2.2 | 2.2 |
| $S$ (m$^2$/g) | 41.2 | 49.3 |
| $\psi$ | 52.6 | 39.5 |

The normalized surface areas determined by equation (3) are plotted as a function of carbon conversion $X$ in Figure 29 for comparison with experimental data. At 1200 °C, the randomly overlapping pore model predicts the same trend of the surface area evolution as the measured data, although it overestimates the surface area. The over-estimation of the surface area is caused by the large $\psi$ value calculated by Equation 4. Feng and Bhatia (2003) found that for fresh chars, the $\psi$ values calculated from Equation 4 were much larger than those determined by fitting the surface area plot. They also found that for low conversion (15–20%) chars, the values of $\psi$ calculated from Equation 4 were closer to those determined by fitting the surface area plot. They attributed this phenomenon to the closed micropores in fresh chars and the re-opening of these micropores in initial reaction. Morimoto et al. (2006) calculated the $\psi$ values at various conversions during $CO_2$ gasification and found that the $\psi$ values decreased dramatically with conversion. They suggested that the calculation of structural parameter $\psi$ should be modified. Therefore, the re-opening of closed micropores during initial reaction should be considered and the low conversion char (15-20%) can be used in the calculation of structural parameter $\psi$ for better predicting the surface area evolution using Equation 3 at temperatures below ash flow temperature.

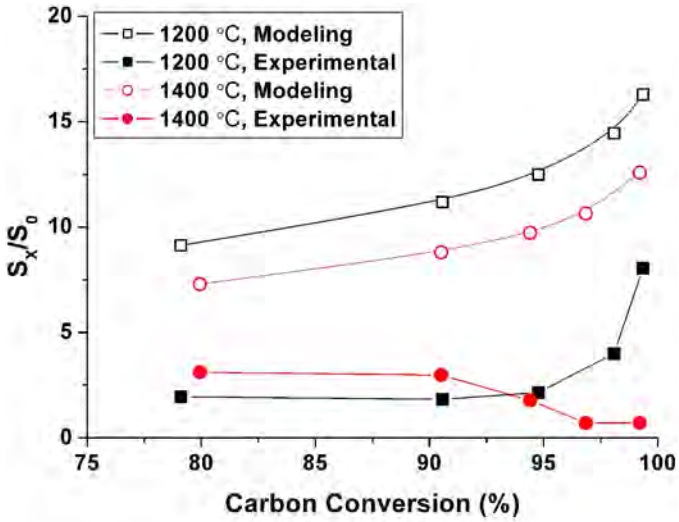


**Figure 29.** Comparison of experimental and modeling results of the surface area evolution at 1200 and 1400°C.

As shown in Figure 29, at 1400 °C, the randomly overlapping pore model does not predict the dramatic decrease in the surface area at high conversion. At high conversion, the structure of the char has changed substantially due to the shrinkage, fragmentation and high ash content of the char, which were not considered by the randomly overlapping pore model. In particular, the melted minerals that exposed on the char surface prevented adsorptive gas diffusing into the pores of char particle by closing some pores in the char. Therefore, the partial coverage of the char surface by melted minerals and the blockage of pores by melted minerals need to be included in the randomly overlapping pore model for predicting surface area at high conversion and temperatures above ash flow temperature.

The comparison between modeling result and experimental data suggests that the randomly overlapping pore model cannot be applied to predict the surface area evolution at high conversion without considering the reopening of micropores at initial reaction and the ash fusion effect.

## Subtask 11.1 – Coal Selection and Characterization

The four coals chosen for the experimental work are Pittsburgh #8, Illinois #6, Black Thunder PRB and Beulah Zap lignite. Typical proximate and ultimate analyses of these fuels, as well as the heating value, are presented in Table 9. Due to the cost of transporting and pulverizing these fuels, it was impractical to get large quantities of all fuels at once. Rather, the experimental teams will work with existing inventories of these fuels and will have these coals subjected to proximate, ultimate and heating value analyses. These fuels will be targeted for follow-on research programs as well. During subsequent

studies, it may be necessary to procure large inventories of particular fuels for testing in the University of Utah's large-scale facilities. When new coal is procured it will be analyzed in a similar manner and records will be kept for the various coals.

**Table 9.** Target fuels with typical proximate, ultimate and heating value analyses.

| **Coal** | **Pittsburgh #8** | **Illinois #6** | **Black Thunder** | **Beulah Zap** |
|---|---|---|---|---|
| **Coal Type** | Bituminous | Bituminous | Sub-Bituminous PRB | Lignite |
| **Proximate Analysis** | | | | |
| Moisture (wt% of as-received fuel) | 1.08 | 2.54 | 21.30 | 26.89 |
| Ash (wt% dry) | 9.00 | 12.33 | 6.46 | 13.86 |
| Volatile matter (wt% dry) | 38.22 | 39.40 | 54.26 | 42.78 |
| Fixed carbon (wt% dry) | 52.64 | 48.28 | 39.28 | 43.36 |
| **Ultimate Analysis** (wt% dry ash-free) | | | | |
| Carbon | 84.07 | 78.91 | 74.73 | 70.49 |
| Hydrogen | 5.58 | 5.50 | 5.40 | 4.75 |
| Nitrogen | 1.53 | 1.38 | 1.00 | 1.22 |
| Sulfur | 3.86 | 4.00 | 0.51 | 2.14 |
| Oxygen | 4.96 | 10.09 | 18.27 | 21.36 |
| Chlorine | n/a | 0.11 | 0.08 | 0.05 |
| **Heating Value** | | | | |
| HHV, dry (Btu/lb) | 13,859 | 12,233 | 12,815 | 10,040 |

## Subtask 11.2 – Modeling of Coal Ash Sintering and Melting

Figure 30 illustrates the geometries used to define the terms in this sintering discussion. In this derivation, two spheres of radius $R$ initially touch at a point. The distance along their common axis of symmetry is measured from this initial point of contact and is designated $Z$ in this discussion. As sintering proceeds, the sphere radius does not change, but the point of contact grows to a neck, with the extent of sintering, $Z_s$, given by the difference between the original point of contact and the horizontal symmetry line between the spheres, which also corresponds to the narrowest section of the neck. The portion of the spheres that is overlapped on either side of $Z_s$ is transferred to the neck, forming a neck that connects with the original spherical body at a point $Z_c$. This model presumes a conservation of both mass and volume.

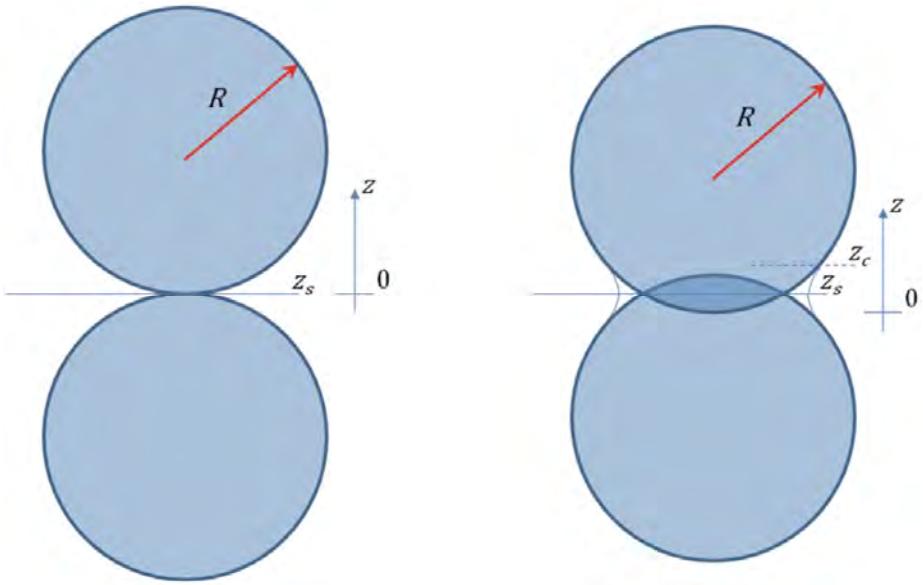


**Figure 30.** Illustration of the geometries used in the sintering discussion.

A surface of revolution contains a volume determined from the formula

$$V = \int_0^L \pi f^2(z)\, dz$$

where *f(z)* is the thickness (distance from the symmetry axis) of the body of revolution as a function of and *L* is the length of the body in the *z* direction.

In the case of sphere with $z = 0$ at the bottom of the sphere as illustrated,

$$f^2(z) = R_s^2 - (R_s - z)^2 = (2R - z)z$$

So,

$$V_{sphere} = \int \pi(2R - z)z\, dz$$

which, with proper choice of an integration constant, becomes

$$V_{sphere} = V_s = \frac{1}{3}\pi(3R - z)z^2$$

The neck thickness (distance from the symmetry axis) must always be larger than the original sphere thickness at any value of $z$ within the neck region, must be a minimum at the point $z = Z_c$, must

have the same value as the sphere radius at the point $z = Z_s$, and must asymptotically approach the sphere surface at the point $z = Z_s$. The following equations express these conditions mathematically

$$\left.\frac{dr_n}{dz}\right|_{z=Z_c} = 0$$

$$\left.\frac{d^2r_n}{dz^2}\right|_{z=Z_c} > 0$$

$$r_n(z = Z_S) = r_s(z = Z_S)$$

$$\left.\frac{dr_n}{dz}\right|_{z=Z_s} = \left.\frac{dr_s}{dz}\right|_{z=Z_s}$$

where $r_n$ and $r_s$ represent the neck and sphere thicknesses, respectively, and the other symbols have already been defined. The simplest polynomial that can satisfy all of these criteria is a quadratic function of $z$, specifically,

$$\begin{aligned} r_n(Z_c \le z \le Z_S) &= \frac{z^2(R - Z_c)}{2\sqrt{Z_c(2R - Z_c)}(Z_c - Z_s)} + \frac{z(Z_c - R)Z_s}{\sqrt{Z_c(2R - Z_c)}(Z_c - Z_s)} - \frac{Z_c(Z_c^2 - 3RZ_c + 2RZ_s)}{2\sqrt{Z_c(2R - Z_c)}(Z_c - Z_s)} \\ &= \frac{R[z^2 + 3Z_c^2 - 2(z + Z_c)Z_s] - Z_c(z^2 + Z_c^2 - 2zZ_s)}{2\sqrt{Z_c(2R - Z_c)}(Z_c - Z_s)} \end{aligned}$$

Placing this expression in the equation for a volume of a solid of rotation yields the total volume (including that of the sphere) of the sintered body in the region of the neck, which is

$$V_t = \frac{\pi(Z_s - Z_c)^2[3RZ_c(3Z_c + 2Z_s) + 2R^2(-Z_s - 6Z_c) - Z_c^2(2Z_c + 3Z_s)]}{15(2R - Z_c)Z_c}$$

The incrementally added volume, that is, the volume of material added to the spheres in the region of the neck, is

$$\begin{aligned} V_n &= \frac{\pi(Z_s - Z_c)^2[3RZ_c(3Z_c + 2Z_s) + 2R^2(-Z_s - 6Z_c) - Z_c^2(2Z_c + 3Z_s)]}{15(2R - Z_c)Z_c} \\ &\quad - \frac{1}{3}\pi[(3R - Z_c)Z_c^2 - (3R - Z_s)Z_s^2] \\ &= \frac{\pi(Z_s - Z_c)^2[3RZ_c(3Z_c + 2Z_s) - 2R^2(6Z_c - Z_s) - Z_c^2(2Z_c + 3Z_s)]}{15(2R - Z_c)Z_c} \end{aligned}$$

The volume of a sphere between any two arbitrary positions along the z-axis is

$$\frac{1}{3}\pi(3R-z)z^2\Big|_{Z_1}^{Z_2}$$

where $Z_1$ and $Z_2$ represent the two locations. The total sphere volume that lies between 0 and $Z_c$ is displaced by sintering and must fill the neck region outside the sphere between $Z_c$ and $Z_s$. Mathematically,

$$\underbrace{\frac{1}{3}\pi(3R-Z_c)Z_c^2}_{\substack{volume\ displaced\\ by\ sintering}} = \underbrace{\frac{\pi(Z_s-Z_c)[Z_c^2(42R^2-34RZ_c+7Z_c^2)+2(8R-3Z_c)(R-zc)Z_cZ_s+2(R-Z_c)^2Z_s^2]}{15(2R-Z_c)Z_c}}_{\substack{total\\ neck\ volume}} - \underbrace{\left[\frac{1}{3}\pi(3R-Z_s)Z_s^2-\frac{1}{3}\pi(3R-Z_c)Z_c^2\right]}_{\substack{volume\ of\ sphere\\ inside\ neck}}$$

or

$$\frac{1}{3}\pi(3R-Z_c)Z_c^2=\frac{\pi(Z_s-Z_c)^2[3RZ_c(3Z_c+2Z_s)+2R^2(Z_s-6Z_c)-Z_c^2(2Z_c+3Z_s)]}{15(2R-Z_c)Z_c}$$

or,

$$(3R-Z_c)Z_c^2=\frac{(Z_s-Z_c)^2[3RZ_c(3Z_c+2Z_s)+2R^2(Z_s-6Z_c)-Z_c^2(2Z_c+3Z_s)]}{5(2R-Z_c)Z_c}$$

This function provides the relationship between $Z_c$ and $Z_s$ for a given value of $R$ that conserves volume/mass. This implicit expression is fifth order in $Z_c$ and third order in $Z_s$. It does not lend itself to explicit solution for $Z_c$ as a function of $Z_s$ and $R$. The three explicit solutions for $Z_s$ are generally complex – meaning having real and imaginary parts – and more complicated than the implicit equation, namely,

$$Z_s=\frac{A_1+2Z_c(16R^2+3RZ_c-4Z_c^2)+\frac{100Z_c^2(2R^2-3RZ_c+Z_c^2)^2}{A_1}}{6(2R^2+6RZ_c-3Z_c^2)}$$

$$Z_s=\frac{i(i+\sqrt{3})A_1+4Z_c(16R^2+3RZ_c-4Z_c^2)-\frac{100i(-i+\sqrt{3})Z_c^2(2R^2-3RZ_c+Z_c^2)^2}{A_1}}{12(2R^2+6RZ_c-3Z_c^2)}$$

$$Z_s = \frac{-(1+i\sqrt{3})A_1 + 4Z_c(16R^2 + 3RZ_c - 4Z_c^2) + \frac{100i(i+\sqrt{3})Z_c^2(2R^2 - 3RZ_c + Z_c^2)^2}{A_1}}{12(2R^2 + 6RZ_c - 3Z_c^2)}\}$$

where

$$A_1 = (2^{2/3}5^{1/3})((2R - Z_c)Z_c^3(524R^5 + Z_c(1036R^4 + Z_c(2546R^3 + Z_c(-4514R^2 + 293(7R - Z_c)Z_c)))) + 3\sqrt{3}\sqrt{((3R - Z_c)Z_c^6(-2R + Z_c)^2(2R^2 + 6RZ_c - 3Z_c^2)^2(724R^5 + Z_c(236R^4 + Z_c(3796R^3 + Z_c(-5464R^2 + 343(7R - Z_c)Z_c))))))^{1/3}$$

$Z_s$ is real valued and the first root above is the physical solution.

The surface radius of curvature, $R_c$, plays an important role in sintering. The definitions of the radius of curvature and its inverse, the curvature ($C$), for an arbitrary, one-dimensional curve are

$$R_c = \frac{\{1 + [f'(x)]^2\}^{3/2}}{f''(x)}$$

and

$$C = \frac{f''(x)}{\{1 + [f'(x)]^2\}^{\frac{3}{2}}} = \frac{1}{R_c}$$

where $f(x)$ describes the surface profile. Since the functions involve only derivatives of $f(x)$, the point of reference of the measurement to the surface is unimportant. In three dimensions, the curvature has two components, expressable as one each in the $z$ and $\theta$ directions of a cylindrical coordinate system for this application. Negative radii of curvatures are taken here to designate convex surfaces.

In this model, using the results from above, the radius of curvature in the $z$ direction is

$$R_{c,z} = \begin{cases} -R & Z_c < z < R \\ \dfrac{\sqrt{(2R - Z_c)Z_c}(1 + \frac{(R - Z_c)^2(z - Z_s)^2}{(2R - Z_c)Z_c(Z_c - Z_s)^2})^{3/2}(Z_c - Z_s)}{R - Z_c} & Z_s \le z \le Z_c \end{cases}$$

In the $\theta$ direction, the radius of curvature is the same as the neck thickness at that location,

$$R_{c,\theta} = \begin{cases} -\sqrt{(2R - z)z} & Z_c < z < R \\ -\dfrac{R[z^2 + 3Z_c^2 - 2(z + Z_c)Z_s] - Z_c(z^2 + Z_c^2 - 2zZ_s)}{2\sqrt{Z_c(2R - Z_c)}(Z_c - Z_s)} = r_n & Z_s \le z \le Z_c \end{cases}$$

The surface curvature in the *z* direction varies from convex to concave and is constant (and convex) for values of *z* greater than $Z_c$, where it is identical to that of the original sphere. Between $Z_s$ and $Z_c$, the surface curvature is convex and varies with *z*. The radius of curvature is smallest (curvature is largest) at $z = Z_s$, as would be expected at the neck. Surface curvature varies as expected with the degree of sintering. Since $Z_s$ is a function of $Z_c$ and vice versa, albeit somewhat complex functions, this function provides the radius of curvature for this idealized system as a smooth function of the extent of sintering. This formalism allows sintering to be described continuously from point contact to formation of a neck the same diameter as the sphere. The substantial current literature rather arbitrarily divides this process into several zones as characterized by curvature. This work contributes to the existing literature by eliminating the need for such divisions, allowing a single model to describe the entire process.

Sintering rates depend on radii of curvature because vapor pressures and surface energies depend on them. For example, the vapor pressure on a concave surface is lower than that on a convex surface, creating one of the several mechanisms by which molecules move from the bulk particles with low curvature and generally convex surfaces to the point contacts that have very high curvature and concave surfaces. Other mechanisms include viscous and plastic flow and volume, grain, and surface diffusion. All are driven by the curvature or, more precisely, the gradient of the curvature. Since the gradient in both radii of curvature is zero in the $\theta$ direction, there should be no net transport of material in that direction. Our interest is on the transport in the *z* direction.

Sintering rates from most materials can be expressed as

$$\frac{dV_n}{dt} = \frac{B}{kTR_{c,z}} = \frac{B(R - Z_c)}{kT\sqrt{(2R - Z_c)Z_c}\left(1 + \frac{(R - Z_c)^2(z - Z_s)^2}{(2R - Z_c)Z_c(Z_c - Z_s)^2}\right)^{3/2}(Z_c - Z_s)}$$

$$= \frac{d}{dt}\frac{\pi(Z_s - Z_c)^2[3RZ_c(3Z_c + 2Z_s) - 2R^2(6Z_c - Z_s) - Z_c^2(2Z_c + 3Z_s)]}{15(2R - Z_c)Z_c}$$

where *k* and *T* are the Boltzman constant and absolute temperature, respectively, and *B* is a constant that depends on material properties and the sintering mechanism and generally exponentially on temperature. Given a generally empirically determined value of *B*, this equation provides estimates of sintering rates.

The above equation could, in principal, be solved for the time dependence $Z_c$ explicitly by inserting the expression for $Z_s$ in terms of $Z_c$ in all locations where $Z_s$ appears and solving the resulting differential equation. However, this solution, if it exists in explicit form at all, would be highly complex. Its numerical solution, however, is straight forward.

The minimum neck radius critically affects the strength and amount of heat transfer through sintered particles. The minimum neck radius as a function of the extent of sintering follows from the above development, namely,

$$r_n(z = Z_S) = \frac{R(3Z_c^2 - Z_s^2 - 2Z_cZ_s) - Z_c(Z_c^2 - Z_s^2)}{2\sqrt{Z_c(2R - Z_c)}(Z_c - Z_s)}$$

where, as before, $Z_s$ could be written as a function of $Z_c$ and there is only one independent variable on the right side. The minimum neck area is, of course

$$A_{min} = \pi r_{n.min}^2 = \pi\left[\frac{R(3Z_c^2 - Z_s^2 - 2Z_cZ_s) - Z_c(Z_c^2 - Z_s^2)}{2\sqrt{Z_c(2R - Z_c)}(Z_c - Z_s)}\right]^2$$

## Subtask 11.3 – Acquisition of Data for Melting Model Verification

Researchers have long established that sintering depends on material temperature, particle size, and material properties (melting point, vapor pressure, surface diffusivity, etc.). Sintering prominently affects such practical deposit properties as strength, thermal conductivity, and emittance. This investigation establishes, possibly for the first time, the critical additional dependence of sintering on deposit structure, deposit initial density, and particle size distribution, especially with respect to the properties of most significance to practical ash management issues such as strength, thermal conductivity, and emittance.

### *Surrogate Materials*

Some of the experiments used in this investigation employed surrogate materials that allow more careful control of particle size and composition than is possible for coal fly ash. Other experiments used coal ash. Experiments were conducted under both reducing and operating conditions.

Sintering is most significant for small particles. The easiest way to generate such small particles is through vapor condensation. Therefore, many of the particles used in the surrogate experiments employed alkali salts (sodium sulfate) mixed with various impurities and formed through vapor condensation. Forming materials by this mechanism requires that essentially all of the initial material be vaporized before recondensing any of it. These recondensation experiments occurred in flow reactors, but it is not possible at the temperature and residence time available in such reactors to completely vaporize nearly any component of coal fly ash. Alkali salts do vaporize and recondense under conditions typical of a flow reactor and do exist in modest amounts in coal ash, and these were used in these experiments. However, they melt at much lower temperatures than coal ash, so the sintering experiments in which they were used were conducted at lower temperatures and in all cases below the first melting point of the

material. These particles typically formed a very narrow size distribution centered near 0.02 micron. The experiments using actual coal ash produced a much broader size distribution, with particles ranging up to 40 microns, and with varying composition and hence melting points and vapor pressures. The sintering experiments in which they were used were conducted at higher temperatures.

Figure 31 illustrates typical sintering progression as a function of time for small particles randomly packed into cubes with initial densities of about 1.4 g/cm$^3$ and initial porosities ranging from 30-50%. The numbers under each SEM represent minutes of sintering. As is seen, the particles rapidly progress from a randomly packed particulate ensemble to a more dense and far more structurally coherent body. This material, sintered in air at 450 °C for up to one hour, represents classical sintering data and results. One of the major conclusions of our work is that it is largely non-representative of the type of sintering that happens on tube deposits.

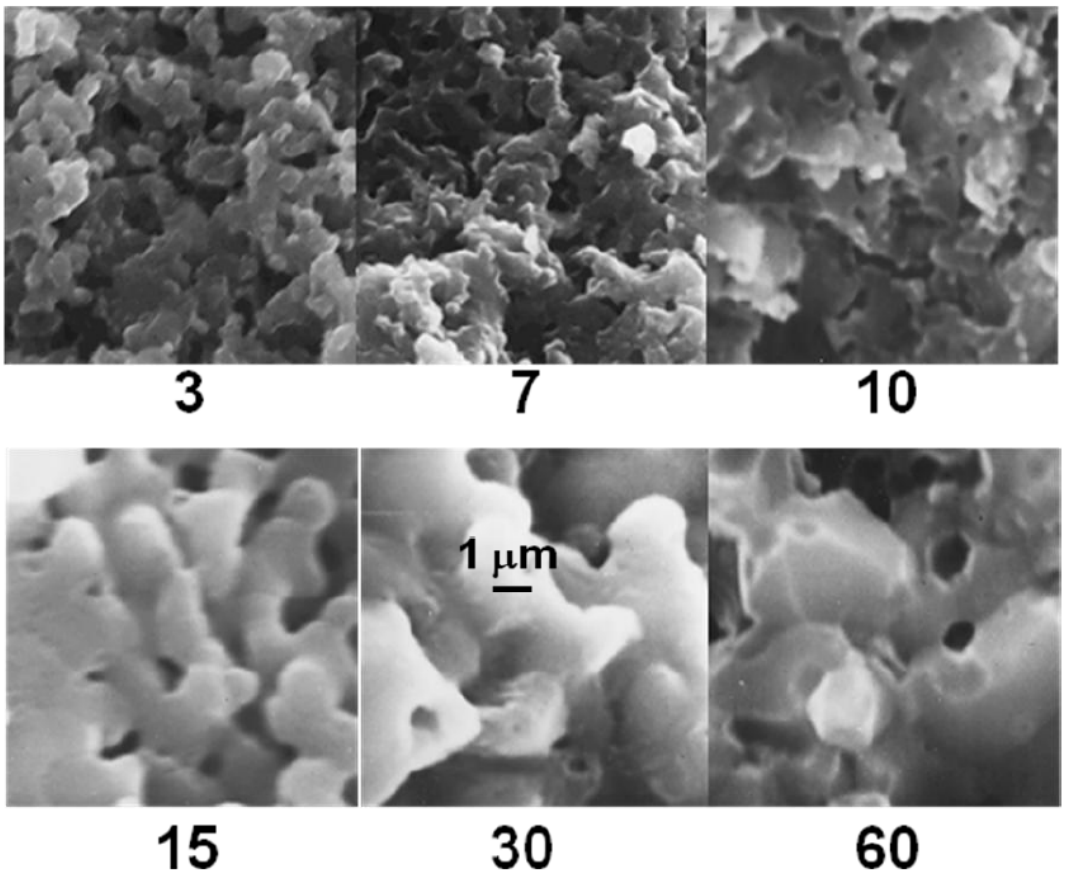


**Figure 31.** Typical sintering progression as a function of time for small particles randomly packed into cubes with initial densities of about 1.4 g/cm$^3$ and initial porosities of about 30-50%. The numbers under each SEM represent minutes of sintering.

Figure 32 illustrates data from a typical small particle deposition experiment on a probe in a furnace (top view). This highly three-dimensional structure differs importantly from the random-packed structures such as those used to generate the data in Figure 31. The structure is difficult to appreciate in micrographs and is schematically illustrated in two dimensions in Figure 33. The structure involves particle filaments with very high aspect ratios and largely singly connected to underlying probe. That is, rather than randomly packed particles, the deposit has a filamentary structure that generally grows radially from the probe surface.

The important consequence of this is that while sintering occurs in such a structure, it occurs dominantly along a filament and not between or among filaments, as illustrated schematically in Figure 33. If temperature is sufficiently high to cause the hottest (top) part of the structure to melt or structurally fail, inter-filament sintering can occur, as illustrated in the last frame of Figure 33. In addition, if large particles impact the surface, they too can bond filaments to one another. As an indication of the dramatically different behavior of real deposits compared to randomly packed experiments, the sample in Figure 32 grew on the probe at 550 °C for 10 hours with essentially no inter-particle sintering, in stark contrast to the much lower temperature and much shorter time experiments that produced the images in Figure 31. Actual deposits commonly exhibit initial porosities of 90% or so, much higher than is reasonably achievable in the randomly packed experiments commonly used to study sintering in other contexts. Deposits maintain high porosity and relatively low strength in boiler deposition much longer than would be the case if they were randomly packed spheres with higher initial and final density and with multiple intra-filament connection points.

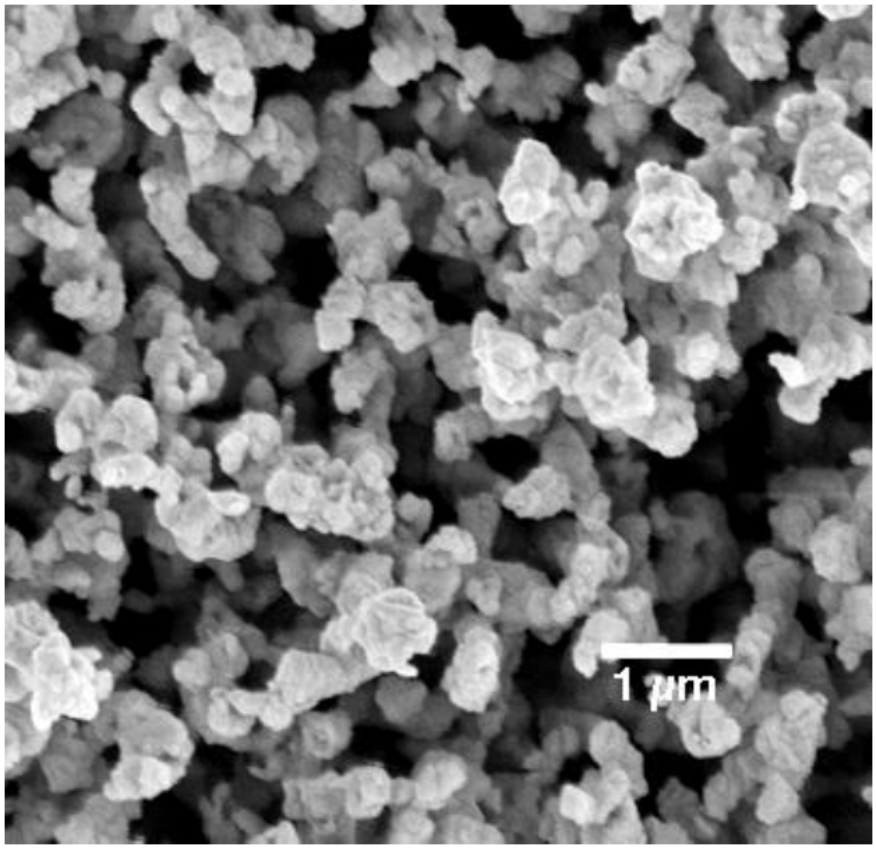


**Figure 32.** Typical small particle deposition on probe in furnace (top view). This highly three-dimensional structure differs importantly from the random-packed structures such as those used to generate the data in Figure 31. The structure is difficult to appreciate in micrographs and is schematically illustrated in two dimensions in Figure 33. This sample was at 550 °C for 10 hours.

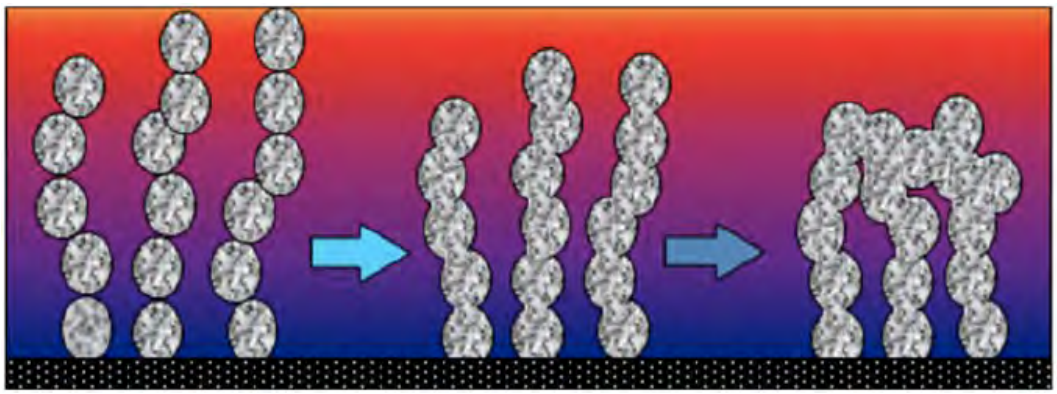

**Figure 33.** Schematic diagram in two dimensions of particle structure observed in experiments such as those in Figure 32. The figure illustrates sintering progression in time in the types of structured deposits typical of boiler deposits.

These differences are relatively insensitive to either particle initial density or particle sintering temperature, as illustrated in Figure 34 and Figure 35. Probe samples maintain higher porosity and more structure despite the much longer sintering time and higher sintering temperature.

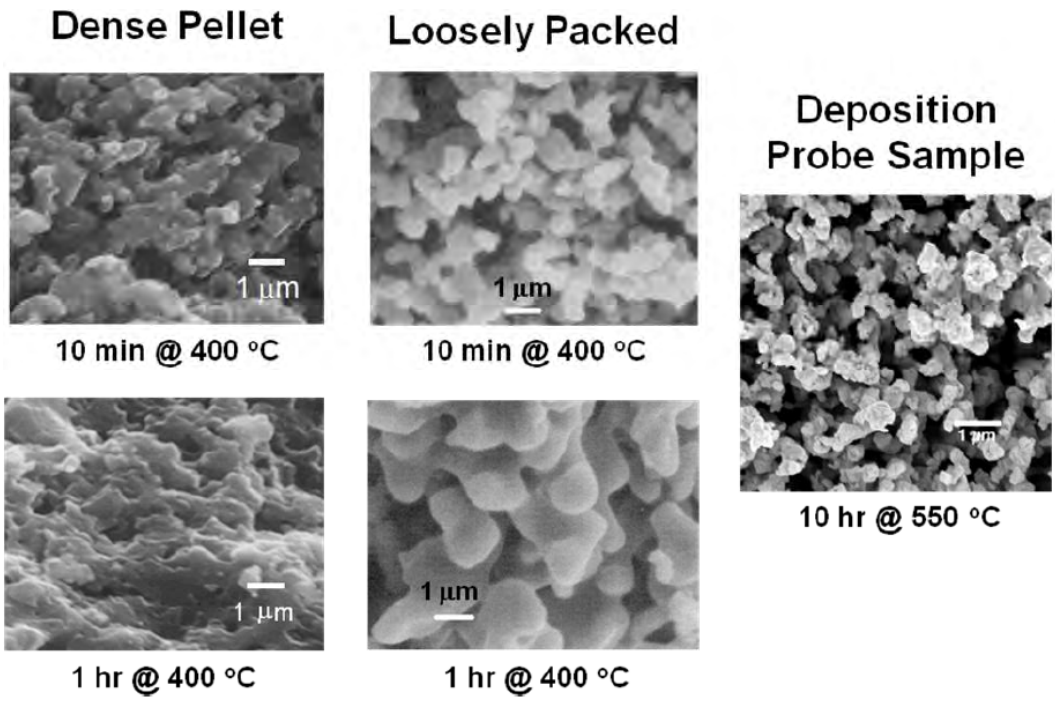


**Figure 34.** Comparison of sintering extents in dense and loosely aggregated samples of randomly packed particles sintered at low temperature with behavior observed particles impacted on probes. Probe samples maintain higher porosity and more structure despite the much longer sintering time and higher sintering temperature.

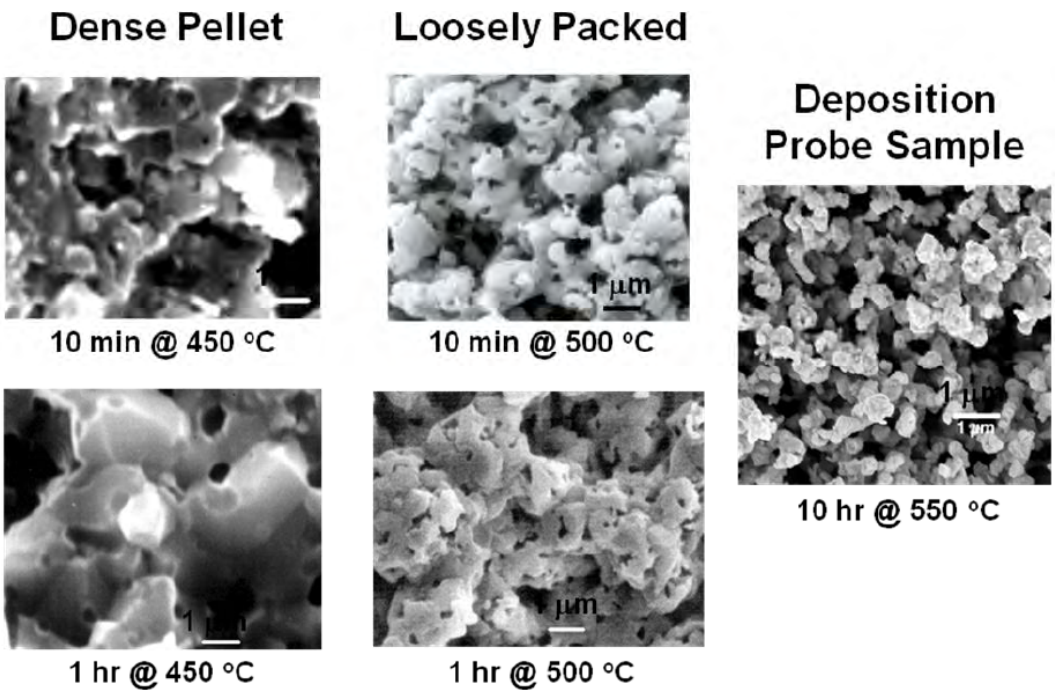


**Figure 35.** Comparison of sintering extents in dense and loosely aggregated samples of randomly packed particles sintered at modest temperature with behavior observed particles impacted on probes. Probe samples maintain higher porosity and more structure despite the much longer sintering time and higher sintering temperature.

Quantitative indications of sintering rate and extent further emphasizes the dependence of sintering on structure. In contrast to the probe deposits that maintain significant porosity for many hours, the quantitative results for a range of sintered materials in random-packed structures indicate rapid and significant porosity loss. The sample compositions for these materials appear in Table 10 and their dynamic sintering rates at 475 °C appear in Figure 36. These data are useful in measuring sintering rates and extents, but because they lack the structure of many boiler and gasifier deposits they are not representative of behavior in these systems. Specifically, they sinter more rapidly and to a much higher extent than occurs in boiler and gasifier deposit samples. Ultimately, most of these deposits approach their true density as sintering temperature increases even though they have not melted. Figure 37 illustrates the ratio of sample density to true material density as a function of sintering temperature and deposit composition. Note nearly all deposits loose essentially all their porosity. The relationship of these data to material melting temperature appears in Figure 38. Since most of these samples are mixtures, they do not have well-defined melting points but rather melting ranges. Here the temperature is normalized by the first melting point, that is, the lowest temperature at which any part of the sample begins to melt.

**Table 10.** Compositions of samples used in surrogate sintering tests.

| Sample: | B Lo Cl Lo $CO_3$ | C Hi Cl/ | D Hi Cl | E Hi $CO_3$ No $CO_3$ | G No Cl/ | #3 Hi K | #4 Hi Cl |
|---|---|---|---|---|---|---|---|
| Na | 32.2 | 31.9 | 33.6 | 32.8 | 29.5 | 26.0 | 29.9 |
| K | 3.7 | 4.0 | 4.4 | 4.7 | 5.2 | 9.9 | 5.9 |
| $SO_4$ | 58.9 | 51.7 | 43.7 | 46.5 | 65.2 | 58.6 | 43.6 |
| $CO_3$ | 6.5 | 0.6 | 5.5 | 13.5 | 0.0 | 3.1 | 4.9 |
| Cl | 0.5 | 12.4 | 13.6 | 2.4 | 0.0 | 2.2 | 13.5 |
| Total | 101.8 | 100.6 | 100.8 | 99.9 | 99.9 | 99.8 | 97.8 |

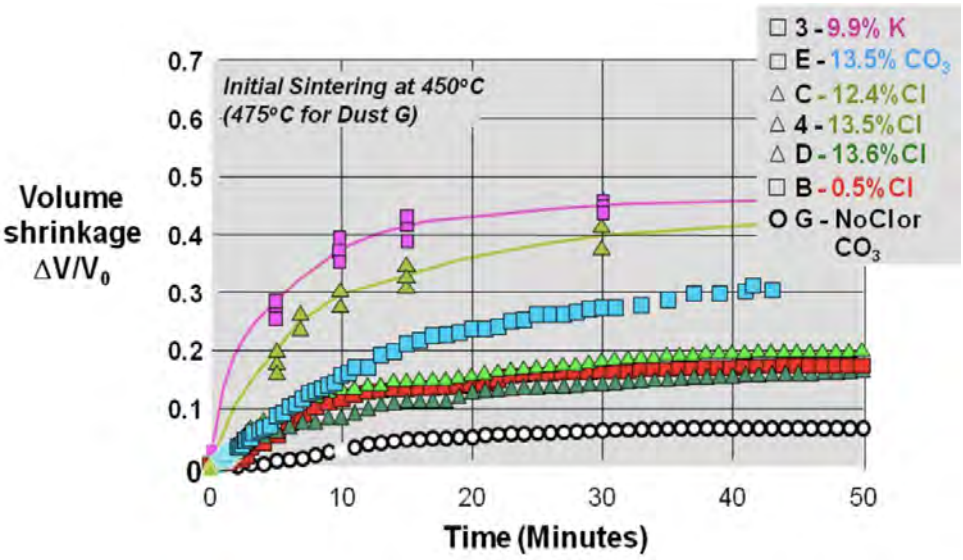


**Figure 36.** Sintering rates and extents as measured by change in the volume for a suite of 7 surrogate samples varying in composition, all sintered at 475 °C.

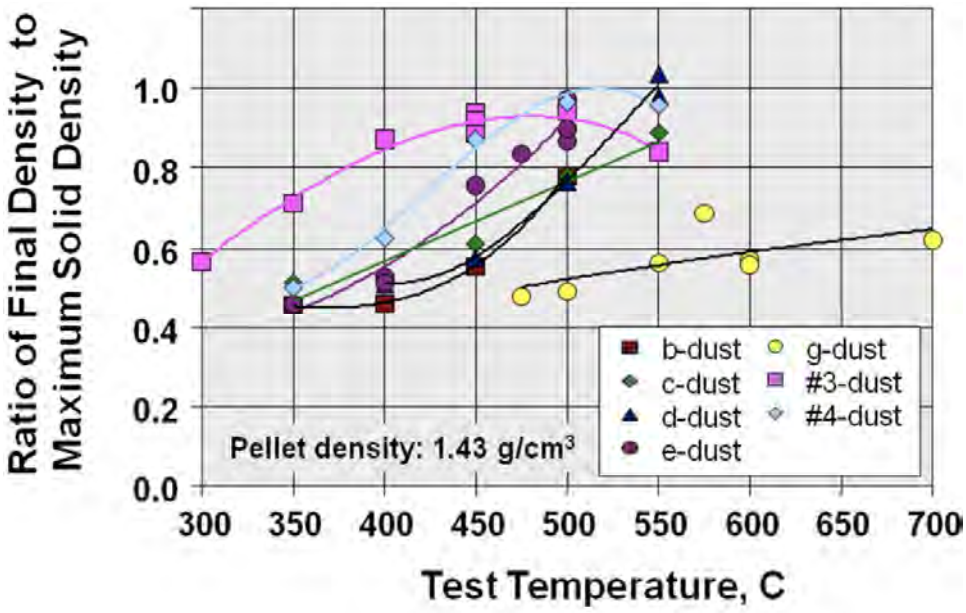


**Figure 37.** Ratio of sample density to true material density as a function of sintering temperature and deposit composition. Note nearly all deposits loose essentially all their porosity. The relationship of these data to material melting temperature appears in Figure 38.

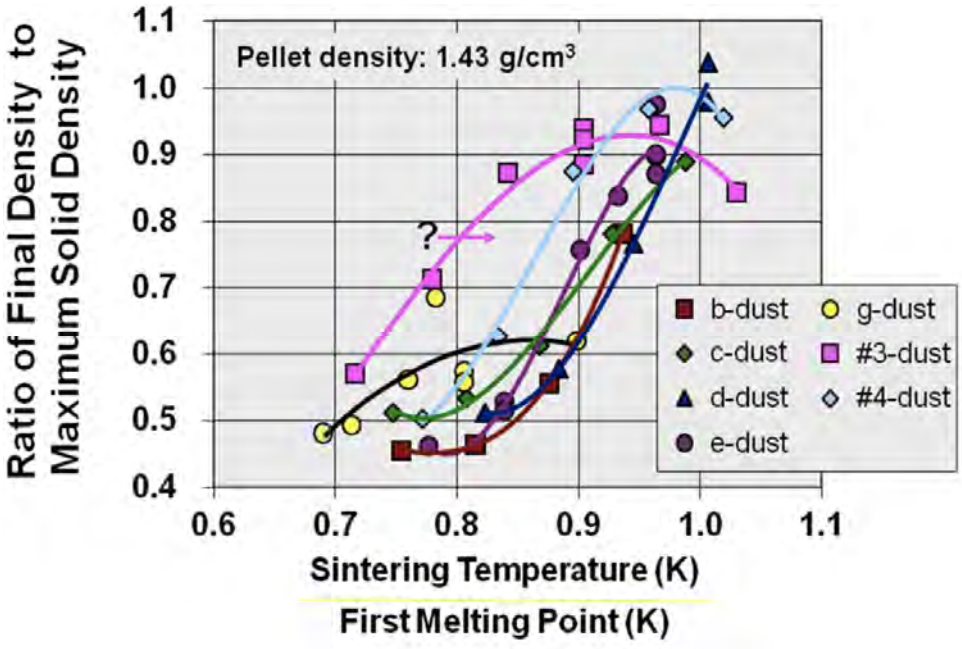


**Figure 38.** Ratio of sample density to true material density as a function of sintering temperature ratio and deposit composition. Note nearly all deposits loose essentially all their porosity. The data with actual temperatures appears in Figure 37.

Material strength depends critically on the extent of sintering. Figure 39 illustrates how strength decreases as porosity increases, with porosity changes occurring through sintering experiments. Strength is predicted in a manner in all ways analogous to thermal conductivity, as discussed later, with upper and lower bounds. The model assumes a structure that is intermediate between these bounds using a structural parameter. The model reasonably captures the trends in the data, though it systematically over-predicts the strength at high porosities. However, the data are derived from pressed pellet experiments and suffer from the same issues discussed above in that they do not accurately incorporate deposit structure and, while representative of sintering, are not representative of deposits in gasifiers or combustors. While the model reasonably succeeds in describing sintering and its effect on material properties, as was our original goal, we are not confident that it is appropriate in this application as a description of gasifier or combustor deposit properties. Specifically, it lacks the structural information of real deposits and hence predicts too rapid of sintering and too rapid of changes in properties.

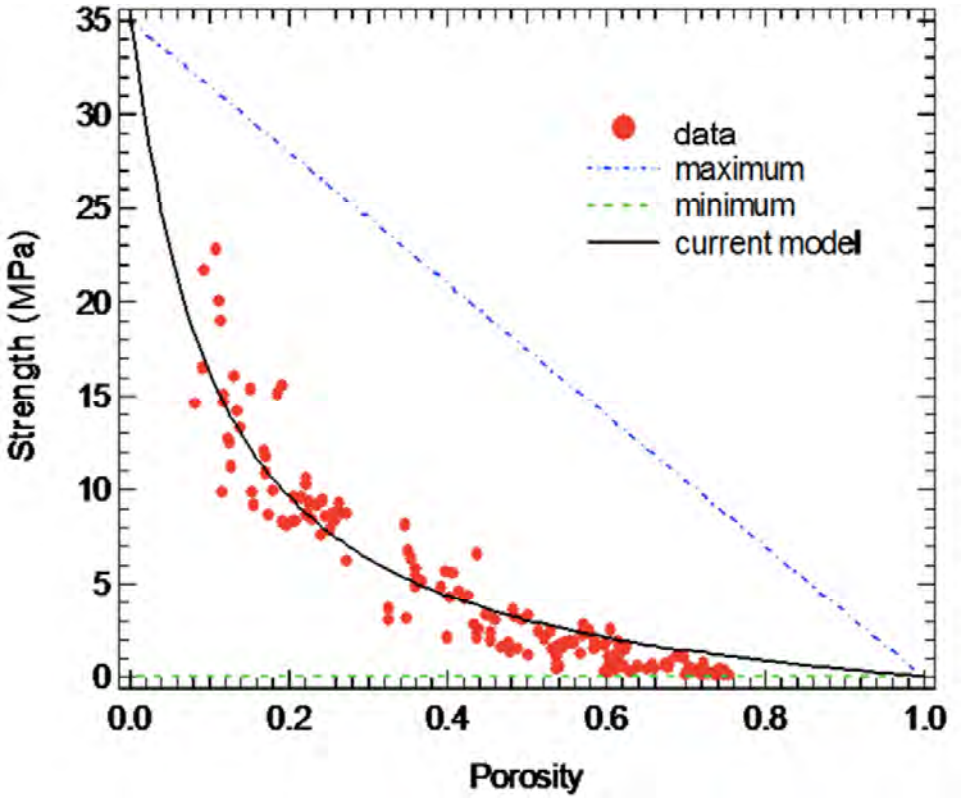


**Figure 39.** Strength development as a function of porosity as measured and as predicted by a sintering model.

## *Coal Fly Ash Deposits*

Similar data on coal fly ash deposits on surfaces illustrate similar trends. The experimental apparatus and procedure used to study coal fly ash deposits were described in the Experimental section.

Quantifying the physical structure and especially things such as the degree of connectedness or neck thickness for deposits generated from actual fuels may not be possible in any practical manner since there is a wide range of particle sizes, the deposits are highly three dimensional, and the connection points that are most important are very small. Rather than attempt this, the approach here monitors important properties that are measurable and uses them to infer structure. Specifically, the thermal conductivity of an ash deposit depends on both solid fraction ($\phi$, or 1-porosity) and structure. Two approximate limits to the structural dependence provide convenient bounds from which structure can be inferred. At the upper limit, heat transfers through the solid and gaseous deposit components in parallel (Figure 40). Solid-phase thermal conductivities for non-metallic samples generally fall in the range of 2-3 W/m·K whereas gas thermal conductivities at the temperatures and pressures of this experiment are nearly two orders of magnitude lower, approximately 0.05 W/m·K. The effective average thermal conductivity at this upper limit is the weighted sum of these two, namely,

$$k_{max} = \phi k_s + (1-\phi)k_g$$

Given the large difference in solid and gaseous thermal conductivities, this equation is highly sensitive to the solid fraction of the deposit.

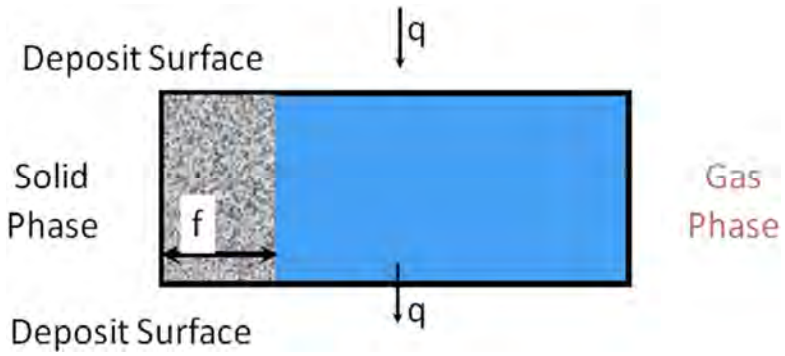


**Figure 40.** Illustration of a deposit structure that leads to its maximum thermal conductivity at a given porosity.

At the lower limit, heat transfers through the solid and gaseous deposit components in series (Figure 41). The effective average thermal conductivity at this lower limit is the inverse weighted sum of these two, namely,

$$k_{min} = \frac{k_s k_g}{\phi k_g + (1-\phi) k_s}$$

Though it is less obvious, the very low value of the gaseous thermal conductivity makes this equation less sensitive to the solid fraction or porosity unless the solid fraction is near unity.

Both equations predict thermal conductivities that approach that of the gas and the the solid phase as the solid fraction approaches zero and unity, respectively, as would be expected. The difference between these two expressions for thermal conductivity at solid volume fractions even modestly removed from these limits is large. Since no deposit can have a solid volume of zero and few particlulare deposits have solid volumes near unity, the thermal conductivity should be a sensitive indicator of deposit structure and, more importantly, of the degree of sintering. Specifically, deposits that are near their upper bound in thermal conductivity must have structures that allow heat transfer to occur in parallel, such as the filamentary structure documented and discussed earlier. Deposits with thermal conductivities near the lower bound tend to not have structures such as that in Figure 41, for if they did the deposit would not remain on the probe. However, particles that have very narrow necks or essentially points at their points of connection approach this lower limit or, more specifically, have thermal conductivities characterized by parallel conduction but through a solid only as large as the neck, which makes them approach this lower limit.

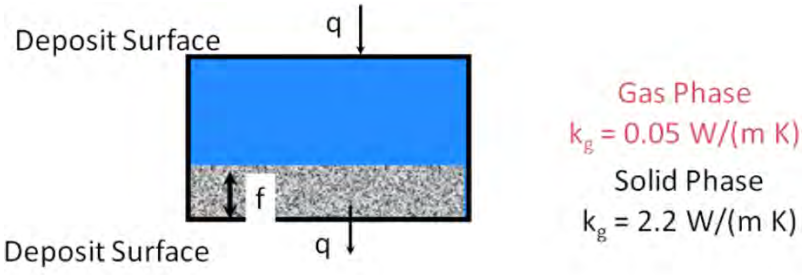


**Figure 41.** Illustration of a deposit structure that leads to its minimum thermal conductivity at a given porosity.

Figure 42 illustrates the efficacy of this approach and typical data. In this experiment, the measured thermal conductivity normalized by its maximum value as predicted from the equations above appears as a function of time in an experiment during which coal flow was halted at about 80 minutes and

temperature increased to more fully sinter the deposit. The success of the sintering is seen by a decrease in deposit thickness without changing deposit mass, that is, an increase in bulk density. As seen, the initial deposit exhibits a thermal conductivity near its lower bound, consistent with a structure of particles minimally connected at their contact points, or with minimal neck formation and little sintering. When the temperature increases, the deposit thermal conductivity rises to near its maximum value, consistent with substantial neck growth approaching its maximum. The thermal conductivity reliably tracks and provides a quantitative measure of the deposit structure.

Data collected without increasing the temperature and sintering the deposit during the experiment appear in Figure 43. The deposit still densifies, but it does so as a consequence of deposit growth and the associated increased temperature and not as a consequence of increasing the overall temperature. As indicated, the deposit conductivity initially rises to near its upper limit when the deposit is young but reaches a plateau and does not change appreciably as the deposit matures and densifies. The deposit behaves very much like the illustration in Figure 33, where the overall thermal conductivity is controlled by the relatively low thermal conductivity of the inner layer and is only modestly influenced by increasing the amount and density of the outer layers.

Similar data for bituminous and subbituminous coals under both oxidizing and reducing conditions appear in Figure 44 (oxidizing) and Figure 45 (reducing). These data are also not normalized to help illustrate differences in rank and stoichiometry. The two types of data symbols represent two alternative ways of reducing the data and are similar, so the differences are not discussed here. There are much stronger dependencies on coal type than on stoichiometry, although all samples are below melting temperatures and hence none represents the behavior of a slag (which would be near its maximum thermal conductivity). Initial thermal conductivities approach the lower limit in all cases, indicative of a sample with minimal particle contact or near point contact among particles. With time, all thermal conductivities increase somewhat from this initial low value. The increase in the subbituminous coal conductivity is modest. These deposits typically consist of small particles that, to the temperatures tested here (up to about 600 °C), do not melt or appreciably sinter. The bituminous coal deposit conductivity rises to much higher values, indicating in part that it sinters more extensively, presumably because its higher iron content lowers its sintering temperature, and in part because it contains larger particles that provide effective thermal coupling among the smaller particles. However, even the bituminous coal particles remain well below their upper bounds for thermal conductivity over the six to eight hours of these experiments. This illustrates that they retain a substantial portion of their radial structure and do not sinter equally in all directions, as occurs in random-packed samples.

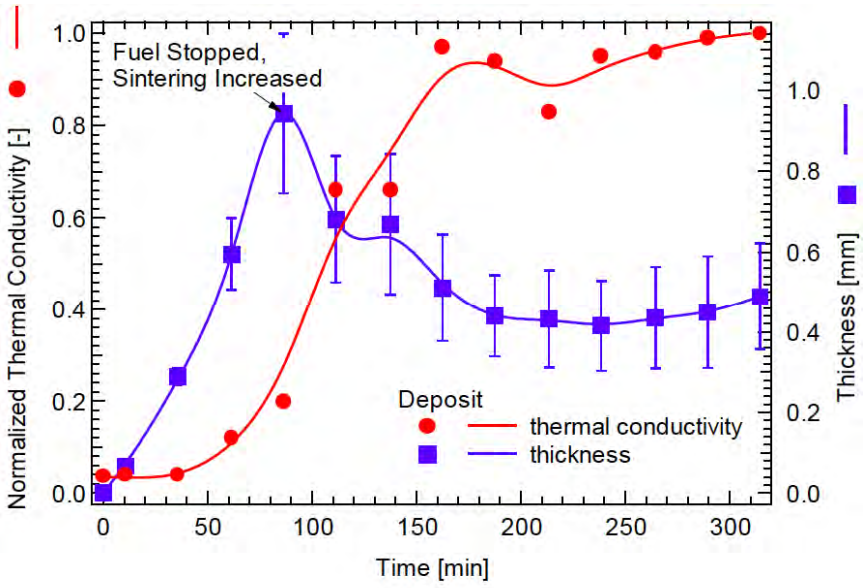


**Figure 42.** Normalized thermal conductivity (normalized by maximum value) as a function of time in an experiment during which coal flow halted, temperature increased, and probe deposit sintered appreciably.

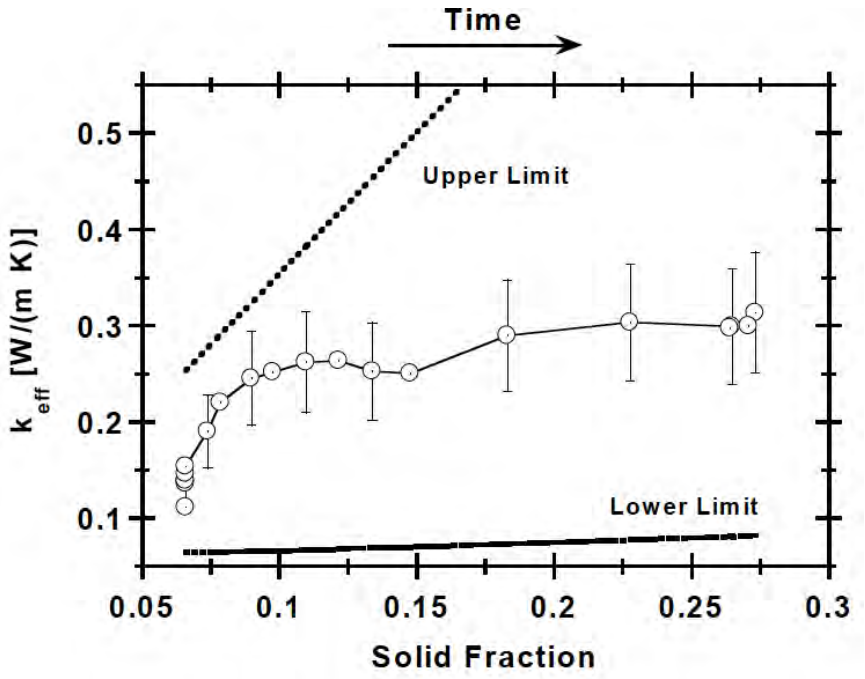


**Figure 43.** Thermal conductivity change with solid fraction as measured for real ash deposits.

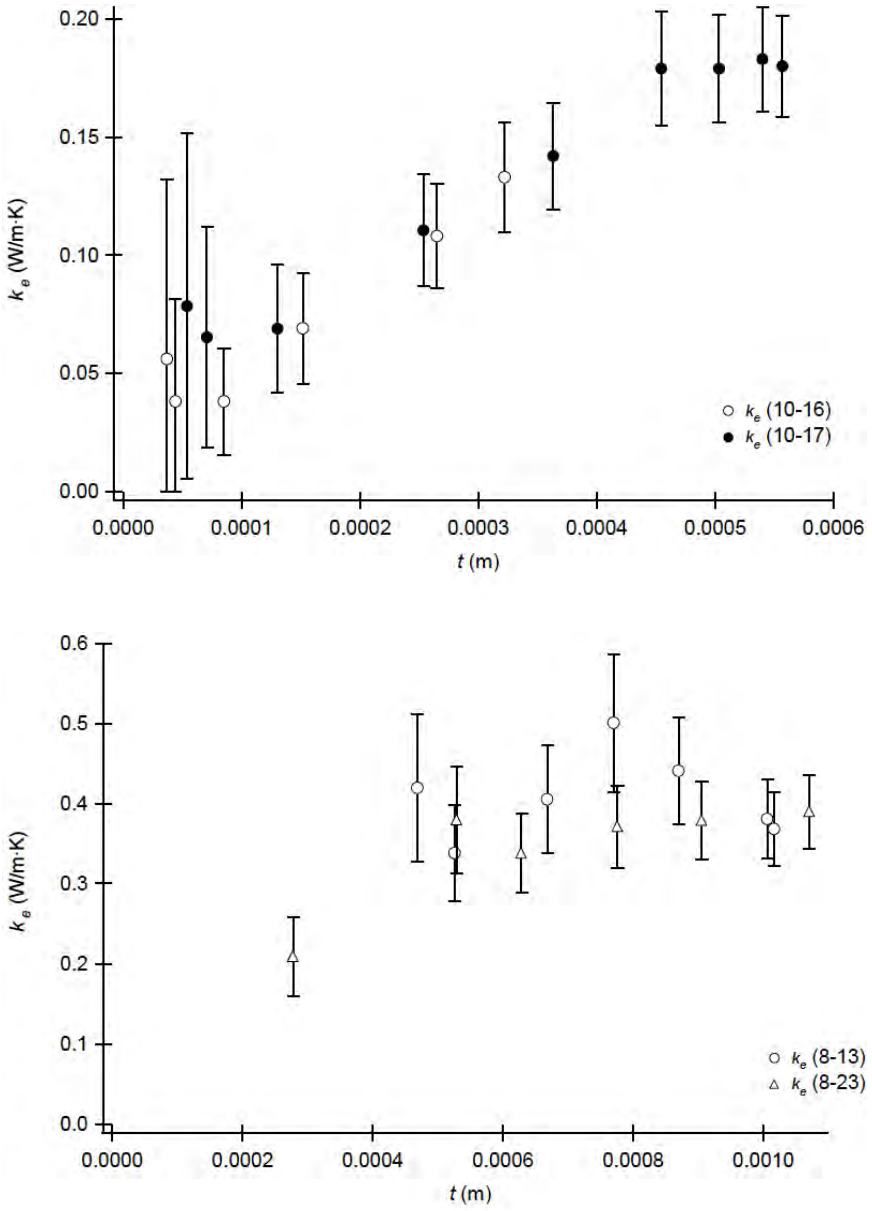


**Figure 44.** Effective thermal conductivity as a function of deposit thickness: top panel - PRB coal, oxidizing conditions ($\Phi$ = 0.71), bottom panel - IL #6 2 coal, oxidizing conditions ($\Phi$ = 0.92).

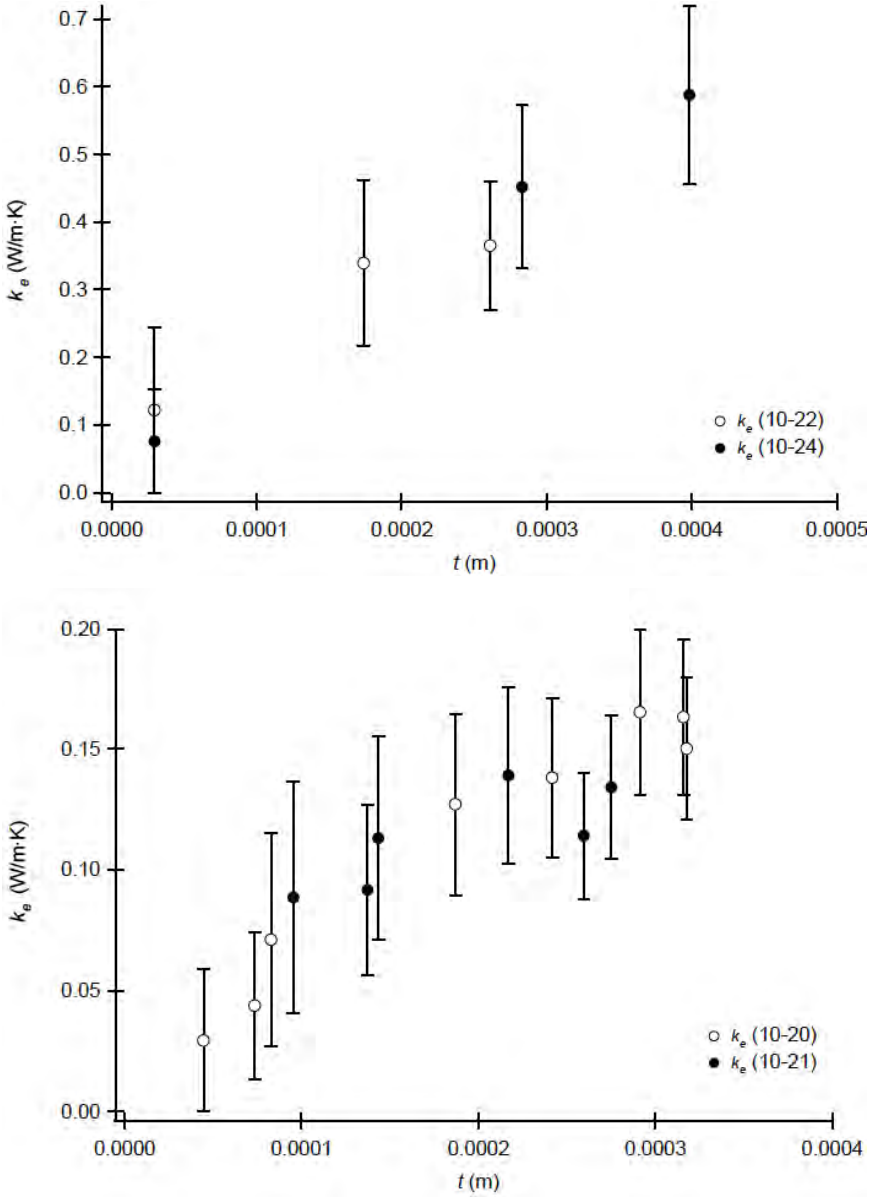


**Figure 45.** Effective thermal conductivity as a function of deposit thickness. top panel - IL #6 1 coal, reducing conditions (Φ = 2.33); bottom panel - PRB coal, reducing conditions (Φ = 3.10).

These results compare favorably with all but possibly one of the literature investigations cited in Table 11, with the one exception exhibiting notably higher conductivities than the others. Based on these investigations, which use differing techniques and different people, overall conclusions about sintering in practical systems as would be implied by the thermal conductivities are consistent.

**Table 11.** Sampling of literature results for thermal conductivity of ash deposits.

| reported in literature | | | |
|---|---|---|---|
| $k_e$ | coal | deposit | reported by |
| 2.5 to 3.0 | not specified | particulate | (Wall, Bhattacharya et al. 1993) |
| 0.10 to 0.25 | blend 65% / 35% (by mass) IL #6 coal / wheat straw | particulate | (Robinson, Buckley et al. 2000) |
| 0.2 to 3.1 | blend 65% / 35% (by mass) IL #6 coal / wheat straw | sintered | (Robinson, Buckley et al. 2000) |
| 0.4 to 0.5 | not specified | | (Rezaei, Gupta et al. 2000) |
| 0.1 to 0.25 | not specified | particulate | (Anderson, Viskanta et al. 1987) |
| 0.25 to 0.5 | not specified | various crushed ("particulate") | (Anderson 1985) |
| **present work** | | | |
| $k_e$ | coal | deposit | |
| 0.2 to 0.5 | IL #6 | particulate | |
| 0.04 to 0.18 | WY | particulate | |

## Subtask 12.1 – Heat Flux Modeling

Heat transfer plays a key role in performance of a gasification system and is largely responsible for limited refractory and injector lifetimes. The entrained-flow gasifier simulation tool being developed at the University of Utah will improve the understanding of heat transfer to the walls and will allow identification of areas prone to excessive heat transfer.

### *Identification of Relevant Parameters*

The gasification group identified factors which play a key role in heat transfer within a gasification system. This analysis was based partly on understanding of the environment within an entrained-flow gasifier, partly on experience with simulation of industrial combustion systems and partly on results from the experimental tasks in this program (e.g., Subtask 10.2). The resulting parameters are indicated below:

- **Soot.** As indicated previously, coal gasification can result in production of carbon-rich soot, which has a very high emissivity and a key player in radiative heat transfer.

- **Char.** Char also has a high emissivity and like soot contributes strongly to radiative heat transfer. Char may exist either entrained in the gas phase or be captured in the slag flowing down the wall of the gasifier.
- **Slag.** The walls of a slagging gasifier are not bare refractory, but instead refractory coated with a layer of viscous slag. Heat transfer from the reacting environment to the refractory walls is thus very dependent on properties of the slag (e.g., emissivity, thickness, coverage).
- **Gas.** Radiation from the gas is more important in entrained-flow gasification systems than combustion systems, primarily because the gas is much more dense due to the pressure, which can exceed 60 atmospheres.

These parameters are expected to be the major contributors to heat flux, which is expected to be driven almost exclusively by radiation at gasification temperatures. The relative importance of each of these will depend on several factors including operating conditions, coal conversion behavior and refractory properties. Models for the first three of these (soot, char, slag) are under development within the gasification thrust area (Subtasks 10.2, 10.3 and 11.2). Gas phase radiation is well enough understood that it can be incorporated into the simulation using existing experience.

### *Integration Strategies*

The University of Utah simulation team is pursuing a multi-phase modeling approach for coal gasification systems using large eddy simulation (LES) as the turbulence closure. Gas transport is represented by the standard, filtered, Navier-Stokes equations wherein LES subgrid closure models are applied to represent the fluctuating scales. The particle phase is represented by transport of the number density function (NDF). Practical representation of the NDF requires some approximation, which in this case leads to directly tracking moments, with numerical quadrature, of the number density function. This approach is termed the direct quadrature method of moments (DQMOM).

The number density function that DQMOM attempts to represent is a function of properties of the particle phase it is representing. One identifies a set of orthogonal properties, termed internal coordinates, that then approximate the NDF. In other words, if $\xi$ is the set of internal coordinates, then the NDF (n) is described by n($\xi$, $X$, i) where $X$ is spatial location and $t$ is time. The distribution then changes through local changes in the internal coordinates, $\xi$ that are dependent on $X$ and $t$. The transport of $\xi$ in internal coordinate space is usually termed phase-space velocity and occurs because of physical processes that affect the NDF. For example, if $\xi$ = length, then one may have a distribution of particles that change size depending on a local concentration of some other quantity, $\phi$. This model then affects the NDF through its affect on an internal coordinate.

Given this background, the modeling approach of the particle phase provides a framework for the experimental team and the simulation team to

1.) define a set of relevant (meaningful) internal coordinates for the coal phase

2.) identify physical models that affect the selected internal coordinates

Once the relevant parameters are defined along with the physical models for the phenomena that affect the NDF, this will be coupled with the LES simulation to provide a simulation tool for heat flux predictions to the wall of the gasifier.

## Subtask 12.2 – Entrained-Flow Gasifier Modification

The aim of this task was to modify the University of Utah's existing pressurized entrained-flow gasifier (Figure 46) so that it could process coal. The system was originally designed to process spent pulping liquor (black liquor) under U.S. Department of Energy cooperative agreement DE-FC26-04NT42261. That program was terminated after the first year due to lack of funding and a redirection of priorities within the Office of Biomass Programs. Consequently, construction of the entrained-flow gasifier was never fully completed and the system was never operated.

Pressurized entrained-flow gasification of coal and black liquor are overall very similar processes. But, there are several important differences between the two processes:

- Black liquor gasification takes place at approximately 975°C while coal gasifiers typically operate much hotter, near 1400°C.
- Black liquor is a homogeneous aqueous solution that does not need to be constantly mixed. Concentrated black liquor does, however, need to be heated in order to flow or to be pumped. Coal slurry is more challenging because the coal will rapidly settle and "harden" if the slurry is not constantly kept well mixed.
- The "ash" or molten smelt from black liquor gasification is soluble in water so no specific solids handling system is necessary. Coal slag, on the other hand, will solidify and settle to the bottom of the water bath below the quench part of the reactor.
- Black liquor smelt is caustic so the quench bath has a high pH (~12). Coal slag is somewhat acidic. Materials of construction must be carefully selected.
- Molten black liquor smelt has a relatively low viscosity and flows readily down the wall of a gasifier. Coal slag is very viscous even at the much higher operation temperature of a coal gasifier, presenting a risk for buildup of slag within the reactor.

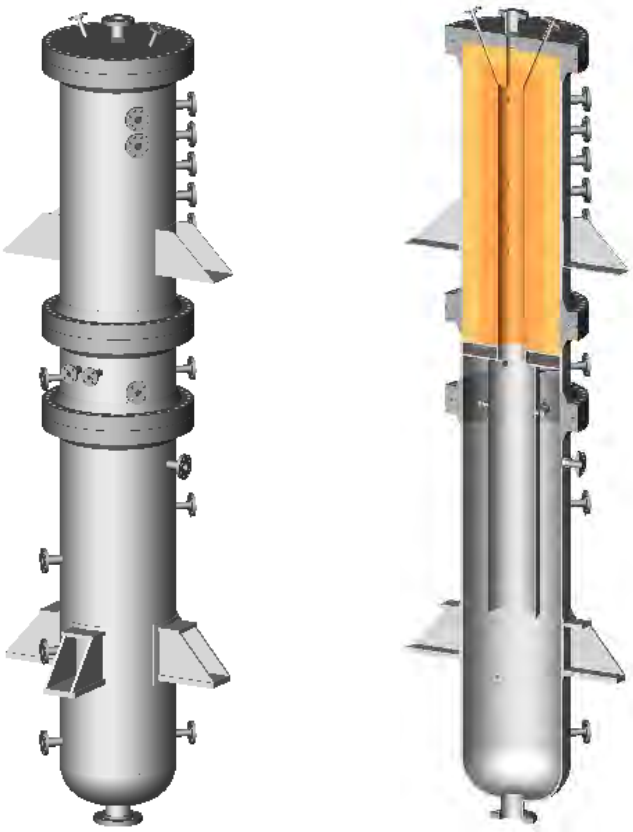

**Figure 46.** Rendering of the entrained-flow gasifier and split view of same.

In order to estimate conditions and performance of the existing entrained-flow gasifier when operating on coal, two Excel-based models were developed. One was very simple and assumed complete conversion of coal slurry to slag and a synthesis gas comprising only CO, $H_2$, $CO_2$ and $H_2O$. Such assumptions result in a maximum volumetric production of syngas and a minimum residence time in the reactor. This model was used to estimate limits of operation and approximate "worst case" flow rates for slurry, oxygen, quench water and syngas. These flow rates were used to specify ranges of the various flow meters, etc. Based on this analysis and a residence time in the reactor of 6 seconds, it is expected that the gasifier should be able to process coal slurry at a rate corresponding to more than 1 ton/day (dry) of coal when operating at pressures greater than 20 bar (300 psi).

The other model developed under this subtask is more involved and uses a Gibbs Free Energy minimization approach to predict the composition of the syngas, syngas flow rate and adiabatic flame temperature based on coal composition, slurry concentration, oxygen/fuel ratio and coal feed rate. This model considers approximately one dozen components in the synthesis gas. Although there are commercial packages such as Aspen and Hysys which can perform equilibrium calculations such as this,

it is desirable to have a portable simulator that can be used without needing expensive, specialized software.

Modification of the gasifier initially focused on the quench system, since it is imperative that the system is able to adequately cool the product from the gasifier before contacting metal components downstream. Water for the primary quench sprays was changed from city water to softened water since deposits quickly formed within the nozzles when using city water. No deposits were observed after this change. A new safety loop was added to the control system which shuts off oxygen and fuel flow if quench recirculation stops, quench spray flow stops or the temperature downstream of the primary quench exceeds a preset temperature (default 500°F). The quench system was tested during operation on natural gas standby and during gasification of isopropyl alcohol and found to efficiently cool the gas exiting the reactor.

Temperature measurement in entrained-flow coal gasifiers is notoriously difficult since the harsh environment quickly corrodes thermocouples. Temperature measurement is critical for this system, however, since it is a research reactor and will ultimately provide validation data to the simulations that are being performed. Two B-type thermocouples were ordered from SynTemp, Inc., a company that specializes in gasifier thermocouples. The thermocouples are able to measure temperatures to 1800°C (3270°F). The thermocouples were installed near the burner and near the exit of the gasifier, positioned such that they protrude approximately 1 cm from the wall of the reactor. Initial testing indicates that the thermocouples perform as intended. The control system was programmed to trip the system if either of the thermocouples exceeds a preset temperature.

The other major activity associated with rebuild of the system was development of a coal slurry preparation and feed system. The University of Utah has no experience making or handling coal slurry. Due to costs associated with a complete feed system able to match the full capacity of the gasifier, it was decided to make a prototype system using existing components available at the University's Industrial Combustion and Gasification Research Facility. The prototype system (Figure 47) comprises a 20-gallon slurry preparation and mixing tank, 2-hp recirculation pump, mixing paddle and a small progressive cavity pump for feeding the coal slurry.

**Figure 47.** Prototype coal slurry feed system. The progressive cavity pump body is seen below the tank, the motor for the mixer is vertically mounted in the upper-left corner of the photo. The recirculation pump is near the center of the photo.

The coal slurry feed system has proven to be able to easily mix and circulate slurry exceeding 60% coal by weight. It was found that the recirculation motor was so powerful that it would actually heat the mixture over time, causing water to evaporate from the slurry, thereby increasing its concentration. The final design will have a variable frequency drive on the motor which will allow it to be operated at lower rotational speeds. The progressive cavity pump was not able to deliver a stable flow of slurry, nor was it able to pressurize the material beyond roughly 15 psi. This was surprising, since several sources indicated that this design of pump is the most appropriate for handling coal slurry in this flow range. Ultimately, after consultation with the pump manufacturer and disassembly of the pump it was observed that the stator was cracked, likely due to its age and lack of contact with fluids for many years. A new rotor and stator set was ordered which should allow pressurizing to approximately 10 bar (150 psi), but these components had a very long lead time and had not arrived by the end of the program.

Most of the effort under this subtask focused on establishing safe operability of the system when processing coal slurry. The quench and downstream systems have been proven to work well. Because the coal slurry feed system was not yet functioning, a test campaign involving gasification of isopropyl alcohol was conducted over several days. The fuel was fed using a 10-gallon vessel pressurized with compressed air to force the fuel out. This test was successful because it provided an opportunity to test heating the reactor on natural gas for several days, establishing a safe procedure for initiating gasification

of the fuel, and experiencing operation at various pressures and oxygen/fuel ratios. The system was operated at pressures to 5 bar (75 psi) and the pressure control valve worked well. Although the objective of this task, getting the system completely ready for operation on coal, was not fully achieved the gasifier has been tested and is expected to be available for operation during the next phase of the research.

# CONCLUSIONS

Key conclusions from this research are summarized in the sections below.

### *Pressurized Pyrolysis of Coal in a Flat Flame Burner System*

After a number of modifications to improve the system, the pressurized flat flame burner system at BYU is now capable of performing high heating rate pyrolysis experiments on pulverized coal. Initial testing on an eastern subbituminous coal resulted in char with a high internal surface area, roughly 360 $m^2/g$. Continued testing is planned for the follow-up CASE research program.

### *Production and Characterization of Coal Tars*

Flat flame burner systems are also suitable for study of tar formation and behavior of tar compounds in a high temperature environment. Two surrogate compounds were tested in an atmospheric pressure FFB system and the products were analyze by NMR spectroscopy. 2,6-dimethylnaphthalene is a disubstituted two-ring compound and 6-(5H)-Phenanthridinone contains both nitrogen and oxygen. The methyl groups are easily stripped from the 2,6-dimethylnaphthalene but the ring structure remains quite stable. 6-(5H)-Phenanthridinone remained relatively intact, even more so than a subbituminous coal that was tested under similar conditions in the flat flame burner system. This result was unexpected and has no obvious explanation. This will be examined further in future campaigns.

### *Transition from Coal Char to Slag*

A new high temperature entrained-flow reactor system was constructed and used to produce a series of coal chars with varying carbon contents corresponding to various degrees of conversion. At temperatures in excess of the coal's ash fusion temperature, a significant decrease in internal surface area was observed at a conversion of roughly 92%. This is a result of the char transitioning ("collapsing") from a highly porous, solid material into a melted, much less porous slag-type material. This collapse

appears to be associated with migration of mineral inclusions to the surface of the char. No such collapse was observed when the temperature of the system was below the ash fusion temperature.

### *Modeling and Verification of Ash Sintering and Melting*

Previous particle sintering models divide sintering rates into several regimes depending mainly on surface curvature. A closed-form and explicit model was developed that describes particle neck size, neck radius of curvature, neck length, and essentially all other geometric properties for the idealized case of two equally sized spheres sintering without change in sphere diameter but with change in neck size and overall shrinkage.

Experimental data describing sintering for both surrogate and ash deposits indicate that ash deposits sinter unlike randomly packed particles in several important ways. Specifically, ash deposits maintain porosity longer, develop strength more slowly and to a lesser extent, and maintain anisotropic structure longer compared to random sphere structures. Random sphere experiments, which are common, can provide useful information on sintering rates and extents, but they are poor representations of deposit structures and cannot generally simulate them directly. In general, low-rank fuels sinter to a lesser extent than high-rank fuels under similar conditions. This fuel-rank dependence is much larger than any detectable dependence on local stoichiometry (gasification vs. combustion) in the limit of no melting or slag formation. The dependence agrees well with known and general properties of deposit composition and particle size between these two fuels. Thermal conductivity provides a quantifiable estimate of the degree of sintering.

# ACKNOWLEDGEMENTS

This material is based upon work supported by the Department of Energy under Award Number DE-FC26-06NT42808. Praxair, GE Energy, ConocoPhillips, Shell, Eastman Chemical Company and Tampa Electric Company all provided valuable input, either formally or informally, to this work. The U.S. Department of Energy's Albany Research Center is thanked for valuable cooperation regarding gasifier refractory performance.

# REPORT FIGURES

# REPORT TABLES

# REFERENCES

Abd-Elhady, M. S., S. H. Clevers, T. N. G. Adriaans, C. C. M. Rindt, J. G. Wijers and A. A. van Steenhoven (2007). "Influence of sintering on the growth rate of particulate fouling layers." *International Journal of Heat and Mass Transfer* 50(1-2): 196-207.

Al-Otoom, A. Y., L. K. Elliott, B. Moghtaderi and T. F. Wall (2005). "The sintering temperature of ash, agglomeration, and defluidisation in a bench scale PFBC." *Fuel* 84(1): 109-114.

Anderson, D. W. (1985). Heat Transfer Through Coal Ash Deposits. West Lafayette, Purdue. Doctor of Philosophy: 305.

Anderson, D. W., R. Viskanta and F. P. Incropera (1987). "Effective Thermal Conductivity of Coal Ash Deposits at Moderate to High Temperatures." *Journal of Engineering for Gas Turbines and Power* 109: 215-221.

Baxter, L. L. (1992). *Combustion and Flame* 90(2):174–184.

Bhatia, S. K.; Perlmutte, D. D. (1980). *AIChE Journal*, 26:379–385.

Bhatia, S. K.; Perlmutte, D. D. (1981). *AIChE Journal*, 27:247–254.

Cundick, D. P. (2009). Characterization of the thermal transport through a temporally varying ash layers. Mechanical Engineering. Provo, UT, Brigham Young University. MS.

Feng, B.; Bhatia, S. K. (2003). *Carbon*, 41:507–523.

Frederick, W. J. and E. Vakkilainen (2003). "Sintering and structure development in alkali metal salt deposits formed in a kraft recovery boiler," Colloquim on Black Liquor Gasification and Combustion, Park City, UT.

Freihaut, J. D., W. M. Proscia and D. J. Seery, "Chemical Characteristics of Tars Produced in a Novel Low-Severity, Entrained-Flow Reactor," *Energy & Fuels,* 3(6), 692-703 (1989).

Gale, T. K., C. H. Bartholomew and T. H. Fletcher, "Decreases in the swelling and porosity of bituminous coals during devolatilization at high heating rates," *Combustion and Flame,* 100(1-2), 94-100 (1995).

Gavalas, G. R. (1980). *AIChE Journal*, 26:577–584.

German, R. (1996). Sintering Theory and Practice. New York, Wiley.

Handwerker, C. A., J. E. Blendell and W. Kaisser (1990). Sintering of advanced ceramics Westerville, Ohio American Ceramic Society.

Hurt, R. H.; Sarofim, A. F.; Longwell, J. P. (1991). *Fuel* 70:1079–1082.

Kang, S.-J. L. (2005). Sintering : densification, grain growth, and microstructure. Amsterdam, Elsevier Butterworth-Heinemann

Kantorovich, I. I.; Bar–Ziv, E. (1994). *Combustion and Flame*, 97:61–78.

Kantorovich, I. I.; Bar–Ziv, E. (1994). *Combustion and Flame*, 97:79–87.

Lan, Z.-Q., X.-Y. Cao, J.-D. Xu, J.-H. Zhou, J.-Z. Liu and K.-F. Cen (2005). "Study on sintering characteristics of the black liquor coal water slurry's slags in test furnace." Meitan Xuebao/Journal of the China Coal Society 30(4): 489-492.

Lien, S. J., H. K. Theliander and J. W. James Frederick (2004). Effect of Gas Composition on Fume Sintering Rates. 2004 International Chemical Recovery Conference, Charleston, South Carolina.

Lin, S. Y.; Hirato, M.; Horio, M. (1994). *Energy & Fuels*, 8:598–606.

Liu, H.; Luo, C.; Kato, S.; Uemiya, S.; Kaneko, M.; Kojima, T. (2006). *Fuel Processing Technology*, 87:775–781.

Llorente, M. J. F. and J. E. C. Garcia (2005). "Comparing methods for predicting the sintering of biomass ash in combustion." Fuel 84(14-15): 1893-1900.

Llorente, M. J. F., P. D. Arocas, L. G. Nebot and J. E. C. Garcia (2008). "The effect of the addition of chemical materials on the sintering of biomass ash." Fuel 87(12): 2651-2658.

Llorente, M. J. F., R. E. Cuadrado, J. M. M. Laplaza and J. E. C. Garcia (2006). "Combustion in bubbling fluidised bed with bed material of limestone to reduce the biomass ash agglomeration and sintering." Fuel 85(14-15): 2081-2092.

Morimoto, T.; Ochiai, T.; Wasaka, S.; Oda, H. (2006). *Energy & Fuels*, 20:353–358.

Perry, S. T., E. M. Hambly, T. H. Fletcher, M. S. Solum and R. J. Pugmire, "Solid-state 13C NMR characterization of matched tars and chars from rapid coal devolatilization," *Proceedings of the Combustion Institute,* 28(2), 2313-2319 (2000).

Rahaman, M. N. (2007). Ceramic Processing. Boca Raton, Taylor & Francis.

Rezaei, H. R., R. P. Gupta, G. W. Bryant, J. T. Hart, G. S. Liu, C. W. Bailey, T. F. Wall, S. Miyamae, K. Makino and Y. Endo (2000). "Thermal Conductivity of Coal Ash and Slags and Models Used." Fuel 79: 1697-1710.

Robinson, A. and L. Baxter (2000). A Framework for Simulating the Effects of Sintering on Ash Deposit Thermal Conductivity. Effects of Coal Quality on Power Plants: Ash Problems, Management and Solutions, Park City, UT.

Robinson, A. L., S. G. Buckley and L. L. Baxter (1998). "In situ measurements of the thermal conductivity of ash deposits." Symposium (International) on Combustion Proceedings of the 1998 27th International Symposium on Combustion,Aug 2-Aug 7 1998 2: 1727-1735.

Robinson, A. L., S. G. Buckley and L. L. Baxter (2001). "Experimental measurements of the thermal conductivity of ash deposits: Part 1. Measurement technique." Energy & Fuels 15: 66-74.

Robinson, A. L., S. G. Buckley, N. Yang and L. L. Baxter (2000). Experimental Measurements of the Thermal Conductivity of Ash Deposits: Part 2. Effects of sintering and deposit microstructure. United States: 37p.

Robinson, A. L., S. G. Buckley, N. Yang and L. L. Baxter (2000). Experimental Measurements of the Thermal Conductivity of Ash Deposits: Part 2. Effects of Sintering and Deposit Microstructure. Albuquerque, NM, Sandia National Laboratories: 1-29.

Robinson, A. L., S. G. Buckley, N. Yang and L. L. Baxter (2001). "Experimental measurements of the thermal conductivity of ash deposits: Part 2. Effects of sintering and deposit microstructure." Energy & Fuels 15: 75-84.

Simons, G. A. (1983). *Progress in Energy and Combustion Science*, 9, 269–290.

Sinquefield, S. (1998). Deposition of Submicron- and Micron-sized Particles from Combustion of Black Liquor. Chemical Engineering. Corvallis, OR, Oregon State UniversityEditor.

U.S. Department of Energy (2002). "Gasification Technologies: Gasification Markets and Technologies – Present and Future. An Industry Perspective," Report DOE/FE-0447.

Wall, T. F., S. P. Bhattacharya, D. K. Zhang, R. P. Gupta and X. He (1993). "Properties and thermal effects of ash deposits in coal-fired furnaces." Progress in Energy and Combustion Science 19(6): 487-504.

Watt, M., T. H. Fletcher, S. Bai, M. S. Solum and R. J. Pugmire, "Chemical structure of coal tar during devolatilization," *Symposium (International) on Combustion*, 26(2), 3153-3160 (1996).

Wu, H.; Bryant, G.; Wall, T. (2000). *Energy & Fuels*, 14:745–750.

Wu, H.; Wall, T.; Liu, G.; Bryant, G. (1999). *Energy & Fuels*, 13:1197–1202.

Xu, M.-L., J.-H. Yan, Z.-Y. Ma, Q. Wang and K.-F. Cen (2006). "Characterization of sintering deposit on the heat-transfer surface of CFB municipal solid waste incinerator." Ranliao Huaxue Xuebao/Journal of Fuel Chemistry and Technology 34(5): 547-552.

# Carbon Dioxide Sequestration: Effect of the Presence of Sulfur Dioxide on the Mineralogical Reactions and on the Injectivity of $CO_2$+$SO_2$ Mixtures

Topical Report

Reporting period: July 1, 2006 to May 31, 2009

*Authors: Prashanth Mandalaparty, Milind Deo, Joe Moore and Brian McPherson*

January 2010

DOE Award Number: DE-FC26-06NT42808

Tasks 13 and 14

University of Utah

**Institute for Clean & Secure Energy**
**380 INSCC, 155 South, 1452 East**
**Salt Lake City, UT 84112**

**Disclaimer**

## Abstract

This report presents experimental and modeling data on certain aspects of carbon dioxide ($CO_2$) sequestration. As different processes are developed and implemented to facilitate the capture of $CO_2$, other contaminant gases (sulfur dioxide, hydrogen sulfide and ammonia) may be present in the sequestration stream. One of the important questions is how $SO_2$ changes the overall chemistry of the system. It is also important to understand how this change impacts practical aspects of sequestration, such as gas injectivity. In this study, a detailed experimental investigation of the reactivity of $CO_2$+$SO_2$ mixtures with brines and rocks of specific mineralogy (typical of sequestration environments) was conducted. $CO_2$ with 10% $SO_2$ was reacted with brine and arkose at $100^0$C and 600 psia, and the mineralogical and brine chemistry changes were compared with base-case experiments with no $SO_2$ in the mixture and with results of experiments carried out at low pH. The base case $CO_2$ experiments carried out over different time periods showed initial calcium carbonate dissolution followed by re-precipitation of calcite. A few other mineral precipitations (notably ankerite) were observed. The brine chemistry changes were consistent with the mineralogical changes observed. When $SO_2$ was present in the mixture, continued dissolution of calcite and precipitation of anhydrite (calcium carbonate) was observed. Numerical simulations of the injection of $CO_2$ and $CO_2$ and $SO_2$ mixtures into rocks of different mineralogy did not show significant differences in injectivity between the two cases. A simulation study about vertical migration and mixing was also carried out. It was shown that absolute permeabilities of the seal play an important role in free-gas and dissolved gas distribution, but relative permeability effects are also important in determining how $CO_2$ distributes in the saline formation into which it is injected.

## Table of Contents

## Executive Summary

Carbon dioxide ($CO_2$) sequestration is considered to be at least a partial solution to decrease $CO_2$ emissions to the atmosphere, thus stemming the rapid rise in atmospheric $CO_2$ concentrations. The process has been conceptualized as being able to inject large quantities of $CO_2$ into saline formations, since saline formations offer the most storage capacity. Mineralogical sequestration, where $CO_2$ gets mineralized to a carbonate or related component, is the permanent storage mechanism. However, as the reactions occur, there are changes in rock properties that can impact the operation of the process. When $CO_2$ is being captured for sequestration, separating small amounts of other gas species from $CO_2$ is expensive, and if these contaminants do not have a significant impact on the sequestration process, they could be co-injected with $CO_2$. One such contaminant is $SO_2$. This project was structured into three tasks to answer the following questions.

1. How does the presence of $SO_2$ change the base mineralogical sequestration reactions? This question was addressed by performing high-temperature, high-pressure sequestration reactions with and without the presence of $SO_2$.

2. Does the presence of $SO_2$ affect the injectivity of $CO_2$ and $SO_2$ mixtures? An experimental system was designed and assembled during this project period.

3. How do the seal properties affect vertical migration of $CO_2$? Numerical simulations of hypothetical sequestration processes were conducted to assess the impact of different domain properties on the distribution of $CO_2$ in the formation.

An experimental program was designed to study the effects of the presence of $SO_2$. First, baseline experiments with mixtures of $CO_2$, brine and rocks of specific compositions were conducted to establish reactions that take place with $CO_2$. A high-temperature and high-pressure reaction system was built, and reactions were carried out from temperatures ranging from $50^0$C to $200^0$C and at pressures from 600 psia to 2000 psia. All of $SO_2$ experiments were carried out with 10% $SO_2$ and 90% $CO_2$ mixtures. Experiments were carried out at multiple times with the identical compositions. The baseline experiments revealed that the initial time period was dominated by dissolution of minerals like calcite.

As the reactions progress, re-precipitation causes the calcium ion concentration to decrease. The presence of $SO_2$ changes the fundamental chemistry of the system. The calcite dissolution continues. However, precipitation of anhydrite (calcium sulfate) is observed later in time. Mineral dissolution and precipitation has implications on permanent sequestration of $CO_2$. These processes also affect the porosity and permeability of the system. Locally, changes in porosity and permeability can affect the injectivity of $CO_2$.

An experimental system was designed and assembled to study changes in injectivity with and without the presence of $CO_2$. The experimental system consists of two precision high-pressure pumps capable of injecting liquid and gases at predetermined rates into cores at formation conditions.

The manner in which $CO_2$ distributes itself in the reservoir is also important in determining the distribution of $CO_2$ in the gas phase and in the dissolved aqueous phase. The dissolved-phase concentration is important in determining the mineralogical reactions that occur. The vertical migration is not only governed by the absolute permeabilities of the interbedded seals but also by the relative permeabilities. In this study, a condition known as “permeability jail”, where, the relative permeabilities to both the gas and the aqueous phases remains low (close to zero) over a certain saturation range, was explored. It was shown that these types of relative permeabilities will result in seals acting as low-permeability barriers, trapping $CO_2$ more effectively.

## Background

Carbon dioxide ($CO_2$) is the most abundant (64%) greenhouse gas (GHG). The atmospheric concentration of $CO_2$ has increased from 280 ppm during the preindustrial period to 385 ppm with about half this increase having occurred since the mid 1960s. In the United States the majority of the $CO_2$ emissions are from power plants which account for about 40% of the total emissions (IPCC 2007). Carbon dioxide sequestration appears to be an important potential method by which emissions into the atmosphere can be reduced. In this method, anthropogenic $CO_2$ is injected into geologic formations such as saline formations, depleted oil reservoirs ($CO_2$ enhanced oil recovery) and unmineable coal seems (enhanced coal bed methane recovery). These formations are widely available and are often in close proximity to majority of the point emission sources (Holloway et al. 1997). Injection of $CO_2$ deep underground is particularly promising because deep sedimentary formations have the potential to retain $CO_2$ in the subsurface for thousands to millions of years (Bachu 2002). In the United States, the capacity of deep saline formations is greater than any other geologic formation with very high estimates (U.S. Department of Energy, 2007, 2008, 2009), and they are also found within close proximity to power plants. Formations with salinities exceeding 10,000 mg/l total dissolved solids are excluded by the U.S. Environmental Protection Agency as underground sources of drinking water (Xu et al. 2005). Hence these form a primary target for the eventual disposal of $CO_2$.

The temperature in these formations ($50^0$-$80^0$C) varies greatly depending on the depth and also the local geothermal gradients (Bachu 2002). Typically, $CO_2$ is injected at depths greater than 800m to ensure that it stays in the super critical state (critical temperature and pressure of $CO_2$ are $31^0$C and 1073 psi, respectively) (Span and Wegner 1996). The notion of $CO_2$ disposal in formations has been discussed in the literature with specific formations as target; for example, in the Netherlands (Lohuis 1993) and the Alberta Basin, Canada (Gunter 1993 Bachu 1994, Perkins and Gunter 1995, Gunter 1996, 1997 Bachu 1996). The comprehensive Carbon Sequestration Atlas (U.S. DOE, 2007 and 2008) provide up-to-date information on capacities in the United States and Canada.

Geologic formations, which are artificially charged with $CO_2$ are called carbon repositories (Kaszuba et al. 2005). Once injected $CO_2$ being more buoyant than water will rise until it hits an impermeable membrane or low permeability seal. This is called structural or stratigraphic trapping of $CO_2$. Subsequently, depending on a rate controlled by several factors such as the rate of $CO_2$ injection, the rate of $CO_2$ dissolution into the pore water, the surface area available for the reaction and the rate of diffusion of the $CO_2$ into the pore water away from the pore water-$CO_2$ interface, $CO_2$ dissolves in the formation water. This process is termed solubility trapping. With time $CO_2$ is trapped as a discontinuous phase (either in supercritical form or as dissolved $CO_2$) in the pores of a formation leading to capillary trapping. $CO_2$ forms carbonic acid, which dissociates to form carbonate and bicarbonate ion leading to ionic trapping of $CO_2$. Finally these anions react with the cations resulting from the dissolution of primary minerals, due to decreased pH, which in turn leads to precipitation of carbonates permanently sequestering $CO_2$ (Bateman et al. 2005). Hence logically, mineral precipitation can be termed sequestration, whereas other mechanisms can be termed as storage (Kaszuba et al. 2005).

Not much importance has been given to mechanisms by which $CO_2$ is actually trapped as immobile mineral phases. Kaszuba et al. (2003) carried out a study to determine the extent of fluid rock interactions in addition to carbonate mineral precipitation that may occur in an experimental system that simulates geologic storage and sequestration of $CO_2$. They reported the precipitation of magnesite, siderite and analcime. Kaszuba et al. (2005) then carried out a study to analyze the effect of $CO_2$ injection on fluid rock reactions and also assess the effect of these geochemical interactions on the integrity of the cap-rock. Shale was used to model the aquitard. Such analyses for the integrity of cap-rock had been performed by Lindeberg (1997) using simple numerical models (Darcy equation and Fick's law). They attributed the leakage of $CO_2$ to gravity migration with subsequent release through sub vertical fractures and faults. Few experimental studies examined geochemical reactions in a saline formation in response to $CO_2$ injection. Gunter et al. (2000) and Perkins and Gunter (1995) carried out numerical geochemical modeling studies that incorporated kinetic laws and some studies combining experiments and modeling, in which dissolution of silicate minerals in brine and precipitation of carbonate are reported. The dominant state of carbonic acid with respect to pH plays an important

role in governing the factors that leads to formation of carbonates in formation (Soong et al. 2002, Drever 1988, Miller et al. 2005). Miller et al. reported the formation of calcite at pressures of around 600 psi and at $150^0$C. Rosenbauer et al. (2005) reported the affect of presence of $SO_4^-$ on geochemical reactions and the solubilities and porosities of the repository.

## Objectives

The objectives of this project were as follows:

1. Develop an experimental assembly to analyze $CO_2$ , brine and rock interactions.
2. Develop an understanding on the effect of the presence of $SO_2$ in the $CO_2$ stream during sequestration on the mineralogical reactions in saline formations.
3. Study the effects of the presence of $SO_2$ on the injectivity of $CO_2$ in formations.
4. Evaluate the effects of different seal properties on vertical migration of $CO_2$ in formations.

## Experimental Methods

### Mineralogical Reactions

Dirty sandstone was selected as the reacting material because of its diverse geochemical reaction basis and common occurrence in sedimentary basins (Kaszuba et al. 2005). The dirty sandstone used in our experiments is comprised of equal proportions of calcite, dolomite, quartz, microcline, andesine and chlorite. The physical properties of these materials are provided in Table 1. The minerals were crushed to 100μm and mixed to create the initial mineral assemblage. The minerals were angular to circular in shape and ranged in size from 80-100μm.

Table 1. Physical properties of the rocks used to construct the dirty sandstone.

| Rock | Quartz | Andesine | Dolomite | Chlorite | Microcline | Calcite |
|---|---|---|---|---|---|---|
| Formula | $SiO_2$ | $Na_xCa_yAlSi_2O_8$ | $CaMg(CO_3)_2$ | $(Fe, Mg, Al)_6(Si, Al)_4O_{10}(OH)_8$ | $KAlSi_3O_8$ | $CaCO_3$ |
| Class | Silicates | Silicates | Carbonates | Silicates | Silicates | Carbonates |

The experimental apparatus is illustrated in Figure 1. It consists of a series of four stainless steel reactors made of 316-grade stainless steel, which were rated for 4000 psi at $600^0$C. The reactors were pressure sealed with high-pressure SWAGELOK fittings. The reactor has the provision for retrieving the rock sample without disturbing it through a detachable cap (Swagelok fitting) at the bottom. The $CO_2$ was pressurized in the reactor using a single cylinder high-pressure positive displacement pump. The flow of $CO_2$ into the reactor was controlled using high-pressure needle valves. Dry $CO_2$ (drawn from a $CO_2$ cylinder equipped with a siphon) was used in all the experiments. High-purity nitrogen was used to pressure test the entire setup at 3000 psi. The temperature was controlled using a bench-top temperature controller with SPECVIEW as the interface via K-type thermocouples. Brine was prepared from laboratory grade NaCl with the initial composition shown in Table 2.

Table 2. Initial composition of the brine for all the experiments (<=detection limits).

| **Na** | **Mg** | **K** | **Ca** | **Al** | **Mn** | **Fe** | **Ba** | **Si** | **S** | **Cl** |
|---|---|---|---|---|---|---|---|---|---|---|
| mg/L | mg/L | mg/L | mg/L | µg/L | µg/L | µg/L | µg/L | mg/L | mg/L | mg/L |
| 23032 | 1 | <6 | <4 | <8 | <1 | 54 | <2 | 0.4 | <6 | 26542 |

High purity nano-filtered de-ionized (DI) water was used to prepare the brine samples. Injection of approximately 7cc of $CO_2$ into the reactor increases the pressure of the experimental system to 2200 psi. Subsequently the pressure decreased to 2000 psi over a period of 37 hrs. The total pressure of the experimental system stabilized around 2000 psi for the duration of the experiment with the exception of a few fluctuations, which can be attributed to changes in the ambient temperature in the laboratory. Three sets of

experiments were carried out at different conditions with different feed gas compositions. Table 3 lists the conditions adopted for each of these experiments.

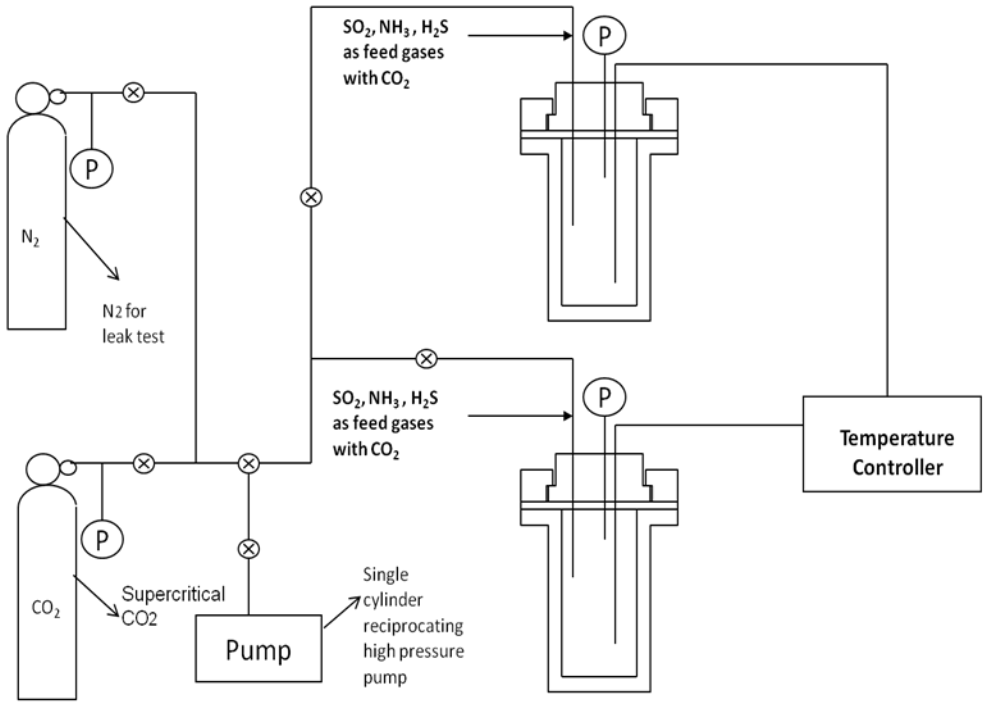


Figure 1. Schematic diagram of the experimental setup.

Table 3. The conditions adopted for each of the experiments

| Experiment | Temperature ($^oC$) | Pressure (psi) | Gas Composition |
|---|---|---|---|
| Set A | 200 | 2000 | $CO_2$ |
| Set B | 100 | 2000 | $CO_2$ |
| Set C | 100 | 600 | $90\%CO_2+10\%SO_2$ |
| Set D | 100 | 2000 | $CO_2$ with an initial pH of 3 |

The advantage of using such apparatus over the previous experimental setup described in Seyfried et al. (1987), which was adopted by Kaszuba et al. (2003, 2005) and Rosenbauer et al. (2005), is that we can correlate the changes in mineralogy with the changes in brine chemistry at each stage the sample is collected. This provides a comprehensive picture of the geochemical interactions taking place. Sampling does not disturb the system, and

mineralogical changes can be viewed in light of the changes in brine chemistry. The rock analysis was carried out using X-ray diffraction (XRD), scanning electron microscope (SEM) and energy dispersive X-ray spectroscopy (EDS) analyses.

The initial sample was prepared by mixing equal proportions of rock (0.5 grams each). After the experiment the sample was retrieved from the reactor by detaching the bottom (wherein the sample rests in a cap) and carefully removing the sample without disturbing the crystals (of the minerals) that might have grown (precipitated) on the surface. The sample was dried overnight at $60^0$C, a temperature not high enough to alter the crystal structure of any minerals. The sample is then retrieved, cooled and split into equal fractions for XRD and SEM/EDS analyses. After the experiments the brine samples were diluted and filtered using Whatman 40 filter paper (retention capacity of 8μm) under a vacuum. The sample was then divided into sub-equal fractions for cation and anion analyses. The sample was acidified with addition of sulfuric acid to prevent any precipitation. The dissolved cations were analyzed using inductively coupled plasma mass spectrometry (ICPMS) and dissolved anions by ion chromatography.

**Injectivity studies**

The experimental setup consists of three dual cylinder Quizix pumps for $CO_2$, brine and the fluid for the overhead burden (Figure 2). The flow is regulated using high-pressure gate valves rated to 15000 psi. All the pumps are automated; the flow is controlled via pump-works software. The flow of the $CO_2$ and brine is directed to a core holder where the absolute and the differential pressures across the core are measured using sensitive pressure transducers. The brine after the breakthrough is collected on a digital scale and preserved for analysis. The whole assembly is mounted in a well-insulated oven maintained at $100^o$F.

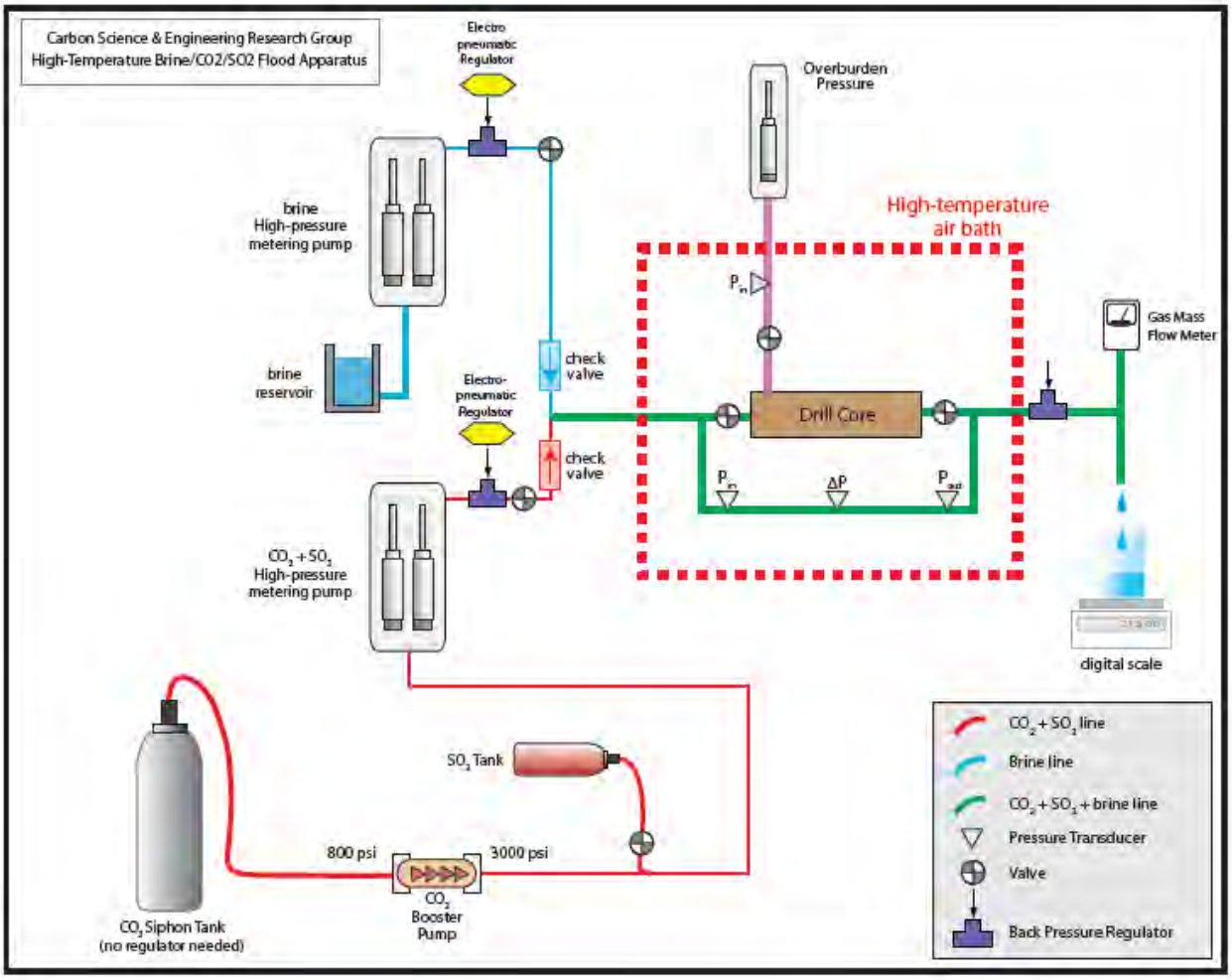


Figure 2. Schematic diagram of the experimental setup.

The experimental system was built, tested and evaluated for experiments. Special provisions were necessary for injecting $SO_2$ into the system.. However, the effort required to accomplish this was more extensive than originally anticipated. The proposed injectivity studies are being performed under separate funding, and the results will be published as they become available.

**Vertical migration studies**

For all simulation experiments, the TOUGHREACT simulator was utilized (Xu et al., 2006), which includes full thermal-hydrologic-chemical coupling – multiphase $CO_2$ flow, heat flow, and reactive transport. TOUGHREACT has a large user community and is widely used for predicting reactive transport and trapping behavior of injected $CO_2$ in

storage reservoirs (Xu et al. 2003, 2004, 2005, 2006, 2007; Audigane et al. 2007, Gherardi et al. 2007, and Zhang et al. 2009). TOUGHREACT utilizes the finite volume method (FVM) to solve the multiphase groundwater flow equation and uses a generalized form of Darcy's Law to evaluate flow velocities. Because all flow experiments and simulations involve brine, a robust chemical model of brine- $CO_2$-$SO_2$ interactions was needed. The original TOUGHREACT code (Xu et al., 2006) computed activity coefficients of charged aqueous species using an extended Debye-Huckel (DH) equation. The DH model can deal with ionic strengths from dilute to moderately saline water. During the course of the Yucca Mountain project, a Pitzer ion-interaction model was implemented into TOUGHREACT (Zhang et al., 2008) using the model formulated by Harvie et al. (1984).

For additional details about the TOUGHREACT simulator, the reader is referred to many recent sequestration publications (e.g., Xu et al. 2007; Audigane et al. 2007, Gherardi et al. 2007, Zhang et al. 2009).

The vertical migration studies were performed by using a multiphase flow simulator (TOUGHREACT) with different seal properties.

## Results

### Mineralogical reactions

***Initial examination of the rock surface*.** SEM and XRD analyses were performed on the rock samples. The SEM analysis was done using a HITACHI SEM equipped with an EDS analyzer. The EDS analyses identified the clay minerals, mainly plagioclase feldspar (Figure 3a) and illite (minor quantities) (Figure 3b) and chlorite to be the major silicate minerals and calcite and dolomite as the carbonate minerals in the starting material. The SEM analysis was performed at different resolutions to measure the exact chemical composition of the mixture and to ensure uniform composition.

Figure 4 shows the XRD analyses for two initial rock samples and indicates the overlap of the spectra for two initial samples, which turn out to be identical. This was done to ensure homogeneity during mixing of the six different rock samples to form the initial

mineral assemblage. The initial sample XRD analysis shows the peaks of the minerals used to prepare the sample. These peaks serve as a reference for the analysis of the reacted sample.

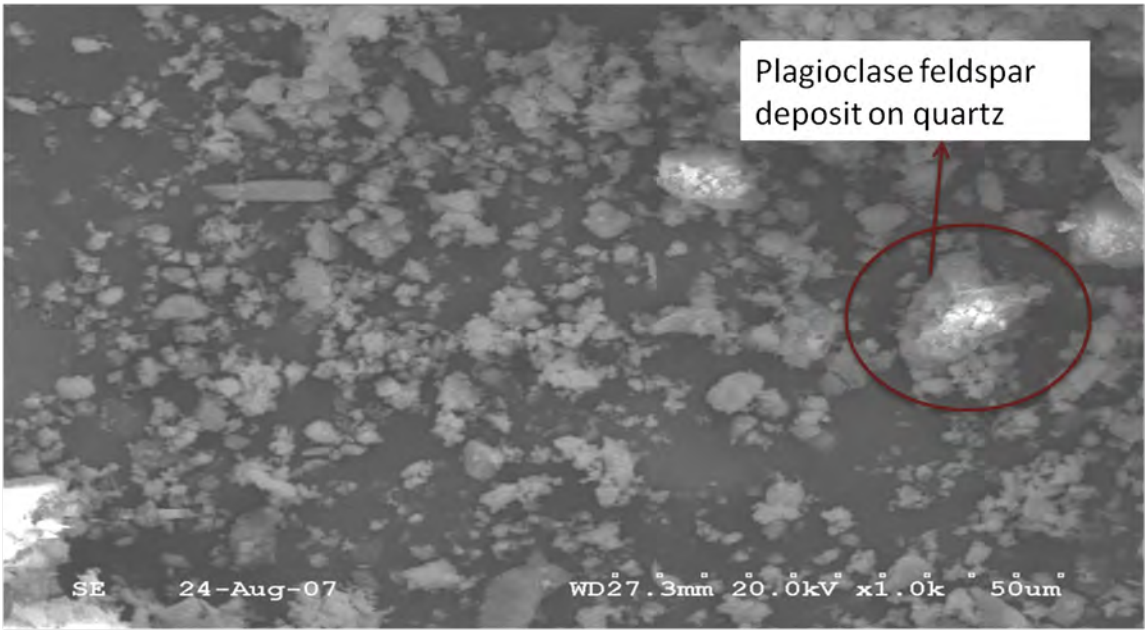


Figure 3a: SEM image of the host rock at 1kx magnification showing plagioclase feldspar deposits on quartz

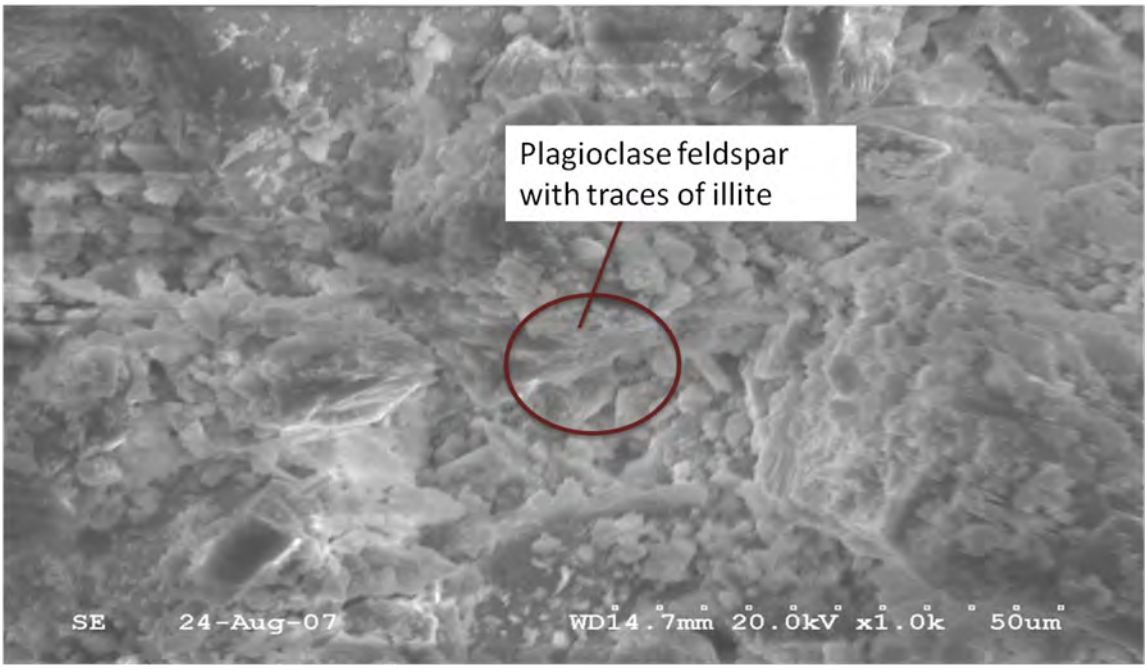


Figure 3b: SEM image of the host rock at 1kx magnification showing branched aggregates of plagioclase feldspar and minor quantities of illite

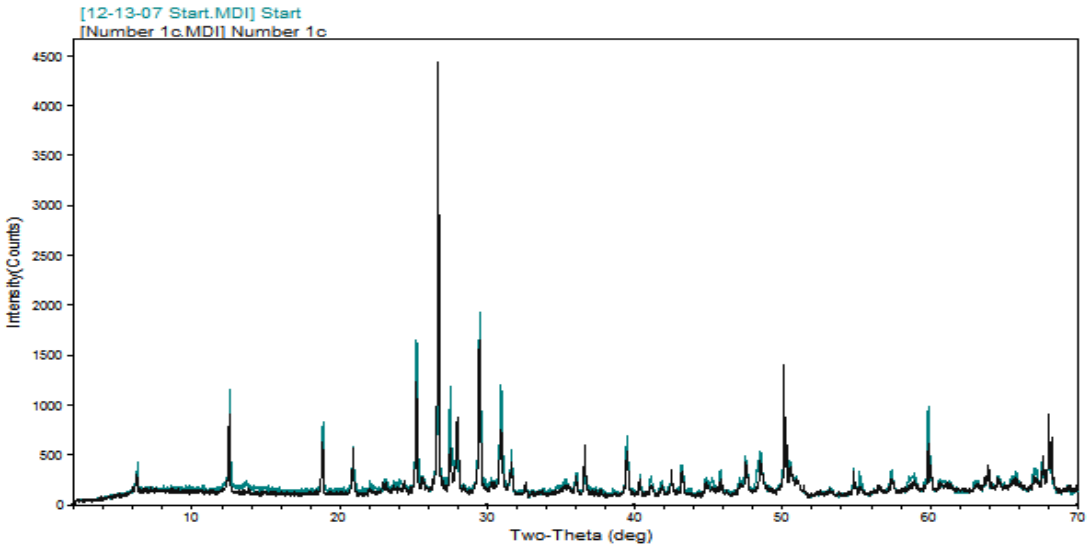


Figure 4: Initial XRD analyses of the host rock

***Experimental set A (200$^{o}$C and 2000 psi).*** The experimental conditions were similar to that of Kaszuba et al. (2003 and 2005). Under these conditions the rates of silicate dissolution are accelerated. However the aqueous solubility of $CO_2$ is generally lower at elevated temperatures and salinity and greater at elevated pressure. Using SUPCRT92 the maximum dissociation for carbonic acid dissolution occurs at 50$^{0}$C, above which log K decreases continuously with increasing temperature as a result of which initially weak acid becomes increasingly weaker at elevated temperatures (Rosenbauer et al. 2005). Consequently these experiments at ~200$^{0}$C were carried out for a relatively longer time period (123 days) to identify detectable changes in the host rock. For the reacted time period, pronounced changes were observed in the starting material. The major change in composition is observed in andesine, chlorite and quartz. While andesine and dolomite were observed to dissolve into the brine, calcite, quartz and chlorite were found to precipitate. The precipitation of quartz was not conclusive since the change in its composition was within the uncertainty in measurement with XRD. This XRD analyses gives a preliminary picture of the changes occurring in mineral phases and a preview of what to expect in the SEM/EDS analyses. To study the surface chemistry and to identify the precipitation or dissolution patterns of the dominant minerals on the samples the initial and the reacted samples were analyzed using SEM. The sample is mounted on a carbon tape and is gold coated in an inert (argon) environment to charge the surface.

SEM analysis requires careful observation of the surface of the sample at a very high resolution. The portions of the surface, which indicate the deposition of calcite as layers or crystals, are usually picked for analysis. The major change in composition is observed in andesine, chlorite and quartz. While andesine and dolomite were observed to dissolve into the brine, calcite, quartz and chlorite were found to precipitate (Table 4). The precipitation of quartz was not conclusive since the change in its composition was within the uncertainty in measurement with XRD. The patterns of XRD analyses of pre and post reaction sample are superposed in Figure 5. Figure shows precipitation of halite and calcite.

Table 4: Quantitative estimates of changes in compositions of the minerals (wt%) before and after the experiment from XRD analysis.

| Mineral | Initial (wt%) | Reacted (wt%) |
|---|---|---|
| Andesine | 23.9 | 18.28 |
| Calcite | 19.1 | 22.4 |
| Dolomite | 17.4 | 14.65 |
| Quartz | 15.7 | 17.8 |
| Chlorite | 14.4 | 17.92 |
| Microcline | 9.4 | 8.96 |

Calcium carbonate was observed to grow on the sample as layers (Figure 6a, 6b). Due to the increased acidity caused by the formation of carbonic acid, the primary minerals such as dolomite and calcite undergo dissolution. The calcium cation should be from dolomite or calcite because the XRD analyses reveal the dissolution of these minerals. The calcium ion thus liberated into the solution forms calcite by combining with the carbonate ion from the acid consuming one mole of $CO_2$ in the process. Calcium carbonate deposition is a clear indication of the consumption of $CO_2$ in this reaction. Chunks of halite were deposited on the reacted surface (Figure 6c). Halite must be from the brine used in the experiment because the sample was dried overnight at $60^0$C before the analysis.

Ankerite, (iron carbonate) was seen growing as aggregates on the reacted surface usually intergrown with the initial minerals (usually quartz) (Figure 6d). The source of iron for ankerite was the dissolution of chlorite, magnesium-rich clay in the initial sample. The

XRD analyses, which shows the dissolution of chlorite, confirms this. The qualitative X-ray analysis by EDS confirmed the identification of ankerite and it was absent in the initial mineral assemblage at the start of the experiment. The growth was seen as aggregated units in the interstitial spaces between the primary minerals especially quartz.

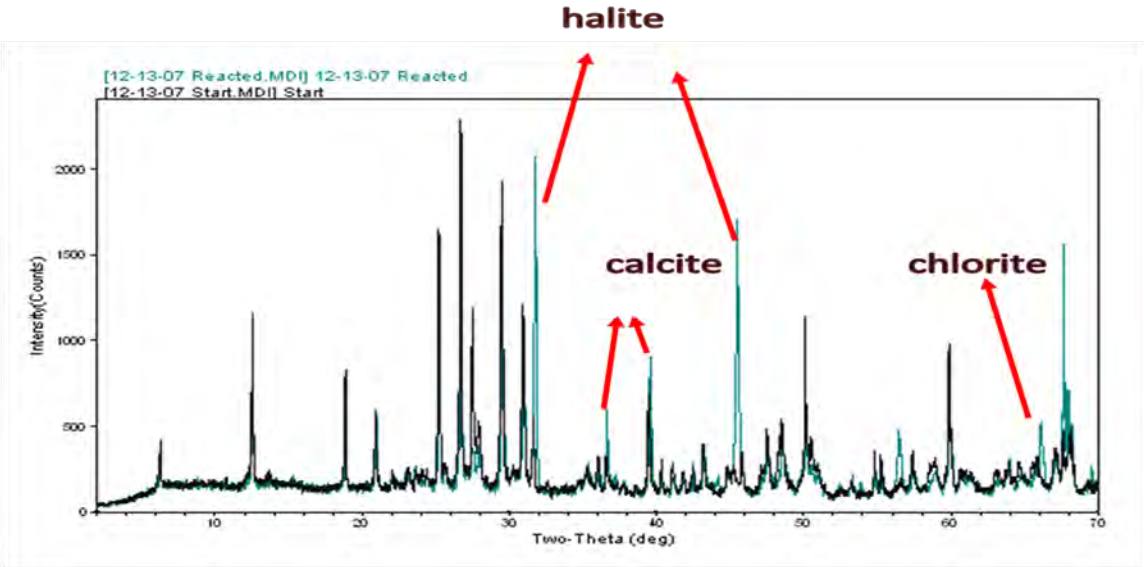


Figure 5: XRD overlap of the initial and the reacted samples for the experiment at 200°C and 2000 psi. The distinctive peaks seen are halite and chlorite and calcite

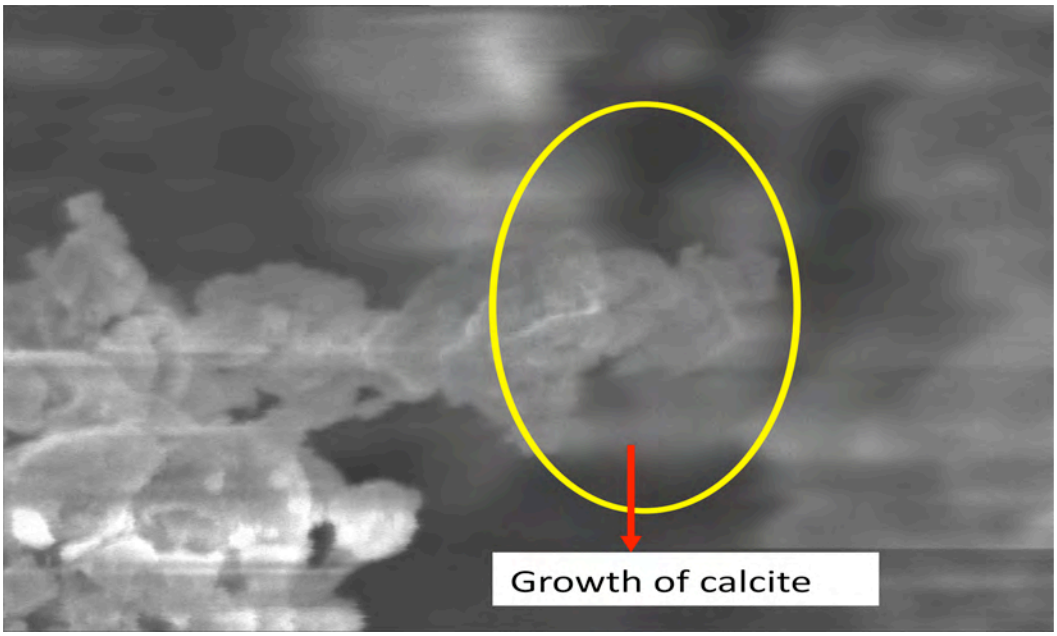


Figure 6a: SEM image at 6kx magnification showing growth of calcite as layers

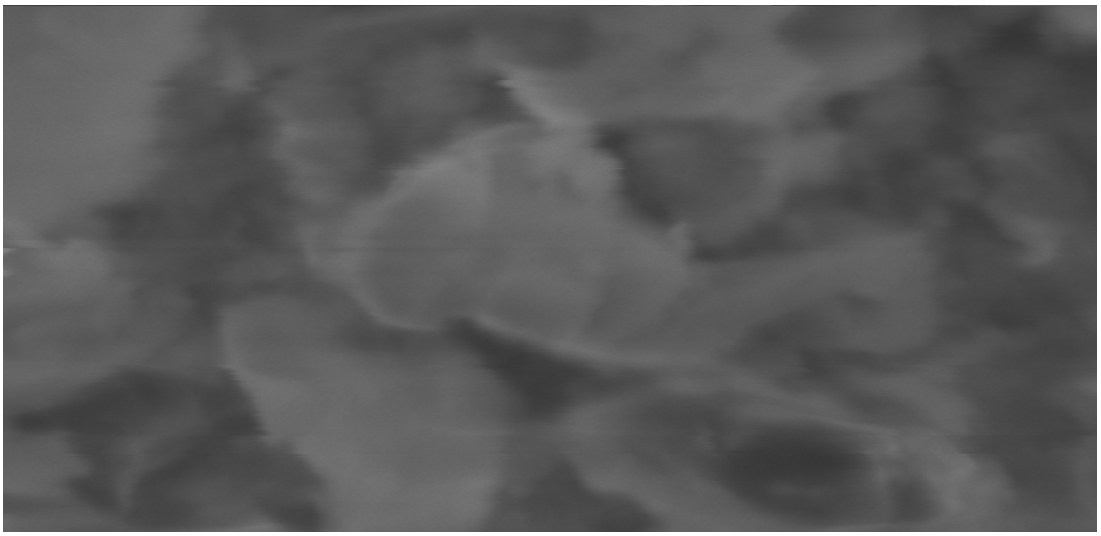

Figure 6b: SEM image at 12kx magnification showing precipitation of calcite aggregates on quartz


Figure 6c: SEM image at 3kx magnification showing deposition of Halite chunks


Figure 6d: SEM image of Ankerite growth in the final sample

***Experimental set B (100$^{o}$C and 2000 psi).*** The experiments were carried out with the same experimental setup used for the Set A experiments with $CO_2$ as feed gas and with the same rock composition at 100$^{0}$C and 2000 psi. As mentioned earlier this experimental setup provides the luxury of analyzing the rock and the brine chemistry at the same time, which enables identification of changes in the rock chemistry and the changes in the concentrations of the corresponding ions in the brine chemistry. The samples were collected from the reactor after 62 days and were heated at 60$^{0}$C overnight and prepared for analysis on both SEM and XRD. Table 5 shows the changes in rock chemistry as identified by the XRD analysis. The quantitative estimates of the minerals before and after the experiments were obtained by XRD. Since small amounts of precipitates formed, attempts to quantify produced solids proved difficult. Hence the changes in the initial mineral assemblage and the mineral assembly after the reaction were calculated. These changes can be corroborated with the precipitated minerals seen in the SEM/EDS analysis, and a reaction mechanism leading to the precipitation of new minerals can

therefore be postulated. In the analysis all the participating minerals (constituents of arkose or dirty sand) participate in the reaction. The major change is seen in the composition of dolomite and feldspars (microcline and andesine) with a small change in calcite and chlorite. The change in quartz composition was not expected and dissolution of quartz usually doesn't occur at pH 5. However as the pH increases to pH of about 7 the $H_4SiO_4$ dissociates leading to the dissociation of silica (Dreever 1988).

Table 5: Quantitative estimates of changes in compositions of the minerals (wt%) before and after the experiment from XRD analysis.

| Mineral | Initial (wt%) | Reacted (wt%) |
|---|---|---|
| Andesine | 25.1 | 29.5 |
| Calcite | 15 | 16 |
| Dolomite | 14.4 | 10.6 |
| Quartz | 22.2 | 15.6 |
| Chlorite | 8.2 | 9 |
| Microcline | 15.2 | 16.2 |

Table 6 shows the XRD analysis of the mineral assemblage after 134 days. While dissolution patterns dominate the XRD analysis in the sample after 62 days, precipitation patterns dominate after 134 days. Andesine, calcite and microcline are found precipitating while dolomite and quartz composition decreased in the final experiment. The reason for the decrease in quartz can be attributed to the same reasoning as given for the 62 days experiment. These results are in good correlation with the brine chemistry analysis and also the SEM/EDS analysis for the rock explained in the sections to follow.

Table 6: Quantitative estimates of changes in compositions of the minerals (wt%) before and after the experiment from XRD analysis after 134 days.

| Mineral | Initial (wt%) | Reacted (wt%) |
|---|---|---|
| Andesine | 25 | 30.5 |
| Calcite | 15 | 19.8 |
| Dolomite | 14.8 | 11 |
| Quartz | 22 | 14.8 |
| Chlorite | 7 | 7.2 |
| Microcline | 15 | 15.2 |

Figures 7 (7a 7b 7c) show the SEM analysis of the initial sample, sample after 62 days and 134 days, respectively. The calcite in the initial samples serves as a standard to examine the precipitation and the dissolution patterns in the samples at different stages of the experiments. The precipitate from the experiment for 134 days was chosen because it was a reaction in which calcite precipitated as determined by the XRD. Figure 7b shows the pronounced dissolution patterns in the sample after 62 days. Dissolution occurs mainly by the formation of few deep etch pits and some shallow ones, almost at the same position in the initial dissolution of the surface. Dissolution occurs quickly which is followed by precipitation as seen in the Figure 7c (experiment carried out for 134 days). These layers and crystals of calcite are seen growing as amorphous mass intergrown with the starting minerals. These calcite crystals (Figure 8a) are highly irregular in shape and show no consistency in size. One calcite crystal had a width of about 10μm and most of the particles appear much smaller than this size. Hence it can be concluded that not all precipitates were collected when the brine was filtered (with a filter paper of 8 μm retention capacity). Figure 7d shows deposition of a new-phase analcime or kaolinite on the reacted surface.

Kaolinite was not identified in the XRD analyses because it shares the same primary peak with one of the minerals in the initial assemblage, chlorite. However, it was identified in the reacted assemblage (Figure 8b). The growth was seen as aggregated units in the interstitial spaces between the primary minerals, especially quartz. Figure 9 confirms the precipitation of ankerite through EDS analysis.

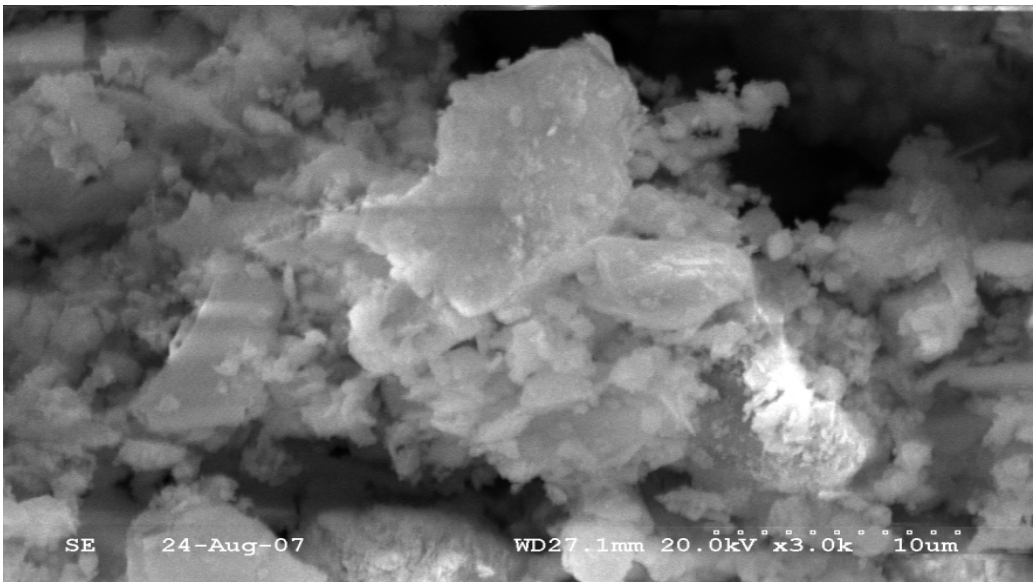


Figure 7a: SEM image showing calcite in the initial samples

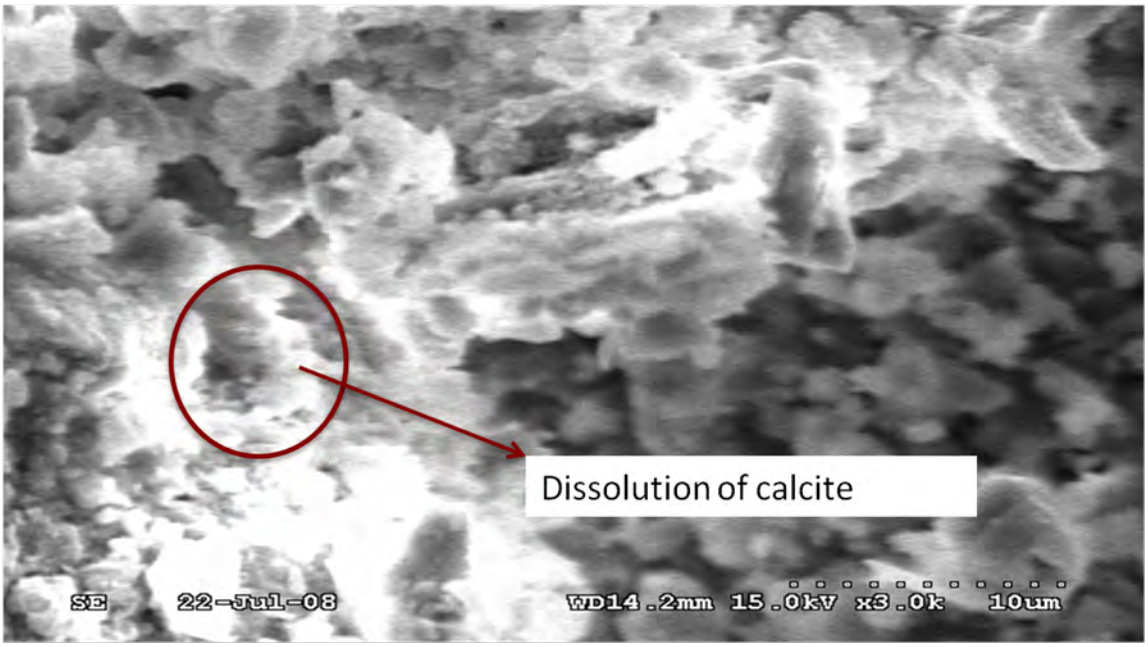


Figure 7b: SEM image showing calcite in the sample showing dissolution after 62days

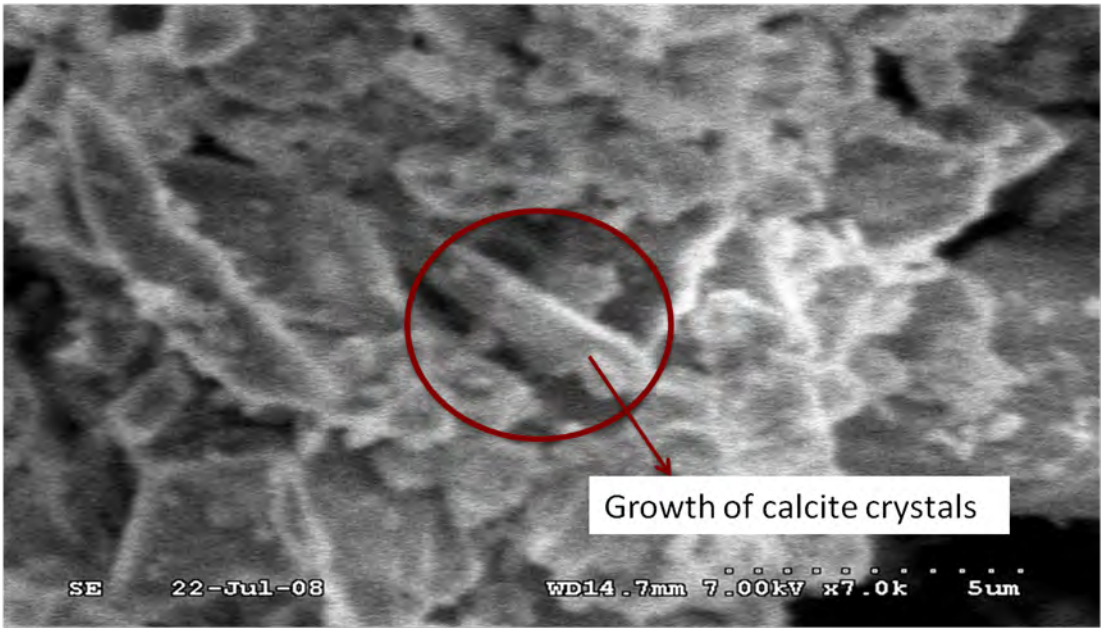


Figure 7c: SEM image showing the growth of calcite after 134 days indicative of mineral precipitation reactions

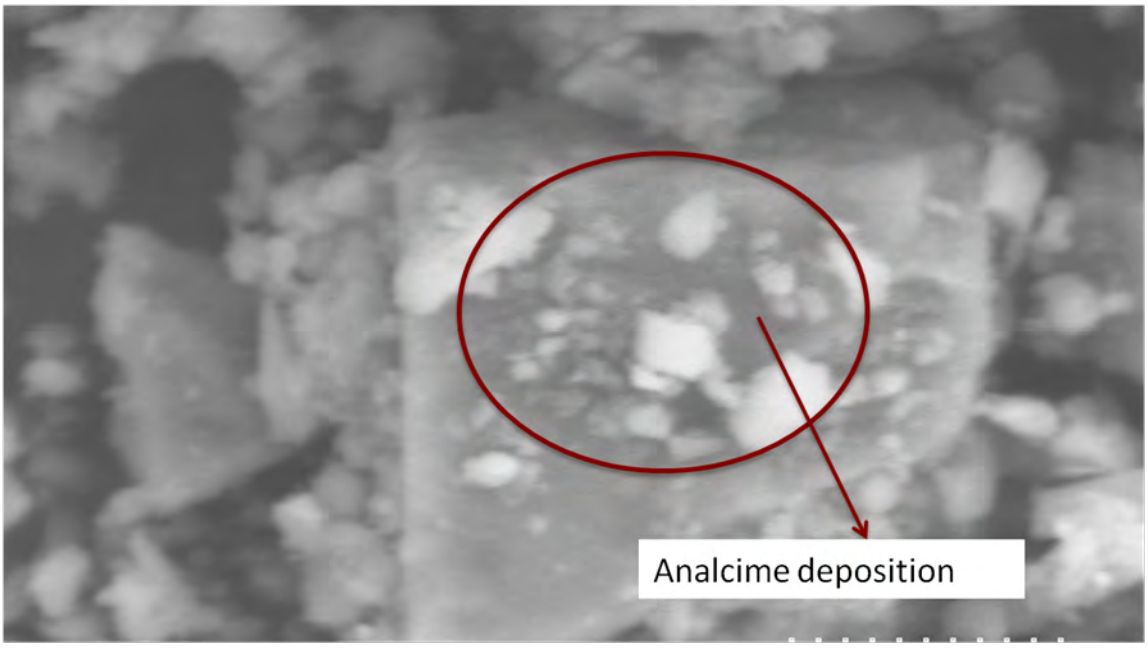


Figure 7d: SEM image showing the growth of growth of new phase probably analcime on the surface


Figure 8a: Calcite crystals growing in interstitial spaces between plagioclase feldspar

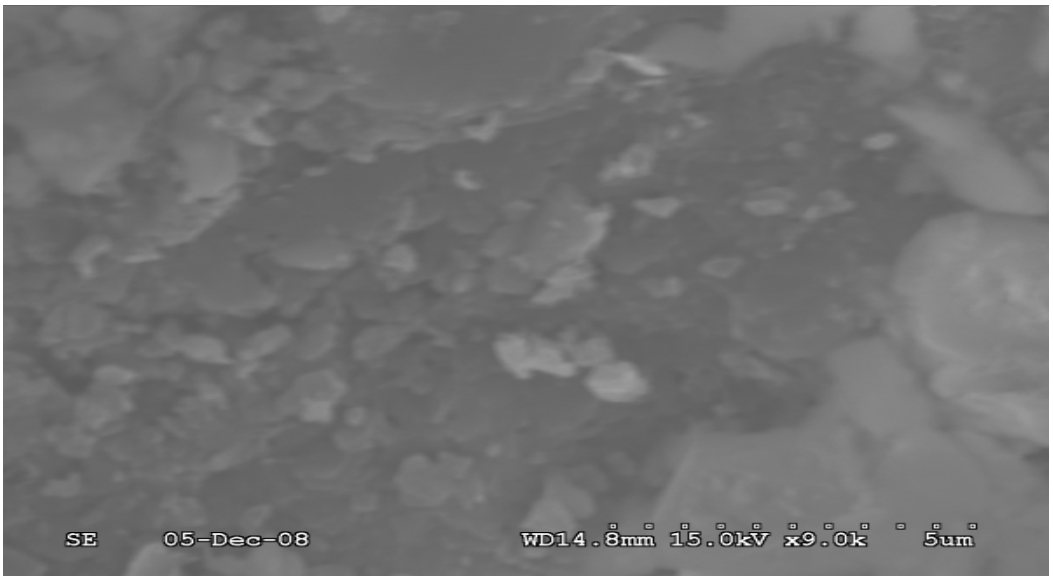


Figure 8b: Kaolinite deposition on quartz

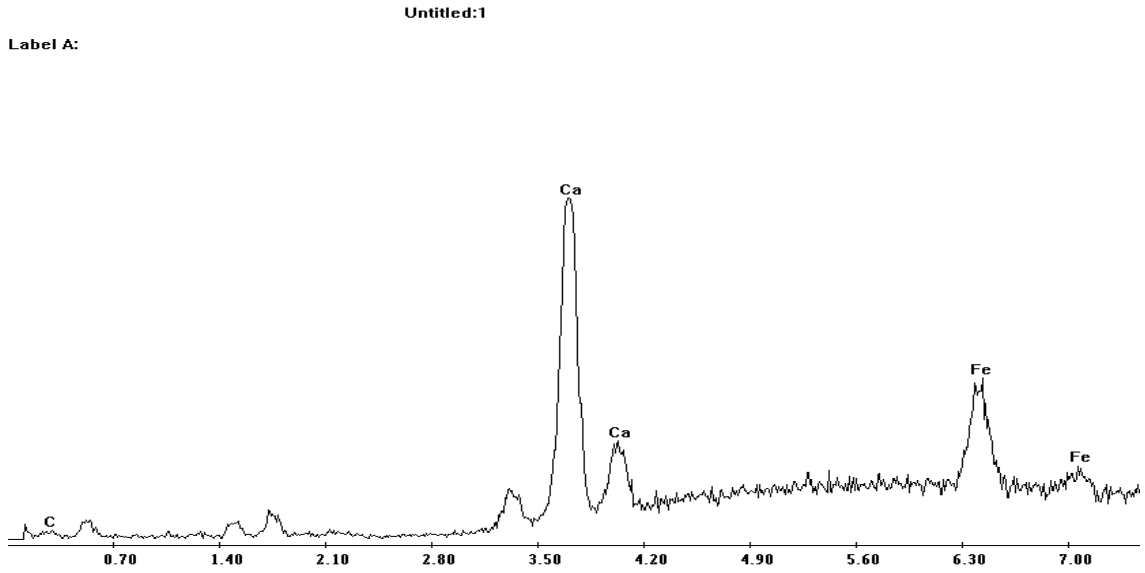


Figure 9: EDS analysis confirming the presence of ankerite in the reacted sample

The analysis of the changes in the concentrations of the principal ions in the brine during the experiment helps provide a clear understanding of the interactions between the rock and dissolved $CO_2$ at the brine-mineral interface (Figure 10). Injection of supercritical $CO_2$ caused significant changes in the brine chemistry. These changes are more evident when compared with the changes in the rock chemistry. The Na ion concentration increased by approximately 17% after 14 days of injection, continued to increase for 62 days (by about 47%) and continued to decrease for the rest of the experiment. The Na concentration prior to the termination of the experiment was 16% less the initial concentration of Na. The Cl concentration followed a similar trend. It increased by approximately 19% at the end of 14 days after injection and increased for 62 days. It then continued to decrease for the rest of the experiment with the final concentration being 5% less than the initial concentration. The pH of the system decreased to approximately 4.5 at the end of 27 days and then stabilized at around 6.7 for the rest of the experiment. All the pH measurements as well as the ion concentrations were calculated by depressurizing the reactors to atmospheric conditions after the experiments. The pH calculated using the Geo-chemists' workbench for this system stabilized around 7.09.

The changes in the concentrations of the principal ions did not follow a particular trend like that of Na and Cl concentrations. The Ca ion concentration increased by about 90% after 14 days and continued to increase for 42 days after, when it decreased with the final concentration approximately 47% less than the highest concentration measured. The K ion concentration exhibited a similar trend to that of Ca ion with the concentration increasing abruptly and continuing to increase until 62 days after which it decreased. The increase in the Ca ion concentration can be attributed to the dissolution of the primary carbonate minerals, calcite and dolomite, liberating Ca ion into the brine. The K ion concentration increase was due to the dissolution of the microcline, which is potassium feldspar, and the silicate dissolution reactions are the fastest in a low pH geochemical system. The Mg ion concentration increased by approximately 52% by 27 days and continued to increase until 62 days, after which it decreased with the final concentration 42% lower than the initial concentration measured at 27 days. This increase was mainly due to the dissolution of dolomite and chlorite. Iron (Fe) concentration decreased throughout the experiment, and the final concentration was approximately 27% lower than the initial concentration. The decrease in the concentrations of the Ca, Mg and K ions by 47%, 42% and 27%, respectively, in the latter stages of the experiment are an indication of new minerals with the primary composition of these ions precipitating in the solid phase. The Si concentration followed a very unique trend. It increased by 14% after 27 days then decreased slightly (2%) and then increased by about 32% until the termination of the experiment. Because the increase of 2% was within the experimental and analytical uncertainty, the concentration can be considered stable from 27 days to 42 days. The Si concentration increase can be attributed to the dissolution of feldspars, microcline and andesine, which are the most sensitive minerals to decreasing pH (Dreever 1988). Hence the silicate dissolution dominates the geochemical reactions in the system. This also is evident from the silica coating on all the samples analyzed in the SEM with a distinctive Si peak in the EDS analyses. This is due to the deposition of Si from the brine on to the rock when the solid sample is dried prior to the analysis.

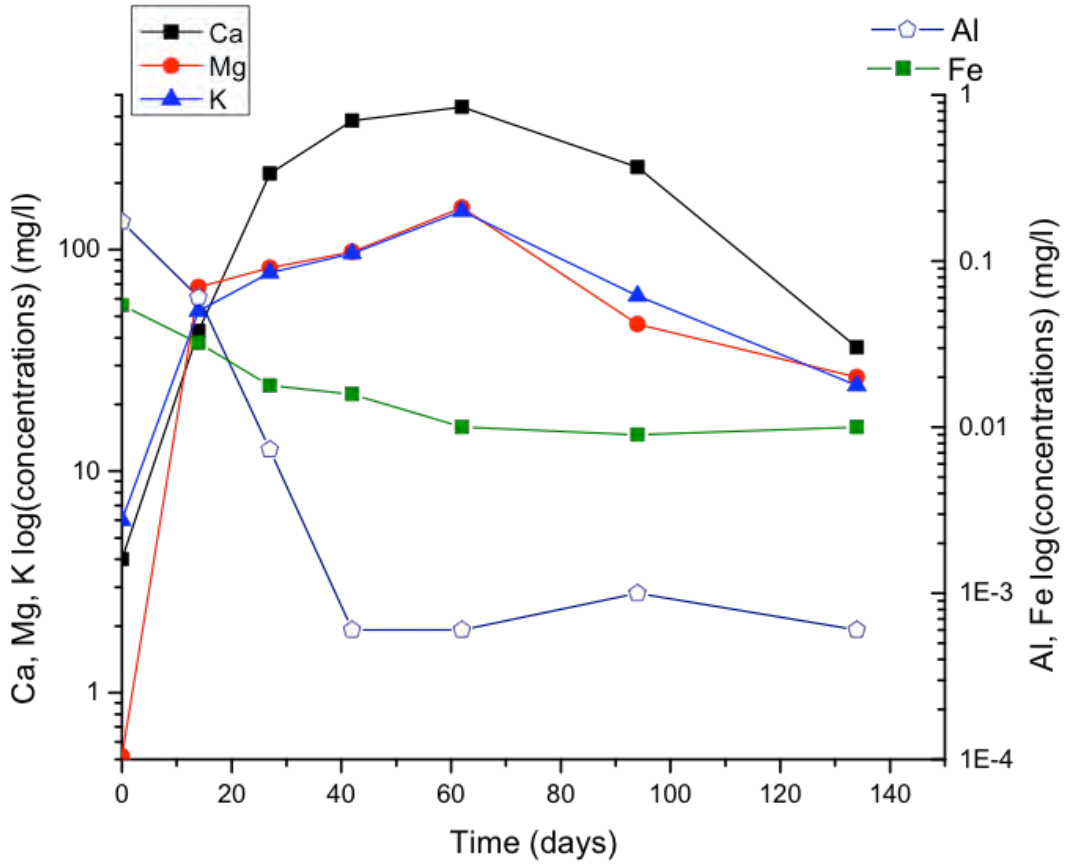


Figure 10: Changes in concentrations of the principal ions during the experiment

Figure 11 is the best example of the changes in the brine chemistry corroborated with the alterations in the solid phase. The changes occurring in the brine reflect in the rock chemistry too. The samples collected at the end of 62 days and 134 days were selected to represent these changes, and Ca ion was chosen as the principal ion undergoing the change. At the end of 62 days and also through the first 62 days, the Ca ion concentration increased in the brine indicating the dissolution of primary carbonate minerals calcite and dolomite in the brine. It is also clearly seen in the SEM analysis of the rock sample collected at the end of 62 days where calcite dissolution pattern dominates. From 62 days through 134 days, the Ca ion concentration decreases, which implies that Ca-bearing minerals should precipitate in the solid phase. This is also evident from the SEM analysis of the sample collected at the end of 134 days where layers and crystals of calcite are seen growing as amorphous mass intergrown with the starting minerals (especially quartz).

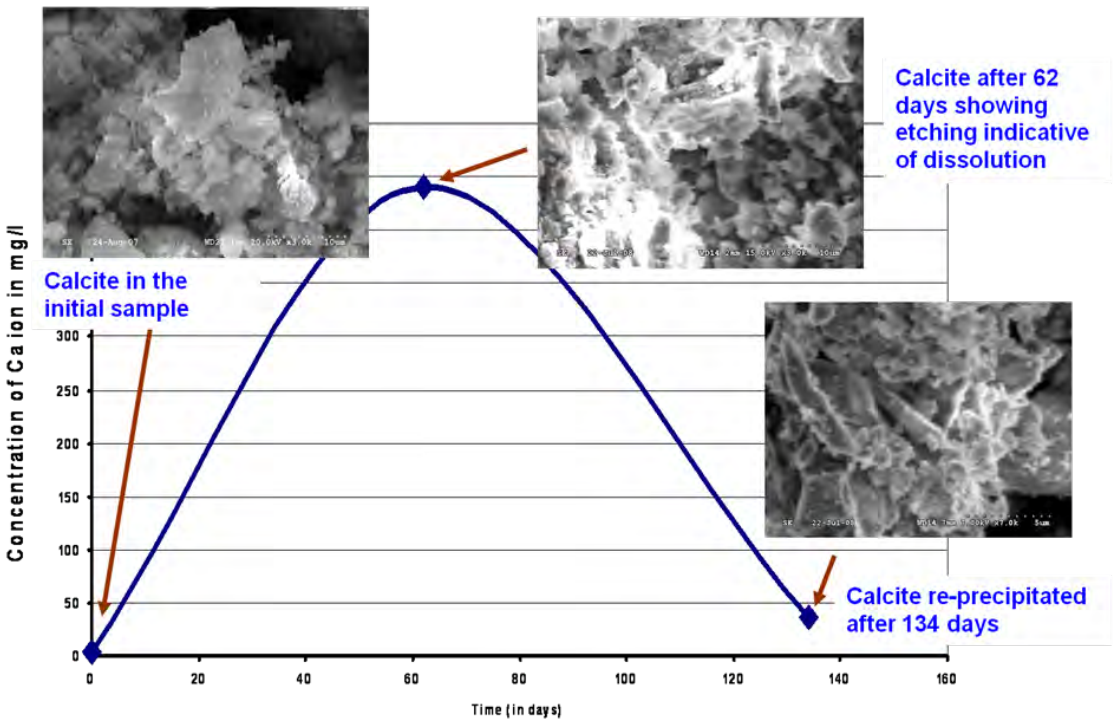


Figure 11: Rock chemistry results corroborated with brine chemistry

***Experiment Set C (100$^{o}$C and 600 psi).*** The experimental setup used for the $CO_2$ experiments was used for these sets of experiments. The temperature was 100$^{0}$C, and pressure was 600 psi. The initial brine composition was the same (Table 7). The composition of the mineral assemblage was also the same. The only change is in the feed gas composition which is 10% $SO_2$ with 90% $CO_2$. The gas is a calibrated mixture provided by AIRGAS in cylinders with a maximum deliverable pressure of 600 psi. There were two reactors running under identical conditions. The rock was equilibrated with brine for a period of 36 days, and then the gas was injected into the system. The first reactor was brought down after 14 days and the second after 37 days.

XRD analyses of the sample show pronounced changes in the rock chemistry (Figure 12). The initial XRD patterns show an almost uniform distribution of the primary minerals in the host rock. For the initial sample i.e., the experiment carried out for 14 days, there is a large dissolution of calcite and dolomite with dissolution of other silicate minerals (plagioclase feldspars and microcline), and also dissolution of the mineral chlorite (Table 8). The XRD pattern also shows the precipitation of hydrated calcium sulfate,

bassanite and some anhydrite, but they were dominated by the pronounced dissolution patterns of the primary minerals calcite, dolomite and chlorite.

Table 7: Brine composition in set C

| Time | Na (mg/l) | Mg (mg/l) | K (mg/l) | Al (µg/l) | Fe (µg/l) | Ca (mg/l) | Si (mg/l) | S (mg/l) | Cl (mg/l) |
|---|---|---|---|---|---|---|---|---|---|
| 0 | 11376 | 587 | 17 | 43 | 27 | 11 | <1 | 296 | 38852 |
| 14 | 12137 | 569 | 26 | 39 | 27 | 14 | 1.5 | 370 | 38742 |
| 21 | 10754 | 461 | 72 | 1 | 21 | 176 | 21.6 | 590 | 34629 |
| 37 | 10599 | 368 | 64 | 4 | 19 | 994 | 34.8 | 1551 | 37157 |

Table 8: Quantitative estimates of changes in compositions of the minerals (wt%) before and after the experiment from XRD analysis after 14 days.

| Mineral | Initial (wt%) | Reacted (wt%) |
|---|---|---|
| Andesine | 17 | 10 |
| Calcite | 17.6 | 4 |
| Dolomite | 12.1 | 8 |
| Quartz | 18.8 | 15 |
| Chlorite | 16 | 13.9 |
| Microcline | 18 | 14 |

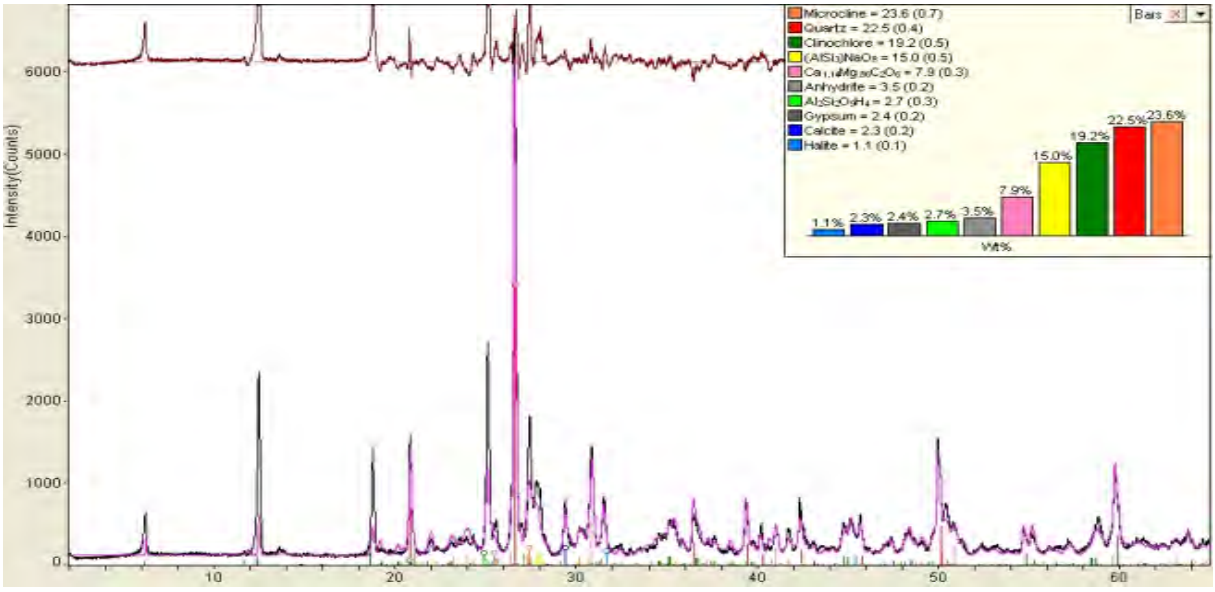


Figure 12: XRD analysis of the reacted sample

For the experiment, which was terminated after 37 days, the XRD pattern shows continued dissolution of calcite, a slight increase in dolomite and the precipitation of bassanite, anhydrite and minute quantities of kaolin (Table 9). Conclusions regarding kaolin deposition in the sample is very difficult because kaolin shares primary peaks with chlorite, which was a part of the initial mineral assemblage. Consequently when a qualitative EDS analysis on the sample was run with the SEM, kaolin was detected which bolstered the finding in the XRD.

Table 9: Quantitative estimates of changes in compositions of the minerals (wt%) before and after the experiment from XRD analysis after 37 days

| Mineral | Initial (wt%) | Reacted (wt%) |
|---|---|---|
| Andesine | 17 | 15 |
| Calcite | 17 | 2 |
| Dolomite | 12 | 8 |
| Quartz | 19 | 22 |
| Chlorite | 16 | 13 |
| Microcline | 18 | 23.7 |

The SEM analyses of the host rock after the experiment showed pronounced dissolution of all the primary minerals involved in the reaction (Figure 13). The product also had widespread deposition of anhydrite crystals. These crystals were usually distinct and were seen growing either on the surface of quartz or in the interstitial spaces between the host rock (especially feldspars anorthite and microcline). The final pH of the system in the two separate experiments was 1.9 after 14 days and 2.48 after 37 days.

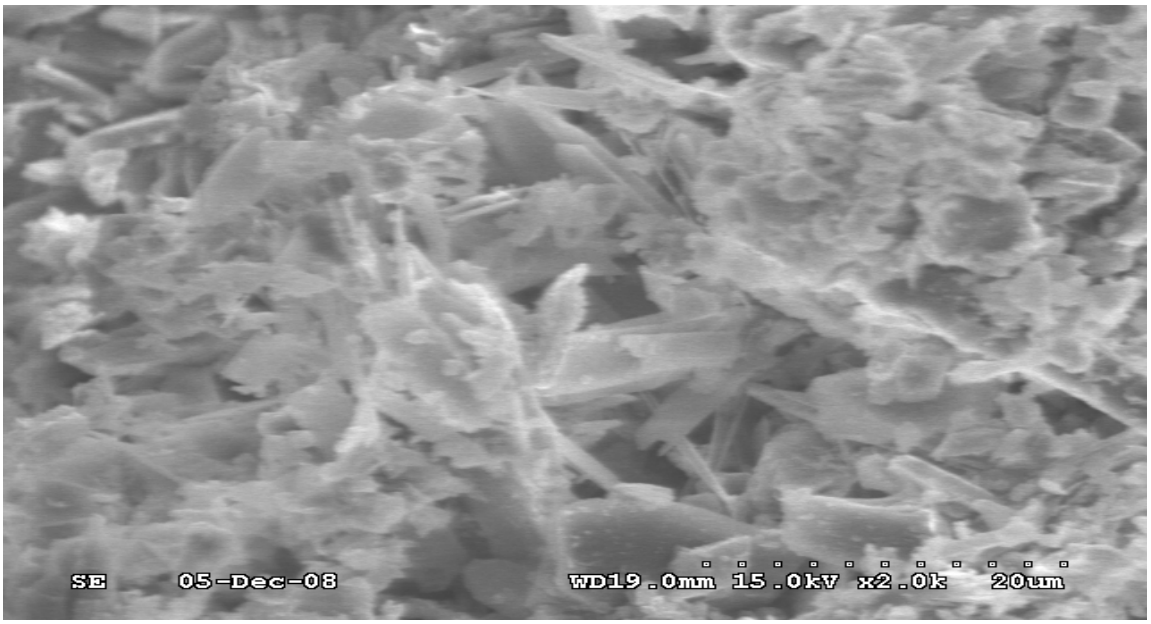


Figure 13a

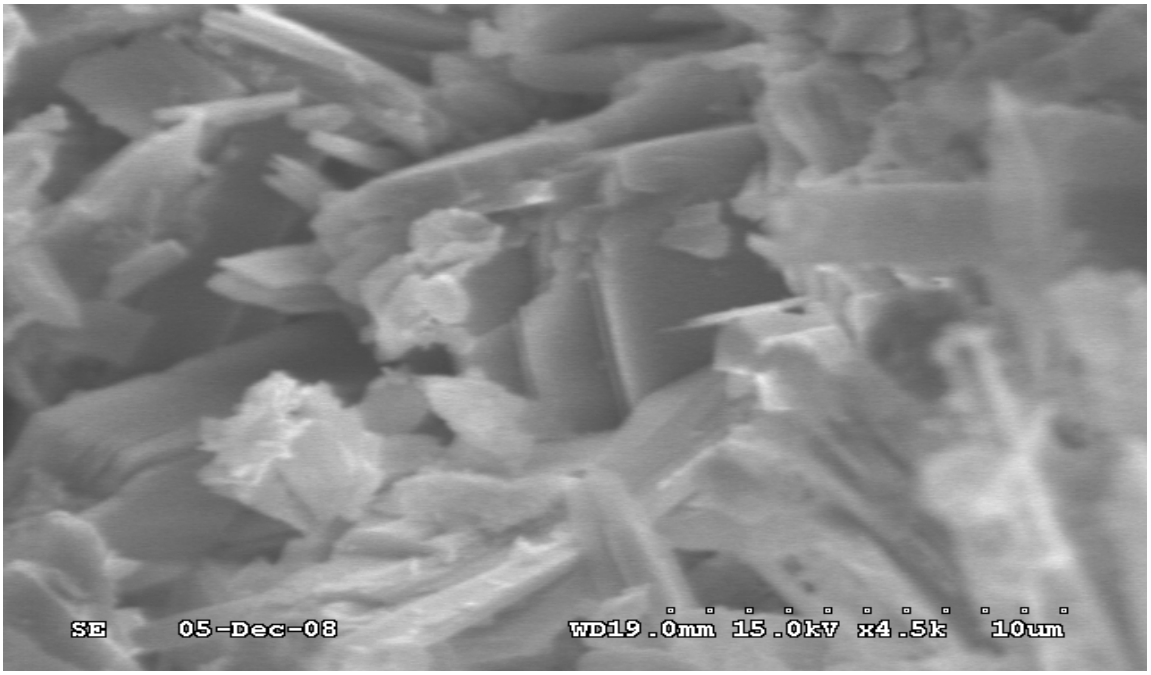


Figure 13b

Figure 13a and 13b: Growth of anhydrite crystals after 37 days

Anhydrite occurs as large discrete bladed crystals on the surface of the host mineral especially on anorthite, which is plagioclase feldspar. The crystals were visible at 2kx resolution usually 6-8μm wide. The crystal faces of anorthite were pitted and rough. EDS analysis confirmed the presence of anhydrite, which was absent in the initial mineral

assemblage (Figure 14). Hence the precipitation of anhydrite can be explained by the increased acidity following the injection of the gas mixture. Primary minerals calcite and dolomite underwent dissolution, and this led to secondary precipitation of anhydrite. The crystalline masses of anhydrite are possibly due to acidity in the brine and the presence of the supercritical $CO_2$ phase, which lead to rapid crystal nucleation and growth. Chunks of silica were seen deposited on these anhydrite crystals (Figure 15a). The increased acidity led to rapid dissolution of silicate bearing phases i.e., plagioclase and potassium feldspar, which led to the release of silica into the brine. When the sample was prepared for analysis (dried overnight), the silica deposited on the surface and the EDS analysis supports this mechanism. The silica chunks are 2-10μm in cross section.

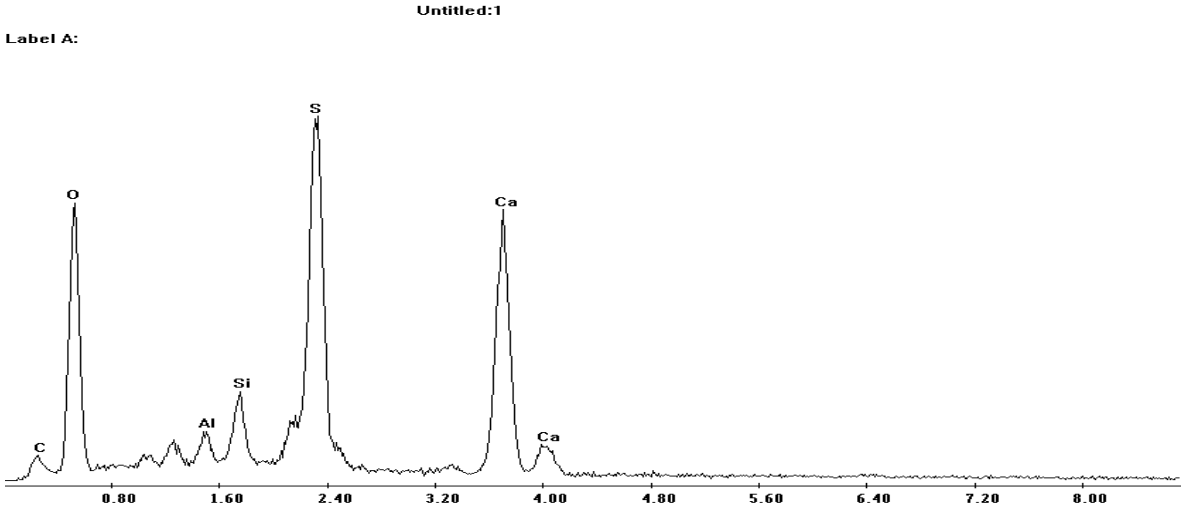


Figure 14: EDS analysis confirming the growth of anhydrite on anorthite and quartz

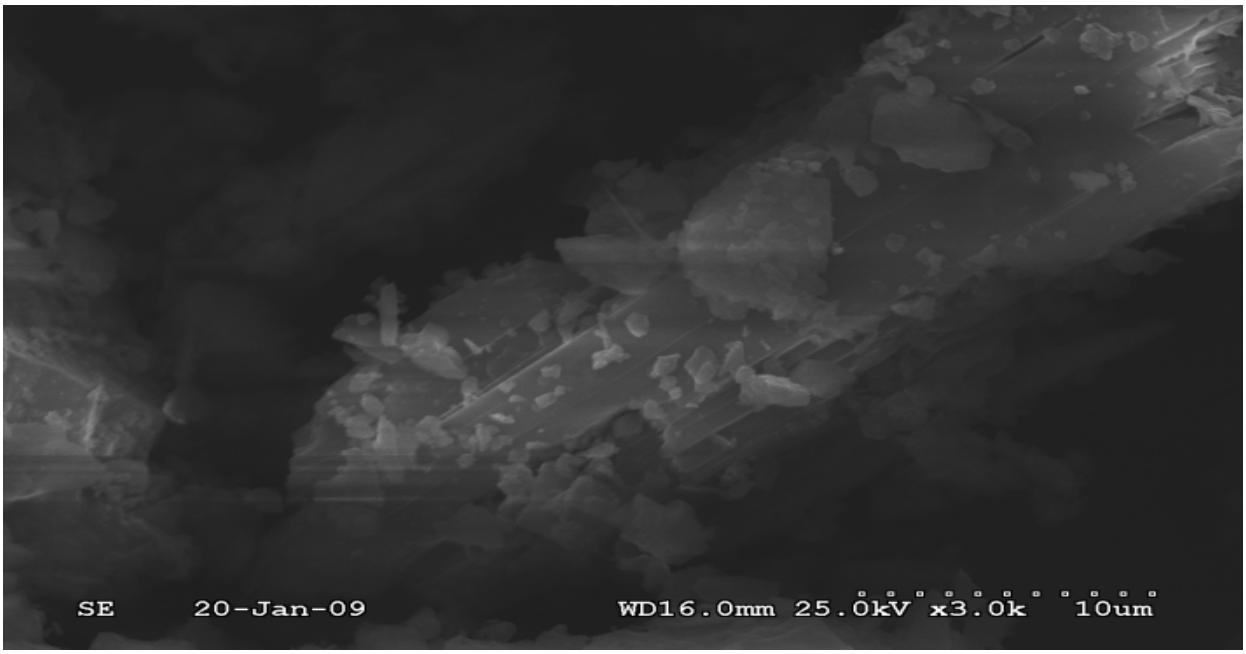


Figure 15a: Anhydrite crystal with some deposits of silica

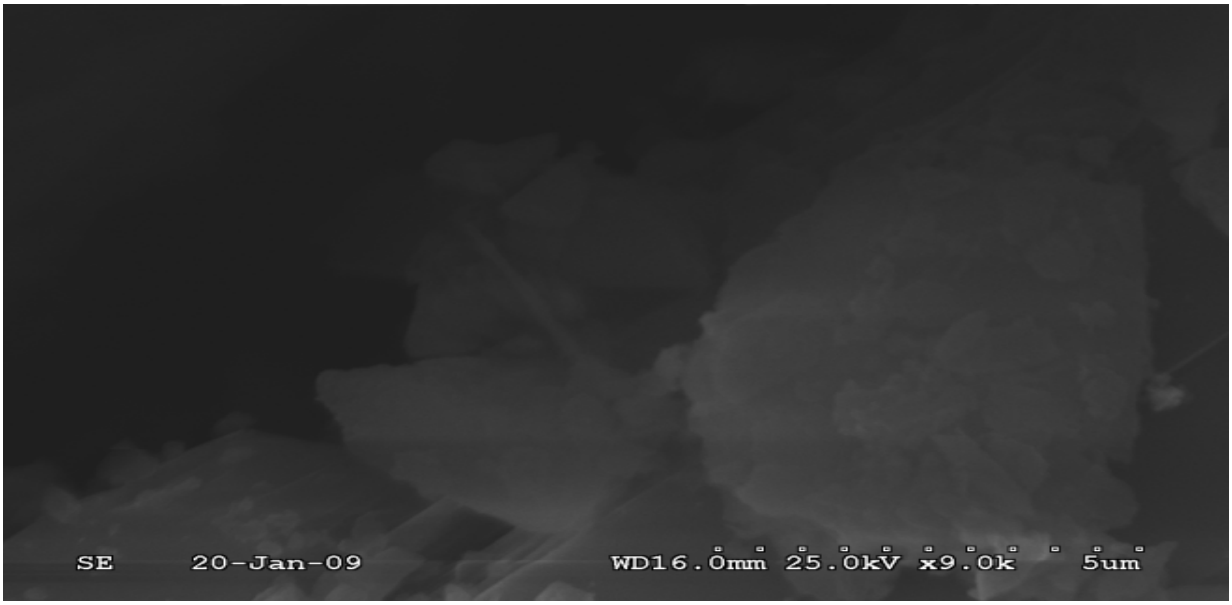


Figure 15b: Growth of discrete anhydrite crystal

There were pronounced dissolution patterns for most of the primary minerals involved in addition to the precipitation of anhydrite. The calcite chunk in Figure 16 shows the dissolution of calcite, which is also evident from the increase in the calcium ion concentration in the brine, which is discussed later. The alteration of the silicate phases

occurs as the dissolution of primary feldspars, the plagioclase feldspar and also the potassium feldspar (microcline). Such dissolution patterns were ubiquitous in addition to the precipitated anhydrite crystals. All the mineral surfaces were rough and pitted, which are the most commonly observed dissolution patterns.

There were other minerals, which were found as traces in the XRD analysis, but their presence was confirmed in the subsequent EDS analysis. Kaolinite was observed growing the interstitial spaces of the host rock (mainly plagioclase feldspar). It was seen growing as hollow crystals (Figure 17), which is the typical manner in which we see crystalline feldspars growing as reported by Moore et al. (2005) in their characterization of natural carbonate reservoirs in Colorado plateau. Figure17 shows one face of the kaolin crystal growing. From the sample collected after 14 days the dissolution patterns dominated with only traces of new mineral precipitation whereas after 37 days there was more prominent precipitation and obvious dissolution.


Figure 16: pronounced dissolution patterns of calcite after 14 days

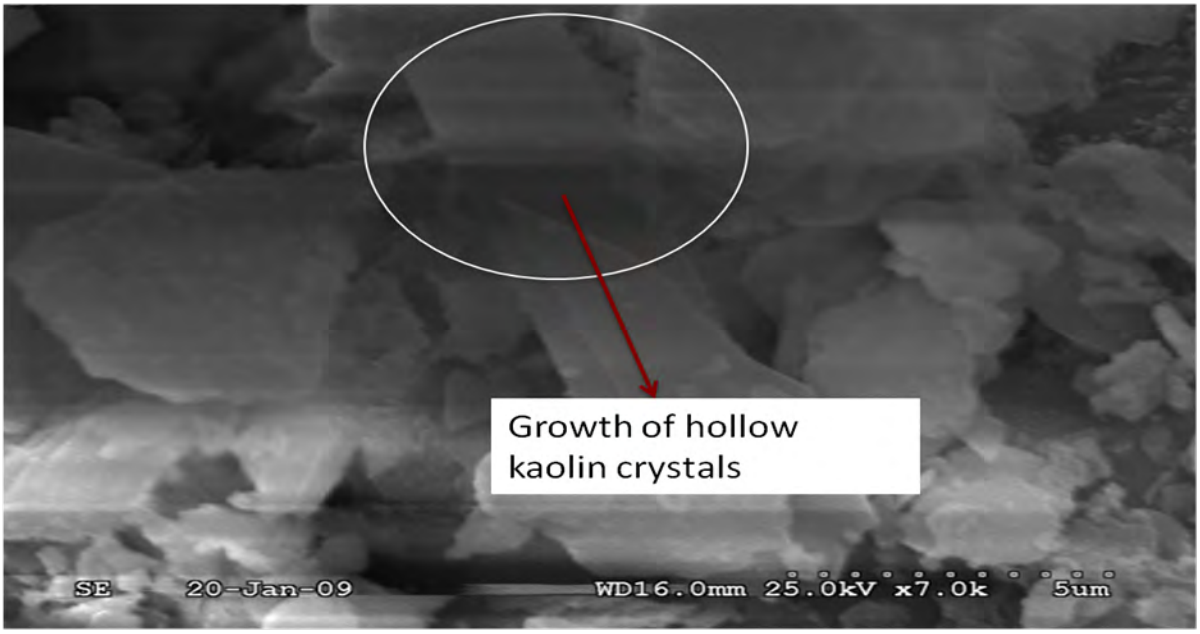


Figure 17: Growth of hollow kaolin crystals

The presence of $SO_2$ in the feed gas stream along with $CO_2$ alters the brine chemistry to a great extent (Figure 18). The Na ion concentration increased for 14 days by about 8% and decreased for the remainder of the experiment. Prior to the termination of experiment there is a 6% decrease when compared to the initial concentration. The Cl concentration decreased by about 11% before increasing in the latter part of the experiment. The principal ion Ca increased throughout the experiment with a final increase of almost 80%, which indicates excessive dissolution of calcite and dolomite in the system. This increase is almost 1.5 times greater than the increase observed in experiments with $CO_2$ as pure gas. The Mg ion concentration decreased by about 18% in the final sample collected, which varies to a great extent from the earlier experiment because Mg was found to increase at the same time in that experiment. The decrease in Mg ion is less than the increase in Ca ion, which implies that Mg ion is precipitating in another phase than dolomite. This might be due to two reasons. The first being the dissolution of calcite or dolomite and the second being the dolomotization of calcite. The slight decrease in magnesium ion concentration leads us to conclude that the latter may be dominant. The dissolution of calcite and dolomite was evident in the XRD analyses. In the experiment the abrupt increase in Ca ion from the dissolution of primary carbonate minerals, calcite and dolomite, causes the $SO_4$ to precipitate as anhydrite, gypsum or bassanite (hydrated

$CaSO_4$). The Al ion concentration decreased by about 1% and decreased rapidly with a slight rise in the latter stages of the experiment. This trend was similar to that observed in the earlier experiment but the decrease was much steeper in this case. The Fe concentration followed a similar trend decreasing throughout. The K ion increased abruptly because of the feldspar dissolution reactions then decreased probably due to kaolin precipitation as observed in the SEM analysis.

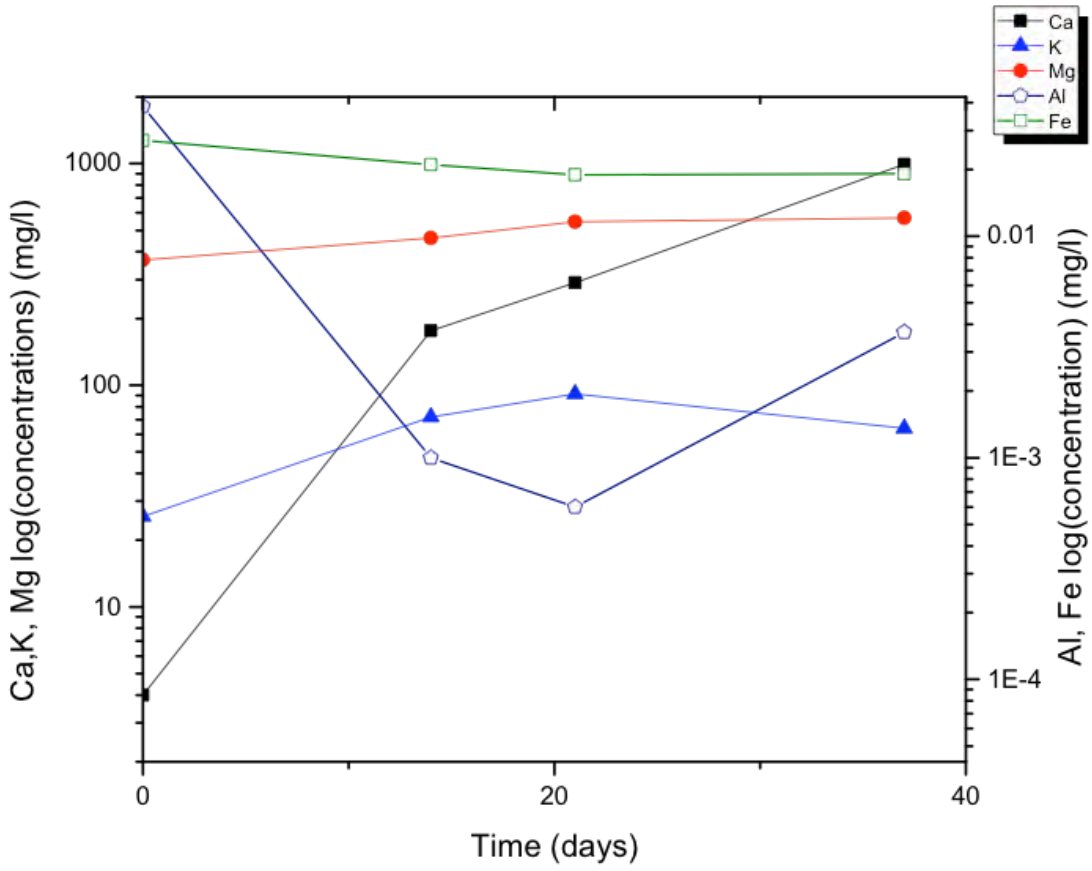


Figure 18: changes in the brine chemistry of principal ions during the experiment

***Experiment set D (100$^o$C and 2000 psi).*** These experiments were performed at an initial pH of 3 by acidifying the brine with 0.1ml of 1M sulfuric acid. The experiments were carried out at 100$^0$C and 2000 psi for 14, 21 and 37 days, respectively. The XRD analyses in Figure 19 and Tables 10 and 11 show dissolution of the primary minerals, calcite and dolomite, and precipitation of other constituents. However precipitation of minerals was not observed in the SEM analyses. The dissolution patters of calcite and dolomite

dominate the reacted rock (Figure 20). Brine chemistry also supports this (Figure 21). The concentrations of the principal ions increase indicating that the carbonate minerals are undergoing dissolution during the course of the experiment.

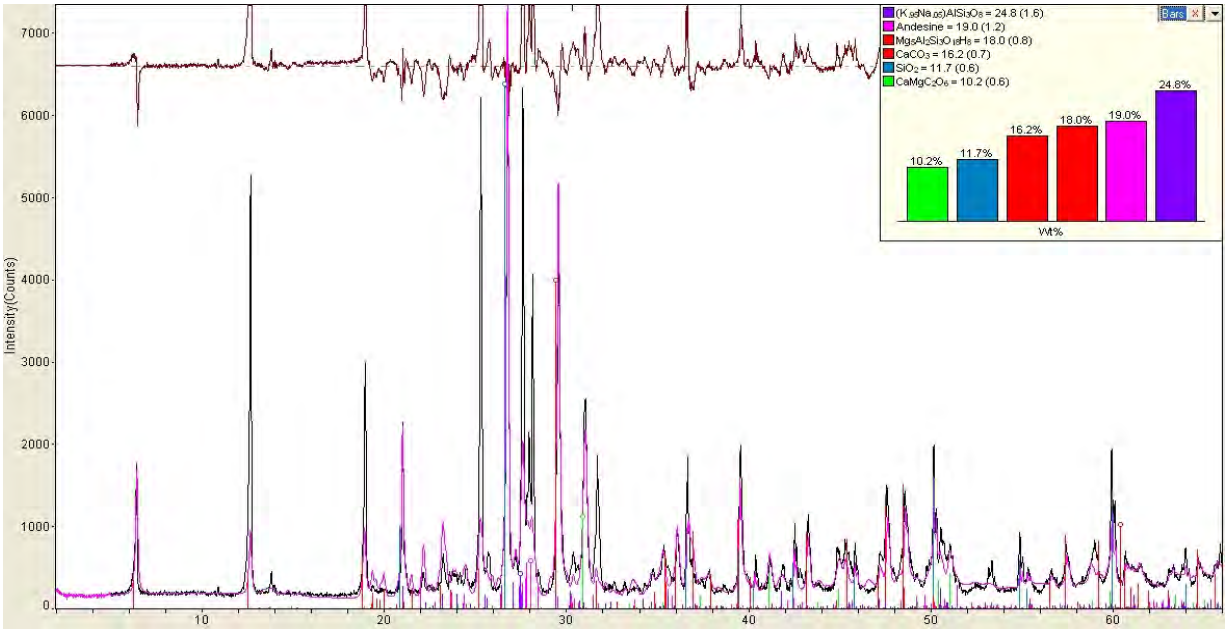


Figure 19: XRD analysis of the reacted sample

Table 10: Quantitative estimates of changes in compositions of the minerals (wt%) before and after the experiment from XRD analysis after 21days

| Mineral | Initial | Reacted |
|---|---|---|
| Andesine | 25.1 | 29.5 |
| Calcite | 15 | 19.1 |
| Dolomite | 14.4 | 10.6 |
| Quartz | 22.2 | 15.6 |
| Chlorite | 8.2 | 9 |
| Microcline | 15.2 | 16.2 |

Table 11: Quantitative estimates of changes in compositions of the minerals (wt%) before and after the experiment from XRD analysis after 37 days

| Mineral | Initial | Reacted |
|---|---|---|
| Andesine | 25.1 | 24.5 |
| Calcite | 15 | 11.1 |
| Dolomite | 14.4 | 10.6 |
| Quartz | 22.2 | 21.6 |
| Chlorite | 8.2 | 9 |
| Microcline | 15.2 | 14.6 |

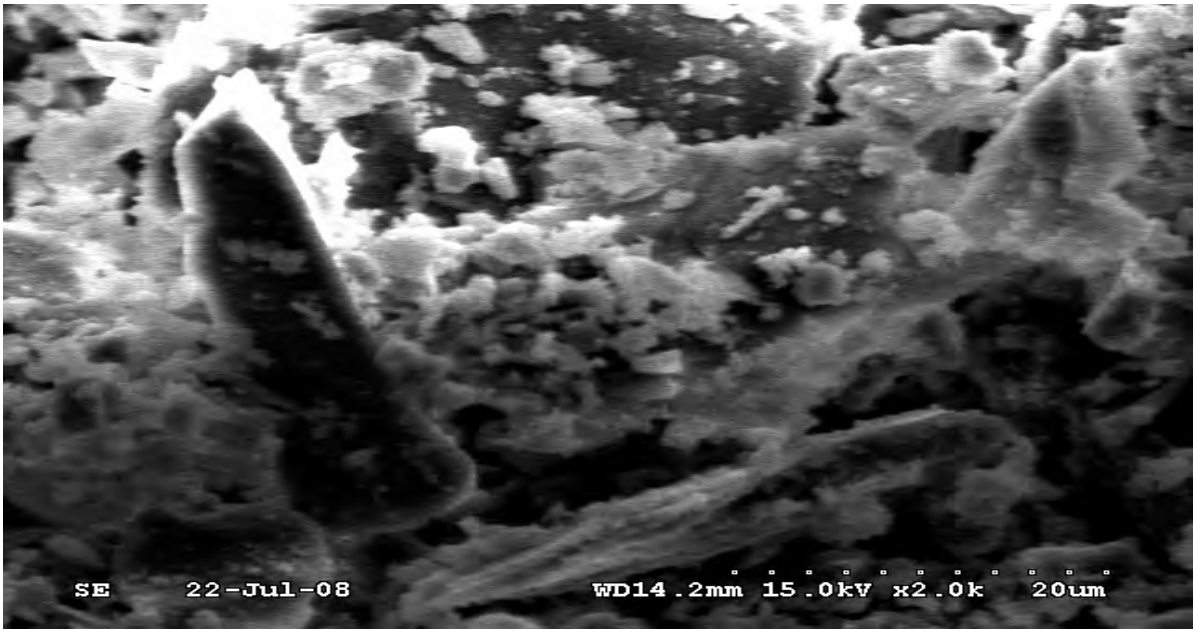


Figure 20a: pronounced dissolution patterns of calcite after 21 days

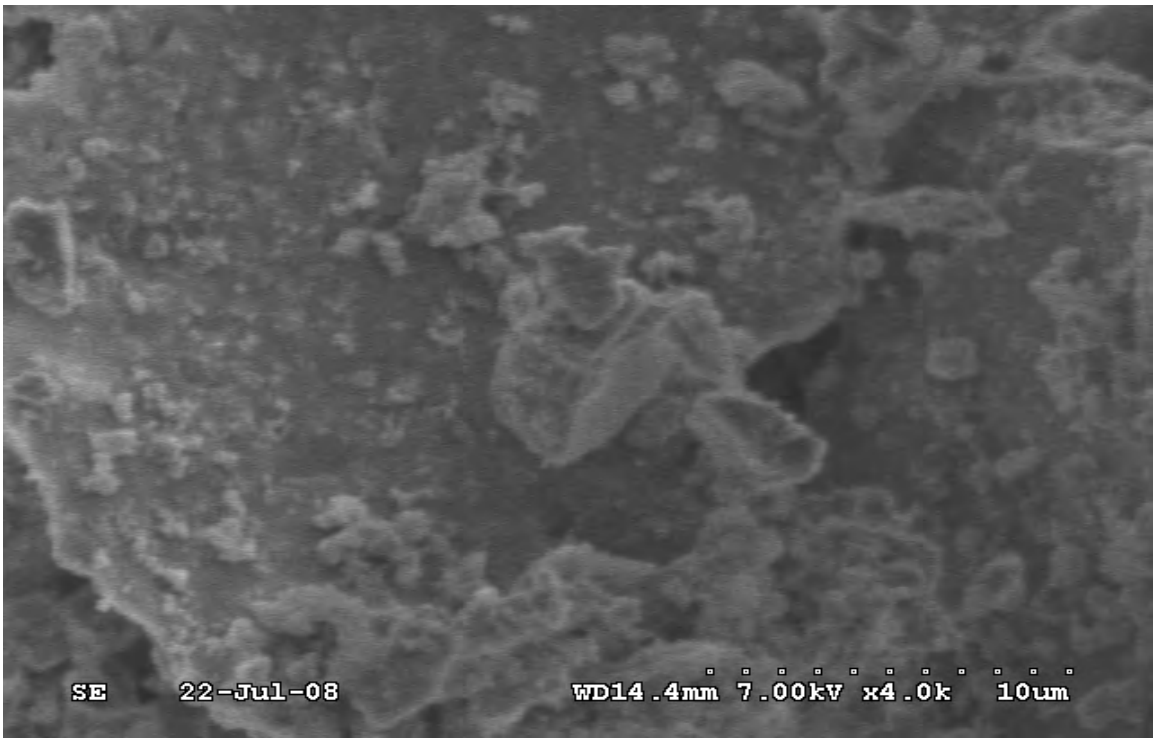


Figure 20b: pronounced dissolution patterns of calcite after 37 days

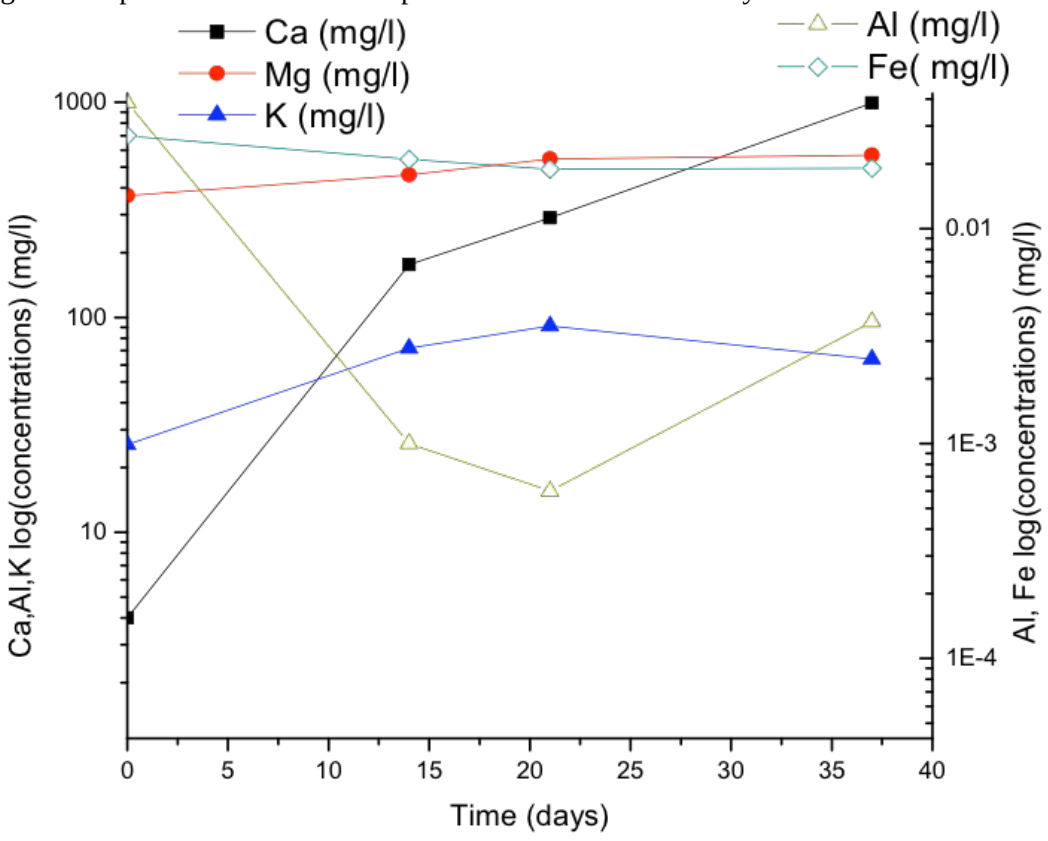


Figure 21: changes in the brine chemistry of principal ions during the experiment

**Injectivity Studies**

The core-scale laboratory flow tests were designed to evaluate the results of explicit processes of reactive transport with matrix chemical diagenesis and associated porosity and permeability changes on CO2 injectivity. Mechanical deformation was not included in this first generation of experiments. Ultimately, these data and results will be used to aid injectivity design of future pilot-scale and commercial-scale sequestration tests, with goals of minimizing risks and maximizing injectivity.

Injectivity studies with $CO_2$ and $CO_2$+$SO_2$ mixtures with the experimental setup described in the Experimental Section were not completed as designing, assembling and testing the state-of-the-art high-pressure, multiphase facility was more extensive than originally planned. They are being performed in the current project phase.

San Juan Basin rock core samples were acquired for laboratory testing (Figure 22). The San Juan Basin of northern New Mexico was selected for this research because it is the site of a pilot-demonstration of $CO_2$ injection under the auspices of the Southwest Regional Partnership on Carbon Sequestration (SWP), a consortium sponsored by NETL. The SWP is in its sixth year and currently deploying multiple injection tests throughout the region. The subject formations for deep saline sequestration testing are the Jurassic-aged Entrada sandstone and the Mississippian-aged Leadville limestone. The core samples were analyzed for fractures and other heterogeneities. To maximize applicability (transferability/portability) of our results to other studies, we elected to focus on pure end-member archetypes of these formations represented by the Indiana Limestone and the Berea Sandstone. In the last few months of this project, we acquired Indiana and Berea core from Fisher Scientific, Inc. and performed repeated mineralogic and hydrologic (porosity and permeability) analyses of the cores (Table 12).

Table 12: Berea and Indiana formation cores subject to final laboratory testing and flow simulation analyses (UCS – Unconfined Compressive Strength).

| Core Lithology | Formation | Permeability (mD) | Porosity (%) | UCS (psi) | Length (in) | Diameter (in) |
|---|---|---|---|---|---|---|
| Berea Sandstone | Kipton | 60 – 100 | 18 - 20 | 6000 -8000 | 24 | 2 |
| Indiana Limestone | Bedford | 2 – 4 | 10-12 | 4500 | 24 | 2 |

Figure 22. Photographs of San Juan basin core taken from the Carson Federal G #1 well

## Study of the vertical movement of the $CO_2$ plume

Vertical migration of $CO_2$ in the formation into which it is injected is an important phenomenon. $CO_2$, being lighter than water, overrides the water and reaches the top of the formation. On a macro-scale, it is important to capture such a buoyancy-driven transport, since it affects all aspects of $CO_2$ trapping. The dissolution of $CO_2$ at the interface, creating a heavier fluid and causing density-driven instabilities has been studied. The gravity fingers created can range in scale from one millimeter to several meters. This particular component of the process embodies all of the elements of the parent sequestration process in the sense that equilibration does not occur over engineering time scales, and several spatial scales govern how the dissolution and equilibration proceeds. In this task we studied the vertical migration of $CO_2$ in the formation and the parameters that control the migration and subsequent distribution of $CO_2$ in the various phases.

All of the simulations were performed using TOUGHREACT. The domain used in the simulations is shown in Figure 23, and the general conditions of simulations are summarized in Table 13. In addition to studying the sensitivity of parameters to the absolute permeability of the seal and the formation, additional simulations were performed with relative permeabilities where both the phases are essentially immobile (a situation that is termed “permeability jail” in some other gas flow applications). The relative permeabilities for the situation with permeability jail are shown in Figure 24.

Distributions of free and dissolved $CO_2$ concentrations are shown in Figure 25. In the uniform permeability case, the free-$CO_2$ concentration is highest at the top of the formation. If the top of the formation is breached, the $CO_2$ will leak outside of the target zone. If permeability-jail type relative permeabilities are used in the seal, the seal becomes an effective trapping layer, and $CO_2$ is better distributed in the aqueous phase as well.

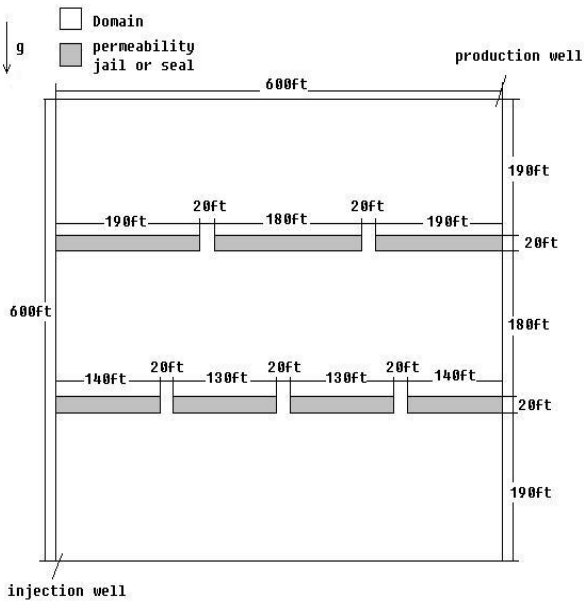


Figure 23: The domain used to study the vertical migration and distribution of $CO_2$

Table 13: Simulation conditions for the study of vertical migration

| Parameter | Values |
|---|---|
| Grid | 1*60*60 |
| Grid block size | 100ft*10ft*10ft |
| Model size | 100ft*600ft*600ft |
| Porosity | 0.30 (0.15 for seal) |
| Permeability (matrix) | 100md |
| Permeability (seal) | 1~100md |
| Temperature | 75°C |
| Pressure | 200bar |
| Salinity | 3-6.0wt% |
| Injection rate | $2.3177*10^3$kg/hr |
| Injection period | 258.4 days |

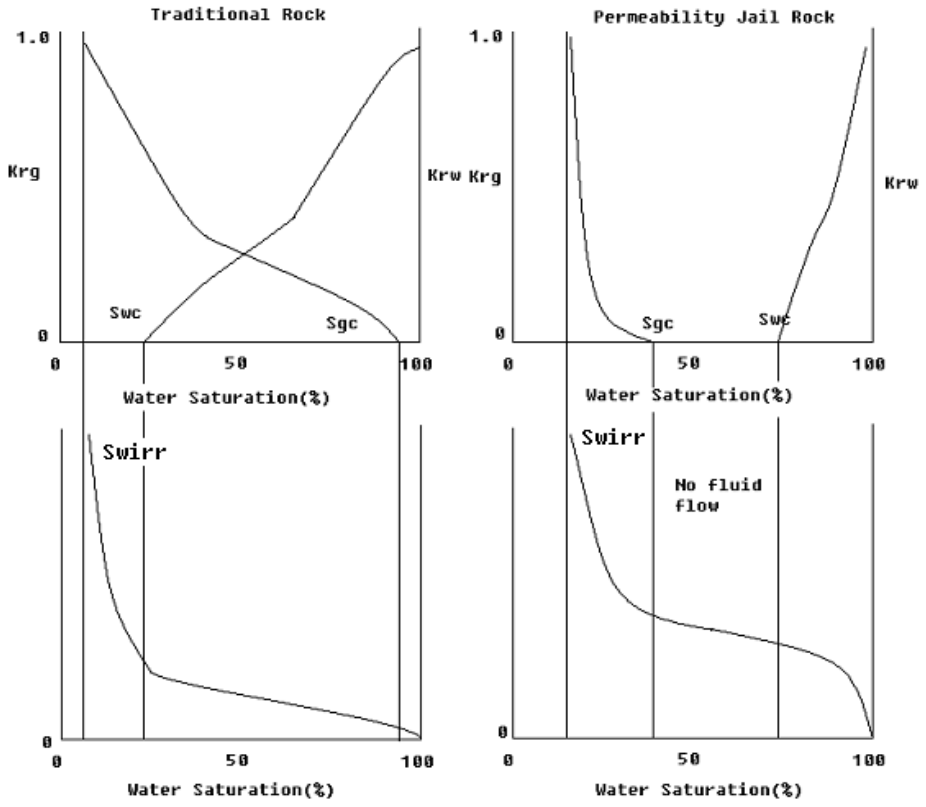


Figure 24: Relative permeability curves for the traditional (base-case) simulations and the set for the "permeability jail" case.

When the permeability of the seal is reduced to 1 md, the vertical migration of $CO_2$ predominantly occurs through the holes in the low permeability seal, and the permeability jail-type relative permeabilities do not change the distributions of the free and dissolved $CO_2$ concentrations significantly (Figure 26).

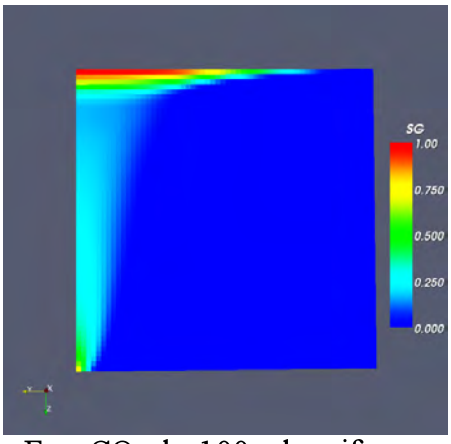


Free $CO_2$: k=100md, uniform

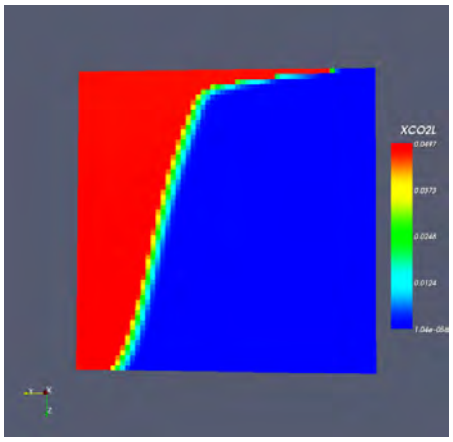


dissolved $CO_2$: k=100md, uniform

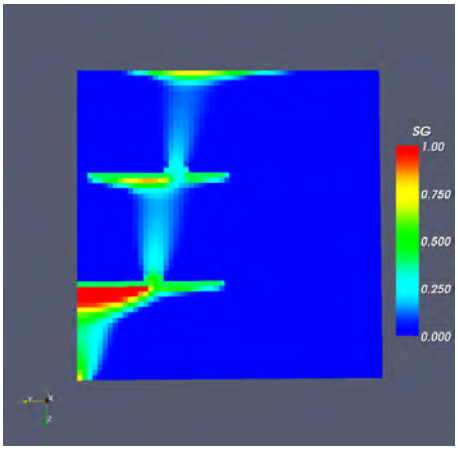


Free $CO_2$: k=100md, permeability jail

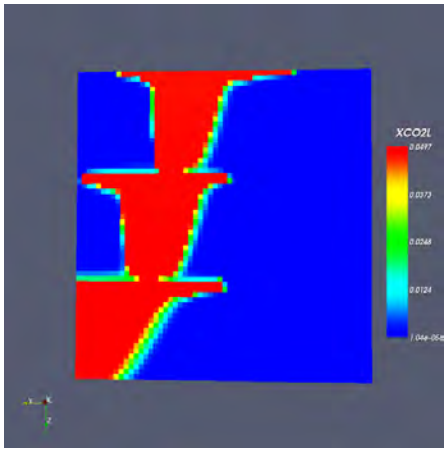


dissolved CO2: k=100md, permeability jail

Figure 25: Vertical distribution of $CO_2$ (as free gas phase, and in the dissolved state) for the domain with uniform permeabilities and in the system with "permeability-jail" relative permeabilities in the seal.

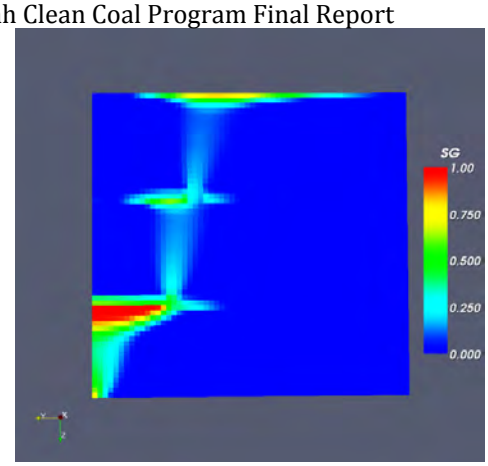


Free $CO_2$: k=1md, low permeability

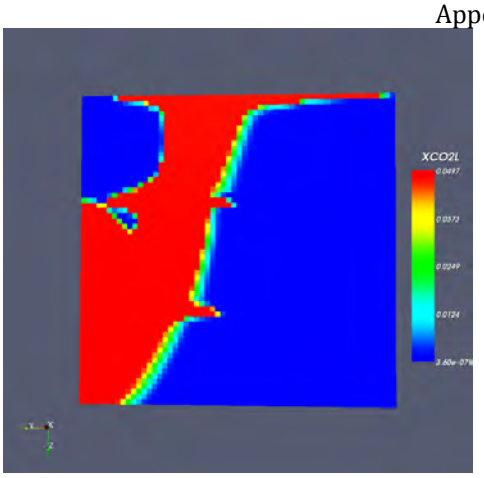


dissolved $CO_2$: k=1md, low permeability

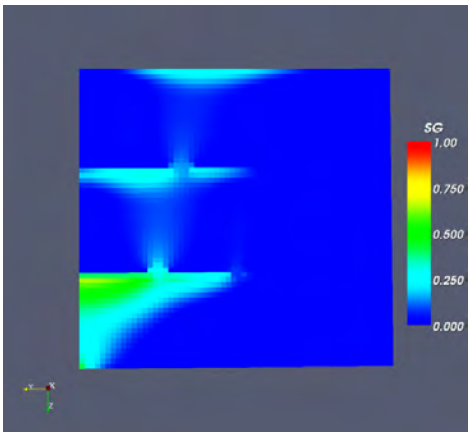


Free $CO_2$: k=1md, permeability jail

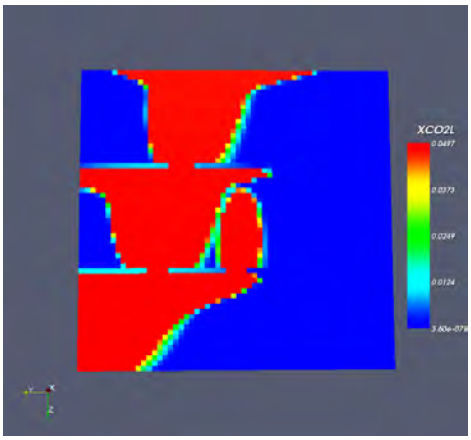


dissolved $CO_2$: k=1md, permeability jail

Figure 26: Vertical distribution of $CO_2$ (as free gas phase, and in the dissolved state) for the domain with uniform permeabilities and in the system with "permeability-jail" relative permeabilities in the seal. The seal permeability is 1 md in all the simulations.

## Conclusions

*Mineralogical Reactions.* In all of the experiments, changes in mineralogy were evident, and in general, observations of changes in rock chemistry mirrored those seen in brine. In experiments with $CO_2$, one of the most important conclusions was the observation of calcite re-precipitation. This indicated that permanent mineralogical sequestration is possible. Chlorite dissolution and analcime and ankerite precipitation were common features in all $CO_2$ experiments. In experiments containing $SO_2$, the mineralogical reactions were significantly different compared to experiments where only $CO_2$ was used. The dissolution patterns continued and no calcite re-precipitation was observed. The most significant findings in these experiments were the precipitation of anhydrite, gypsum and bassanite. These results are highlighted in Mandalaparty et al. (2009).

*Vertical Migration and Seal Properties.* The distribution of $CO_2$ in the free gas and dissolved forms in a layered reservoir depends on the absolute permeability of the seals, and also on the relative permeabilities employed.

## Acknowledgement

This material is based upon work supported by the Department of Energy under Award Number DE-FC26-06NT42808.

## List of Tables

## List of Figures

## Abbreviations

$CO_2$ : carbon dioxide

$H_2SO_4$ : sulfuric Acid

$SO_2$ : sulphur dioxide

μm : micrometers

C: Celsius

DH: debye huckel equation

EDS: energy dispersive X-ray spectroscopy

EOR: enhanced oil recovery

g: grams

GHG: greenhouse gas

IC: ion chromatography

ICPMS: inductively coupled plasma mass spectroscopy

IPCC: inter governmental panel on climate change

m: meters

K: Kelvin

mg/l: milligrams per liter

md: milli darcy

ppm: parts per million

psi: pounds per square inch

SEM: scanning electron microscope

XRD: X-ray diffraction

# References

Audigane, P., I. Gaus, I. Czernichowski-Lauriol, K. Pruess and T. Xu, Two-dimensional reactive transport modeling of $CO_2$ injection in a saline aquifer at the Sleipner Site, American Journal of Science, v. 307, p. 974-1008, 2007.

Bachu, S. Sequestration of Carbon dioxide in geological media in response to climate change: road map for site selection using the transform of the geological space into the $CO_2$ phase space. *Energy Convers. Manage* **2002**. 43 (1), 87-102.

Bachu, S.; Gunter, W.D; Perkins, E.H. Aquifer disposal of $CO_2$ : hydrodynamic and mineral trapping. *Energy Converse. Manage* **1994**. 35 (4), 269-279.

Bateman, K.; Turner, G. Large scale column experiment: Study of carbon dioxide, pore water, rock reactions and model test case. *Oil and Gas Tech* **2005.** 60, 161–175.

Bergman, P.D.; Winter, E.M. Disposal of $CO_2$ in aquifers in the U.S. *Energy Conver. Manage* **1995**. 36, 523-526.

Bergman, P.D.; Winter, E.M.; Chen, Z.Y. Disposal of power plant $CO_2$ in depleted oil and gas reservoirs in Texas. Energy Converse. Manage (1997). 38, S211-S216.

Climate Change. An assessment of the Intergovernmental panel on climate change, 2007. http://www.ipcc.ch/pdf/assessment-report/ar4/syr/ar4_syr.pdf

Drever, J.I.; The Geochemistry of Natural Waters: Surface and Groundwater Environments, Prentice Hall, INC, 1988.

Druckenmiller, M. L.; Maroto-Valer, M. M.; Hill, M. Investigation of carbon sequestration via induced calcite formation in natural gas well brine. *Energy and Fuels* **2005.**

Garcia E.J. Fluid Dynamics of Carbon dioxide disposal into saline aquifers. Ph.D. Dissertation, University of California, Berkeley, CA, 2003.

Gherardi, F., T. Xu, and K. Pruess, Numerical modeling of self-limiting and self-enhancing caprock alteration induced by $CO_2$ storage in a depleted gas reservoir, Chemical Geochemistry, v. 244, p. 103-129, 2007.

Gunter, W.D.; Perkins, E.H.; McCann, T.J. Aquifer disposal of $CO_2$ rich gases: reaction design for added capacity. *Energy Converse. Manage* **1993**. 34, 941-948.

Gunter, W.D.; Bachu, S.; Law, D.H.S.; Marwaha, V.; Drysdale, D.L.; McDonald, D.E. Technical and economic feasibility of $CO_2$ disposal in aquifers within the Alberta Sedimentary Basin, Canada. *Energy Convers. Manage* **1996**. 37, 1135-1142.

Gunter, W.D.; Wiwchar, B.; Perkins, E.H. Aquifer disposal of $CO_2$ rich greenhouse gases: extension of time scale of experiment for $CO_2$ sequestering reactions by geochemical modeling. *Mineral. Petrol* **1997**. 59, 121-140.

Gunter, W.D.; Perkins, E.H.; Hutcheon, I. Aquifer disposal of acid gases: modeling of water rock reactions for trapping of acid wastes. *Appl. GeoChem* **2000**. 15 (8), 1085-1095.

Harvie, C. E., N. Moller, and J. H. Weare, The prediction of mineral solubilities in antural waters: The Na-K-Mg-Ca-H-Cl-$SO_4$-OH-$HCO_3$-$CO_3$-$H_2O$-system to high ionic strengths at 25 $^oC$, *Geochim. Cosmochim. Acta*, *48*(4), 723-751, 1984.

Holloway, S. An overview of the underground disposal of carbon dioxide. *Energy Convers. Manag*., 1997. 38 (SS), S193-198.

Jacquemet, N.; Pironon, N.; Marc, J. S. Mineralogical changes of a well cement in various $H_2S$-$CO_2$ (brine) fluids at high pressure and temperature. *Environ. Sci. Technol* **2008.** 42, 282–288.

Kaszuba, J. P. ; Janecky, D. R. ; Snow, M. G. Experimental evaluation of mixed fluid reactions between supercritical carbon dioxide and brine: Relevance to the integrity of a geologic carbon repository. *Chem Geol* **2005.** 217, 277-293.

Kaszuba, J. P. ; Janecky, D. R. ; Snow, M. G. Carbon dioxide reaction processes in a model brine aquifer at 2000 C and 200 bar: Implications for geologic sequestration of carbon. *Appl Geo. Chem* **2003**. 18, 1065–1080.

Law, D.H.S.; Bachu, S. Hydrogeological and numerical analysis of $CO_2$ disposal in deep saline aquifers in the Alberta Sedimentary basin. *Energy Converse. Manage* **1996**. 37(6-8), 1167-1174.

Lindeberg, E. Escape of Carbon Dioxide from aquifers. *Energy converse. Manage* **1997.** 38, 238–240.

Lohuis, J.A.O. Carbon Dioxide disposal and sustainable development in The Netherlands. *Energy. Convers. Manage* **1993**. 34 (9-11), 815-821.

Mandalaparty P.; Deo, M.; Moore, J. $CO_2$ sequestration: temperature and gas compositional effects on the kinetics of mineralogical reactions, *Society of Petroleum Engineers*, Paper 124909.

Moore, J.; Adams, M.; Allis, R.; Lutz, S.; Rauzi, S. Mineralogical and geochemical consequences of long term presence of $CO_2$ in natural reserviors: An example from the Springerville-St.Johns field, Arizona and New Mexico, U.S.A. *Chem Geol* **2005**. 217, 365–385.

Perkins, E.H.; Gunter, W.D. A users manual for PATHARC.94: a reaction path-mass transfer program, Alberta research council report ENVTR (1995) 95-11, 179, Canada.

Rosenbauer, R. J.; Koksalan, T; Palandri, J.L Experimental investigation of $CO_2$ -brine-rock interactions at elevated temperature and pressure : Implications for $CO_2$ sequestration in deep-saline aquifers," *Fuel Process. Tech* **2005**. 86, 1581–1597.

Seyfried Jr.; Janecky, W.E.; Berndt, D.R. Rocking autoclaves for hydrothermal experiments, II. The flexible reaction cell system. In: Ulmer, G.C.; Barnes, H.L. (1987).

Soong, Y.; Goodman, A. L.; Hedges, S. W.; Jones, J. R.; Harrison, D. K. $CO_2$ Sequestration and importance of pH. *Am. Chem. Soc* **2002**. 47, 43–48.

Span, R.; Wagner, W. A new equation of state for carbon dioxide covering the fluid region from the triple point temperature to 1100K at pressures up to 800 MPa. *J. Phys. Chem. Ref. Data* **1996.** 25 (6), 1509-1596.

U.S. Department of Energy, 2007, Carbon Sequestration Atlas of the United States, National Energy Technology Laboratories.

U.S. Department of Energy, 2008, Carbon Sequestration Atlas of the United States, Version 2, National Energy Technology Laboratories.

U.S. Department of Energy, 2009, Storage of Captured Carbon Dioxide on Federal Lands, National Energy Technology Laboratories, DOE/NETL-2009/1358.

Xu, T.; John, A.; Pruess, K. Mineral Sequestration of carbon dioxide in a sandstone-shale system. *Chem Geol* **2005** 217 , 295-318.

Xu, T, Apps, J.A., Pruess, K., Mineral sequestration of carbon dioxide in a sandstone-shale system. Chem. Geol. 217, 295-318, 2005.

Xu, T, J. A. Apps, and K. Pruess, Numerical simulation of $CO_2$ disposal by mineral trapping in deep aquifers, Applied Geochemistry, 19, 917-936, 2004.

Xu, T, J. A. Apps, and K. Pruess, Reactive geochemical transport simulation to study mineral trapping for CO2 disposal in deep arenaceous formations, Journal of Geophysical Research, v. 108 (B2), 2071, doi:10.1029/2002JB001979, 2003.

Xu, T., and K. Pruess, Modeling multiphase non-isothermal fluid flow and reactive geochemical transport in variably saturated fractured rocks: 1. Methodology, American Journal of Science, v. 301, p. 16-33, 2001.

Xu, T., Apps, J.A., Pruess, K., Yamamoto, H., Numerical modeling of injection and mineral trapping of CO2 with H2S and SO2 in a sandstone formation. Chem. Geol., 242, 319-346, 2007.

Xu, T., E.L. Sonnenthal, N. Spycher, and K. Pruess, TOURGHREACT: A simulation program for non-isothermal multiphase reactive geochemical transport in variably saturated geologic media. Computer & Geosciences 32, 145-165, 2006.

Xu, T., Sonnenthal, E., Spycher, N., Pruess, K., 2006, TOUGHREACT—A simulation program for non-isothermal multiphase reactive geochemical transport in variably saturated geologic media: Applications to geothermal injectivity and $CO_2$ geological sequestration. Computers & Geoscience 32, 145-165.

Zhang, W., Li, Y., Xu, T., Cheng, H., Zheng, Y., Xiong, P., Long-term variations of CO2 trapped in different mechanisms in deep saline formations: A case study of the Songliao Basin, China, Greenhouse Gas Control Technologies, v3(2), p. 161-180, 2009.

Zhang, G., N. Spycher, E. Sonnenthal, C. Steefel, and T. **Xu**, Implementation of a Pitzer Activity Model into TOUGHREACT for modeling concentrated solutions, Nuclear Technology, v. 164, p. 180-195, 2008.